

UNCLASSIFIED

AD NUMBER

AD855019

LIMITATION CHANGES

TO:

Approved for public release; distribution is unlimited.

FROM:

Distribution authorized to U.S. Gov't. agencies and their contractors; Critical Technology; MAY 1969. Other requests shall be referred to U.S. Army Aviation Materiel Laboratories Fort Eustis, VA. This document contains export-controlled technical data.

AUTHORITY

USAAMRDL ltr, 30 Mar 1976

THIS PAGE IS UNCLASSIFIED

THIS REPORT HAS BEEN DELIMITED
AND CLEARED FOR PUBLIC RELEASE
UNDER DOD DIRECTIVE 5200.20 AND
NO RESTRICTIONS ARE IMPOSED UPON
ITS USE AND DISCLOSURE,

DISTRIBUTION STATEMENT A

APPROVED FOR PUBLIC RELEASE;
DISTRIBUTION UNLIMITED.

AD

USAAVLABS TECHNICAL REPORT 68-38A
RADIAL OUTFLOW COMPRESSOR COMPONENT DEVELOPMENT
VOLUME I
PHASE I - AERODYNAMIC AND MECHANICAL DESIGN
ANALYSIS AND DIFFUSER TESTS

By

John R. Erwin

Nickolas G. Vitale

May 1969

U. S. ARMY AVIATION MATERIEL LABORATORIES
FORT EUSTIS, VIRGINIA

CONTRACT DA 44-177-AMC-180(T)
GENERAL ELECTRIC COMPANY
CINCINNATI, OHIO

This document is subject to special export controls and each transmittal to foreign governments or foreign nationals may be made only with prior approval of US Army Aviation Materiel Laboratories, Fort Eustis, Virginia 23604.



DDC
RECEIVED
JUL 17 1969
REGISTRATION
A

AD855019

Disclaimers

The findings in this report are not to be construed as an official Department of the Army position unless so designated by other authorized documents.

When Government drawings, specifications, or other data are used for any purpose other than in connection with a definitely related Government procurement operation, the United States Government thereby incurs no responsibility nor any obligation whatsoever; and the fact that the Government may have formulated, furnished, or in any way supplied the said drawings, specifications, or other data is not to be regarded by implication or otherwise as in any manner licensing the holder or any other person or corporation, or conveying any rights or permission, to manufacture, use, or sell any patented invention that may in any way be related thereto.

Disposition Instructions

Destroy this report when no longer needed Do not return it to the originator.

ACCESSION FOR

WFOI

DDC

UNANNOUNCED

JUSTIFICATION

WHITE SECTION ☐

DIFF SECTION ☒

BY

DISTRIBUTION/AVAILABILITY CODES

DIST. 'X' MAIL 'N' AIR 'S' SPECIAL

2



DEPARTMENT OF THE ARMY
U. S. ARMY AVIATION MATERIEL LABORATORIES
FORT EUSTIS, VIRGINIA 23604

This report has been reviewed by the U. S. Army Aviation Materiel Laboratories and is considered to be technically sound.

The research completed during this phase of the program was based on the development and refinement of the compressor integral parts as separate elements. The data and information contained herein will be used to design the experimental compressor to be tested and developed as a full component in Phase II.

A final experimental compressor configuration will be designed and developed in Phase III based on the experimental results of Phase II.

Task 1M121401D14413
Contract DA 44-177-AMC-180(T)
USAAVLABS Technical Report 68-38A
May 1969

RADIAL OUTFLOW COMPRESSOR COMPONENT DEVELOPMENT

Volume I

Phase I - Aerodynamic and Mechanical Design Analysis and Diffuser Tests

By

**John R. Erwin
Nickolas G. Vitale**

Prepared by

**General Electric Company
Cincinnati, Ohio**

for

**U. S. ARMY AVIATION MATERIEL LABORATORIES
FORT EUSTIS, VIRGINIA**

This document is subject to special export controls and each transmittal to foreign governments or foreign nationals may be made only with prior approval of US Army Aviation Materiel Laboratories, Fort Eustis, Virginia 23604.

SUMMARY

The report contains the results and analysis of investigations conducted during Phase I of the small gas turbine engine compressor technology program. Phase I contract work consisted of compressor component analyses and investigations conducted, using the existing low-speed compressor model and the transonic cascade tunnel to provide aerodynamic information for the design of the high-speed radial outflow supersonic compressor to be investigated in Phase II. A stress analysis and bench tests of several possible rotor designs and an investigation of methods of fabricating and joining blades, rotating shroud, and disc were conducted.

Compressor component aerodynamic performance goals along with levels demonstrated from the Phase I investigation are summarized in Table I (see page 10). Numerical calculations of the design point demonstrated for each component are included in Appendix I. Also included in Appendix I is a complete step-by-step calculation of the overall performance of the high-speed radial outflow compressor based on the Phase I demonstrated component performance levels. The following comparison shows these results relative to target values at the sea level standard design point:

<u>Parameter</u>	<u>Target Value</u>	<u>Calculated Value</u>
Efficiency, percent	81	81.6
Pressure ratio	11	11.3
Airflow, lb/sec	4.5	4.7

The accomplishment of Phase I of the small gas turbine engine compressor technology program has yielded valuable and encouraging results. This information was used to advantage in the design of the high-speed radial outflow supersonic compressor. Results of rotating diffuser tests using the low-speed compressor indicated that greater diffusion could be obtained in the high-speed rotor. Stress analyses verified that a larger rotor outside diameter of 13 inches could be used. This diameter has been selected rather than the original 12-inch diameter because the Mach number of the flow entering the stator vanes is reduced and the compressor performance will be improved. The major conclusion derived from Phase I of this program is that all investigations have provided results which approach or exceed the expected goals. The radial outflow compressor will be sensitive to inlet distortion, and further inlet system investigation is recommended to provide for a uniform flow in entering the rotor when large inlet guide turning angles are used. No problem areas were discovered that would prevent the achievement of the design performance levels from the radial outflow compressor to be tested in Phase II of this program.

FOREWORD

Under United States Army Contract DA-177-AMC-180(T), the Flight Propulsion Division of the General Electric Company in Cincinnati, Ohio, is conducting a program to advance and demonstrate high-pressure-ratio compressor technology for small gas turbine engines. The investigation concerning the analysis, design, construction, and testing of a Radial Outflow Compressor (ROC) is presented in 3 volumes, each volume generally describing 1 of the 3 phases of the program. Volume I presents the ROC design philosophy, mechanical analysis and bench test results, inlet system and rotating wall vaneless diffuser studies using a low-speed compressor, the design and supersonic cascade tests of the rotor blade sections, and high-speed transonic and supersonic cascade tests of single row and tandem row stator vanes. The design of the high-speed compressor test vehicle used in the Phase II and III investigations is also presented in Volume I.

Volume II describes the Phase II investigation including the aerodynamic and mechanical design of the high-speed rotor and the stator system. The experiments conducted consisted of testing 6 major buildups (A through F) of the compressor. A number of aerodynamic, mechanical, and operational problems were encountered during testing of the new compressor using a new test vehicle. During Buildup F, encouraging rotor performance was obtained at 70 percent speed, with a maximum rotor efficiency of 92.1 percent recorded at a rotor exit total pressure ratio of 3.97, and a rotor exit static pressure ratio of 1.97. This performance was accomplished by elimination of the inlet guide vanes, the use of a circular inlet vane, the Phase III rotor blades, and the subsonic stators. Analysis of the rotating wall vaneless diffuser was described and further low-speed compressor test results were presented. The rotating diffuser configuration selected for the Phase III rotor was also presented in Volume II.

Volume III describes the Phase III investigation of 3 major buildups (A through C) of the high-speed compressor. Buildup A was intended to provide direct comparison of the Phase III rotor performance with the best performance obtained with the Phase II rotor during Buildup F. The circular inlet vane was not used in Buildup A (Phase III) because the rotor inlet curvature was more gradual and it was hoped that the assembly, balancing and installation difficulties inherent with the circular inlet vane could be avoided. Operating problems with the bellmouth liner used to form the air path into the new rotor were encountered. Fracture of the liner occurred at low speed. Continued operation of the compressor was obtained by machining the liner back to eliminate interference with the rotor. Although an unsatisfactory rotor entrance condition existed, some aerodynamic and mechanical data were obtained. A satisfactory inlet was constructed by modifying the bellmouth with a liner composed of pyrolytic graphite and glass fibers bonded with phenolic resin.

For the final test phases, the circular inlet vane was used, the rotor strain gages and leads were removed, and the supersonic stator vanes were installed upstream of the subsonic stators. An improved seal was employed upstream of the rotor for Buildup B. Buildup C was similar to Buildup B except that reduced seal clearance was established, reduced rotor to casing offset (cold, nonrotating) was used, and greater capacity to remove flow from the forward cavity was provided. A systematic series of stator vane settings was tested during Buildup C at speeds up to 100 percent.

The manager of the Small Gas Turbine Engine Compressor Technology Program is J. R. Erwin, and the principal contributing engineers are N. G. Vitale, R. G. Giffin, E. L. Timperman, C. H. Gay, and R. E. Troeger. Volume I was compiled and edited by Mr. D. V. Robinett. The assistance and consultations provided by Dr. D. C. Prince, Jr. and Dr. L. H. Smith, both of the General Electric Company, are gratefully acknowledged, as are the services of Dr. G. F. Wislicenus of Pennsylvania State University, who served as consultant on the program. Mr. LeRoy H. Hubert is Project Engineer for this program on behalf of the U.S. Army.

CONTENTS

	<u>Page</u>
SUMMARY.	iii
FOREWORD	v
LIST OF ILLUSTRATIONS.	viii
LIST OF TABLES	xxiv
INTRODUCTION	1
INLET GUIDE VANES.	11
ROTOR BLADES	92
ROTATING VANELESS DIFFUSER	127
SUPERSONIC AND SUBSONIC STATORS.	180
SCROLL COLLECTOR, DIFFUSER, AND ELBOW	241
AERODYNAMIC ANALYSIS	275
MECHANICAL ANALYSIS.	300
MECHANICAL BENCH TESTS	314
DESCRIPTION OF HIGH- SPEED COMPRESSOR	327
CONCLUSIONS.	333
RECOMMENDATIONS.	335
BIBLIOGRAPHY	336
APPENDIXES	
I. Compressor Performance Calculations	339
II. Derivation of Characteristic Equations.	357
III. ROC Instrumentation	371
DISTRIBUTION	378

ILLUSTRATIONS

<u>Figure</u>		<u>Page</u>
1	Cross Section of Supersonic Radial Outflow Compressor	4
2	Vector Diagrams of Radial Outflow Compressor	7
3	Axial Flow Inlet Design	14
4	Installation of Axial Flow Inlet	17
5	Axial Flow Inlet Optional Rotating Walls	18
6	Radial Inflow Inlet Design	19
7	Installation of Radial Inflow Inlet	21
8	Radial Inflow Inlet Optional Rotating Walls	22
9	Yaw Angle and Total Pressure Probe	25
10	Rotor Discharge Pressure Coefficient, Axial Flow IGV at 60°, Hub and Housing 1 Rotating	27
11	Compressor Efficiency, Axial Flow IGV at 60°, Hub and Housing 1 Rotating	28
12	Rotor Discharge Pressure Coefficient, Axial Flow IGV at 60°, Hub Rotating	29
13	Compressor Efficiency, Axial Flow IGV at 60°, Hub Rotating	30
14	Rotor Discharge Pressure Coefficient, Radial Inflow IGV at 60°, Hub and Housings 1 and 2 Rotating	31
15	Compressor Efficiency, Radial Inflow IGV at 60°, Hub and Housings 1 and 2 Rotating	32
16	Rotor Discharge Pressure Coefficient, Radial Inflow IGV at 60°, Hub and Housing 2 Rotating	33
17	Compressor Efficiency, Radial Inflow IGV at 60°, Hub and Housing 2 Rotating	34
18	Rotor Discharge Pressure Coefficient, Radial Inflow IGV at 60°, Hub Rotating	35

<u>Figure</u>		<u>Page</u>
19	Compressor Efficiency, Radial Inflow IGV at 60°, Hub Rotating	36
20	Compressor Efficiency, Radial Inflow IGV at 60°, Hub Rotating	37
21	Rotor Discharge Pressure Coefficient, Axial Flow IGV at 60°, Hub and Housings 1 and 2 Rotating.	38
22	Compressor Efficiency, Axial Flow IGV at 60°, Hub and Housings 1 and 2 Rotating.	39
23	Rotor Discharge Pressure Coefficient, Axial Flow IGV at 60°, Hub and Housing 1 Rotating	40
24	Compressor Efficiency, Axial Flow IGV at 60°, Hub and Housing 1 Rotating	41
25	Rotor Discharge Pressure Coefficient, Axial Flow IGV at 50°, Hub and Housing 1 Rotating.	42
26	Compressor Efficiency, Axial Flow IGV at 50°, Hub and Housing 1 Rotating	43
27	Rotor Discharge Pressure Coefficient, Axial Flow IGV at 35°, Hub and Housing 1 Rotating.	44
28	Compressor Efficiency, Axial Flow IGV at 50°, Hub and Housing 1 Rotating	45
29	Rotor Discharge Pressure Coefficient, Axial Flow IGV at 50°, Hub and Housing 1 Rotating.	46
30	Compressor Efficiency, Axial Flow IGV at 35°, Hub and Housing 1 Rotating	47
31	Rotor Discharge Pressure Coefficient, Axial Flow IGV at 18.5°, Hub and Housing 1 Rotating.	48
32	Compressor Efficiency, Axial Flow IGV at 18.5°, Hub and Housing 1 Rotating.	49
33	Rotor Discharge Pressure Coefficient, Axial Flow IGV at 0°, Hub and Housing 1 Rotating.	50
34	Compressor Efficiency, Axial Flow IGV at 0°, Hub and Housing 1 Rotating.	51

<u>Figure</u>		<u>Page</u>
35	Rotor Discharge Pressure Coefficient, Axial Flow IGV at -18.5° , Hub and Housing 1 Rotating	52
36	Compressor Efficiency, Axial Flow IGV at -18.5° , Hub and Housing 1 Rotating	53
37	Rotor Discharge Pressure Coefficient, Radial Inflow IGV at 60° , Hub and Housings 1 and 2 Rotating . .	54
38	Compressor Efficiency, Radial Inflow IGV at 60° , Hub and Housings 1 and 2 Rotating.	55
39	Rotor Discharge Pressure Coefficient, Radial Inflow IGV at 50° , Hub and Housings 1 and 2 Rotating . .	56
40	Compressor Efficiency, Radial Inflow IGV at 50° , Hub and Housings 1 and 2 Rotating.	57
41	Rotor Discharge Pressure Coefficient, Radial Inflow IGV at 35° , Hub and Housings 1 and 2 Rotating.	58
42	Compressor Efficiency, Radial Inflow IGV at 35° , Hub and Housings 1 and 2 Rotating.	59
43	Rotor Discharge Pressure Coefficient, Radial Inflow IGV at 18.5° , Hub and Housings 1 and 2 Rotating .	60
44	Compressor Efficiency, Radial Inflow IGV at 18.5° , Hub and Housings 1 and 2 Rotating.	61
45	Rotor Discharge Pressure Coefficient, Radial Inflow IGV at 0° , Hub and Housings 1 and 2 Rotating. . .	62
46	Compressor Efficiency, Radial Inflow IGV at 0° , Hub and Housings 1 and 2 Rotating	63
47	Rotor Discharge Pressure Coefficient, Radial Inflow IGV at -18.5° , Hub and Housings 1 and 2 Rotating.	64
48	Compressor Efficiency, Radial Inflow IGV at -18.5° , Hub and Housings 1 and 2 Rotating	65
49	Compressor Pressure Coefficient Characteristics, Axial Inlet	66
50	Compressor Efficiency Characteristics, Axial Inlet.	67

<u>Figure</u>		<u>Page</u>
51	Compressor Pressure Coefficient Characteristics, Radial Inflow Inlet	68
52	Compressor Efficiency Characteristics, Radial Inflow Inlet	69
53	Rotor Inlet Total Pressure Loss Profile, Axial and Radial IGV Setting of 60°	70
54	Rotor Inlet Total Pressure Loss Profile, Axial IGV Setting of 50°	71
55	Rotor Inlet Total Pressure Loss Profile, Axial and Radial IGV Setting of 60°	72
56	Rotor Inlet Total Pressure Loss Profile, Axial and Radial IGV Setting of 50°	73
57	Rotor Inlet Total Pressure Loss Profile, Axial and Radial IGV Setting of 35°	74
58	Rotor Inlet Total Pressure Loss Profile, Axial and Radial IGV Setting of 18.5°	75
59	Rotor Inlet Total Pressure Loss Profile, Axial and Radial IGV Setting of 0°	76
60	Rotor Inlet Total Pressure Loss Profile, Axial and Radial IGV Setting of -18.5°	77
61	Rotor Inlet Flow Angle Profiles with Axial Flow Inlet Guide Vanes, Rotor Speed at 1600 RPM.	78
62	Rotor Inlet Flow Angle Profiles with Radial Inflow Inlet Guide Vanes, Rotor Speed at 1600 RPM.	79
63	Rotor Discharge Characteristics from Mass Averaged Data, Axial Flow IGV at 0° , Hub and Housing 1 Rotating	81
64	Rotor Discharge Characteristics from Mass Averaged Data, Axial Flow IGV at 35° , Hub and Housing 1 Rotating	82
65	Rotor Discharge Characteristics from Mass Averaged Data, Axial Flow IGV at 50° , Hub and Housing 1 Rotating	83

<u>Figure</u>		<u>Page</u>
66	Rotor Blade Velocity Triangles.	86
67	Plot of Total Pressure Ratio and Loss Coefficient as a Function of Entering Mach Number for Blade Sec- tions in Cascade.	93
68	Rotor Blade Schematic Flow Diagram with Cusped Leading Edges	96
69	Rotor Blade Schematic Flow Diagram with Finite Leading Edges	97
70	Two-Dimensional Supersonic Rotor Blade.	100
71	Rotor Blade Cascade Assembly, Side View	102
72	Rotor Blade Cascade Assembly, Oblique View.	103
73	Schlieren Photograph, Rotor Blade Cascade Tests, Case Number 20216	109
74	Schlieren Photograph, Rotor Blade Cascade Tests, Case Number 20242	110
75	Schlieren Photograph, Rotor Blade Cascade Tests, Case Number 20316	111
76	Schlieren Photograph, Rotor Blade Cascade Tests, Case Number 20317	112
77	Schlieren Photograph, Rotor Blade Cascade Tests, Case Number 20320	113
78	Schlieren Photograph, Rotor Blade Cascade Tests, Case Number 21969	114
79	Schlieren Photograph, Rotor Blade Cascade Tests, Case Number 21981	115
80	Schlieren Photograph, Rotor Blade Cascade Tests, Case Number 21983	116
81	Schlieren Photograph, Rotor Blade Cascade Tests, Case Number 21984	117
82	Schlieren Photograph, Rotor Blade Cascade Tests, Case Number 21985	118

<u>Figure</u>		<u>Page</u>
83	Schlieren Photograph, Rotor Blade Cascade Tests, Case Number 21986.	119
84	Schlieren Photograph, Rotor Blade Cascade Tests, Case Number 21986.	120
85	Test Results of Existing Rotor Blades at Nominal Blade Setting (Leading Edge Suction Surface Angle = 55.6°) (Inlet Air Angle = 59.6°) (Solidity = 2.0). . .	122
86	Test Results of the Modified Existing Rotor Blades at Nominal Blade Setting (Leading Edge Suction Surface Angle = 55.6°) (Solidity = 2.0). . . .	123
87	Test Results of New Rotor Blades (Solidity - 2.5) at Design Inlet Angle of 60°	124
88	Effect of Inlet Angle Variation on New Design Rotor Blade (Solidity = 2.5)	125
89	Supersonic Vortex Characteristics Net Showing Streamlines (Dash-Dot Curves), a Stator Blade with a Weak Shock Propagating from Its Leading Edge (Dashed Line)	129
90	Characteristics Net Showing Several Stators, Streamlines and Weak Shock Waves	130
91	Calculated Diffuser Relative Velocity Ratio as a Function of Rotor Exit and Diffuser Exit Flow Angles. Test Points Investigated Are Shown as Circles.	132
92	Low-Speed Radial Outflow Compressor Installation in Test Facility.	133
93	Low-Speed Air Test Radial Outflow Compressor	136
94	Low-Speed Radial Outflow Compressor.	137
95	Vaneless Diffuser Test Nomenclature, Low- Speed ROC.	139
96	Rotor Discharge Pressure Coefficient from Preliminary Test Results of the Low-Speed Radial Outflow Compressor.	140

<u>Figure</u>		<u>Page</u>
97	Compressor and Rotor Efficiencies from Preliminary Test Results of the Low-Speed Radial Outflow Compressor. . .	141
98	Rotor Discharge Pressure Coefficient with Vaneless Diffuser Radius Ratio of 1.45 and Rotor Blade Trailing Edge Angle of 60°.	148
99	Compressor Efficiency with Vaneless Diffuser Radius Ratio of 1.45 and Rotor Blade Trailing Edge Angle of 60°.	149
100	Rotor Discharge Pressure Coefficient with Vaneless Diffuser Radius Ratio of 1.45 and Rotor Blade Trailing Edge Angle of 65°.	150
101	Compressor Efficiency with Vaneless Diffuser Radius Ratio of 1.45 and Rotor Blade Trailing Edge Angle of 65°.	151
102	Rotor Discharge Pressure Coefficient with Vaneless Diffuser Radius Ratio of 1.45 and Rotor Blade Trailing Edge Angle of 55°.	152
103	Compressor Efficiency with Vaneless Diffuser Radius Ratio of 1.45 and Rotor Blade Trailing Edge Angle of 55°.	153
104	Rotor Discharge Pressure Coefficient with Vaneless Diffuser Radius Ratio of 1.69 and Rotor Blade Trailing Edge Angle of 55°.	154
105	Compressor Efficiency with Vaneless Diffuser Radius Ratio of 1.69 and Rotor Blade Trailing Edge Angle of 55°.	155
106	Rotor Discharge Pressure Coefficient with Vaneless Diffuser Radius Ratio of 1.69 and Rotor Blade Trailing Edge Angle of 60°.	156
107	Compressor Efficiency with Vaneless Diffuser Radius Ratio of 1.69 and Rotor Blade Trailing Edge Angle of 60°.	157
108	Rotor Discharge Pressure Coefficient with Vaneless Diffuser Radius Ratio of 1.69 and Rotor Blade Trailing Edge Angle of 65°.	158

<u>Figure</u>		<u>Page</u>
109	Compressor Efficiency with Vaneless Diffuser Radius Ratio of 1.69 and Rotor Blade Trailing Edge Angle of 65°	159
110	Rotor Discharge Pressure Coefficient with Vaneless Diffuser Radius Ratio of 1.45 and Rotor Blade Trailing Edge Angle of 55°	160
111	Compressor Efficiency with Vaneless Diffuser Radius Ratio of 1.45 and Rotor Blade Trailing Edge Angle of 55°	161
112	Rotor Discharge Pressure Coefficient with Vaneless Diffuser Radius Ratio of 1.45, Rotor Blade Trailing Edge Angle of 60°, and Scroll Collector Installed. . .	162
113	Compressor Efficiency with Vaneless Diffuser Radius Ratio of 1.45, Rotor Blade Trailing Edge Angle of 60°, and Scroll Collector Installed.	163
114	Rotor Discharge Pressure Coefficient with Vaneless Diffuser Radius Ratio of 1.45, Rotor Blade Trailing Edge Angle of 60°, and Scroll Collector Installed . . .	164
115	Compressor Efficiency with Vaneless Diffuser Radius Ratio of 1.45, Rotor Blade Trailing Edge Angle of 60°, and Scroll Collector Installed.	165
116	Dynamic Rotor Wake Responses. Rotor Speed = 1400 RPM. Horizontal Scope Sweep = 500 Micro- seconds/CM. Blade Trailing Edge Angle $\beta_2^* = 55^\circ$. Exit Vanes Removed	166
117	Dynamic Rotor Wake Responses. Rotor Speed = 1400 RPM. Horizontal Scope Sweep = 500 Micro- seconds/CM. Blade Trailing Edge Angle $\beta_2^* = 55^\circ$. Exit Vanes Removed	167
118	Dynamic Rotor Wake Responses. Rotor Speed = 1400 RPM. Horizontal Scope Sweep = 500 Micro- seconds/CM. Blade Trailing Edge Angle $\beta_2^* = 55^\circ$. Exit Vanes Removed	168
119	Low Speed ROC Installation with Scroll Collector, Exit Arm Ducts, Elbow Turning Vanes and Throttle Valves	169

<u>Figure</u>		<u>Page</u>
120	Preliminary Carpet Plot Rotor Efficiency Characteristics as a Function of Effective Static Pressure Rise Coefficient with Rotating Vaneless Diffuser Radius Ratio of 1.50.	171
121	Rotor Efficiency Characteristics as a Function of Effective Pressure Rise Coefficient with Rotating Vaneless Diffuser Radius Ratio of 1.45. . . .	172
122	Rotor Efficiency Characteristics as a Function of Effective Static Pressure Rise Coefficient with Rotating Vaneless Diffuser Radius Ratio of 1.69.	173
123	Effect of Vaneless Diffuser Geometry on Effective Static Pressure Rise Coefficient	175
124	Effect of Vaneless Diffuser Geometry on Rotor Discharge Flow Angle and Mach Number	176
125	Resultant Effect of Vaneless Diffuser Geometry on Compressor Pressure Ratio and Efficiency.	177
126	Rotor Discharge Mach Number, Flow Angle, Compressor Pressure Ratio and Efficiency for Two Vaneless Diffuser Configurations with Variations in Rotor Blade Area Ratio and Discharge Flow Angle	178
127	Stator Test Cascade Assembly	183
128	Stator Test Cascade Assembly, View of Inlet.	185
129	Stator Test Cascade Assembly, Side View Showing Supersonic Stators Installed	186
130	Stator Test Cascade Assembly	187
131	Supersonic Stator Test Blade Design, Long.	188
132	Supersonic Stator Test Blade Design, Medium and Short.	189
133	Subsonic Stator Test Blade Design.	190

<u>Figure</u>		<u>Page</u>
134a	Straight Stator Blades with Upper Surface Wedge	191
134b	Stator Blade with Upper and Lower Surface Wedges	191
135	Installation of Stator Test Vehicle in Transonic Cascade Facility	193
136	Schlieren Photograph of Supersonic Stator Cascade Tests, Case Number 22277	210
137	Schlieren Photograph of Supersonic Stator Cascade Tests, Case Number 22288	211
138	Schlieren Photograph of Supersonic Stator Cascade Tests, Case Number 22291	212
139	Schlieren Photograph of Supersonic Stator Cascade Tests, Case Number 22293	213
140	Schlieren Photograph of Supersonic Stator Cascade Tests, Case Number 22294	214
141	Schlieren Photograph of Supersonic Stator Cascade Tests, Case Number 22908	215
142	Schlieren Photograph of Supersonic Stator Cascade Tests, Case Number 22905	216
143	Schlieren Photograph of Supersonic Stator Cascade Tests, Case Number 22898	217
144	Schlieren Photograph of Supersonic Stator Cascade Tests, Case Number 22900	218
145	Schlieren Photograph of Supersonic Stator Cascade Tests, Case Number 22901	219
146	Schlieren Photograph of Supersonic Stator Cascade Tests, Case Number 22902	220
147	Schlieren Photograph of Supersonic Stator Cascade Tests, Case Number 22903	221
148	Results of Preliminary Testing with Original Design Medium Length Supersonic Stator Blades at Nominal Throttle Setting	223

<u>Figure</u>		<u>Page</u>
149	Schlieren Photograph of Preliminary Supersonic Stator Cascade Tests, Original Medium Length Design, Inlet Mach Number = 1.56 and Inlet Angle = 80°	224
150	Schlieren Photograph of Preliminary Supersonic Stator Cascade Tests, Original Medium Length Design, Inlet Mach Number = 1.56 and Inlet Angle = 82°	225
151	Schlieren Photograph of Preliminary Supersonic Stator Cascade Tests, Original Medium Length Design, Inlet Mach Number = 1.495 and Inlet Angle = 80°	226
152	Schlieren Photograph of Preliminary Supersonic Stator Cascade Tests, Original Medium Length Design, Inlet Mach Number = 1.59 and Inlet Angle = 78°	227
153	Performance of Modified Design Supersonic Stator Vanes of Three Different Lengths at Design Inlet Angle of 80°	228
154	Effect of Contraction Ratio on Performance of Medium Length Supersonic Stators (Modified Design) at Design Inlet Angle of 80°	229
155	Effect of Area Ratio on Performance of Medium Length Supersonic Stators (Modified Design) at Design Inlet Angle of 80°	231
156	Modified Medium Length Supersonic Stator Vane	232
157	Performance of Subsonic Stator Vanes of Three Different Lengths at Design Inlet Angle of 75°	234
158	Effect of Inlet Angle Variation on Performance of Subsonic Stators at Design Inlet Mach Number of 0.7	235
159	Effect of Area Ratio on Performance of Medium Length Subsonic Stators at Design Inlet Angle of 75°	236
160	Effect of Spacing Between Supersonic and Subsonic Stators in Tandem Cascade Arrangement at Design Inlet Angle of 80°	238

<u>Figure</u>		<u>Page</u>
161	Effects of Throttling on Performance of Tandem Supersonic and Subsonic Stators at Inlet Mach Number of 1.3 and Inlet Angle of 80°.	239
162	Installation of Scroll Collector, Transition Diffuser and Elbow on Low-Speed Radial Outflow Compressor	242
163	Scroll Collector Assembly, Low-Speed ROC	243
164	View of Instrumentation Spool Piece at Discharge of Scroll Exit Arm, Low-Speed Radial Outflow Compressor.	245
165	Flow Discharge Ducting, Low-Speed ROC	247
166	Elbow Turning Vane Profile	249
167	Low-Speed Radial Outflow Compressor with Axial Flow Inlet Installed	250
168	Scroll Collector and Transition Diffuser Static Pressure Tap Locations	258
169	Scroll Exit Arm Total Pressure Rake	259
170	Total Pressure Rake, Elbow Turning Vane Discharge	260
171	Scroll Collector Exit Arm Loss Coefficient Profiles, Flow Splitter 1	261
172	Scroll Collector Exit Arm Loss Coefficient Profiles, Flow Splitter 2	262
173	Scroll Collector Exit Arm Loss Coefficient Profiles, Flow Splitter 3	263
174	Scroll Collector Exit Arm Loss Coefficient Map, Flow Splitter 1	264
175	Scroll Collector Exit Arm Loss Coefficient Map, Flow Splitter 2	265
176	Scroll Collector Exit Arm Loss Coefficient Map, Flow Splitter 3	266
177	Scroll Collector Static Pressure Rise Coefficient, Flow Splitter 1	267

<u>Figure</u>		<u>Page</u>
178	Scroll Collector Static Pressure Rise Coefficient, Flow Splitter 2	268
179	Scroll Collector Static Pressure Rise Coefficient, Flow Splitter 3	269
180	Scroll Collector Static Pressure Profile, Flow Splitter 1	270
181	Scroll Collector Static Pressure Rise Coefficient Versus Circumferential Location	271
182	Elbow Turning Vane Loss Coefficient Profiles With Scroll Flow Splitter 1	272
183	Elbow Turning Vane Loss Coefficient Profiles With Scroll Flow Splitter 2	273
184	Elbow Turning Vane Loss Coefficient Profiles With Scroll Flow Splitter 3	274
185	Axial Inlet Calculated Streamlines Based on Incompressible Flow	277
186	Axial Inlet Mach Number Contours for Rotor Inlet Mach Number of 0.50	278
187	Axial Inlet Mach Number Contours for Rotor Inlet Mach Number of 0.70	279
188	Axial Inlet Mach Number Contours for Rotor Inlet Mach Number of 0.75	280
189	Axial Inlet Calculated Streamlines Based on Incompressible Flow with Splitter	281
190	Axial Inlet Mach Number Contours with Flow Splitter for Rotor Inlet Mach Number of 0.50	283
191	Two-Dimensional Rotor Blade Mach Number Distribution.	287
192	Rotor Blade Sketch	288
193	Three-Dimensional Rotor Blade Radial Orientation.	290
194	Three-Dimensional Rotor Blade Mach Number Distribution.	291

<u>Figure</u>		<u>Page</u>
195	Finite Thickness Leading Edge Effects	293
196	Mach Number Distribution for Final Rotor Blade Shape	296
197	Characteristics Network and Passage Shape for Three-Dimensional Rotor Blade (Final Design)	297
198	Rotor Blade Surface Pressure Distribution	298
199	Rotor Blade Tangential Force Distribution	299
200	Rotor Assembly, High-Speed ROC	301
201	Disc Cross Sections for Optimum Stress Design	303
202	Stable, Converging Flow Channel Design	303
203	Blade Attachment Alternatives	306
204	Preloaded Blade Attachment	308
205	Campbell Diagram, Titanium Shroud	313
206	Blade Attachment Test Pieces of 6-6-2 Titanium with Shear Lug Design	315
207	Hollow Titanium Blades Manufactured by Removing Center Material by Electric Discharge Machining	316
208	Assembly of Several Hollow Blades on Shear Lugs	317
209	Fir-Tree Stud Fastener Evaluated for Use With the Shear Lug Design	319
210	Illustration of Assembly of Fir-Tree Stud Fastener. . .	319
211	Tensile Test Failure Comparison With and Without Closely Fitted Hollow Blade	320
212	Half Sections of Hollow Blade with Diffusion Bonded Titanium End Plates Compared with Hollow Blade Not Bonded.	321
213	Fiber Glass Reinforced Shroud	325
214	Shroud with Honeycomb and Fiber Glass on Inside Edges.	326

<u>Figure</u>		<u>Page</u>
215	Radial Outflow Compressor, High Speed	329
216	Radial Outflow Compressor Subsonic Map	356
217	Radial Outflow Compressor Supersonic Map	357
218	Mesh Point Location by Characteristic Curves and by Characteristic Slopes	358
219	Mesh Point Location by Characteristic Curves and by Characteristic Average Slopes	359
220	Rotating Reference Frame	361
221	Stream Element.	362
222	Radial Outflow Compressor Instrumentation Station Numbers	373

TABLES

<u>Table</u>		<u>Page</u>
I	Phase I Demonstrated Component Performance	10
II	Inlet Guide Vane Run Summary	24
III	Rotor Blade Run Summary	104
IV	Rotor Blade Cascade Test Results	105
V	Rotating Vaneless Diffuser Test Run Summary	142
VI	Instrumentation Summary - Rotating Vaneless Diffuser Tests	143
VII	Supersonic Stators Test Run Summary	194
VIII	Subsonic Stators Test Run Summary	196
IX	Tandem Cascade Test Run Summary	197
X	Supersonic Stator Cascade Test Results	198
XI	Subsonic Stator Cascade Test Results	202
XII	Tandem Cascade Test Results	205
XIII	Scroll Collector, Diffuser and Elbow Test Run Summary	256
XIV	Instrumentation Summary - Scroll Collector, Diffuser and Elbow Tests	257
XV	Correlation of Method of Characteristics and Transformed Free Vortex Flow Solutions	285
XVI	6-6-2 Titanium Properties	322
XVII	Aluminum Shroud Resonant Frequency - cps	324
XVIII	ROC Station Definition	374
XIX	Radial Outflow Compressor Research Instrumentation (Phase II)	375

SYMBOLS

A	area, feet ²
\bar{A}	acceleration, feet/second ²
a	speed of sound, feet/second
B	blockage factor
C _p	specific heat at constant pressure, Btu/lb/°F
\bar{C}_p	static pressure rise coefficient ($P_{s2} - P_{s1}/P_{t1} - P_{s1}$)
C _{Peff}	effective static pressure rise coefficient (see Figure 120 or Appendix I)
D	diameter, inches
F	force, pounds
g	gravitational constant, feet/second ²
h	passage height (width), inches
i	incidence angle, degrees
\bar{i}	unit vector
J	Joule's mechanical equivalent of heat, foot-pounds/Btu
\bar{j}	unit vector
l	chord length, or distance, inches
M	Mach number
\dot{M}	mass flow rate, pounds/second
m	slope
N	rotating speed, rpm
n	stream tube width, inches
P	pressure, pounds/inch ²
P _s	static pressure, pounds/inch ²
P _t	total pressure, pounds/inch ²

\bar{P}_t	reference total pressure, pounds/inch ²
P	pressure ratio, P/\bar{P}_t
q	dynamic pressure, pounds/inch ² ($1/2 \rho v^2$)
R	radius, reference frame (Appendix II)
R	radius ratio (when used with subscripts)
R	gas constant, ft-lb/lb/°F
\bar{R}	position vector, reference frame
R*	reference radius, feet
r	radius, inches
\bar{r}	position vector of intrinsic frame
s_p	pitch, inches
s	distance along streamlines, feet
T	temperature, degrees Rankine
T_s	static temperature, degrees Rankine
T_t	total temperature, degrees Rankine
\bar{T}_t	reference total temperature, degrees Rankine
t	blade thickness, inches
U	tangential velocity, feet/second
u	particle velocity in \bar{i} direction, feet/second
V	absolute velocity, feet/second
v	particle velocity in \bar{j} direction, feet/second
W	relative velocity, feet/second
w	flow rate, pounds/second
X	distance along blade chord line measured from center of rotation, inches
z	passage height, inches

α	angle between radial line and absolute velocity, degrees
β	angle between radial line and relative velocity, degrees
θ^*	angle between radial line and rotor blade mean line, degrees
$\bar{\theta}$	direction of velocity vector \bar{R} with respect to rotating reference frame (Appendix II), degrees
γ	ratio of specific heats
$\epsilon(+)$	characteristic function dependent on flow properties
$\epsilon(-)$	characteristic function dependent on flow properties
ζ	lower edge wedge angle, rotor blade, degrees
η	efficiency (isentropic ΔT_t /Actual ΔT_t)
θ	flow angle with respect to rotating reference frame (Appendix II), degrees
A_s	angle between blade surface tangent and the local radius, degrees
λ	direction of vector r with respect to intrinsic coordinate system, degrees
λ^*	leading edge suction surface angle (rotor blade), degrees
μ	Mach angle, degrees
ν	upper edge wedge angle, rotor blade, degrees
$\xi(+)$	characteristic flow property
$\xi(-)$	characteristic flow property
ρ	density, pounds/feet ³
τ	blade setting angle (stator), degrees
ϕ	flow coefficient (V_R/U)
ϕ	flow direction with respect to \bar{R} , degrees
ψ	total pressure rise coefficient ($P_{t2} - P_{t1}/\frac{1}{2} \rho U_2^2$)
ω	angular velocity, radians/second
$\bar{\omega}$	total pressure loss coefficient ($P_{t1} - P_{t2}/P_{t1} - P_{s1}$)

Subscripts

o thru 9 refer to stations as defined in Table XVIII

AMB ambient

BM bellmouth

e exit

F area corrected for blockage factor

f.v. free vortex

i inlet

R relative

r component in radial direction

RA rotor aerodynamic

s static

s.b. solid body

t total

u component in tangential direction

BLANK PAGE

INTRODUCTION

Advancement of component technology is required to permit the development of small, lightweight, high-performance gas turbine engines to meet the future needs of the United States Army for aircraft propulsion units as well as ground vehicle and stationary power units. The current gas turbine engine component efficiencies have been developed to a high level, and major improvement of engine performance is likely to come from advancing the state of the art for higher turbine inlet temperatures, higher compression ratios, and lightweight high-effectiveness regenerators. The program under which this report is submitted is concerned with advanced compressor technology.

The engine cycle conditions required to yield excellent gas turbine fuel economy over a broad operating range demand that the compressor produce a high pressure ratio at high efficiency. The design pressure ratio at full speed should be about 10 to 12 with an adiabatic efficiency of at least 80 percent. In order to achieve good engine performance in the 30- to 50-percent power range, the compressor should also be capable of producing pressure ratios in the range of 4 to 6 with high efficiencies.

Within the present state of the art, the only way of meeting these stringent efficiency requirements in a 2- to 5-pound-per-second-size machine would be to use a multistage axial compressor with many variable stator blade rows, or possibly a two-spool compressor. The potentiality of meeting these requirements by the use of a single-stage radial outflow supersonic compressor appears to be very promising. Aerodynamic representations of the elements of this type of compressor have been demonstrated in cascade tests at supersonic speed or in compressor tests at low speeds. The demonstration of the appropriate aerodynamic and mechanical design at high speeds will represent a long step forward toward the production of a gas turbine engine ideally suited to the needs of the United States Army.

DISCUSSION OF COMPRESSOR TYPES

Multistage Axial Flow Compressors

The possibility exists of producing the required pressure ratio in a multistage axial compressor of from 8 to 14 stages. The smaller number of stages would require the utilization of transonic compressor technology throughout and might result in a slightly lower efficiency than a largely subsonic multistage axial compressor.

The forward stages of a many-row axial subsonic compressor would have high efficiency, but the clearance and blade fabrication problems of the miniature rear-blade rows would probably result in much less efficiency, perhaps resulting in unsatisfactory performance. In order to meet the off-design requirements, about half of the stationary blade rows would

have to be variable. Because of the many blades and many variable parts required, it is likely that multistage axial compressors in the very small size required would be expensive to construct, susceptible to foreign object damage, and difficult to maintain and repair. Growth potential by adding lower hub/tip ratio forward stages is limited but may be adequate.

Multistage Centrifugal Compressors

Because of the nonuniformity of flow in conventional centrifugal compressor rotors designed for high pressure ratios, the efficiency of such machines is less than required. In multistage centrifugal compressors, further losses are encountered in ducting the flow from the stator exit into later stages. The second stage (for the low corrected airflows encountered) would be quite small, and clearance and vane construction difficulties, similar to the rear stages of axial machines, would be encountered. A matching problem exists because of the significant difference in size and flow areas in subsequent stages, compared to the first stage, required for high overall pressure ratios. The cost of multistage centrifugal compressors will probably be less than multistage axial compressors. For very small compressors, improvement in ruggedness, maintenance, and repair should be obtained. A multistage centrifugal compressor would probably be heavier than the multistage axial compressor. Growth potential is limited.

Multistage Axial-Centrifugal Compressors

The combination of high-efficiency subsonic axial stages and a relatively high pressure ratio centrifugal stage offers the best opportunity using the present state of the art to approach the performance requirements of the engine cycle under consideration herein. In order to achieve satisfactory performance for part-power operation, matching of the axial stages and the centrifugal stage will require the use of variable vanes in many of the axial stages. Variable blade rows not only add to the cost of the compressor, but also subtract from the efficiency because of the larger clearances which are required. Therefore, it is likely that a combination compressor of this type will be more expensive than a multistage centrifugal compressor and only slightly more efficient. A combination compressor will probably be intermediate in weight between multistage axials and centrifugals, as will be the cost of maintenance and repair. The ruggedness and growth potential would be essentially the same as those of a multistage axial compressor.

Radial Outflow Compressor

The Radial Outflow Compressor (ROC) is a new type of turbomachine conceived to meet the requirements of a small, efficient gas turbine. The ROC combines axial flow compressor technology with the flow path of a centrifugal compressor. The use of supersonic rotor blades in conjunction with a rotating wall vaneless diffuser and supersonic stator blades

of new design offers the potentiality of producing very high pressure ratios in a single stage with very good efficiency.

Because the compressor type selected is a single stage, the cost of the radial outflow compressor should be much less than that of a multistage axial machine and significantly less than that of a multistage centrifugal compressor or a combination of the two. Analysis indicates that the problem of matching the compressor and turbine for off-design performance can be solved with a single variable inlet guide vane row. The radial outflow compressor is expected to be simpler, more rugged, and easier to maintain and repair than a multistage centrifugal compressor. Large growth potential can be achieved by supercharging with one or more transonic axial stages. It is because of these advantages that the single stage radial outflow compressor has been selected for development in this program. Although all of the individual aerodynamic elements have been demonstrated, either at supersonic speed in cascade tunnels or at low speed in compressors, the combination of these elements in a high speed machine has not yet been tested; in particular, the performance of the rotating vaneless diffuser under compressible flow conditions has not been demonstrated. However, the results obtained in a low speed compressor have been very encouraging. The significant step forward which this compressor offers strongly justifies further investigation and development.

A sketch of the radial outflow compressor is shown in Figure 1. The conventional axial flow inlet guide vane system is employed in this configuration even though other configurations are considered. The rotor blade sections have the appearance of typical impulse turbine sections. They are different from such turbine sections in that, at the design speed, the entering Mach number and the exiting Mach number are supersonic. The rotor blades are followed by a vaneless diffuser, with the walls of the vaneless diffuser being an integral part of the rotor. Following the rotor, supersonic stator blades are employed. Subsonic stator blades are used in tandem with the supersonic stators. A scroll collector, having two collector ducts, will probably be employed to deliver the compressor exit flow to the regenerator or to the combustor.

The specific flow handling capacity of the compressor in small engines is not a critical quantity. The reason for this is seen by examination of production engines in the 250- to 1000-horsepower class. The compressor frontal area is small in comparison to the gearbox and, in some smaller engines, to the combustor as well. It seems likely, for small regenerative engines, that the compressor frontal area will be relatively the same as the frontal area of the regenerator. Thus, the relatively low specific air handling capacity of centrifugal compressors or of the radial outflow compressor will not significantly affect the total frontal area of small gas turbine engines. The fact that the radial outflow compressor has a narrow profile, when viewed normal to the axis of rotation, may be an advantage for some installations.

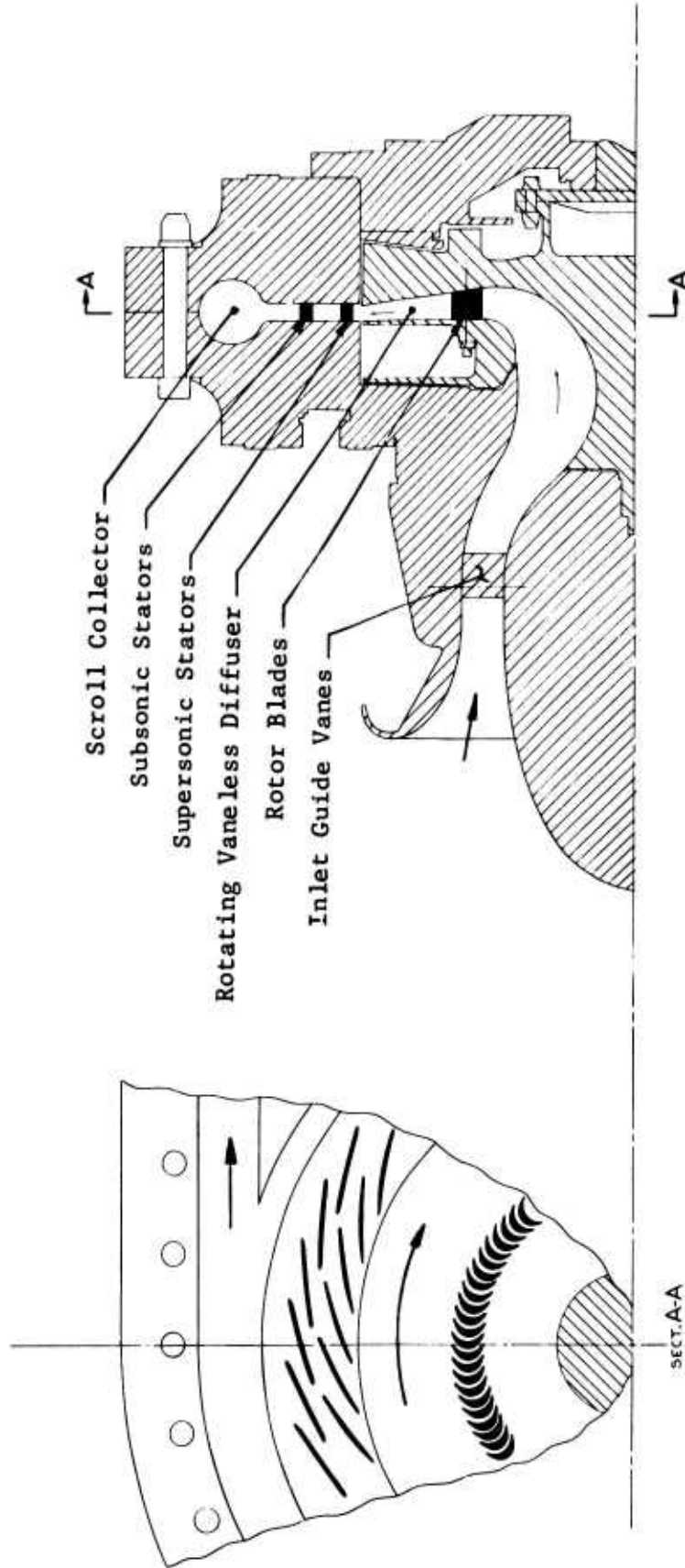


Figure 1. Cross Section of Supersonic Radial Outflow Compressor.

DISCUSSION OF THE SUPERSONIC RADIAL OUTFLOW COMPRESSOR

Compressors can impart high energy to air by accepting the flow at supersonic velocity while rotating at high speed and turning the velocity vector direction through large angles to produce high tangential exit velocity. The supersonic radial outflow compressor will accomplish high work input efficiently in this manner by employing rotor blade sections which have been demonstrated in supersonic cascade tests. The flow leaving the rotor blades will have a tangential velocity of about 2856 fps (absolute Mach number about 2.66). This flow will be permitted to form a powerful supersonic vortex within the rotating walls of the vaneless diffuser, which is an integral part of the rotor. Free vortex flow is a "natural" flow occurring in tornados and whirlpools and is characterized by conservation of angular momentum, with the tangential velocity decreasing inversely as the radius increases, and a corresponding large increase in static pressure with increasing radius.

Ideally, supersonic vortex flow, as well as subsonic vortex flow, exists with minimum energy losses, and the strong static pressure increase as radius increases is obtained with minimum loss. In conventional vaneless diffusers, much friction results between the stationary walls and the high velocity airstream. Secondary flows, separated zones, and large losses occur. By permitting the vaneless diffuser walls to rotate at high speed, the relative velocity between the walls and airstream is greatly reduced. The powerful centrifugal force field energizes boundary layer particles and should prevent the occurrence of separated zones. The losses are greatly reduced and a close approach to loss-free vortex flow should be obtained. Diffusion of the absolute velocity to a Mach number of 1.3 or less will be accomplished by this means.

An important feature of the radial outflow compressor is the design intent to obtain two-dimensional flow in all of the elements. Thus, the flow of the inlet guide vanes will be a close approximation of two-dimensional cascade flow. Since the rotor blade elements are parallel to the axis, the leading and trailing edges rotate at constant speed along their span. The rotor blade sections and the airflow through them will be two-dimensional. The rotor blade and passage wall surface boundary layers are energized by the centrifugal force field to maintain closely the two-dimensional flow. The purpose of these considerations is to produce a flow into the rotating diffuser that is essentially uniform in total pressure, static pressure and flow direction. There have been many indications (References 1 through 6) that vaneless diffuser performance is much affected by the uniformity of the flow entering the diffuser. Excellent diffuser performance and exit velocity profile are required to permit the stator blades to perform their important function efficiently. It is believed that these design features are essential to high efficiency and to high-pressure-ratio compressor performance and are unique to this new type of turbomachine.

The vector diagrams for the radial outflow compressor are shown in Figure 2. The absolute flow enters the rotor blades at a Mach number of 0.776 with an angle of 18.4 degrees from radial, in the direction to increase the relative velocity into the rotor blades. Relative to the rotor, the flow enters the blades at a Mach number slightly above 1.47 with an angle of 60 degrees from the radial direction. The total pressure, relative to the rotor blades, is about 2.37 times atmospheric pressure. Due to the change in radius through the rotor, the relative total pressure at rotor discharge is increased to about 1.24 times the entrance value, or to about 2.8 atmospheres. The assumed total pressure loss occurring in the rotor blades reduces the exit relative total pressure to about 2.55 atmospheres.

The rotor blade area ratio is selected so that at transonic speed, and particularly at the relative entering Mach number of 1, the effective rotor exit area is such that the exit Mach number is also near 1. This design consideration, intended to minimize discontinuous performance at transonic speeds, will produce a rotor exit Mach number at design speed that is slightly greater than the rotor entrance Mach number. The rotor blade discharge angle is 60 degrees from radial, which is necessary at the design exit rotational speed of 1300 fps to produce the work input required for a compression ratio of 11.34 with a stage efficiency of 81.6 percent.

The absolute Mach number entering the vaneless diffuser is about 2.66. The radius ratio of the vaneless diffuser has been selected so that the absolute Mach number entering the stator will be 1.3 or lower. Satisfactory supersonic static performance has been obtained in cascade tests conducted in this Mach number range by the General Electric Company (Reference 7). The Mach number of the flow entering the stator will be influenced by mechanical design considerations as well as by the amount of diffusion which can be obtained efficiently in the rotating vaneless diffuser. Greater diffusion will improve compressor efficiency.

In passing through the supersonic stators, the flow experiences a normal shock and subsonic diffusion to a Mach number of about 0.70. Subsonic stators are employed to reduce the Mach number to about 0.35. The scroll collector and the diffusing scroll arms will reduce the flow Mach number to about 0.30 before a 90-degree turn in vaned elbows is encountered. Total pressure loss coefficients obtained from rotor and stator blade cascade tests are assigned to the flow in the rotor, to the vaneless diffuser, and to the combined stator blade row. Calculated values of the various flow properties at the appropriate radial stations are given in the following example which is typical of the compressor shown in Figure 1.

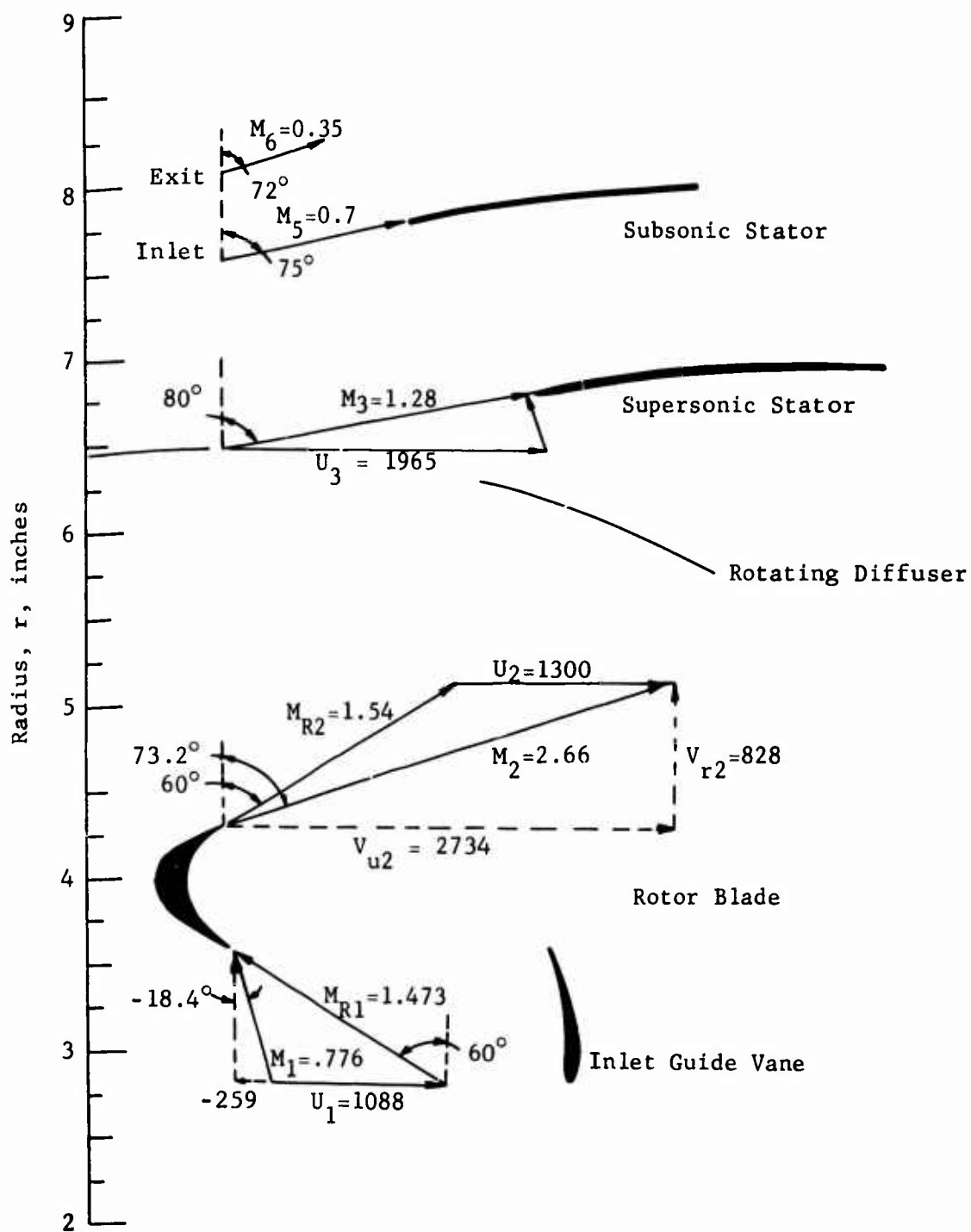


Figure 2. Vector Diagrams of Radial Outflow Compressor.

Calculation Example (See Figure 2)

Compressor Inlet Conditions

$$P_t = 1.0$$

$$T_t = 520^\circ\text{R}$$

Guide Vane Exit (Absolute)

$$V = 819$$

$$M = 0.776$$

$$\alpha = -18.4$$

$$P_s = 0.671$$

$$P_t = 1.0$$

Rotor Inlet (Relative)

$$V = 1555$$

$$M = 1.473$$

$$\beta = -60$$

$$D = 7.20$$

$$P_s = 0.671$$

$$P_t = 2.370$$

Rotor Exit (Relative)

$$V = 1656$$

$$M = 1.54$$

$$\beta = 60$$

$$D = 8.60$$

$$P_s = 0.653$$

$$P_t = 2.55$$

Rotating Diffuser Inlet (Absolute)

$$V = 2856$$

$$M = 2.66$$

$$\alpha = 73.2$$

$$D = 8.60$$

$$P_s = 0.653$$

$$P_t = 14.30$$

Supersonic Stator Inlet (Absolute)

$$V = 1855$$

$$M = 1.28$$

$$\alpha = 80$$

$$D = 13.0$$

$$P_s = 4.71$$

$$P_t = 12.7$$

Subsonic stator exit total pressure = 11.34 atmospheres; compressor efficiency = 81.6 percent.

Note: Velocities are given in feet per second, pressures are given in atmospheres, diameters are given in inches, and angles are given in degrees from radial.

STATUS OF DEVELOPMENT AT BEGINNING OF PROGRAM

Although the radial outflow compressor applies certain features of axial and centrifugal compressors, it represents a necessary radical departure from current practice for either type in order to obtain advanced performance in small-size turbomachines. Rotor blades and stator blades of this new compressor had been developed in cascade and tested in axial flow compressors, but they had not been used in the radial outflow configuration. Single-stage performance of the pressure ratio and efficiency calculated to be obtainable with the radial outflow supersonic compressor is far advanced from the present state of conventional compressor design. The combination of high work input impulse rotor blades,

rotating wall vaneless diffuser and advanced stator systems, with uniform, two-dimensional flow closely approached throughout, should make possible this advanced performance.

A low-speed water flow model having transparent rotor and stator walls was constructed to explore the potentiality of this new concept and to observe flow details in this unusual configuration. The early configuration was done with water as the fluid medium because of the ease of flow visualization using dye traces and the high Reynolds number obtained at low speed.

Since the results obtained with the water flow model were very encouraging, a low-speed air test model compressor was constructed utilizing the same geometry. This low-speed compressor is capable of running at higher rotor speeds than the water flow model and, thus, produces high enough pressures for adequate water manometer deflections to give accurate readings. Prior to the beginning of this program, the low-speed compressor had run at only one rotor blade setting, the design value for impulse flow. The results were most encouraging in that they produced a peak rotor efficiency slightly over 95 percent, including rotating diffuser losses.

The low-speed models represented operation of a high pressure ratio radial outflow compressor running at 2 to 5 percent design speed. A direct indication of excellent low-speed operating characteristics had, therefore, been obtained. The powerful effect of compressibility on rotating diffuser and supersonic stator performance could only be estimated from existing theory and cascade tests. However, all of the evidence available from these tests, from supersonic cascade tests and theory, strongly indicated that the radial outflow compressor had the potential of producing very high pressure ratios in a single stage with efficiencies now obtainable only in multistage axial flow compressors of much greater airflow capacity.

SMALL GAS TURBINE ENGINE COMPRESSOR TECHNOLOGY PROGRAM

The radial outflow compressor is being developed by the General Electric Company under contract to the United States Army. The objectives of the program are the advancement and demonstration of high pressure ratio compressor technology for small gas turbine engines.

Phase I of this program, reported herein, has been completed. It included investigations relating to the design and performance of the basic components to determine optimum configurations to be incorporated in the high-speed radial outflow compressor. The low-speed air model radial outflow compressor was used to investigate the aerodynamic performance characteristics of inlet guide vanes, rotating vaneless diffusers, scroll collector, transition diffuser and elbow. Optimum aerodynamic performance characteristics for rotor blade cascades, supersonic and subsonic stator cascades, and tandem arrangement of supersonic and subsonic cascades were determined from transonic cascade tunnel

tests. Aerodynamic analysis programs were conducted to investigate the inlet flow passage of the high-speed machine and to determine the required rotor blade shape to be used in the high-speed machine that duplicates the optimum performance characteristics of the two-dimensional cascade tested in the transonic cascade tunnel. Stress analysis and bench tests of several possible rotor designs and investigation of fabricating and joining blades, rotating shroud, and disc were conducted.

A high-speed radial outflow compressor will be designed, fabricated, and used for further investigations during Phase II of this program. Phase III of the program will include the full demonstration of compressor characteristics using a second experimental compressor incorporating the improved mechanical and aerodynamic design information generated from all previous investigations.

TABLE I
PHASE I DEMONSTRATED COMPONENT PERFORMANCE

Component	Inlet Mach No.	Inlet Angle (degrees)	Design Point Parameters	Goal	Demonstrated
Rotor Blades	1.42(Rel)	60	\bar{w} \bar{C}_P	0.15 0	0.185 0
Vaneless Rotating Diffuser	1.60(Rel)*	60	$C_{P_{eff}}$ η_{RA}	0.32 0.90	0.32 0.885
Supersonic Stator	1.28	80	\bar{w} \bar{C}_P	0.14 0.45	0.144 0.46
Subsonic Stator	0.70	75	\bar{w} \bar{C}_P	0.08 0.60	0.066 0.652
Tandem (Supersonic and Subsonic) Stators	1.28	80	\bar{w} \bar{C}_P	0.22 0.60	0.244 0.612

Where: \bar{w} is total pressure loss coefficient
 \bar{C}_P is static pressure rise coefficient
 $C_{P_{eff}}$ is effective static pressure rise coefficient
 η_{RA} is aerodynamic rotor efficiency

* The goal and demonstrated performance levels presented for the rotating vaneless diffuser are representative of the low-speed radial outflow compressor and not at the design inlet Mach number.

INLET GUIDE VANES

INTRODUCTION

Gas turbine engine cycle studies aimed at providing efficient operation over a wide range indicate that a matching problem exists between a fixed-geometry compressor and a fixed-geometry turbine. This matching problem can be solved with a single variable inlet guide vane (IGV) row.

To achieve satisfactory matching down to the 30- to 40-percent power range, the cycle studies indicated that the inlet guide vanes must be closed from 30 to 40 degrees from radial. Since the present design inlet guide vane setting is 18.4 degrees open from radial, a relatively large swing in inlet guide vane turning is required.

A prime objective of the radial outflow compressor design is to produce a two-dimensional flow into the rotor blades, entering the vaneless diffuser and into the following stators. This consideration suggests that the spanwise elements of the inlet guide vanes should lie parallel to the axis of rotation. The radial inflow and radial outflow inlet guide vane configurations included this desirable characteristic. For conventional axial flow inlet guide vanes, a design should be considered that produces flow turning in a manner that approximates constant angular momentum at all radii over a range of IGV closure angles.

The possibility of supercharging radial outflow compressors by the use of one or more transonic axial stages exists and offers significant growth potential. The axial flow inlet guide vane configuration would probably be used with this design.

During Phase I of this program, radial inflow, radial outflow, and axial flow inlet guide vane systems were designed and built. Investigations were conducted on the low-speed radial outflow compressor using the radial inflow and axial flow IGV systems. Even though the radial outflow inlet guide vane system appears in theory to be the best aerodynamic approach, this configuration has not been tested owing to questionable mechanical integrity of the small fixed part of the variable vanes. This inlet system requires that the vanes be installed directly in front of the rotor. Since the back wall of the passage rotates, a cantilever design supporting both the fixed and variable parts of the vanes from the front wall seems to be required. A satisfactory radial outflow vane system for high-speed application capable of maintaining close end clearances at all guide vane angles has not yet been designed.

DESCRIPTION

In order to select the inlet guide vane system for the high-speed radial outflow compressor, a series of tests was conducted using the low-speed compressor. The basic configuration consists of the rotor (containing rotor blades and a vaneless diffuser), diffuser, scroll collector, transition diffusers, turning vanes, and throttle valves. Stator blades

were not installed in the nonrotating diffuser. This low-speed machine originally employed a bellmouth inlet. This inlet was removed and the test compressor modified to accommodate either an axial flow, a radial inflow, or a radial outflow inlet guide vane assembly.

The axial flow inlet induces flow into the machine parallel to the compressor axis. A tangential component of velocity is produced by inlet guide vanes installed in the inlet annulus. The passage then turns inward toward the axis of rotation. After the flow enters the rotor, the air is directed radially outward to the rotor blades. A drawing of the axial flow inlet is given in Figure 3. A photograph of this inlet installed on the low-speed radial outflow compressor is shown in Figure 4. This inlet was designed not only to investigate the influence of inlet guide vanes upon the flow but also to investigate the effects of rotating passage walls upon the boundary layer growth associated with the tangential component of velocity. Figure 5 defines these optional rotating and nonrotating walls as rotor housing 1 and rotor housing 2. The clearance gap that necessarily occurs between these rotating and stationary parts is sealed against external leakage by the use of a rotor housing seal.

In a similar manner, the radial inflow inlet was designed to induce a radial velocity vector directed inward toward the machine centerline. A tangential component of velocity is produced by the action of inlet guide vanes placed on a circumferential inlet area. This two-component velocity vector is then turned 180 degrees in a plane which contains the axis of the compressor so that the inward radial vector becomes an outward radial vector. Therefore, the rotor inlet sees a two-component velocity vector similar to the axial flow inlet. A drawing of the radial inflow inlet guide vane assembly is shown in Figure 6. A photograph of this inlet mounted on the low speed radial outflow compressor is shown in Figure 7. This inlet guide vane assembly is also intended to investigate the action of the inlet guide vanes and also the effects of various rotating walls upon the boundary layer growth associated with the tangential component of velocity. Figure 8 describes the notation used throughout the test procedure. Rotor housing 1 and rotor housing 2 are optional rotating parts. The rotor housing seal is again employed to prevent external leakage through the clearance gap.

It is to be noted that the inlet guide vanes of the radial inflow inlet are positioned at a larger radius than are the axial flow guide vanes. Positive and negative inlet guide vane deflections are defined in Figures 5 and 8. The positive deflections are in the direction of rotor blade rotation. Guide vanes of the type described in Reference 8 are employed because of their wide range of operation with low losses.

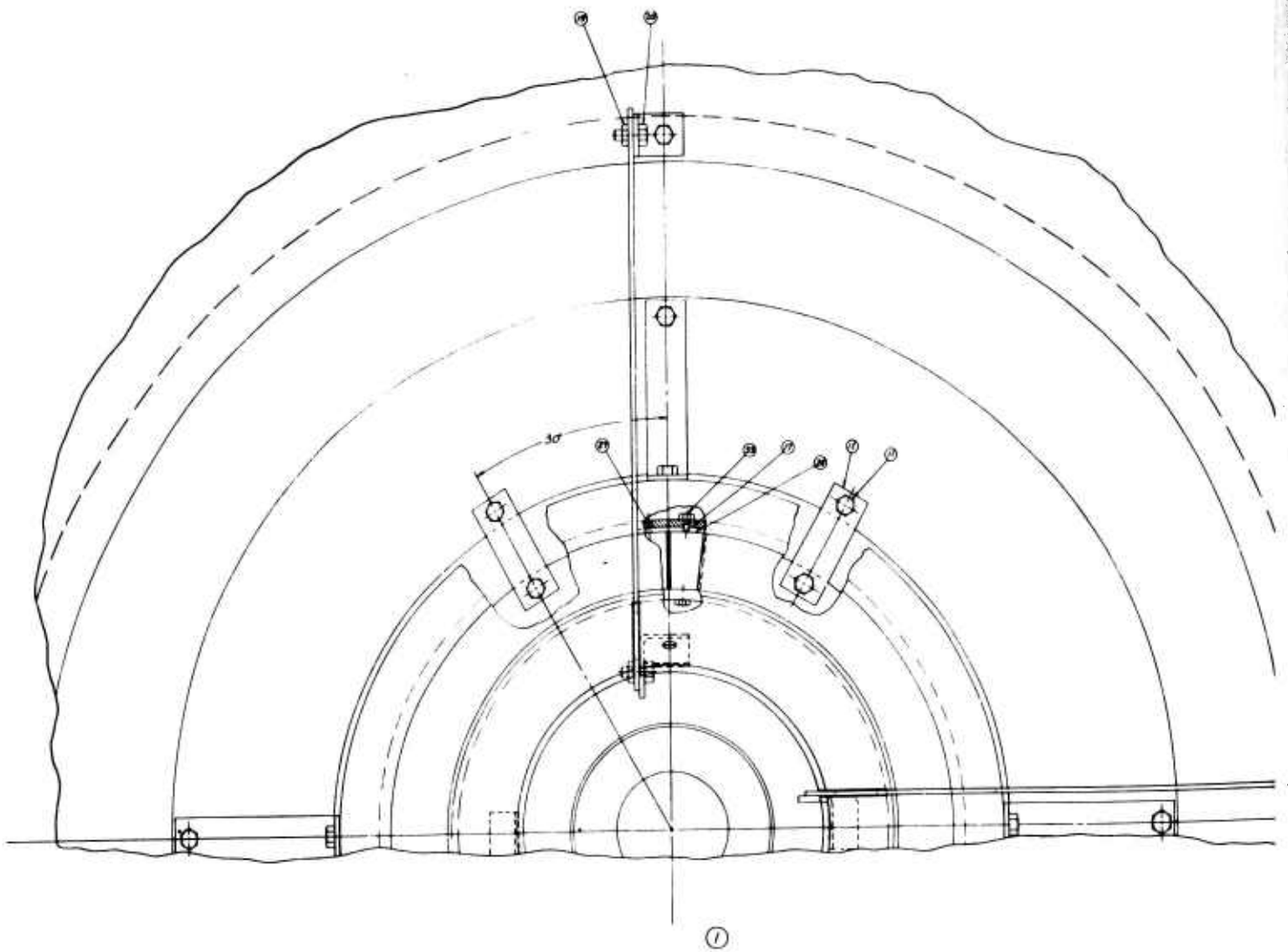
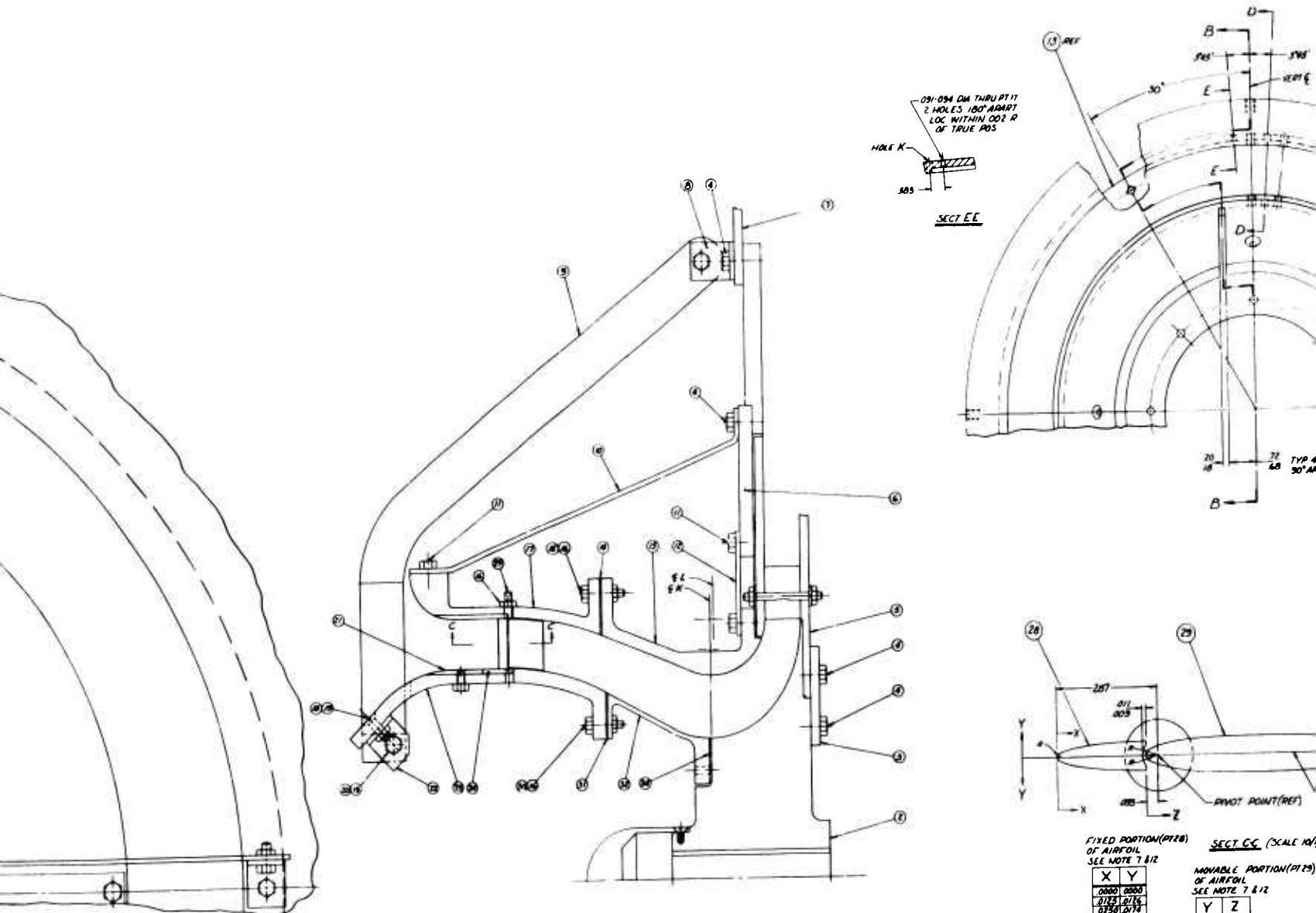


Figure 3. Axial Flow Inlet Design.

A



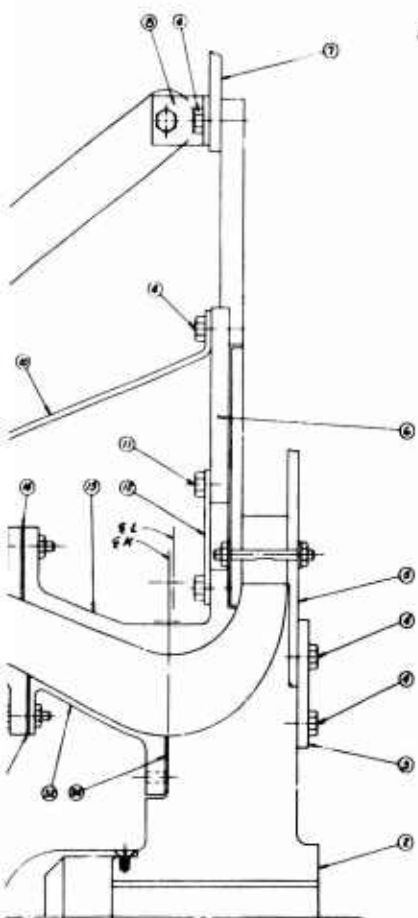
B

FIXED PORTION (PI 28)
OF AIRFOIL
SEE NOTE 7 & 12

X	Y
0.000	0.000
0.125	0.175
0.250	0.350
0.375	0.525
0.500	0.700
0.625	0.875
0.750	1.050
0.875	1.225
1.000	1.400
1.125	1.575
1.250	1.750
1.375	1.925
1.500	2.100
1.625	2.275
1.750	2.450
1.875	2.625
2.000	2.800
2.125	2.975
2.250	3.150
2.375	3.325
2.500	3.500
2.625	3.675
2.750	3.850
2.875	4.025
3.000	4.200
3.125	4.375
3.250	4.550
3.375	4.725
3.500	4.900
3.625	5.075
3.750	5.250
3.875	5.425
4.000	5.600
4.125	5.775
4.250	5.950
4.375	6.125
4.500	6.300
4.625	6.475
4.750	6.650
4.875	6.825
5.000	7.000
5.125	7.175
5.250	7.350
5.375	7.525
5.500	7.700
5.625	7.875
5.750	8.050
5.875	8.225
6.000	8.400
6.125	8.575
6.250	8.750
6.375	8.925
6.500	9.100
6.625	9.275
6.750	9.450
6.875	9.625
7.000	9.800
7.125	9.975
7.250	10.150
7.375	10.325
7.500	10.500
7.625	10.675
7.750	10.850
7.875	11.025
8.000	11.200
8.125	11.375
8.250	11.550
8.375	11.725
8.500	11.900
8.625	12.075
8.750	12.250
8.875	12.425
9.000	12.600
9.125	12.775
9.250	12.950
9.375	13.125
9.500	13.300
9.625	13.475
9.750	13.650
9.875	13.825
10.000	14.000

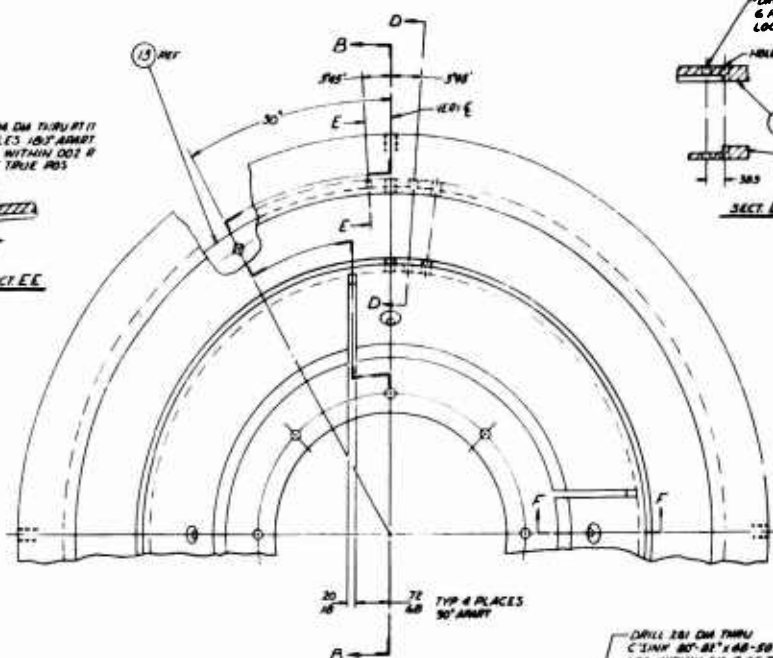
SECT CC (SCALE 10/1)
MOVABLE PORTION (PI 29)
OF AIRFOIL
SEE NOTE 7 & 12

Y	Z
0.000	0.000
0.125	0.175
0.250	0.350
0.375	0.525
0.500	0.700
0.625	0.875
0.750	1.050
0.875	1.225
1.000	1.400
1.125	1.575
1.250	1.750
1.375	1.925
1.500	2.100
1.625	2.275
1.750	2.450
1.875	2.625
2.000	2.800
2.125	2.975
2.250	3.150
2.375	3.325
2.500	3.500
2.625	3.675
2.750	3.850
2.875	4.025
3.000	4.200
3.125	4.375
3.250	4.550
3.375	4.725
3.500	4.900
3.625	5.075
3.750	5.250
3.875	5.425
4.000	5.600
4.125	5.775
4.250	5.950
4.375	6.125
4.500	6.300
4.625	6.475
4.750	6.650
4.875	6.825
5.000	7.000
5.125	7.175
5.250	7.350
5.375	7.525
5.500	7.700
5.625	7.875
5.750	8.050
5.875	8.225
6.000	8.400
6.125	8.575
6.250	8.750
6.375	8.925
6.500	9.100
6.625	9.275
6.750	9.450
6.875	9.625
7.000	9.800
7.125	9.975
7.250	10.150
7.375	10.325
7.500	10.500
7.625	10.675
7.750	10.850
7.875	11.025
8.000	11.200
8.125	11.375
8.250	11.550
8.375	11.725
8.500	11.900
8.625	12.075
8.750	12.250
8.875	12.425
9.000	12.600
9.125	12.775
9.250	12.950
9.375	13.125
9.500	13.300
9.625	13.475
9.750	13.650
9.875	13.825
10.000	14.000



DRILL .034 DIA THRU PT 11
2 HOLES 180° APART
LOC WITHIN .002 R
OF TRUE POS

HOLE H
M3
SECT EE

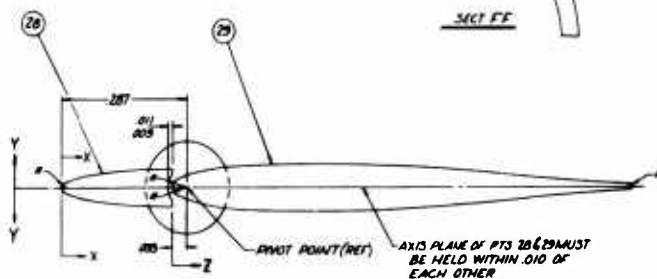


DRILL .130 DIA THRU PTS 17 & 23
6 HOLES EQ SP AS SHOWN
LOC WITHIN .010 R OF TRUE POS

HOLE H
17
23
M3
SECT DD

DRILL .251 DIA THRU
C 1/4" DIA .001" DIA .50 DIA
LOC WITHIN .010 R OF TRUE
POS - 4 HOLES EQ SP

25
26
SECT FF



FIXED PORTION (PT 28)
OF AIRFOIL
SEE NOTE 7 & 12

X	Y
.0000	.0000
.0112	.0176
.0224	.0278
.0336	.0377
.0448	.0473
.0560	.0565
.0672	.0653
.0784	.0736
.0896	.0814
.1008	.0887
.1120	.0955

SECT CC (SCALE 1/2)

MOVABLE PORTION (PT 29)
OF AIRFOIL
SEE NOTE 7 & 12

Y	Z
.0000	.0000
.0112	.0176
.0224	.0278
.0336	.0377
.0448	.0473
.0560	.0565
.0672	.0653
.0784	.0736
.0896	.0814
.1008	.0887
.1120	.0955

C

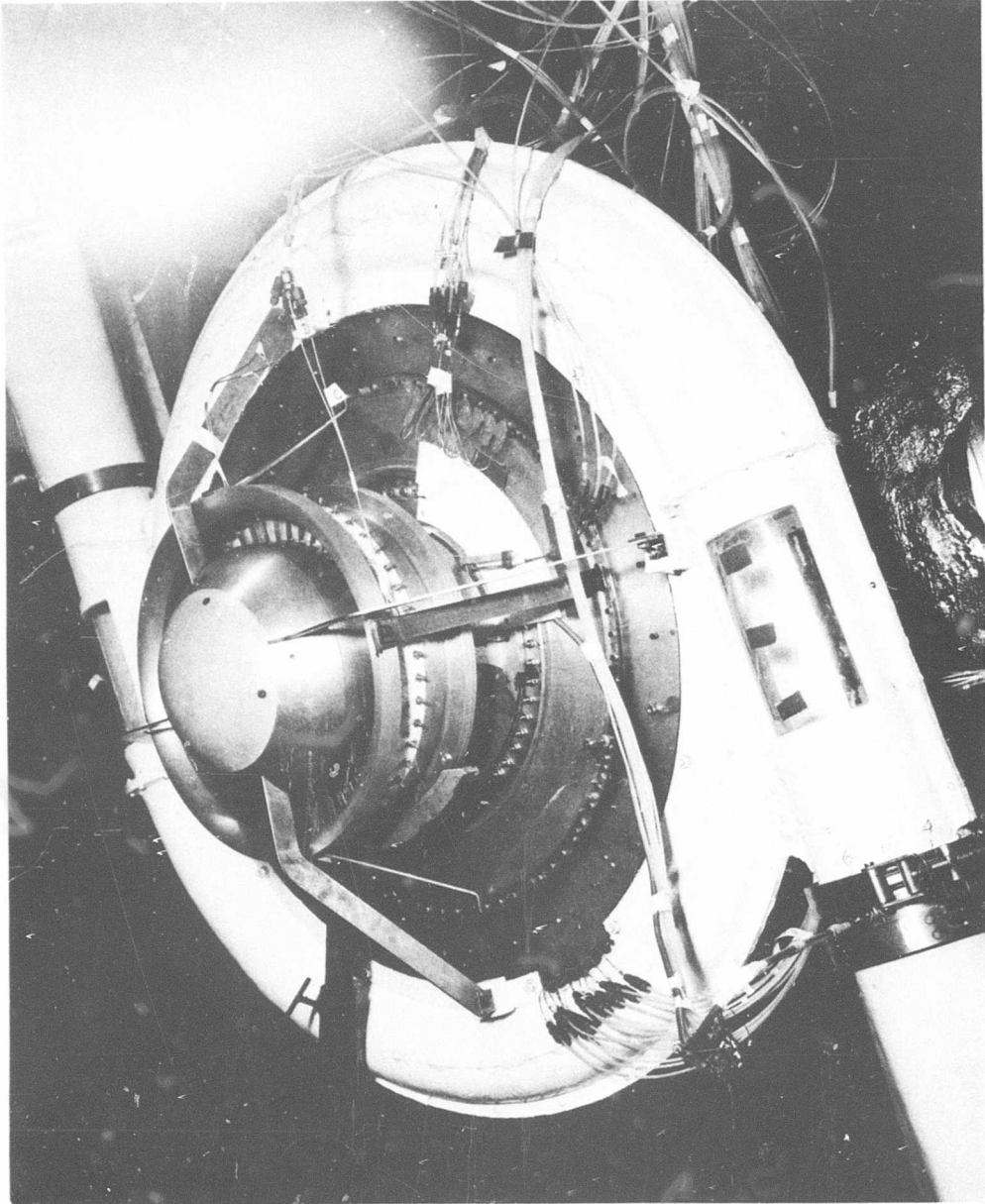


Figure 4. Installation of Axial Flow Inlet.

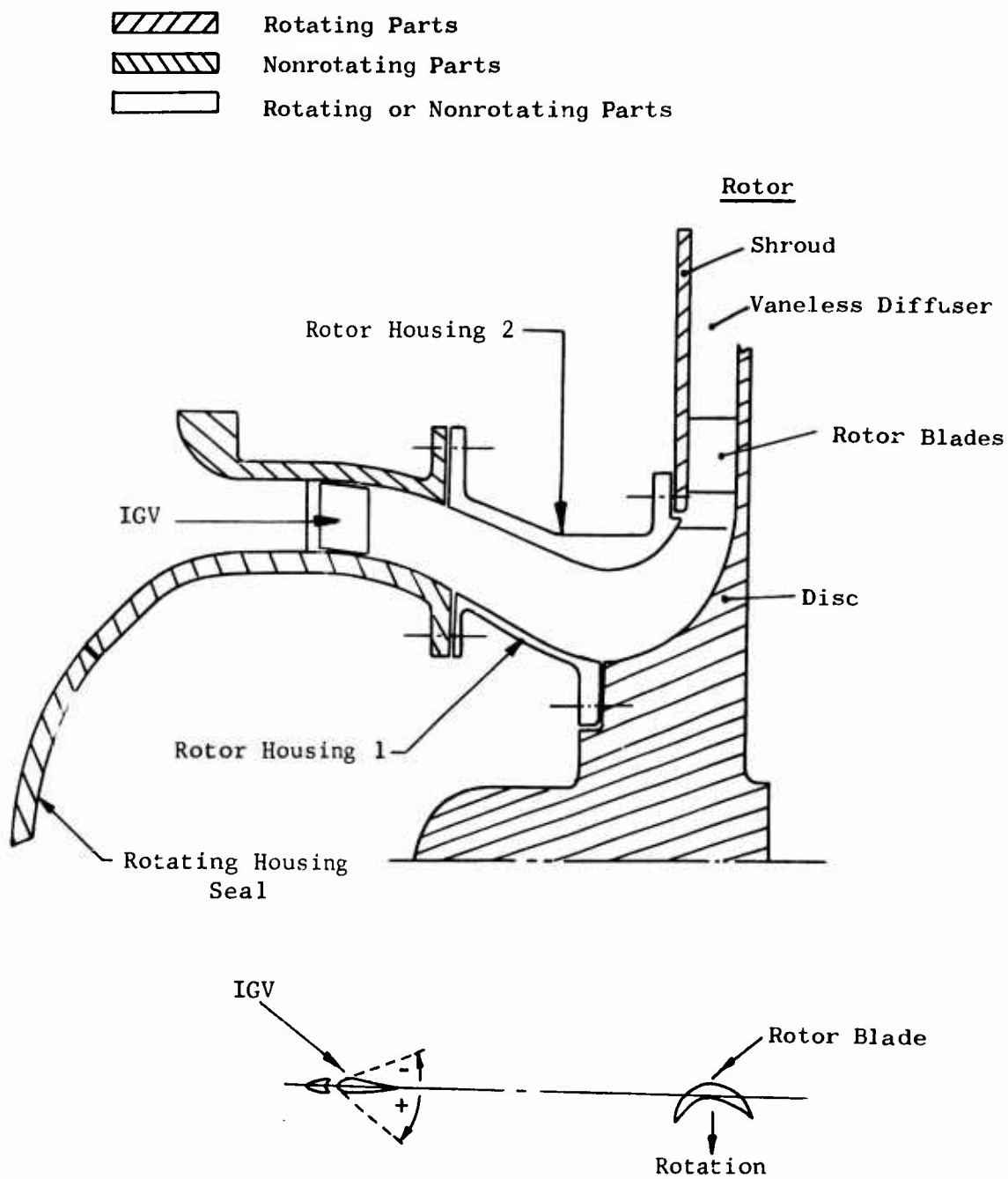


Figure 5. Axial Flow Inlet Optional Rotating Walls.

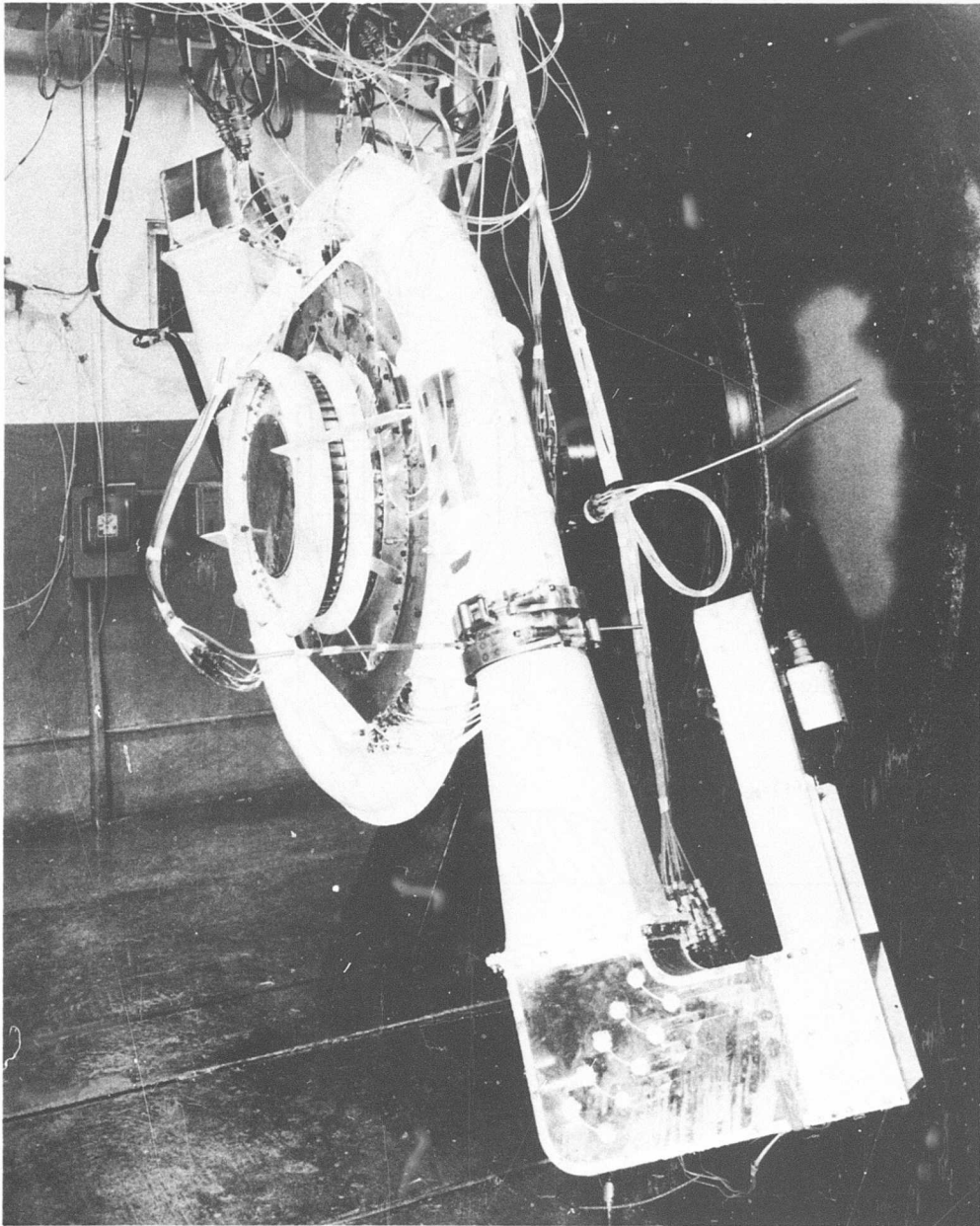


Figure 7. Installation of Radial Inflow Inlet.

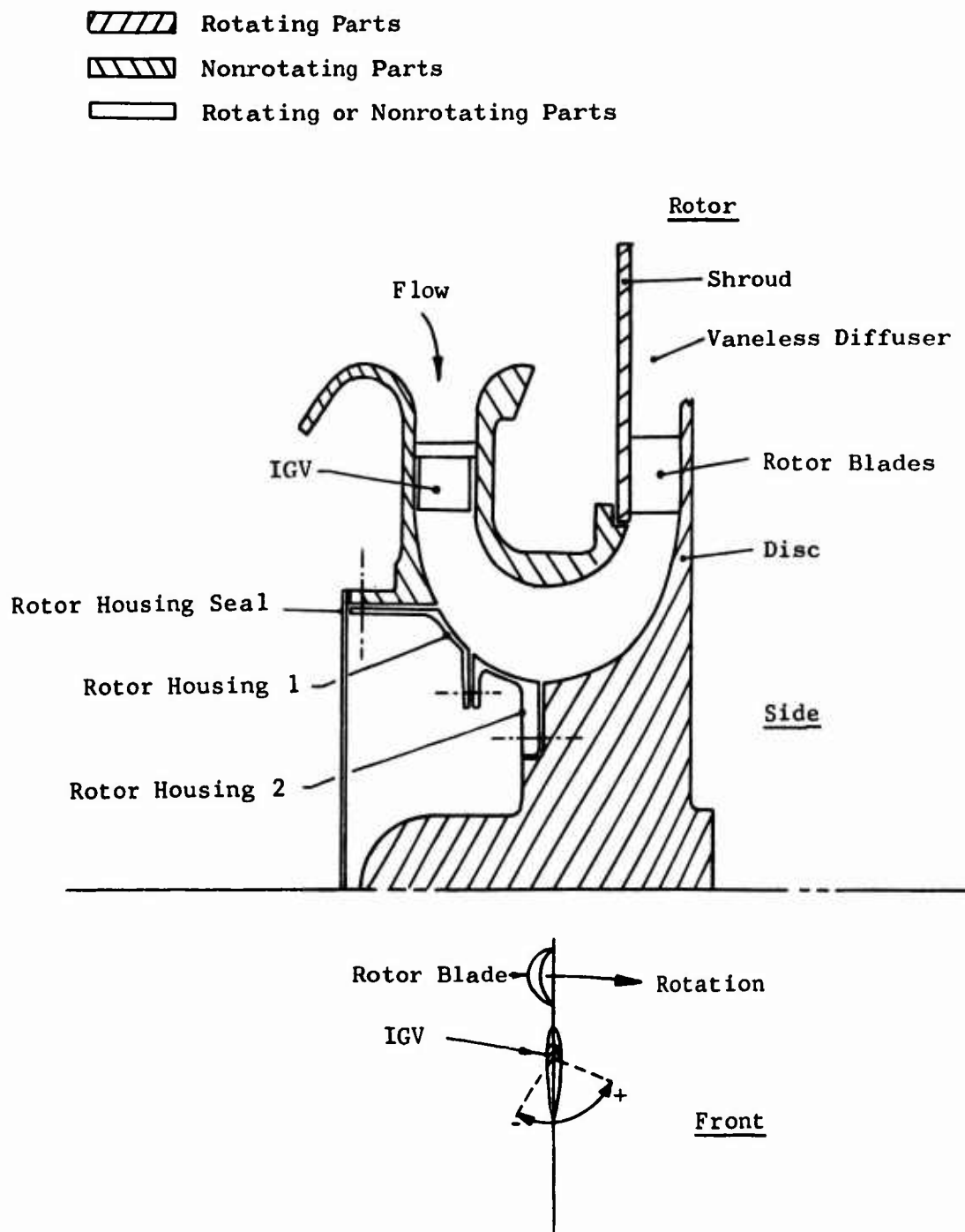


Figure 8. Radial Inflow Inlet Optional Rotating Walls.

EXPERIMENTAL PROCEDURE

The inlet guide vane systems were tested with the low-speed radial outflow compressor in the following configuration: the buildup consisted of the small rotating diffuser, rotor blades set with a 60-degree trailing edge angle, scroll collector, turning vanes, throttle valves, and flow splitter number 1. The variable parts of the configuration consisted of the axial and radial inlet, the inlet guide vane angle setting, and various (optional) rotating inlet parts. A chronological list of all these various changes, along with their appropriate run numbers, is to be found in Table II.

The instrumentation peculiar to this investigation is as follows. A six-element total pressure probe was installed at the exit of the rotating diffuser along with eight static pressure orifices. A combination total pressure and yaw probe, equipped to rotate automatically until equal yaw tube pressures are sensed, thus indicating the direction of flow, was used. The actuator permitted continuous traversing of the flow passage at the exit of the rotating diffuser. A combination manual total pressure and angle probe was installed just upstream of the rotor blades. This probe and its orientation are shown in Figure 9. Various static pressure orifices were installed at the inlet of each guide vane assembly. Four static pressure orifices were installed just upstream of the inlet guide vanes of the axial inlet. These orifices are on relatively flat surfaces and were employed in measuring the mass flow through the machine. In like manner, eight static pressure orifices were located just upstream of the inlet guide vanes of the radial flow inlet. All other instrumentation is the same as was employed in the investigation concerning the scroll collector, flow splitter, and turning vane evaluations.

The general procedure employed in operating the compressor is as follows. At each throttle valve setting, the machine characteristics were measured at 1400, 1600, and 1800 rpm. The throttle valve settings employed in the procurement of the compressor characteristics are as follows: 90, 80, 70, 65, 60, 55, 47.5, 45, 40, 35, 30, and 25 percent (of exit area) open. The first tests in this series were for the purpose of finding the best rotating wall configurations. The uniformity of the flow angle and total pressure near the rotor blade inlet were considered to be significant in making evaluations. To make these measurements, the inlet probe was set at the same angle as the inlet guide vanes. It was considered that the geometric angle setting of the guide vanes would produce a fluid turning at the rotor blades that would not deviate appreciably from the setting angle; therefore, the inlet probe remained stationary (not nulled) throughout the tests, the yaw tube pressure differences were recorded, and the flow angle was calculated from a calibration curve. The static pressures indicated from orifices upstream of the inlet guide vanes on both inlets were read on vertical manometers. After Runs 1235 and 1236 were completed and the data reduced, it became apparent that two changes would have to be made in the test procedure. First, at large inlet guide

TABLE II
INLET GUIDE VANE RUN SUMMARY

Run	Inlet	IGV Angle	Rotating Parts	Objective
1235	Radial	60	Hub	Compressor Characteristics
↓	↓	↓	Hub & Housing 2	Compressor Characteristics
↓	↓	↓	Hub, Housings 1 & 2	Compressor Characteristics
1236	Axial	60	Hub	Compressor Characteristics
↓	↓	↓	Hub & Housing 1	Compressor Characteristics
1237	Radial	50	Hub, Housings 1 & 2	Compressor Characteristics
1238	Radial	35	Hub, Housings 1 & 2	Compressor Characteristics
1239	Radial	18.5	Hub, Housings 1 & 2	Compressor Characteristics
1241	Radial	0	Hub, Housings 1 & 2	Compressor Characteristics
1242	Radial	-18.5	Hub, Housings 1 & 2	Compressor Characteristics
1243	Radial	60	Hub	Rotor Inlet Profile
↓	↓	↓	Hub & Housing 2	Rotor Inlet Profile
↓	↓	↓	Hub, Housings 1 & 2	Rotor Inlet Profile
↓	↓	50	Hub	Rotor Inlet Profile
↓	↓	↓	Hub & Housing 2	Rotor Inlet Profile
↓	↓	↓	Hub, Housings 1 & 2	Rotor Inlet Profile
1244	Radial	35	Hub, Housings 1 & 2	Rotor Inlet Profile
1245	Radial	18.5	Hub, Housings 1 & 2	Rotor Inlet Profile
1246	Axial	60	Hub & Housing 1	Rotor Inlet Profile
1247	Axial	60	Hub, Housings 1 & 2	Compressor Characteristics
1248	Axial	60	Hub	Rotor Inlet Profile
1249	Axial	50	Hub & Housing 1	Compressor Characteristics
1250	Axial	35	Hub & Housing 1	Compressor Characteristics
1251	Axial	18.5	Hub & Housing 1	Compressor Characteristics
1252	Axial	0	Hub & Housing 1	Compressor Characteristics
1253	Axial	-18.5	Hub & Housing 1	Compressor Characteristics
1255	Radial	60	Hub, Housings 1 & 2	Compressor Characteristics
1256	Radial	60	Hub	Rotor Inlet Profile
1257	Axial	60	Hub & Housing 1	Compressor Characteristics
1258	Axial	60	Hub	Rotor Inlet Profile
1259	Axial	50	Hub & Housing 1	Compressor Characteristics

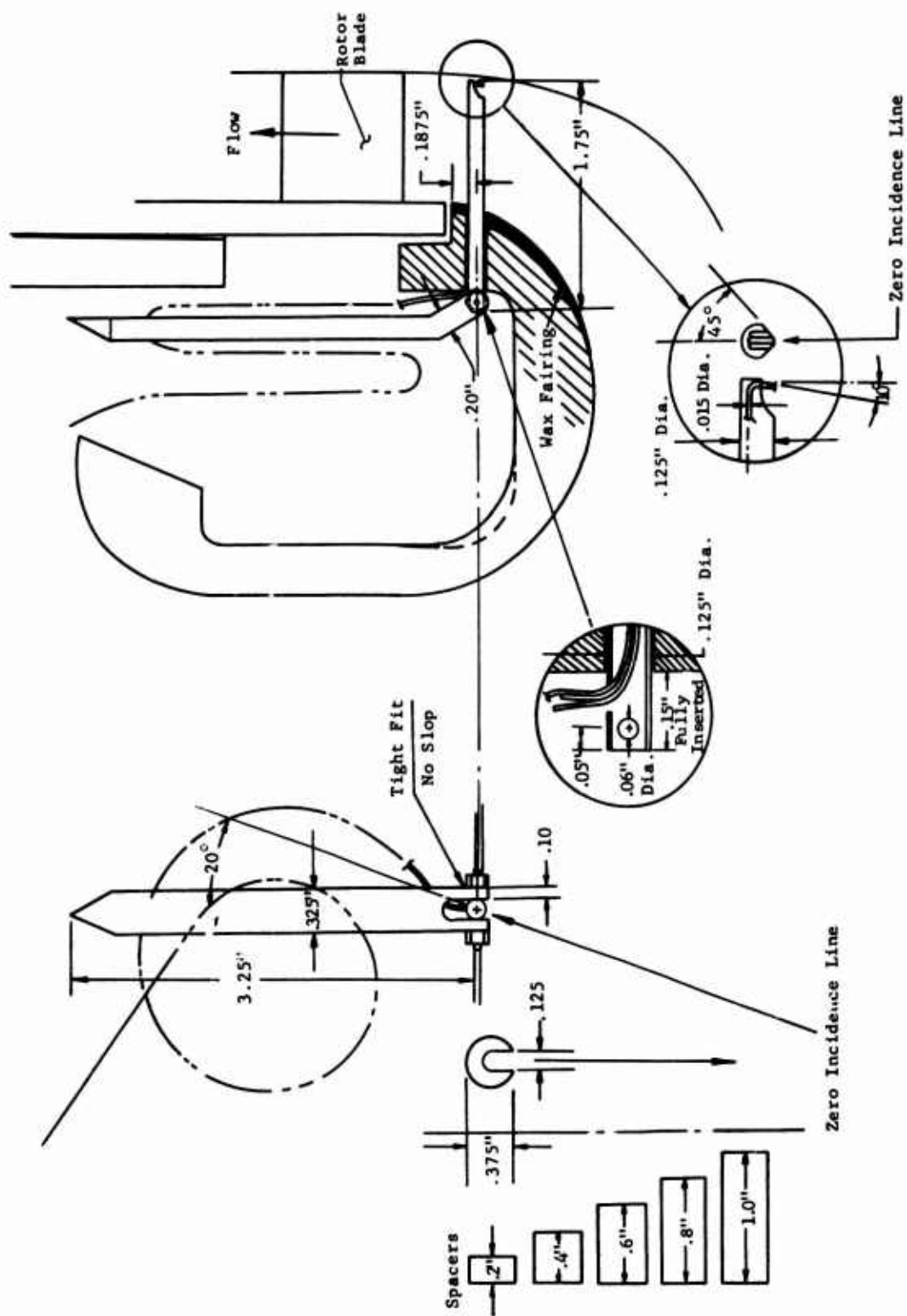


Figure 9. Yaw Angle and Total Pressure Probe.

vane setting angles, the fluid turning at the rotor blade deviated significantly from the geometric setting angle of the guide vanes. Therefore, it was decided that the inlet total pressure and angle probe would have to be nulled for each test point. Second, at large inlet guide vane turning angles, the mass flow was reduced significantly, and the static pressures taken from the inlet entrance were not being recorded with sufficient accuracy to produce reliable data. Inclined manometers were substituted to obtain the required accuracy.

In selecting the optimum rotating parts, an inlet guide vane angle setting of 60 degrees was employed since the 60-degree setting should produce a large growth in inlet wall boundary layer associated with the tangential component of velocity. This condition should make the evaluation of inlet performance more definitive than with lower flow angles.

The effect of inlet guide vane turning angle was then investigated for turning angles of 60, 50, 35, 18.5, 0, and -18.5 degrees. As was previously stated, positive turning angles are in the direction of rotor blade rotation.

EXPERIMENTAL RESULTS

In general, compressor characteristics are plotted as pressure coefficient versus flow coefficient and rotor aerodynamic efficiency versus flow coefficient for all inlet guide vane settings in Figures 10 through 48. Since the total of these characteristics comprises many figures, a composite presentation of the results is also plotted (Figures 49 through 52), giving rotor aerodynamic efficiency and pressure coefficient versus rotor inlet flow angle for lines of constant flow coefficient. The rotor inlet flow angle presented is the angle, measured from radial, of the absolute velocity vector entering the rotor blades.

At design flow coefficient, the rotor inlet probe was traversed to obtain the flow conditions that exist across the passage width. Therefore, a total pressure profile and flow angle profile were obtained at the rotor inlet. This information is presented in Figures 53 through 62 as a function of passage width. Since the flow passage at the rotor inlet has a 1-inch depth, the data are presented with zero defining the disc wall and 1 inch defining the shroud wall of the compressor. Since the 1-inch spacer shown in Figure 9 did not permit the head of the total pressure and yaw probe to reach the flow passage wall, data were not obtained for the position adjacent to the shroud wall.

A sampling of rotating diffuser exit profiles was taken at design flow coefficient. This information was obtained from the automatic total pressure and flow angle equipment previously described. A mass weighting program was written to utilize these data and to determine the velocity profiles and efficiency at the exit of the rotating diffuser. The results are presented in Figures 63 through 65 as tangential velocity, radial velocity, and efficiency profiles.

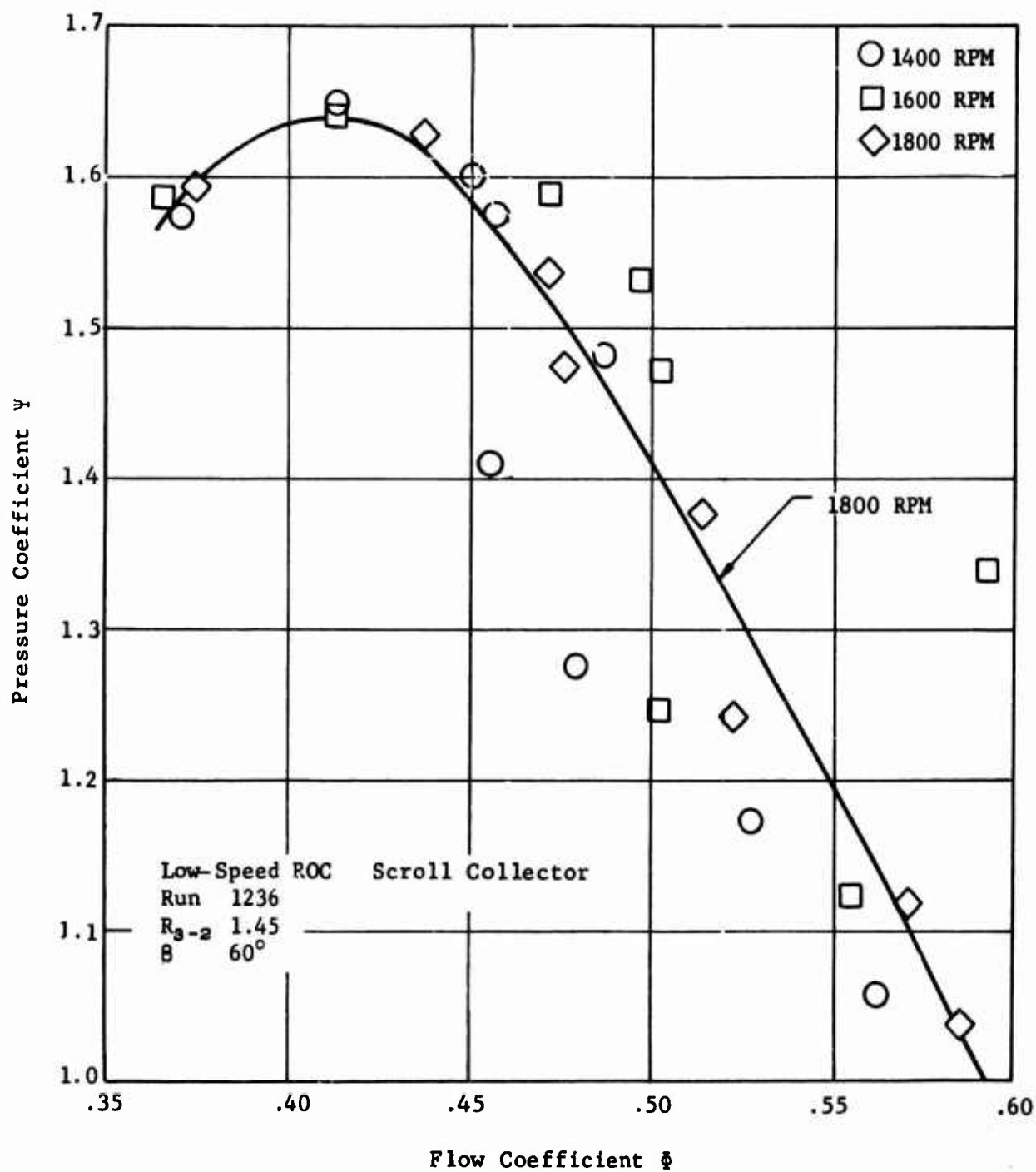


Figure 10. Rotor Discharge Pressure Coefficient, Axial Flow IGV at 60° , Hub and Housing 1 Rotating.

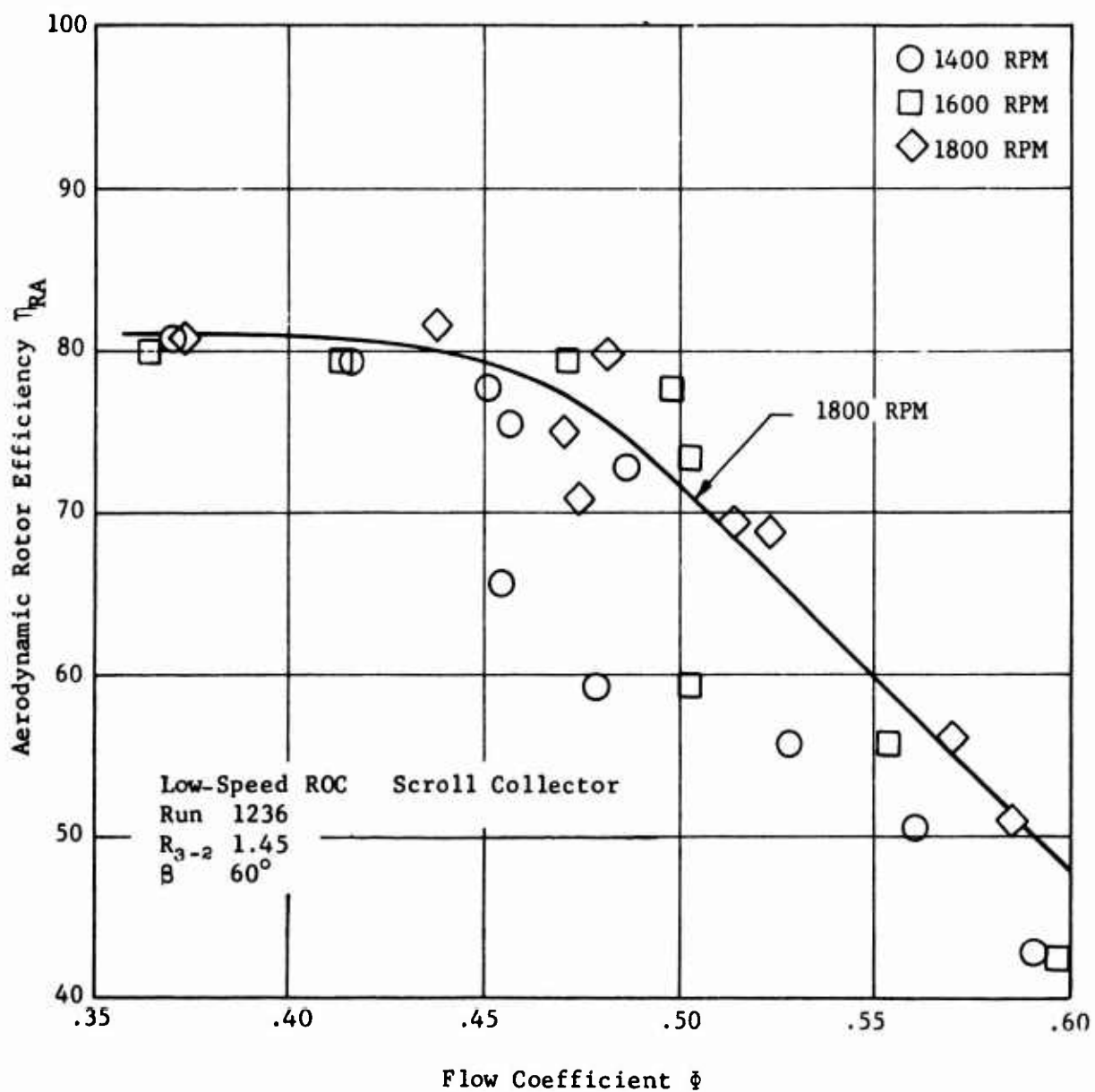


Figure 11. Compressor Efficiency, Axial Flow IGV at 60° , Hub and Housing 1 Rotating.

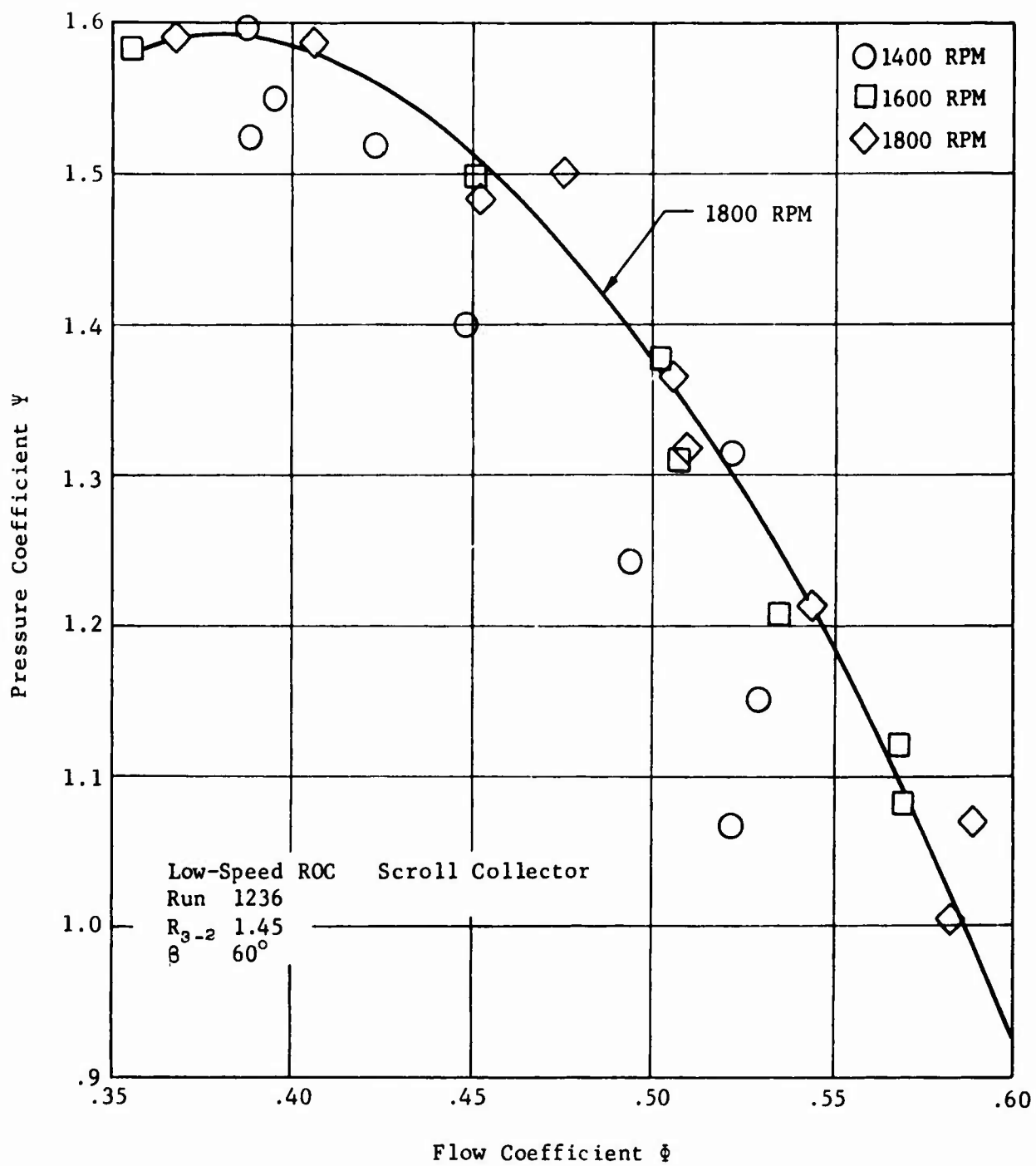


Figure 12. Rotor Discharge Pressure Coefficient, Axial Flow IGV at 60°, Hub Rotating.

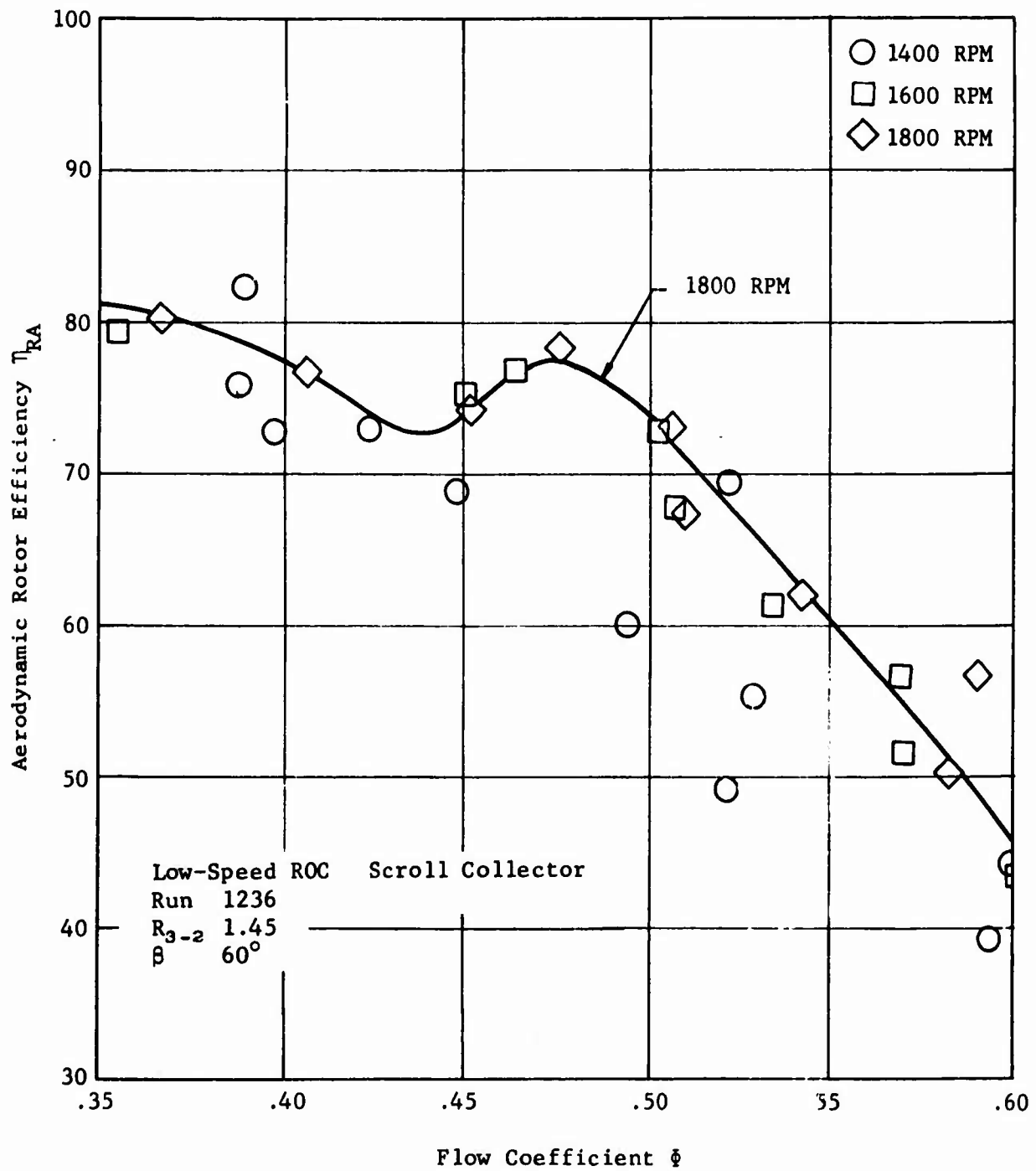


Figure 13. Compressor Efficiency, Axial Flow IGV at 60° , Hub Rotating.

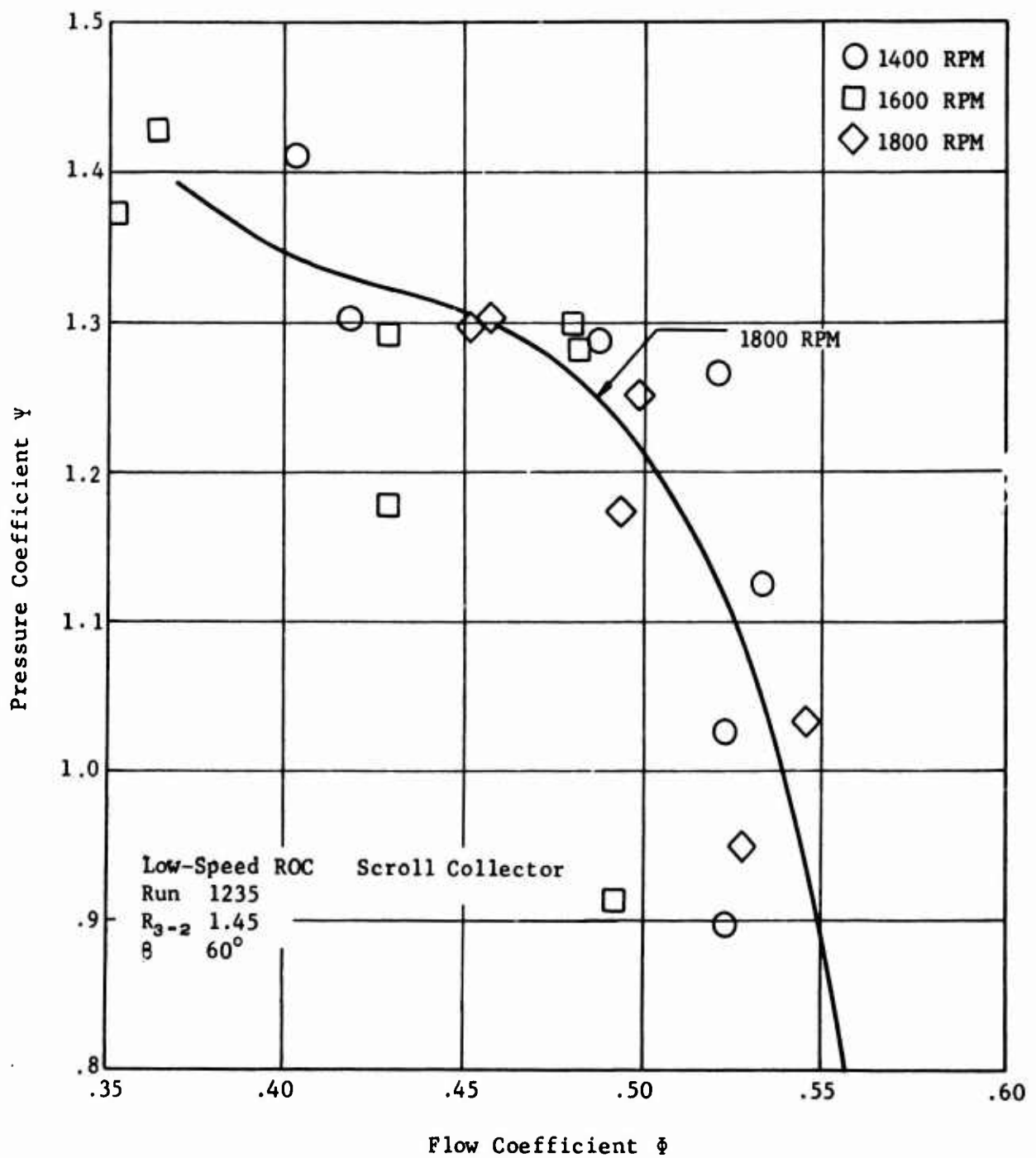


Figure 14. Rotor Discharge Pressure Coefficient, Radial Inflow IGV at 60°, Hub and Housings 1 and 2 Rotating.

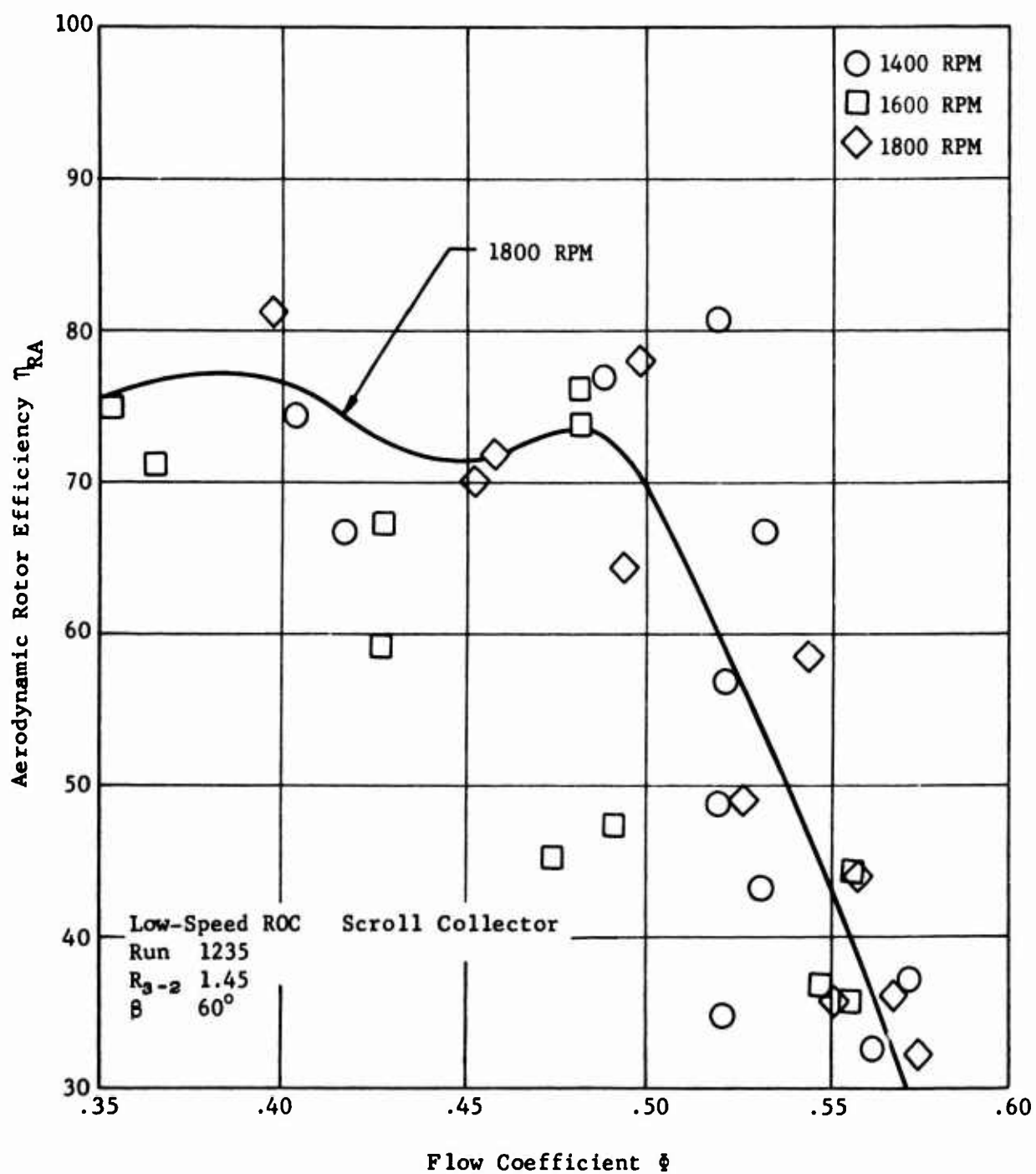


Figure 15. Compressor Efficiency, Radial Inflow IGV at 60° , Hub and Housings 1 and 2 Rotating.

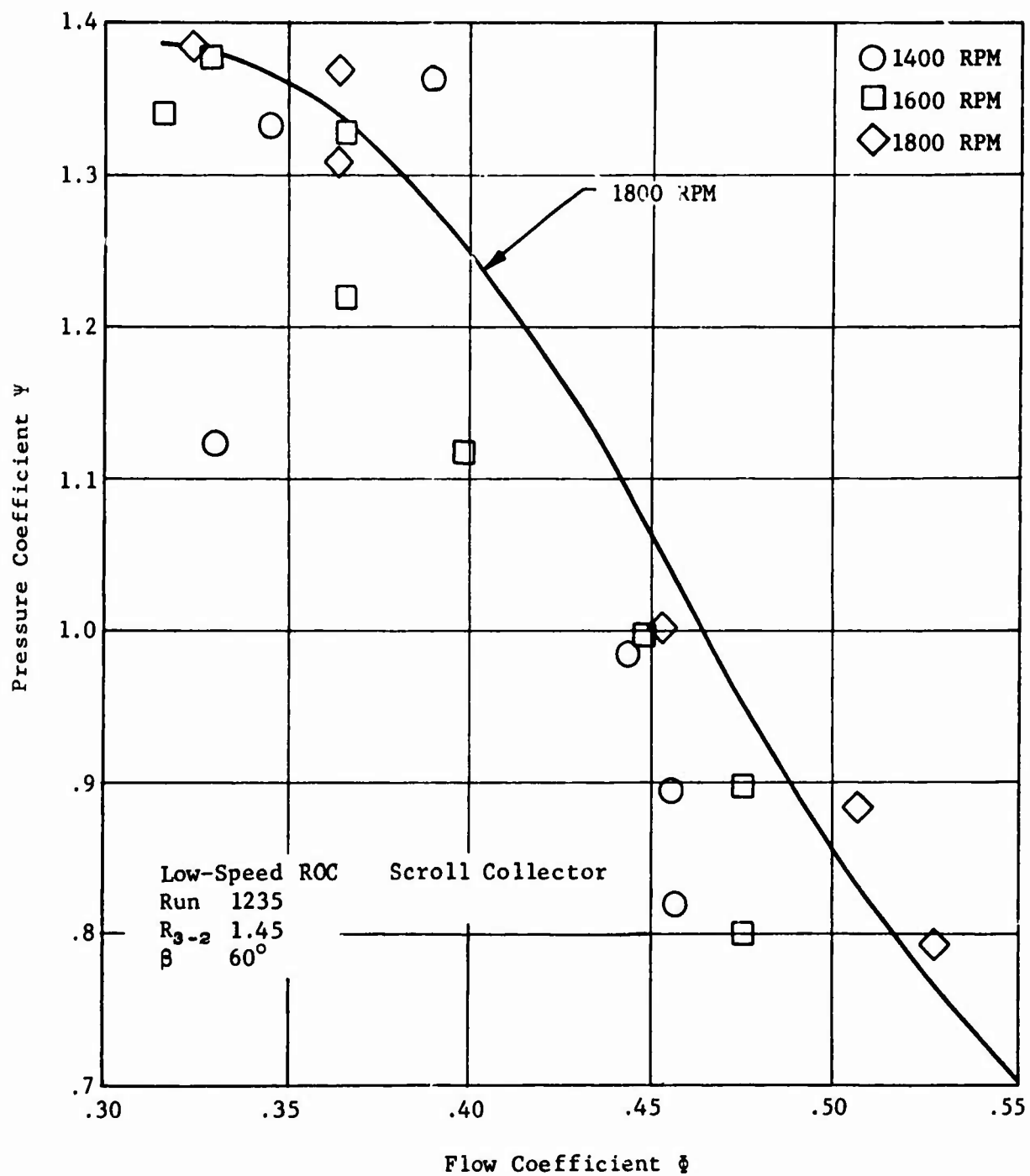


Figure 16. Rotor Discharge Pressure Coefficient, Radial Inflow IGV at 60° , Hub and Housing 2 Rotating.

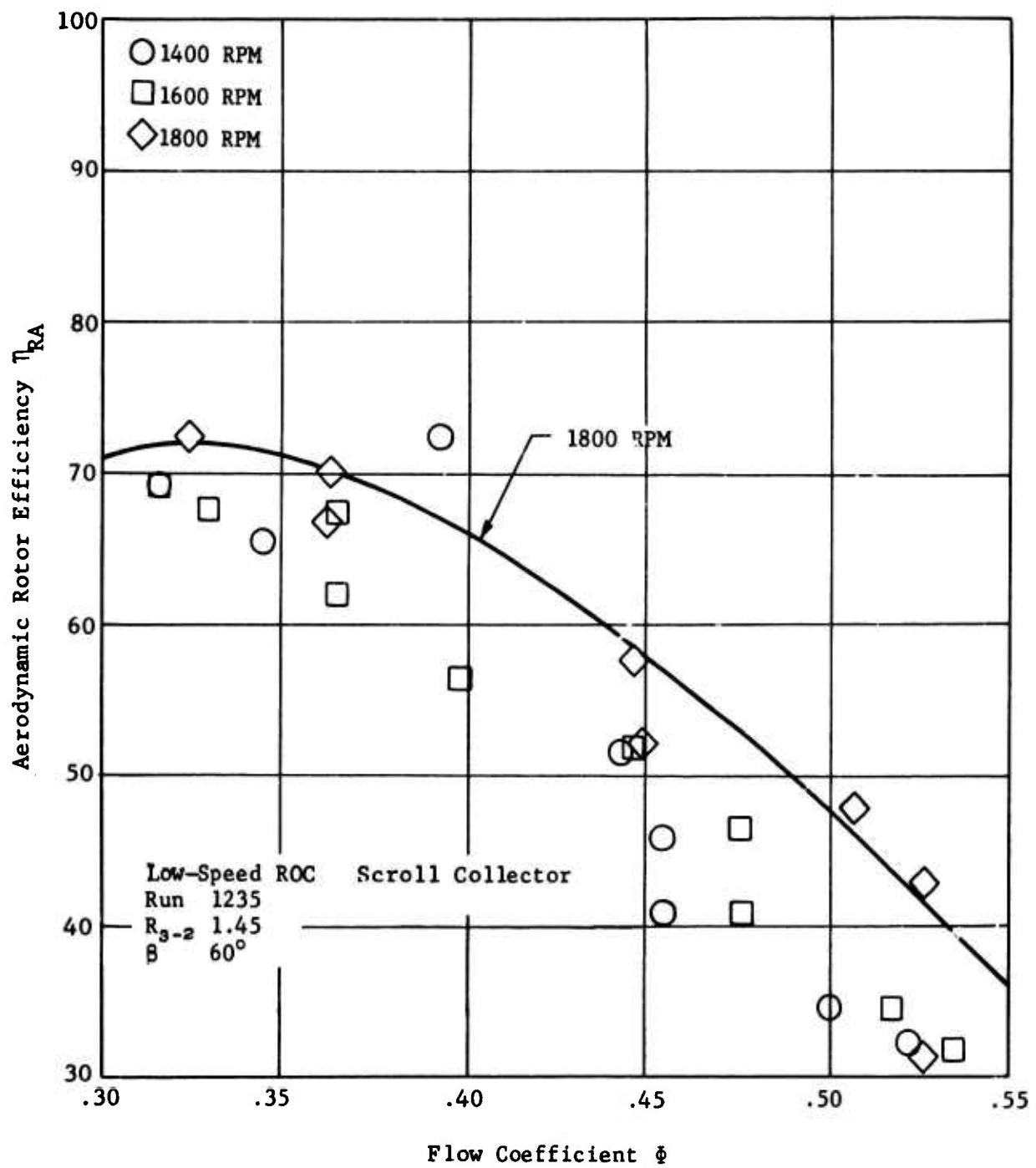


Figure 17. Compressor Efficiency, Radial Inflow IGV at 60° , Hub and Housing 2 Rotating.

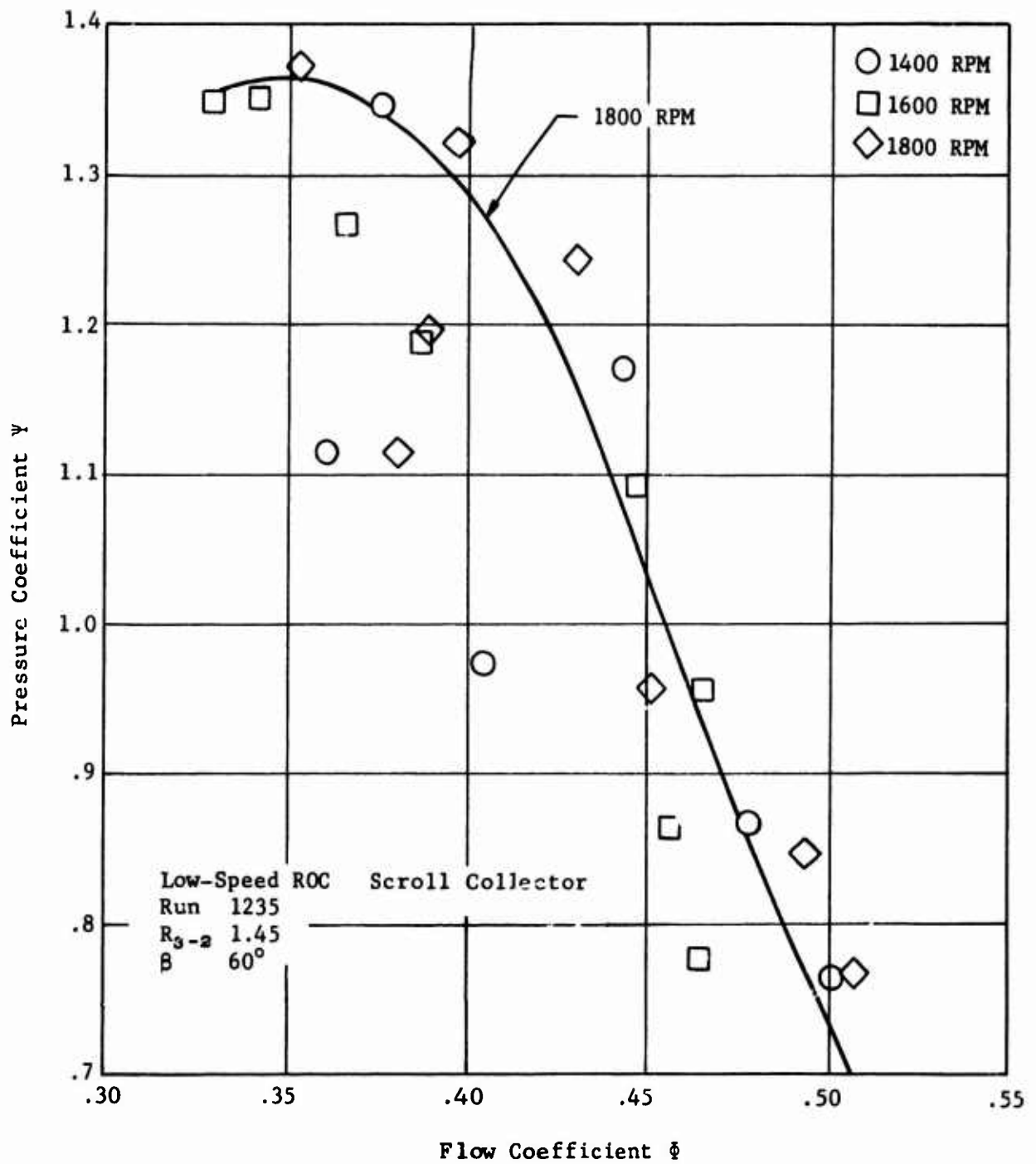


Figure 18. Rotor Discharge Pressure Coefficient, Radial Inflow IGV at 60°, Hub Rotating.

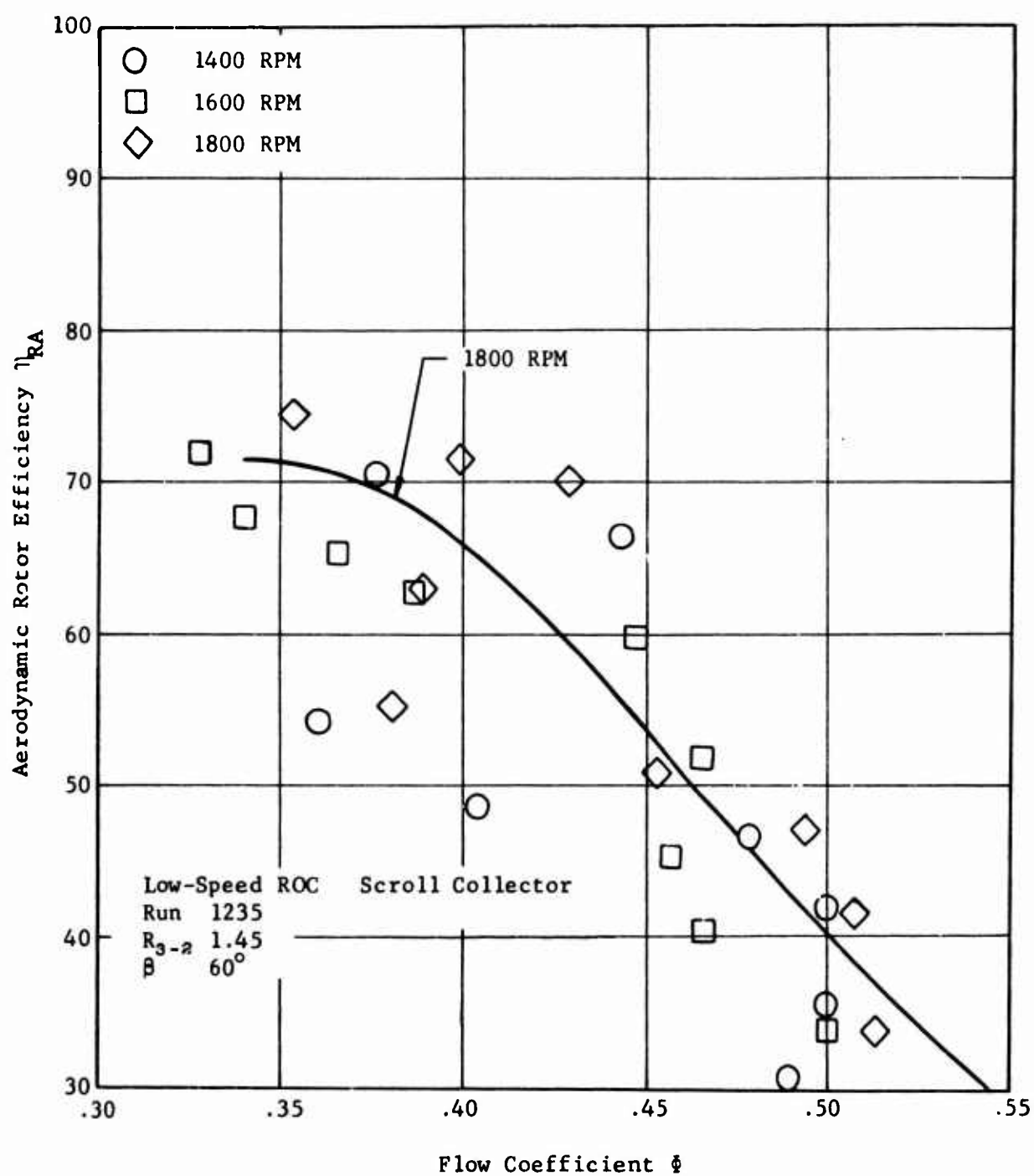


Figure 19. Compressor Efficiency, Radial Inflow IGV at 60°, Hub Rotating.

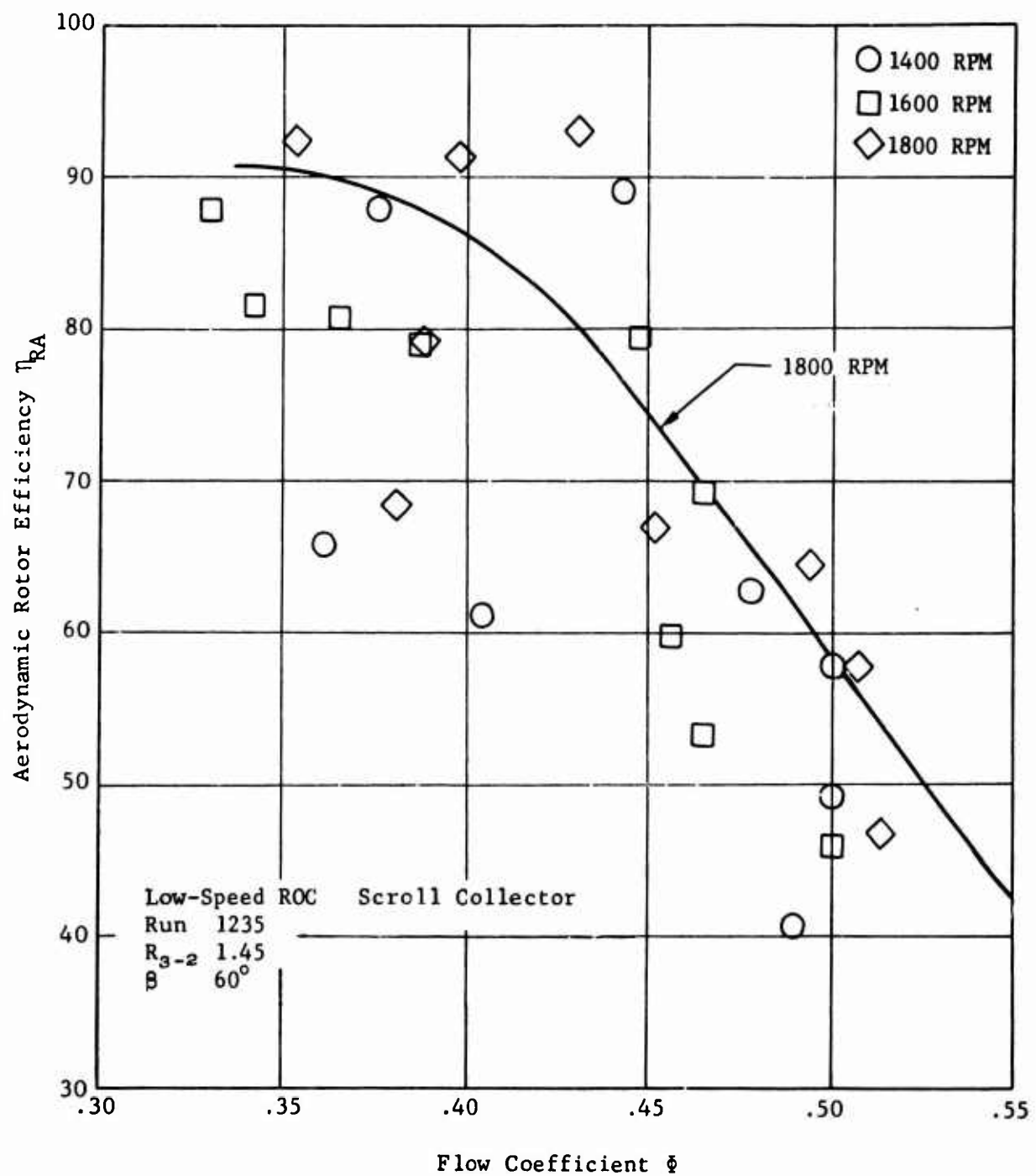


Figure 20. Compressor Efficiency, Radial Inflow IGV at 60° , Hub Rotating.

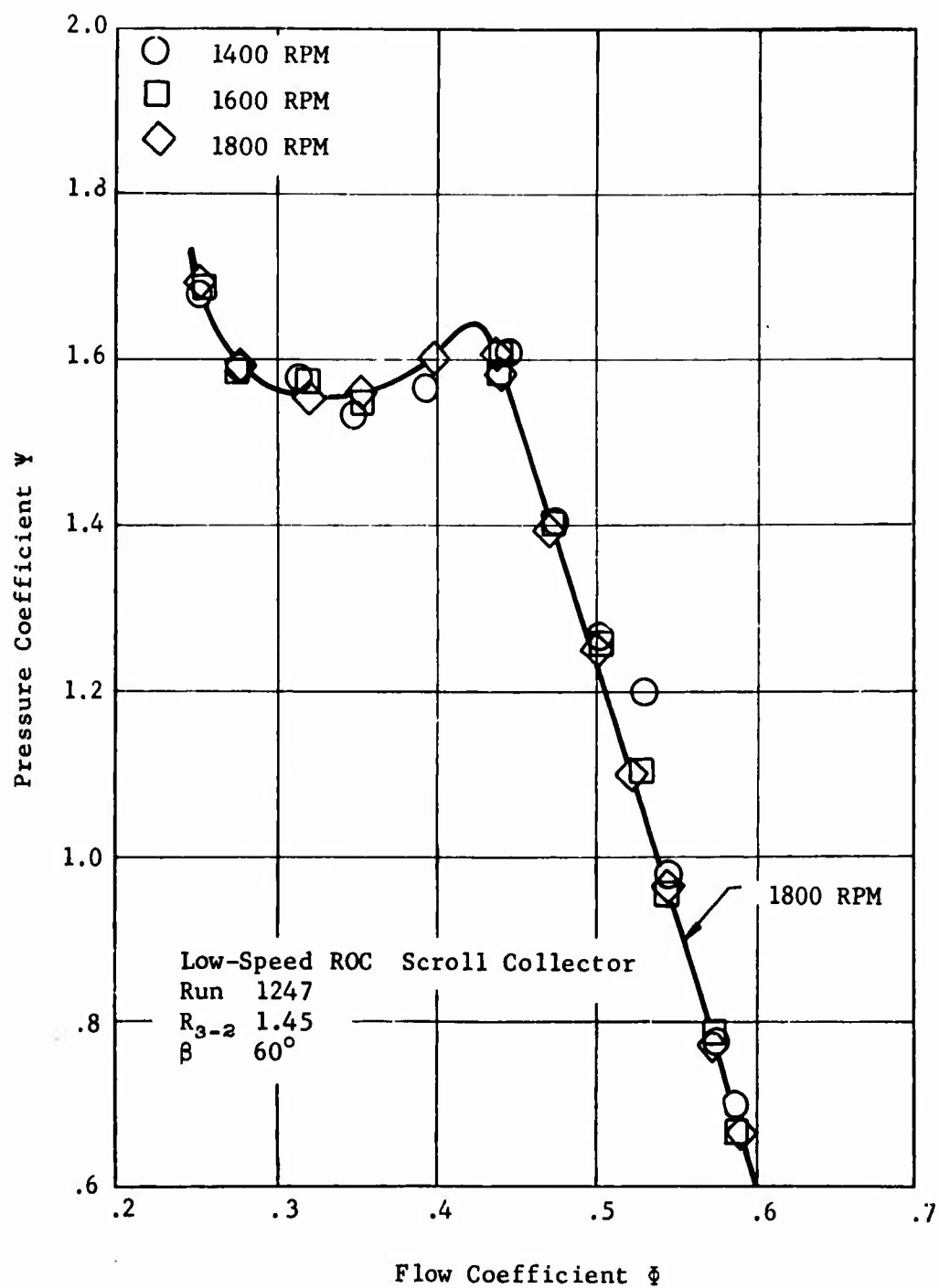


Figure 21 Rotor Discharge Pressure Coefficient, Axial Flow IGV at 60°, Hub and Housings 1 and 2 Rotating.

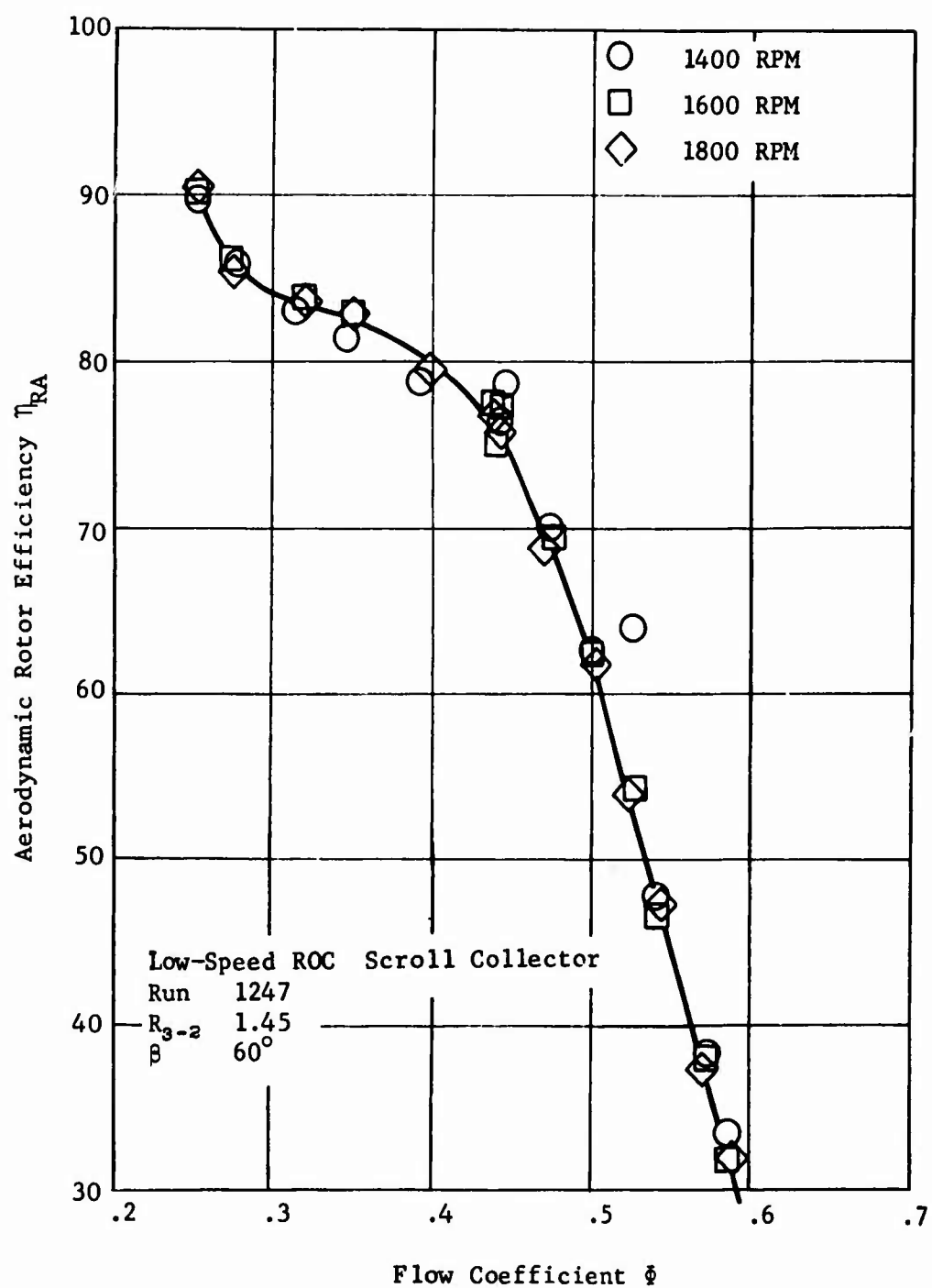


Figure 22. Compressor Efficiency, Axial Flow IGV at 60°, Hub and Housings 1 and 2 Rotating.

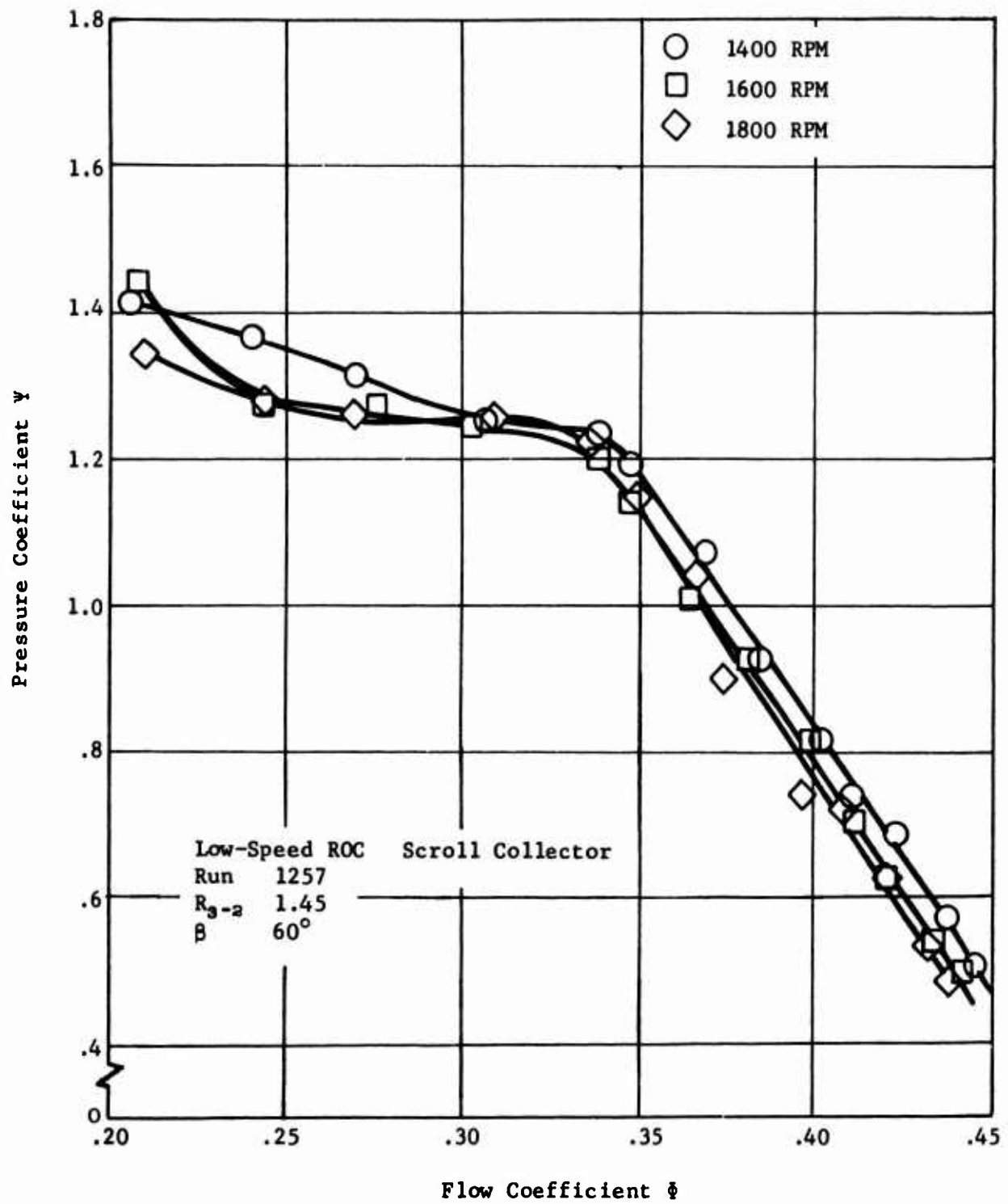


Figure 23. Rotor Discharge Pressure Coefficient, Axial Flow IGV at 60° , Hub and Housing 1 Rotating.

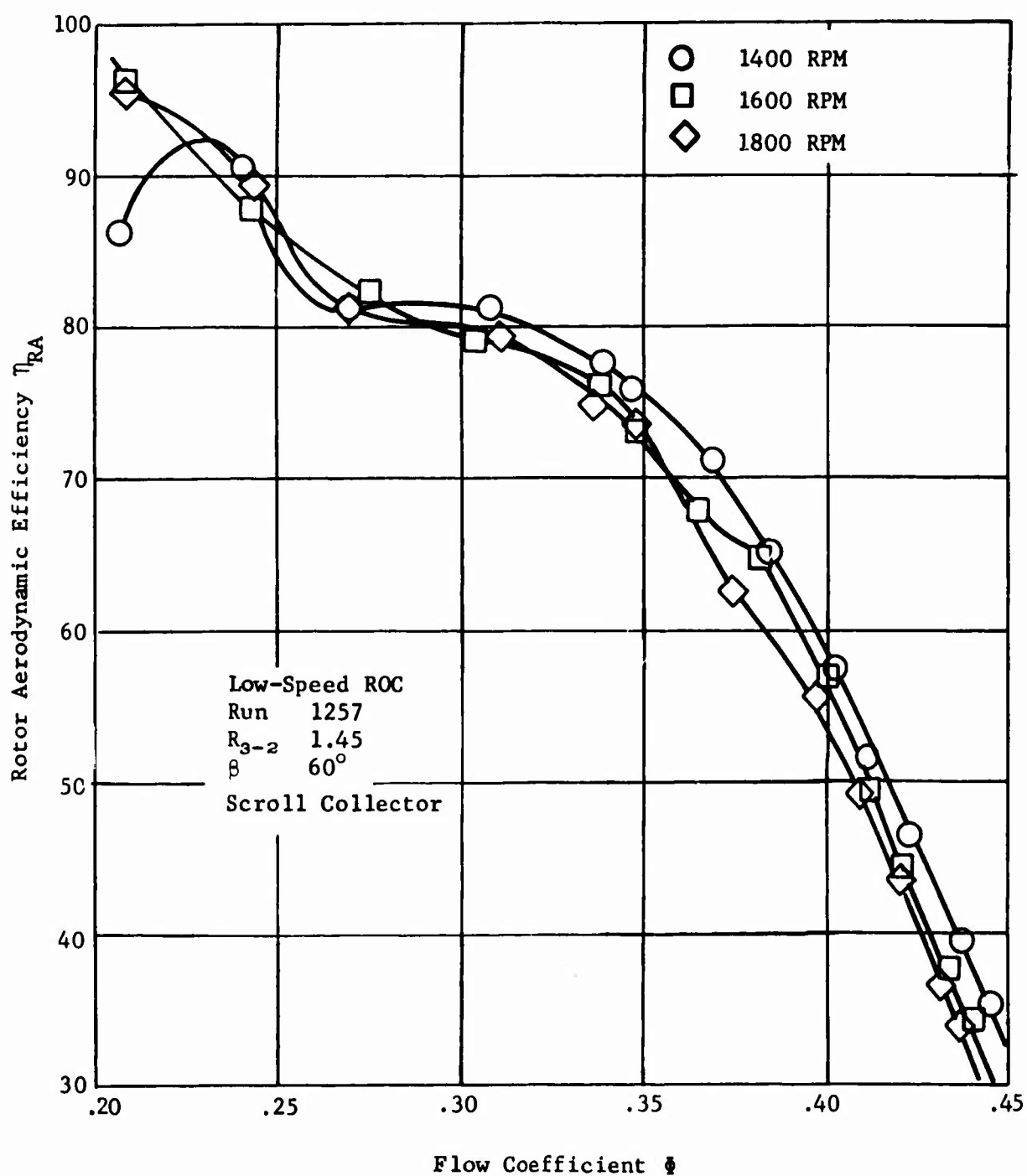


Figure 24. Compressor Efficiency, Axial Flow IGV at 60°, Hub and Housing 1 Rotating.

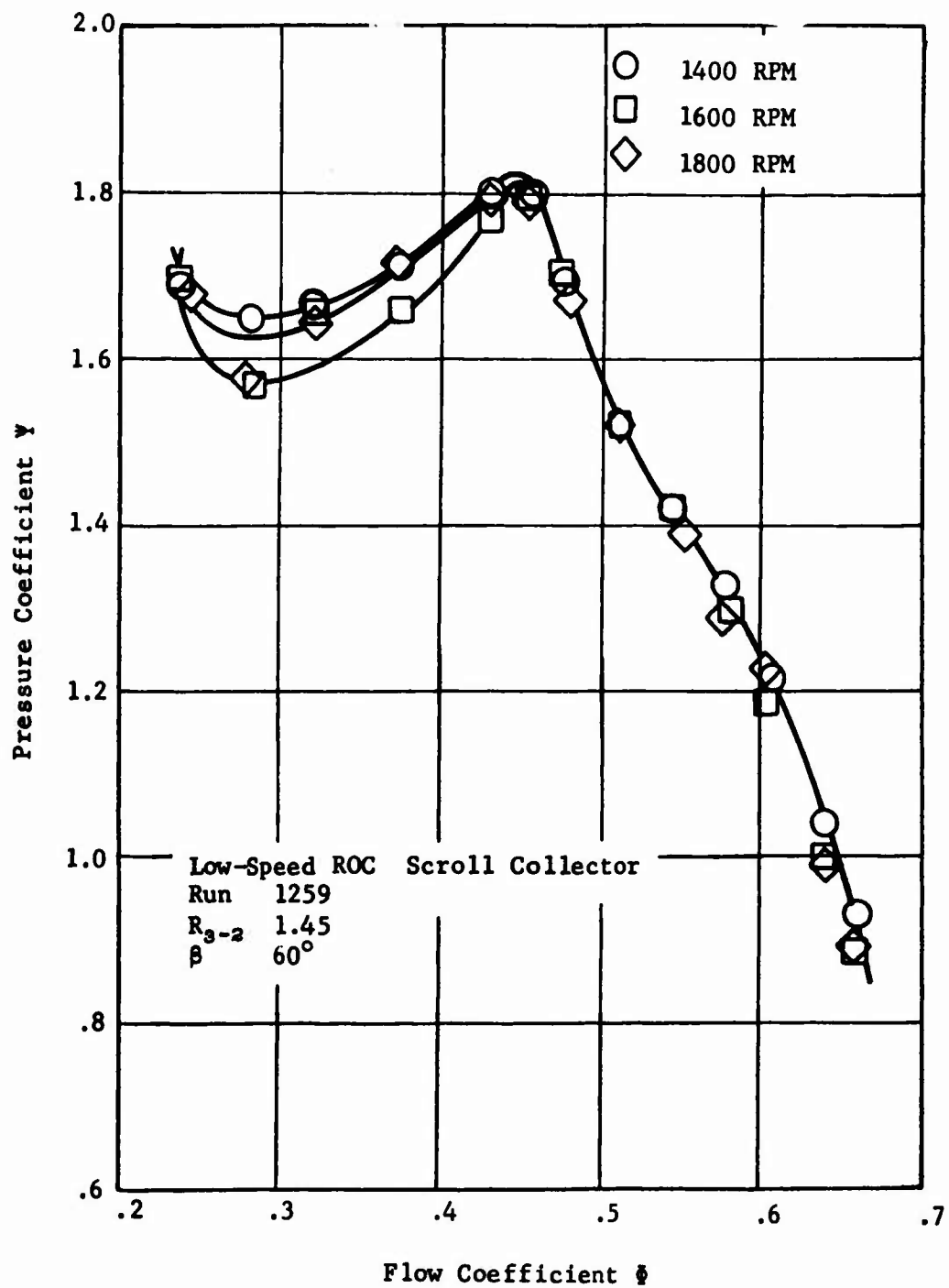


Figure 25. Rotor Discharge Pressure Coefficient, Axial Flow IGV at 50°, Hub and Housing 1 Rotating.

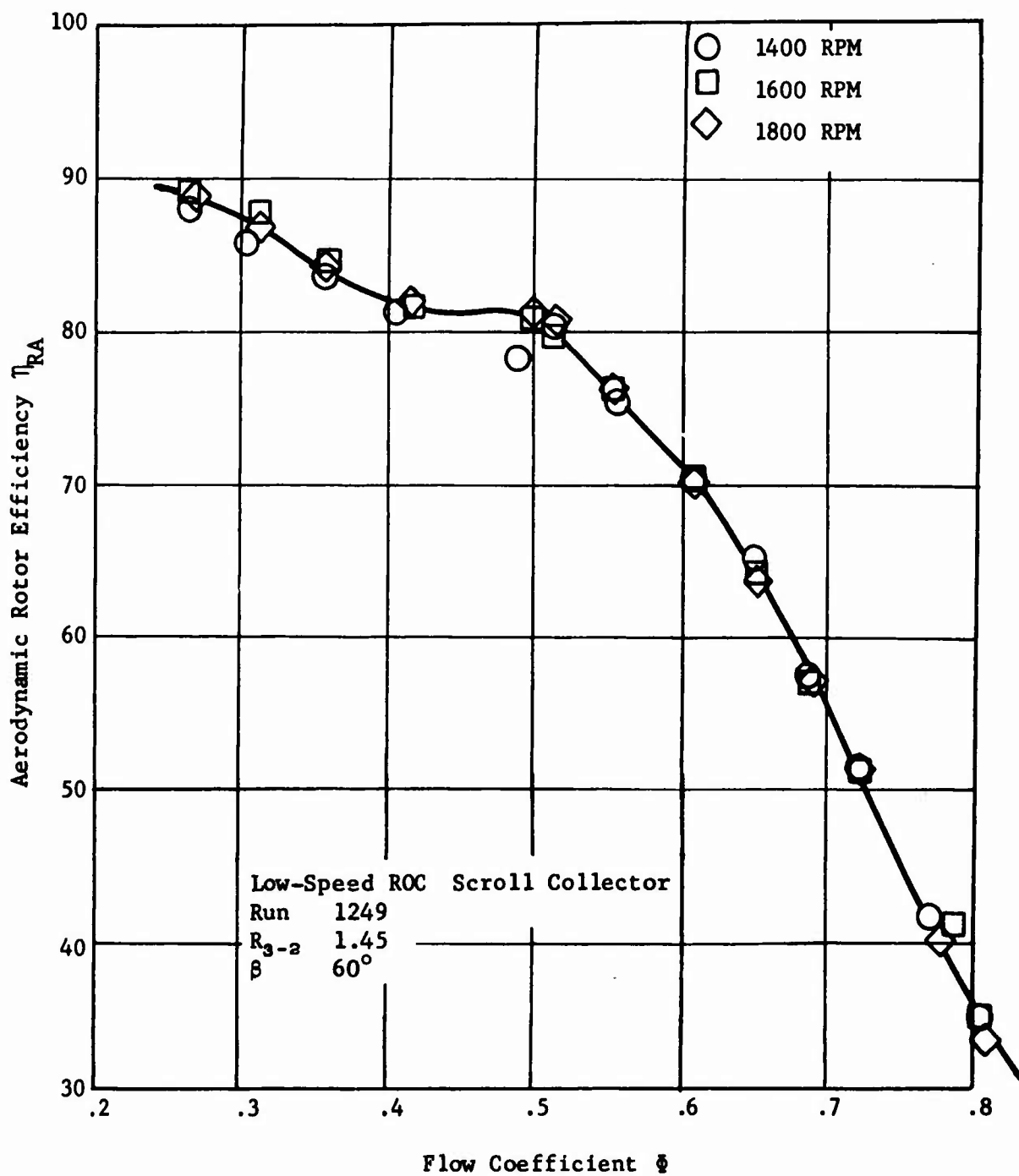


Figure 26. Compressor Efficiency, Axial Flow IGV at 50°, Hub and Housing 1 Rotating.

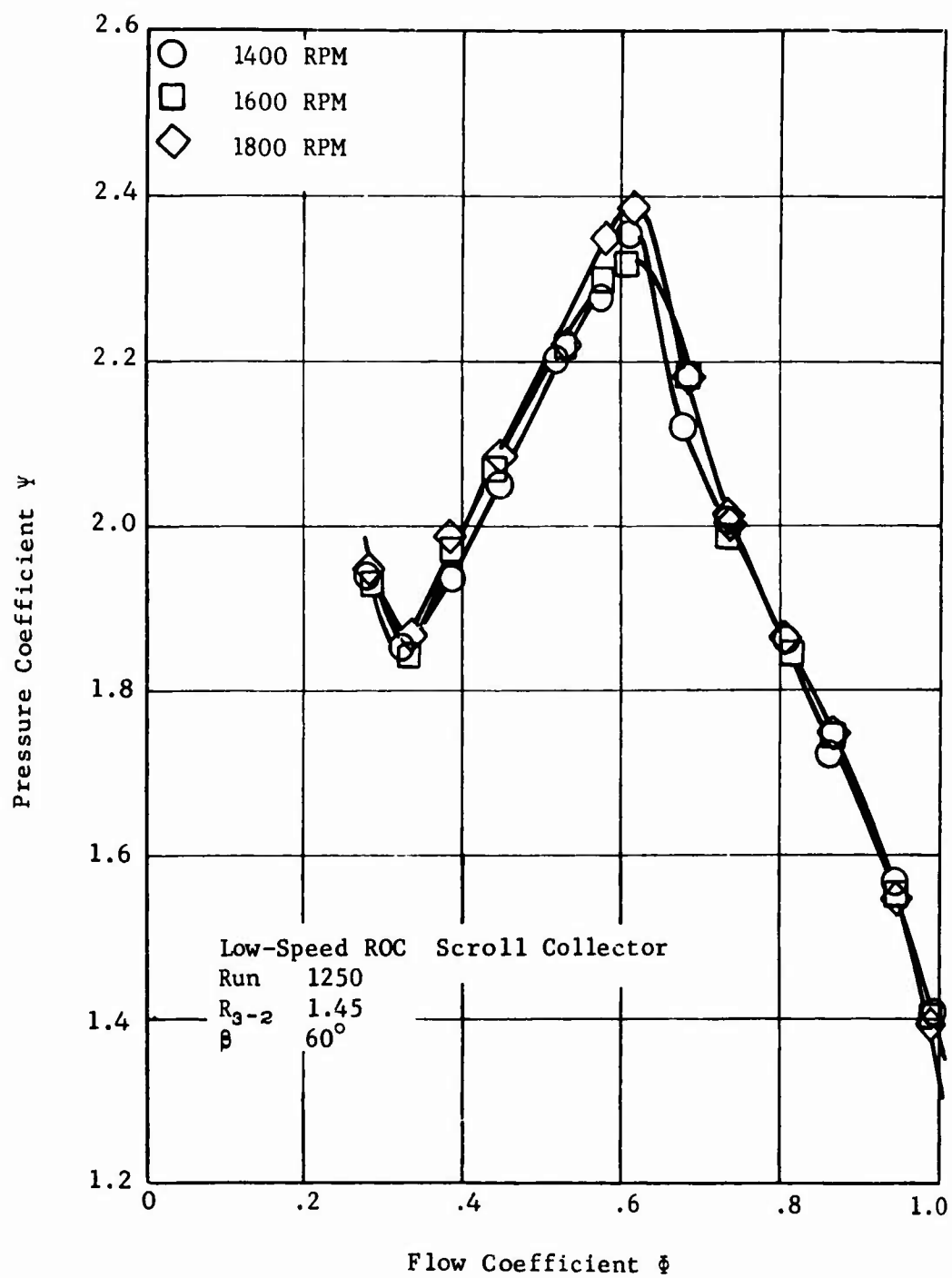


Figure 27. Rotor Discharge Pressure Coefficient, Axial Flow IGV at 35° , Hub and Housing 1 Rotating.

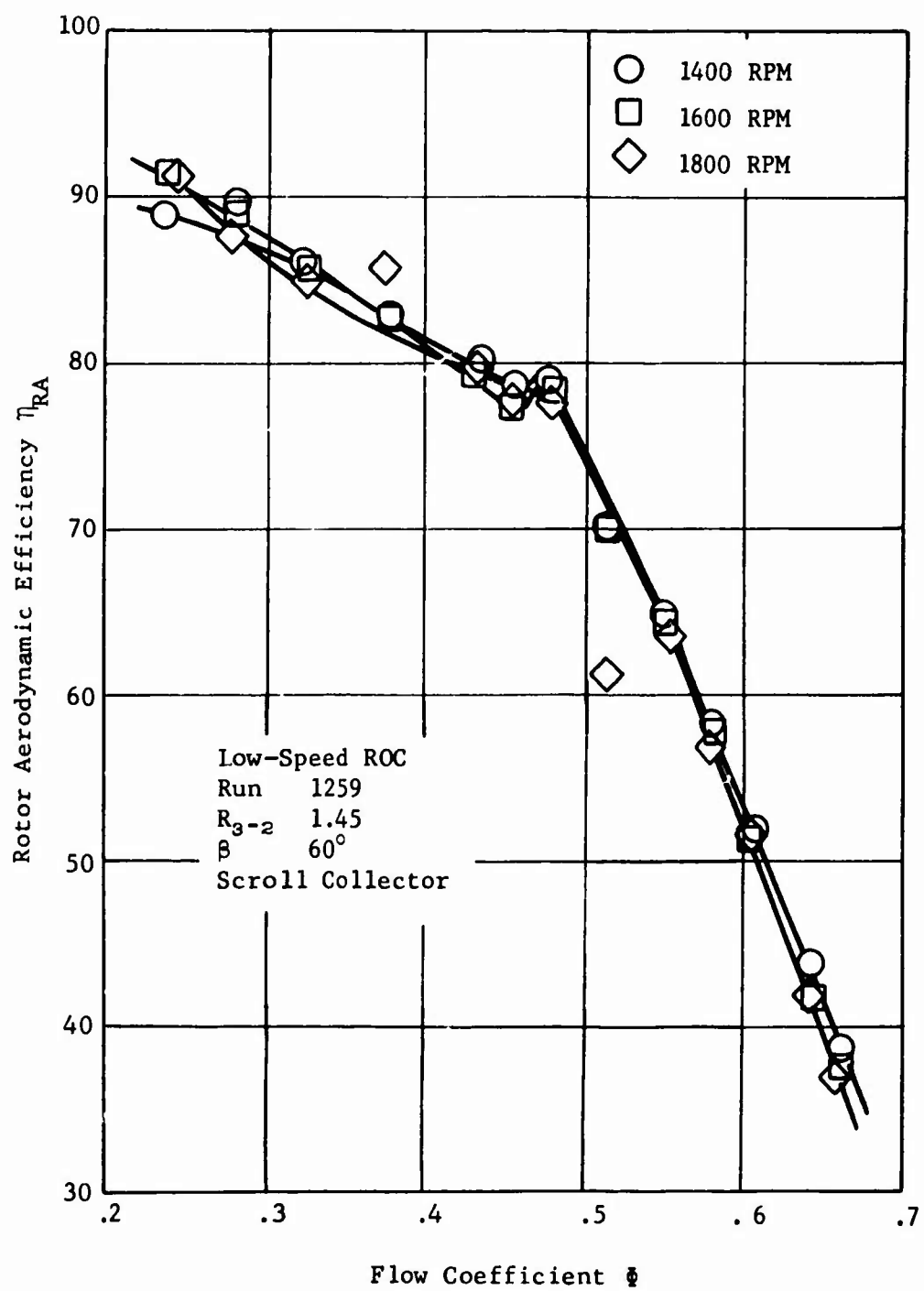


Figure 28. Compressor Efficiency, Axial Flow IGV at 50°, Hub and Housing 1 Rotating.

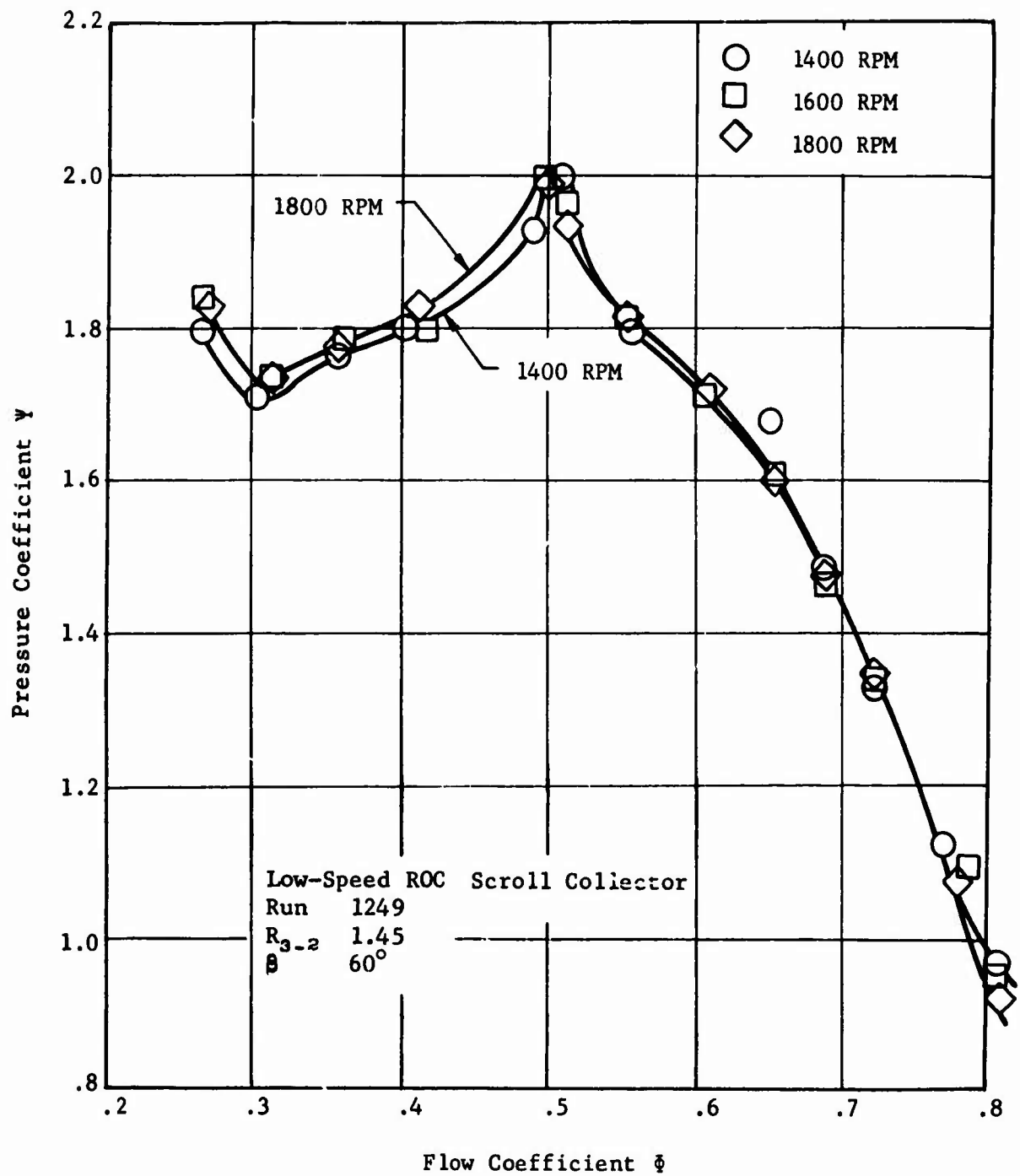


Figure 29. Rotor Discharge Pressure Coefficient, Axial Flow IGV at 50°, Hub and Housing 1 Rotating.

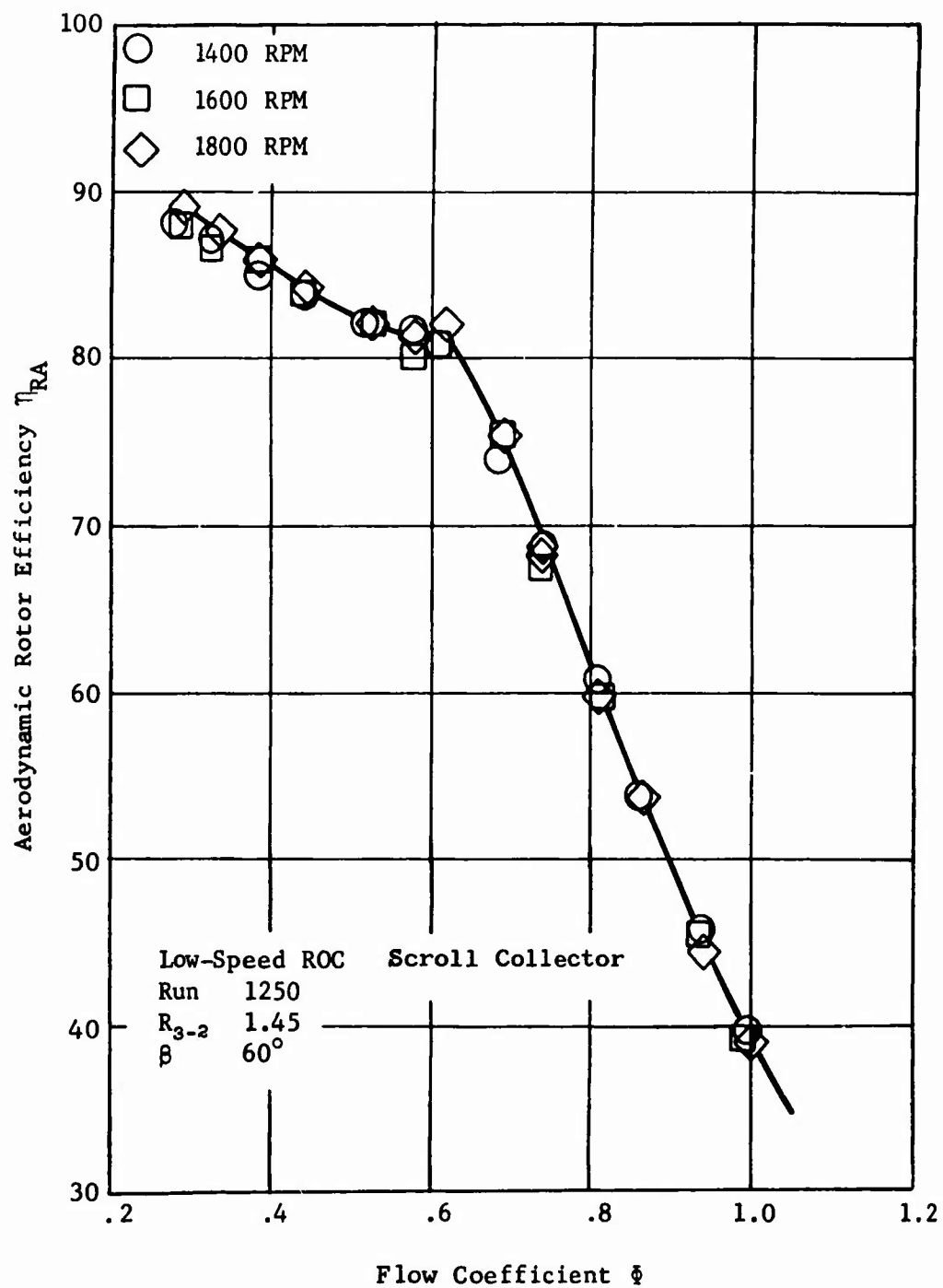


Figure 30. Compressor Efficiency, Axial Flow IGV at 35°, Hub and Housing 1 Rotating.

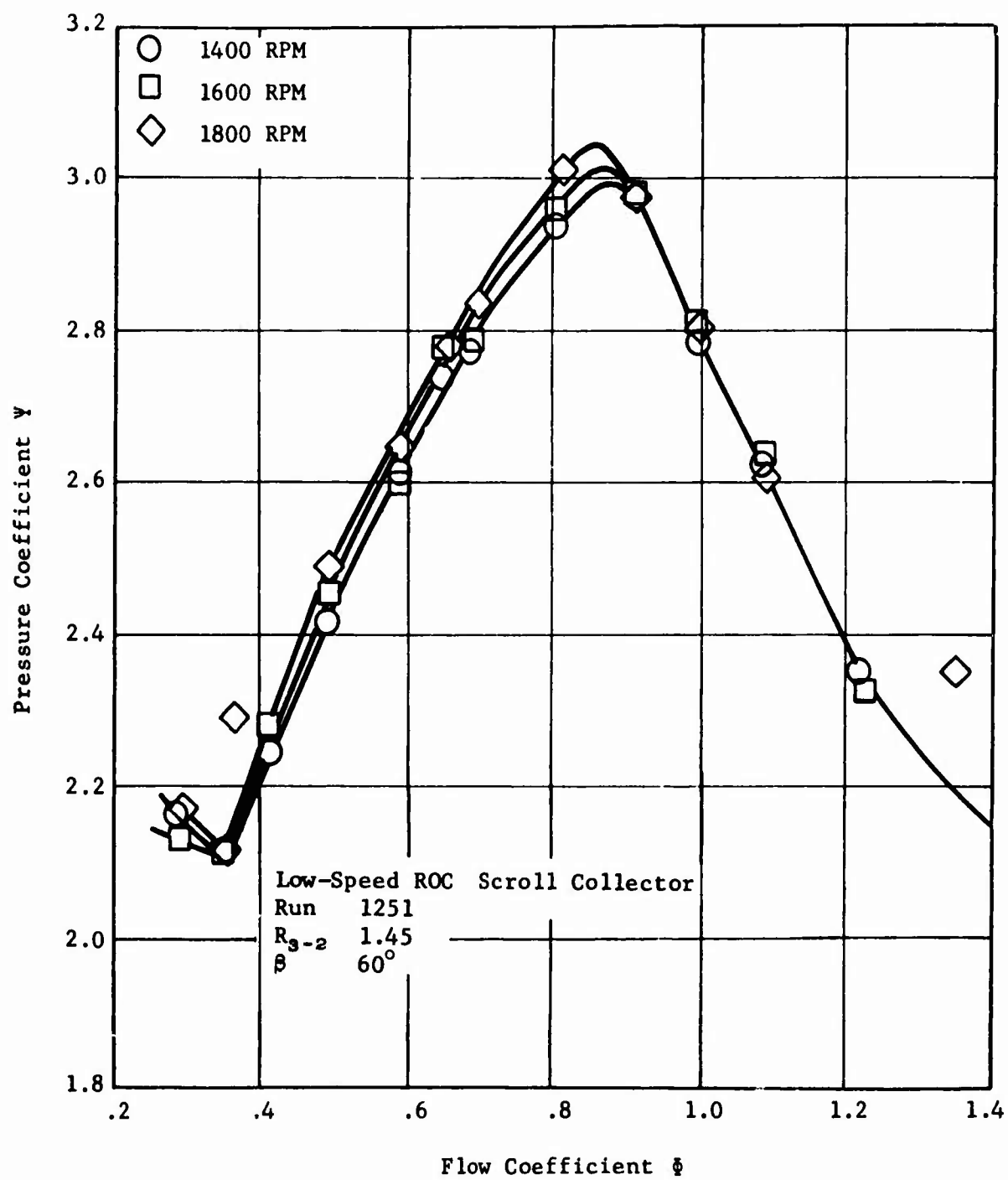


Figure 31. Rotor Discharge Pressure Coefficient, Axial Flow IGV at 18.5°, Hub and Housing 1 Rotating.

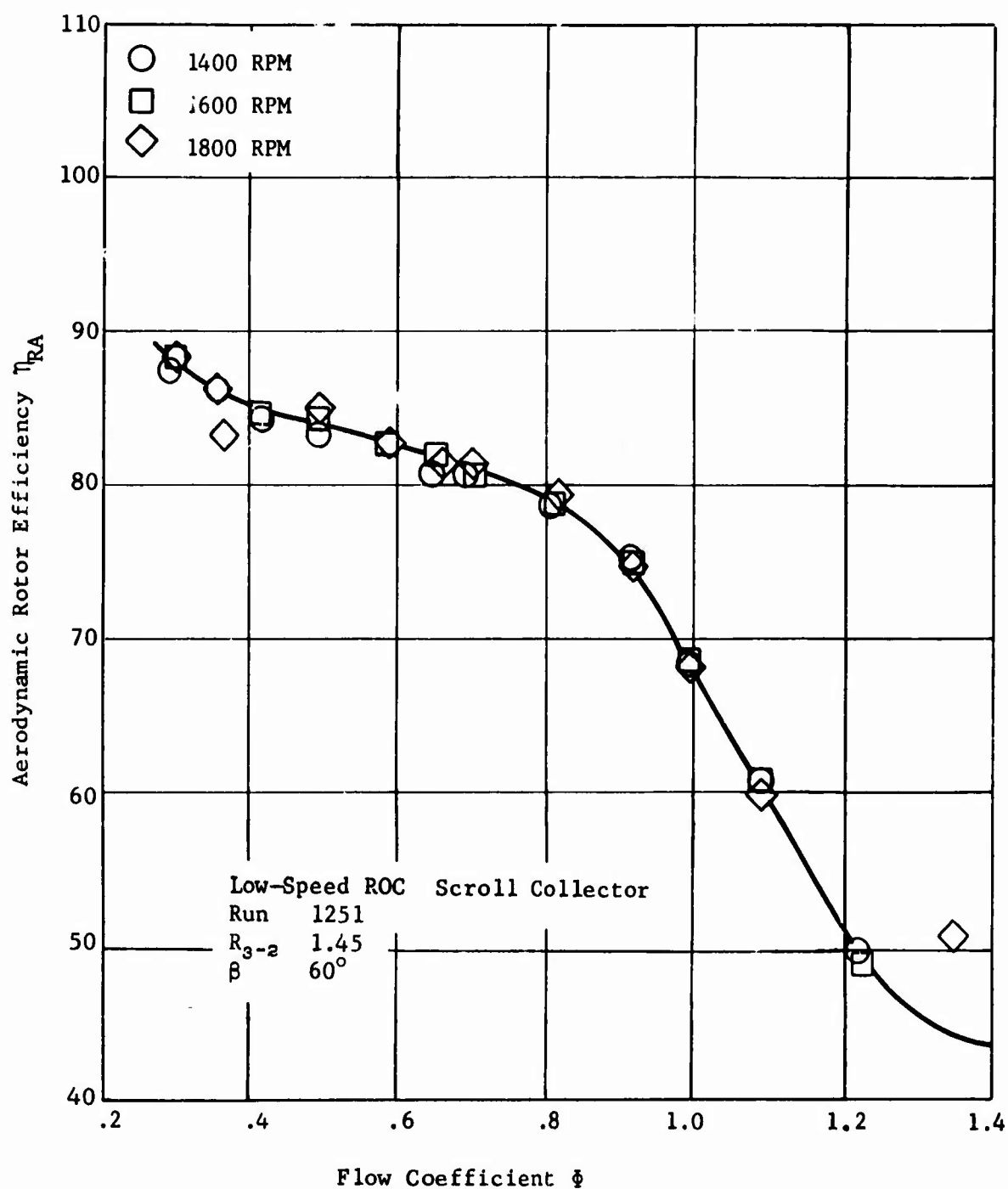


Figure 32. Compressor Efficiency, Axial Flow IGV at 18.5° , Hub and Housing 1 Rotating.

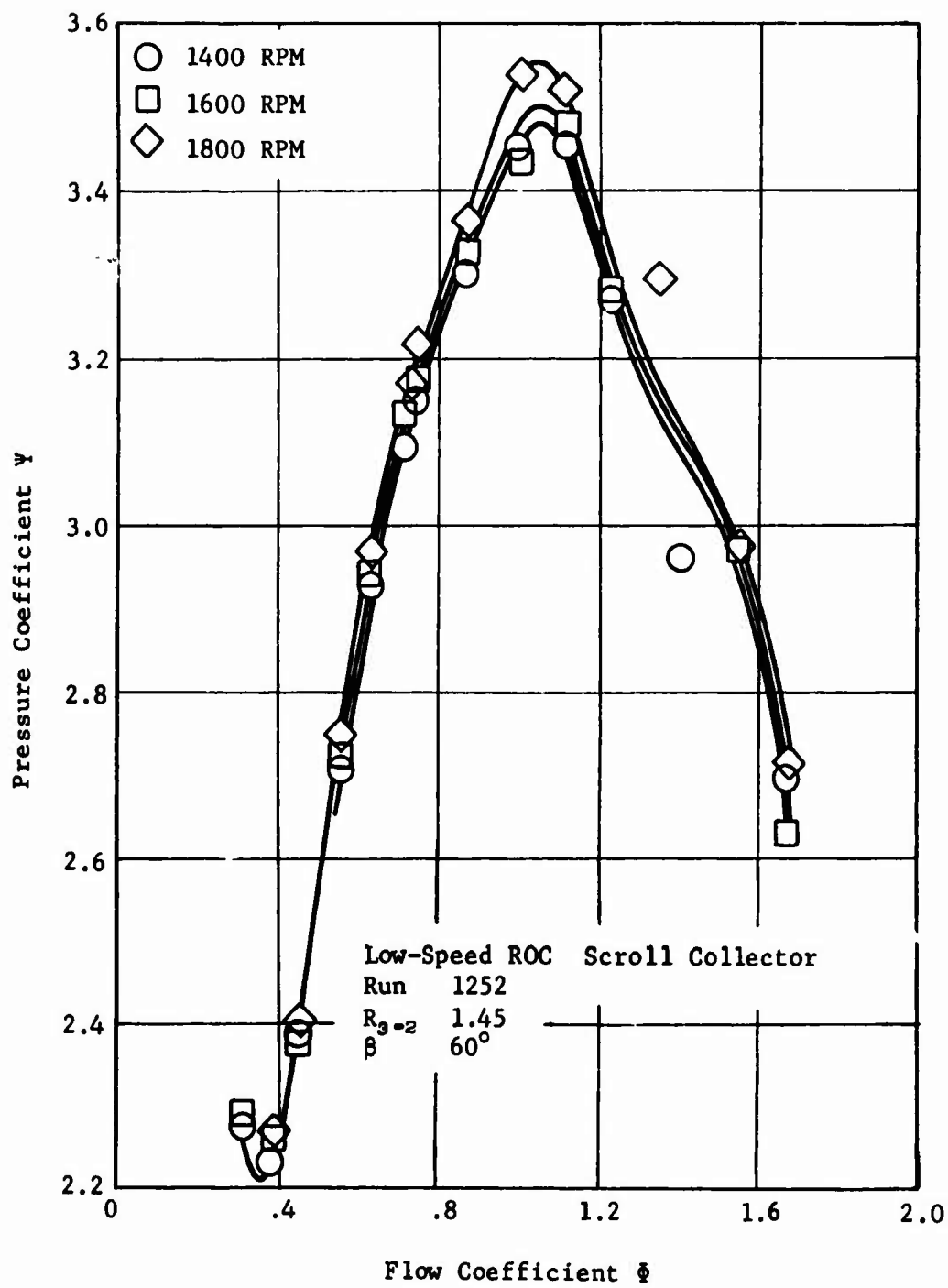


Figure 33. Rotor Discharge Pressure Coefficient, Axial Flow IGV at 0° , Hub and Housing 1 Rotating.

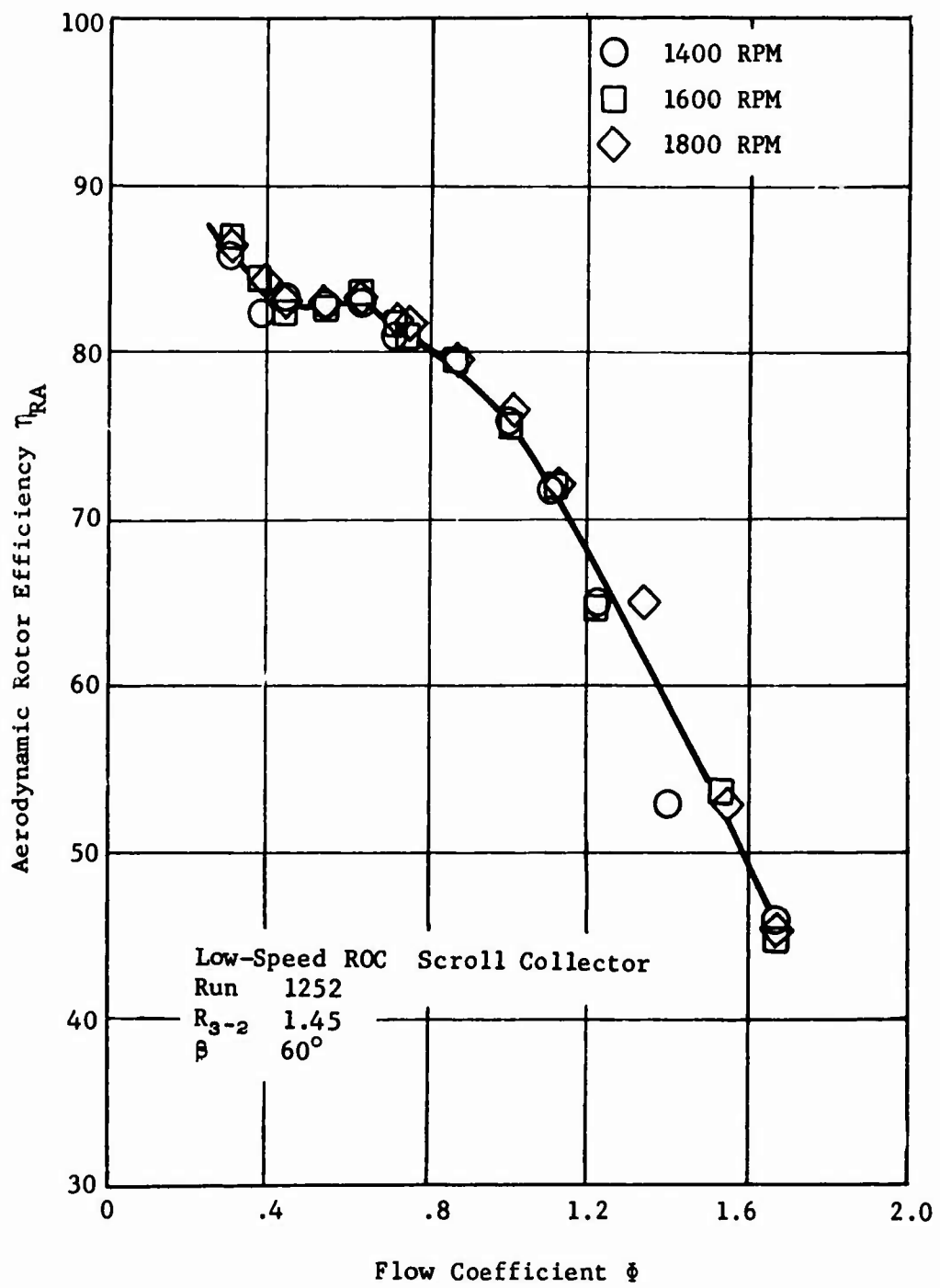


Figure 34. Compressor Efficiency, Axial Flow IGV at 0°, Hub and Housing 1 Rotating.

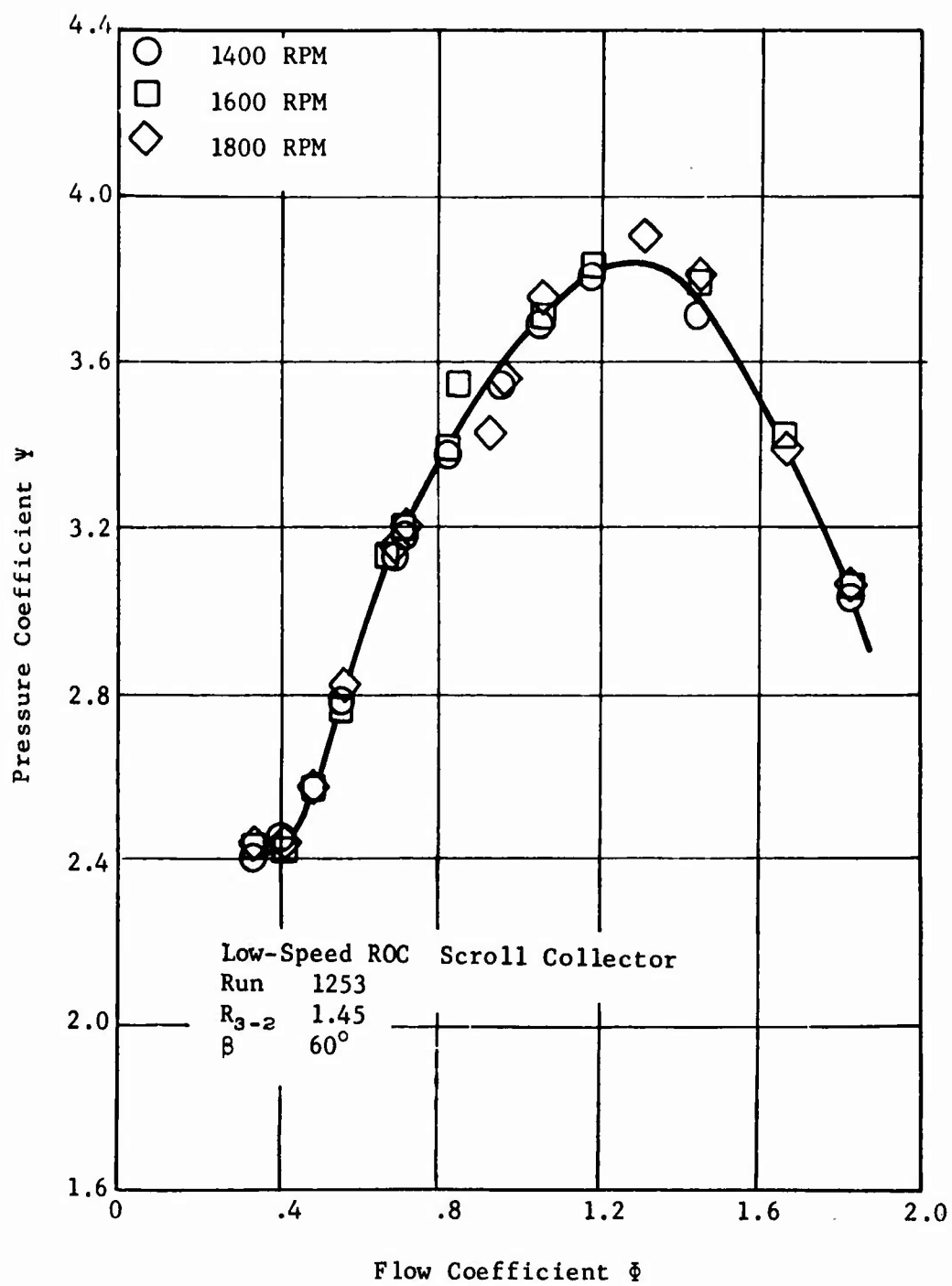


Figure 35. Rotor Discharge Pressure Coefficient, Axial Flow IGV at -18.5°, Hub and Housing 1 Rotating.

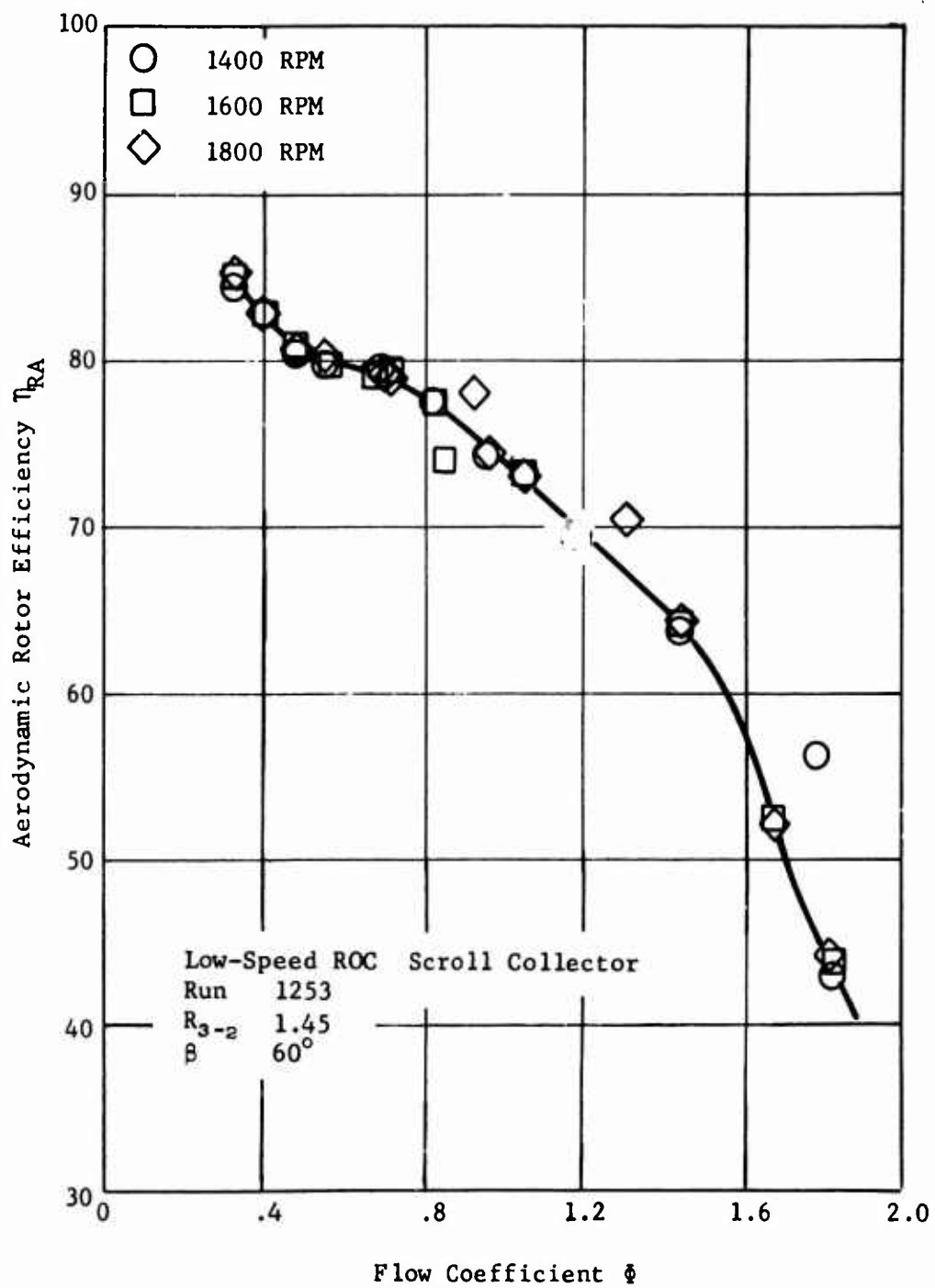


Figure 36. Compressor Efficiency, Axial Flow IGV at -18.5° , Hub and Housing 1 Rotating.

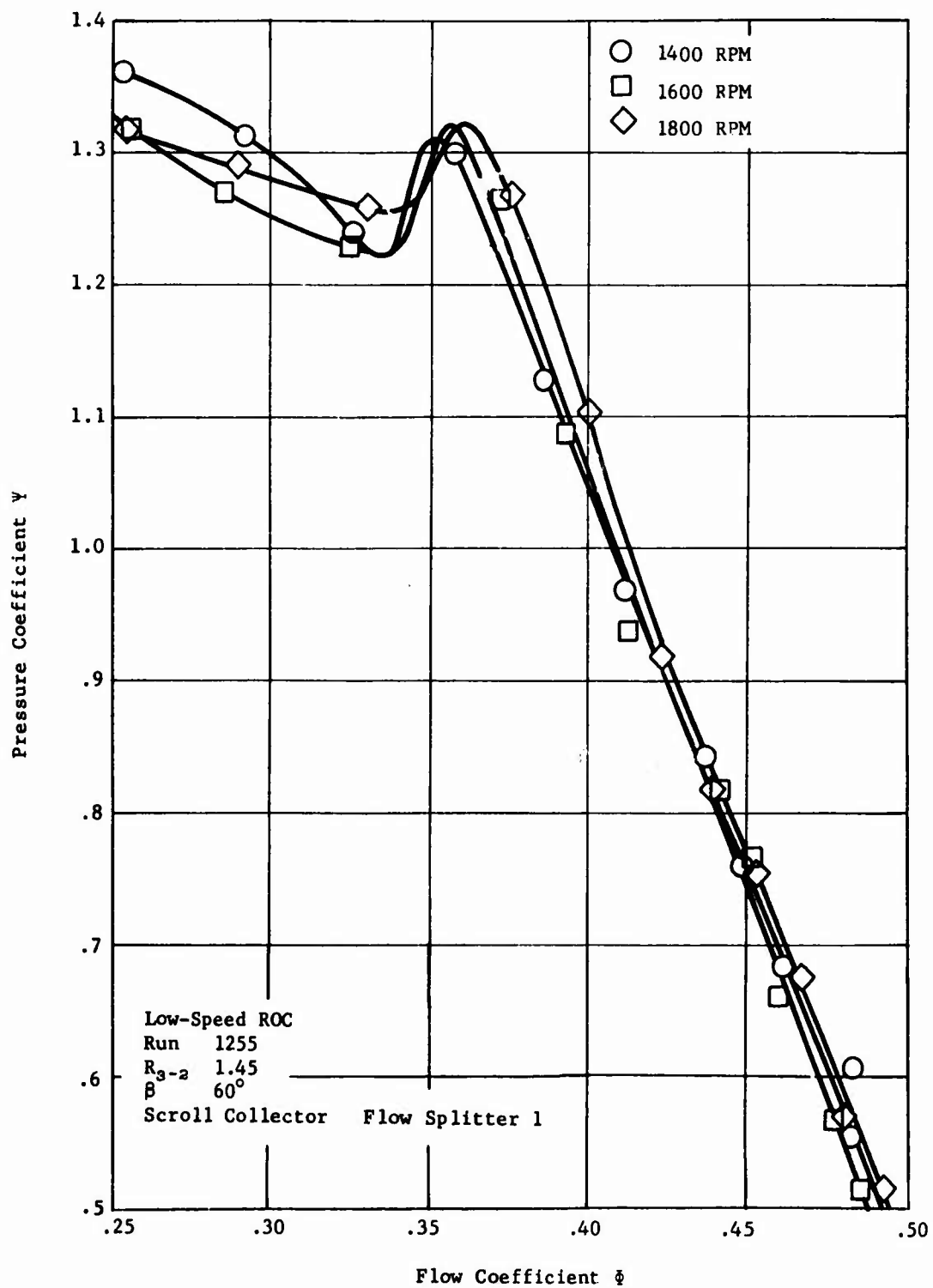


Figure 37. Rotor Discharge Pressure Coefficient, Radial Inflow IGV at 60°, Hub and Housings 1 and 2 Rotating.

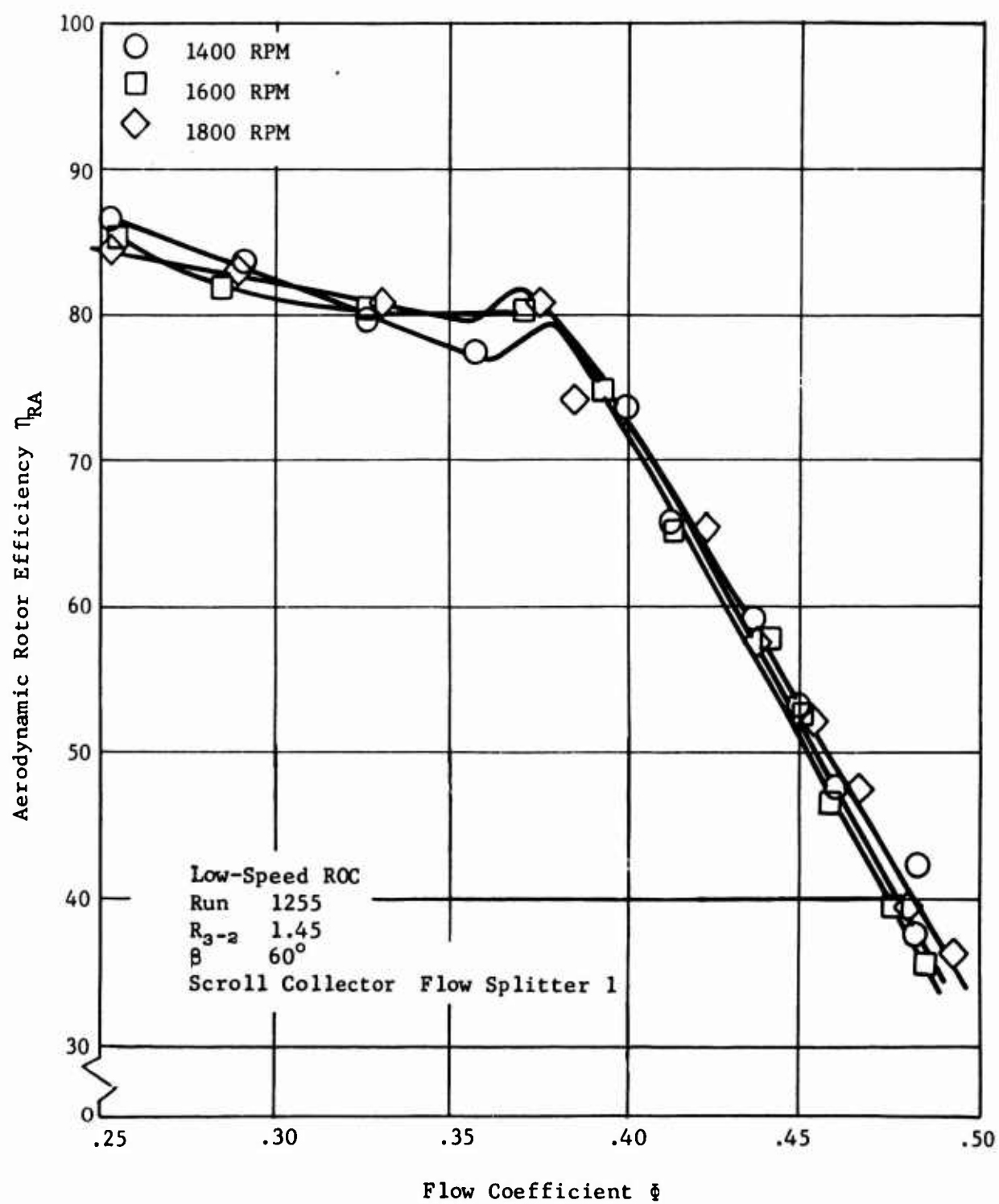


Figure 38. Compressor Efficiency, Radial Inflow IGV at 60° , Hub and Housings 1 and 2 Rotating.

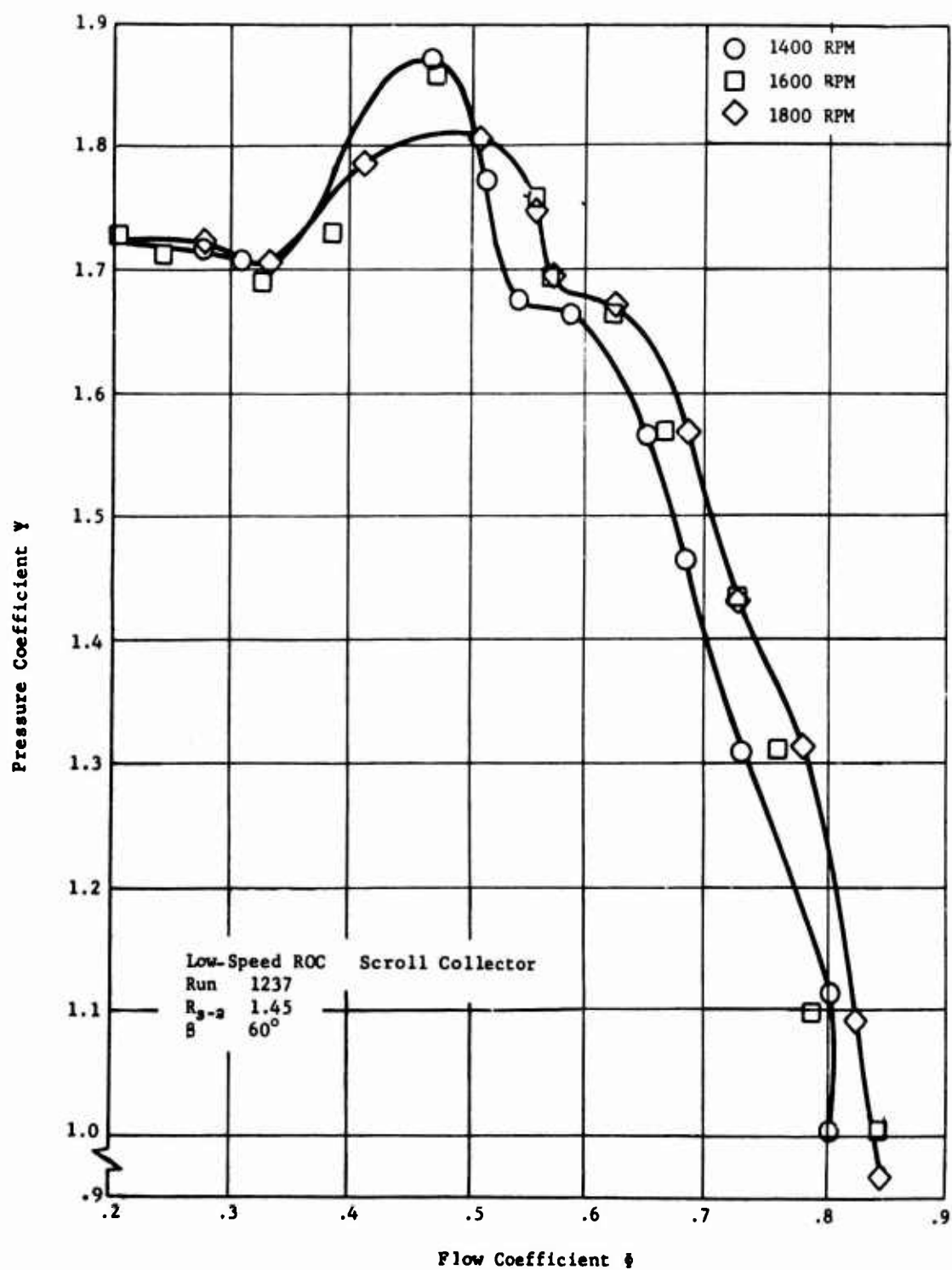


Figure 39. Rotor Discharge Pressure Coefficient, Radial Inflow IGV at 50°, Hub and Housings 1 and 2 Rotating.

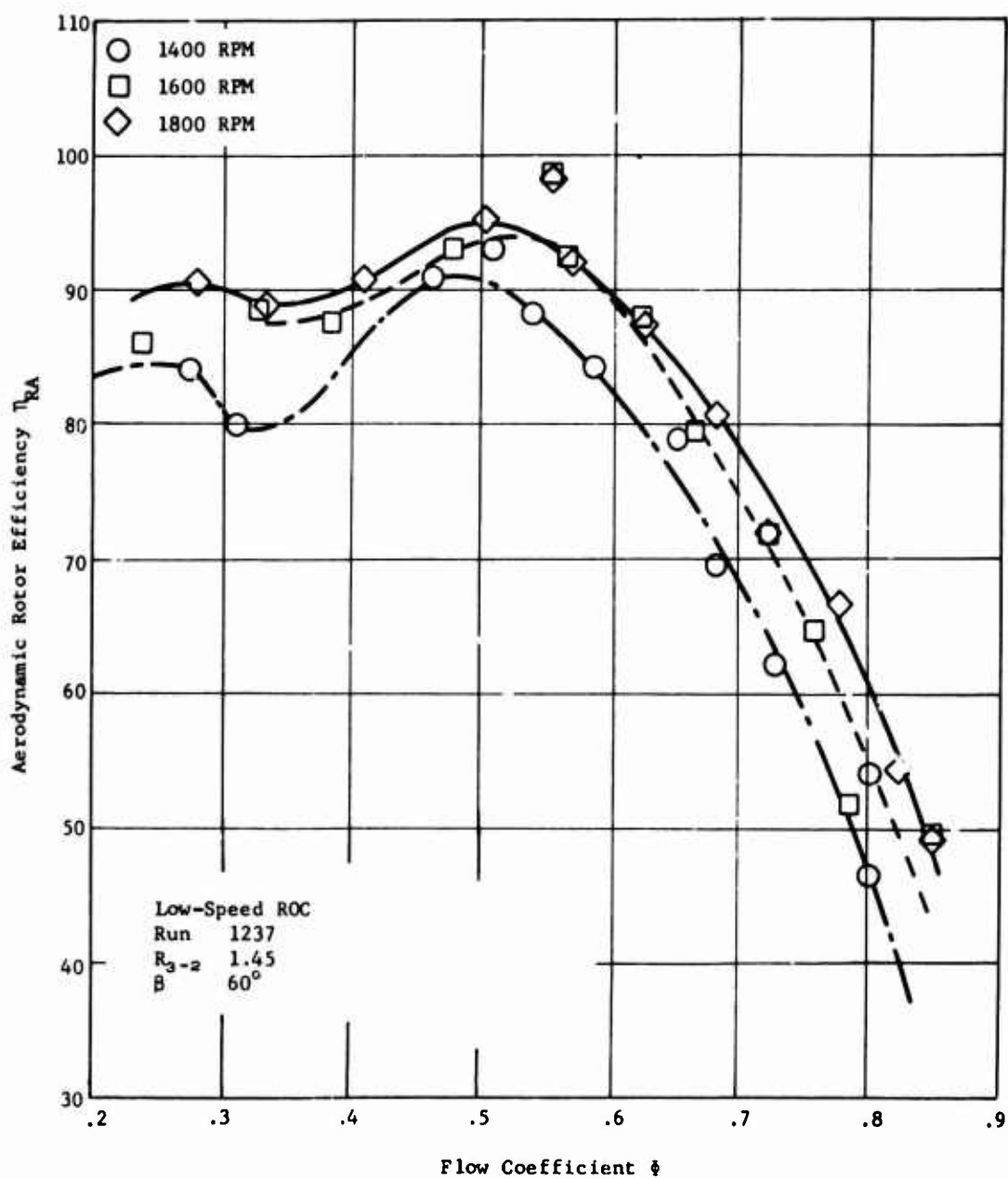


Figure 40. Compressor Efficiency, Radial Inflow IGV at 50°, Hub and Housings 1 and 2 Rotating.

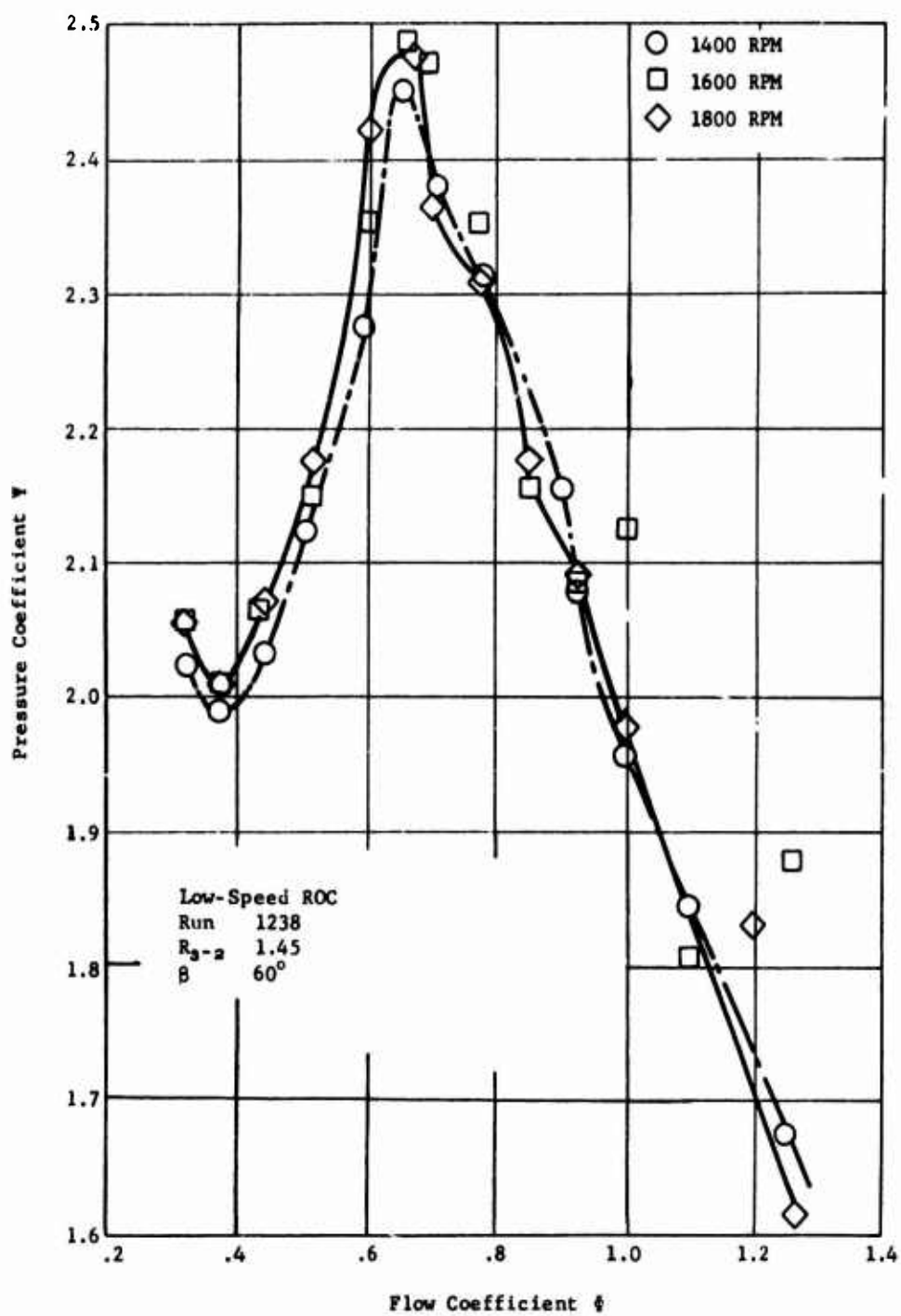


Figure 41. Rotor Discharge Pressure Coefficient, Radial Inflow IGV at 35°, Hub and Housings 1 and 2 Rotating.

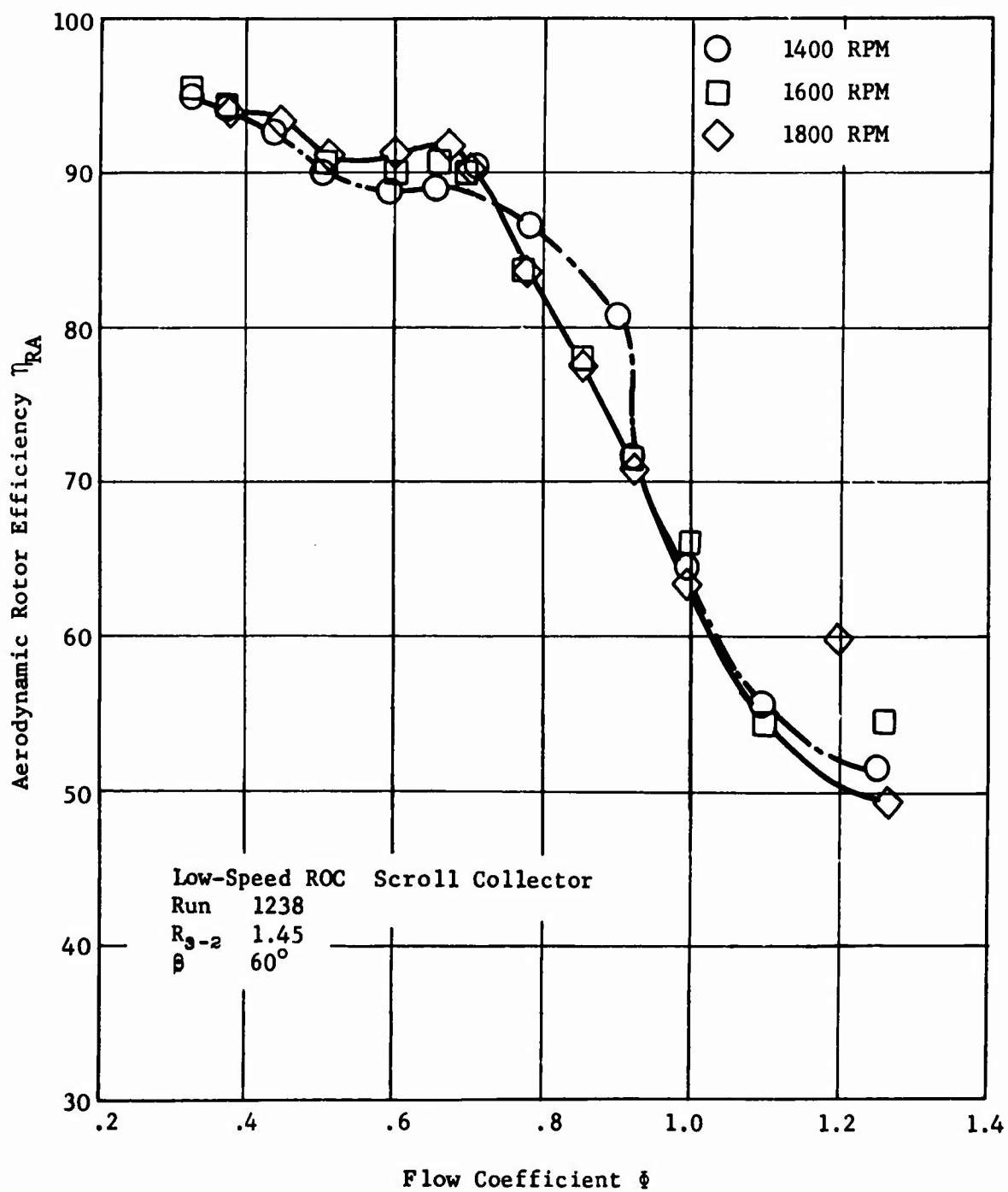


Figure 42. Compressor Efficiency, Radial Inflow IGV at 35°, Hub and Housings 1 and 2 Rotating.

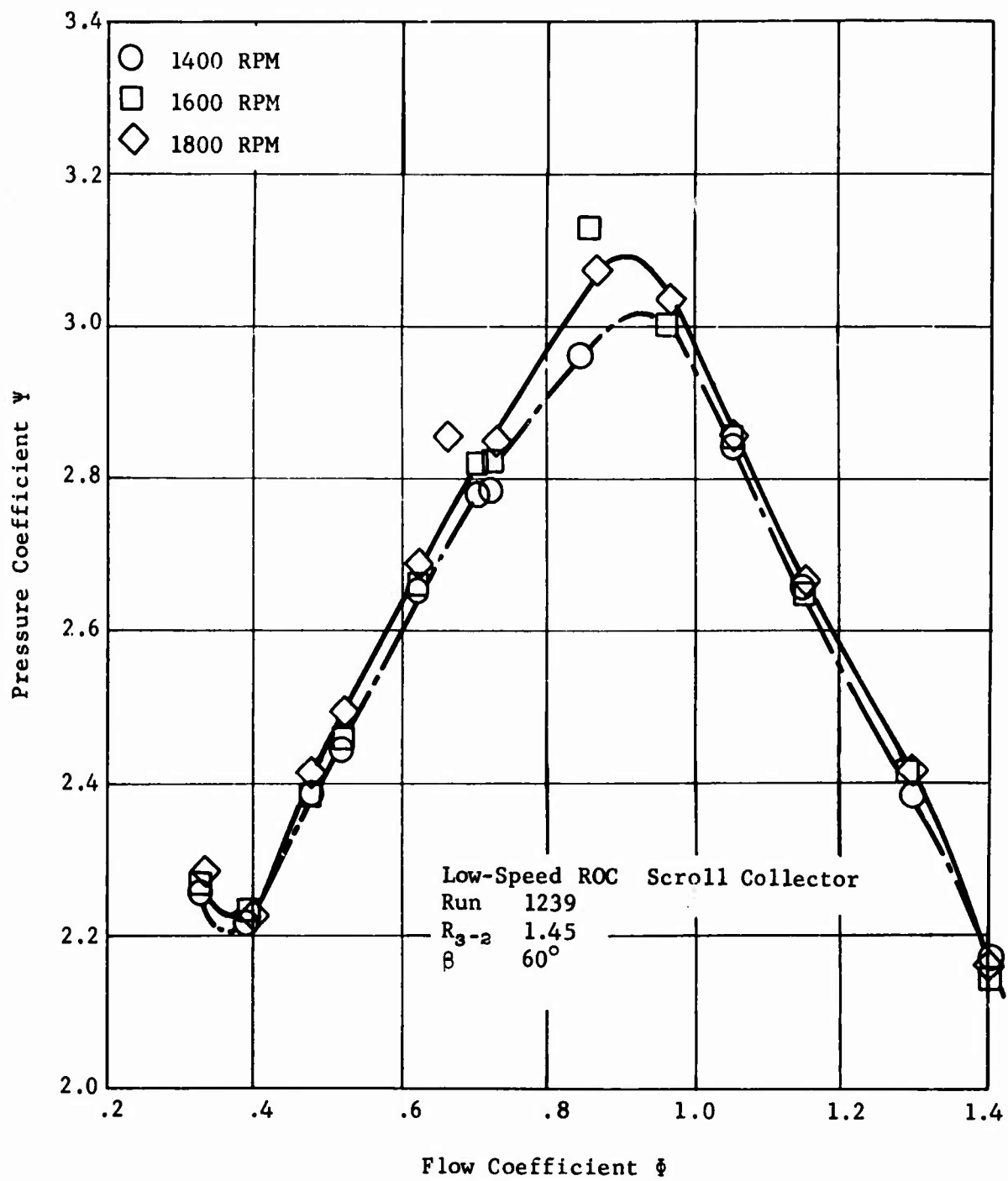


Figure 43. Rotor Discharge Pressure Coefficient, Radial Inflow IGV at 18.5°, Hub and Housings 1 and 2 Rotating.

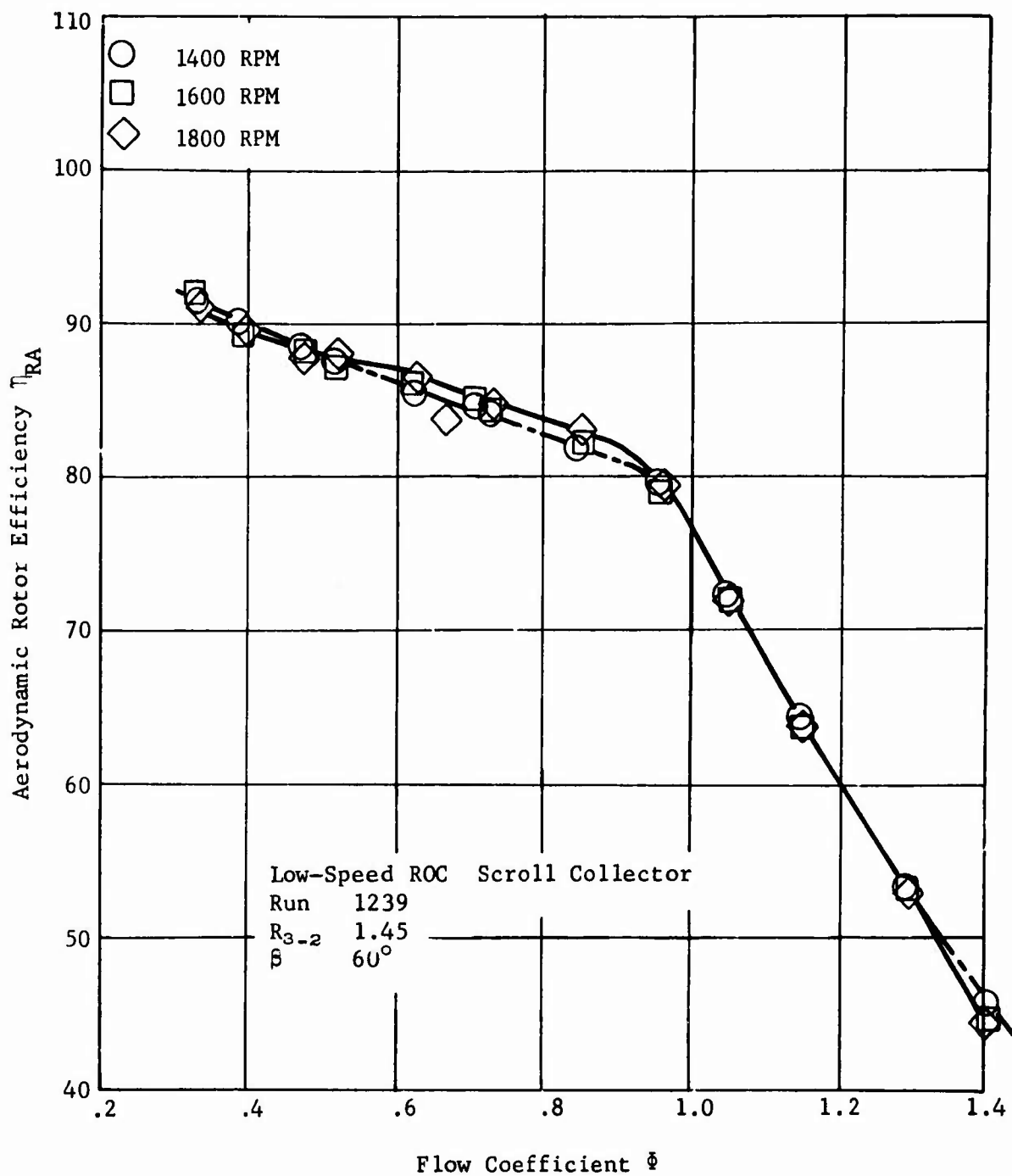


Figure 44. Compressor Efficiency, Radial Inflow IGV at 18.5°, Hub and Housings 1 and 2 Rotating.

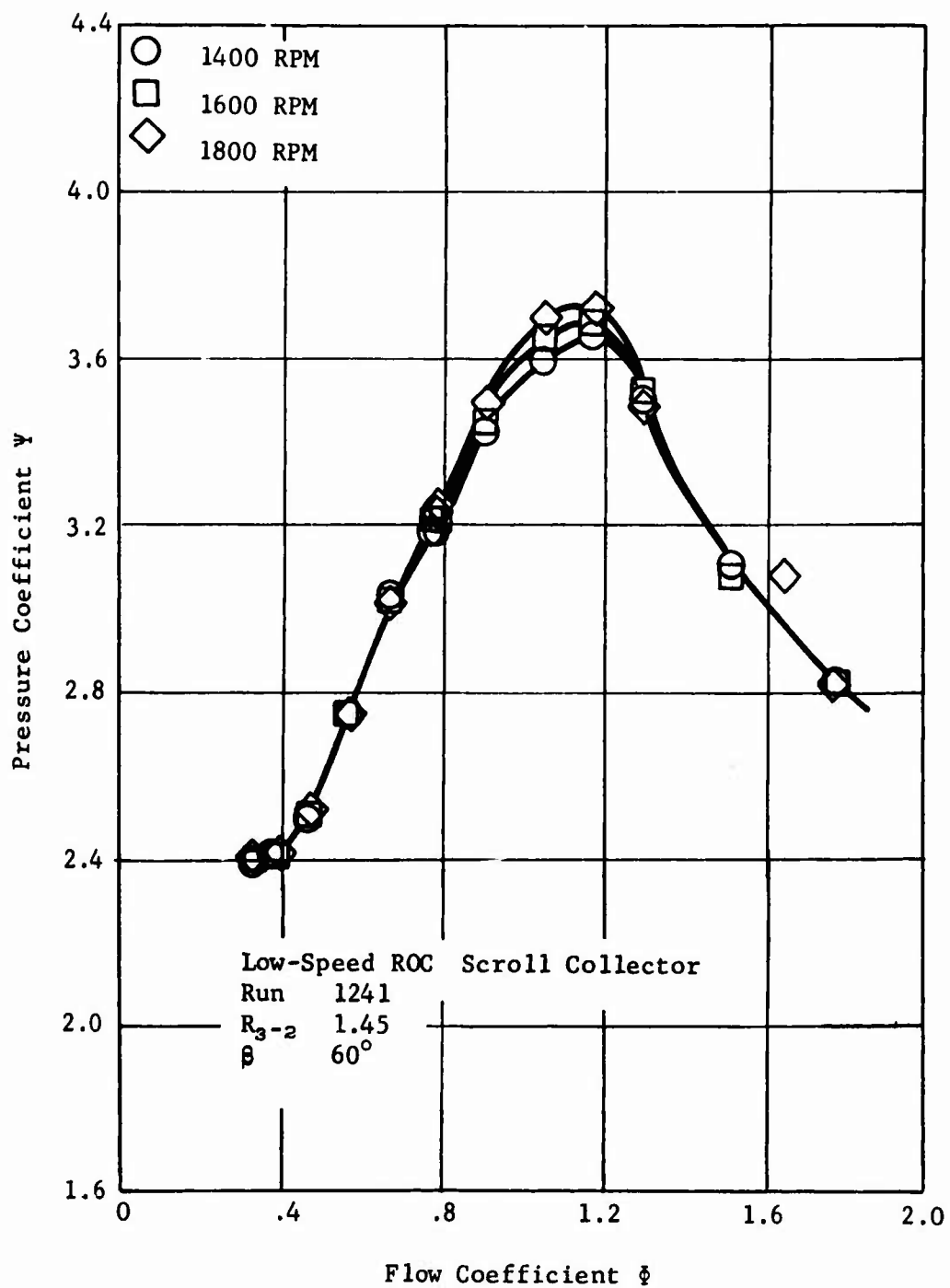


Figure 45. Rotor Discharge Pressure Coefficient, Radial Inflow IGV at 0°, Hub and Housings 1 and 2 Rotating.

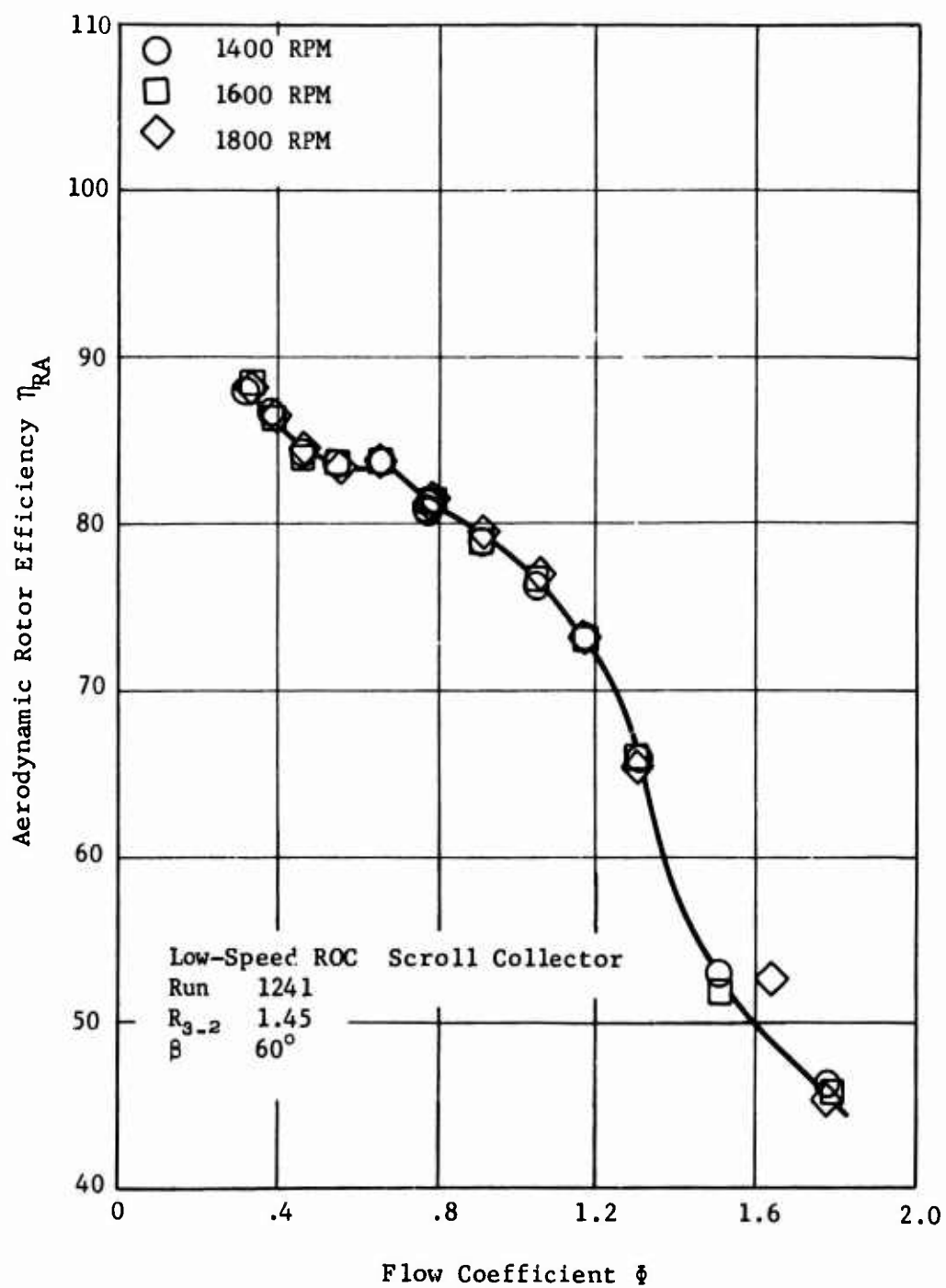


Figure 46. Compressor Efficiency, Radial Inflow IGV at 0°, Hub and Housings 1 and 2 Rotating.

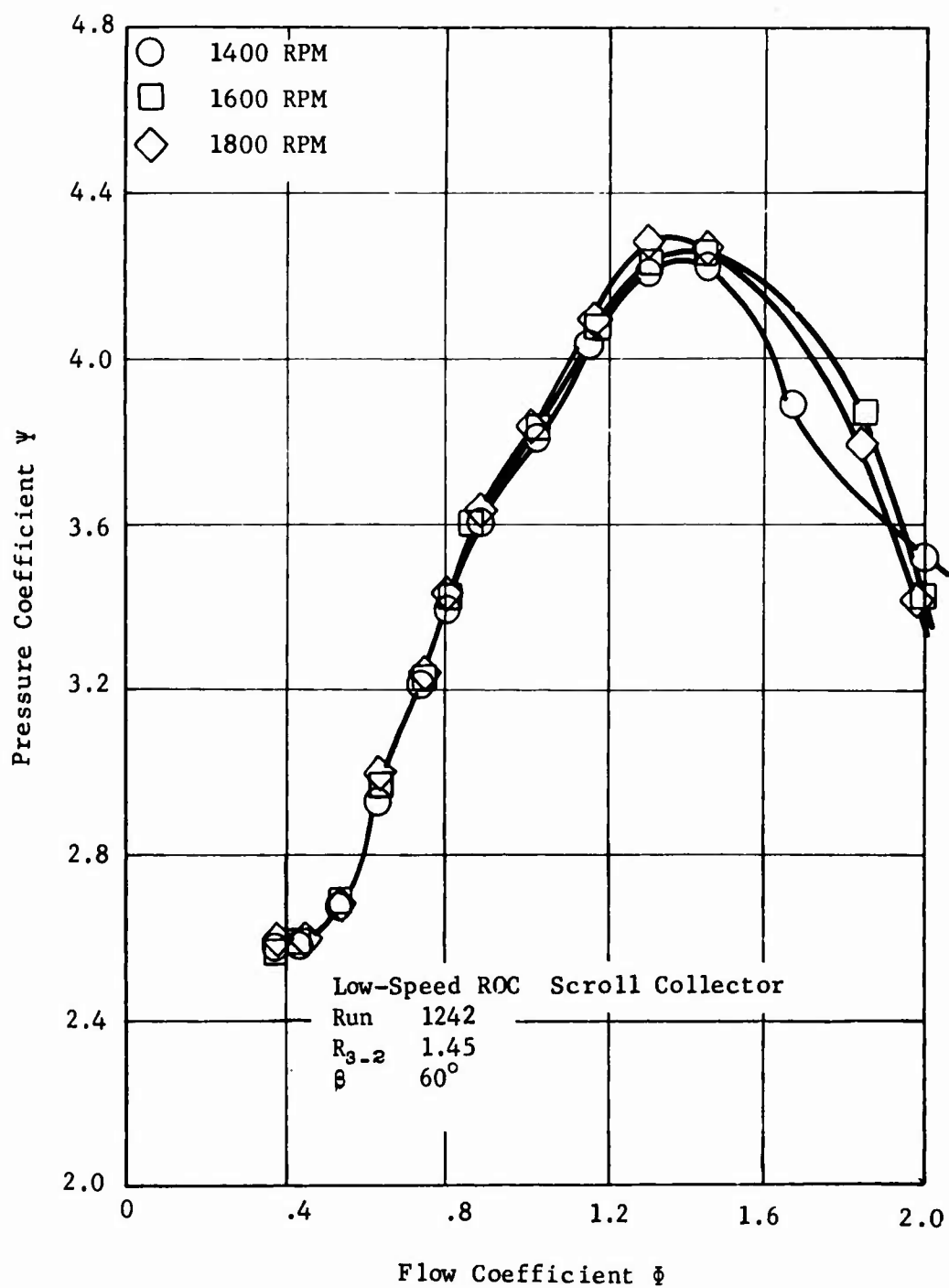


Figure 47. Rotor Discharge Pressure Coefficient, Radial Inflow IGV at -18.5° , Hub and Housings 1 and 2 Rotating.

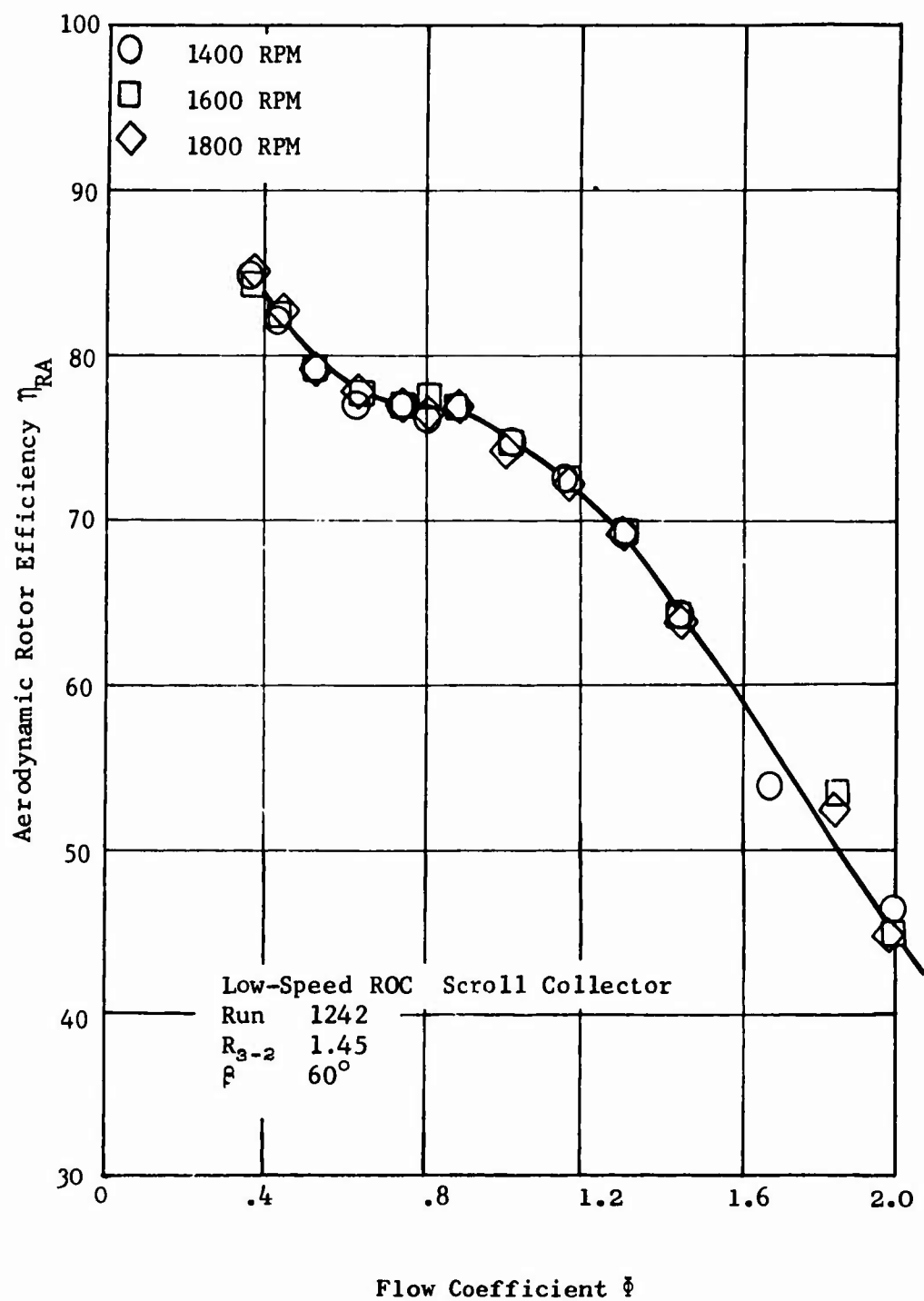


Figure 48. Compressor Efficiency, Radial Inflow IGV at -18.5° , Hub and Housings 1 and 2 Rotating.

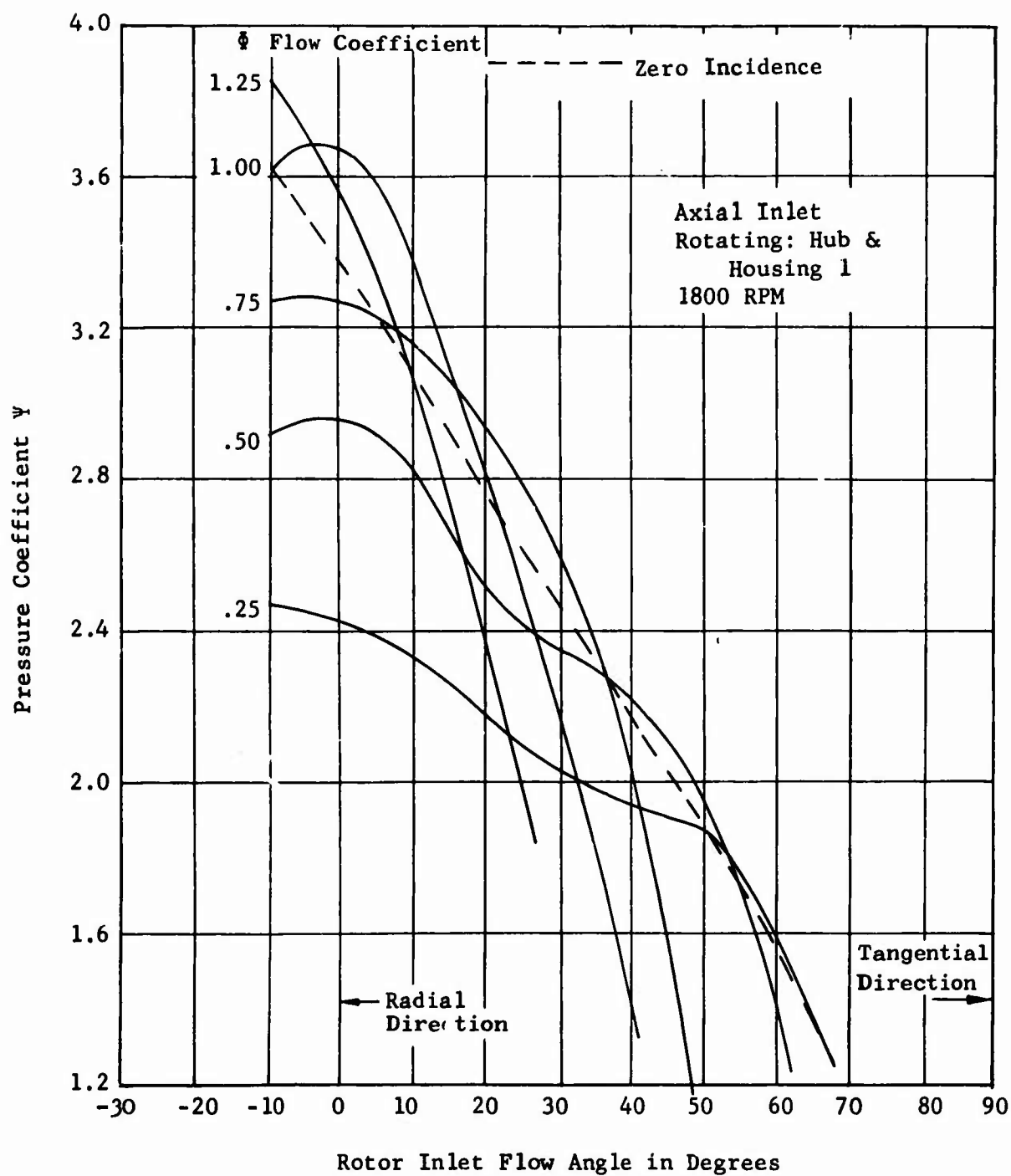


Figure 49. Compressor Pressure Coefficient Characteristics, Axial Inlet.

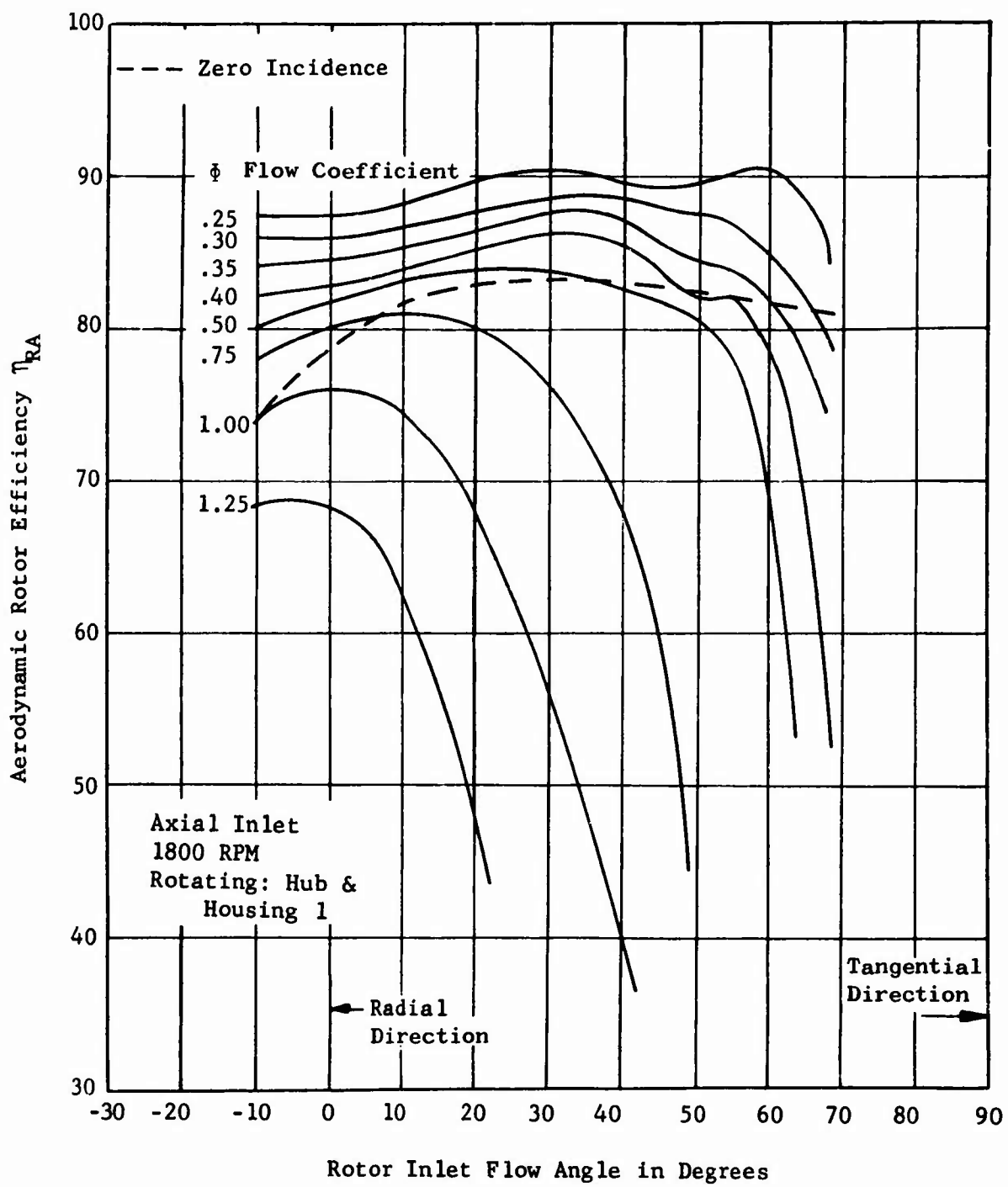


Figure 50. Compressor Efficiency Characteristics, Axial Inlet.

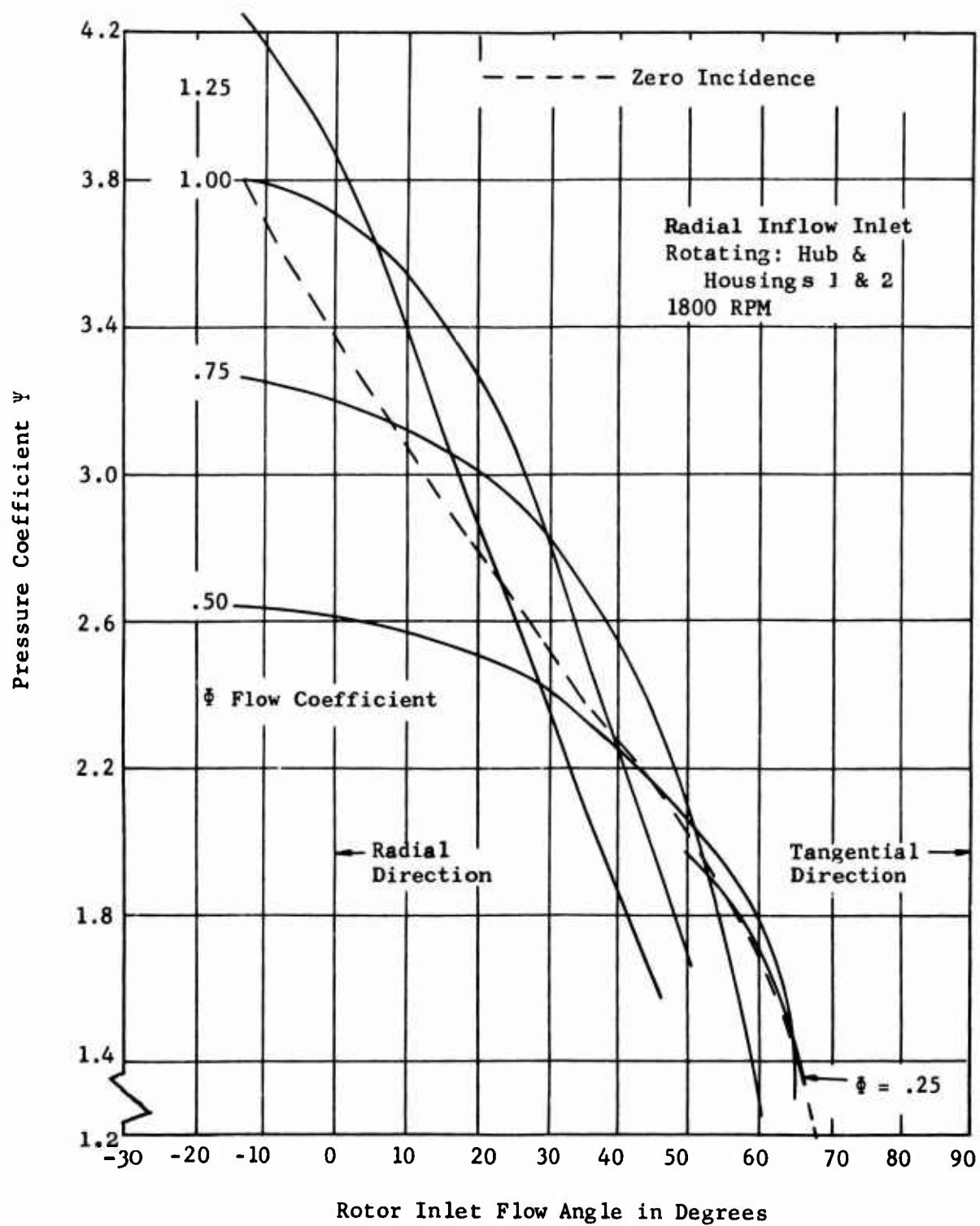


Figure 51. Compressor Pressure Coefficient Characteristics, Radial Inflow Inlet.

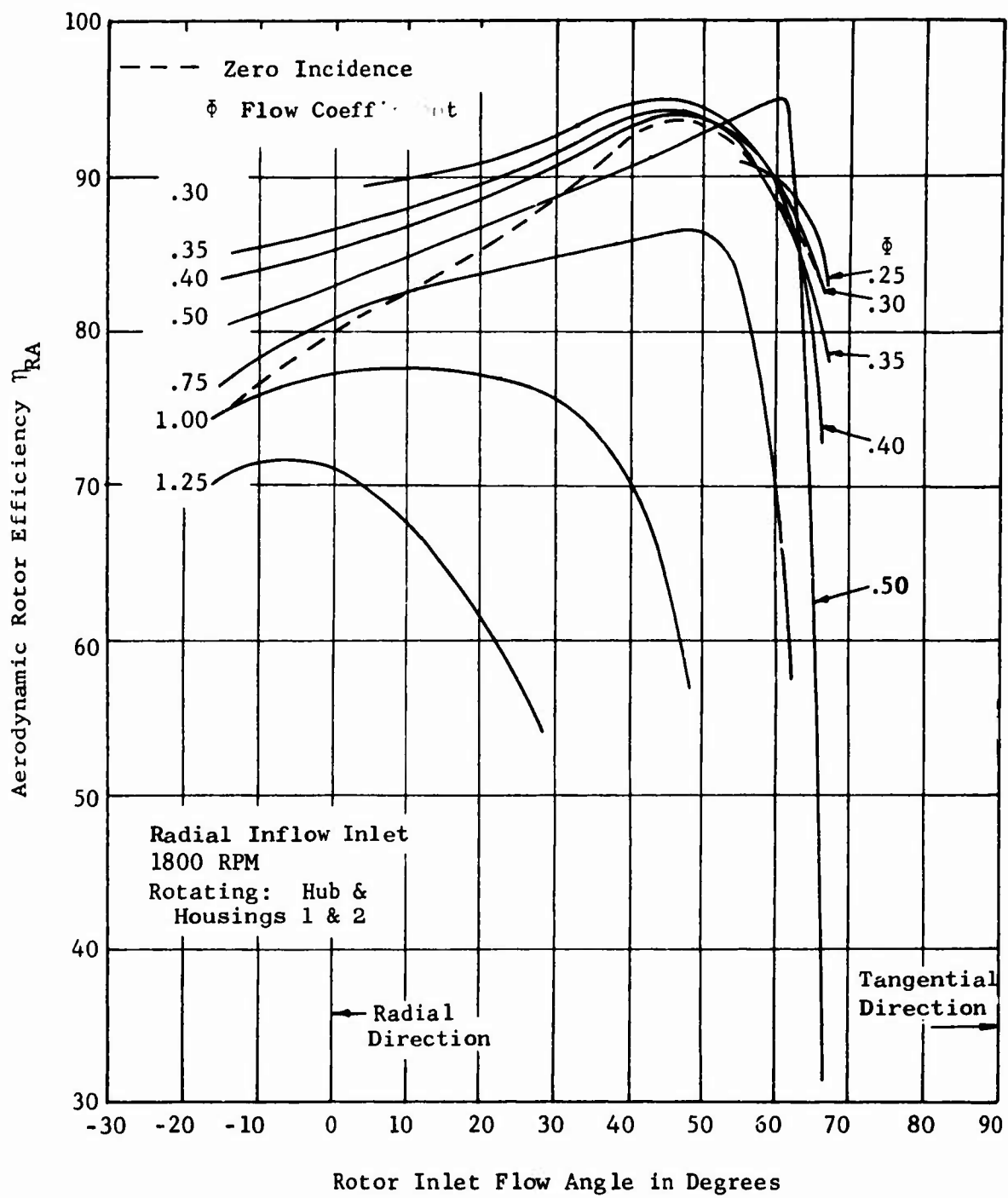


Figure 52. Compressor Efficiency Characteristics, Radial Inflow Inlet.

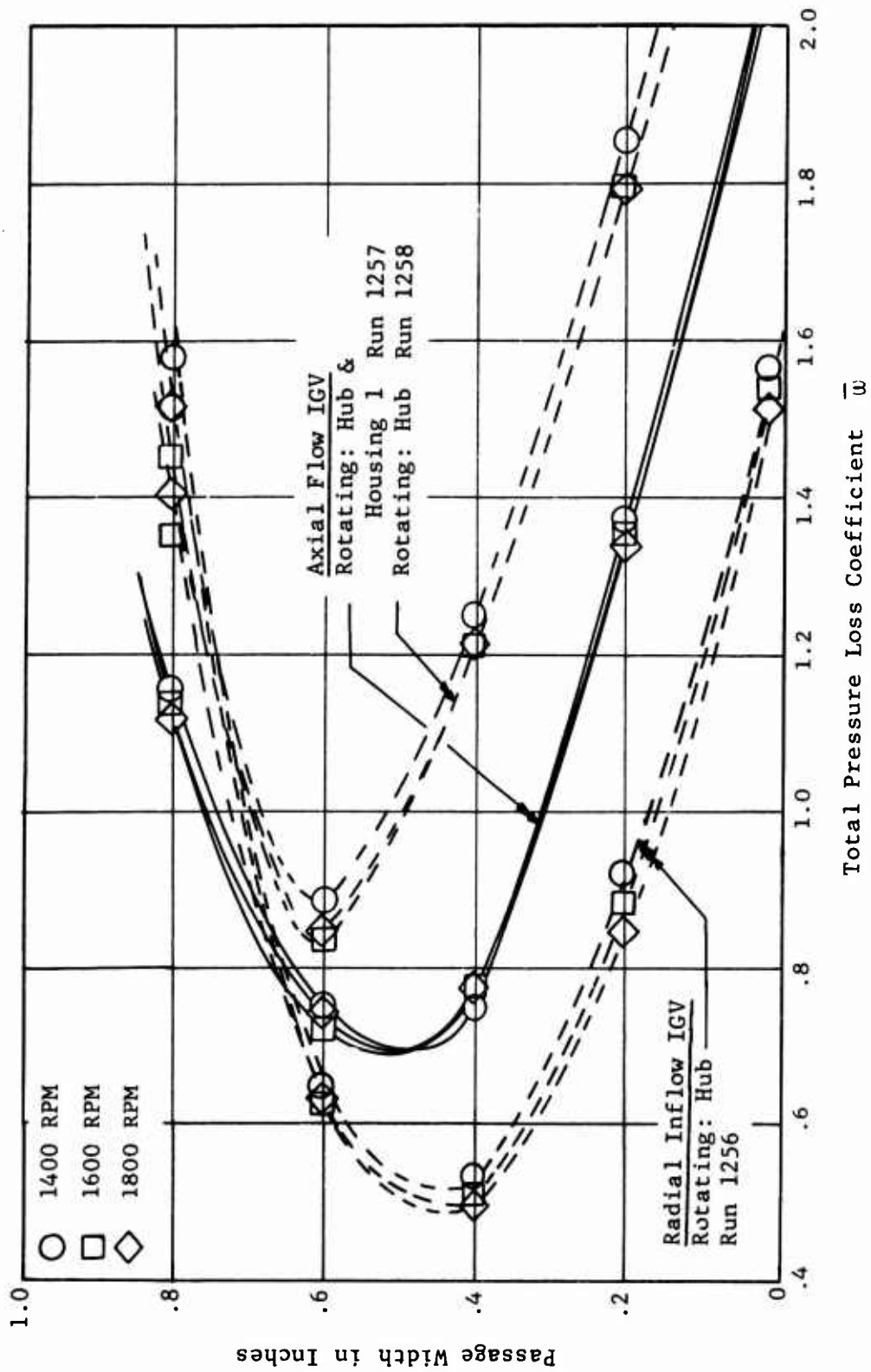


Figure 53. Rotor Inlet Total Pressure Loss Profile, Axial and Radial IGV Setting of 60°.

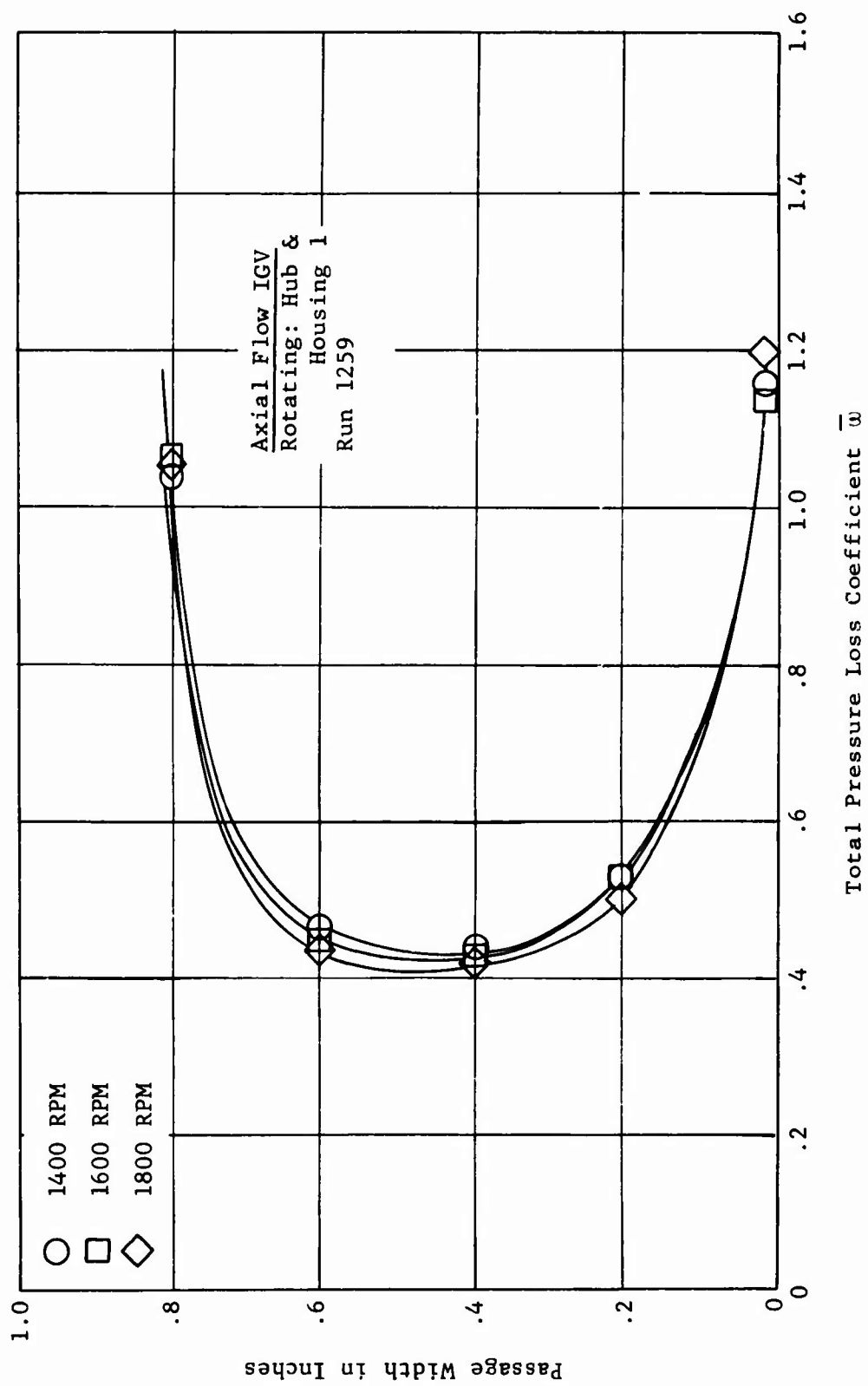


Figure 54. Rotor Inlet Total Pressure Loss Profile, Axial IGV Setting of 50°.

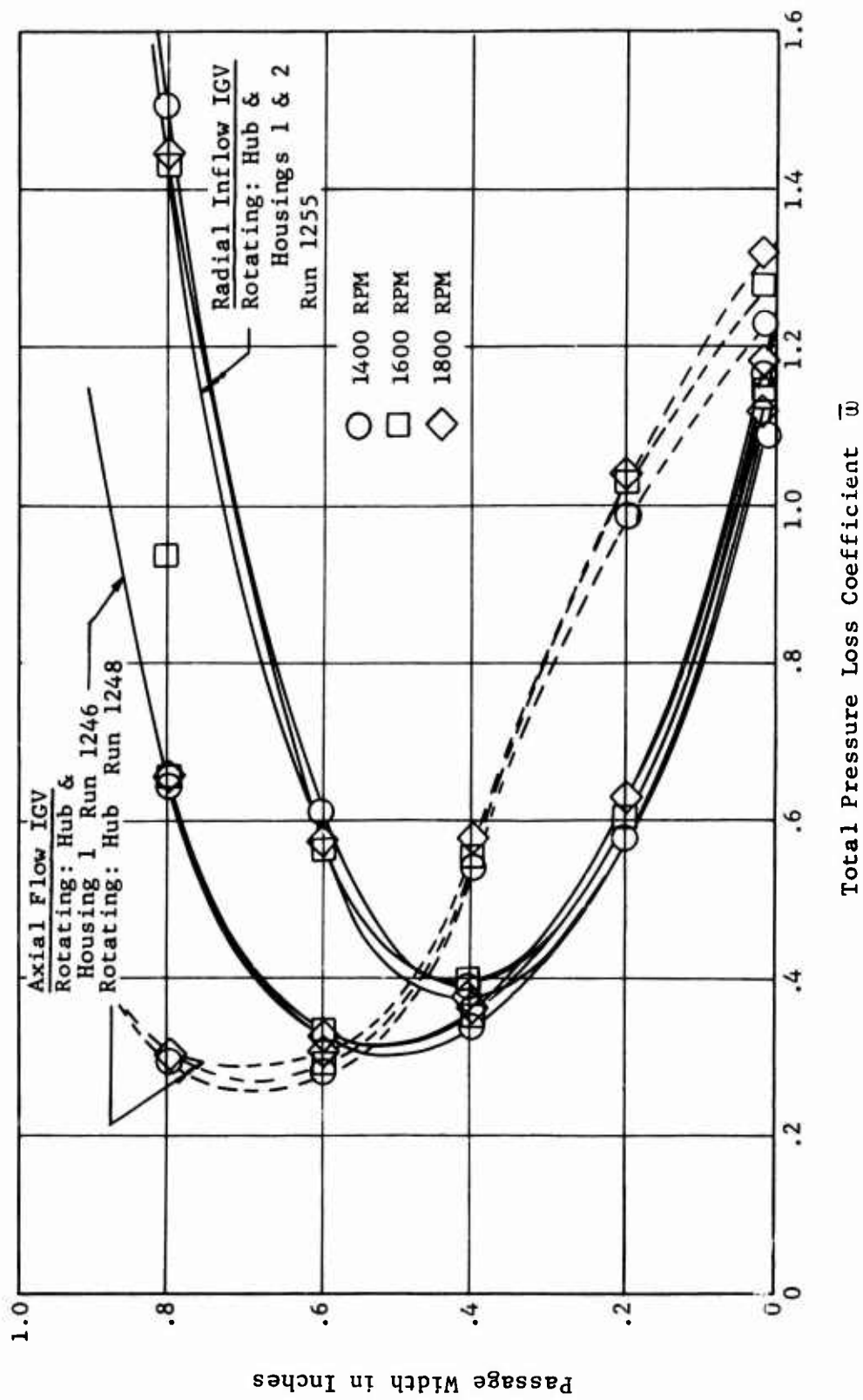


Figure 55. Rotor Inlet Total Pressure Loss Profile, Axial and Radial IGV Setting of 60°.

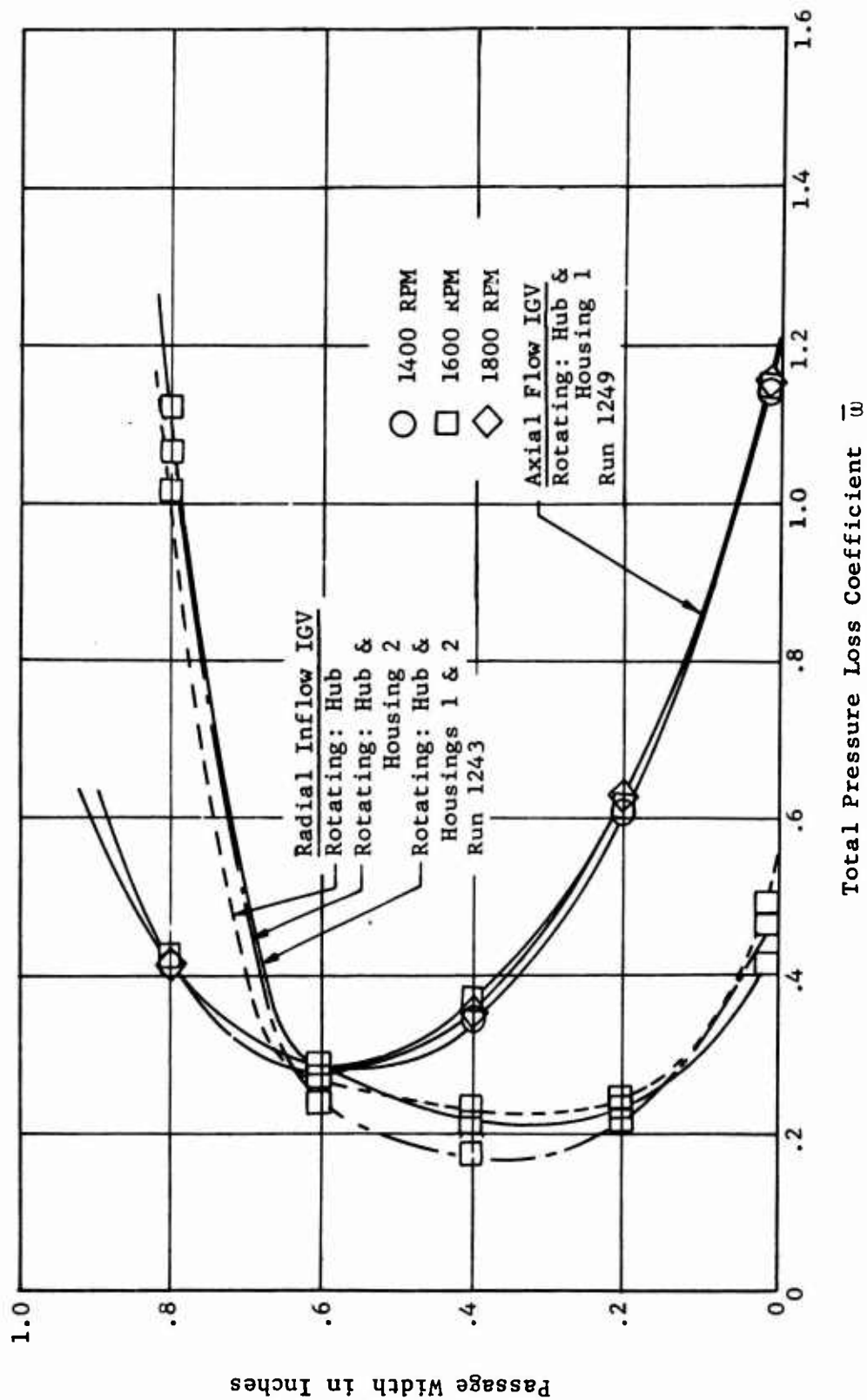


Figure 56. Rotor Inlet Total Pressure Loss Profile, Axial and Radial IGV Setting of 50°.

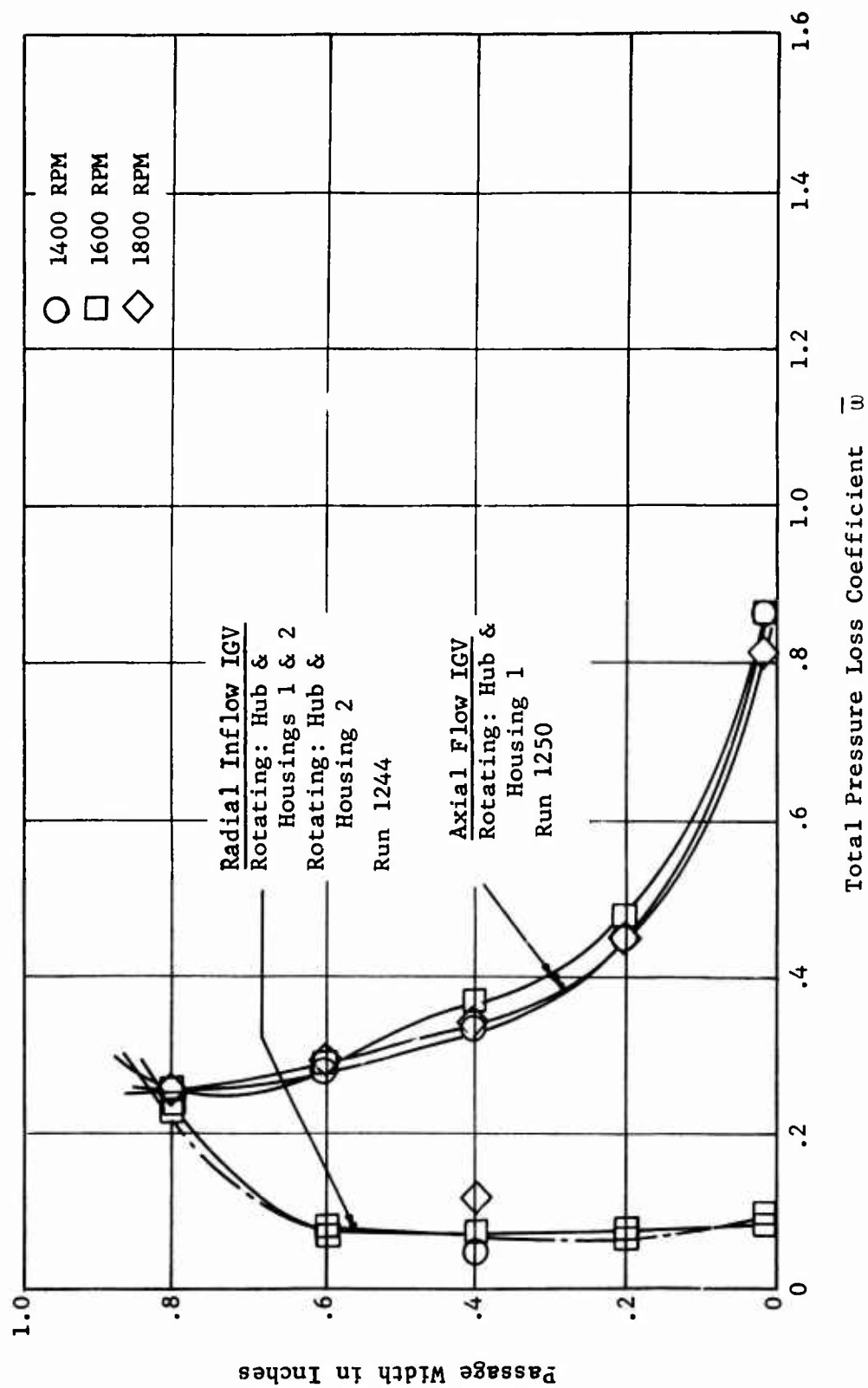


Figure 57. Rotor Inlet Total Pressure Loss Profile, Axial and Radial IGV Setting of 35°.

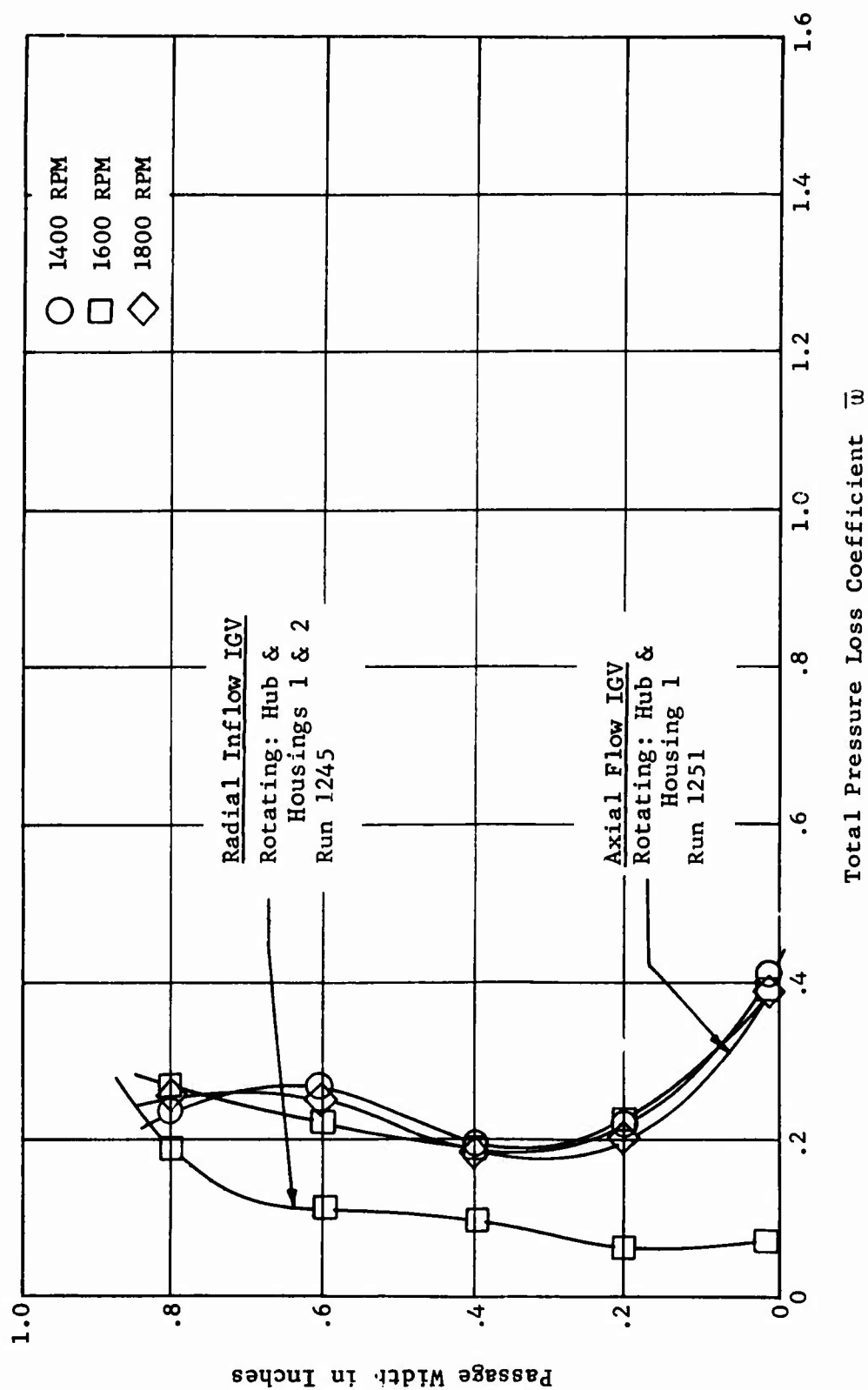


Figure 58. Rotor Inlet Total Pressure Loss Profile, Axial and Radial IGV Setting of 18.5°.

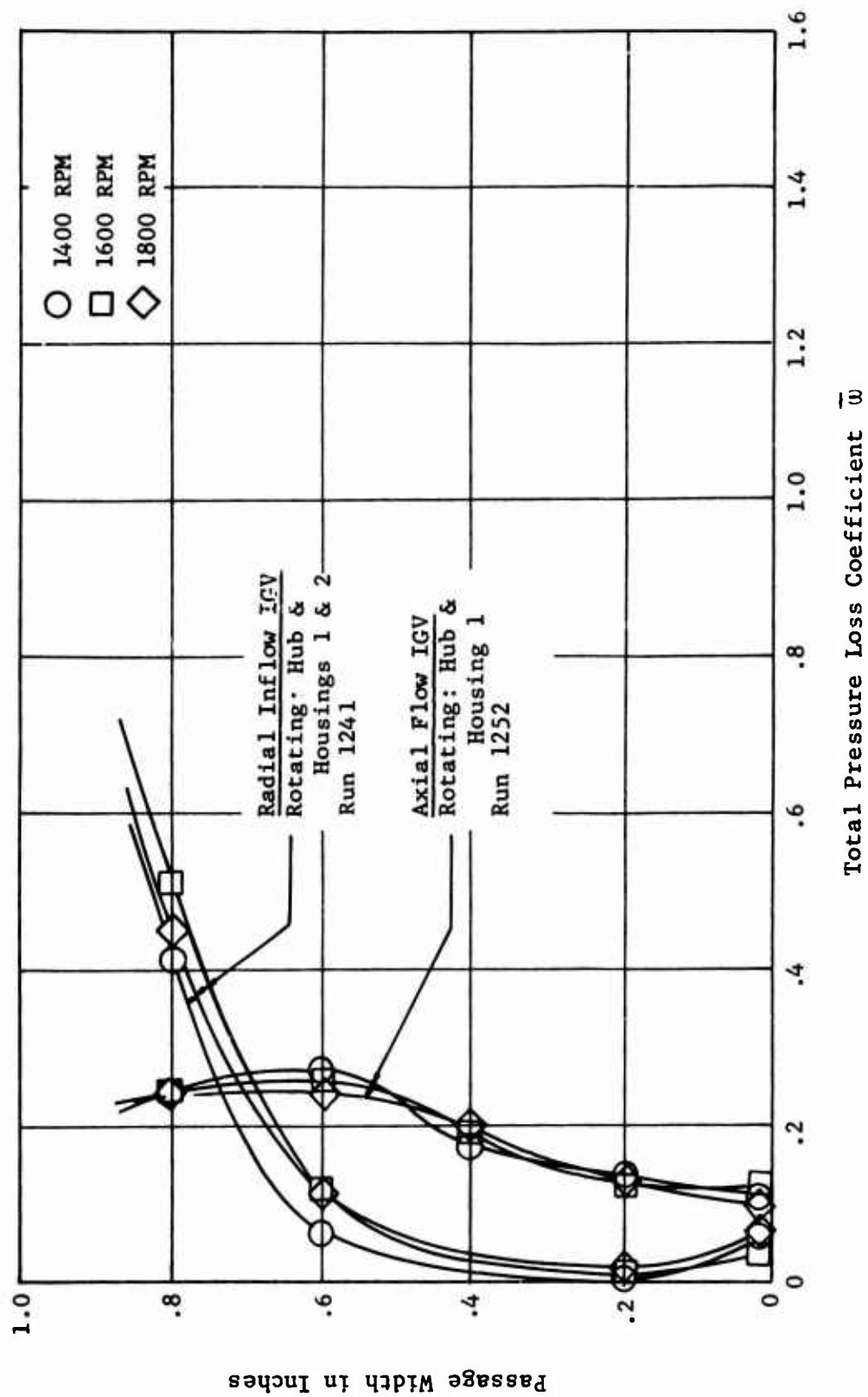


Figure 59. Rotor Inlet Total Pressure Loss Profile, Axial and Radial IGV Setting of 0°.

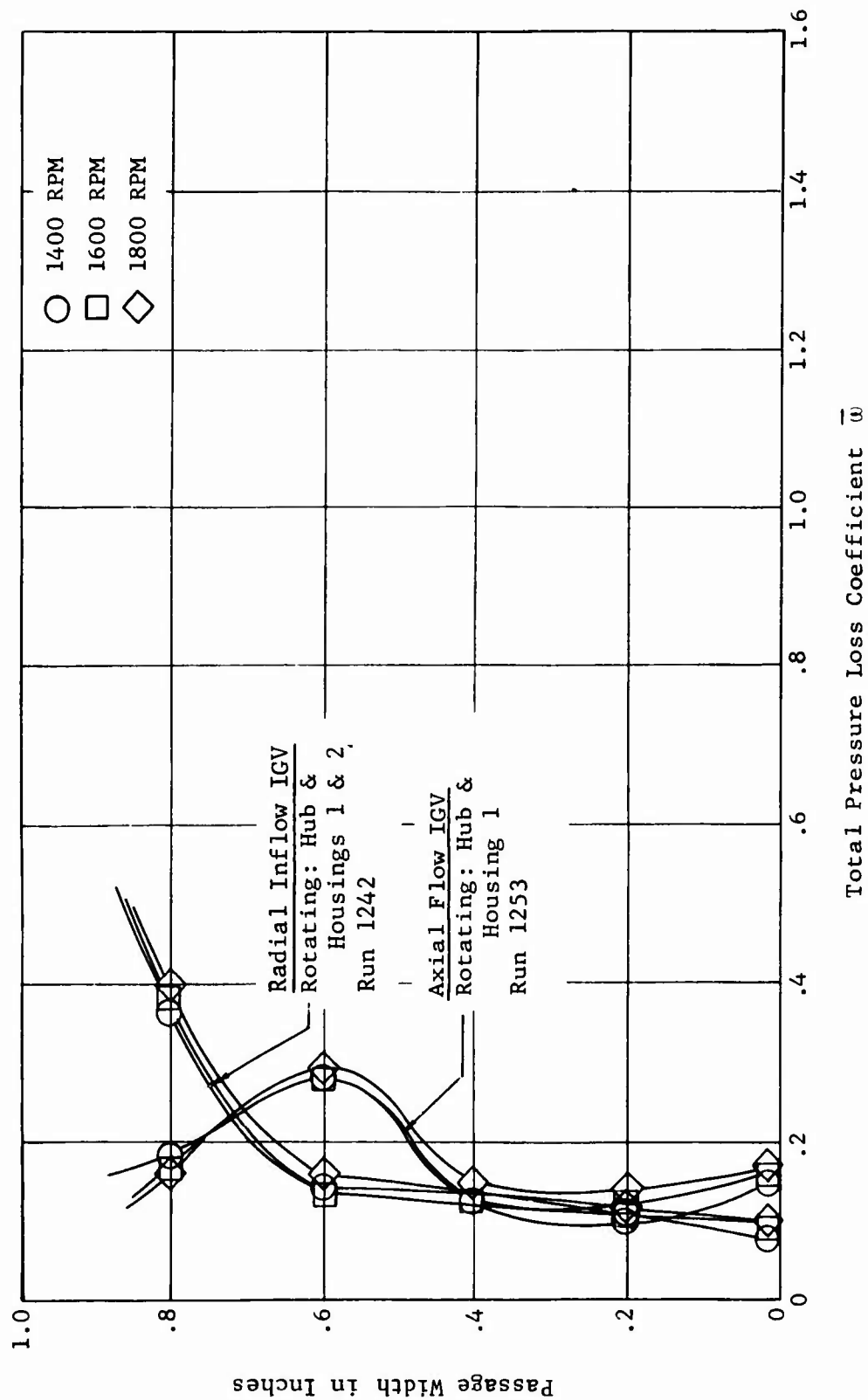


Figure 60. Rotor Inlet Total Pressure Loss Profile, Axial and Radial IGV Setting of -18.5° .

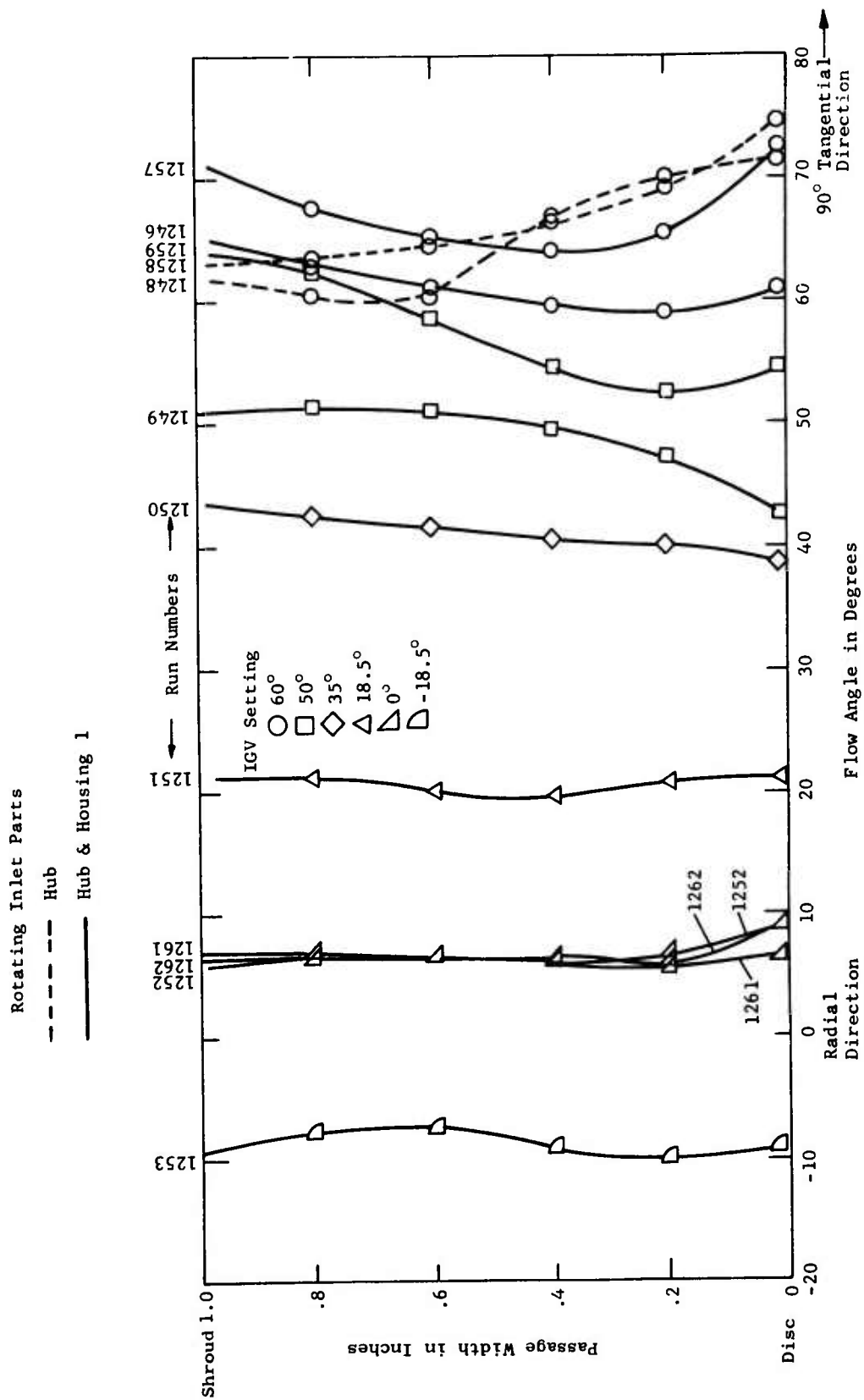


Figure 61. Rotor Inlet Flow Angle Profiles with Axial Flow Inlet Guide Vanes, Rotor Speed at 1600 RPM.

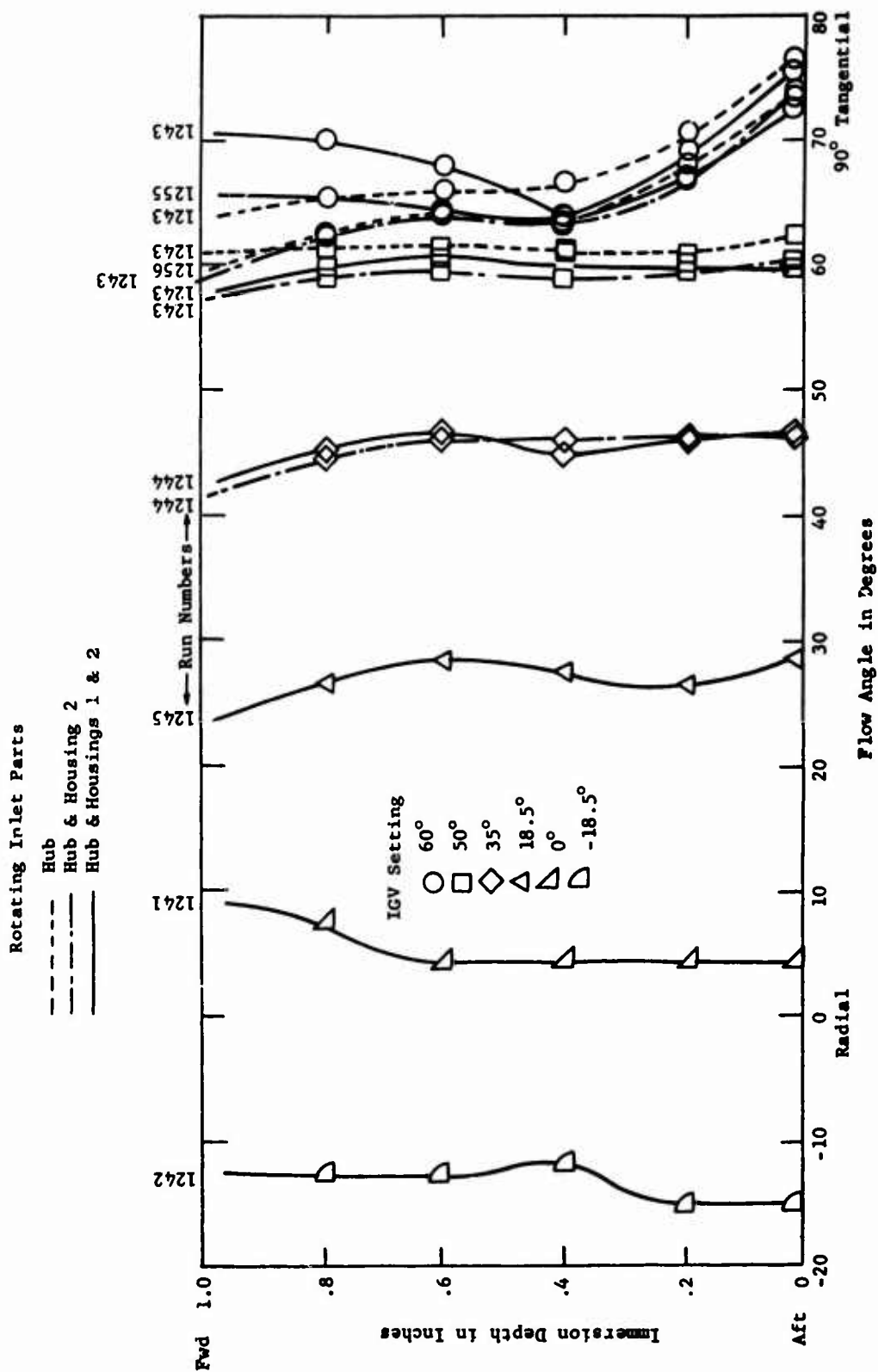


Figure 62. Rotor Inlet Flow Angle Profiles with Radial Inflow Inlet Guide Vanes, Rotor Speed at 1600 RPM.

ANALYSIS

Wall Rotation

The first portion of this investigation was concerned with determining the most advantageous combination of rotating passage walls for both inlets. Run 1236 was concerned with testing of the axial flow inlet guide vane assembly in the following two configurations: hub only rotating, and hub and housing 1 rotating. The configuration with hub and housings 1 and 2 rotating was not tested at this time since the inlet total pressure probe could not be installed in the rotating parts. The data obtained from these configurations are presented in Figures 10 through 13. The comparison of pressure coefficient and rotor aerodynamic efficiency indicates that the configuration employing the rotating hub and housing 1 has a slight advantage in performance; therefore, this configuration was selected to be tested through all axial flow inlet guide vane setting angles.

In like manner, the radial inflow inlet guide vane assembly was tested in Run 1235 in the following configurations: hub rotating, hub and housing 2 rotating, and hub and housings 1 and 2 rotating. The compressor characteristics for these tests are presented in Figures 14 through 19. Careful comparison of the compressor characteristics shows that hub alone and hub and housing 2 configurations are for the most part identical, but hub and housings 1 and 2 rotating shows a slight advantage in pressure coefficient and rotor aerodynamic efficiency. Therefore, the configuration involving the rotating hub and housings 1 and 2 was selected, and this configuration has been extensively tested through all radial inflow inlet guide vane turning angles.

It is to be noted in these tests that the rotor aerodynamic efficiency is consistently low. This is due to the procedure employed in reducing the data, since the geometric setting angle of the guide vanes was employed in the efficiency calculation rather than the measured angle of the absolute velocity vector entering the rotor blades. Figure 20 is a second data reduction using the absolute flow angle and shows a major increase in efficiency to the level consistent with previous data.

In the design of the high-speed radial outflow compressor, the outside wall leading to the rotor blade rotates, since it is an integral part of the rotor. Therefore, the low-speed compressor with the axial inlet installed was tested in a corresponding configuration. This configuration consisted in rotating the hub and housings 1 and 2 of the low-speed axial inlet (see Figure 5), thus simulating the rotating outer wall of the high-speed machine. It was not possible to install the rotor inlet total pressure probe in this configuration, so analysis of this test is dependent upon the rotating diffuser exit characteristics. These data are shown in Figures 21 and 22 in the usual manner. Comparison of these results with previous runs concerning the axial flow inlet at an inlet guide vane setting angle of 60 degrees shows that a slight advantage

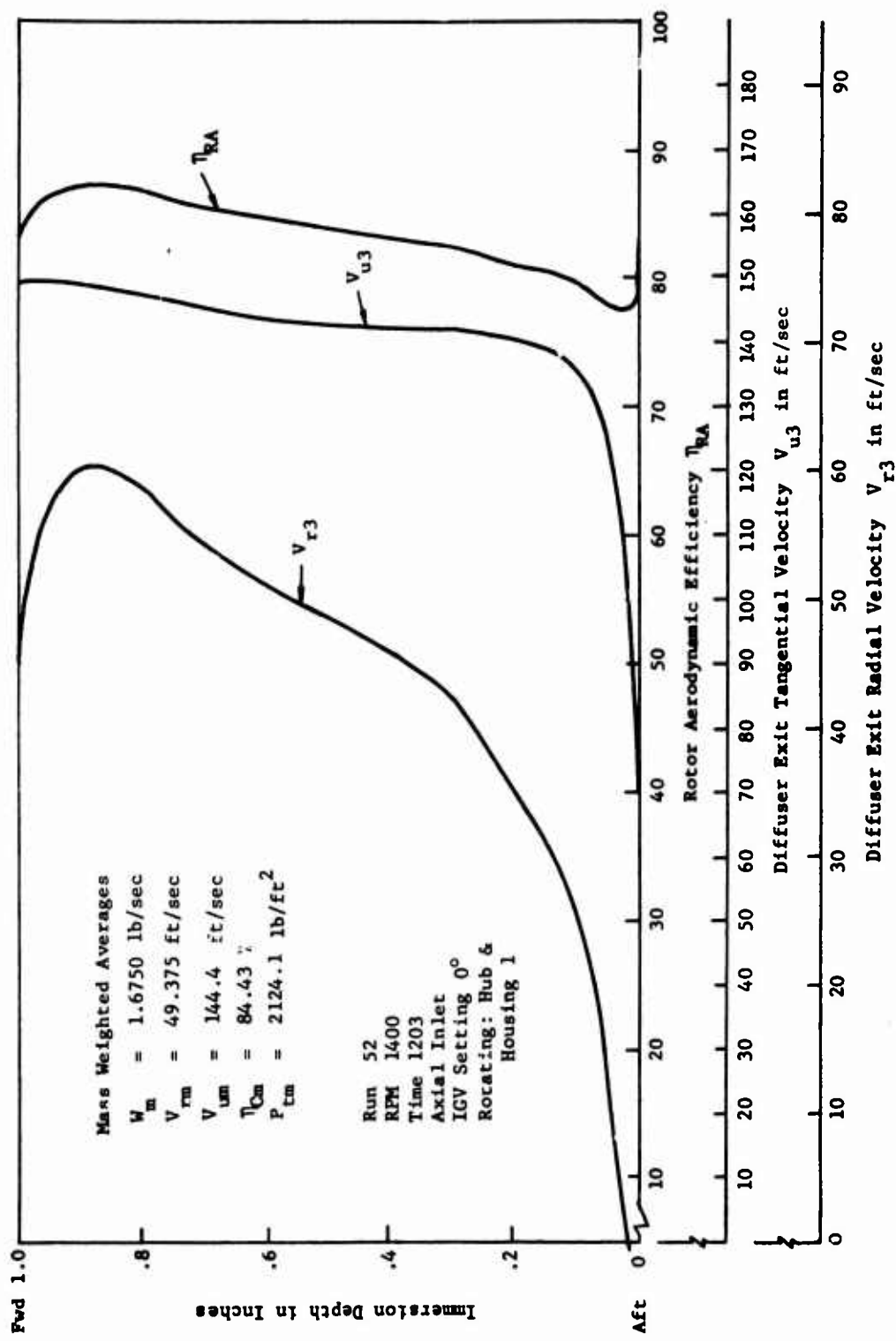


Figure 63. Rotor Discharge Characteristics from Mass Averaged Data, Axial Flow IGV at 0° , Hub and Housing 1 Rotating.

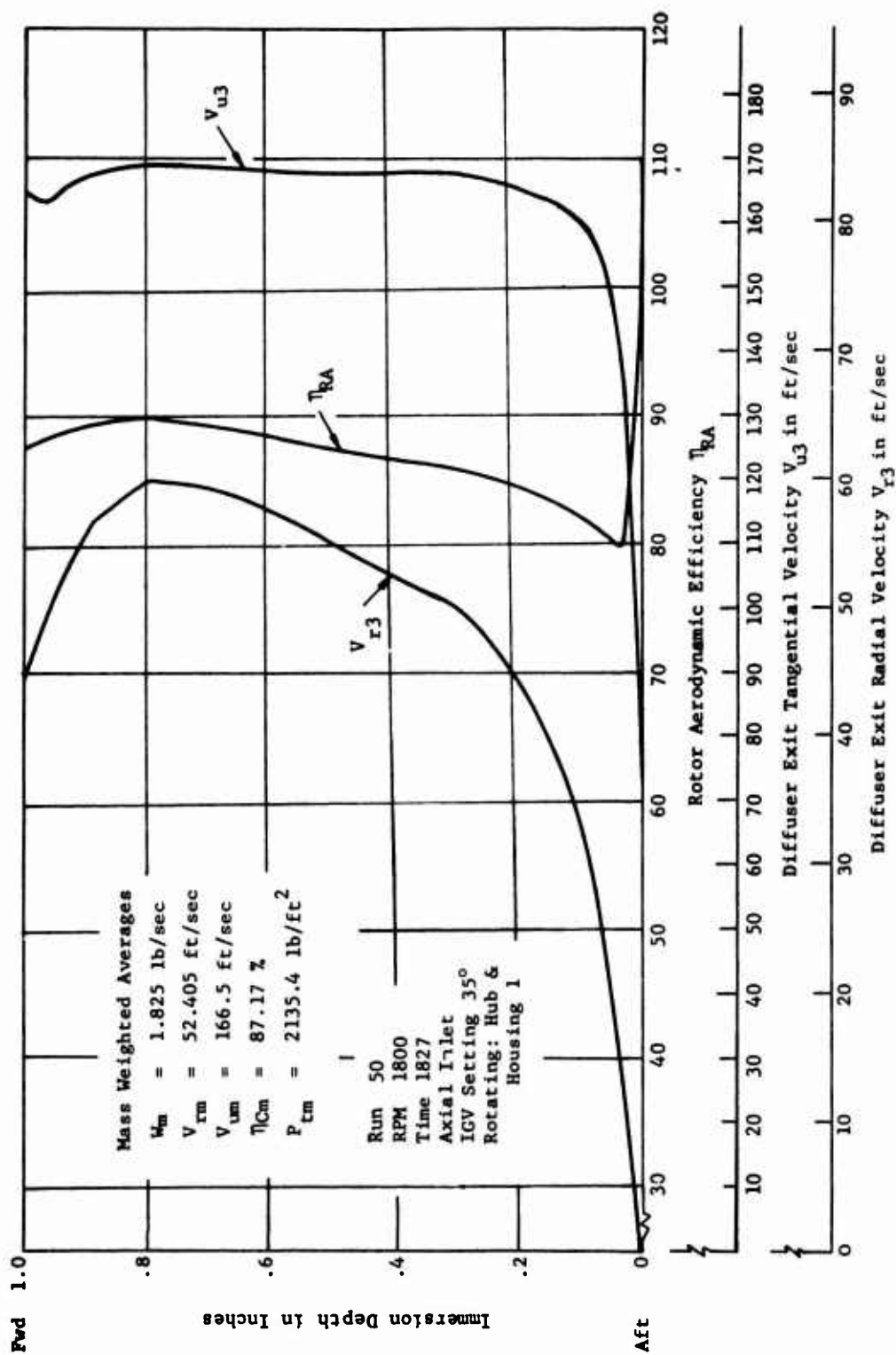


Figure 64. Rotor Discharge Characteristics from Mass Averaged Data, Axial Flow IGV at 35°, Hub and Housing 1 Rotating.

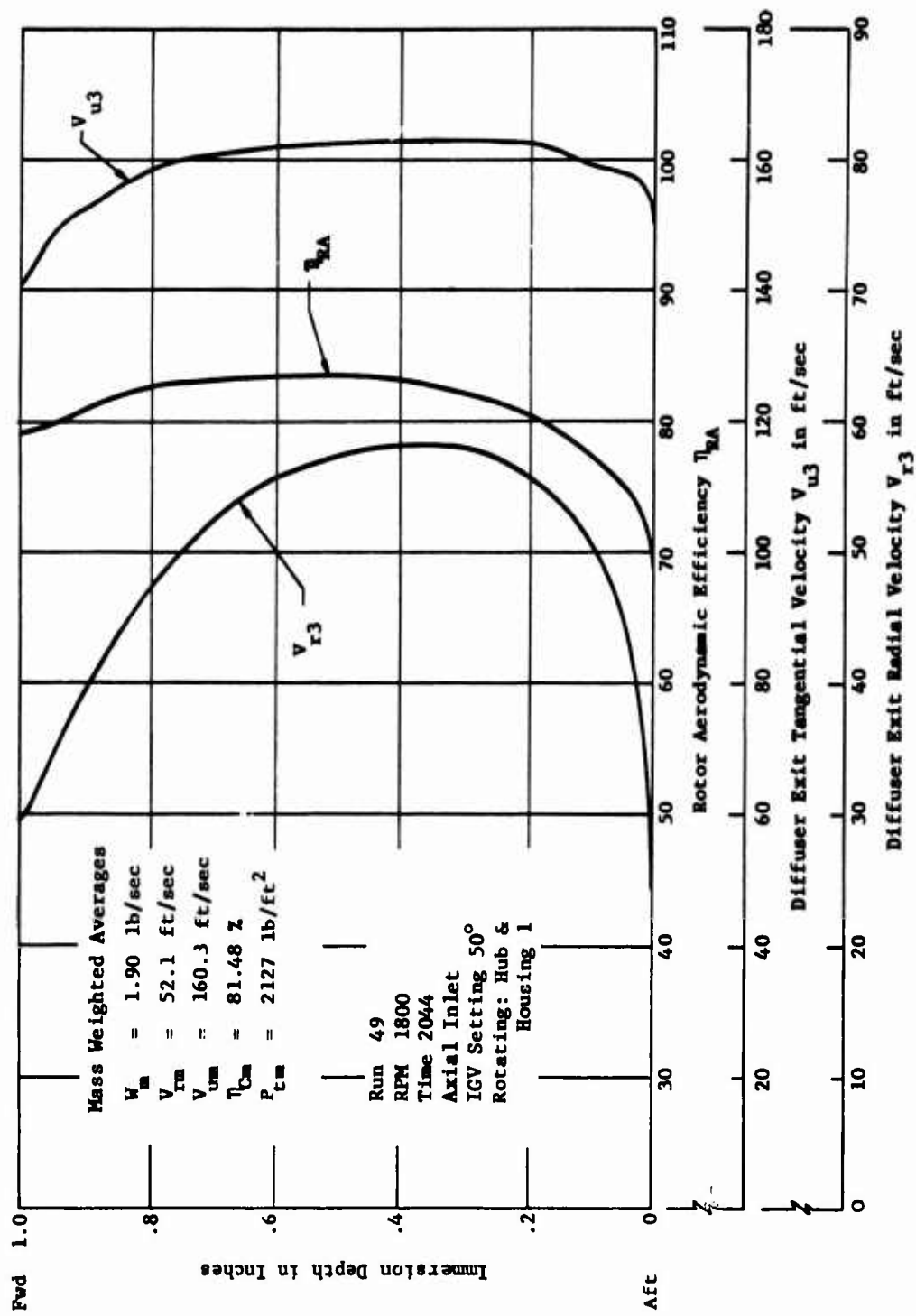


Figure 65. Rotor Discharge Characteristics from Mass Averaged Data, Axial Flow IGV at 50°, Hub and Housing 1 Rotating.

may be obtainable by rotating the inner and outer walls of the flow passage. Comparison of Figures 21 and 22 with Figures 23 and 24 will indicate the performance advantage. This advantage at first sight appears to be large, but the results are considered to be somewhat dubious. This is due to the fact that these two runs are completely independent in the sense that the axial flow inlet guide vanes were reset and the inlet reinstalled for each test. Experience has shown that this procedure will not produce an identical set of compressor characteristics; but since the apparent differences in these two runs (Runs 1247 and 1257) are large, it is felt that, by rotating both sides of the passage, at least a small gain in performance is possible.

Rotor Pressure Coefficient and Efficiency

The axial flow inlet guide vane assembly with hub and housing 1 rotating was subsequently tested through all inlet guide vane setting angles. The test results are presented in Figures 23 through 36. Run 1257 presented in Figures 23 and 24 is a repeat of Run 1237 presented in Figures 10 and 11. This was necessary to obtain more accurate inlet static pressure readings and therefore more accurate flow coefficients.

Run 1259 presented in Figures 27 and 28 is a repeat of Run 1249 presented in Figures 25 and 26. This repeat was deemed necessary to substantiate the compressor characteristics obtained for the axial flow inlet with inlet guide vanes set at 50 degrees with hub and housing 1 rotating. In comparing these two runs, it is observed that the same general trends in pressure coefficient and efficiency occur, but at reduced flow coefficient. This does not invalidate either run, since it is most difficult to reset manually and individually the inlet guide vanes to their exact initial setting, which would hopefully produce an identical set of compressor characteristics. These runs must be compared on the basis of rotor inlet flow angle as measured in each test.

The compressor characteristics of the remaining inlet guide vane setting angles are presented in sequence. A composite presentation of these characteristics will be discussed in the following paragraph. The same procedure was followed to obtain similar results for the radial inflow inlet guide vane assembly. These results are presented in Figures 37 through 48. Run 1255 presented in Figure 37 is a repeat of parts of Run 1235. The reason for this retest was to obtain more accurate inlet static pressure readings. The corresponding results of the remaining inlet guide vane settings follow in sequence.

Figures 49 through 52 are composite plots of compressor characteristics for the axial flow and radial inflow inlet guide vane assemblies. These figures present the pressure coefficient and rotor aerodynamic efficiency data as functions of rotor inlet flow angle. The rotor inlet flow angle is defined as the angle of the absolute velocity vector entering the rotor blades. This angle is measured from a radial line intersecting the leading edge of the appropriate rotor blade and is shown as α in

Figure 66. In Figures 49 and 51, it can be seen that the pressure coefficient rises as the flow through the machine increases. This is easily explained when the velocity triangles at the inlet and exit of the rotor blades are examined. As the mass flow increases, the energy input by the rotor blades also increases, producing higher total pressures (Figure 66). As the mass flow increases through the compressor blade row, the relative velocity vector approaches the rotor with an increasingly negative angle of attack with respect to the blades. This seems to indicate a rotor stall or, more accurately, a separated flow region between the blades that remains stable but whose effect is magnified in the rotating diffuser. When high inlet guide vane turning angles are employed, the effect becomes large, as can be seen in the figures.

The design operating conditions are shown in Figures 49 and 51, and for both inlets are approximately identical. This design line, shown dashed in the figures, is defined as zero incidence of the rotor blades.

In Figures 50 and 52, a composite representation of rotor aerodynamic efficiency versus rotor inlet flow angle for lines of constant flow coefficient is shown. The shape of these curves shows that with increasing flow, the rotor aerodynamic efficiency gradually decreases, further indicating that the flow separation through the compressor rotor is increasing. As inlet guide vane angle is increased, the efficiency decreases more and more rapidly under the combined growing inefficiencies of inlet guide vanes and rotor blades. The characteristics are generally true for both axial flow and radial inflow inlets. Again the design operating line is shown as the zero incidence line for both inlets.

When the design operating efficiency lines (Figures 50 and 52) are compared, it becomes obvious that the radial inflow inlet enjoys a large advantage in efficiency while producing an identical pressure operating line. The radial inlet is approximately 1 percent more efficient at zero rotor inlet flow angle, and it steadily increases until a 10-percent increase in efficiency occurs at approximately 45 degrees of inlet flow turning. This advantage then decreases with further increases in fluid turning. Only at the highest turning angles tested does it appear that the axial inlet is more efficient.

Inlet Loss Coefficient

Figures 53 through 60 demonstrate the performance on a comparative basis of the axial and radial inlets. These plots give the total pressure loss coefficient, which is defined as $\Delta P_t / k(q_{BM})$,

where

$$\Delta P_t = (P_{AMB} - P_{t1}) = \text{total pressure loss at rotor inlet with respect to ambient pressure}$$

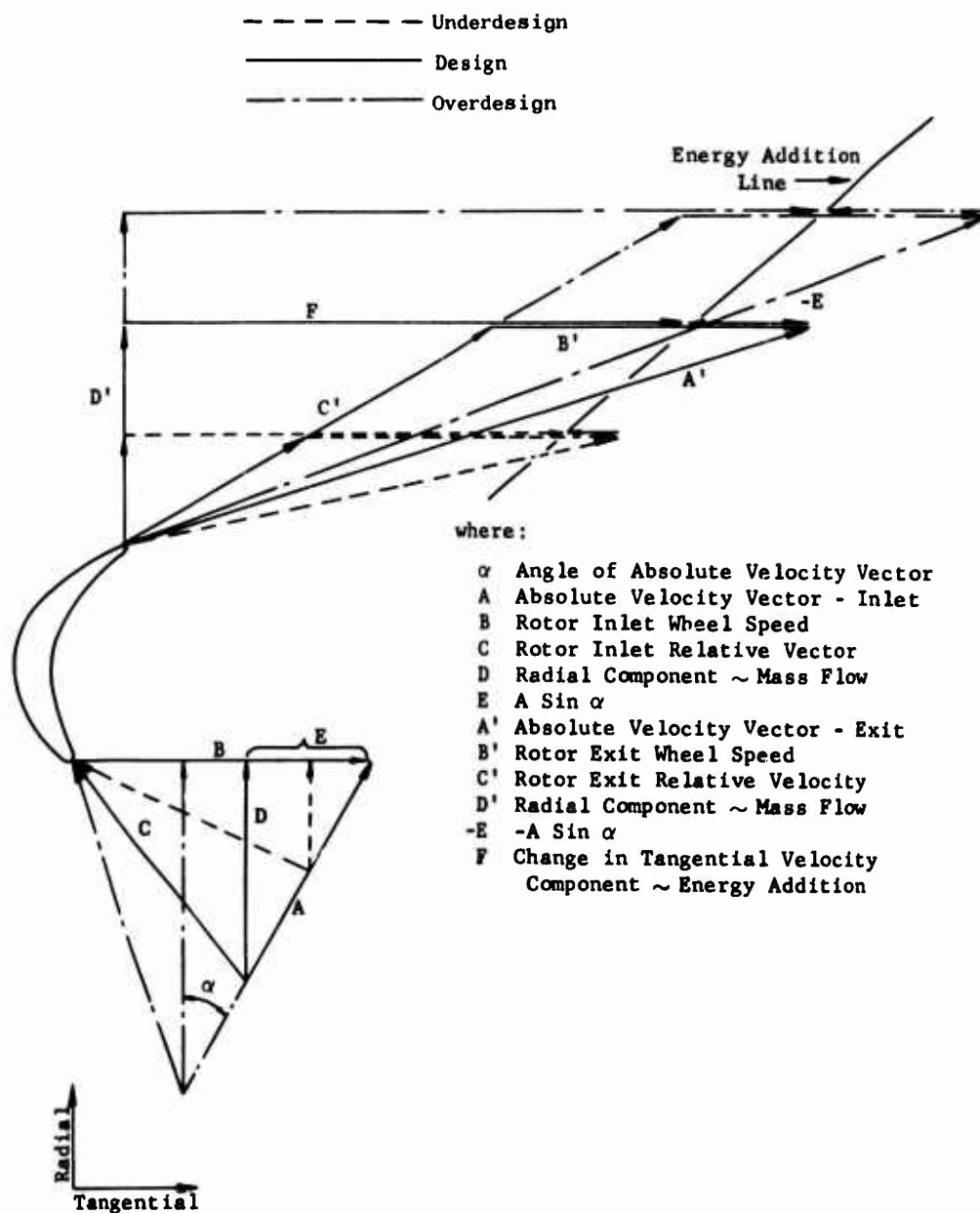


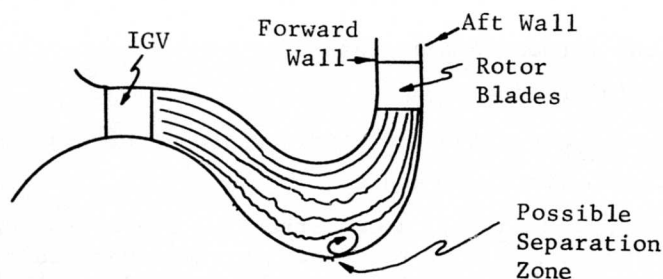
Figure 66. Rotor Blade Velocity Triangles.

P_{AMB} = ambient (atmospheric) pressure
 P_{t1} = rotor inlet total pressure
 q_{BM} = $P_{AMB} - P_{sBM}$ = dynamic pressure upstream of inlet guide vanes
 P_{sBM} = bellmouth static pressure
 k = $\left[(r_i/r_e) / \cos \alpha \right]^2$ = area correction factor to change the reference dynamic pressure from the inlet to the exit plane of the inlet guide vanes

 r_i = radius of IGV inlet
 r_e = radius of IGV exit
 α = IGV angle setting

Runs 1257 and 1258 in Figure 53 are repeats of Runs 1246, 1248, and 1255 as given in Figure 55. Run 1259 given in Figure 54 is also a repeat of Run 1249 given in Figure 56. Again the direct comparison of these data is hindered by the inability to reset all variable geometry features precisely. Figures 61 and 62 are composite plots of absolute rotor inlet flow angle profiles obtained by setting the inlet guide vanes at the angles called out in the test procedure. This inlet angle again serves as a common base upon which to compare the rotor inlet loss profiles.

In general, the total pressure loss increases gradually for both the axial and the radial inflow inlets as inlet guide vane angle setting is increased until a setting of approximately 50 degrees is attained. Then the pressure loss begins to increase more and more rapidly, and the angularity of the flow begins to deviate considerably from a relatively constant profile as demonstrated at the lower angle settings. In examining these figures, several characteristics become apparent. The radial inflow inlet shows a lower level of losses for most turning angles. The pressure profiles for the axial inlet indicate that the higher losses are located on the aft wall of the inlet as the flow approaches the rotor inlet, especially at the higher inlet flow angles. As this angle decreases, the loss on this wall decreases proportionately until, at zero degrees axial inlet guide vane setting, an almost constant profile is obtained. As the inlet flow angle becomes negative, it appears that the losses become greater on the forward wall of the inlet. This coincides with the observation of turbulence on the aft wall of this inlet when visual investigation was made with a tuft. A region of flow separation could be occurring in this inlet as shown in the following diagram.



Conversely, the radial inflow inlet develops its larger losses on the forward wall as the flow approaches the rotor inlet. This apparently never diminishes completely, but does reach a minimum at 18.5 degrees of inlet guide vane setting. These losses are associated with the velocity increase that develops on the forward wall as the flow accomplishes its 180-degree turn. Otherwise, the radial inlet pressure profile is quite constant over the remainder of the passage. From the information available, the various rotating parts seem to have a very mild effect upon the inlet total pressure losses. Consider Figure 57. For the radial flow inlet, there seems to be a negligible effect at 35 degrees of inlet guide vane turning. Figure 56 substantiates this if the data point for hub and housing 2 configuration at 0.6 inch of passage depth is in error. Therefore, from these data the radial inlet seems to be affected very little by the additional rotating parts with the hub rotating. The axial inlet shows a marked deviation at 60 degrees of inlet guide vane setting. Figure 55 indicates that the lack of rotating inlet walls will aggravate the losses incurred on the aft wall of the passage.

Exit Profiles

In considering the influence of the axial flow inlet upon the pressure coefficient and rotor aerodynamic efficiency produced at the exit of the rotating diffuser, several effects of the inlet must be considered in combination. Figures 63 through 65 represent a sampling of the data that were obtained at the rotating diffuser exit by the automatic total pressure and yaw angle probe. The basic data of total pressure and flow angle have been entered into a mass weighting program from which one obtains the tangential and radial components of the velocity along with the rotor aerodynamic efficiency. These quantities are then plotted against passage width. Figure 63 is the result of Run 1252, which was a test of the axial flow inlet with zero degrees of inlet guide vane turning and hub and housing 1 rotating. It can be seen from the figure that the radial and tangential components of velocity are severely deficient near the aft wall of the diffuser. Figure 64 is the result of Run 1250, which investigated the axial inlet with 35 degrees of inlet guide vane turning and hub and housing 1 rotating. The velocity profiles are somewhat improved near the aft wall but do not peak out as

sharply near the forward wall when compared with the previous case with inlet guide vanes at zero degrees. Figure 65 shows the results of Run 1249, which investigated the axial flow inlet with 50 degrees of inlet guide vane turning and hub and housing 1 rotating. The velocity profiles in this figure indicate definite deficiency on the forward wall of the rotating diffuser with much improved flow near the aft wall of the diffuser. When these three figures are considered in combination, a definite trend exists such that at low inlet guide vane turning angles a reduction in radial velocity exists on the aft wall; and as the inlet guide vane angles increase, this effect is overcome and the low radial velocities appear on the forward wall. This is due to the fact that the inlet static pressure gradient is counteracted by an opposing pressure gradient produced by the tangential velocity. The rotor aerodynamic efficiency near the forward wall decreases with increasing inlet guide vane turning angle, since a deepening boundary layer is produced on rotor housing 2 as the tangential component of velocity is made larger. Rotating this wall could improve this situation. This can be seen by again referring to Figures 55 through 60. This efficiency near the aft wall can probably be improved when the cause of the turbulent flow in this region is determined and eliminated.

CONCLUSIONS

Compressor rotors employing impulse-type blading exhibit an increasing work input and increasing total pressure coefficient as the flow coefficient increases. This characteristic is perhaps best illustrated in Figure 33, which presents results for the axial flow inlet without guide vane turning. Impulse rotors, therefore, tend to be strongly affected by inlet flow distortion. Regions of low total pressure entering the rotor blades will probably be amplified in passing through the rotor blades.

Another flow behavior, described by Hawthorne in Reference 9, is the rotation of a total pressure gradient as a flow is turned through a bend (the bend being the rotor blades in this case). For small turning angles in a circular bend, the angle through which the total pressure gradient is rotated is twice the angle of the bend. In the low-speed rotor, the rotor blade camber is about 110 degrees, and the flow passage between blades is rectangular. Because of these differences, Hawthorne's analysis of secondary flow in circular bends cannot be applied directly.

The behavior of the radial velocity leaving the rotor for axial inlet guide vane settings of 0, 35, and 50 degrees (Figures 63, 64, and 65) when compared with the respective inlet total pressure loss coefficients (Figures 59, 57, and 56) suggests that the impulse rotor flow-pressure characteristic and secondary rotation are acting in combination to produce the exit radial velocity distributions observed for the several guide vane angle settings tested. The relatively small changes in tangential velocity and rotor efficiency across the span are encouraging to observe in spite of the distorted inlet flow existing for all three axial flow inlet guide vane angle settings.

Because of the positive slope of the flow-pressure characteristic, rotors using impulse blading are sensitive to distortion of the flow entering the rotor. Inlet distortions tend to be amplified as the flow passes through the rotor. Uniformity of flow is probably important to obtain efficient rotating diffuser, stator, and exit system performance. The selection of an inlet guide vane system to produce a uniform flow entering the rotor is necessary for efficient radial outflow compressor performance.

The difficulties encountered in previous attempts to use radial inflow systems with high swirl angles (Reference 10) did not occur in the present investigation. The results of these tests indicate that permitting the surfaces of the inlet flow path to rotate is generally beneficial to the performance of the radial outflow compressor inlet and rotor for both the radial inflow and axial flow inlet guide vane systems.

The flow angle distribution produced by both inlet systems appeared to be quite satisfactory over the wide range of guide vane angles tested.

Although the static pressure distribution in the spanwise direction across the rotor inlet was not measured, the rapid turning of the flow from the axial to the radial direction requires the existence of a static pressure gradient which probably persisted at the rotor blade leading edges. A higher radial velocity would, therefore, occur at the forward face (rotating shroud) than at the aft face (disc) of the rotor inlet. The rotor blade angle of incidence will be lower in the forward region and higher in the aft region than that calculated for the mean flow. The inlet guide vanes can be twisted to alleviate this condition. The rotor blade leading edge directions could be adjusted to accommodate this flow angle variation, but this was not done in the low-speed radial outflow compressor, and is not presently anticipated for the high-speed compressor. As a result, some reduction in the useful (high efficiency) angle of incidence range occurs compared to the ideal case of uniform radial velocity entering the rotor blades.

The persistence of the upstream static pressure gradient through the rotor blades to the trailing edges seems unlikely to occur in either low- or high-speed radial outflow compressor, since the passage walls are straight in the region of the blades. An inlet static pressure variation is, therefore, not a distortion in the usual sense, since the tangential velocity change (the work input) should not be affected.

The efficiency of the low-speed radial outflow compressor rotor was higher with the radial inlet than with the axial inlet over a wide range of inlet guide vane angular settings.

The reason for the greater losses in the axial flow inlet, particularly for the zero swirl condition, is not clear. For high swirl angles, the inability of untwisted axial inlet guide vanes to impart constant angular

momentum probably accounts for some of the observed nonuniformity in flow. A region of unsteady, fluctuating, turbulent flow has been observed near the inner surface of the inlet flow path.

RECOMMENDATIONS

A sector of the inner passage wall of the high-speed radial outflow compressor inlet should be permitted to rotate with the rotor.

Since the axial flow inlet has been selected for the high-speed radial outflow compressor on the basis of compatibility with an axial flow supercharging stage, further investigation should be conducted using the low-speed radial outflow compressor to determine and eliminate the cause of the unsteady flow and high losses observed in the axial flow inlet. Boundary layer removal and inlet contour changes are methods applicable to both low- and high-speed radial outflow compressors.

If the high-speed radial outflow compressor test results indicate that improved rotor performance can be obtained, the possibility of twisting the inlet guide vanes or the rotor blades to match the airflow and rotor blade leading edge direction should be considered.

ROTOR BLADES

GENERAL

The rotor blade section of the radial outflow compressor has the requirement of turning the relative flow through about 120 degrees with relative inlet Mach numbers up to about 1.4 under approximately impulse conditions. High turning blade sections employing subsonic flow on the concave surfaces and supersonic flow in the convex surfaces have demonstrated superior performance in the NACA Langley supersonic cascade tests. The purpose of the tests conducted during Phase I of the radial outflow compressor program was to obtain sufficient information to select the optimum combination of blade solidity and camber for the particular conditions of this compressor. These tests have also provided information as to the performance of these blade sections at speeds ranging from subsonic to supersonic and as to the range of angle of attack over which these blade sections will operate efficiently.

The radial outflow compressor has its origins in the axial flow impulse compressor which was designed and investigated at the Langley laboratory of NACA (References 11 and 12). The possibility of obtaining high pressure ratios in a single axial flow stage by using a supersonic impulse rotor was also investigated at the Langley laboratory (Reference 13). This axial flow rotor produced a pressure ratio of about 8 to 1 with a rotor efficiency of 90 percent. An axial flow compressor rotor having higher turning and, hence, higher work input was also investigated (Reference 14). This latter rotor produced a pressure ratio of 13 to 1 in the outer streamlines with a high element efficiency that is not reliable because of nonuniformity of the exit flow.

An investigation of supersonic turning passages for compressors or turbines was conducted by NACA (Reference 15). These blade sections employed supersonic free vortex flow through the majority of the passages using a vortex net derived by Dr. A. Busemann. This approach is recommended because it yields a systematic series of blade profiles which exhibit minimum local values of surface Mach number. However, all of the profiles reported in Reference 15 employed fully supersonic flow. This was done because at the time it was believed advantageous to avoid subsonic flow and the normal shock which was anticipated to occur if subsonic flow were employed. The validity of this argument was questioned, however, and in a later incompleted and unreported series of tests, blade sections designed for free vortex flow, but with the pressure surfaces subsonic, were investigated. Total pressure losses for these sections as a function of Mach number are presented in Figure 67. Scatter of the results is attributed to the fact that this program was not completed in the systematic manner which was proposed. These test results did prove that high turning blade sections employing subsonic flow on the concave surfaces and supersonic flow on the convex surfaces were superior to the all-supersonic blades reported in Reference 15. However, the information obtained was insufficient to select the optimum

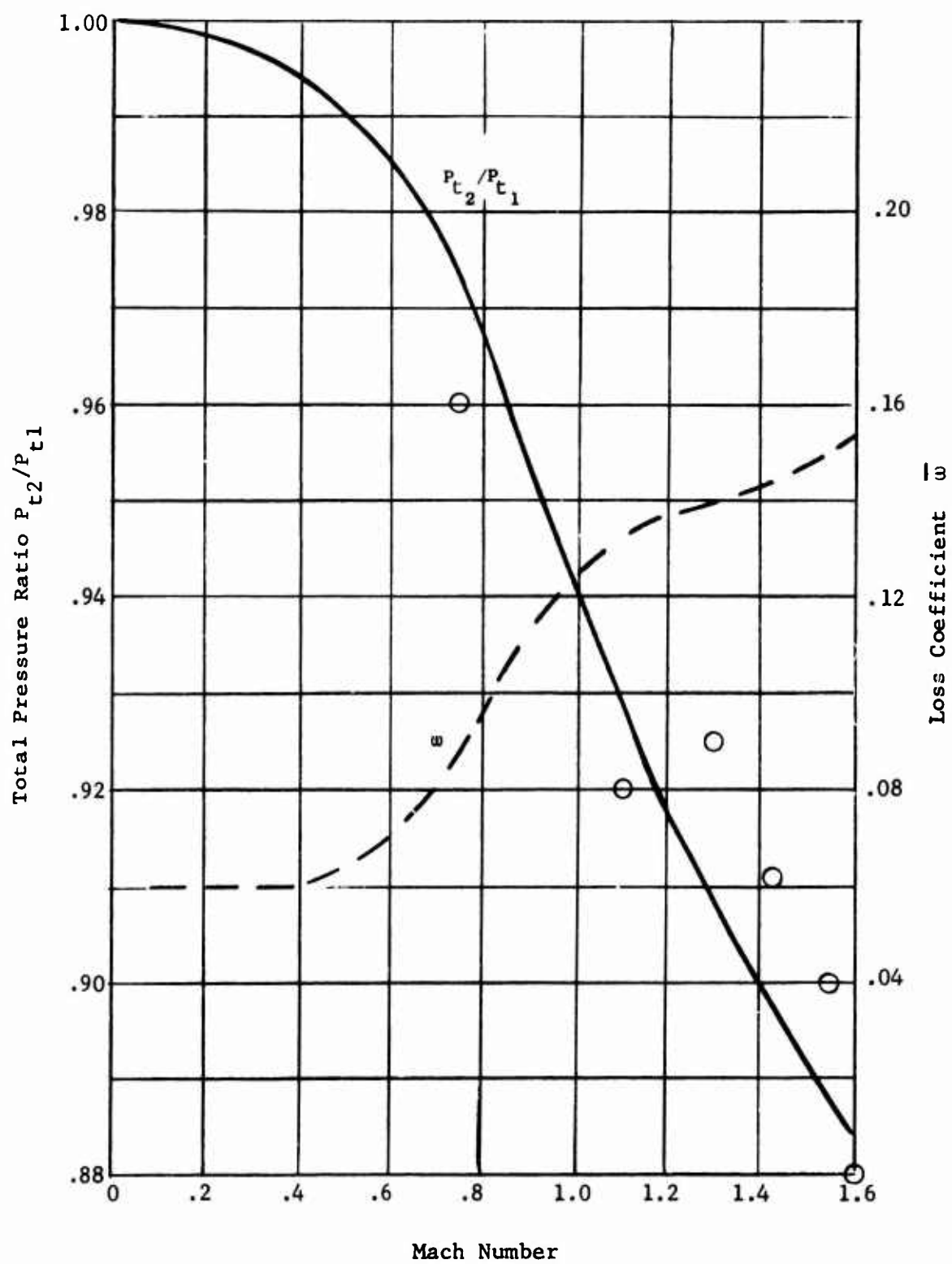


Figure 67. Plot of Total Pressure Ratio and Loss Coefficient as a Function of Entering Mach Number for Blade Sections in Cascade.

combination of blade solidity and camber for the particular conditions of the radial outflow compressor. The requirements of radial outflow compressor rotor blades are different in inlet Mach number and turning angle from the blade sections tested by NACA. An improvement in design technique, combining the waves from the leading edge wedge and the transition section waves, was developed. A reduction in blade solidity resulted. The supersonic cascade investigation conducted in Phase I of this program and reported herein completes the information required for selection of optimum supersonic impulse rotor blade sections for the radial outflow compressor.

DESCRIPTION OF THE TEST ITEM

Existing Blades

A previous program undertaken by the General Electric Company required the design and cascade test of a transonic impulse turbine rotor blade section. These blades were designed for mixed free vortex flow and operation up to an inlet Mach number of unity with about 112 degrees of turning. Examination of this blade shape for operation at inlet Mach numbers of 1.4 indicated the need for a higher solidity, a trend borne out by the tests on similar configurations by NACA. Because of the similarity of the existing blades to matching the overall vector diagram requirements, these sections with the solidity increased to two were selected for performing the initial cascade tests. Higher solidity was believed to be optimum but could not be obtained with the existing sections without voiding vortex flow requirements.

This blading had a relatively thick leading edge which was permissible for the original design conditions for "unstarted" transonic operation. However, for supersonic "started" operation, the effective blockage of 5.7 percent produced by 0.040 inch leading edges was judged to be excessive. The increase in solidity from the original transonic design indicated the desirability of a slightly modified contour for improved area distribution and better matching for the mixed vortex flow design. The modified blades included a 0.010-inch leading edge and a 7-degree leading edge wedge angle which gave an effective blockage of about 1.4 percent.

New Blade Sections

In designing new blade sections using higher solidities, difficulty was encountered in achieving subsonic surface Mach numbers without exceeding the allowable contraction ratio to permit supersonic flow entry. A new design procedure was established for blade sections of this type.

The design requirements of this two-dimensional rotor blade cascade were as follows:

Upstream inlet Mach number	1.42
Upstream inlet flow angle	60 degrees from axial
Solidity	2.5
Turning angle	120 degrees

In addition, it was required that the cascade be nearly impulse and that it be capable of "supersonic starting" at the design inlet conditions or, if possible, at a slightly lower inlet Mach number.

The design approach used was similar to that presented in Reference 15. In this design method, the blade passage is essentially the space between two concentric circular arcs. The blade entrance is designed to convert the uniform entering flow to the required vortex distribution in the circular arc passage, and vice versa at the exit. If the blade edges are cusped, the supersonic flow pattern will be as shown in Figure 68. The flow in region I will be identical to the flow far upstream. The flow in region IV will be the desired vortex flow within the circular arc portion of the passage. In region II, the flow is expanding through expansion waves generated by the convex transition arc; and in region III, the flow is compressed by compression waves generated by the concave transition arc. Coordinates for the concave and convex transition arcs are given in Reference 15 for many combinations of entrance and blade surface Mach numbers.

In the more general case, where the blade leading edges have a finite thickness and wedge angle, the flow pattern becomes somewhat more complicated, as shown in Figure 69. Shock waves and expansion waves from the leading edges extend upstream of the cascade, and the flow immediately ahead of the cascade will be altered from conditions far upstream. Also, shock waves from the leading edges may extend into the blade passage and must be considered in designing the passage entrance region.

Figure 69 shows a schematic diagram of the supersonic flow for this cascade design. For a given upstream Mach number, the upstream flow angle and the flow angle and Mach number in region III, just ahead of the cascade, will adjust themselves to satisfy continuity across the blade passage entrance. This adjustment is accomplished through the action of the shock waves aa' and the expansion fan generated by the corner at b . For uniform flow far upstream, the shock waves and expansion fans from points b must exactly cancel, and thus their strengths must be equal. A particle entering region III from far upstream is seen to cross shocks and expansion waves alternately from all the lower blades in the cascade. However, as the particle enters region III, it will have crossed some expansion waves which go to cancel the shock from the next higher blade in the cascade. Therefore, the flow in region III is uniform but slightly expanded from upstream conditions, and it has a more nearly axial (or radial in the radial outflow compressor) flow direction.

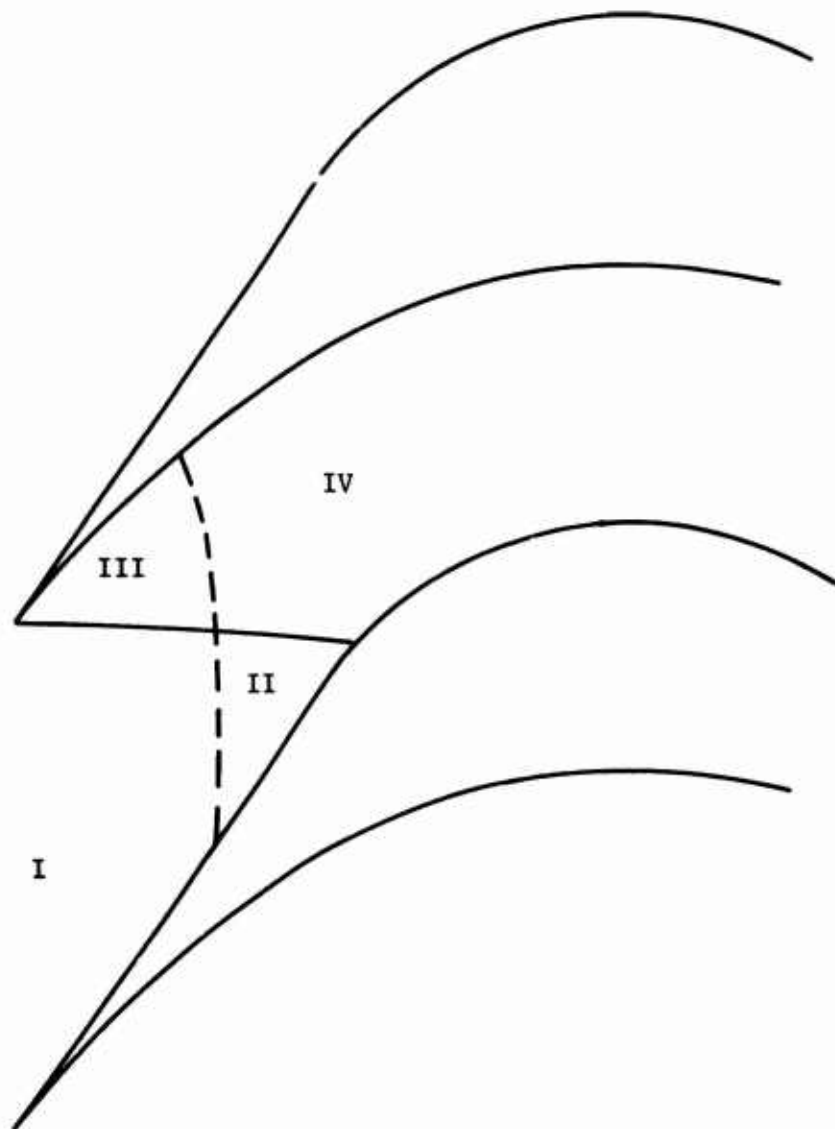


Figure 68. Rotor Blade Schematic Flow Diagram with Cusped Leading Edges.

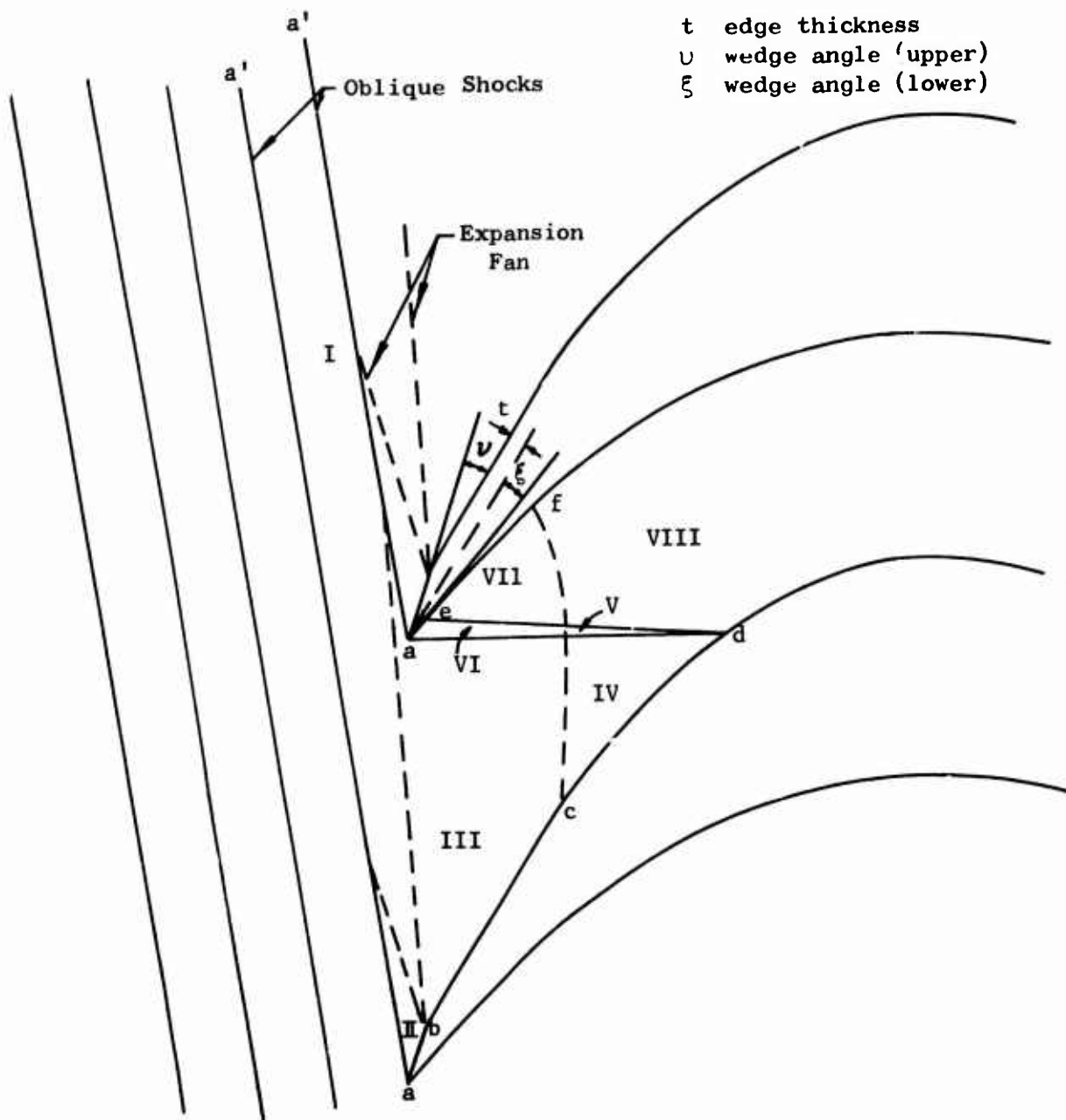


Figure 69. Rotor Blade Schematic Flow Diagram with Finite Leading Edges.

The amount of expansion and flow direction change that takes place depends only on the upstream conditions and leading edge thickness if we assume there is no entropy change across the shock waves. If the edge thickness is zero, the flow in region III is unchanged from upstream conditions. It is also evident now that the angle of the blade surface bc , in combination with the edge thickness t , determines the upstream flow angle for any supersonic Mach number where the shock aa' is attached to the blade leading edge.

The strength of the weak oblique shock aa' and of the expansion fan from b are determined by the wedge angle ν , which should be chosen to be small enough to assure attachment of the shock. The flow in region II is seen to be uniform but compressed somewhat from upstream conditions.

At the passage entrance, the uniform flow in region III must be transformed into the desired vortex flow in region VII. In the case where the leading edge wedge angle is zero, the shock ad vanishes and the transition arcs cd and ef can be constructed exactly by the methods of Reference 15. If the wedge angle ζ is not zero, the shock ad extends across the passage and is cancelled by the expansion corner at d . The transition arc ef can now be designed by using, as the entering conditions, the conditions in region VI following the shock. The transition arc cd is designed using as entering conditions the conditions in region III, and at point d using a property angle (which is a function of the Mach number) higher than that desired on convex blade surface by an amount ζ . The Mach wave ed and the shock ad are not quite coincident, so there must be a short straight line segment, ae , on the concave surface of the blade.

If an impulse cascade is desired, the exit region of the passage may be made identical to the entrance region and the resulting blade will be symmetrical.

Using this design approach, the final blade shape and solidity are determined by the choice of five design parameters.

1. Edge thickness, t , as a fraction of blade spacing
2. Lower edge wedge angle, ζ
3. Upper edge wedge angle, ν
4. Lower or concave surface Mach number within the passage
5. Upper or convex surface Mach number within the passage

The choice of edge thickness is limited by the following consideration. As the edge thickness is increased, the Mach number in region III increases until the last expansion wave from the corner, b , intersects the leading edge of the next higher blade in the cascade. If the edge thickness is increased beyond this point, the blade passage cannot pass the required flow and the upstream conditions cannot be satisfied. For this design, an edge thickness of 1.0 percent of the blade spacing was chosen. This resulted in a Mach number in region III of 1.503 and an incidence angle of 2.44 degrees for the surface bc .

Angles ζ and ν were chosen to be 5 degrees to give a total wedge angle of 10 degrees to the leading edge. This assured that the shocks would be attached and also gave an acceptable leading edge from a strength standpoint.

The concave surface Mach number was chosen as 1.0, and the convex surface Mach number was chosen as 2.0. These choices were based on the resulting solidity and starting characteristics of the cascade. It would have been desirable to lower the convex surface Mach number below 2.0 in order to minimize the amount of diffusion necessary on the aft side of this surface. Attempts to do so, however, resulted in either increased solidity or decreased passage width, or a combination of both. Decreased passage width was undesirable because of the starting problem. With increased solidity, it was doubtful whether there would be any net decrease in blade losses because of the increased blade surface area. The cascade resulting from these choices then had a solidity of 2.52 and an effective passage area 1.9 percent larger than the theoretical minimum to permit starting at the design inlet conditions (see Figure 70).

EXPERIMENTAL PROCEDURE

When the initial series of tests was conducted, the existing supersonic blade sections were used. The range of solidity variation with this blade section, which would yield reasonable passage area distributions, was limited to values near 2.0.

The first test series on these blades was done to determine the allowances which should be made for boundary layer growth within the blade passage. Solidity was maintained at 2.0, and the blade passage area ratio was varied by resetting the blades.

The blade settings were:

1. Exit area equal to inlet area (nominal)
2. Exit area 4 percent larger than inlet area (a blade closure of 0.7 degree from nominal)
3. Exit area 8 percent larger than inlet area (a blade closure of 1.4 degrees from nominal)

The tests were conducted with solid walls for schlieren viewing.

The second test series on these blades was conducted to determine the effect of using porous sidewalls. The nominal and 4-percent open setting angles were investigated. Past experience with General Electric's Transonic Cascade Tunnel and with the cascade tunnel of NACA (Reference 16) has shown that porous sidewalls are beneficial and in many cases required (for cascades with pressure rise) for achieving two-dimensional flow conditions.

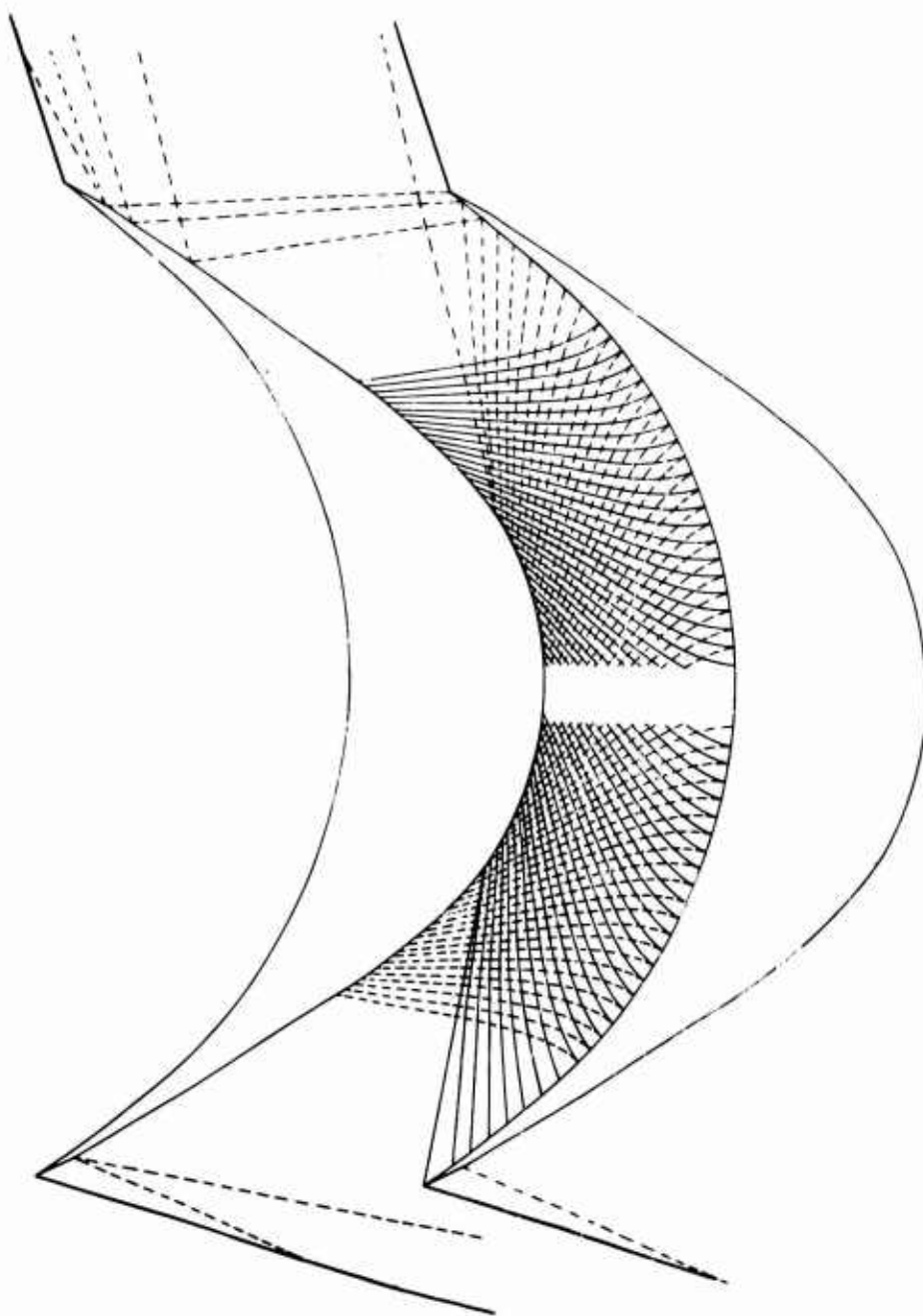


Figure 70. Two-Dimensional Supersonic Rotor Blade.

For the third test series, the blading was modified to incorporate a 0.010-inch leading edge and a 7-degree leading edge wedge angle. This configuration was tested at the nominal setting angle with both schlieren and porous sidewalls.

New blade sections were designed and built specifically to match free vortex flow at the operational requirements of the radial outflow compressor (see Figure 70). These blade sections were tested at subsonic, transonic, and supersonic speeds and at variable inlet angles.

All of the rotor blade testing was done in the General Electric Transonic Cascade Tunnel. The rotor blade cascade assembly is shown in Figures 71 and 72. The inlet and exit static pressure instrumentation can be seen in this view. The measured test parameters were: inlet total pressure, inlet total temperature, inlet static pressure, inlet flow angle, inlet Mach number, exit total pressure, exit static pressure, and exit flow angle.

The rotor blade cascade assembly is mounted to the tunnel so that the tunnel flow enters the cascade at the proper angle. The support arms on the cascade assembly (Figures 71 and 72) were made so that fine adjustment of inlet flow angle could be made. The transonic cascade tunnel supplies the inlet flow at the desired Mach number. A Mach number meter is provided on the tunnel control panel for this purpose.

The rotor blade testing on both the existing and the new blade sections is summarized in Table III.

EXPERIMENTAL RESULTS

A tabulation of test results for test runs on the existing rotor blade sections, the existing rotor blade sections with modified leading edge, and the new rotor blade sections is included in Table IV. The more significant schlieren photographs are also included (Figures 73 through 84) and are referenced to the test case number each represents.

EVALUATION

As indicated in Table III, the test variable during the first four runs on the existing blade sections was blade setting angle. The following blade settings (λ^*) were used:

1. Nominal - exit area equal to inlet area
2. 0.7 degree closed - exit area 4 percent larger than inlet area
3. 1.4 degrees closed - exit area 8 percent larger than inlet area

Schlieren observation of the flow indicated that a strong shock wave existed upstream of each leading edge and that supersonic entry was not established. For the two blade settings closed from nominal, the

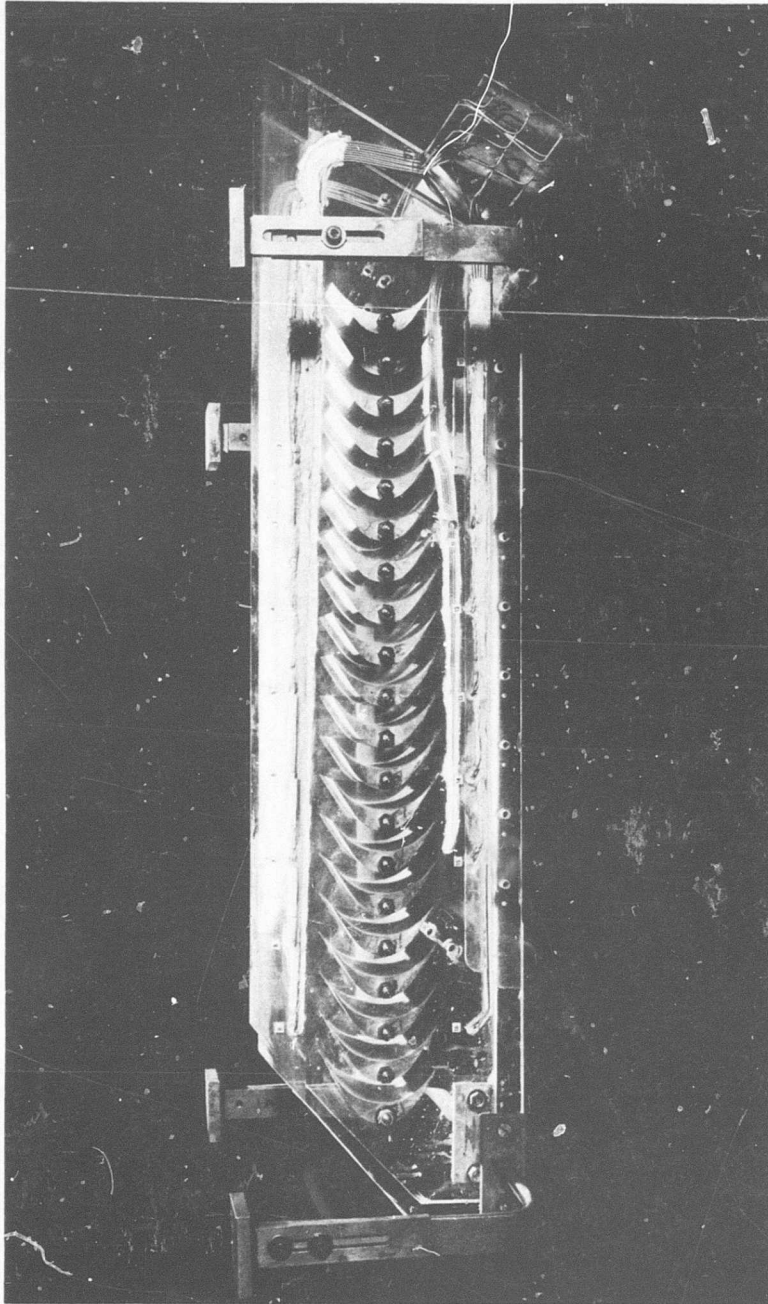


Figure 71. Rotor Blade Cascade Assembly, Side View.

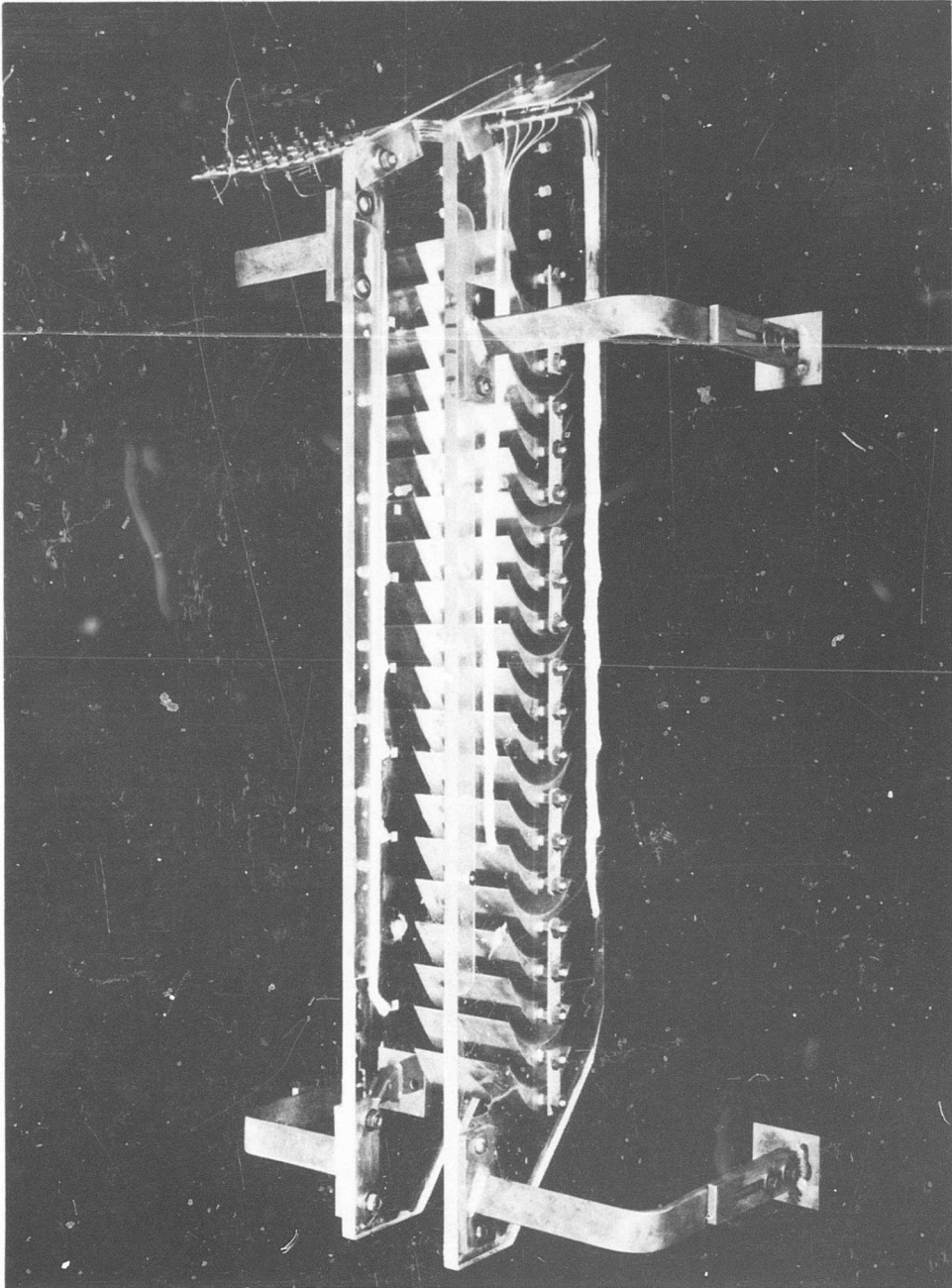


Figure 72. Rotor Blade Cascade Assembly, Oblique View.

TABLE III
ROTOR BLADE RUN SUMMARY

Date	Run No.	Cascade	Blade Setting	Sidewalls	Test Variables
5/19/64	1	Existing	Closed 0.7°	Solid	Mach Number
5/20/64	2	Existing	Closed 0.7°	Solid	Mach Number & Inlet Angle
5/21/64	3	Existing	Closed 1.4°	Solid	Mach Number & Inlet Angle
5/22/64	4	Existing	Nominal	Solid	Mach Number & Inlet Angle
5/25/64	5	Existing	Nominal	Porous	Mach Number & Inlet Angle
6/1/64	6	Existing	Closed 0.7°	Porous	Mach Number & Inlet Angle
6/2/64	7	Existing-Modified	Nominal	Porous	Mach Number & Inlet Angle
6/3/64	8	Existing-Modified	Nominal	Solid	Mach Number & Inlet Angle
12/4/64	1	New	Nominal	Solid	Mach Number & Inlet Angle
12/7/64	2	New	Nominal	Solid	Mach Number & Inlet Angle
12/8/64	3	New	Nominal	Solid	Mach Number & Inlet Angle

TABLE IV
 ROTOR BLADE CASCADE TEST RESULTS
 Existing Rotor Blade Tests Solidity = 2.0

Date	Run No.	Case	Inlet Mach No.	Air Inlet Angle	\bar{C}_P	$\bar{\omega}$	λ^*
5/19/64	1	20186	.366	56.3	-.0135	.0514	56.3
5/19/64	1	20187	.545	56.3	-.0535	.0576	56.3
5/19/64	1	20188	.758	56.3	-.244	.1085	56.3
5/20/64	2	20190	.525	56.3	-	.054	56.3
5/20/64	2	20191	.615	56.3	-.064	.074	56.3
5/20/64	2	20192	.69	56.3	.0914	.0905	56.3
5/20/64	2	20193	.30	56.3	.036	.073	56.3
5/20/64	2	20194	.30	58.3	-.095	.074	56.3
5/20/64	2	20195	.515	58.3	.0595	.046	56.3
5/20/64	2	20196	.615	58.3	.033	.0548	56.3
5/20/64	2	20197	.805	58.3	-.045	.0874	56.3
5/20/64	2	20198	.985	58.3	-.358	.222	56.3
5/20/64	2	20200	.987	59.3	-.205	.191	56.3
5/20/64	2	20201	.987	60.3	-.092	.192	56.3
5/20/64	2	20202	1.14	60.3	-.183	.248	56.3
5/20/64	2	20203	1.14	61.3	-.164	.248	56.3
5/20/64	2	20204	1.0	61.3	-.0685	.297	56.3
5/20/64	2	20205	.82	61.3	.0876	.0706	56.3
5/20/64	2	20206	.512	60.6	.129	.0603	56.3
5/20/64	2	20207	.513	61.3	.14	.0587	56.3
5/21/64	3	20208	.515	57	.022	.06	57
5/21/64	3	20209	.515	57	.022	.069	57
5/21/64	3	20210	.61	57	0	.0765	57
5/21/64	3	20211	.7	57	-.041	.097	57
5/21/64	3	20212	.755	57	-.17	.156	57
5/21/64	3	20213	.76	59	.041	.085	57
5/21/64	3	20214	.865	59	-.0645	.165	57
5/21/64	3	20215	.868	60	.0615	.148	57
5/21/64	3	20216	1.12	60	.0476	.227	57
5/21/64	3	20217	1.12	61	.019	.217	57
5/21/64	3	20218	1.21	61	-.076	.257	57
5/21/64	3	20219	.92	61	.116	.144	57
5/21/64	3	20220	.705	61	.159	.088	57
5/22/64	4	20222	.535	55.6	-.080	.053	55.6
5/22/64	4	20223	.535	55.6	-.080	.064	55.6
5/22/64	4	20224	.535	55.6	-	.090	55.6
5/22/64	4	20225	.535	55.6	-	.278	55.6
5/22/64	4	20226	.535	55.6	-	.233	55.6
5/22/64	4	20227	.535	55.6	-	.074	55.6
5/22/64	4	20228	.605	55.6	-.112	.061	55.6
5/22/64	4	20229	.705	55.6	-.194	.087	55.6

TABLE IV, Continued

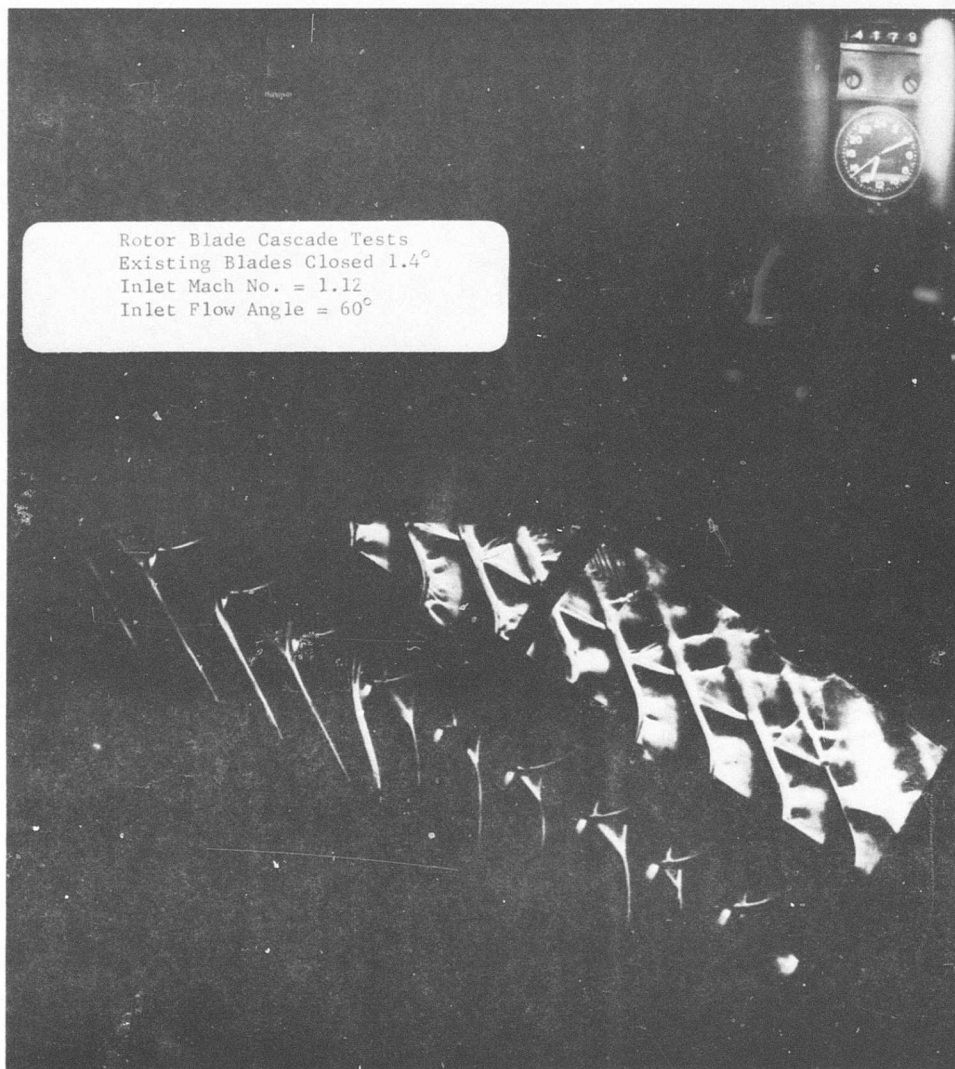
Date	Run No.	Case	Inlet Mach No.	Air Inlet Angle	\bar{C}_P	\bar{w}	λ^*
5/22/64	4	20230	.705	55.6	-	.112	55.6
5/22/64	4	20231	.705	55.6	-	.131	55.6
5/22/64	4	20232	.705	57.6	-.033	.056	55.6
5/22/64	4	20233	.705	57.6	-	.086	55.6
5/22/64	4	20234	.705	57.6	-	.130	55.6
5/22/64	4	20235	.705	57.6	Incomplete		55.6
5/22/64	4	20236	.855	57.6	-.189	.096	55.6
5/22/64	4	20237	.922	58.6	-.177	.123	55.6
5/22/64	4	20238	1.035	59.6	-.108	.152	55.6
5/22/64	4	20239	1.03	59.6	-	.175	55.6
5/22/64	4	20240	1.034	59.6	-.106	.170	55.6
5/22/64	4	20241	1.331	60.6	-.023	.232	55.6
5/22/64	4	20242	1.33	59.6	-.027	.228	55.6
5/22/64	4	20243	1.231	59.6	-.049	.206	55.6
5/22/64	4	20244	1.295	59.6	-.025	.219	55.6
5/22/64	4	20245	1.173	59.6	-.043	.185	55.6
5/22/64	4	20247	1.098	59.6	-.014	.156	55.6
5/22/64	4	20248	1.028	59.6	-.030	.129	55.6
5/22/64	4	20249	.933	59.6	.026	.101	55.6
5/22/64	4	20250	.796	59.6	.043	.075	55.6
5/22/64	4	20251	.654	59.6	.069	.069	55.6
5/22/64	4	20252	.504	59.6	.097	.063	55.6
5/25/64	5	20254	.31	55.6	.002	.0382	55.6
5/25/64	5	20256	.56	55.6	0	.056	55.6
5/25/64	5	20257	.655	55.6	0	.0629	55.6
5/25/64	5	20258	.655	55.6	-.12	.064	55.6
5/25/64	5	20259	.765	55.6	-.183	.0824	55.6
5/25/64	5	20260	.765	57.6	-.057	.074	55.6
5/25/64	5	20261	.89	57.6	-.0837	.0784	55.6
5/25/64	5	20262	.95	57.6	-.119	.103	55.6
5/25/64	5	20263	.957	59.6	.004	.114	55.6
5/25/64	5	20264	1.38	59.6	-.04	.260	55.6
5/25/64	5	20265	1.38	59.6	-.04	.282	55.6
5/25/64	5	20266	1.379	59.6	-.037	.364	55.6
5/25/64	5	20267	1.379	59.6	-.038	.334	55.6
5/25/64	5	20268	1.379	59.6	-.037	.307	55.6
5/25/64	5	20269	1.346	59.6	-.048	.230	55.6
5/25/64	5	20270	1.295	59.6	-.062	.213	55.6
5/25/64	5	20271	1.19	59.6	-.040	.162	55.6
5/25/64	5	20272	1.122	59.6	-.030	.139	55.6
5/25/64	5	20273	1.047	59.6	-.016	.127	55.6
5/25/64	5	20274	.965	59.6	.020	.106	55.6
5/25/64	5	20275	.815	59.6	.091	.087	55.6
5/25/64	5	20276	.522	59.6	.155	.067	55.6
5/25/64	5	20277	.353	59.6	.138	.059	55.6
6/1/64	6	20279	.519	58.3	.110	.062	56.3

TABLE IV, Continued

Date	Run No.	Case	Inlet Mach No.	Air Inlet Angle	\bar{C}_P	\bar{w}	λ^*
6/1/64	6	20280	.705	58.3	.040	.074	56.3
6/1/64	6	20281	.797	58.3	.016	.078	56.3
6/1/64	6	20282	.799	60.3	.149	.080	56.3
6/1/64	6	20283	1.351	60.3	-.025	.276	56.3
6/1/64	6	20284	1.3	60.3	-.018	.240	56.3
6/1/64	6	20285	1.244	60.3	-.020	.206	56.3
6/1/64	6	20286	1.188	60.3	-.013	.187	56.3
6/1/64	6	20287	1.119	60.3	-.019	.171	56.3
6/1/64	6	20288	1.053	60.3	-.009	.143	56.3
6/1/64	6	20289	.956	60.3	.055	.096	56.3
6/1/64	6	20290	.903	60.3	.080	.085	56.3
6/1/64	6	20291	.796	60.3	.119	.073	56.3
6/2/64	7	20293	.515	57.6	.109	.060	55.6
6/2/64	7	20294	.703	57.6	.040	.062	55.6
6/2/64	7	20295	.803	57.6	.003	.091	55.6
6/2/64	7	20296	.910	57.6	-.073	.122	55.6
6/2/64	7	20297	1.359	57.6	-.062	.223	55.6
6/2/64	7	20298	1.227	57.6	-.071	.201	55.6
6/2/64	7	20299	1.101	57.6	-.132	.165	55.6
6/2/64	7	20300	.912	57.6	-.073	.126	55.6
6/2/64	7	20301	.915	59.6	.087	.082	55.6
6/2/64	7	20302	1.393	59.6	-.040	.233	55.6
6/2/64	7	20303	1.349	59.6	-.014	.210	55.6
6/2/64	7	20304	1.346	58.1	-.029	.210	55.6
6/2/64	7	20305	1.391	57.1	-.045	.219	55.6
6/2/64	7	20306	1.254	59.6	-.021	.207	55.6
6/2/64	7	20307	1.101	59.6	-.007	.163	55.6
6/2/64	7	20308	.954	59.6	.057	.104	55.6
6/2/64	7	20309	.714	59.6	.124	.080	55.6
6/3/64	8	20311	.521	57.6	.006	.059	55.6
6/3/64	8	20312	.805	57.6	-.089	.103	55.6
6/3/64	8	20313	.881	57.6	-.195	.143	55.6
6/3/64	8	20314	.885	59.6	.027	.085	55.6
6/3/64	8	20316	1.357	59.6	-.050	.267	55.6
6/3/64	8	20317	1.335	57.6	-.066	.228	55.6
6/3/64	8	20318	1.325	56.6	-.073	.209	55.6
6/3/64	8	20319	1.312	56.1	-.083	.209	55.6
6/3/64	8	20320	1.328	57.1	-.071	.258	55.6

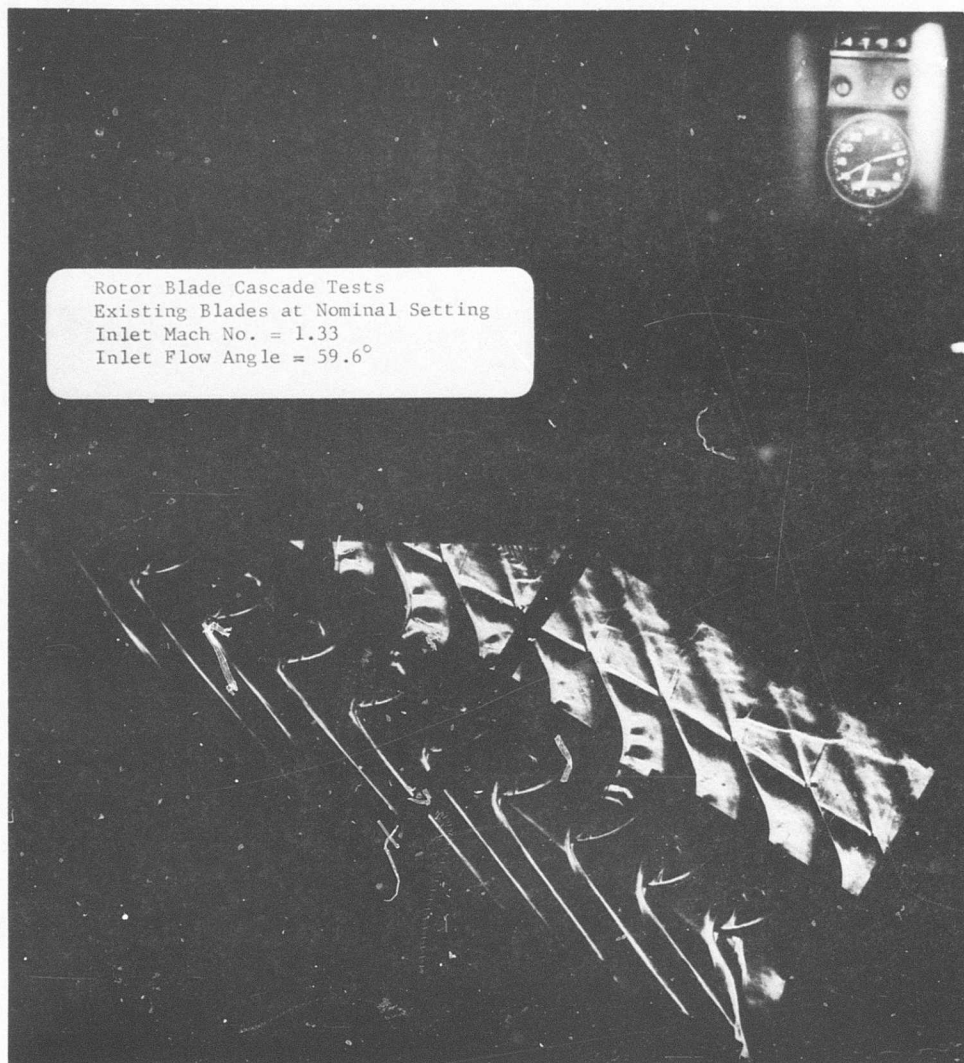
TABLE IV, Continued

New Rotor Blade Test Solidity = 2.5						
Date	Run No.	Case	Inlet Mach No.	Air Inlet Angle	\bar{C}_P	$\bar{\omega}$
12/4/64	1	21949	1.130	60	.016	.154
12/4/64	1	21950	1.258	60	-.048	.172
12/4/64	1	21951	1.373	60	-.049	.211
12/4/64	1	21952	1.406	60	-.030	.191
12/4/64	1	21953	1.436	60	-.016	.190
12/4/64	1	21954	1.497	60	-.010	.187
12/4/64	1	21955	1.296	61	-.009	.185
12/4/64	1	21956	1.334	61	-.008	.210
12/4/64	1	21957	1.380	61	-.013	.194
12/4/64	1	21958	1.421	61	-.009	.194
12/4/64	1	21959	1.484	61	-.008	.199
12/4/64	1	21960	1.289	59	-.003	.195
12/4/64	1	21961	1.358	59	-.006	.211
12/4/64	1	21962	1.419	59	-.008	.184
12/4/64	1	21963	1.470	59	-.003	.186
12/4/64	1	21964	1.460	58	-.001	.197
12/4/64	1	21965	1.389	62	.001	.202
12/7/64	2	21967	.619	60	-.004	.088
12/7/64	2	21968	.806	60	0	.090
12/7/64	2	21969	.995	60	.002	.139
12/8/64	3	21971	.604	60	0	.079
12/8/64	3	21972	.604	59	.001	.081
12/8/64	3	21973	.604	61	-.001	.081
12/8/64	3	21974	.799	61	.002	.089
12/8/64	3	21975	.798	60	.003	.086
12/8/64	3	21976	.798	59	.003	.083
12/8/64	3	21977	.997	59	.001	.125
12/8/64	3	21978	.997	60	.002	.128
12/8/64	3	21979	.997	61	.002	.134
12/8/64	3	21980	1.175	61	.004	.155
12/8/64	3	21981	1.176	60	.005	.153
12/8/64	3	21982	1.176	59	.002	.146
12/8/64	3	21983	1.291	60	.003	.185
12/8/64	3	21984	1.340	60	.002	.222
12/8/64	3	21985	1.392	60	.001	.206
12/8/64	3	21986	1.441	60	-.001	.203
12/8/64	3	21988	.801	63	.003	.091
12/8/64	3	21989	.801	57.45	.001	.086
12/8/64	3	21990	.603	57.42	.002	.074
12/8/64	3	21991	.603	63	.004	.091



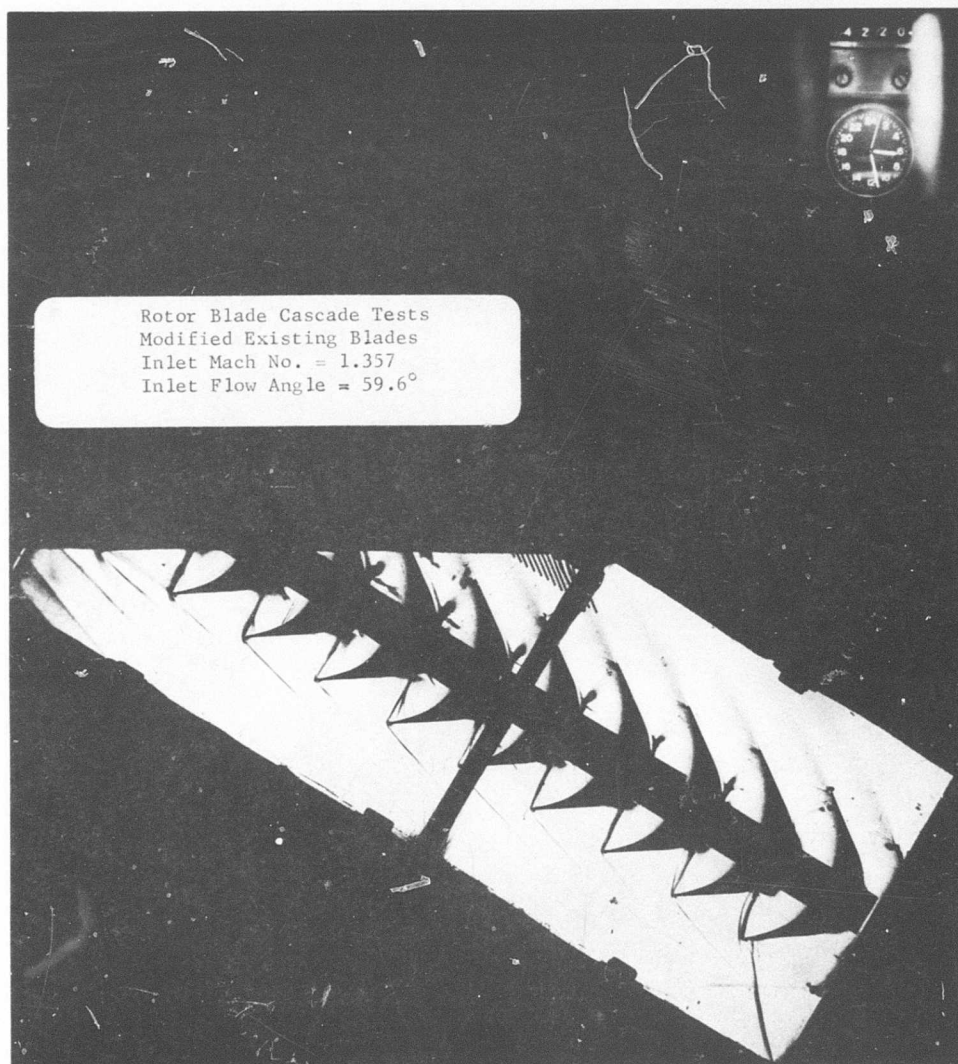
Rotor Blade Cascade Tests
Existing Blades Closed 1.4°
Inlet Mach No. = 1.12
Inlet Flow Angle = 60°

Figure 73. Schlieren Photograph, Rotor Blade Cascade Tests, Case Number 20216.



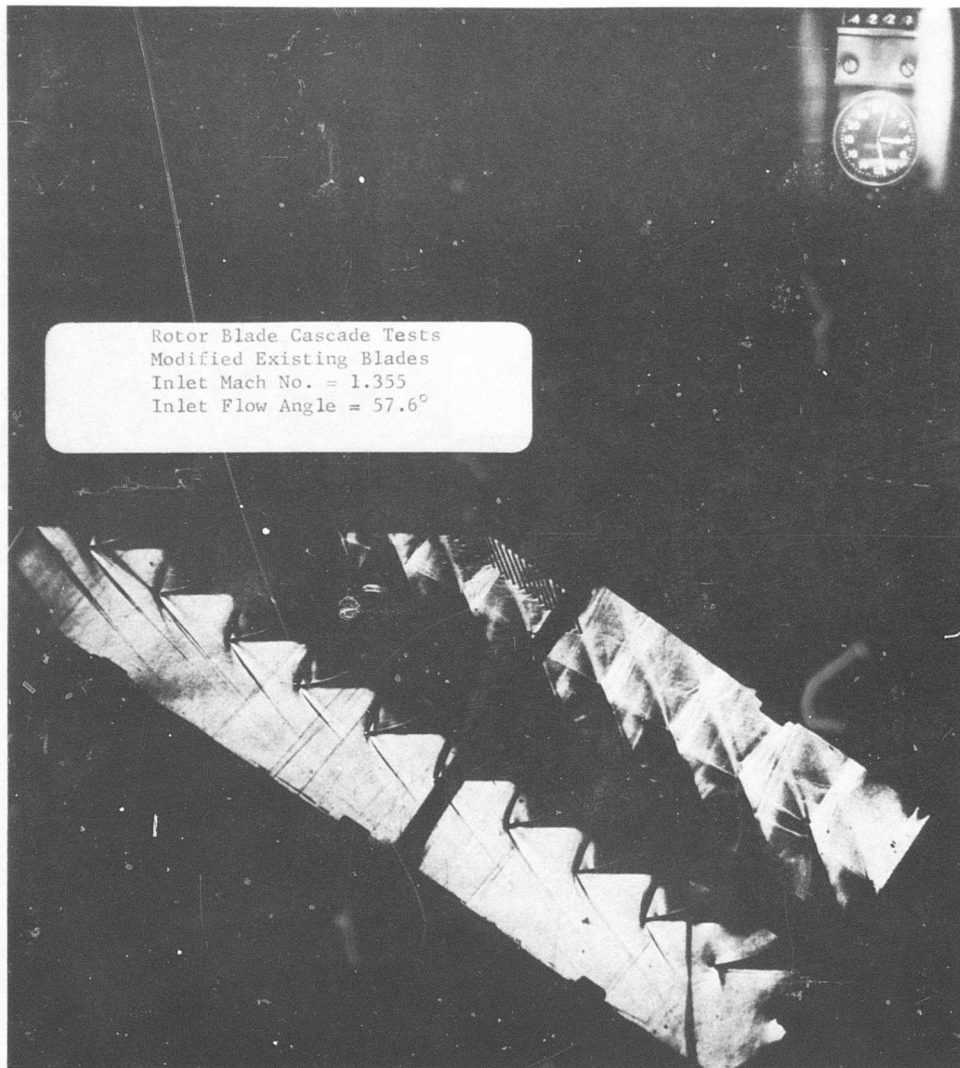
Rotor Blade Cascade Tests
Existing Blades at Nominal Setting
Inlet Mach No. = 1.33
Inlet Flow Angle = 59.6°

Figure 74. Schlieren Photograph, Rotor Blade Cascade Tests, Case Number 20242.



Rotor Blade Cascade Tests
Modified Existing Blades
Inlet Mach No. = 1.357
Inlet Flow Angle = 59.6°

Figure 75. Schlieren Photograph, Rotor Blade Cascade Tests, Case Number 20316.



Rotor Blade Cascade Tests
Modified Existing Blades
Inlet Mach No. = 1.355
Inlet Flow Angle = 57.6°

Figure 76. Schlieren Photograph, Rotor Blade Cascade Tests,
Case Number 20317.

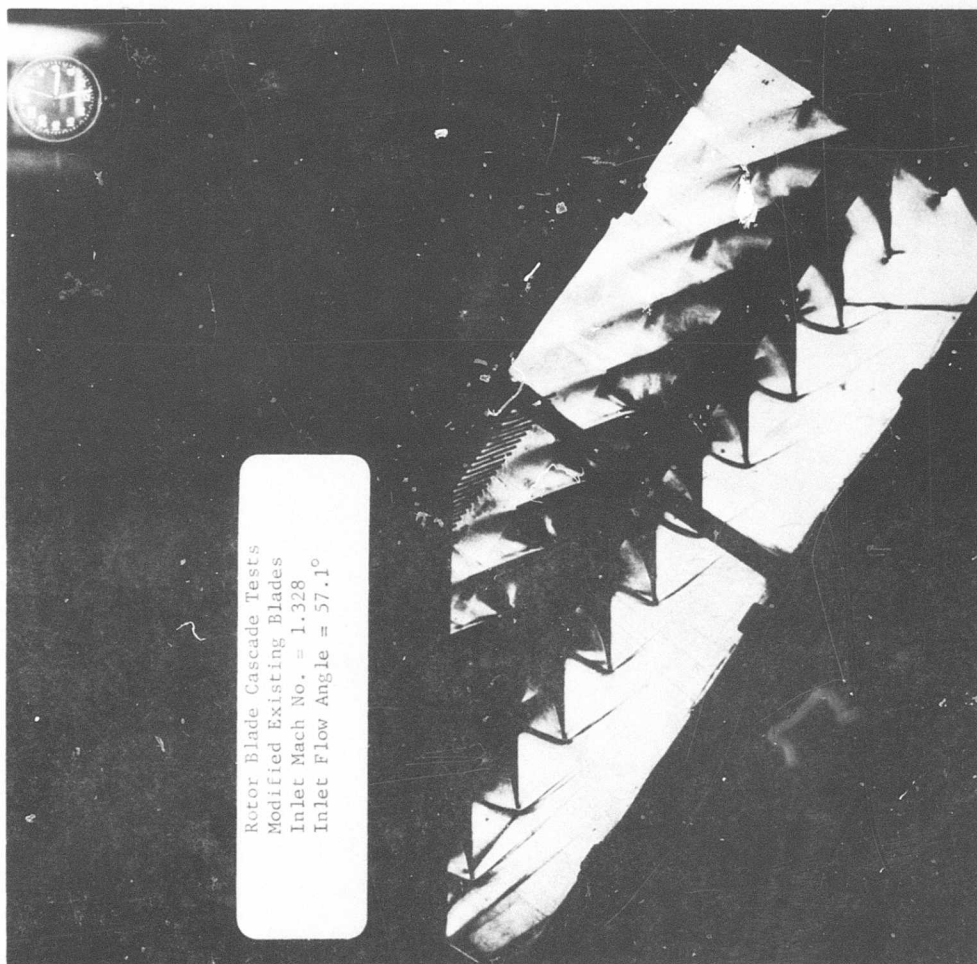


Figure 77. Schlieren Photograph, Rotor Blade Cascade Tests, Case Number 20320.

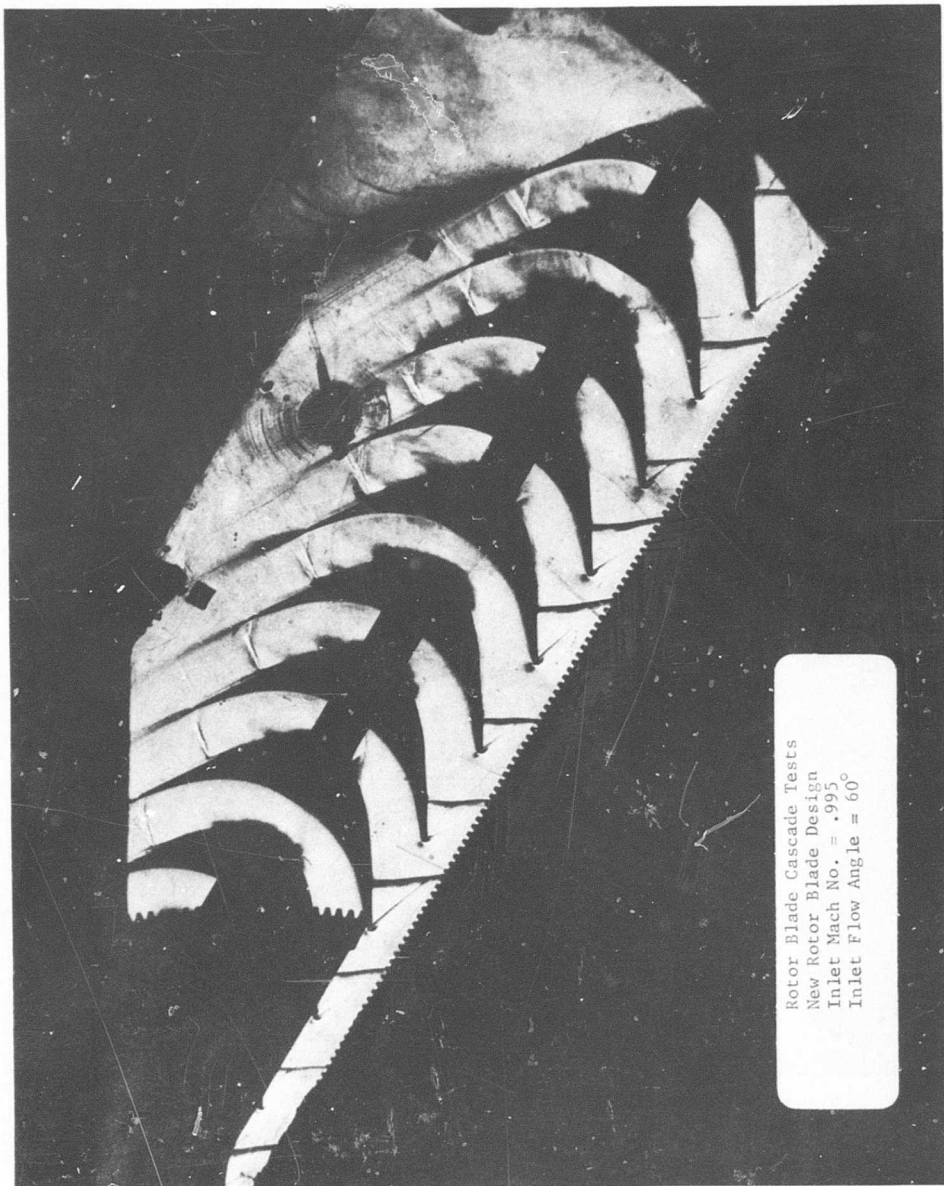


Figure 78. Schlieren Photograph, Rotor Blade Cascade Tests, Case Number 21969.



Rotor Blade Cascade Tests
New Rotor Blade Design
Inlet Mach No. = 1.176
Inlet Flow Angle = 60°

Figure 79. Schlieren Photograph, Rotor Blade Cascade Tests, Case Number 21981.



Rotor Blade Cascade Tests
New Rotor Blade Design
Inlet Mach No. = 1.291
Inlet Flow Angle = 60°

Figure 80. Schlieren Photograph, Rotor Blade Cascade Tests, Case Number 21983.

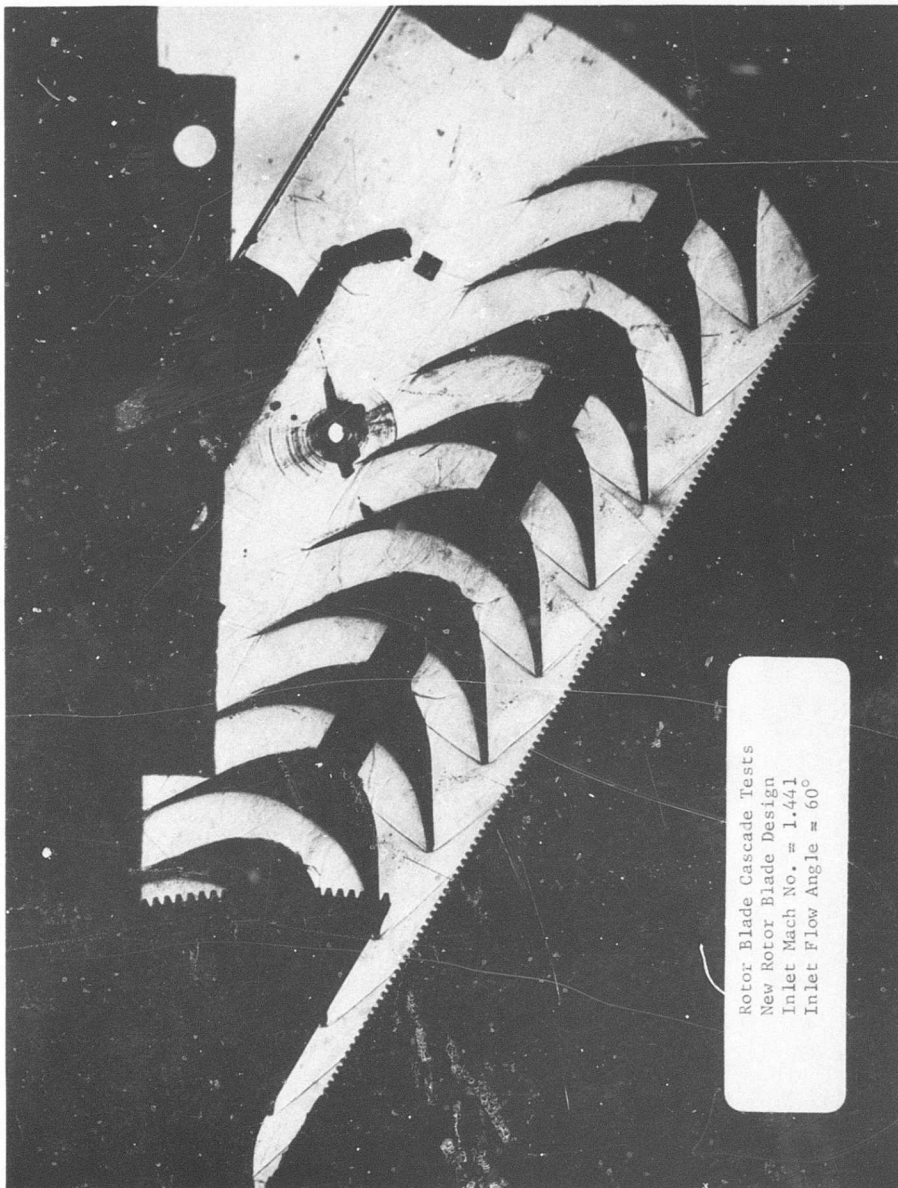


Figure 81. Schlieren Photograph, Rotor Blade Cascade Tests, Case Number 21984.



Rotor Blade Cascade Tests
New Rotor Blade Design
Inlet Mach No. = 1.392
Inlet Flow Angle = 60°

Figure 82. Schlieren Photograph, Rotor Blade Cascade Tests, Case Number 21985.



Rotor Blade Cascade Tests
New Rotor Blade Design
Inlet Mach No. ≈ 1.441
Inlet Flow Angle $\approx 60^\circ$

Figure 83. Schlieren Photograph, Rotor Blade Cascade Tests, Case Number 21986.



Rotor Blade Cascade Tests
New Rotor Blade Design
Inlet Mach No. = 1.441
Inlet Flow Angle = 60°

Figure 84. Schlieren Photograph, Rotor Blade Cascade Tests, Case Number 21986.

losses were very high and a large static pressure drop occurred across the cascade. The nominal configuration ran in a more conventional manner but did not achieve "started" supersonic flow.

Porous sidewalls were used during the next two runs (Runs 5 and 6), and blade setting angles of nominal and 0.7 degree closed were investigated. The nominal configuration was again found to be superior. The test results for the existing blade sections at the nominal blade setting angle with solid and porous sidewalls are presented in Figure 85. These sections operated with a loss coefficient of about 0.22 at an inlet Mach number of 1.30. With the existing blade sections, "started" supersonic flow entry was not achieved with solid or porous sidewalls.

The existing blade sections modified to incorporate a 0.010-inch leading edge and a 7-degree leading edge wedge angle provided improved area distribution and better matching for the mixed vortex flow design. The nominal blade setting angle with both solid (for schlieren viewing) and porous sidewalls was investigated (see Figure 86). At an indicated inlet Mach number of 1.35, the loss coefficient was 0.21. Calculation of the inlet Mach number from the Mach wave angles seen in the flow shadowgraph, Figure 79, yields a value of 1.41. At this high inlet Mach number, the loss coefficient is reduced to 0.202 compared to the target value of 0.15 at an inlet Mach number of 1.42.

New rotor blade sections with higher solidity (2.5) were tested over a range of Mach numbers from 0.6 to 1.5 and a range of inlet angles from 57.4 to 63 degrees. At the design inlet angle of 60 degrees, the flow through the blades was fully supersonic at the design inlet Mach number of 1.42. At an inlet angle of 58 degrees, supersonic flow started at an inlet Mach number of 1.45; at an inlet angle of 62 degrees, it started at an inlet Mach number of 1.38. Loss coefficient and static pressure rise coefficient at the design inlet angle of 60 degrees are presented in Figure 87. At the design inlet Mach number of 1.42, the minimum loss coefficient was about 0.185, which is slightly higher than the target value of 0.15. The loss coefficient variation with inlet angle changes was very slight, as can be seen in Figure 88.

CONCLUSIONS

When the existing rotor blade sections were used, the value of solidity was limited to values close to two to maintain mixed free vortex flow conditions. An investigation was undertaken to determine the allowances which should be made for boundary layer growth within the blade passage maintaining solidity constant. Supersonic flow entry was not achieved with solid or porous sidewalls, but the configuration that yielded the best performance had the exit area equal to the inlet area.

By reducing the blade leading edge from 0.040 to 0.010 and by modifying the blade contour to give a 7-degree leading edge wedge angle, the effective blockage was reduced from 5.7 to 1.4 percent. This resulted

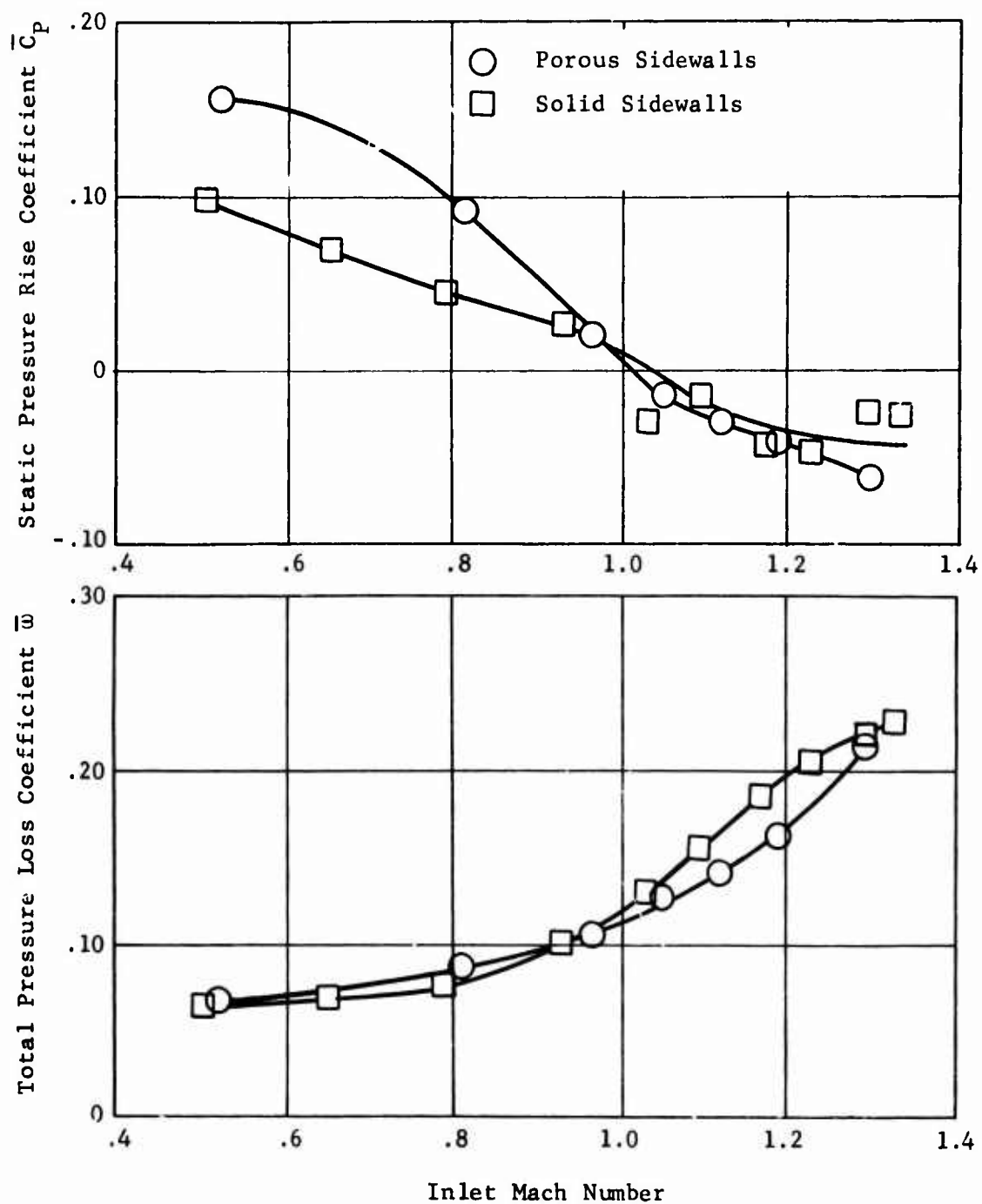


Figure 85. Test Results of Existing Rotor Blades at Nominal Blade Setting (Leading Edge Suction Surface Angle = 55.6°), Inlet Air Angle = 59.6° (Solidity = 2.0).

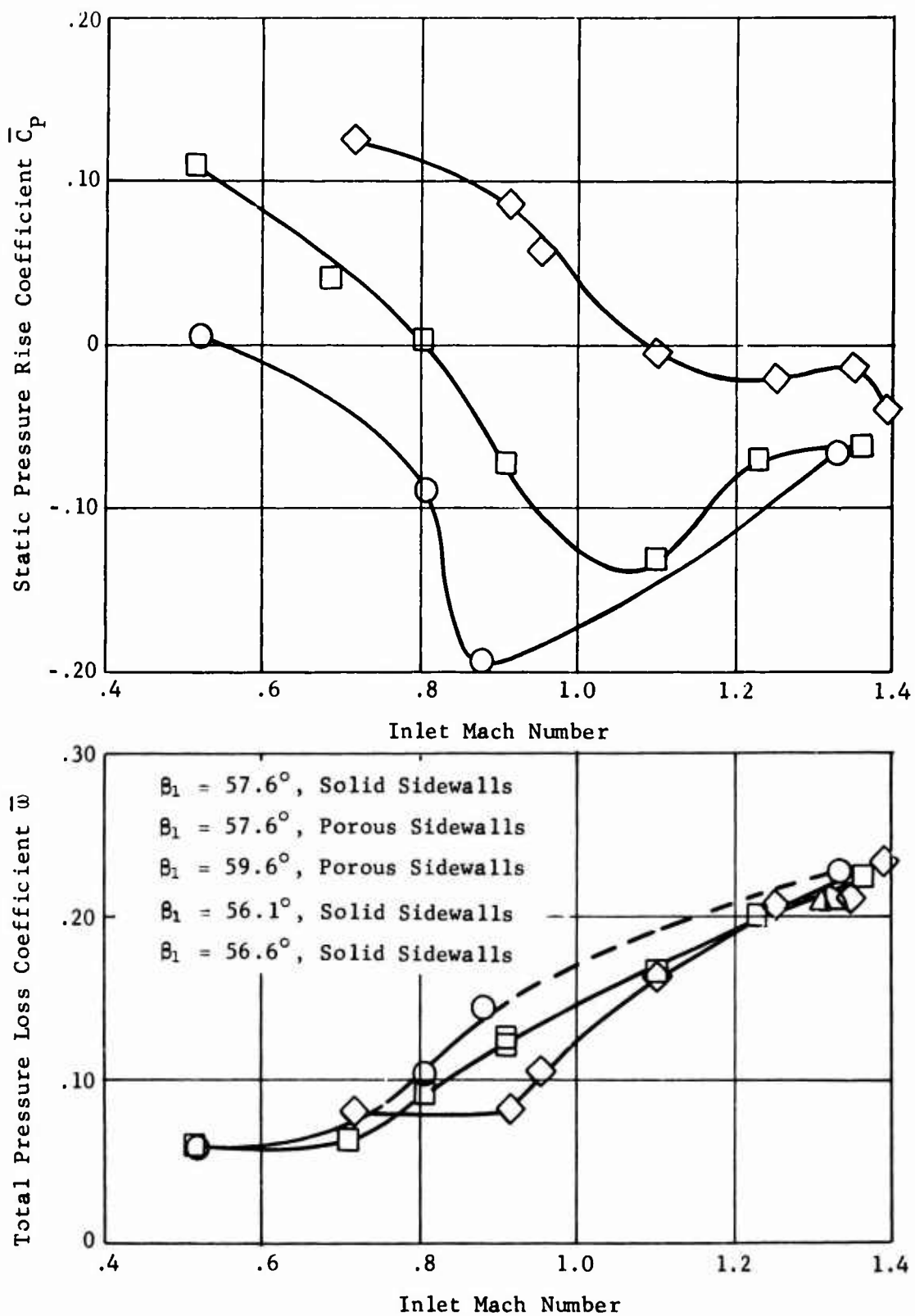


Figure 85. Test Results of the Modified Existing Rotor Blades at Nominal Blade Setting (Leading Edge Suction Surface Angle = 55.6°) (Solidity = 2.0).

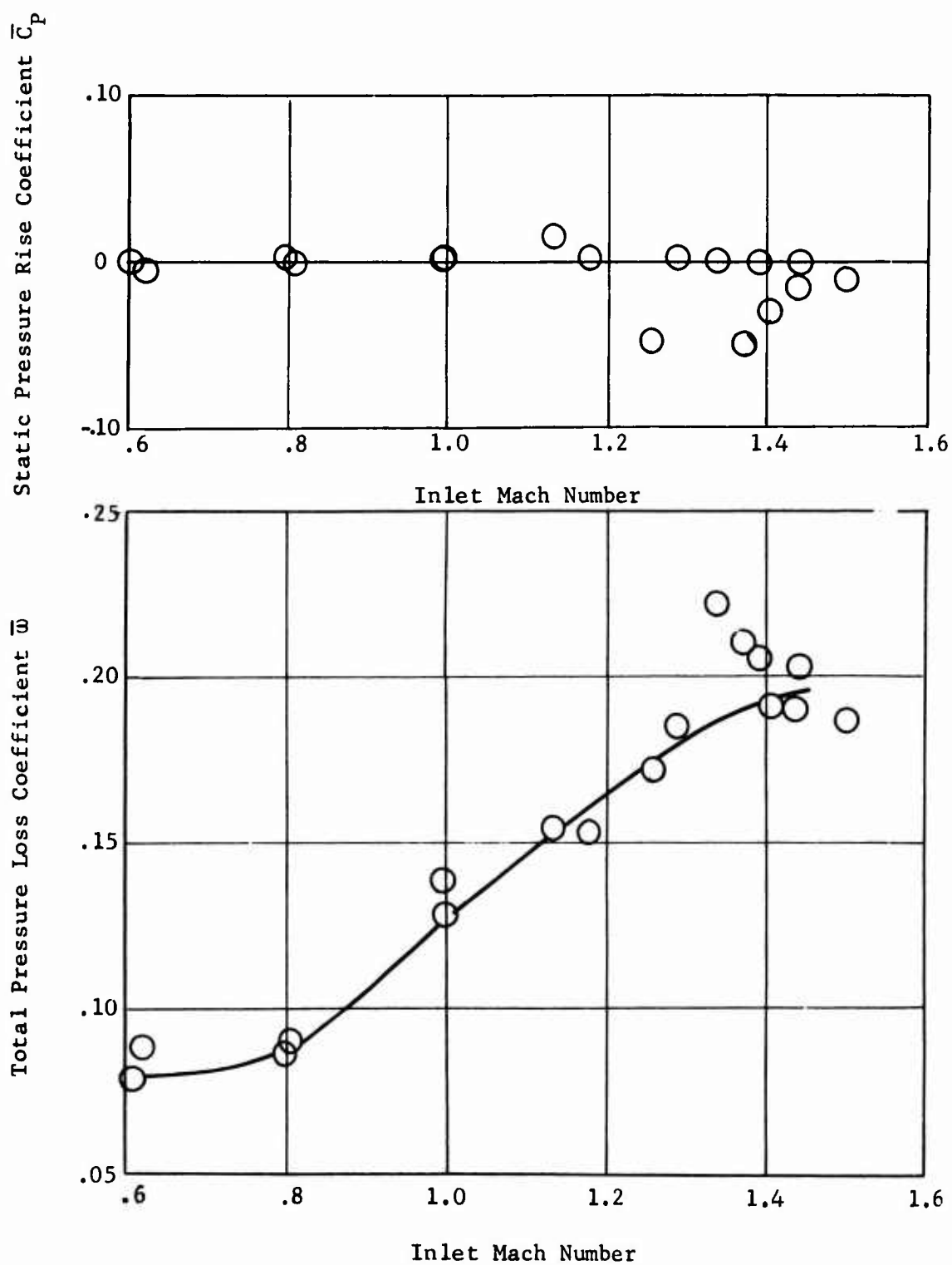


Figure 87. Test Results of New Rotor Blades (Solidity = 2.5) at Design Inlet Angle of 60° .

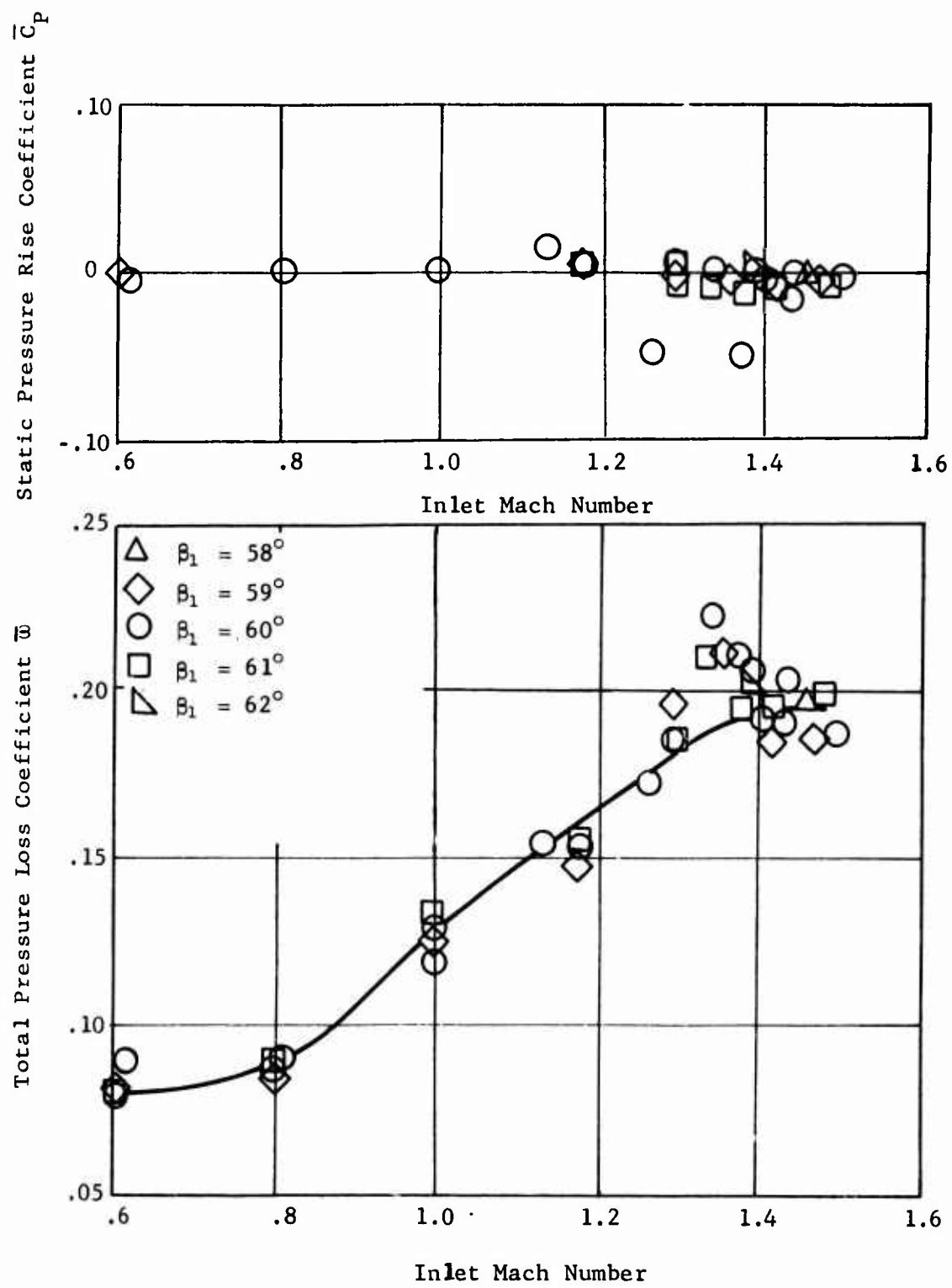


Figure 88. Effect of Inlet Angle Variation on New Design Rotor Blade (Solidity = 2.5).

in improved area distribution for this blade and provided a better match for mixed free vortex flow for the higher inlet Mach requirements of the radial outflow compressor. Improved performance did result ($\bar{w} = 0.202$ at $M = 1.41$), and more improvement is anticipated for the new blades designed at a more optimum value of solidity.

The new blades had a solidity of 2.5 and exhibited very satisfactory performance characteristics. The flow through the blades was fully supersonic at the design inlet angle of 60 degrees and the design inlet Mach number of 1.42. The blade sections were relatively insensitive to inlet angle changes and produced a minimum loss coefficient near 0.185 at the design inlet conditions. This value is slightly higher than the 0.15 goal and was considered to be acceptable.

ROTATING VANELESS DIFFUSER

GENERAL

An extremely important feature of the radial outflow compressor is the rotating wall vaneless diffuser. The purpose of this device is to reduce the absolute Mach number from a level of about 2.7 as the flow leaves the rotor blades to 1.28 as it enters the stator blades. The flow leaving the rotor blades at this high tangential velocity will be permitted to form a powerful supersonic vortex within the walls of the vaneless diffuser, which is an integral part of the rotor. Free vortex flow is a "natural" flow occurring in tornadoes and whirlpools and is characterized by conservation of angular momentum, with tangential velocity decreasing inversely as the radius increases, and with a corresponding increase in static pressure with increasing radius.

Ideally, supersonic vortex flow, as well as subsonic vortex flow, exists with minimum energy losses; and the strong static pressure increase, as radius increases, is obtained with minimum loss. In conventional vaneless diffusers, much friction results between the stationary walls and the high velocity airstream. Secondary flows, separated zones, and large losses occur. By permitting the vaneless diffuser walls to rotate at high speed, the relative velocity between the walls and the airstream is greatly reduced. The powerful centrifugal force field energizes boundary layer particles and acts to prevent the occurrence of separated zones. The losses are greatly reduced and a close approach to loss-free vortex flow is obtained.

Information Pertinent to the Design of Rotating Vaneless Diffusers

Although rotating wall vaneless diffusers added to conventional centrifugal compressor rotors appear in the patent literature starting about 1910, the only present use of the principle appears to be in ventilating fans offered in 1963 by the Joy Manufacturing Company (Reference 17). Literature searches have been made, through the General Electric automatic information retrieval system, to determine whether theoretical or experimental results concerning rotating diffusers exist. The problem has been discussed with Professor E. S. Taylor of the Gas Turbine Laboratory at MIT, with Professor S. J. Kline of the Thermo-Sciences Laboratory at Stanford University, and with Dr. G. F. Wislicenus of Pennsylvania State University. The various discussions and searches have turned up information concerning flow over rotating discs in quiescent air, the flow between two rotating discs with and without a small amount of radial flow, and information as to the frictional losses between a rotating and a stationary disc with and without a small amount of radial flow (References 18 through 20). The conditions existing in a rotating wall vaneless diffuser have not been investigated previously.

Strong inward flow of the wall boundary layer and strong spanwise secondary flow on stationary vanes in centrifugal compressor diffusers have been observed by Johnston (Reference 1). The presence of axisymmetric separated flow in a torus attached to one wall of a vaneless diffuser was observed by Gardow (Reference 2). The occurrence of a sinusoidal flow and the presence of axisymmetric regions of separation appearing systematically on alternate sides of a vaneless diffuser were observed by Jansen (Reference 3). Jansen was also able to apply a transformation to the incompressible flow to predict the probable effect of compressible flow on the boundary layer growth in a vaneless diffuser having stationary walls (Reference 4). For conditions quite similar (except wall rotation) to those that will be encountered in the radial outflow compressor (flow angle 70.5 degrees from radial and $M = 1.3$), Jansen calculates that the boundary layer will occupy about three-fourths passage width at a radius 1.1 times the diffuser inlet radius. This boundary layer growth is much more rapid than the incompressible flow boundary layer growth would be. Unsteady flow conditions in vaneless diffusers have been treated by Dean and Senoo (Reference 21) and Jansen (Reference 5). The analyses of Stewartson (Reference 18) and Moore (Reference 22) indicate, as would be expected, that laminar wall boundary layers will migrate inward whenever the rotational speed of the wall is less than the tangential velocity of the main stream. The formulation of turbulent boundary layer flow relations in a rotating wall diffuser has not been accomplished. This is the condition anticipated to occur in the high-speed radial outflow compressor. It is estimated that the greater radial and tangential shear forces occurring with turbulent boundary layer flow will drive more of the boundary flow outward, thus minimizing rotating wall boundary layer thickness.

Shock Waves in Vortex Flow

The behavior of a shock wave in a supersonic vortex flow field is important in predicting the off-design performance of this compressor. Analytical investigation of this behavior was done by Dr. D. C. Prince, Jr., of the General Electric Company. Supersonic flow net characteristics of the undisturbed Mach lines and one weak shock wave are shown in Figure 89. The propagation of several weak shocks radially inward and thus traversing a flow field of increasing Mach number is shown in Figure 90. The question is whether a shock wave of given strength would become stronger or would be attenuated in this flow. Dr. Prince's analysis indicates that the wave strength will be increased as the shock wave traverses inward through the supersonic field. This is of importance to the off-design operation of the compressor because it means that the expansion wave fan which will exist at the rotor exit under transonic operating conditions will be influenced by the interaction with the pressure wave. If the wave is discrete and strong, the expansion fan will be neutralized and a subsonic flow region will momentarily result. This collapse of the expansion fan will permit the information that a static pressure increase is being impressed upon the rotor discharge flow field to propagate forward and affect the air weight flow of the

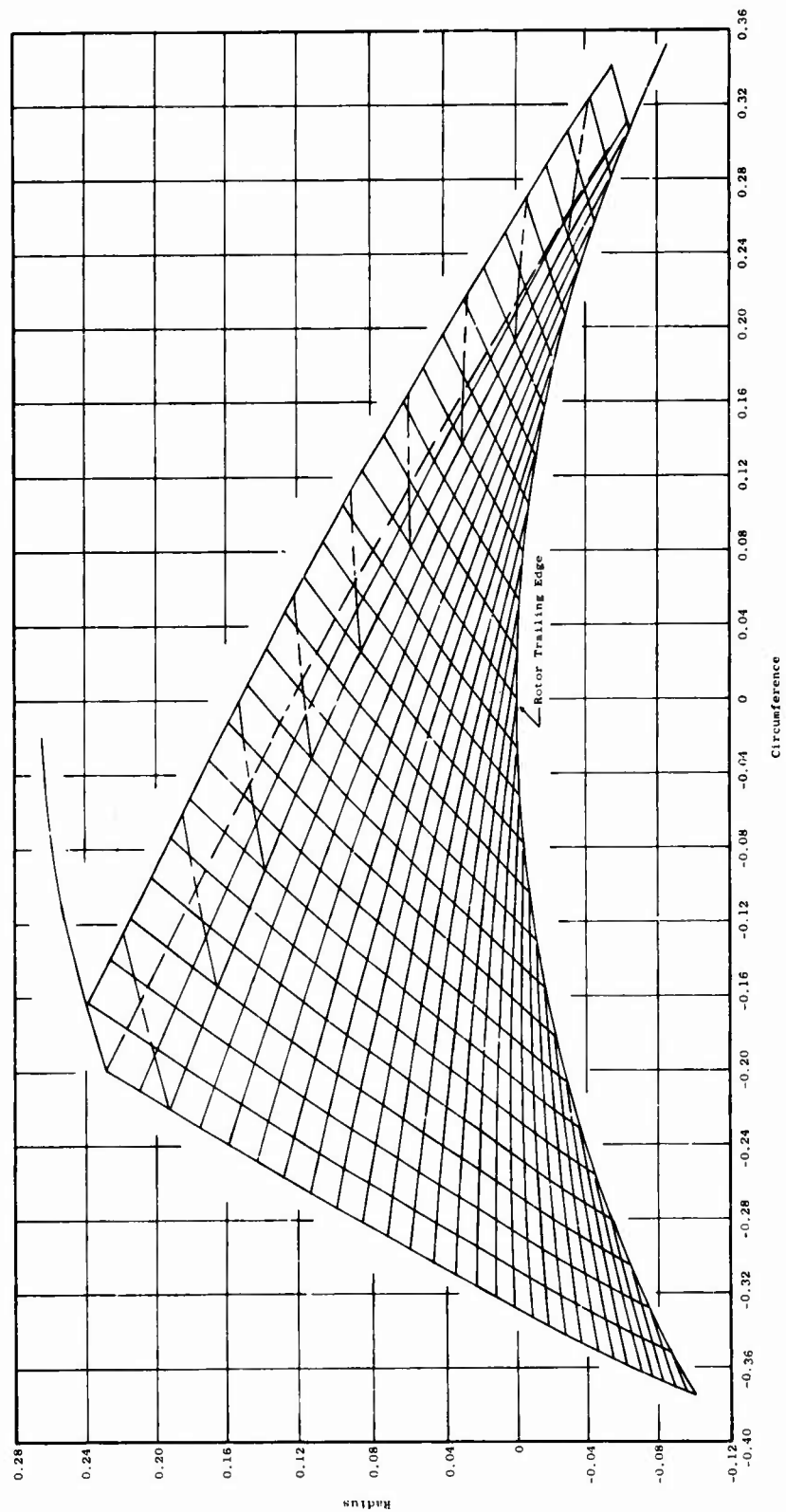


Figure 89. Supersonic Vortex Characteristics Net Showing Streamlines (Dash-Dot Curves, a Stator Blade with a Weak Shock Propagating from Its Leading Edge (Dashed Line)).

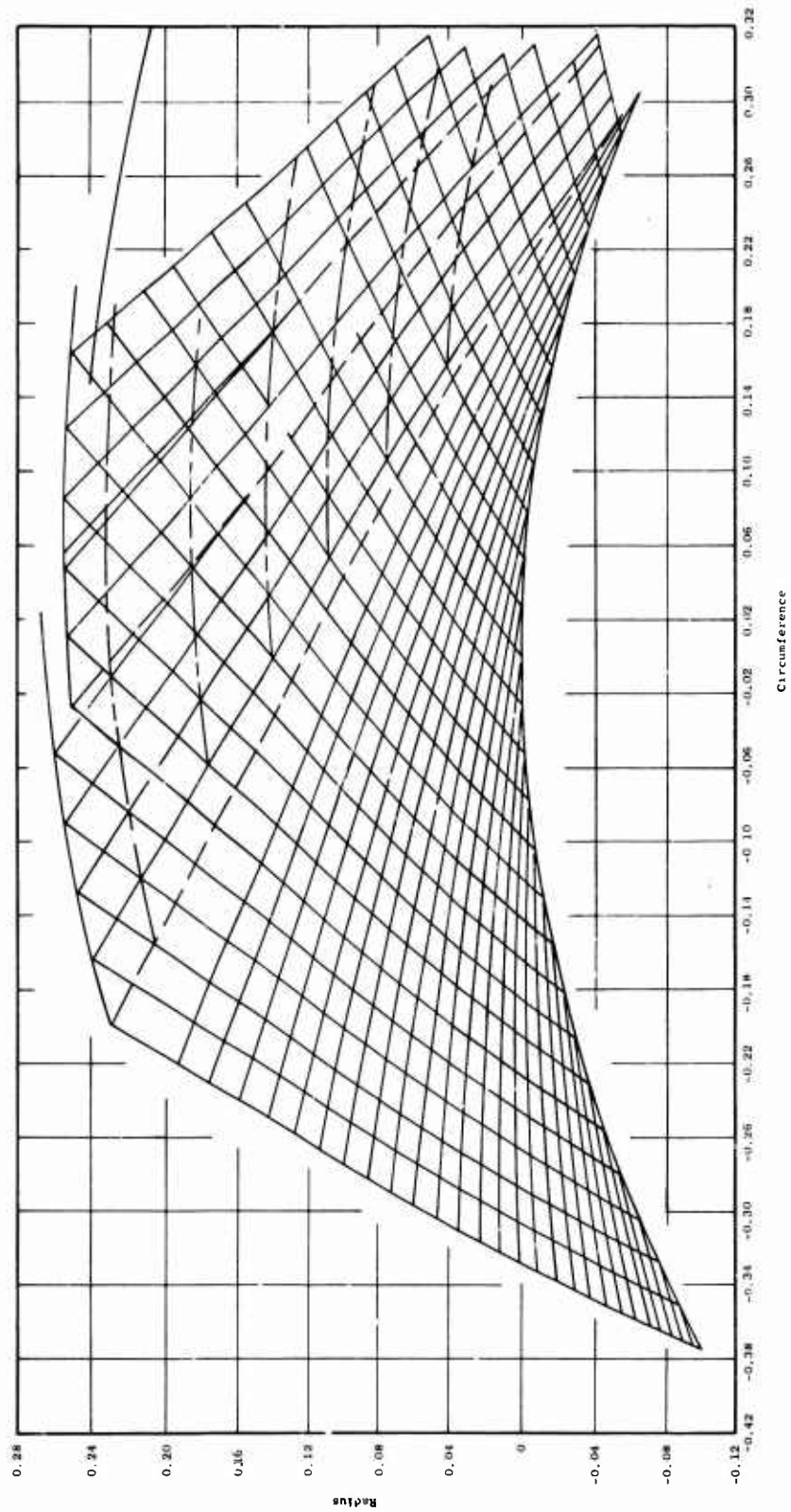


Figure 90. Characteristics Net Showing Several Stators, Streamlines and Weak Shock Waves.

compressor. Because of this behavior, the radial outflow compressor, when operating at transonic speeds, is expected to exhibit a "normal" compressor characteristic; i.e., decreasing weight flow with increased throttling. This normal operation characteristic should thus make it possible for this compressor to match the usual combustor and turbine operating conditions without resorting to special devices other than variable inlet guide vanes and possibly stators to accomplish such matching.

Preliminary Test Results

The only experimental evidence available on rotating vaneless diffusers at the beginning of Phase I of the radial outflow compressor program was obtained from the water flow model and the low-speed air model tests which were conducted at General Electric. The water flow model was constructed with transparent rotor and stator walls. Water was selected as the fluid rather than air to produce higher Reynolds numbers at low speed and to provide ease of flow visualization using dye traces and bubbles. By varying the rotor blade angles and the pressure head produced, the vaneless diffuser was forced to work over a range of relative velocity ratios that extended both higher and lower than required in the high-speed machine (Figure 91). Although total pressure measurements were not accurate owing to the very low flow velocities, measurements that were made confirmed the tuft surveys and dye traces which indicated a very uniform flow over the range of diffusion examined.

Because of the encouraging results obtained with the water flow model, the low-speed air test model (Figure 92) was constructed using the same geometry. The pressure rise produced in this compressor is high enough to produce adequate water manometer deflections for accurate pressure measurements. Prior to the beginning of Phase I of the radial outflow compressor program, this compressor had been run at only one rotor blade setting, the design value for impulse flow, and the rotating diffuser had not been examined over a large range of flow conditions.

The peak rotor efficiency obtained, slightly over 95 percent, was not out of line with values obtained in the impulse rotor investigations presented in References 11 and 12 and with conventional axial flow rotors at low speed presented in Reference 23. Since these rotor efficiency values included the rotating diffuser losses, the results were most encouraging.

Investigations at MIT had indicated that when a blade wake traverses a strong adverse static pressure gradient, the wake may grow rapidly and may exhibit reverse flow (References 24 and 25). There was some concern, therefore, that the rotor blade wakes in the proposed compressor would not be attenuated, that the flow into the stator blades would be non-uniform, and that poor stator performance would result. This situation was investigated in the low-speed air test model. The data indicated

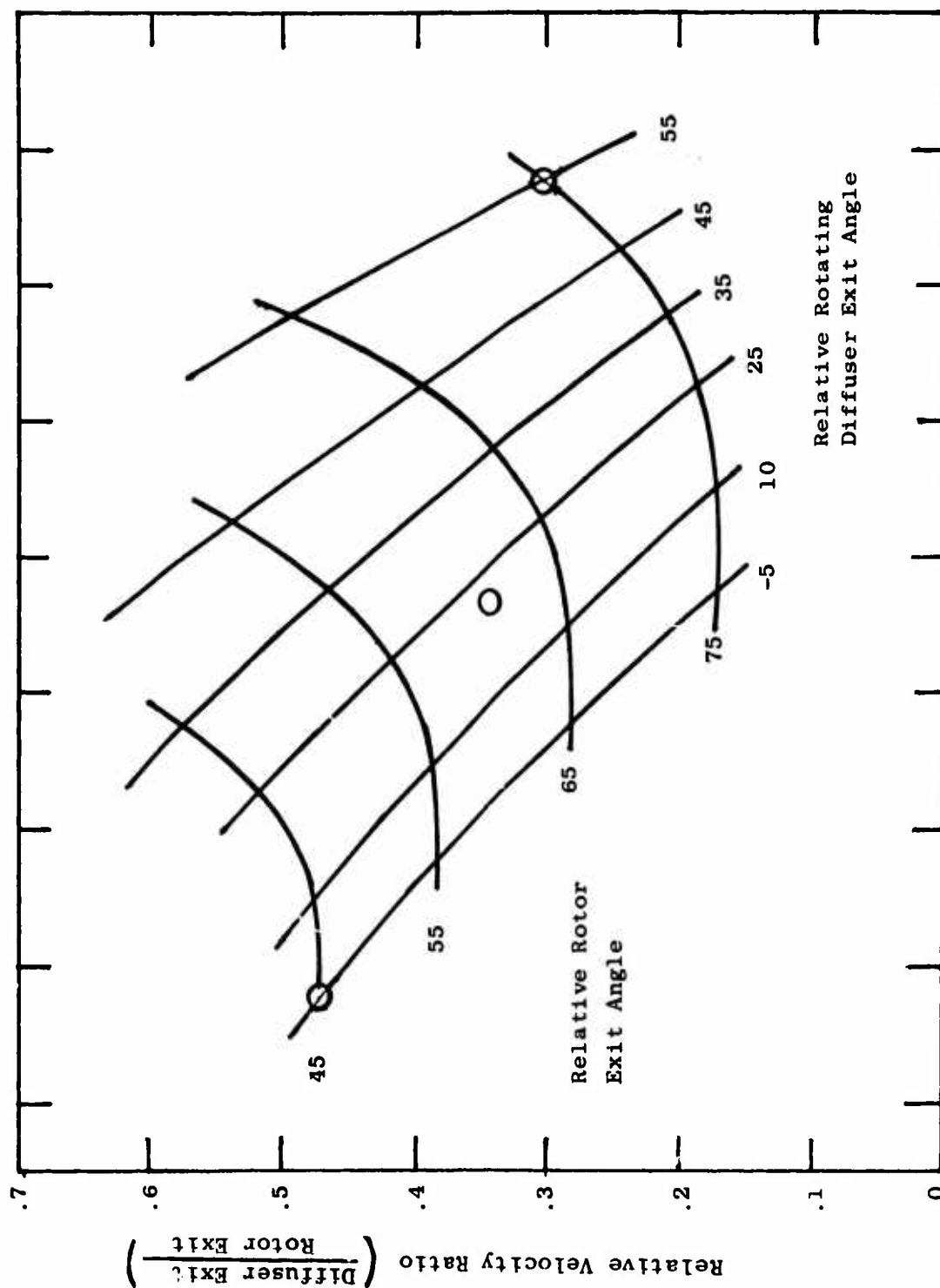


Figure 91. Calculated Diffuser Relative Velocity Ratio as a Function of Rotor Exit and Diffuser Exit Flow Angles. Test Points Investigated Are Shown as Circles.

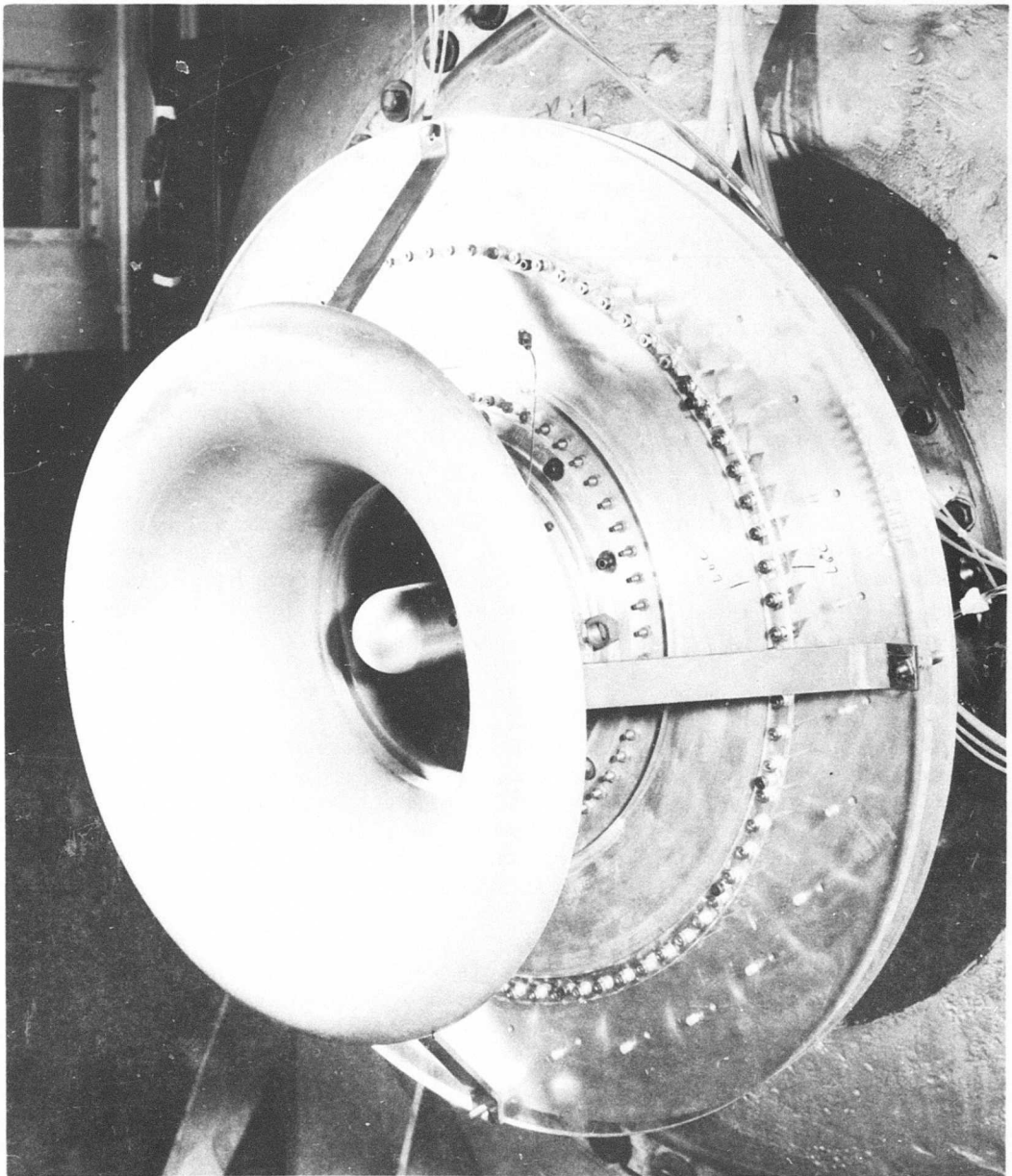


Figure 92. Low-Speed Radial Outflow Compressor Installation in Test Facility.

that the rotor blade wakes were strongly attenuated within the vaneless diffuser despite the strong adverse static pressure gradient. This result confirmed the hypothesis of Dean and Senoo (Reference 21), in which they predicted that wakes in vaneless diffusers would disappear rapidly, both because of the turbomachine-type work performed on the wake fluid by the main stream fluid and because of viscous mixing; the result also provided further evidence that radial outflow compressors can be efficient while demonstrating high work output.

Scope of Phase I Investigations

The vaneless diffuser is the least known item of the radial outflow compressor. No practical means have as yet been conceived for determining the performance of a vaneless diffuser without incorporating it in a rotor. For this reason, the rotating diffuser investigations in Phase I of this program were confined to the investigations using the low-speed compressor. The purpose of these investigations was to measure the vaneless diffuser performance in the air model over a wide range of operating conditions and to determine the efficiency under varying conditions of diffuser operation. High frequency response pressure measurements within the vaneless diffuser were to be conducted to determine whether the rotor blade wakes will continue to be attenuated under conditions of greater diffuser static pressure rise.

DESCRIPTION OF TEST ITEM

The low-speed air model radial outflow compressor used for the rotating vaneless diffuser investigations is shown in Figure 92. Figure 93 is a closer view of the compressor with the inlet bellmouth removed, exposing more of the rotor and rotor blades. More details of the radial outflow compressor test rig are shown in Drawing 4012153-734 (Figure 94). The rotating vaneless diffuser is an integral part of the rotor and is the area bounded by parts 9 and 22 extending outward from the rotor blade exit. Figure 95 illustrates the nomenclature more clearly and defines appropriate symbols and station designations used during this test. The radius of the rotating vaneless diffuser exit shown is 12 inches. A larger vaneless diffuser having an exit radius of 14 inches was also built and tested to determine vaneless diffuser performance under conditions of greater diffusion.

EXPERIMENTAL PROCEDURE

The low-speed radial outflow compressor with the smaller (12-inch radius) rotating vaneless diffuser was the configuration used for the initial series of tests. The rotor blade trailing edge angle of 60 degrees was investigated first to verify earlier test results reported in Proposal P63-102 (Figures 96 and 97). Compressor bellmouth calibrations were performed prior to these tests to assure more accurate airflow calculations.

More extensive investigations were conducted during the next series of tests with the rotor blade trailing edge angle set at 55 degrees. These included the following:

1. Performance and repeatability tests.
2. The addition of a rotor blade trailing edge probe (diffuser inlet) to determine pressure drop across the rotating diffuser.
3. The addition of a yaw probe to determine the flow angle leaving the vaneless diffuser.
4. Dynamic pressure measurements at three radial locations in the rotating vaneless diffuser to determine if the rotor blade wakes are being attenuated, particularly at higher static pressure rise coefficients.

The rotor blade trailing edge angle was changed back to 60 degrees, and runs were repeated with the additional instrumentation. It was during these tests that some of the static pressures measured at the exit of the rotating vaneless diffuser were found to be leaking. Since it was not known when the leaks first occurred, it was necessary to repeat the performance data at 60- and 55-degree rotor blade trailing edge angles. A rotor blade angle at 65 degrees was also tested.

The test procedure was essentially the same as before. At each blade angle setting, flow coefficient was varied over a range from wide open throttle to near stall. At each throttle setting, data were taken at three compressor rotor speed settings. This same procedure was repeated for a larger radius rotating vaneless diffuser.

In this way, the radial outflow compressor characteristics were investigated incorporating rotating vaneless diffusers of two different sizes operated over a range of flow conditions. The purpose was to determine how flow angle into the diffuser, flow coefficient, and rotating diffuser radius ratio affect the efficiency of the compressor. Through analysis of the results, the attempt would be made to synthesize a parameter which would correlate the data and guide the design of high-speed rotating-wall vaneless diffusers.

Test runs and configurations are summarized in Table V. A summary of the instrumentation used on the low-speed radial outflow compressor for this investigation is presented in Table VI.

Preliminary Testing

The initial test runs at the rotor blade trailing edge angle of 60 degrees were made to verify earlier test results. Compressor bellmouth calibrations were performed prior to these tests to assure more accurate airflow calculations. The earlier test results had produced efficiencies

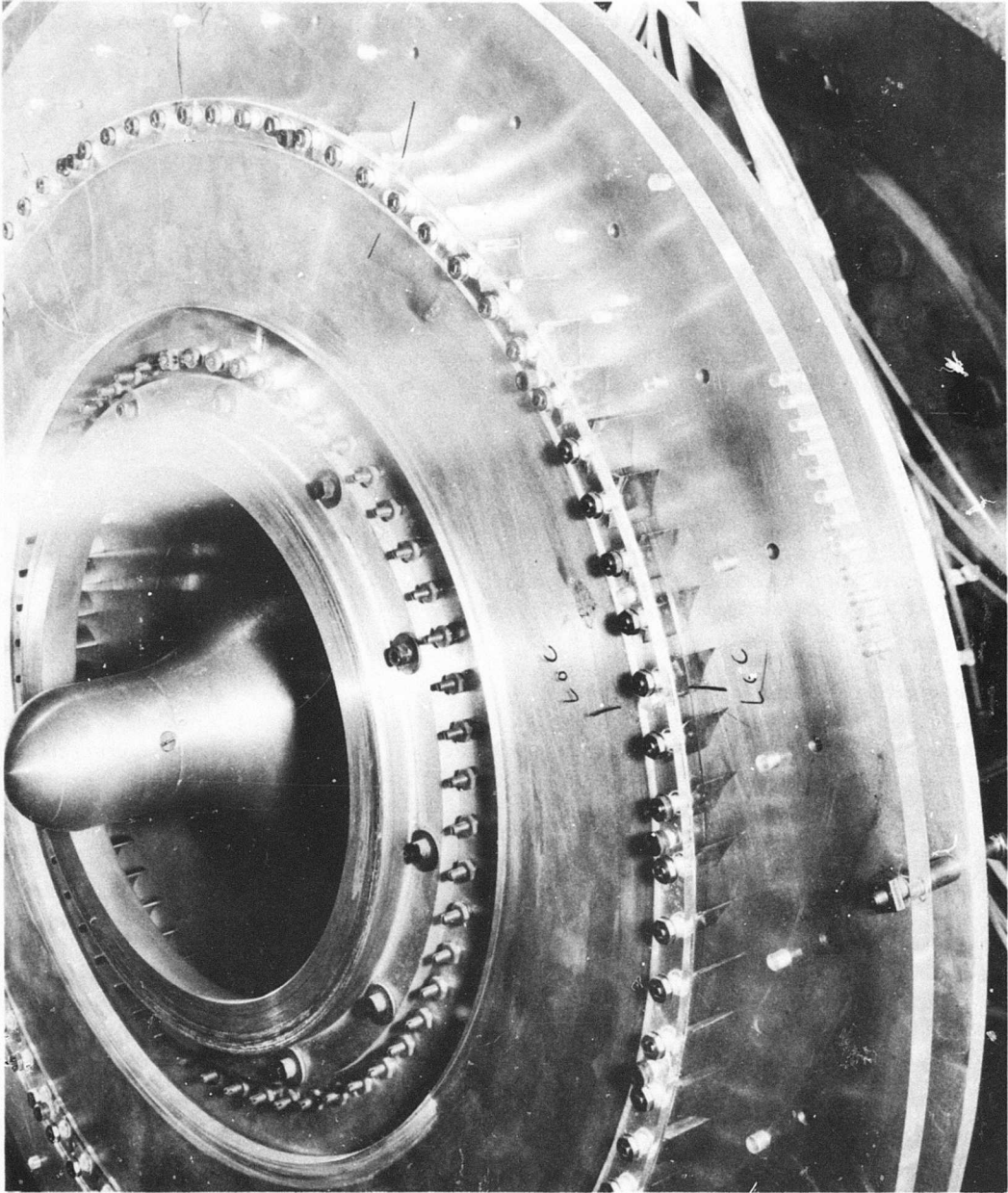
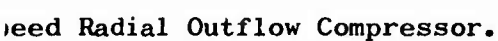
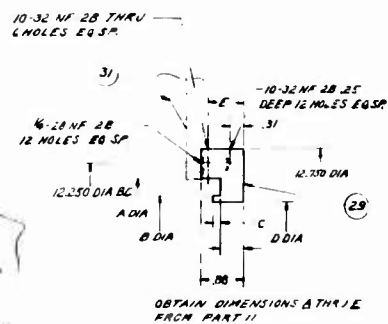
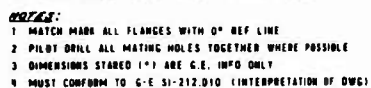


Figure 93. Low-Speed Air Test Radial Outflow Compressor.



B

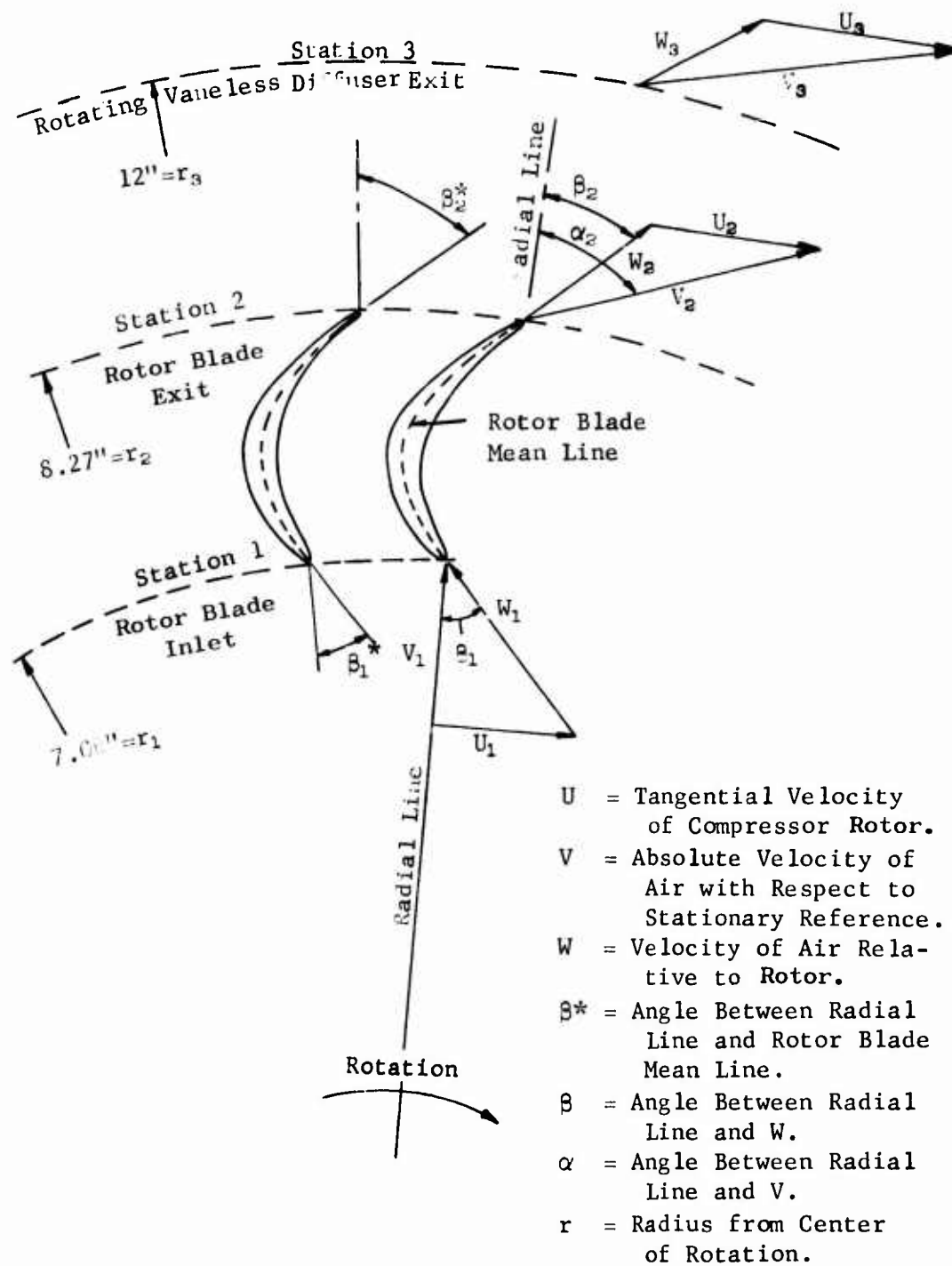


Figure 95. Vaneless Diffuser Test Nomenclature, Low-Speed ROC.

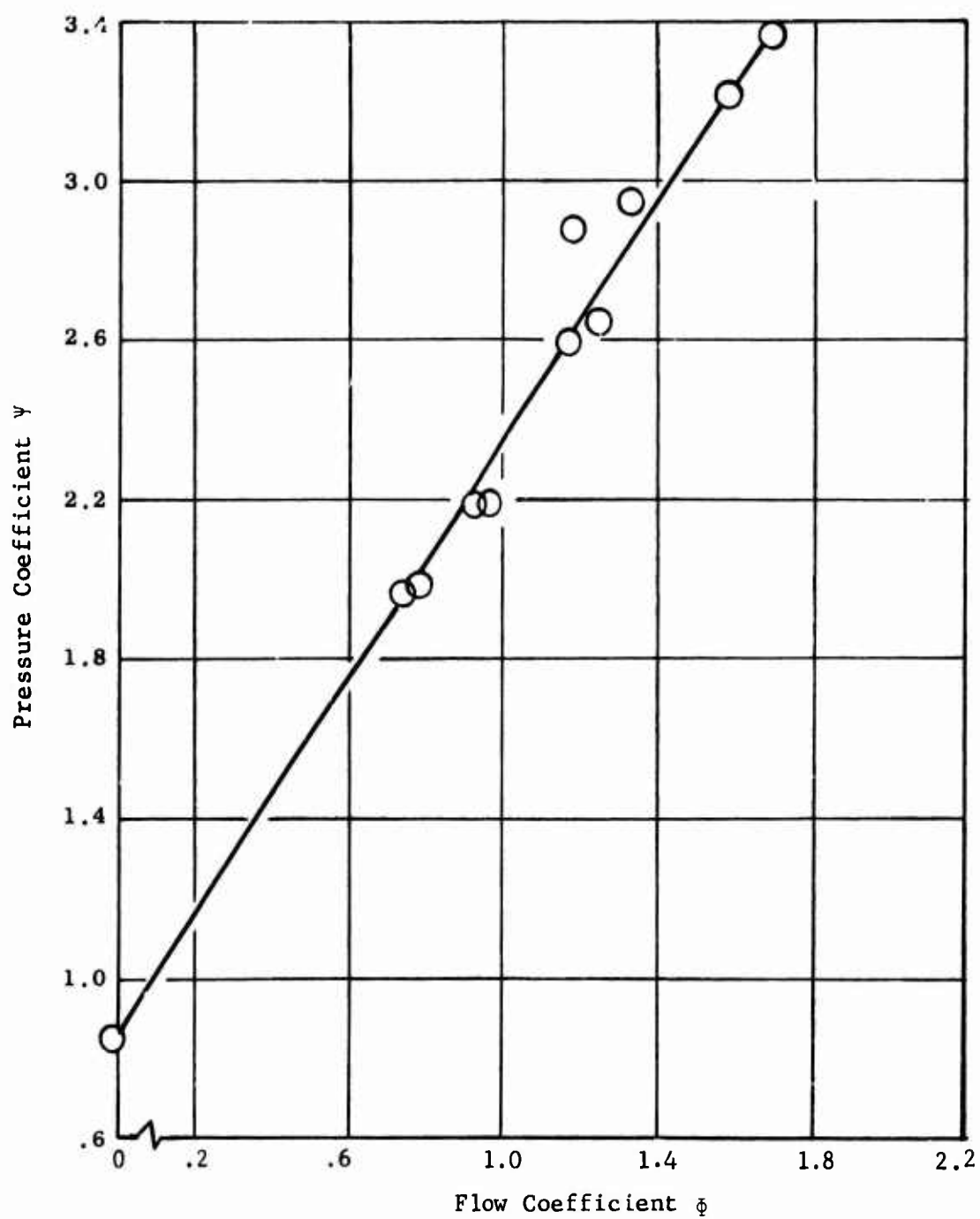


Figure 96. Rotor Discharge Pressure Coefficient from Preliminary Test Results of the Low-Speed Radial Outflow Compressor.

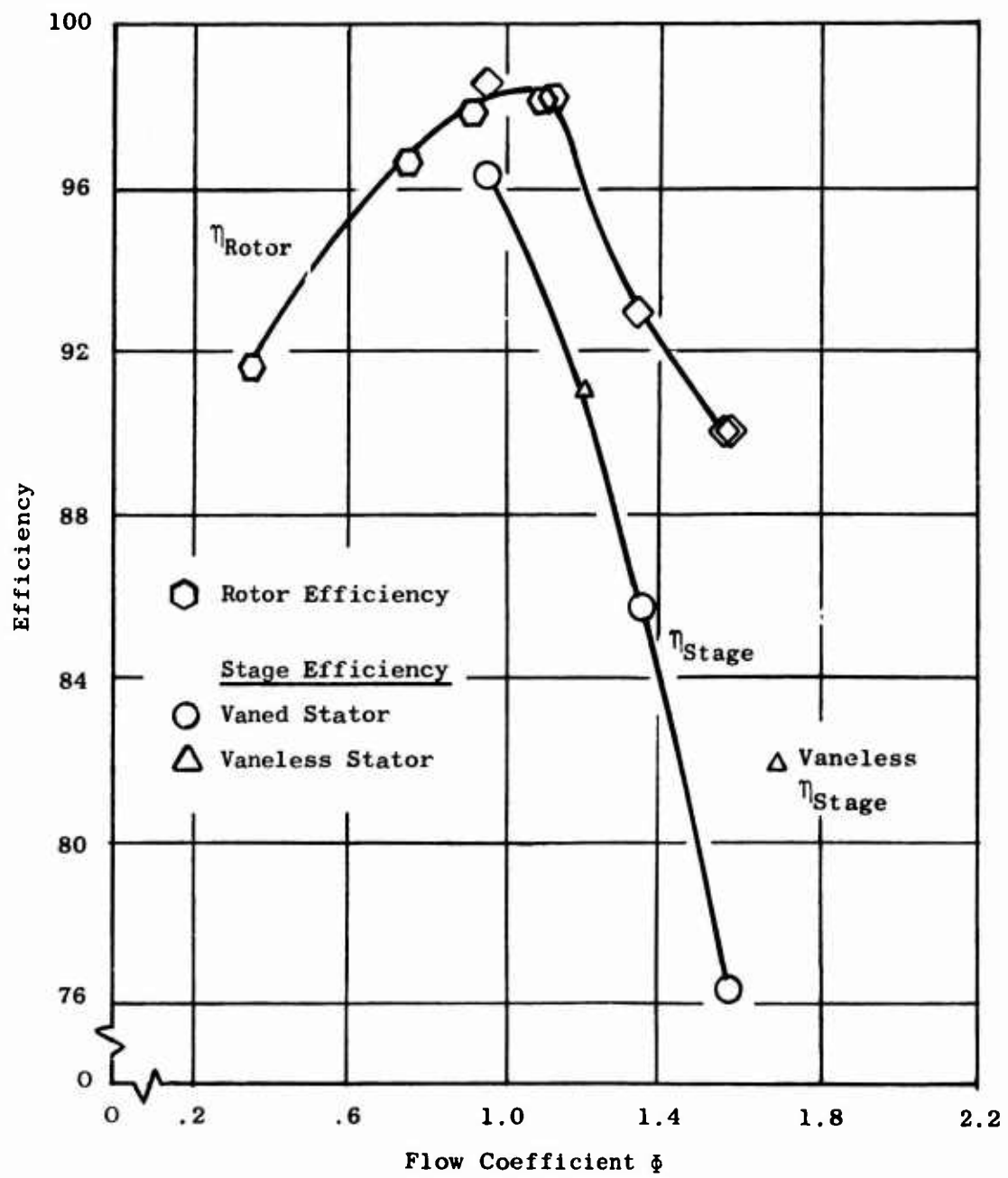


Figure 97. Compressor and Rotor Efficiencies from Preliminary Test Results of the Low-Speed Radial Outflow Compressor.

TABLE V

ROTATING VANELESS DIFFUSER TEST RUN SUMMARY

Run No.	Run No. Designation	Date	Rotor Blade Trailing Edge Angle 3/2* (degrees)	Rotating Vaneless Diffuser Radius (inches)	Exit Vanes	Trailing Edge Probe	Yaw Probe	Remarks
1	1201	3/9/64	60	12	In	-	-	Performance verification - repeatability
2	1202	5/15/64	60	12	In	-	-	Performance at 52* of 55 degrees
3	1103	5/25/64	55	12	In	-	-	Performance repeatability
4	1104	6/2/64	55	12	In	-	-	Trailing edge probe added to determine pressure drop in rotating vaneless diffuser
5	1105	6/3/64	55	12	In	In	-	Repeat with exit stator vanes removed
7	1107	6/9/64	55	12	Out	In	-	Dynamic pressure measurements for rotor blade wake attenuation study
8	1108	6/16/64	55	12	Out	Out	-	Dynamic pressure measurements for rotor blade wake attenuation study
9	1109	5/17/64	55	12	Out	Out	-	Dynamic pressure measurements for rotor blade wake attenuation study
10	1110	6/18/64	55	12	Out	Out	-	Dynamic pressure measurements for rotor blade wake attenuation study
11	1111	7/16/64	55	12	Out	In	-	Performance repeatability
12	1112	8/19/64	55	12	Out	Out	In	Yaw probe added to determine flow angle out of diffuser
13	1113	8/25/64	55	12	Out	Out	In	Performance repeatability
14	1114	8/31/64	55	12	Out	Out	In	Attempt to repeat earlier data
15	1215	9/2/64	60	12	Out	Out	In	Attempt to repeat earlier data
16	1216	9/4/64	60	12	Out	In	In	Instrumentation Leak Check - Leaks Corrected
17	1217	9/11/64	60	12	Out	Out	In	Performance at 52* of 60 degrees
18	1218	9/14/64	60	12	Out	In	In	Performance repeatability
19	1219	9/15/64	60	12	Out	In	In	Performance at 52* of 65 degrees
20	1320	9/19/64	65	12	Out	Out	In	Trouble setting rotor speeds
21	1321	9/22/64	65	12	Out	Out	In	Trailing edge traverse data
22	1322	11/24/64	65	12	Out	Out	In	Performance repeatability
23	1323	12/1/64	65	12	Out	In	In	Dynamic coupling broke terminating this run
24	1124	12/11/64	55	12	Out	Out	In	Computer performance program corrected
25	1125	12/14/64	55	12	Out	Out	In	
26	1126	2/15/65	55	12	Out	Out	In	
27	1127	2/16/65	55	12	Out	Out	In	
28	2128	2/22/65	55	14	Out	Out	In	
29	2229	2/25/65	60	14	Out	Out	In	
30	2330	2/27/65	65	14	Out	Out	In	
31	1131	3/3/65	55	12	Out	Out	In	
32	1132	3/5/65	55	12	Out	Out	In	
33	1233	3/17/65	60	12	Out	Out	In	Scroll collector installed
34	1234	4/12/65	60	12	Out	Out	In	Scroll collector installed

Run number designation defines the basic buildup.

The first digit denotes vaneless rotating diffuser radius; 1 for 12 and 2 for 14.

The second digit gives the rotor blade trailing edge angle; 1 for 55 degrees, 2 for 60 degrees and 3 for 65 degrees.

The last two digits indicate the individual run number.

TABLE VI
INSTRUMENTATION SUMMARY - ROTATING VANELESS DIFFUSER

Item	Location	Symbol	Quantity	Purpose
1	Bellmouth Static Pressures	P_{BM}	4	Airflow Measurement
2	Rotor Discharge Total Pressures (Vaneless Diffuser Exit)	P_{t3}	12 ⁽¹⁾	Rotor Performance
3	Rotor Discharge Static Pressures (Vaneless Diffuser Exit)	P_{s3}	16	Rotor Performance
4	Compressor Discharge Total Pressure (Stator Exit)	P_{t6}	12 ⁽²⁾	Stator and Stage Performance
5	Compressor Discharge Static Pressure (Stator Exit)	P_{s6}	4	Stator and Stage Performance
6	Rotor Discharge Total Pressure (Rotor Blade Exit)	P_{t2}	1 ⁽³⁾	Vaneless Diffuser Performance
7	Rotor Discharge Total Pressure	P_{t3}	1	Flow Direction - Vaneless Diffuser Performance
8	Rotor Discharge Dynamic Pressure	P_{t3}	1	Rotor Blade Wake Attenuation in Vaneless Diffuser
9	Rotor Exit Static Pressure Radial traverse from edge of rotor blades to exit of rotating vaneless diffuser	P_{s2-5}	1	From Edge of Rotor to Exit of Rotating Diffuser

(1) When rotor discharge probe was used, it affected the pressures measured on one rake reducing the number used to six.

(2) These were located on a circumference at mid passage. Each element was at slightly different angles. Only one representing highest pressure was used.

(3) Single probe that was installed on an arm that could be rotated in or out of the airstream. This probe was out (not used) generally when the yaw probe was being used.

based on torque meter readings that were too high. This was believed to have been caused by errors in airflow resulting from the assumption of a uniform static pressure across the measuring plane of the compressor bellmouth. The use of improved airflow values, however, did not prove to be the complete solution, since efficiencies based on torque meter readings still came out too high.

The generally erratic and nonrepeatable data from these initial test runs seemed to indicate that with the blade trailing edge angle set at 60 degrees from radial, the diffusion limit of the compressor had been encountered. It is very possible that some of the erratic data problems were caused by poor throttle setting methods.

Improved throttle setting methods were devised for the next series of runs with the rotor blade trailing edge angle setting of 55 degrees. The results were much more consistent and well behaved, but still not repeatable from one day to the next. Maximum calculated aerodynamic efficiency was about 82 percent, which was approximately 10 percent lower than the 60-degree configuration. A dip occurred in the efficiency curve in the range of flow coefficient from 1.0 to 1.1. Minimum relative velocity ratio occurs for the 55-degree angle setting at a flow coefficient of 1.1, and the coincidence between the minimum velocity ratio and the efficiency dip suggested a connection between these two occurrences.

To further investigate the low efficiency and the dip in the efficiency characteristic, a total pressure probe was placed near the rotor blade trailing edge. The data indicated that there was no significant total pressure loss in the rotating vaneless diffuser even at the flow function of 1.1. This result is very important because no evidence of separation was found, and there is reason to believe that the high-speed vaneless diffuser will also exhibit low losses.

The exit stator vanes were removed from the low-speed radial outflow compressor at this point to make it easier to install other instrumentation such as the total pressure probe for the rotor wake attenuation survey in the rotating vaneless diffuser. The stators were left out for all of the succeeding vaneless diffuser tests.

Additional testing of the 55-degree rotor blade angle setting was done with exit stator vanes removed. The problem of data repeatability from one day to the next persisted. The data indicated that the minimum value of relative velocity ratio was less and had shifted so that it occurred at a lower value of flow coefficient without the exit vanes in place. Rotor aerodynamic efficiency appeared to be lower than before but was disguised in the data repeatability problem. A yaw probe was installed to measure flow angle at the rotating vaneless diffuser exit to provide another check on the performance calculation methods.

Finally, the rotor blade trailing edge angle was reset to 60 degrees to repeat earlier test data to verify the high performance originally observed at this setting. The efficiency obtained using the torque meter readings to calculate power input agreed with previous data. Efficiencies obtained from aerodynamic measurements fell below previous readings. Careful search revealed that the majority of the rotor exit static pressure taps were leaking.

EXPERIMENTAL RESULTS

Rotor exit total pressure rise coefficient and rotor aerodynamic efficiency are plotted versus flow coefficient in Figures 98 through 115. These results are based on test runs made after the rotor exit static pressure instrumentation was corrected. Test results from prior runs are deleted, since it is not known when the leaks first occurred and since these test configurations were subsequently repeated.

Results of the rotor wake attenuation survey in the rotating vaneless diffuser are presented in Figures 116 through 118.

EVALUATION

Radius Ratio 1.69 Diffuser

The characteristics of the 1.69 radius ratio diffuser with rotor blade angles of 55, 60, and 65 degrees are shown in Figures 104 through 109. The pressure coefficient generally increases with increasing blade angle. At a flow coefficient of 1.0, the pressure coefficient increased by 19 percent in going from the 55- to the 60-degree blade setting, and increased by 15 percent when the blade angle was increased from 60 to 65 degrees. The aerodynamic efficiency obtained was relatively constant, with the 60-degree blade setting giving a slightly higher result of 90 percent at a flow coefficient of 1.0.

Radius Ratio 1.45 Diffuser

Using the 24-inch-diameter vaneless diffuser (radius ratio 1.45), the 60-degree blade setting was tested over a range of flow coefficients. The results are presented in Figures 98 and 99. Rotor aerodynamic efficiencies were as high as 98 percent at a flow coefficient of about 1.0.

The rotor blade trailing edge angle was changed to 65 degrees. As shown in Figures 100 and 101, the rotor efficiency peaks at about 94 percent at a flow coefficient of 0.6. Above a flow coefficient of 0.8, the pressure coefficient and efficiency drop off rapidly.

At a rotor blade angle of 55 degrees, two tests were conducted. The first one is represented by the lower set of curves in Figures 102 and 103. For the second test, the angular setting of the rotating diffuser

exit total pressure probes was increased by 11.75 degrees with respect to radial. The repeat points are the upper set of curves in Figures 102 and 103. This procedure exposed another factor to be considered in obtaining consistent repeatable data. For all test configurations after this, the rotating diffuser discharge total pressure probe angle was set at its optimum value (to read maximum total pressure at midstream) at the design flow coefficient.

The data at the 55-degree blade angle were again repeated to increase curve definition. The probe angle setting procedure described above was used. Results are presented in Figures 110 and 111.

For the run at 60 degrees with the 1.45 radius ratio diffuser, the scroll collector, turning vanes, and remotely controlled throttle valves were added to the buildup (Figure 119). These changes to the compressor exit should not have affected the characteristics of the rotating diffuser, but should have made possible a more accurate and consistent setting of the desired airflow.

Figures 110 through 113 show the rotor performance characteristics for the radius ratio 1.45 vaneless rotating diffuser at blade angles of 55 and 60 degrees. For the 60-degree setting, the test was repeated to get a better definition of the curves as shown in Figures 114 and 115. The plot of pressure coefficient versus flow coefficient was repeated exactly at the lower value of flow coefficient but exhibited less abrupt and smoother curves at the higher values of flow coefficient. The rotor efficiency curve, Figure 115, is very well defined and has a small dip in efficiency at a flow coefficient near 1.0.

Comparison of Diffusers

Direct comparisons can be made between the rotor performance with vaneless diffuser radius ratios of 1.69 and 1.45 at rotor blade angles of 55 and 60 degrees.

Comparing the two different radius ratio diffusers at the 60-degree rotor blade angle, the pressure coefficient and efficiency characteristics are about the same at flow coefficients below 1.65. The maximum rotor discharge pressure coefficient is higher and occurs at a proportionately higher flow coefficient for the large radius ratio vaneless diffuser. The maximum efficiency is about 88 percent for both diffusers and occurs at a flow coefficient of about 1.0.

At the 55-degree blade setting, the smaller vaneless diffuser produces a higher pressure coefficient over the range of flow coefficients to 1.55. The maximum value of pressure coefficient is less but occurs at a higher value of flow coefficient for the large vaneless diffuser. The efficiency characteristic is not very consistent in the region near design flow coefficient and also appears to be sensitive to rotor speed. At flow coefficients of 0.8 and 1.0 for 1800 rpm, the efficiencies of the

two vaneless diffusers appear to be about the same (87 to 88 percent) at the 55-degree blade setting.

Wake Attenuation

The rotor blade wake attenuation study was done at the 55-degree setting with exit stator vanes removed. A total pressure probe connected to a high frequency response transducer was used for these measurements. Wake traces were recorded on tape and on film at 1400, 1600, and 1800 rpm for three throttle settings at the following radial locations in the rotating vaneless diffuser:

1. 1/8 inch out from rotor blade trailing edges
2. Midway out in the vaneless diffuser
3. At the vaneless diffuser exit

For all speeds and throttle settings, the rotor blade wakes dissipated greatly in passing through the diffuser in spite of the strong adverse static pressure gradient. Typical results are presented in Figures 116 through 118 at 1400 rpm. Each picture displays two sets of traces. The upper set of traces in each picture is a 1/25-second time exposure, while the lower set of traces is a 10-second time exposure at the same conditions. Note the smaller vertical scale sensitivity to display the signal properly at midpassage when the probe is located 1/8 inch from the rotor exit in Figure 116. At 2 inches from rotor exit in this same figure, the rotor wake at midpassage appears to be as small or smaller than the wakes at either the front or the back wall. Similar results are presented in Figure 117 for a flow function of 1.0. Figure 118 compares the wake responses at the rotating diffuser exit at flow functions of 0.8 and 1.0.

Discussion

Initially, it had been decided to evaluate the rotating diffuser on the basis of relative velocity ratio; that is, the ratio of the relative velocity leaving the rotating diffuser (W_3) to the relative velocity leaving the rotor blades (W_2). The relative velocity ratio was chosen because: (a) it is not related to the total pressure (which varies with radius in this machine) as is the usual static pressure rise coefficient; and (b) it has been employed in pump design practice. In pump design, it is conventional not to reduce the relative velocity to less than 50 percent of the entering velocity. An early design of the radial outflow compressor called for a relative velocity ratio of 0.44, or a 56-percent reduction in relative velocity in the rotating diffuser. Further reduction in relative velocity in the rotating diffuser could be controlled by either increasing the exit diameter of the diffuser or increasing the diffuser passage width. For this reason, the initial objectives were to investigate the vaneless diffuser over a range of velocity ratios and to determine the limiting value. The desired velocity ratio range was to be accomplished by operating the low-speed air model over a range of flow coefficient value at three rotor blade trailing edge angles.

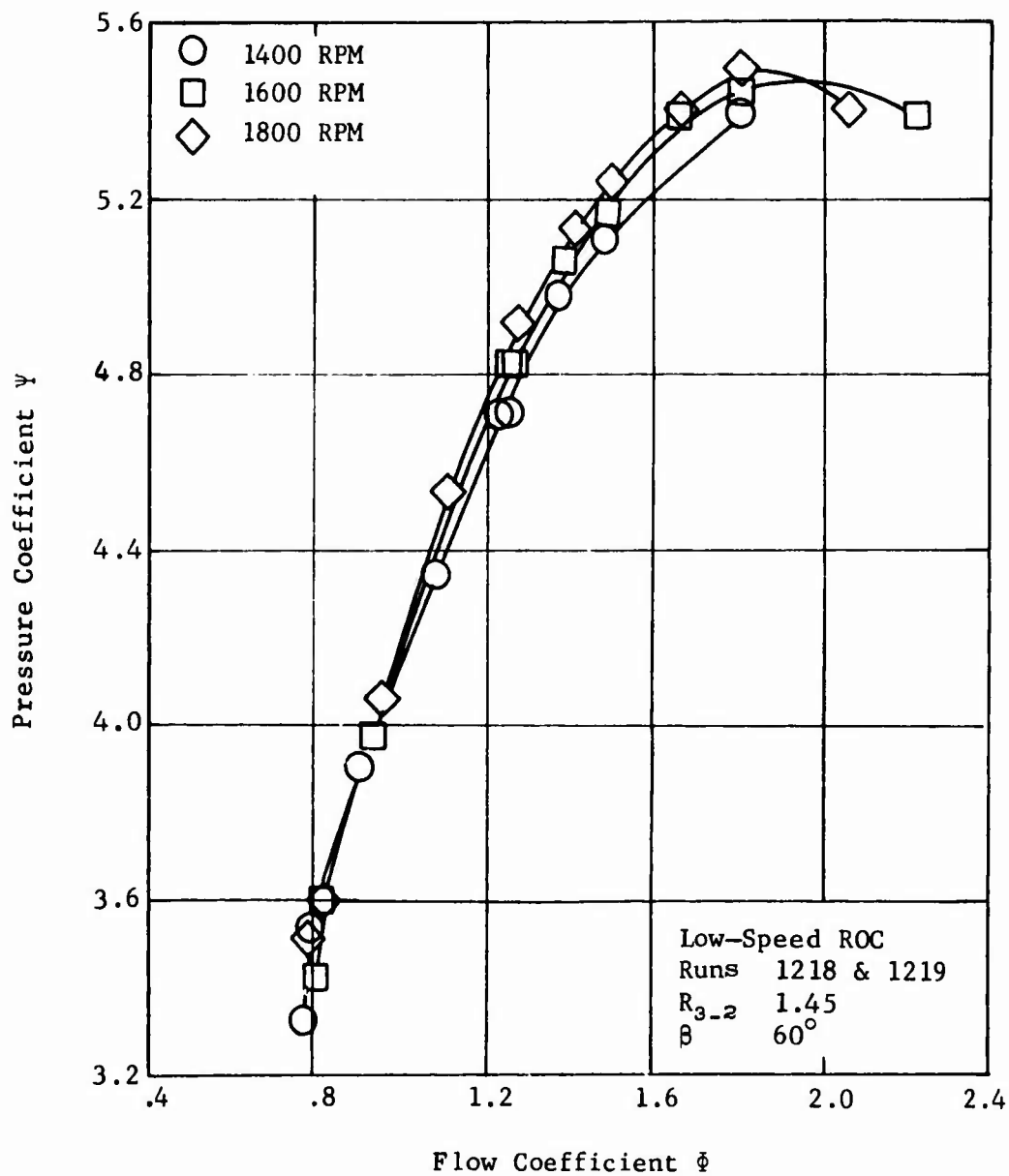


Figure 98. Rotor Discharge Pressure Coefficient with Vaneless Diffuser Radius Ratio of 1.45 and Rotor Blade Trailing Edge Angle of 60°.

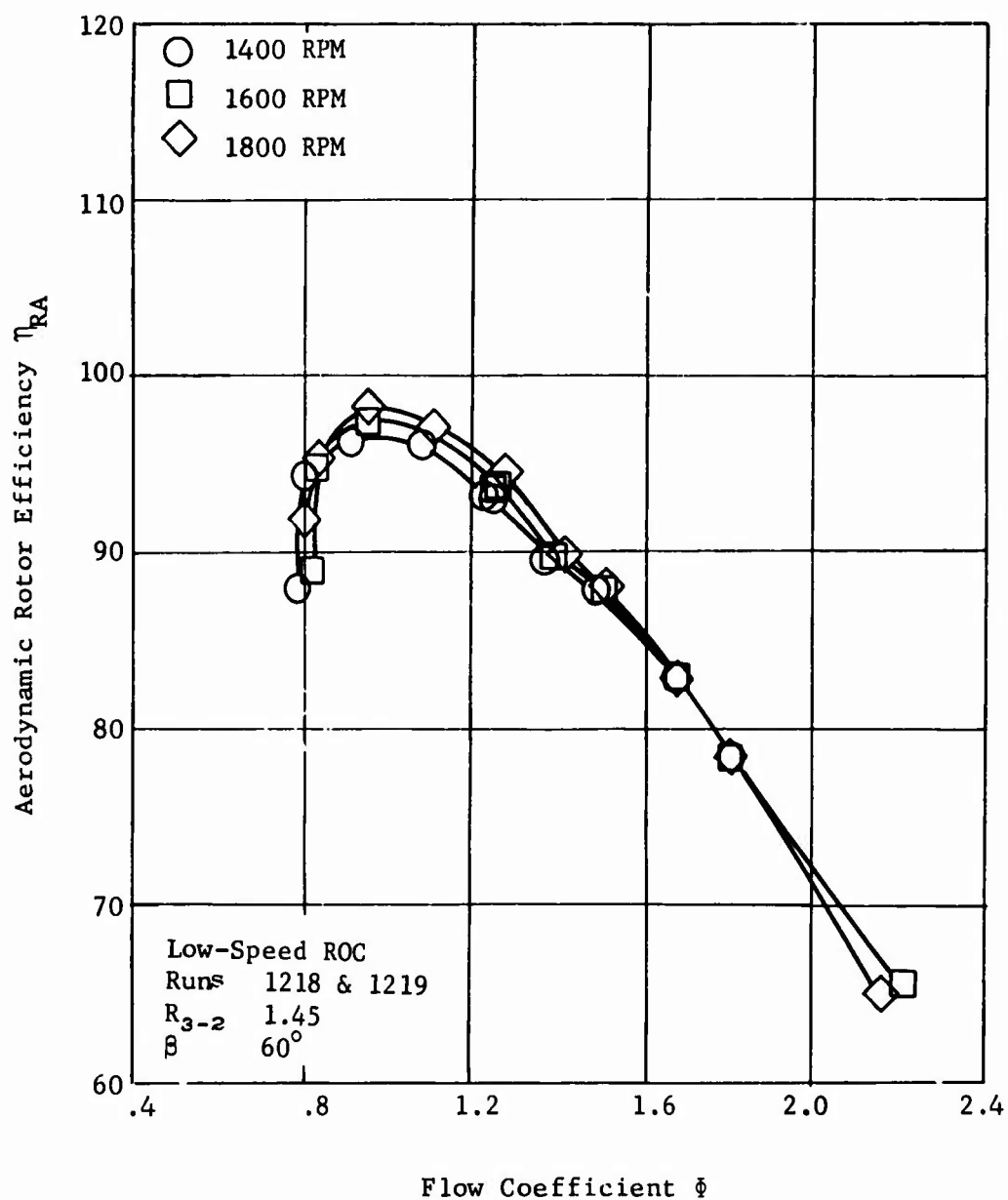


Figure 99. Compressor Efficiency with Vaneless Diffuser Radius Ratio of 1.45 and Rotor Blade Trailing Edge Angle of 60° .

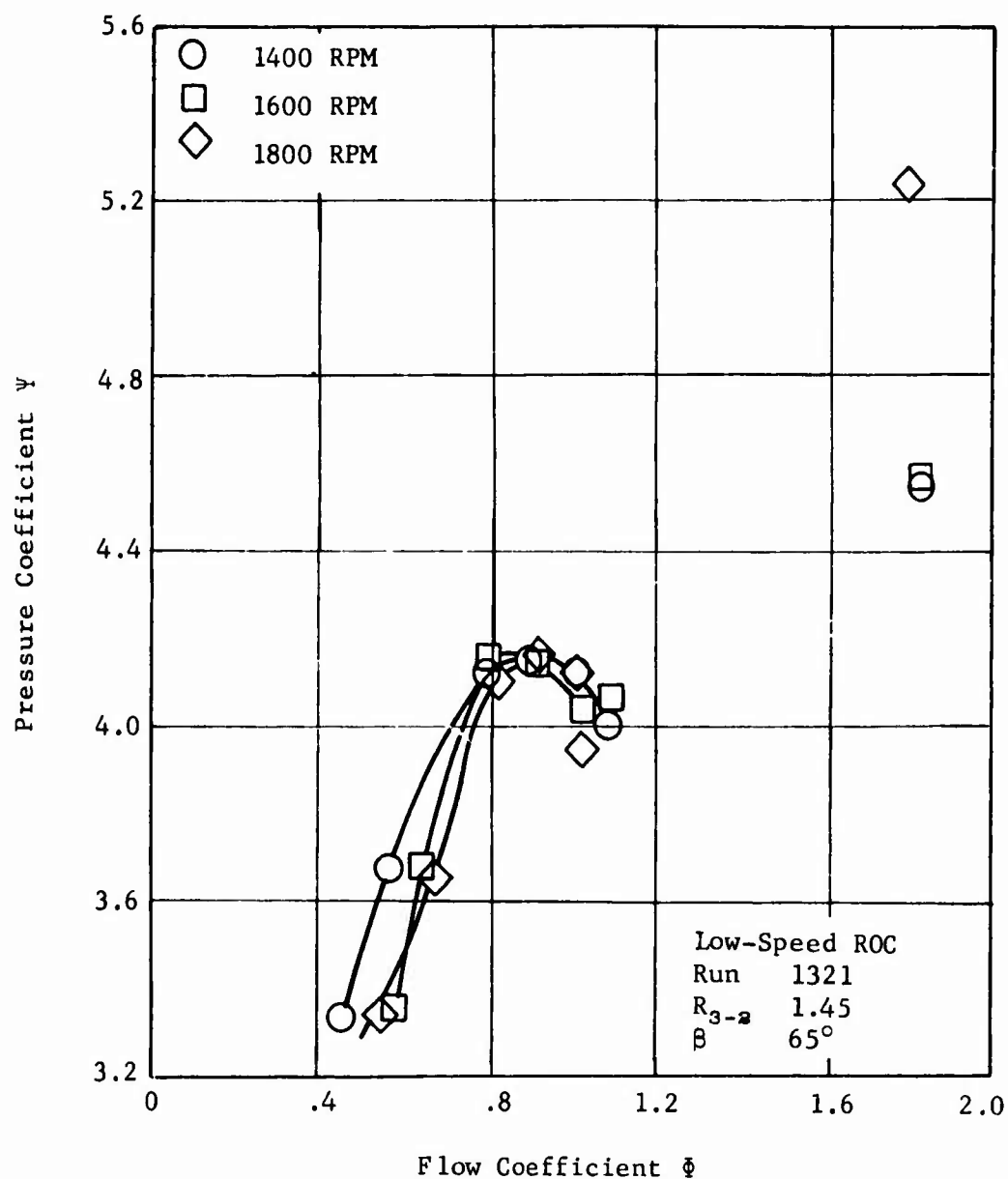


Figure 100. Rotor Discharge Pressure Coefficient with Vaneless Diffuser Radius Ratio of 1.45 and Rotor Blade Trailing Edge Angle of 65° .

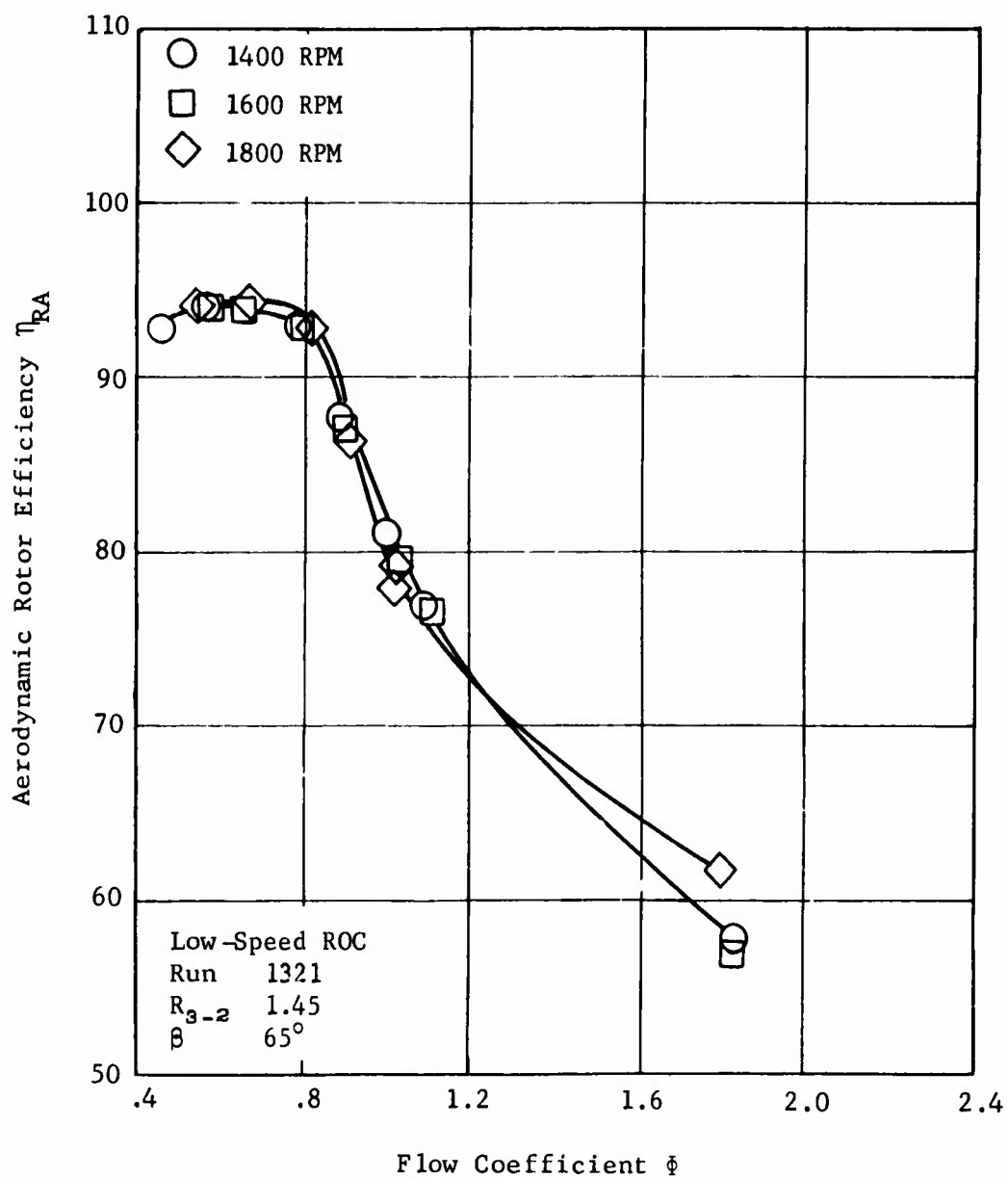


Figure 101. Compressor Efficiency with Vaneless Diffuser
Radius Ratio of 1.45 and Rotor Blade Trailing
Edge Angle of 65° .

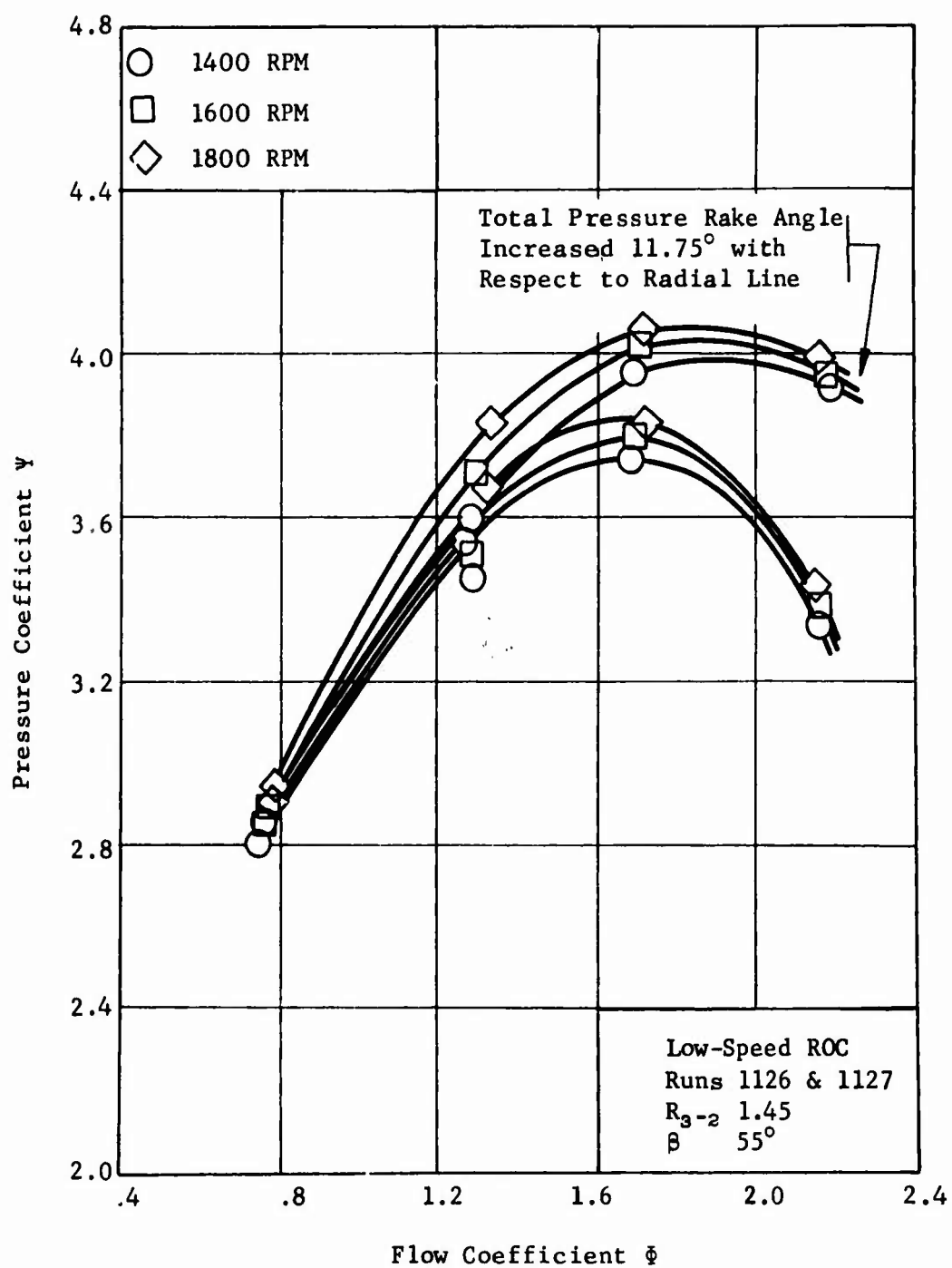


Figure 102. Rotor Discharge Pressure Coefficient with Vaneless Diffuser Radius Ratio of 1.45 and Rotor Blade Trailing Edge Angle of 55° .

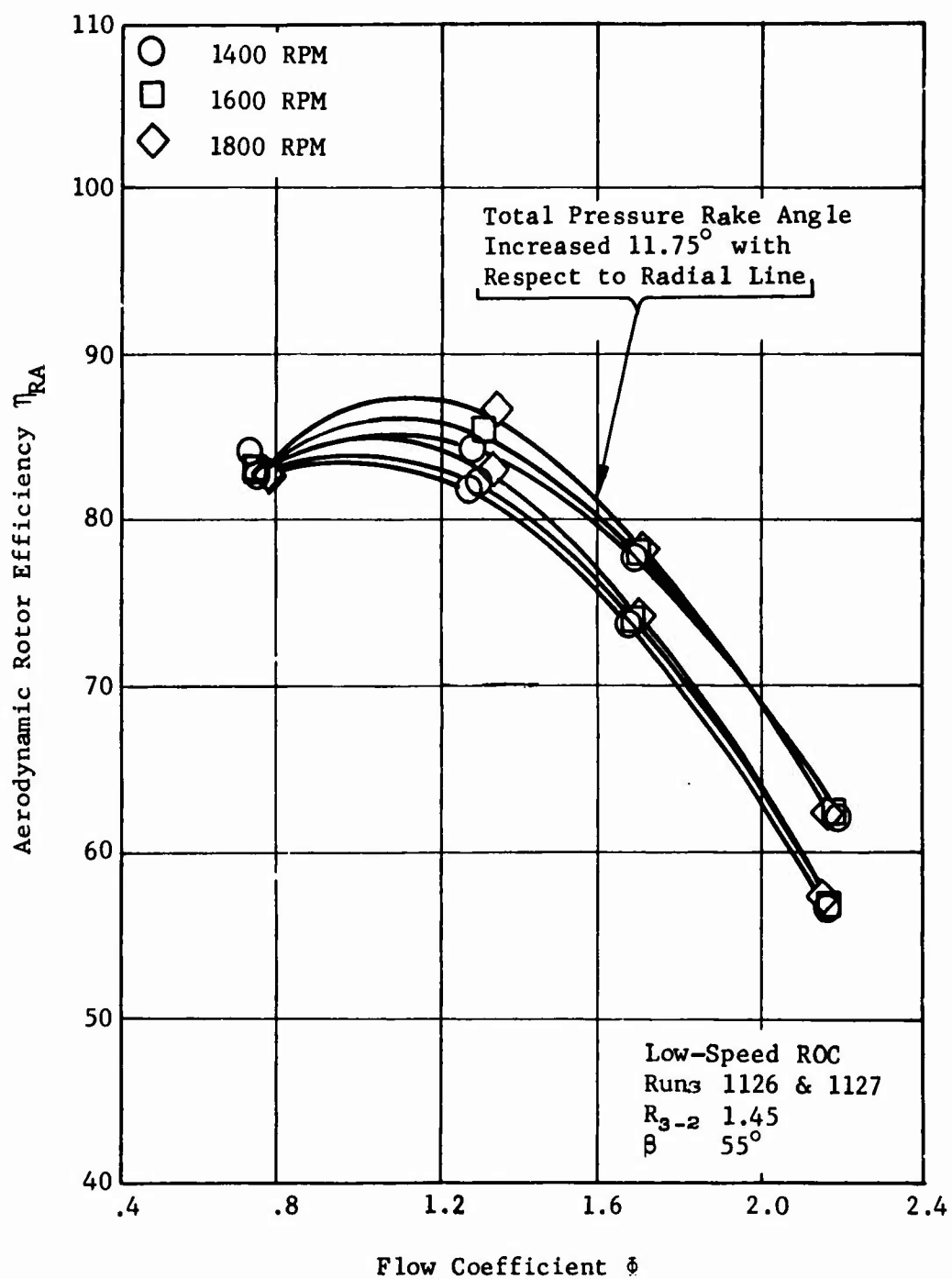


Figure 103. Compressor Efficiency with Vaneless Diffuser Radius Ratio of 1.45 and Rotor Blade Trailing Edge Angle of 55° .

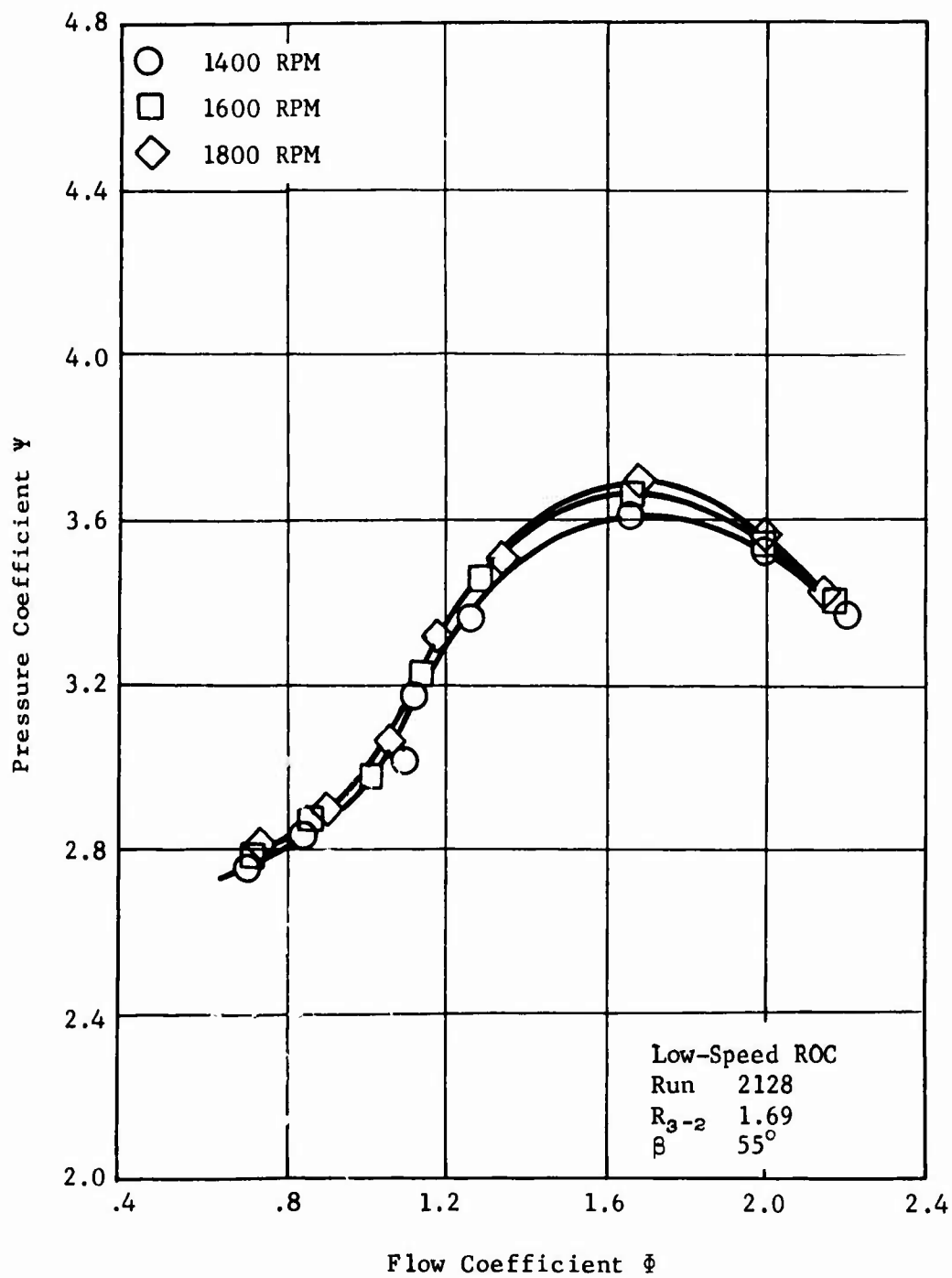


Figure 104. Rotor Discharge Pressure Coefficient with Vaneless Diffuser Radius Ratio of 1.69 and Rotor Blade Trailing Edge Angle of 55° .

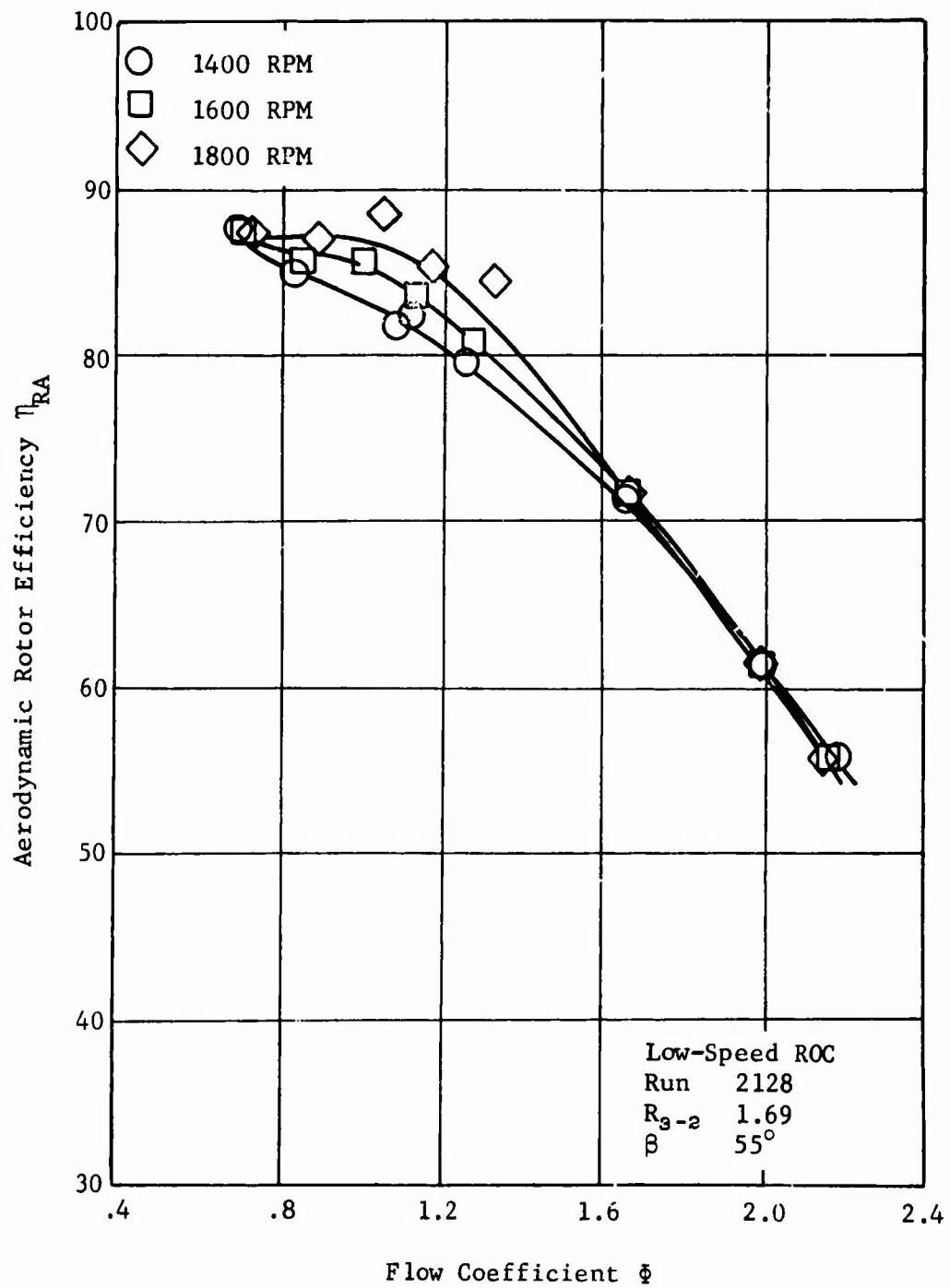


Figure 105. Compressor Efficiency with Vaneless Diffuser Radius Ratio of 1.69 and Rotor Blade Trailing Edge Angle of 55°.

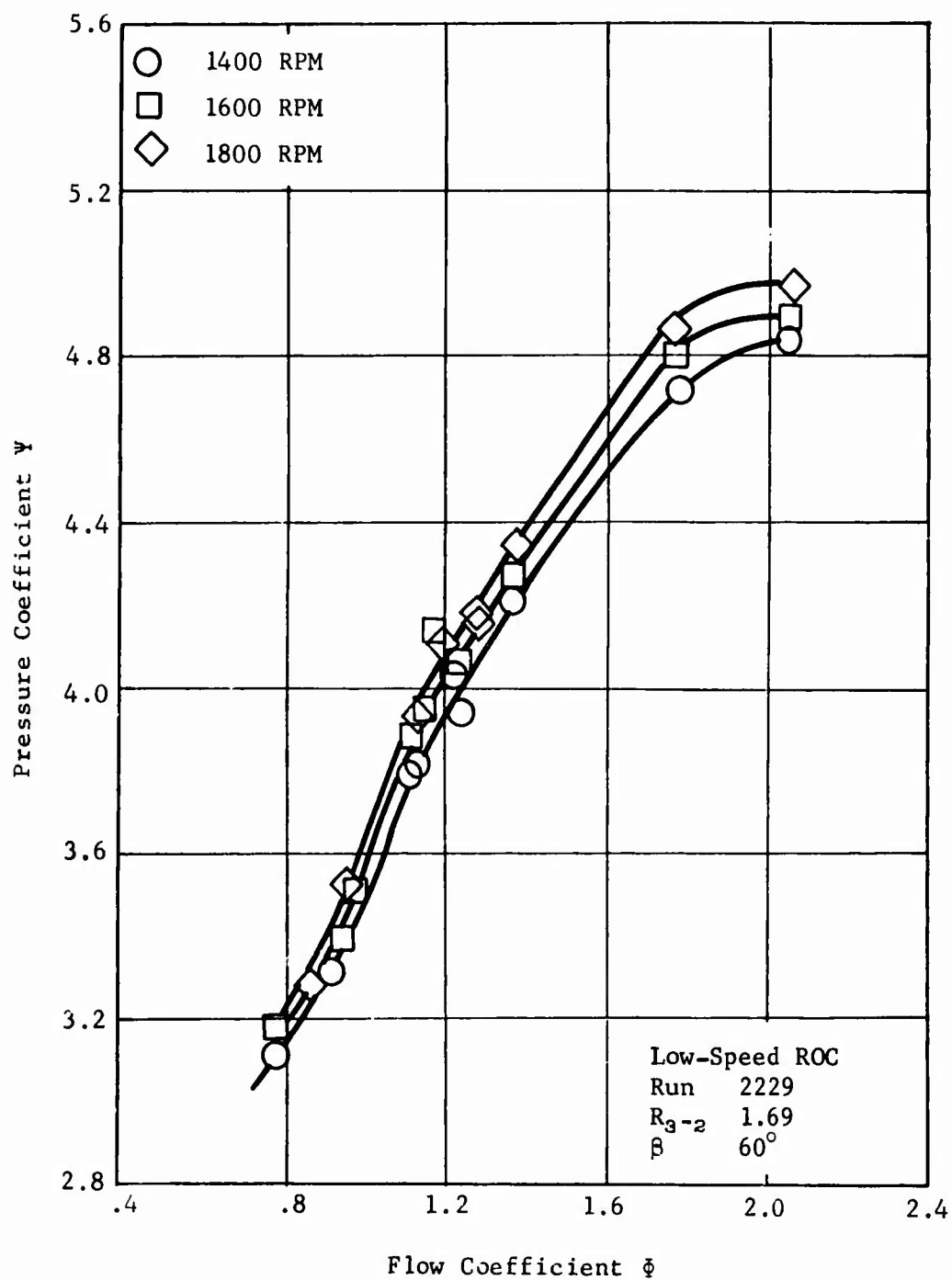


Figure 106. Rotor Discharge Pressure Coefficient with Vaneless Diffuser Radius Ratio of 1.69 and Rotor Blade Trailing Edge Angle of 60°.

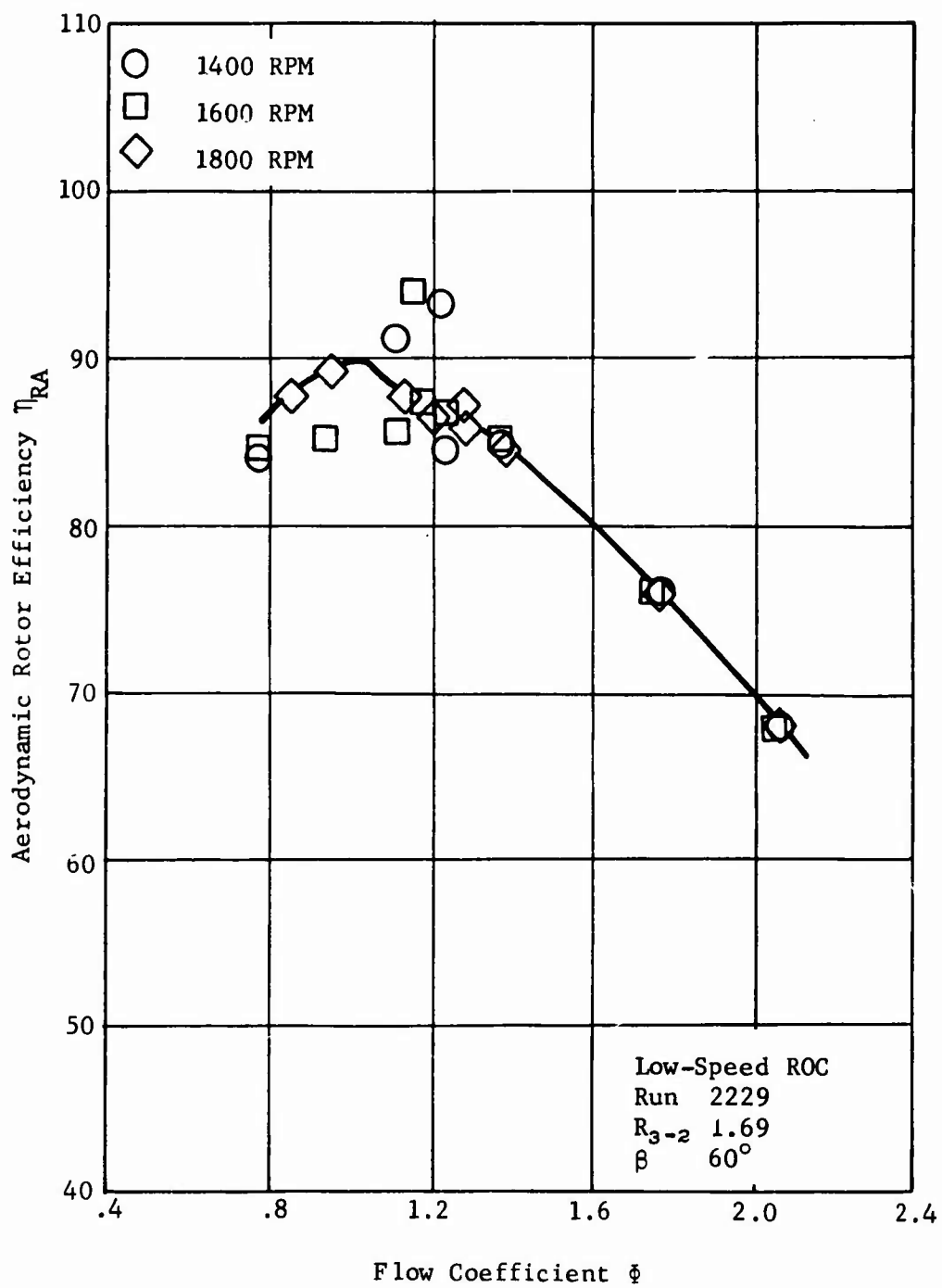


Figure 107. Compressor Efficiency with Vaneless Diffuser
Radius Ratio of 1.69 and Rotor Blade Trailing
Edge Angle of 60°.

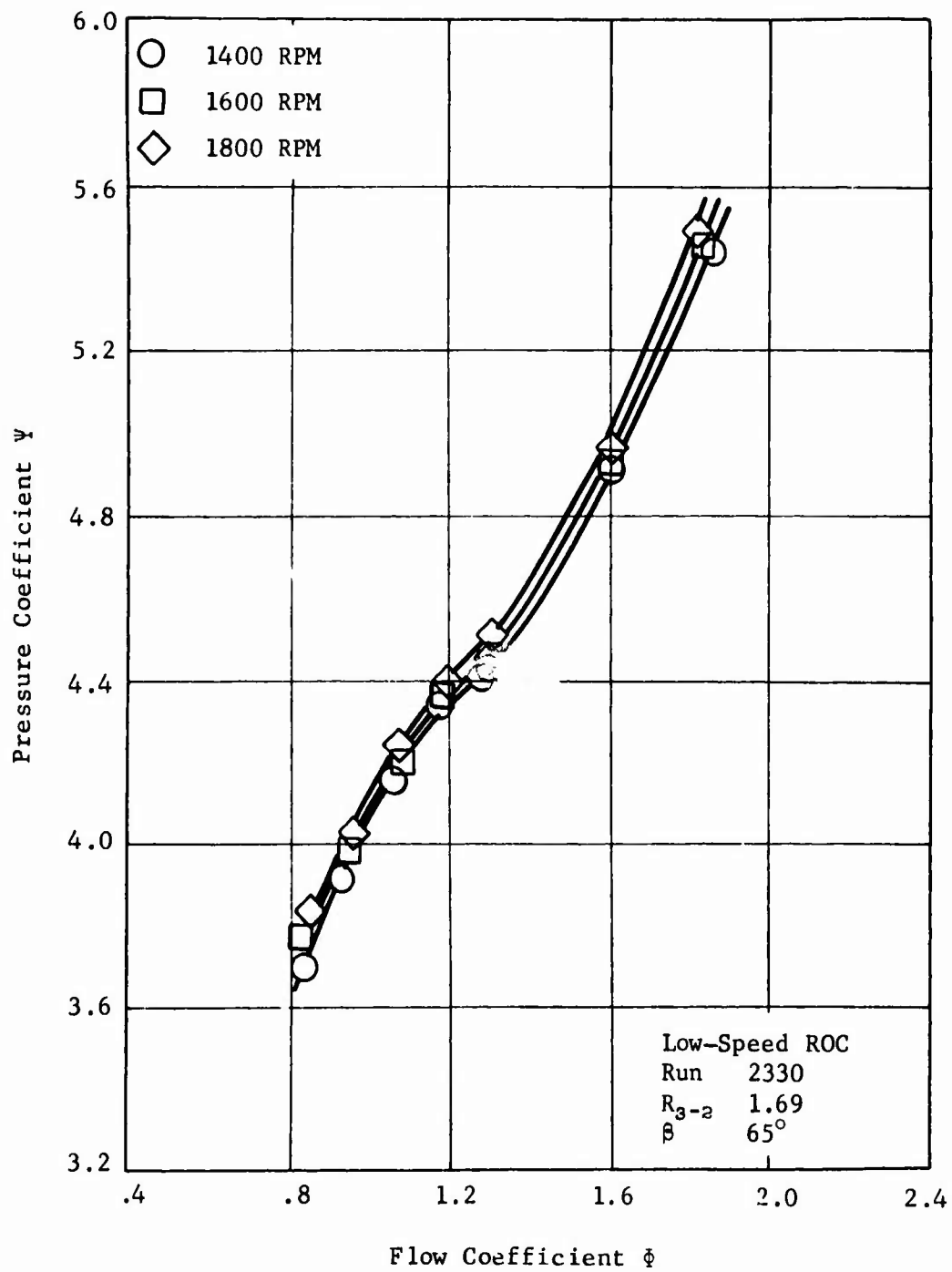


Figure 108. Rotor Discharge Pressure Coefficient with Vaneless Diffuser Radius Ratio of 1.69 and Rotor Blade Trailing Edge Angle of 65° .

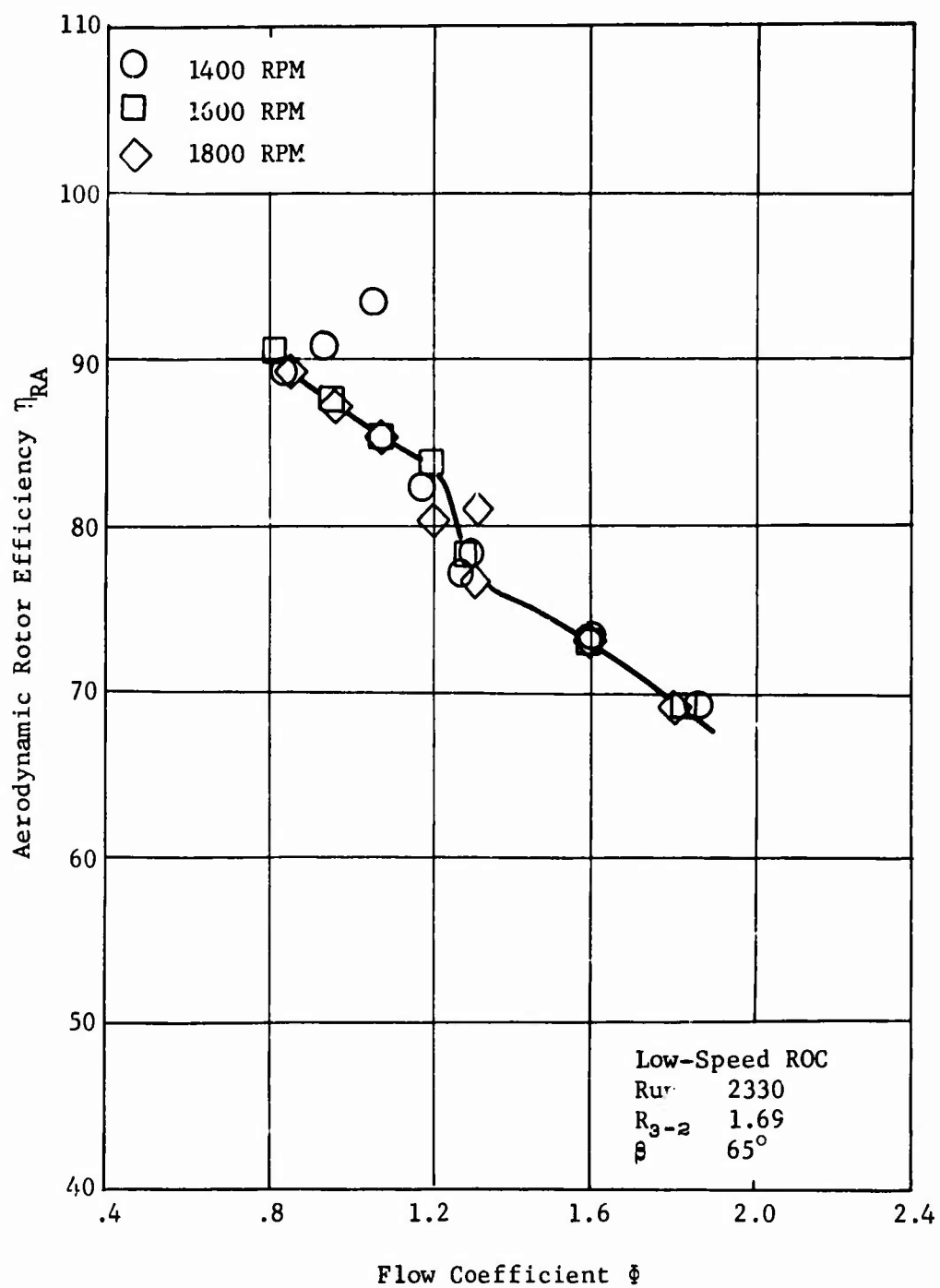


Figure 109. Compressor Efficiency with Vaneless Diffuser
 Radius Ratio of 1.69 and Rotor Blade Trailing
 Edge Angle of 65°.

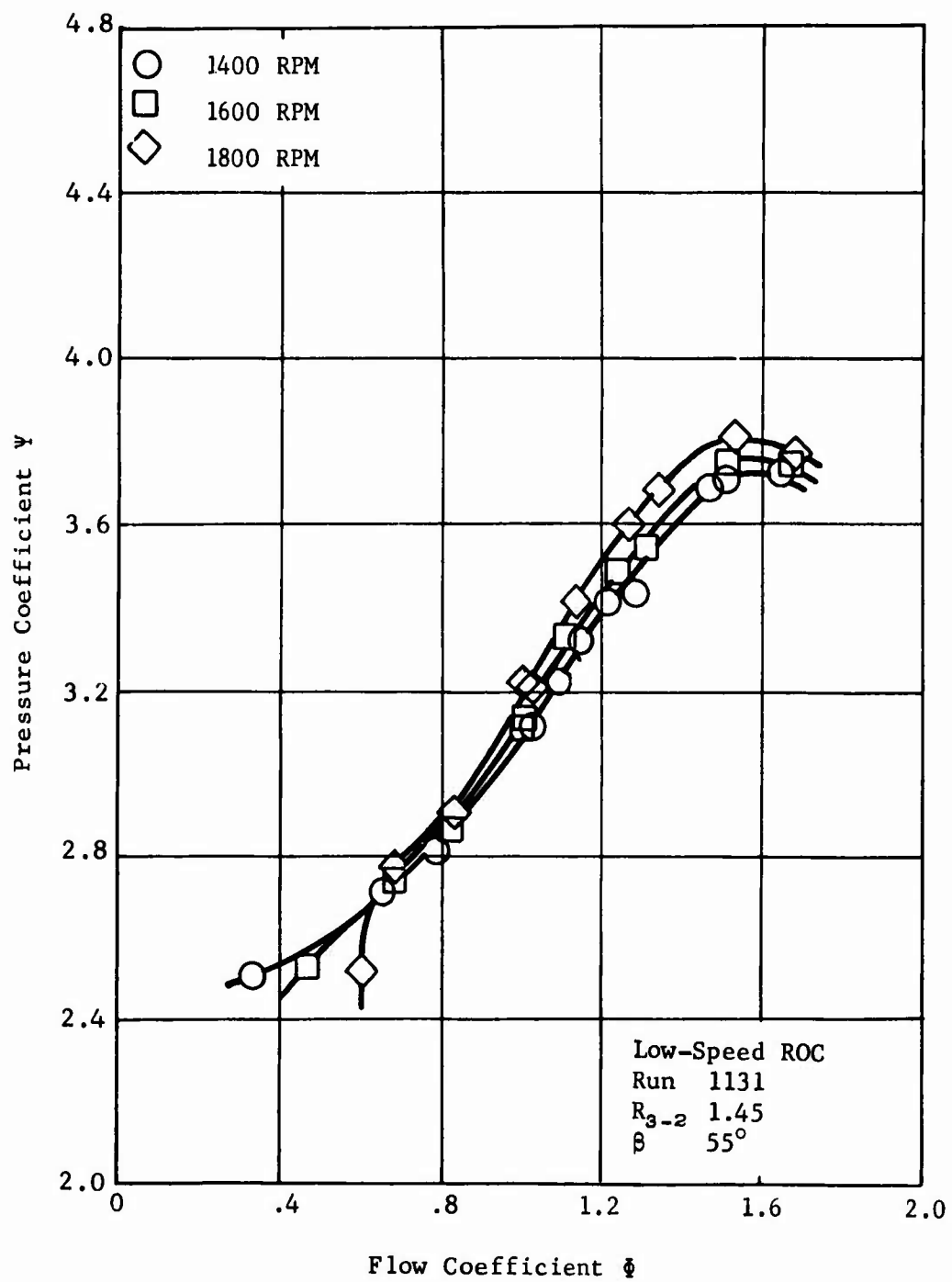


Figure 110. Rotor Discharge Pressure Coefficient with Vaneless Diffuser Radius Ratio of 1.45 and Rotor Blade Trailing Edge Angle of 55°.

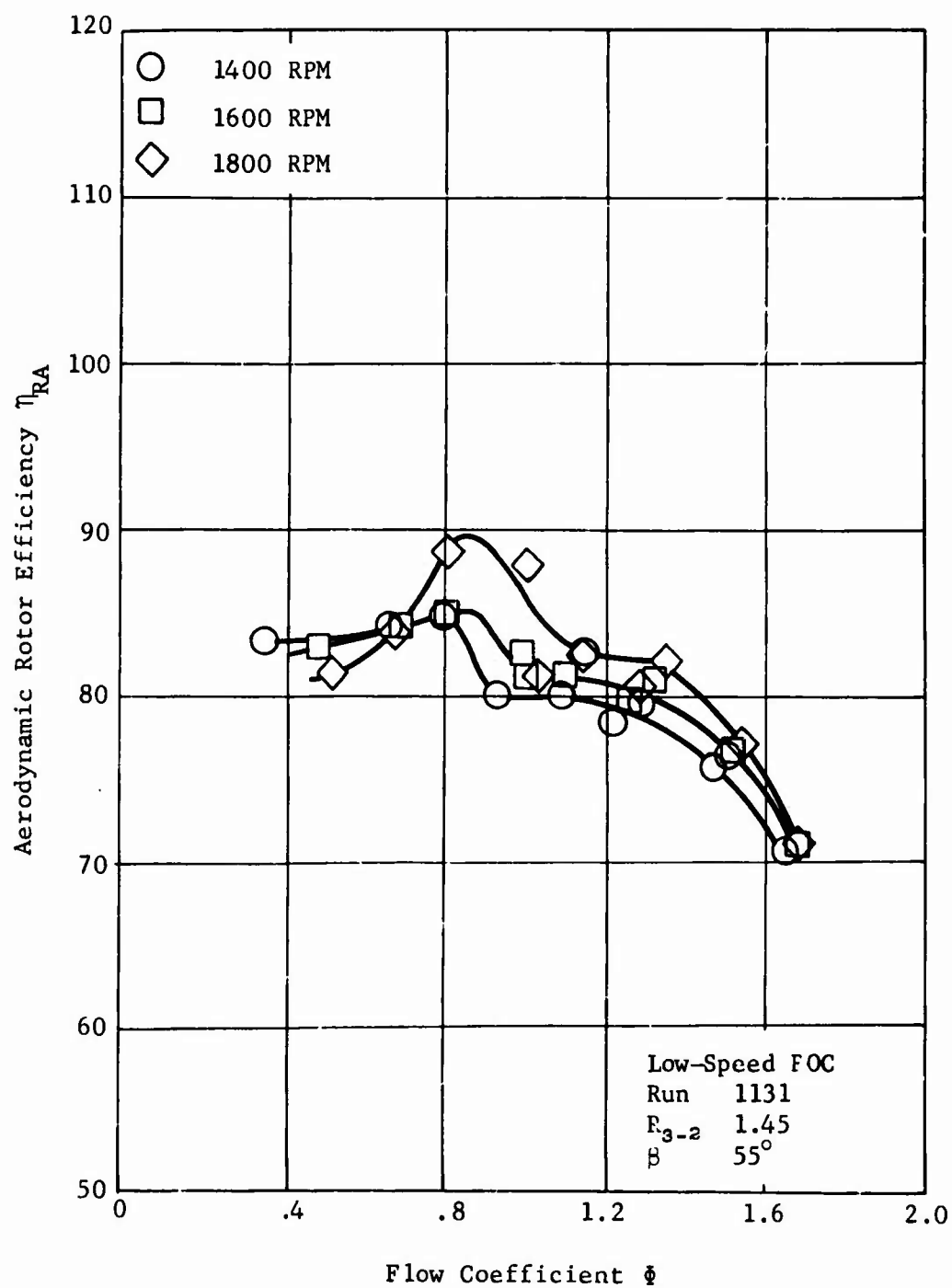


Figure 111. Compressor Efficiency with Vaneless Diffuser
 Radius Ratio of 1.45 and Rotor Blade Trailing
 Edge Angle of 55°.

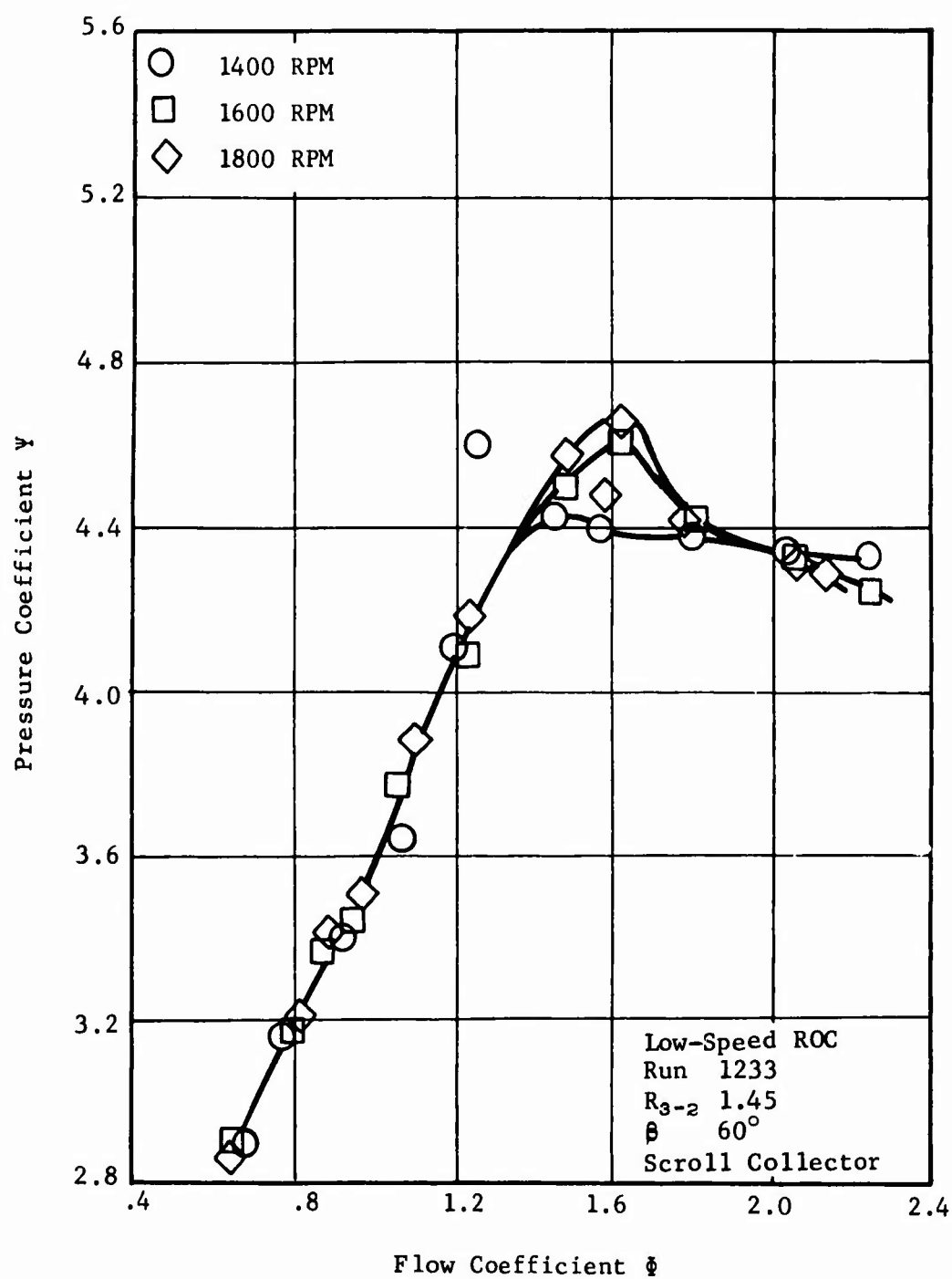


Figure 112. Rotor Discharge Pressure Coefficient with Vaneless Diffuser Radius Ratio of 1.45, Rotor Blade Trailing Edge Angle of 60° , and Scroll Collector Installed.

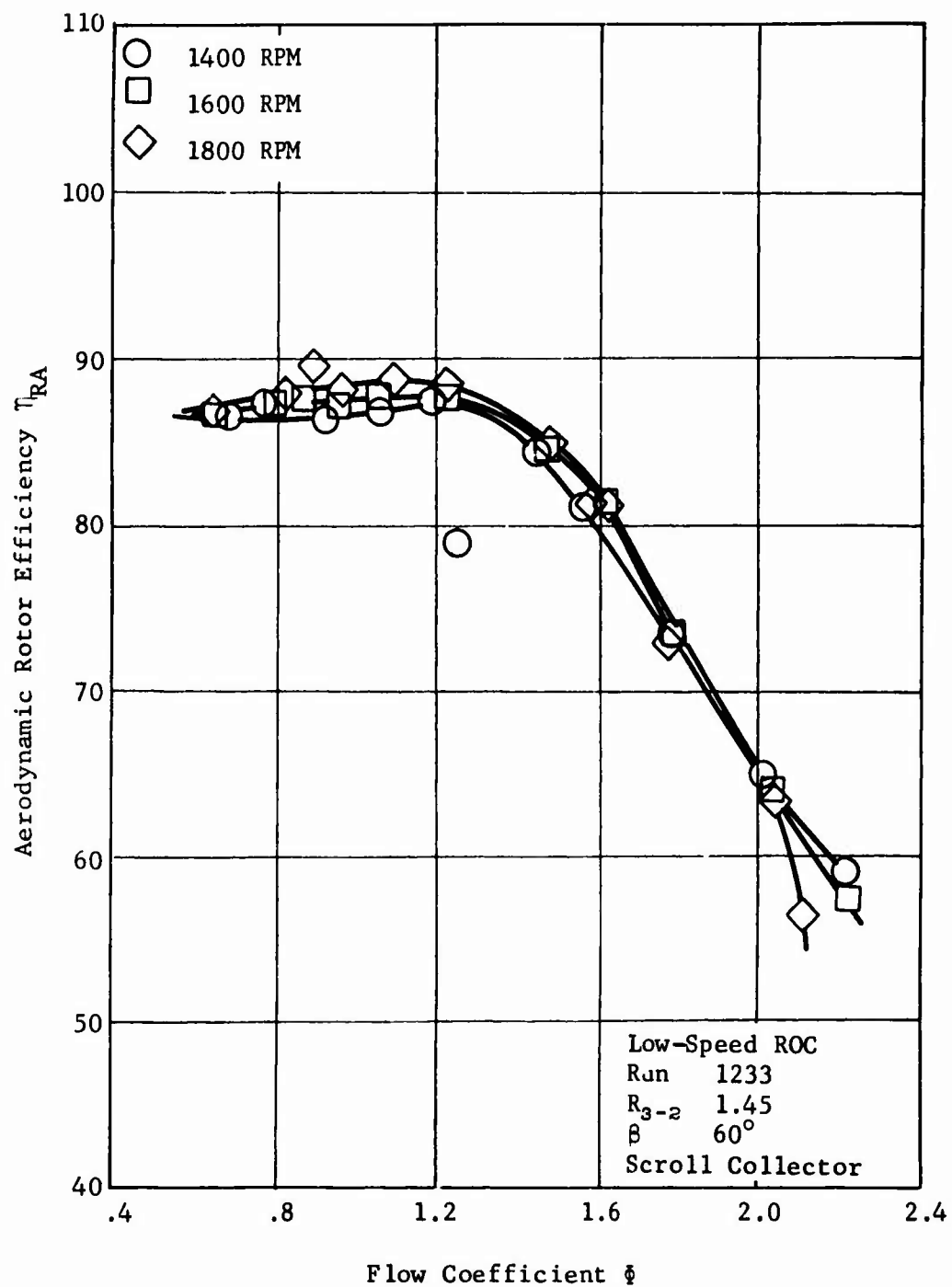


Figure 113. Compressor Efficiency with Vaneless Diffuser Radius Ratio of 1.45, Rotor Blade Trailing Edge Angle of 60° , and Scroll Collector Installed.

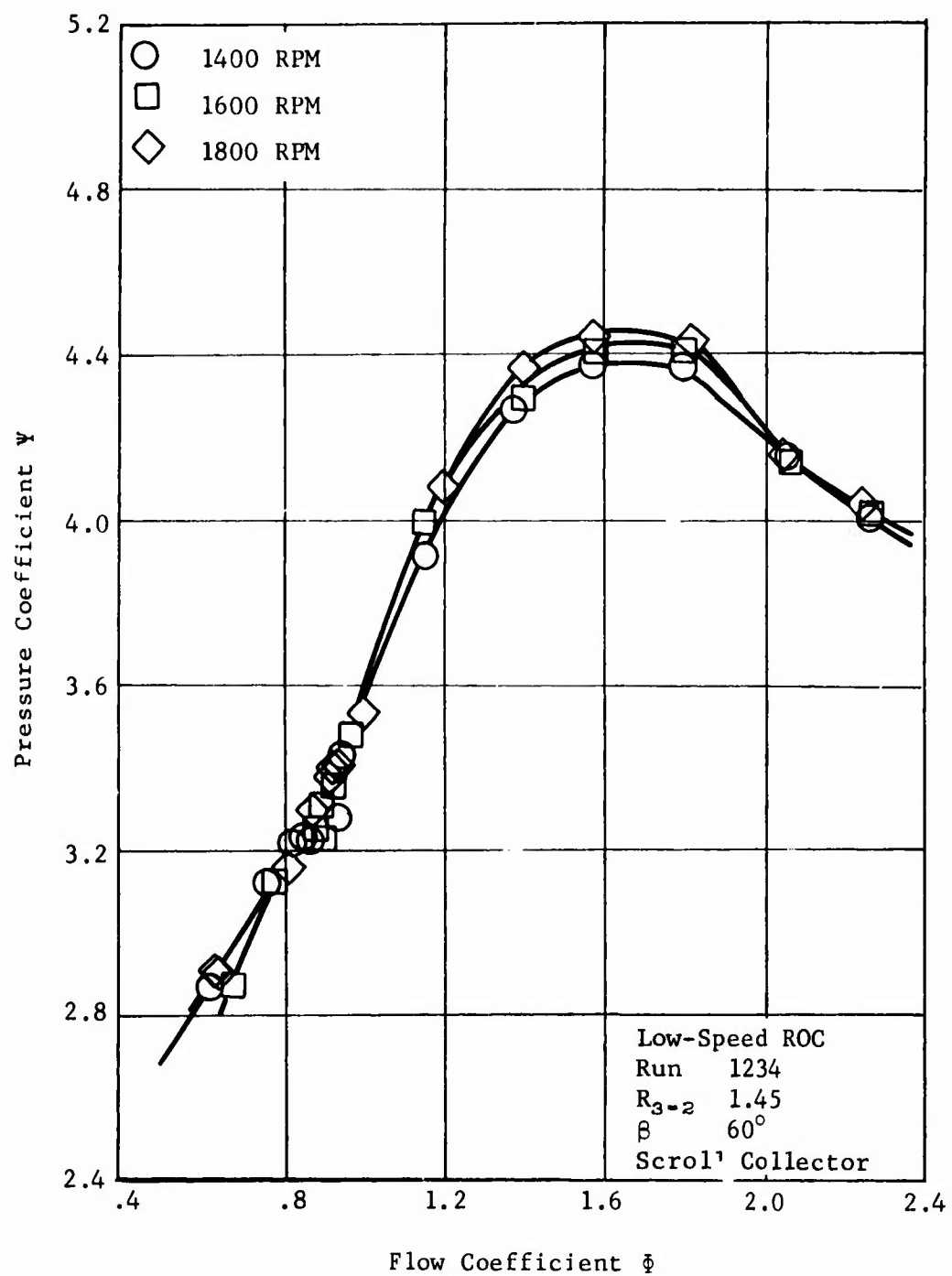


Figure 114. Rotor Discharge Pressure Coefficient with Vaneless Diffuser Radius Ratio of 1.45, Rotor Blade Trailing Edge Angle of 60° , and Scroll Collector Installed.

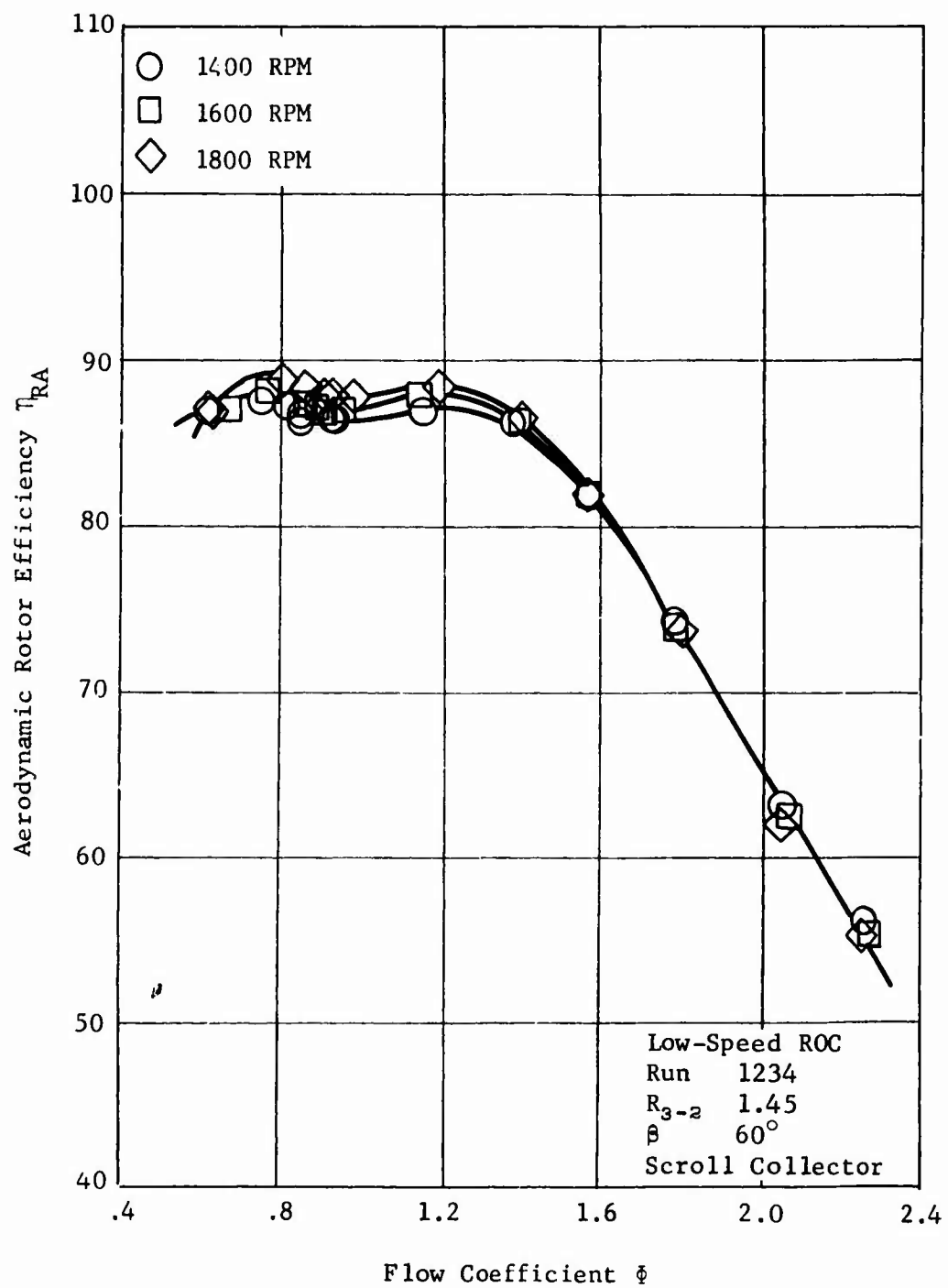
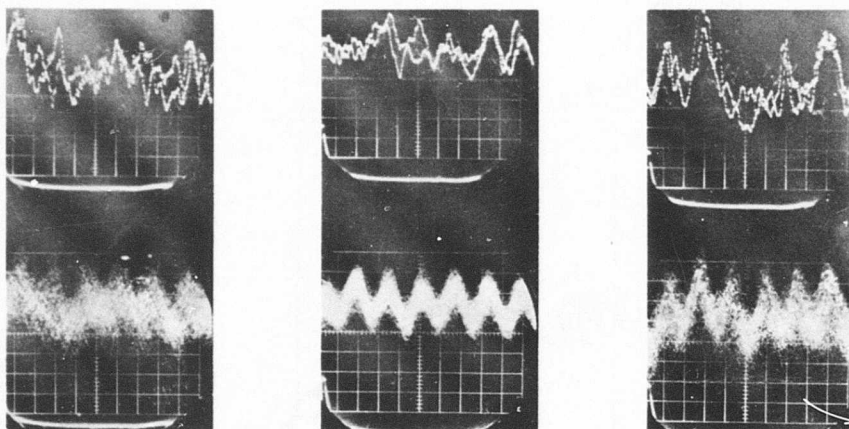
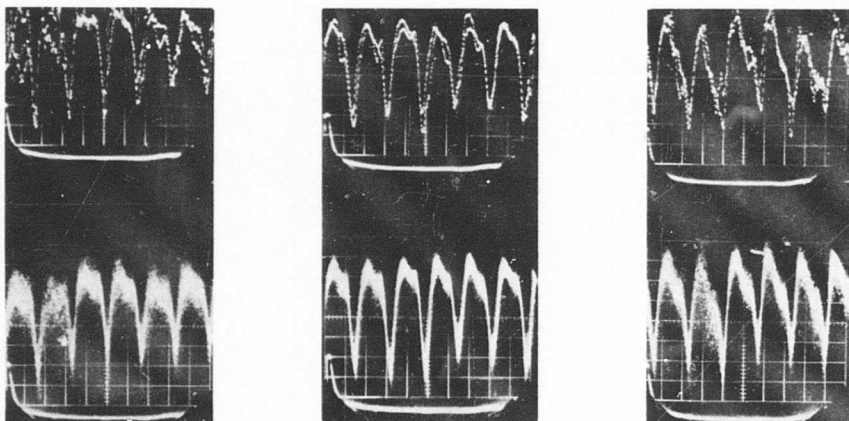


Figure 115. Compressor Efficiency with Vaneless Diffuser
Radius Ratio of 1.45, Rotor Blade Trailing Edge
Angle of 60°, and Scroll Collector Installed.

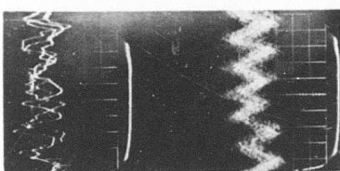


Front Wall Middle Back Wall
 Scale = 0.5V/CM. Scale = 0.5V/CM. Scale = 0.5V/CM.
 Radial Location of Probe from Rotor Exit = 2 Inches



Front Wall Middle Back Wall
 Scale = 0.5V/CM. Scale = 1.0V/CM. Scale = 0.5V/CM.
 Radial Location of Probe from Rotor Exit = 1/8 Inch
 Flow Function Φ 2.1

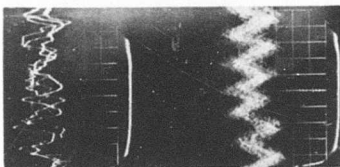
Figure 116. Dynamic Rotor Wake Responses. Rotor Speed = 1400 RPM.
 Horizontal Scope Sweep = 500 Microseconds/CM. Blade
 Trailing Edge Angle $\beta_{2*} = 55^\circ$. Exit Vanes Removed.



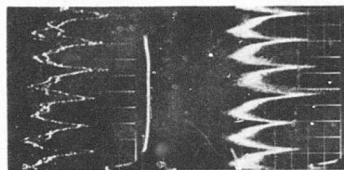
Front Wall
Scale = 0.5V/CM.



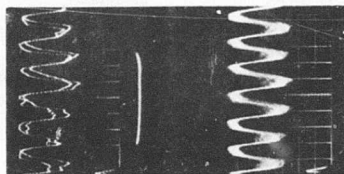
Middle
Scale = 0.5V/CM.
Radial Location of Probe from Rotor Exit = 2 Inches



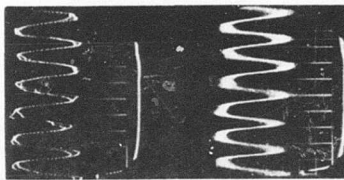
Back Wall
Scale = 0.5V/CM.



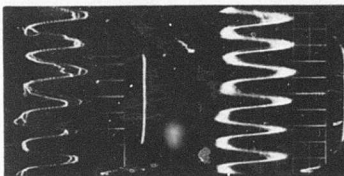
Front Wall
Scale = 0.5V/CM.



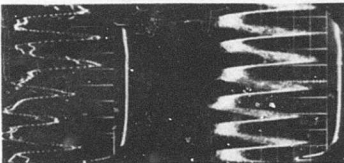
1/4" from Front Wall
Scale = 1.0V/CM.
Radial Location of Probe from Rotor Exit = 1/8 Inch



Middle
Scale = 1.0V/CM.
Radial Location of Probe from Rotor Exit = 1/8 Inch



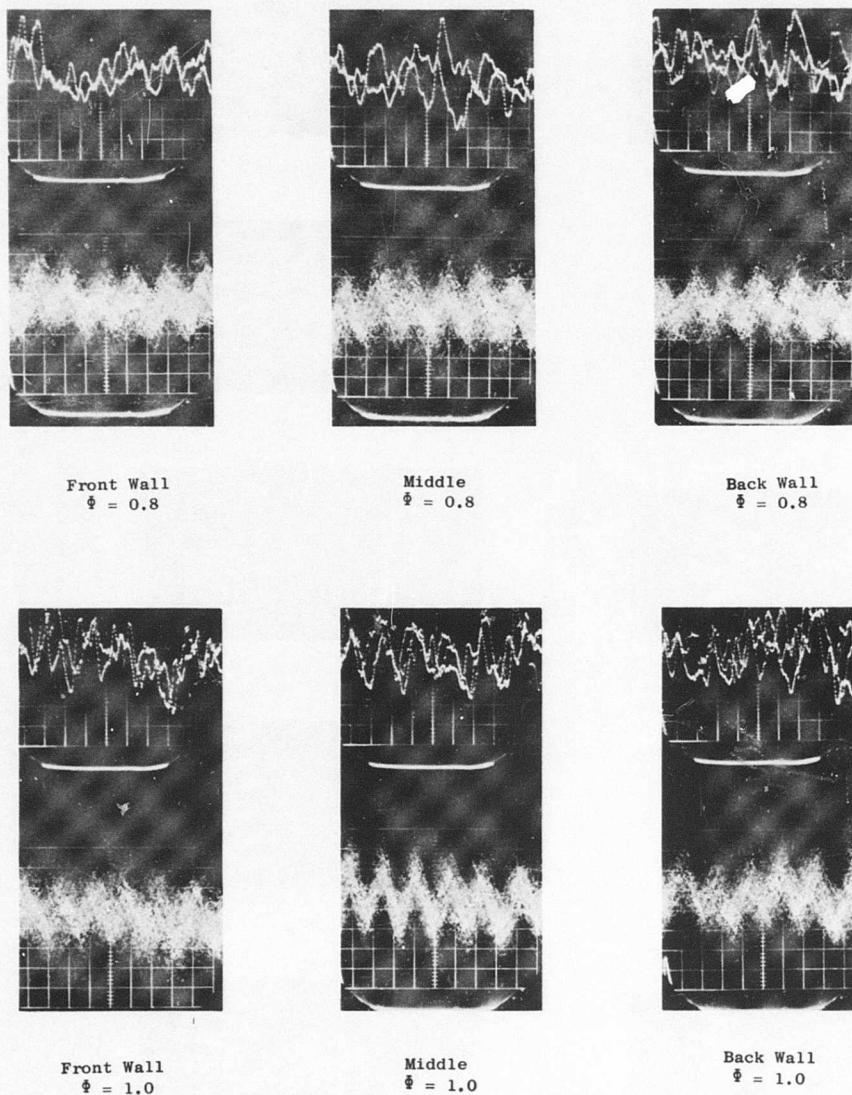
1/4" from Back Wall
Scale = 1.0V/CM.



Back Wall
Scale = 0.5V/CM.

Flow Function $\Phi = 1.0$

Figure 117. Dynamic Rotor Wake Responses. Rotor Speed = 1400 RPM. Horizontal Scope Sweep = 500 Microseconds/CM. Blade Trailing Edge Angle $\beta_2^* = 55^\circ$. Exit Vanes Removed.



Probe Located at Rotating Diffuser Exit.
Vertical Scale = 0.2 Volt/CM.

Figure 118. Dynamic Rotor Wake Responses. Rotor Speed = 1400 RPM. Horizontal Scope Sweep = 500 Microseconds/CM. Blade Trailing Edge Angle $\beta_{2*} = 55^\circ$. Exit Vanes Removed.

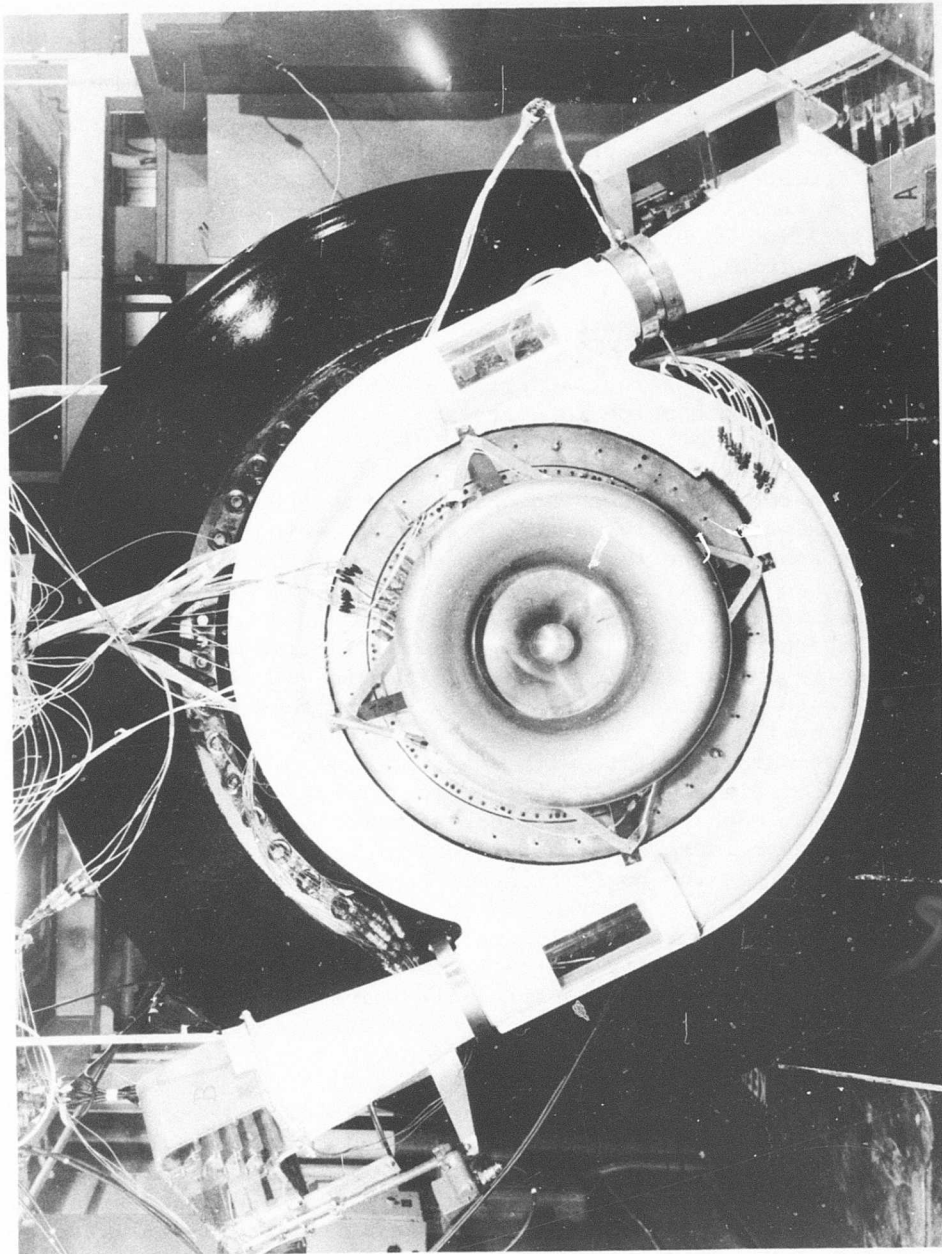


Figure 119. Low-Speed ROC Installation with Scroll Collector, Exit Arm Ducts, Elbow Turning Vanes and Throttle Valves.

The generally erratic and nonrepeatable results from the early tests at the 60-degree rotor blade setting seemed to indicate that the rotating diffuser was already in trouble. The minimum velocity ratio achieved was 0.338. It was decided to open up the rotor blade angle to 55 degrees and to test the rotating diffuser at a higher velocity ratio in an attempt to achieve consistent repeatable data as a base for further analysis. The data for any one run were consistent and well behaved, but test points were still not repeatable from one day to the next. The maximum measured rotor aerodynamic efficiency at 55 degrees was down by about 10 percent from the maximum obtained at 60 degrees. This result was contrary to the expected improvement in efficiency that should accompany what appeared to be an easier flow problem at this higher relative velocity ratio. Further investigation at this blade setting using a rotor trailing edge total pressure probe indicated that there was no significant total pressure loss in the rotating diffuser.

Comparison of Correlating Parameters

Along with the continued testing, analytical studies were begun in search of a better parameter with which to correlate rotor aerodynamic efficiency. Based on later test results after the instrumentation leaks were corrected, a preliminary carpet plot (Figure 120) was made using the effective pressure coefficient as the ordinate. This coefficient is defined as the maximum effective static pressure rise normalized to the absolute dynamic head, where the effective static pressure rise represents the difference in the static pressure rise of the free stream treated as a free vortex and the boundary layer treated as rotating at wall speed (solid body rotation). The maximum effective static pressure rise is obtained by evaluating the pressure rise in both cases from diffuser inlet to the radial position where the absolute flow velocity is equal to the wheel speed. The carpet plot, Figure 120, indicates that the low-speed test data correlate with the effective pressure coefficient and do not correlate with relative velocity ratio or rotor blade angle of incidence. High rotor efficiency appears to be associated with an effective static pressure rise coefficient of about 0.30, with decreasing efficiency as the coefficient increases.

It was decided to test a larger radius ratio vaneless diffuser to permit the attainment of lower velocity ratios in conjunction with differing values of the effective pressure coefficient. More information showing the effects of these two parameters on vaneless diffuser performance would be obtained.

Test results showing the performance characteristics of the rotating vaneless diffuser as determined from the low-speed radial outflow compressor are presented in Figures 104 through 115. Figure 121 is a carpet plot of the measured rotor aerodynamic efficiency characteristics for the 24-inch-diameter rotating diffuser (radius ratio of 1.45) at a speed of 1800 rpm. The characteristics of the 28-inch-diameter diffuser (radius ratio of 1.69) at a speed of 1800 rpm are shown in Figure 122. In general, the peak efficiencies occur in the same portion of each map.

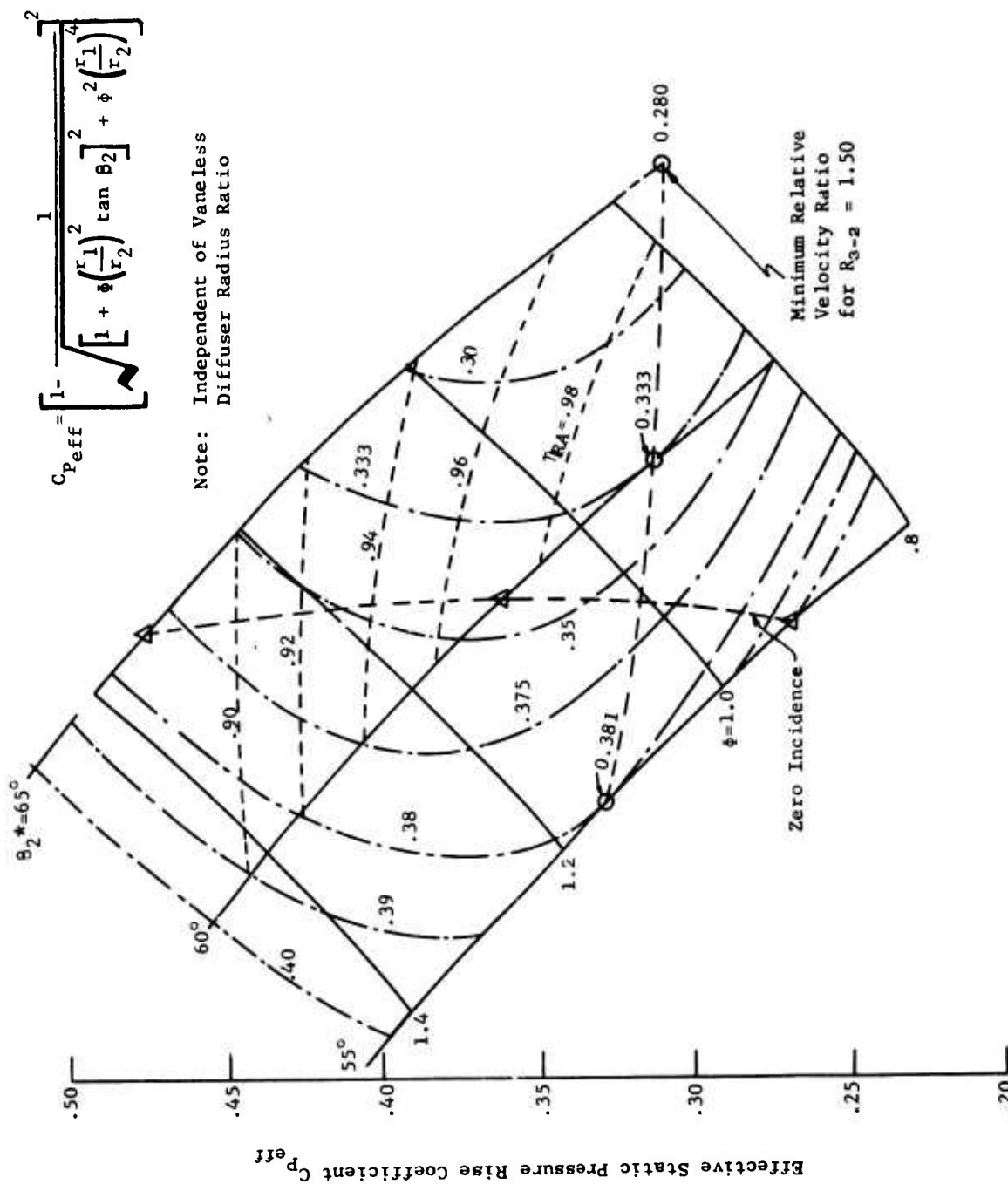


Figure 120. Preliminary Carpet Plot Rotor Efficiency Characteristics as a Function of Effective Static Pressure Rise Coefficient with Rotating Vaneless Diffuser Radius Ratio of 1.50.

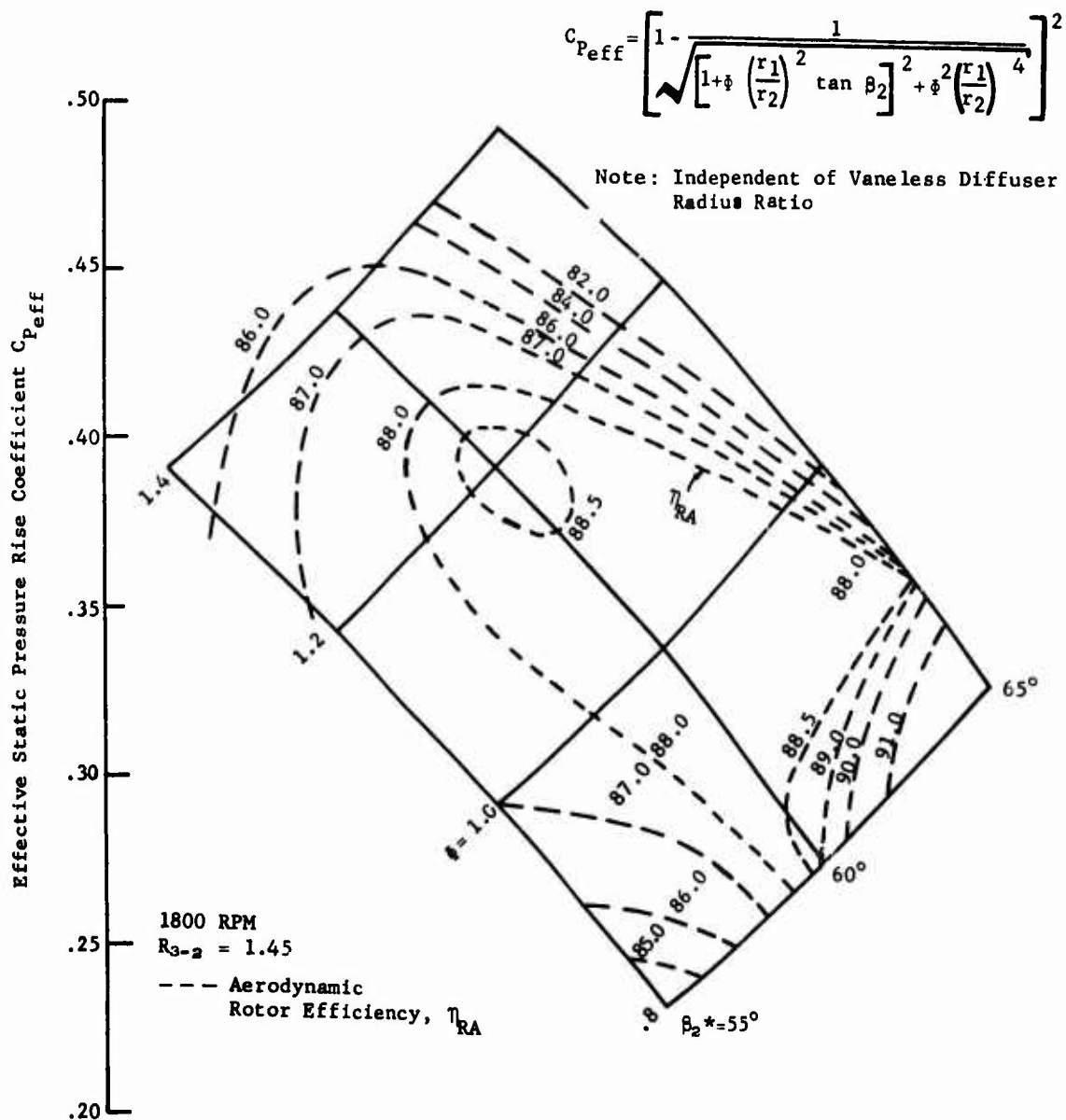


Figure 121. Rotor Efficiency Characteristics as a Function of Effective Pressure Rise Coefficient with Rotating Vaneless Diffuser Radius Ratio of 1.45.

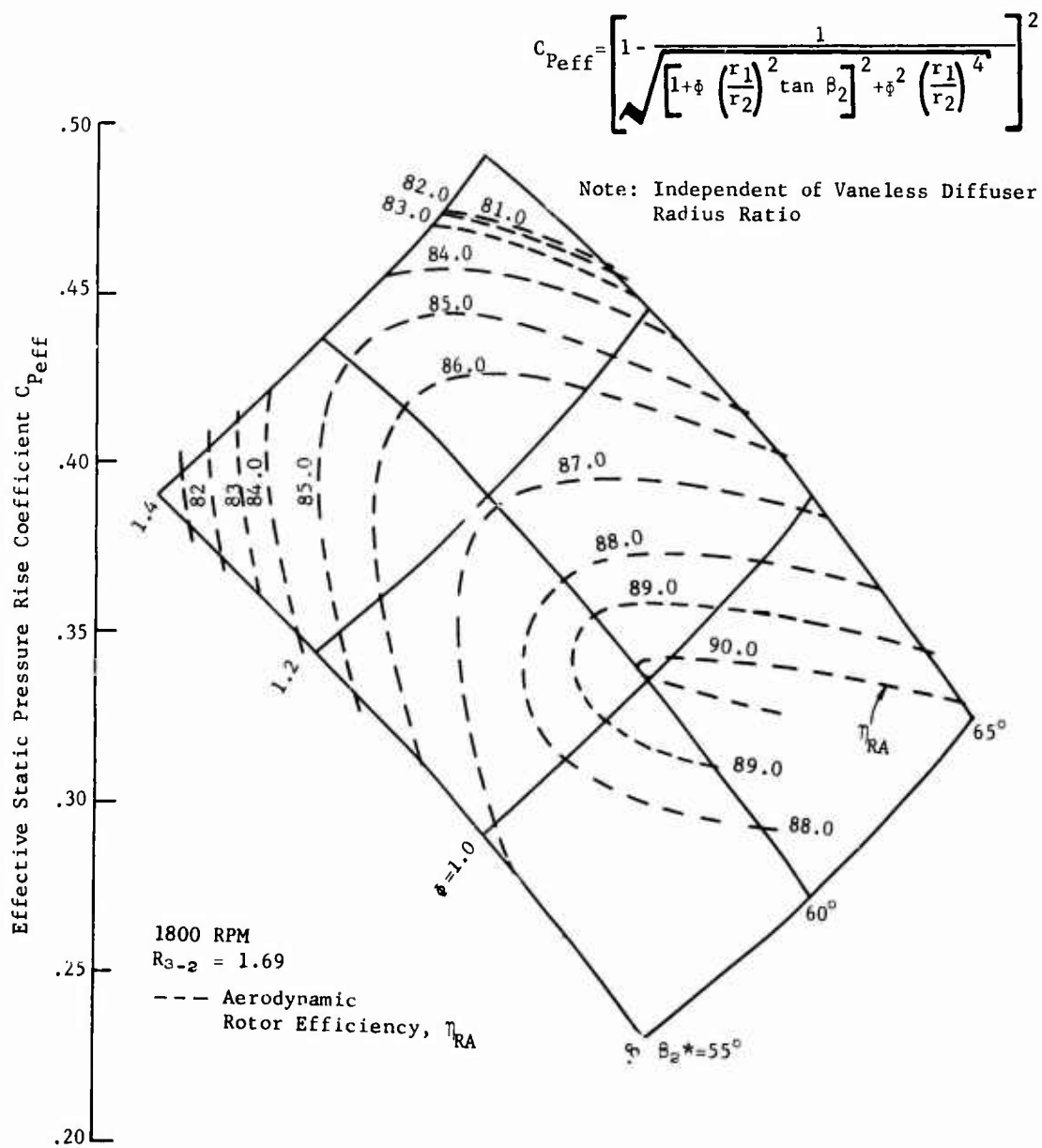


Figure 122. Rotor Efficiency Characteristics as a Function of Effective Static Pressure Rise Coefficient with Rotating Vaneless Diffuser Radius Ratio of 1.69.

Analysis of High-Speed Compressor

An analytical study was conducted to examine the effects of vaneless diffuser geometry variations on radial outflow compressor performance. The original design point of the high-speed machine was selected as a base. The effect of varying vaneless diffuser geometry on effective pressure rise coefficient is shown in Figure 123. Radius ratio is expressed as the exit radius in inches and width ratio as h_3/h_2 . The effect of these same parameters on the flow angle and Mach number entering the stators is presented in Figure 124. Figure 125 shows the resultant effect on the calculated pressure ratio and efficiency. Two values of vaneless diffuser radius ratio and width ratio (indicated by r_3 and h_3) were selected to show the effects of rotor blade exit direction (β^*_2) and rotor blade area ratio (A_2/A_1) on the flow angle and Mach number entering the stators and overall pressure ratio in Figure 126. At the time that this study was being made, the variation in vaneless diffuser efficiency and the inlet angle effects on stator efficiency were not determined and were not incorporated. The high-speed radial outflow compressor is designed to operate at an effective pressure coefficient between 0.26 and 0.30. Based on the low-speed data, the high-speed machine will operate in a range of high efficiencies.

CONCLUSIONS

Being an integral part of the rotor, rotating vaneless diffuser performance characteristics were based on variations in overall rotor performance. The change in rotor blade trailing edge angle was initially adopted as a means of varying the relative velocity ratios at which the rotating diffuser would operate. The desired variation of relative velocity ratio was accomplished, but its effect on vaneless diffuser performance was not directly apparent owing to the very significant influence that the trailing edge angle variation had on rotor performance. For this reason, the comparison in performance levels achieved with the two radius ratio vaneless diffusers was very important and valuable. The effective pressure rise coefficient was found to provide satisfactory correlation of rotor efficiency.

The rotating vaneless diffuser performed well over a range of flow coefficients for all test conditions investigated. Best performance occurred at effective static pressure rise coefficients in the range from 0.30 to 0.36.

Based on the vaneless diffuser characteristics presented in the carpet plots, Figures 121 and 122, the high-speed radial outflow compressor, designed to operate at an effective static pressure coefficient of 0.32, should operate in a range of high rotor efficiencies.

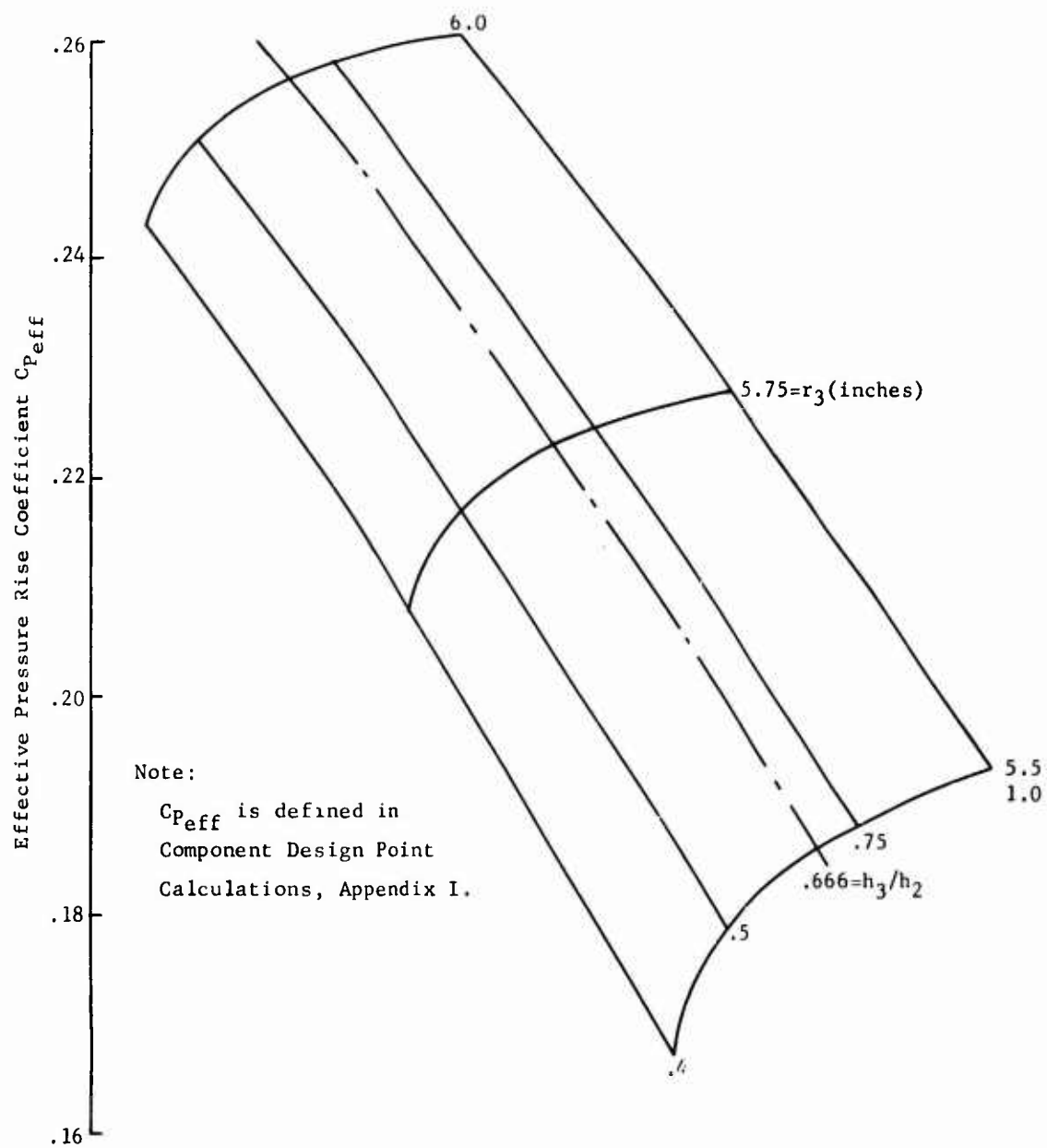


Figure 123. Effect of Vaneless Diffuser Geometry on Effective Static Pressure Rise Coefficient.

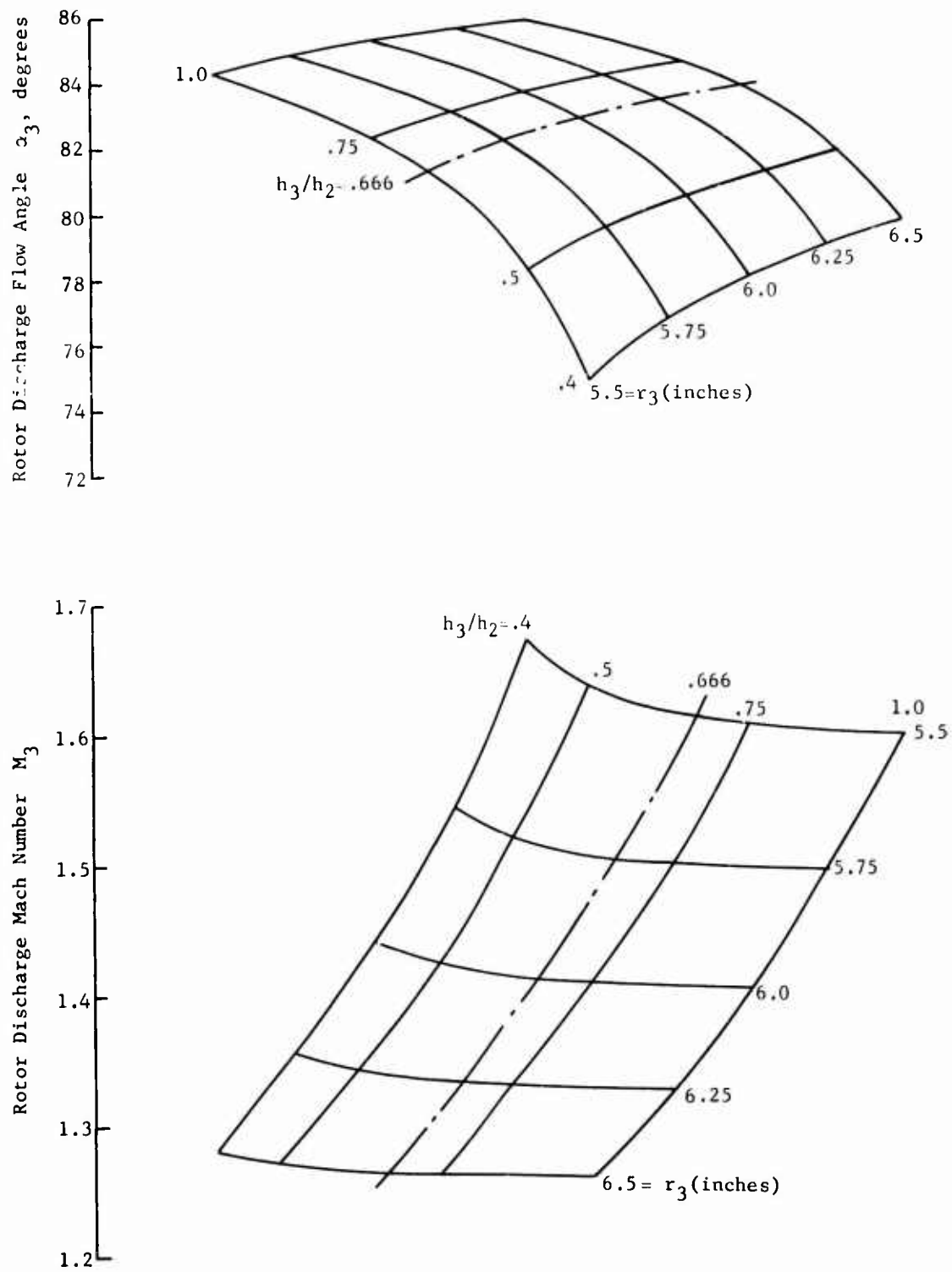


Figure 124. Effect of Vaneless Diffuser Geometry on Rotor Discharge Flow Angle and Mach Number.

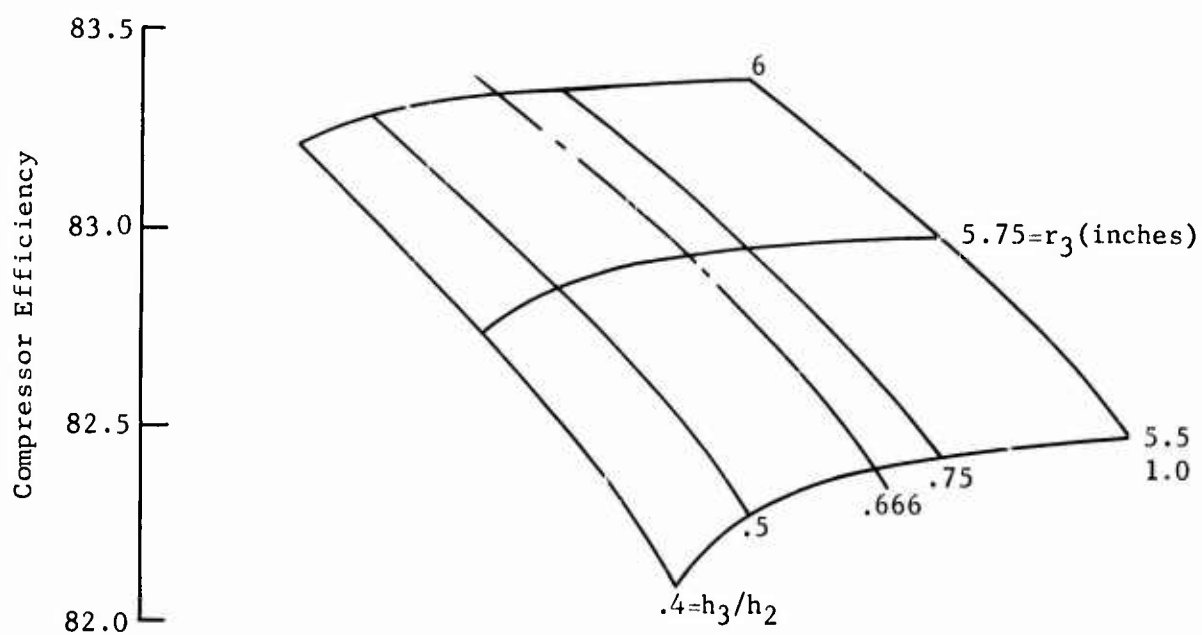
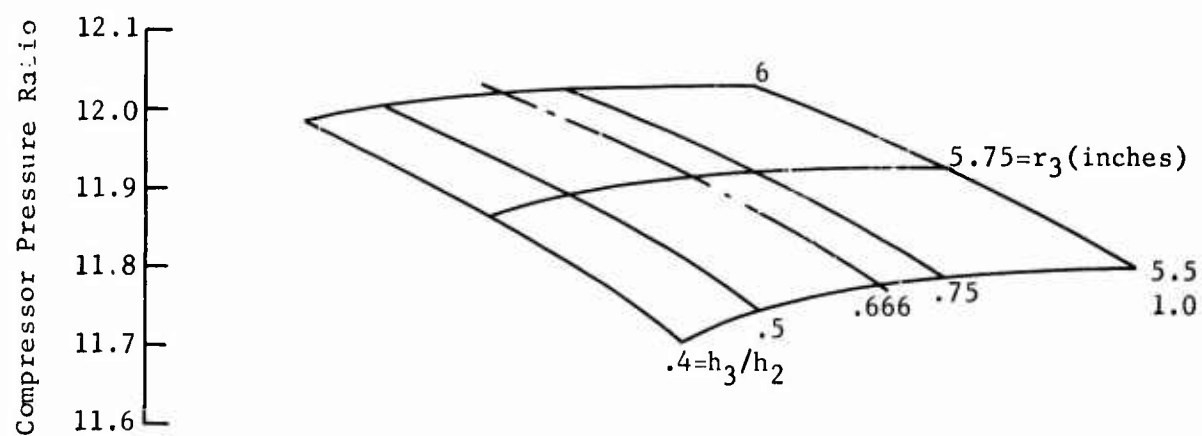


Figure 125. Resultant Effect of Vaneless Diffuser Geometry on Compressor Pressure Ratio and Efficiency.

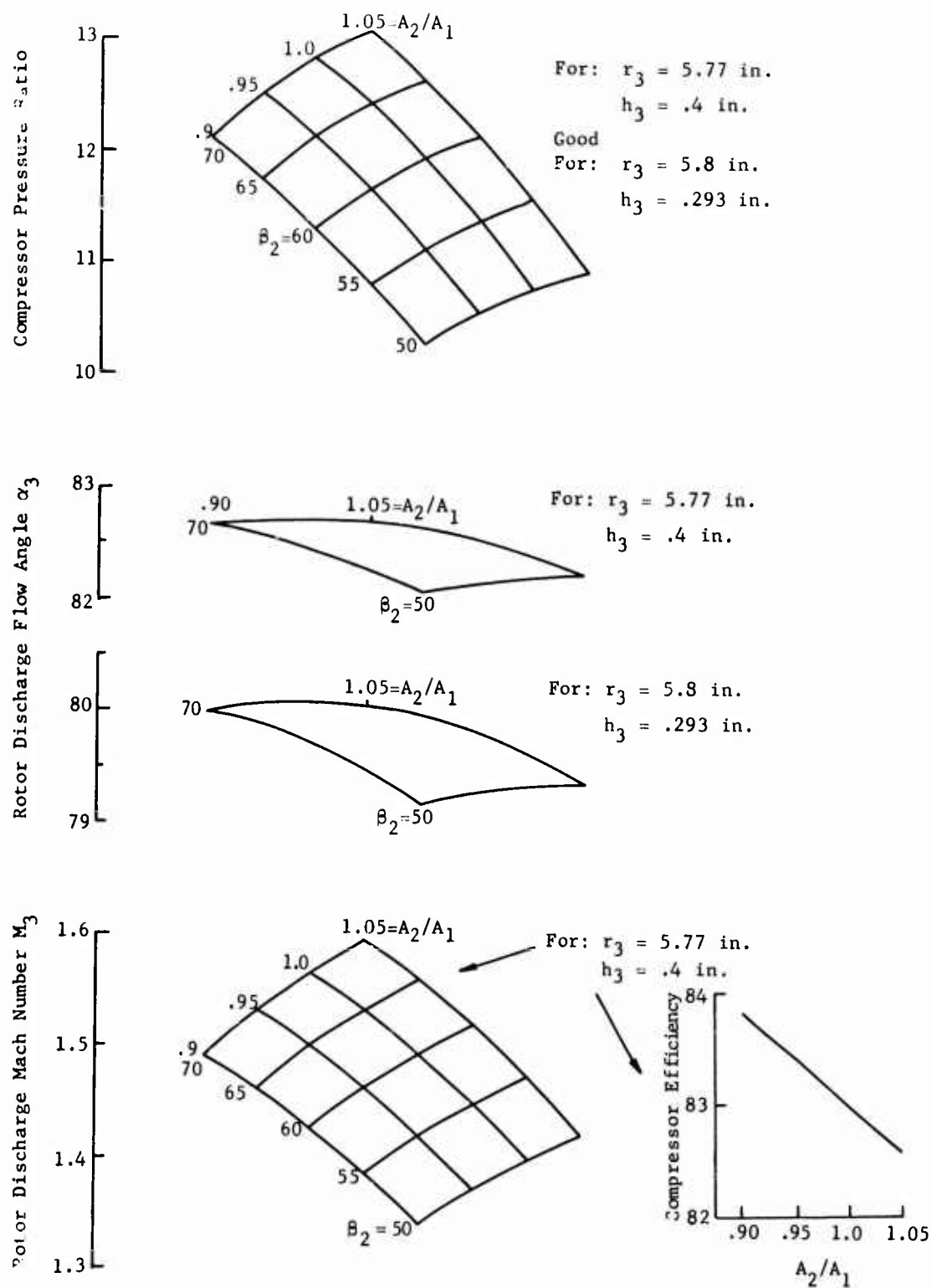


Figure 126. Rotor Discharge Mach Number, Flow Angle, Compressor Pressure Ratio and Efficiency for Two Vaneless Diffuser Configurations with Variations in Rotor Blade Area Ratio and Discharge Flow Angle.

High frequency response pressure measurements within the rotating vaneless diffuser at a rotor blade trailing edge angle of 55 degrees substantiated earlier results showing that the rotor blade wakes are strongly attenuated in passing through the diffuser.

- A survey of the flow in the rotating wall vaneless diffuser indicated no loss in total pressure from near the rotor blade trailing edges to the rotating diffuser exit. This result is very encouraging, since significant losses in this zone have been anticipated and included in all calculations of high-speed compressor performance. Therefore, these calculations may be conservative.

SUPERSONIC AND SUBSONIC STATORS

GENERAL

The purpose of the supersonic and subsonic statots in the radial outflow compressor is to accept the supersonic flow from the rotating vaneless diffuser and to diffuse it efficiently to a low subsonic Mach number (0.4) for entry into the scroll collector. The process of this diffusion is to be as follows: The flow from the rotating vaneless diffuser enters the supersonic statots at a Mach number of 1.6 or lower. In passing through the supersonic statots, the flow experiences a normal shock and subsonic diffusion to a Mach number of about 0.7. A region of essentially constant pressure follows the supersonic statots to permit mixing of the stator wakes before the flow enters the subsonic statots. The subsonic statots are used to reduce the tangential and radial velocity further before the flow enters the scroll collector.

Attempts to develop efficient supersonic statots for axial flow compressors were made at the NACA Langley laboratory from 1942 through 1956. Stator investigations were also carried out at the Lewis laboratory. The general result was that the total pressure recovery in supersonic statots was always less than that obtainable with conical supersonic inlets. At Mach numbers above about 1.4, the recovery of various supersonic statots was not as good as that theoretically obtainable with a normal shock.

Some information on the performance of constant area channels used as supersonic diffusers had appeared in the literature (Reference 26). These diffusers are referred to as "pseudo shock" diffusers and are reported to produce recovery equal to an ideal normal shock, at least at Mach numbers of the order of 3.0. No information had appeared with regard to pseudo shock performance at Mach numbers of less than 2.0. In 1961, the General Electric Company conducted an investigation of high solidity, low camber statots to determine whether high performance could be obtained at Mach numbers of 1.5 or 1.6. Although the flow patterns observed did not correspond to those expected of pseudo shock operation, high static pressure rises were obtained with total pressure losses about equal to normal shock losses for an inlet flow angle (θ) of 57 degrees.

These tests also included the investigation of tandem arrangements of supersonic and subsonic statots tested at supersonic speeds. With the best location of the subsonic statots, results indicated that at Mach numbers slightly in excess of 1.5, a static pressure rise equivalent to 60 percent of the inlet dynamic pressure could be recovered with a total pressure loss of slightly less than 10 percent (Reference 7).

Investigations performed during Phase I of this program were conducted to provide detailed design information for the radial outflow compressor. Even though the design inlet Mach number of the supersonic statots was

near those investigated by General Electric in 1961, similar performance information was required at the significantly higher (80 degrees versus 57 degrees) inlet flow angle. Cascade tests of supersonic stators, subsonic stators, and tandem arrangements of supersonic and subsonic stators were conducted to determine optimum design parameters for the radial outflow compressor design inlet conditions.

DESCRIPTION OF THE TEST ITEM

Initial design of the supersonic and subsonic stators was done by personnel of the Applied Research Operation. The designs were based on the supersonic cascade tests conducted in Evendale during the period 1961 to 1963. The selection of the solidities and area ratios to be investigated was based on the diffuser design rules developed by Professor S. Kline of Stanford University (Reference 27).

The test cascade assembly, Figure 127, was designed to serve as a vehicle for testing supersonic stators as a single cascade, subsonic stators as a single cascade, and a tandem arrangement of supersonic and subsonic stator cascades. Figures 128, 129, and 130 show the test cascade assembly with the supersonic stator vanes in the proper location as required for the first test. Stator vane configurations to be tested are shown in Figures 131, 132, and 133. Stator vane Number 1, shown in Figures 131 and 132, describes the supersonic stators; stator vane Number 2, in Figure 133, describes the subsonic stators.

These vanes are four times the actual size of the stators to be used with the high-speed compressor. The operating pressure in the transonic cascade tunnel is atmospheric compared to about 12 atmospheres in the high-speed radial outflow compressor, resulting in a test Reynolds number that is about one-fourth of the design value. Therefore, similar stator cascades should operate at higher performance levels in the radial outflow compressor since the boundary layer decreases with increasing Reynolds number.

Based on the performance from the first test of the supersonic stator blades, the design was reviewed and compared to previous test configurations investigated during the 1963 tests at Evendale. The decision was made to reduce the supersonic stator design inlet Mach number to less than 1.3 by increasing the rotor exit diameter. The supersonic stator design philosophy that developed from this review is described here and was incorporated in the modified supersonic stator configurations in all the tests that followed.

Supersonic Stator Design Philosophy

The supersonic stator row is the first blade row following the rotor discharge. The primary responsibility of this blade row is to reduce the flow velocities from supersonic to subsonic efficiently, thus increasing the static pressure significantly.

The reduction from supersonic to subsonic velocity is accomplished primarily by means of a normal shock. Because of the flow losses inherently involved in the normal shock process and the adverse effect of a strong normal shock on the boundary layer, a major design criterion is that the normal shock be kept as weak as possible. Normal shocks occurring at Mach numbers greater than about $M = 1.25$ are believed to cause separation of a turbulent boundary layer (Reference 28). Supersonic compression is accomplished by establishing weak oblique shock waves upstream of the stator minimum (throat) area.

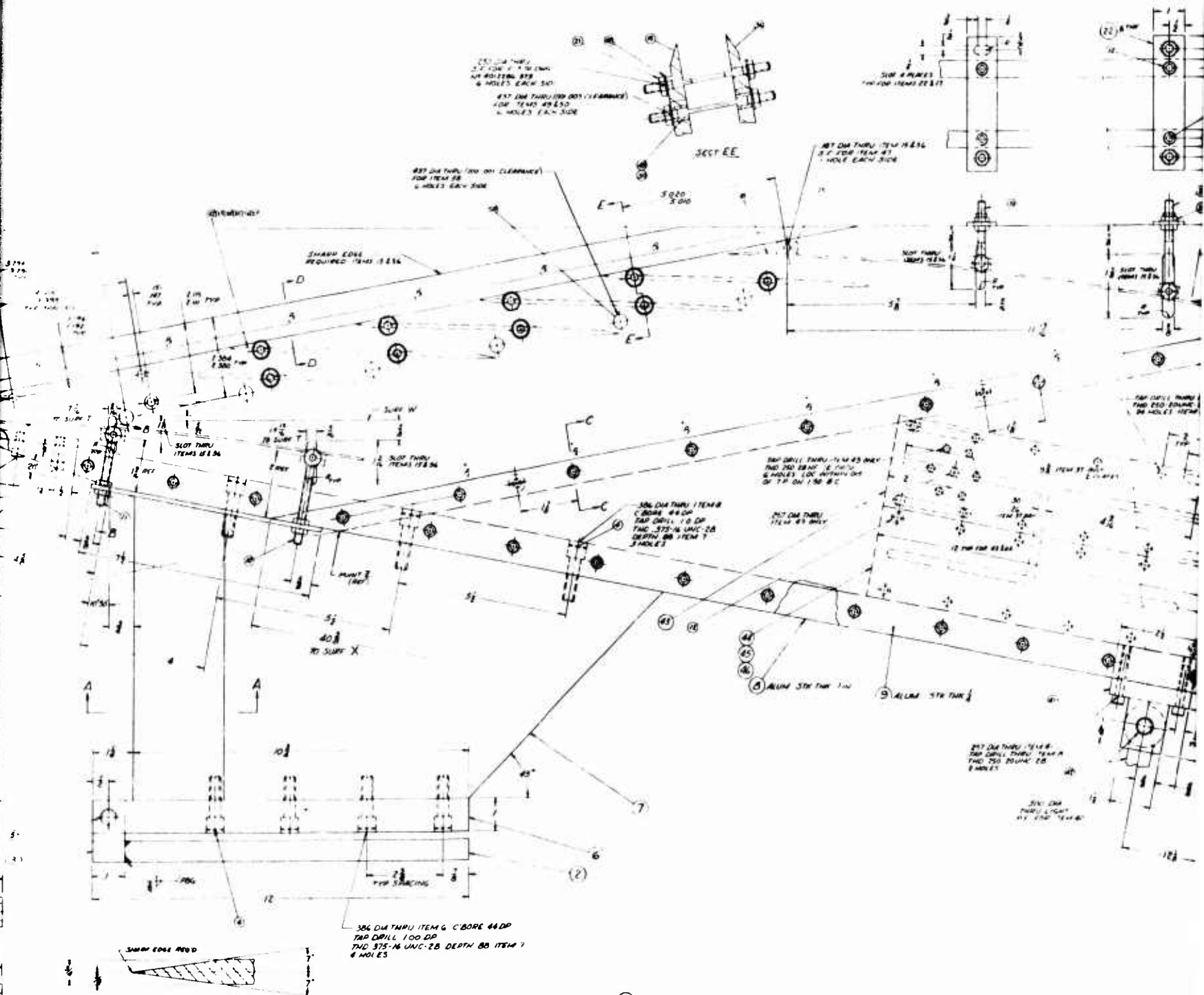
The major stator design parameters are the supersonic starting Mach number; the operating Mach number design; the minimum blade thickness, t ; the pitch, s ; the chord length, l ; the contraction ratio, A_1/A_2 ; and the expansion ratio, A_3/A_2 (see Figure 134a). The minimum thickness is determined from mechanical design factors. The thickness distribution for any given minimum thickness is determined from starting considerations, following the approach presented in Reference 15.

For simplicity, consider a straight blade, as shown in Figure 134a, with an upper surface wedge only. Let the Mach number for starting be known from overall compressor calculations. For a given thickness to pitch ratio, t/s , there is one blade setting angle, τ , for which an attached shock solution will exist. This angle can be determined by considering the shock and expansion processes to be isentropic.

The angle, τ , for which the conditions in region II satisfy continuity is the desired setting angle. With the angle determined, the Mach number in region II is known. Since it is desired that the blade start at the inlet conditions described above, the Mach number in region II is also the Mach number into the leading edge normal shock just before the passage starts. This Mach number determines the theoretical minimum passage area ratio A_1/A_2 , consistent with the ability of the passage to swallow the starting normal shock. This area ratio was divided by 1.05 to account for boundary layer effects. The resulting area ratio A_1/A_2 represents the allowable physical contraction ratio. It was decided that the allowable reduction in area would be accomplished by placing a wedge section on the blade lower surface, reflecting the resulting oblique shock from the adjacent blade and then cancelling the reflection with an expansion corner (see Figure 134b). Supersonic compression is accomplished by the oblique shock generated by the leading edge and the oblique shock reflection from the adjacent blade.

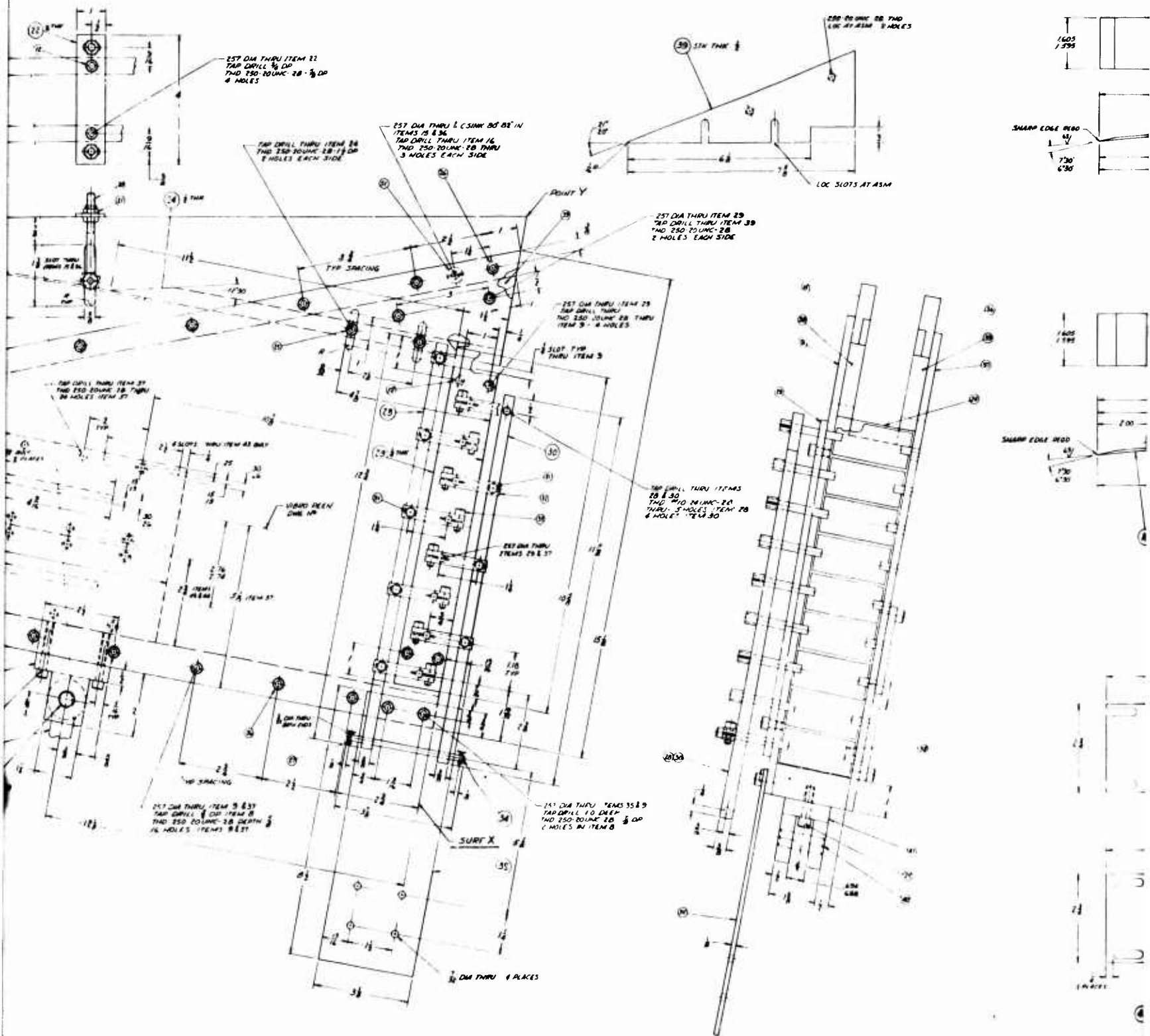
The shock wave pattern shown in Figure 134b is for the starting condition. The strength of the shocks is chosen such that the previously determined physical area ratio will exist in the passage. After point A, the passage is expanded and the normal shock is taken at some point within this expanding region determined by the downstream conditions. It should be noted that the lower surface wedge does not influence the starting criteria previously discussed, since this wedge does not affect the





SECT. 4A

B



C

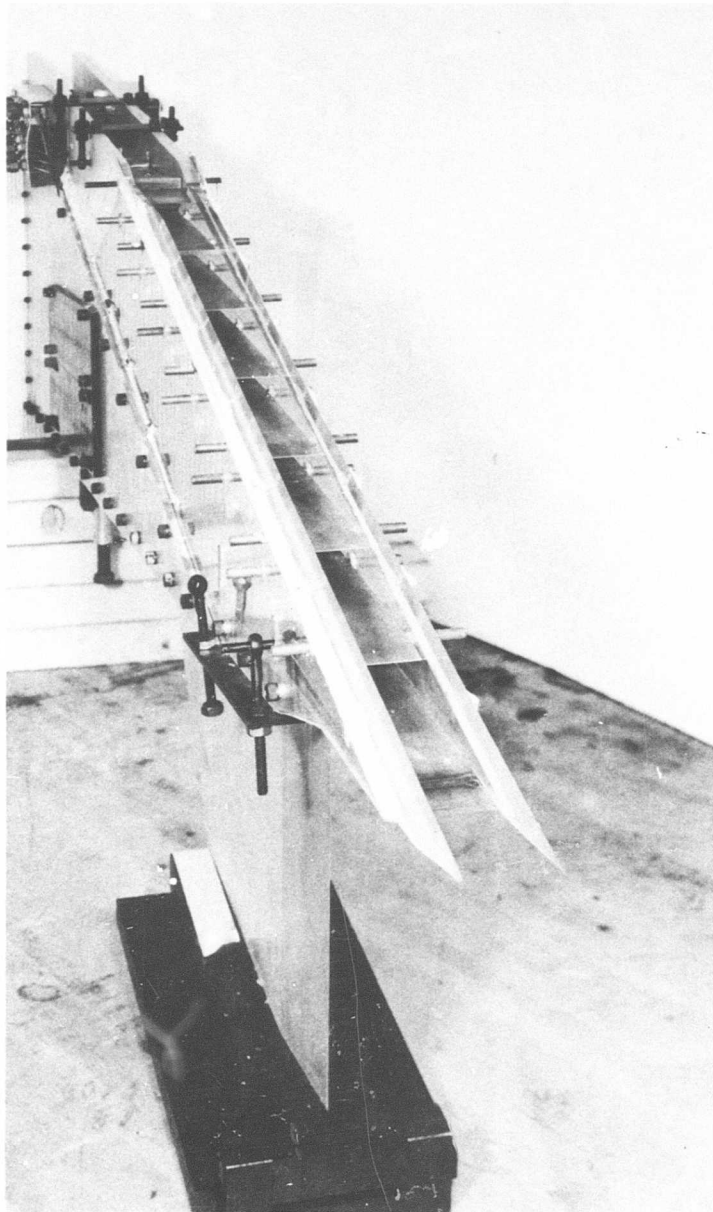


Figure 128. Stator Test Cascade Assembly,
View of Inlet.

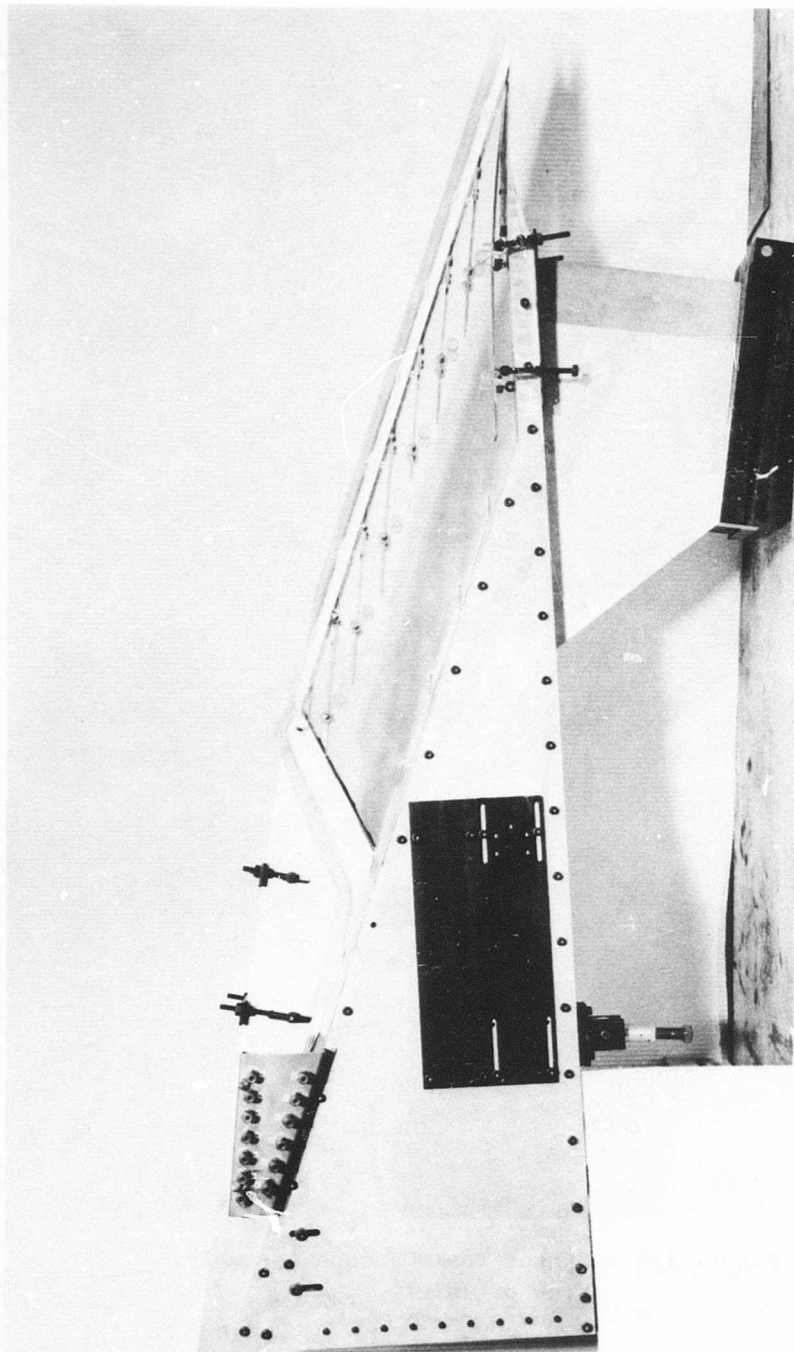


Figure 129. Stator Test Cascade Assembly, Side View Showing Supersonic Stators Installed.

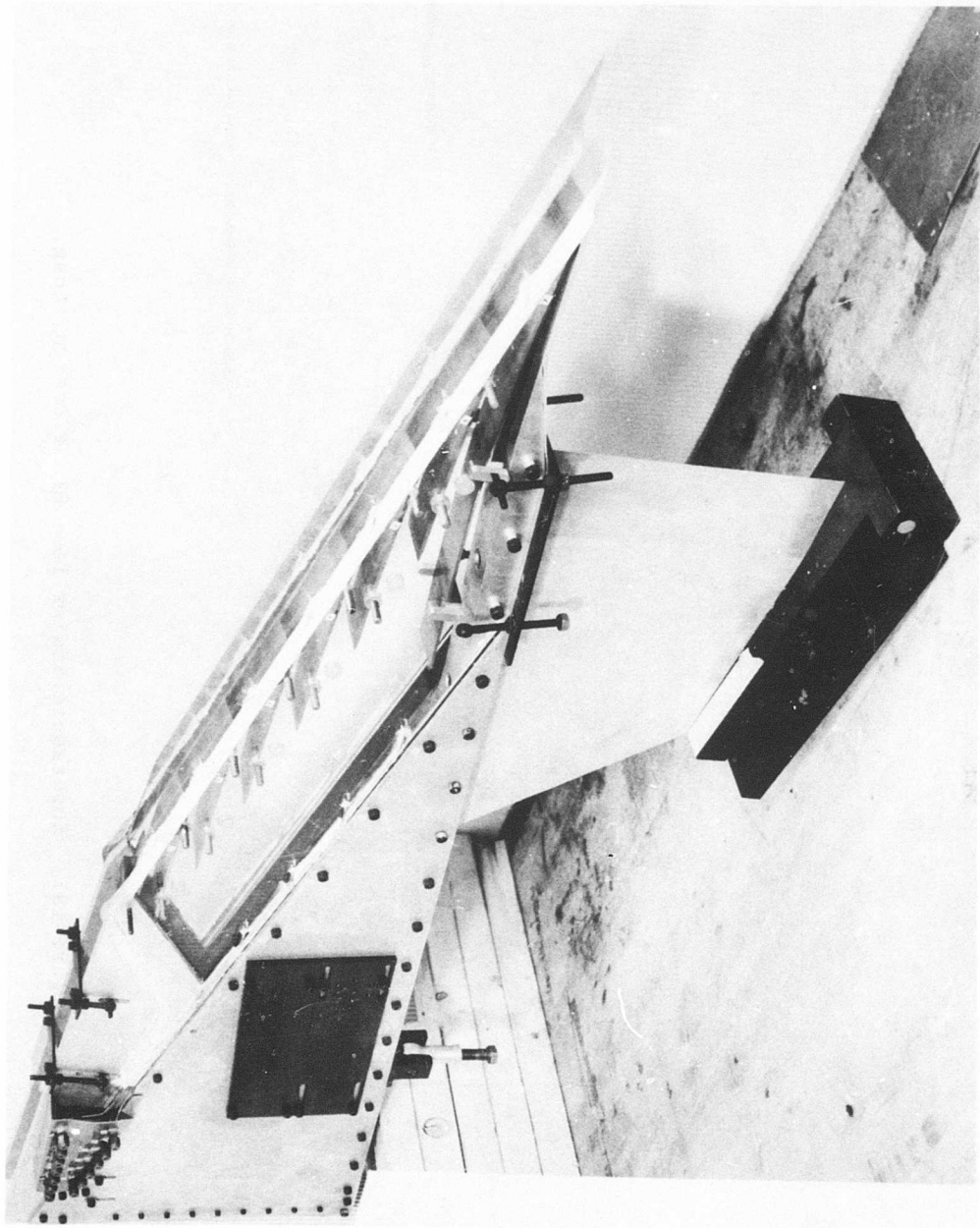


Figure 130. Stator Test Cascade Assembly.

ITEM		DESCRIPTION OR NAME		GROUP NO. & QTY		REVISIONS		DATE	
1	2	3	4	5	6	7	8	9	10
1		BLADE		1					
2		STUD		1					
3									

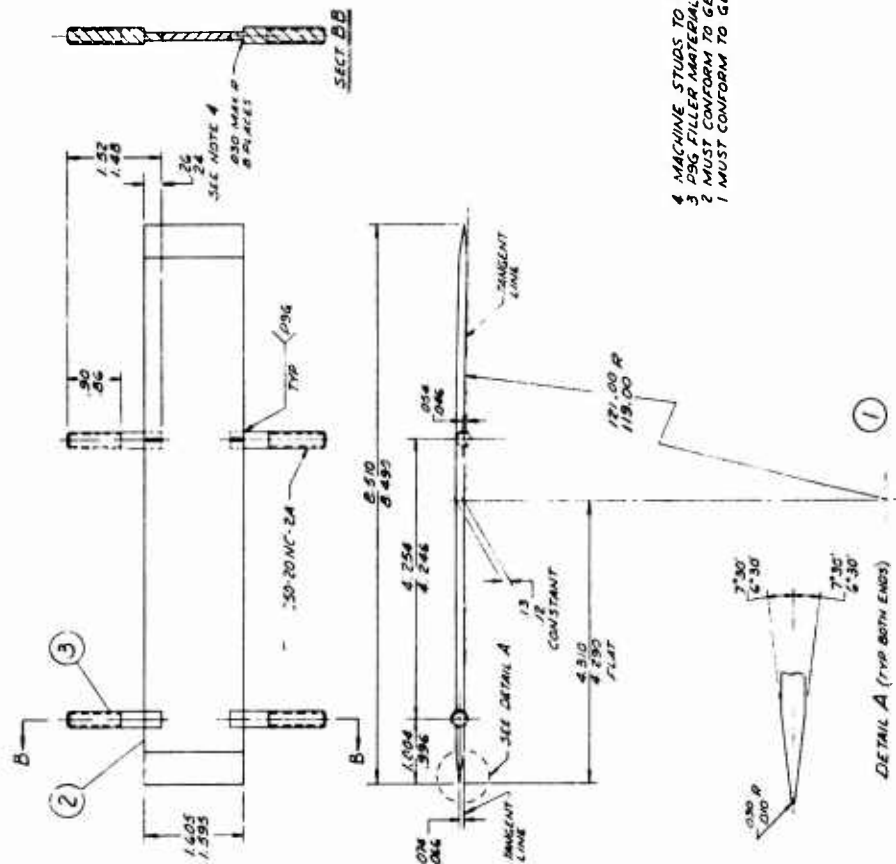


Figure 131. Supersonic Stator Test Blade Design, Long.

PART NO				DESCRIPTION OR NAME		GROUP NO. & QTY				REVISIONS	
ITEM				DESCRIPTION OR NAME		ZONE				SYN. ZONE	
				DESCRIPTION OR NAME							

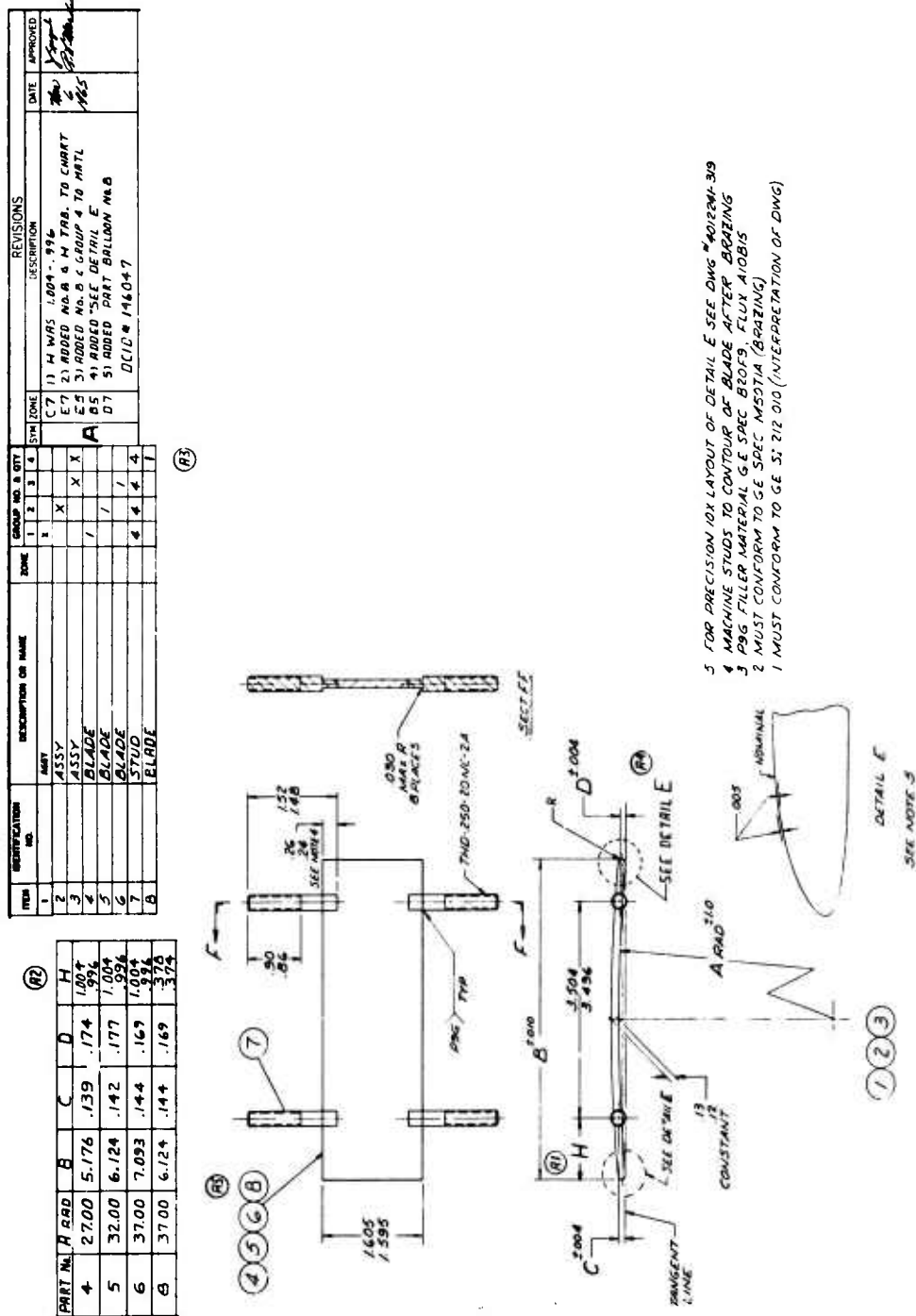


Figure 133. Subsonic Stator Test Blade Design.

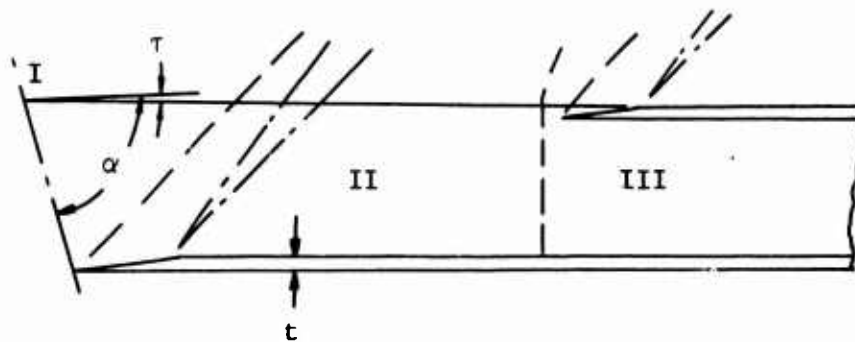


Figure 134a. Straight Stator Blades with Upper Surface Wedge.



Figure 134b. Stator Blade with Upper and Lower Surface Wedges.

average upstream Mach number. It does, however, result in a distribution of the available blade thickness between upper and lower surface, and it reduces the Mach number at which the normal shock will occur.

EXPERIMENTAL PROCEDURE

The test model with the tandem arrangement of supersonic and subsonic stators is shown installed in the Transonic Cascade Tunnel in Figure 135. The Transonic Cascade Tunnel supplies the inlet flow at the desired Mach number. The test model was installed so that the desired inlet angle could be set by means of the variable mounting system. Also in Figure 135, the actuating mechanism to throttle the flow at the discharge of the test model assembly is shown in the lower right-hand corner.

Supersonic Stators

The first series of tests was conducted to identify the best supersonic stator configuration for the radial outflow compressor. The initial three sets of supersonic stator blades are referred to as vane Number 1 in Figures 131 and 132. The characteristics of these blades were as follows:

<u>Blade Dwg. No.</u>	<u>Length-Inches</u>	<u>Solidity</u>	<u>Area Ratio</u>
4012286-373	8.50	2.125	1.15
4012286-374G1	7.62	1.905	1.15
4012286-374G2	6.12	1.530	1.15

The planned procedure was to test each of the above supersonic stator configurations over the Mach number range from 0.7 to 1.5 and an inlet angle variation of 78 to 82 degrees. From these tests, the stator cascade with the optimum solidity would be selected. This configuration would then be used in further tests varying area ratio A_3/A_2 while maintaining solidity constant. The optimum supersonic stator configuration would be identified based on the above performance results.

The medium length blades were used in the first test and showed very poor performance. Vane modifications to reduce the edge wedge angles were necessary before the planned test procedure could begin.

A summary of test runs, which lists the configurations tested and range of inlet Mach number and flow angle investigated, is included in Table VII.

Subsonic Stators

The second series of tests was conducted to identify the best subsonic stator configuration for the radial outflow compressor. The initial three sets of subsonic stator blades were of three different lengths,

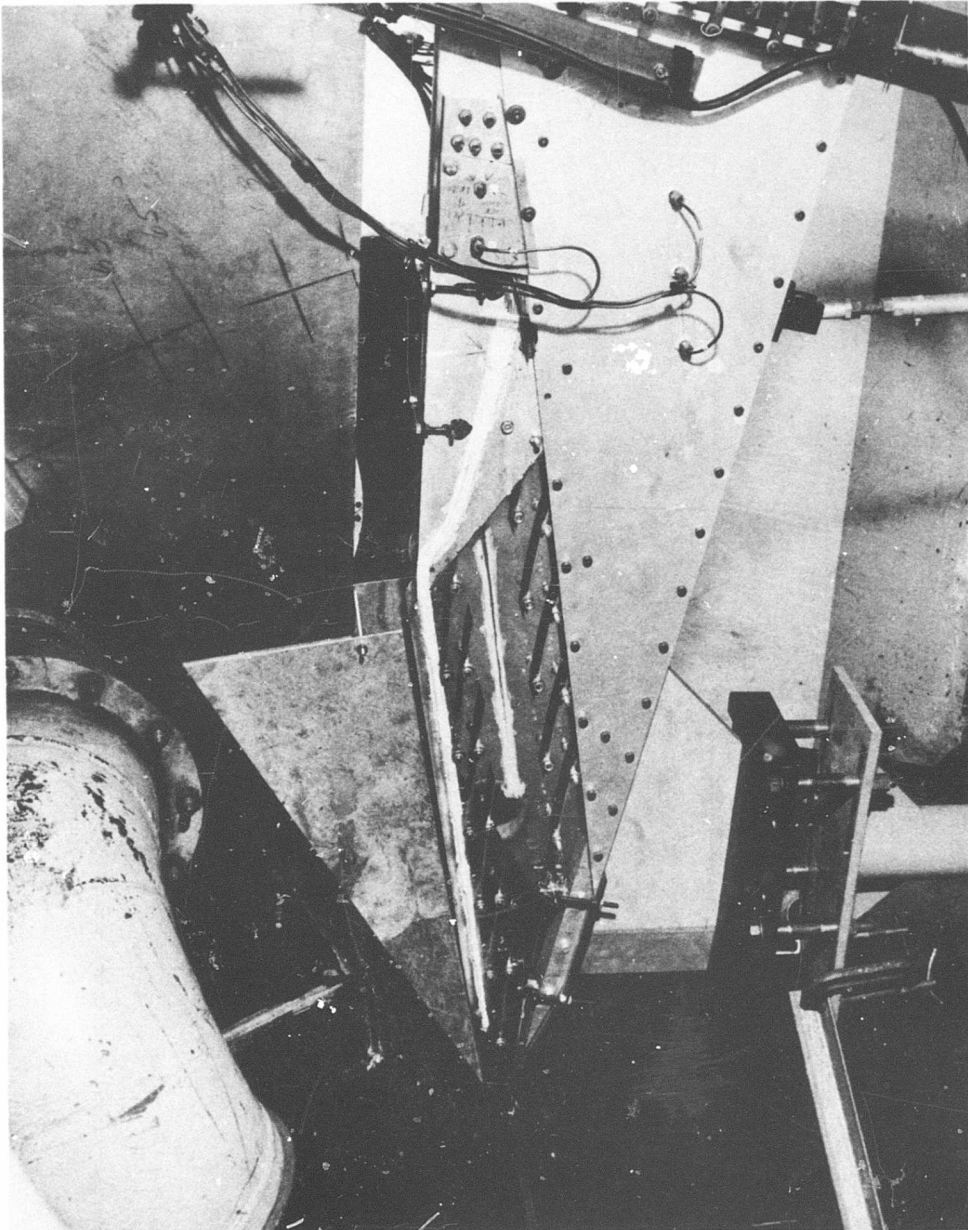


Figure 135. Installation of Stator Test Vehicle in Transonic Cascade Facility.

TABLE VII
SUPERSONIC STATORS TEST RUN SUMMARY

Run No.	Date	Inlet Mach No.	Inlet Flow Angle (degrees)	Length (inches)	Solidity	Contraction Ratio	Area Ratio	Configuration Description
-	11/64	1.3-1.6	78-82	7.62	1.905	1.02	1.15	Medium length, original design, Drawing 4012286-374, failed to start supersonic flow.
1	1/22/65	1.3-1.35	79-81	8.20	2.05	1.02	1.15	Modified long vanes shown in Drawing 4012286-373B.
2	1/23/65	1.35-1.46	80-81	8.20	2.05			Modified long vanes (Drawing 4012286-373B) with No. 2 modification wedge on upper surface 3.3 inches behind leading edge. Resulted in increased contraction ratio.
3	1/25/65	0.8-1.5	79-81	6.08	1.52	1.02	1.10	Modified short vanes as shown in Drawing 4012286-374G2. Tested with drum trailing edge extensions to within 1 inch of model leading edge. This was done for all subsequent runs as well.
4	1/25/65	0.8-1.5	80	7.62	1.905	1.02	1.165	Modified medium vanes as shown in Drawing 4012286-374G1.
5	1/27/65	1.35-1.5	80	7.62	1.905	1.06	1.09	Modified medium recambered - contraction ratio 1.06.
6	1/27/65	0.6-1.5	80	7.62	1.905	1.03	1.10	Modified medium recambered - contraction ratio 1.03.
7	1/28/65	1.1-1.2	80	7.62	1.905	1.02	1.23	Modified medium recambered - contraction ratio 1.02, area ratio 1.23.
8	1/29/65	0.7-1.5	79-82	7.62	1.905	1.02	1.23	Same as run No. 7.
9	1/29/65	0.7-1.4	80	7.62	1.905	1.02	1.28	Modified medium with area ratio of 1.28.

and all had a nominal camber of 11 degrees. Details of these vanes are shown in Figure 133.

Each of the above sets of stators tested over the Mach number range from 0.5 to 0.9 at the design inlet angle of 75 degrees. At the design Mach number of 0.70, all of the sections were tested at inlet angles of 74 and 76.5 degrees. From these tests, the best set of stators (medium length or solidity) was selected for further tests of varying area ratio. The optimum subsonic stator configuration was identified from these tests.

A summary of test runs, listing configurations tested and the range of inlet Mach numbers and flow angles investigated, is included in Table VIII.

Tandem Cascade

The third series of tests was conducted to identify the best relative position of the subsonic stators with respect to the supersonic stators. Three variations of the spacing between bladerows in addition to the nominal value were tested over the Mach number range from 0.6 to 1.4. Table IX gives a summary of the tandem cascade test runs.

The "nominal" or "zero" spacing was identified as 2 inches in the radial direction between the trailing edge of the supersonic stators and the leading edge of the subsonic stators. Spacing in the direction of air-flow was about 8 inches. All other spacings were identified relative to the subsonic stator position at the nominal setting. Thus, the spacing identified as 1.248 indicates that the subsonic stators are positioned 1.248 inches closer to the supersonic stators in the flow direction than nominal.

A number of difficulties were encountered during the first several runs. One had to do with flow in the lower passage of the model. This problem was solved by extending the lower tailboard shown in Figure 127 (position K6 on Drawing 4012286-372). This lower boundary surface was extended rearward until a short overlapping passage was obtained between the tailboard and the lowest subsonic stator blade. The second problem involved locating the total pressure rake downstream of the central subsonic stator blade. The slot through which the probe is positioned had to be extended in the downstream direction. Runs 4 through 8 represent data taken after the "shakedown" problems were solved.

EXPERIMENTAL RESULTS

A tabulation of test results for supersonic stators, subsonic stators, and tandem cascade investigations is included in Tables X, XI and XII, respectively. Numerous schlieren photographs were taken as deemed appropriate throughout these tests. The more significant ones are included in Figures 136 through 147 and are referenced to the test case numbers they represent.

TABLE VIII
SUBSONIC STATORS TEST RUN SUMMARY

Run No.	Date	Inlet Mach No.	Inlet Flow Angle (degrees)	Length (inches)	Solidity	Camber (degrees)	Area Ratio	Configuration Description
10	2/2/65	0.5-0.9	74.3-76.5	6.124	1.53	11	1.23	Medium length subsonic staters.
11	2/3/65	0.5-0.9	74-76.5	5.176	1.29	11	1.15	Short length subsonic staters.
12	2/3/65	0.5-0.9	74-76.5	7.093	1.77	11	1.29	Long subsonic staters.
13	2/4/65	0.5-0.9	74-76.5	6.124	1.53	12.13	1.29	Medium length subsonic staters - modified camber.
14	2/4/65	0.5-0.9	74-76.5	6.124	1.53	7.67	1.16	Medium length subsonic staters - modified camber.

TABLE IX
TANDEM CASCADE TEST RUN SUMMARY

Run No.	Date	Contraction Ratio	Area Ratio	Inlet Angle (degrees)	Inlet Mach No.	Spacing* (inches)	Area Ratio	Configuration Description
1	3/15/65	1.02	1.285	80	0.8-1.4	Nominal	1.254	Subsonic stators at nominal (zero) position.
2	3/17/65	1.02	1.22	80-82	0.5-1.4	Nominal	1.254	Subsonic stators at nominal (zero) position.
3	3/19/65	1.02	1.23	79.75	1.3-1.57	Nominal	1.254	Improved supersonic stator performance by extending lower tailboard into area of subsonic blade leading edge. Bleed holes in lower passage did not help.
4	3/22/65	1.02	1.22	78-82	0.6-1.4	+1.248	1.254	Subsonic stators at +1.248 inches forward from nominal leading edge position; extended lower tailboard.
5	3/23/65	1.02	1.22	79.75	1.2-1.4	+1.248	1.254	Took color schlieren.
6	3/24/65	1.02	1.22	79.75	0.6-1.4	-0.624	1.254	Subsonic -0.624 leading edge.
7	3/25/65	1.02	1.22	79.75	0.6-1.4	Nominal	1.254	Nominal (zero) subsonic.
8	3/26/65	1.02	1.22	79.75	0.6-1.4	+0.624	1.254	Subsonic +0.624 leading edge.

*Spacing tabulated is relative to a nominal or zero position. At nominal position the spacing between the subsonic blade leading edge and the supersonic stator trailing edge is 2 inches in the flow direction.

TABLE X
SUPERSONIC STATOR CASCADE TEST RESULTS

Date	Run No.	Case	Inlet Mach No.	Inlet Angle (degrees)	\bar{C}_P	$\bar{\omega}$	Exit Mach No.
1/22/65	1	22155	1.35	80	0.4066	0.1970	0.7365
1/22/65	1	22156	1.35	80	0.4369	0.1934	0.7034
1/22/65	1	22157	1.35	80	0.4480	0.2128	0.6729
1/22/65	1	22158	1.35	79	0.4009	0.1966	0.7424
1/22/65	1	22159	1.35	85	0.4204	0.1923	0.7234
1/22/65	1	22160	1.28	80	0.3947	0.1808	0.7369
1/23/65	2	22162	1.46	80	0.4812	0.2842	0.5895
1/23/65	2	22163	1.46	80	0.4431	0.2959	0.6302
1/23/65	2	22164	1.46	80	0.4310	0.3005	0.6429
1/23/65	2	22165	1.36	81	0.4716	0.2603	0.6013
1/23/65	2	22166	1.36	81	0.4404	0.2689	0.6333
1/23/65	2	22167	1.36	81	0.3763	0.2803	0.7049
1/23/65	2	22168	1.35	81	0.4927	0.2509	0.5819
1/23/65	2	22169	1.35	81	0.4540	0.2474	0.6355
1/25/65	3	22170	1.35	80	0.4065	0.1458	0.7775
1/25/65	3	22171	1.35	80	0.3700	0.1485	0.8157
1/25/65	3	22172	1.35	80	0.3998	0.1460	0.7839
1/25/65	3	22173	1.35	80	0.3450	0.1440	0.8470
1/25/65	3	22174	1.35	79	0.4052	0.1472	0.7766
1/25/65	3	22175	1.35	79	0.3587	0.1543	0.8237
1/25/65	3	22176	1.35	81	0.3880	0.1514	0.7927
1/25/65	3	22177	1.35	81	0.4185	0.1478	0.7608
1/25/65	3	22178	1.30	80	0.3734	0.1529	0.7894
1/25/65	3	22179	1.30	80	0.4014	0.1487	0.7617
1/25/65	3	22180	1.30	80	0.3421	0.1556	0.8217
1/25/65	3	22181	1.30	79	0.3897	0.1486	0.7748
1/25/65	3	22182	1.30	79	0.3722	0.1510	0.7921
1/25/65	3	22183	1.30	79	0.3587	0.1528	0.8053
1/25/65	3	22184	1.30	81	0.3479	0.1504	0.8185
1/25/65	3	22185	1.30	81	0.3906	0.1495	0.7726
1/25/65	3	22186	1.30	81	0.4159	0.1496	0.7449
1/25/65	3	22187	1.40	80	0.3879	0.1568	0.8097
1/25/65	3	22188	1.40	80	0.4126	0.1606	0.7776
1/25/65	3	22190	1.40	80	0.4296	0.1632	0.7552
1/25/65	3	22191	1.45	80	0.3728	0.1490	0.8537
1/25/65	3	22192	1.45	80	0.4013	0.1729	0.7999
1/25/65	3	22193	1.50	80	0.3387	0.1746	0.8979
1/25/65	3	22194	1.50	80	0.3934	0.2463	0.7645
1/25/65	3	22195	1.25	80	0.3607	0.1413	0.7884
1/25/65	3	22196	1.20	80	0.4024	0.1460	0.7182
1/25/65	3	22197	1.10	80	0.4169	0.1087	0.6841
1/25/65	3	22198	1.00	80	0.4237	0.0921	0.6385

Table X, Continued

Date	Run No.	Case	Inlet Mach No.	Inlet Angle (degrees)	\bar{C}_P	\bar{w}	Exit Mach No.
1/25/65	3	22199	0.90	80	0.4235	0.0864	0.5870
1/25/65	3	22200	0.80	80	0.4214	0.0784	0.5377
1/25/65	3	22201	0.80	80	0.3915	0.0773	0.5564
1/25/65	3	22202	1.40	80	0.3940	0.2255	0.7476
1/25/65	3	22203	1.40	80	0.3941	0.1964	0.7719
1/25/65	3	22204	1.40	80	0.3949	0.1644	0.7967
1/25/65	3	22205	1.40	80	0.3963	0.1506	0.8055
1/25/65	3	22206	1.40	80	0.3957	0.1510	0.8058
1/25/65	3	22207	1.40	80	0.3953	0.1530	0.8048
1/25/65	3	22208	1.40	80	0.3951	0.1540	0.8043
1/25/65	3	22209	1.40	80	0.3950	0.1544	0.8038
1/25/65	3	22210	1.40	80	0.3946	0.1547	0.8041
1/25/65	3	22211	1.40	80	0.3936	0.1590	0.8020
1/25/65	3	22212	1.40	80	0.3934	0.1765	0.7881
1/25/65	3	22213	1.40	80	0.3935	0.1927	0.7749
1/25/65	4	22215	1.33	80	0.4248	0.1601	0.7395
1/25/65	4	22216	1.40	80	0.3710	0.1742	0.8151
1/25/65	4	22217	1.40	80	0.4399	0.1802	0.7278
1/25/65	4	22218	1.39	80	0.2747	0.1900	0.9182
1/25/65	4	22219	1.39	80	0.3922	0.1585	0.8000
1/25/65	4	22220	1.39	80	0.4175	0.1539	0.7739
1/25/65	4	22221	1.39	80	0.4479	0.1645	0.7292
1/25/65	4	22222	1.40	80	0.4623	0.1757	0.7044
1/25/65	4	22223	1.46	80	0.4333	0.1603	0.7725
1/25/65	4	22224	1.46	80	0.4527	0.1787	0.7327
1/25/65	4	22225	1.46	80	0.4621	0.1904	0.7102
1/25/65	4	22226	1.29	80	0.3915	0.1402	0.7717
1/25/65	4	22227	1.29	80	0.4260	0.1400	0.7353
1/25/65	4	22228	1.29	80	0.4456	0.1449	0.7104
1/25/65	4	22229	1.51	80	0.4158	0.1968	0.7820
1/25/65	4	22230	1.51	80	0.4301	0.2259	0.7365
1/25/65	4	22231	1.39	80	0.4198	0.2009	0.7305
1/25/65	4	22232	1.39	80	0.4195	0.1830	0.7461
1/25/65	4	22233	1.39	80	0.4201	0.1659	0.7594
1/25/65	4	22234	1.39	80	0.4197	0.1583	0.7660
1/25/65	4	22235	1.39	80	0.4194	0.1562	0.7679
1/25/65	4	22236	1.39	80	0.4188	0.1545	0.7699
1/25/65	4	22237	1.39	80	0.4182	0.1552	0.7701
1/25/65	4	22238	1.39	80	0.4196	0.1559	0.7679
1/25/65	4	22239	1.39	80	0.4188	0.1581	0.7669
1/25/65	4	22240	1.39	80	0.4195	0.1641	0.7612
1/25/65	4	22241	1.38	80	0.4201	0.1771	0.7499
1/25/65	4	22242	1.38	80	0.4191	0.1927	0.7382
1/25/65	4	22243	1.19	80	0.4363	0.1340	0.6889
1/25/65	4	22244	1.09	80	0.4433	0.1059	0.6559
1/25/65	4	22245	0.99	80	0.4496	0.0832	0.6161

Table X, Continued

Date	Run No.	Case	Inlet Mach No.	Inlet Angle (degrees)	\bar{C}_P	\bar{w}	Exit Mach No.
1/25/65	4	22246	0.90	80	0.4509	0.0215	0.5695
1/25/65	4	22247	0.79	80	0.4522	0.0709	0.5130
1/27/65	5*	22249	1.50	80	0.346	0.185	-
1/27/65	5	22251	1.50	80	0.374	0.195	-
1/27/65	5	22252	1.40	80	0.421	0.1725	-
1/28/65	6*	22253	1.46	80	0.366	0.185	-
1/28/65	6	22254	1.46	80	0.439	0.189	-
1/28/65	6	22255	1.52	80	0.3815	0.2195	-
1/28/65	6	22256	1.52	80	0.405	0.227	-
1/28/65	6	22257	1.30	80	0.426	0.146	-
1/28/65	6	22266	1.30	80	0.428	0.146	-
1/28/65	6	22267	1.30	80	0.381	0.142	-
1/28/65	6	22268	1.20	80	0.385	0.119	-
1/28/65	6	22269	1.10	80	0.387	0.110	-
1/28/65	6	22270	1.00	80	0.393	0.1037	-
1/28/65	6	22271	0.90	80	0.39	0.098	-
1/28/65	6	22272	0.80	80	0.39	0.0874	-
1/28/65	6	22273	0.70	80	0.394	0.0844	-
1/28/65	6	22274	0.60	80	0.401	0.0838	-
1/28/65	6	22275	0.60	80	0.488	0.0918	-
1/28/65	6	22276	0.60	80	0.548	0.115	-
1/28/65	7	22277	1.22	80	0.2566	0.2066	0.8366
1/28/65	7	22278	1.22	80	0.4541	0.1456	0.6733
1/28/65	7	22280	1.21	80	0.4998	0.1388	0.6305
1/28/65	7	22281	1.11	80	0.2842	0.1637	0.7692
1/28/65	7	22282	1.11	80	0.5193	0.1149	0.5880
1/28/65	7	22283	1.11	80	0.5641	0.1287	0.5343
1/29/65	8	22285	1.33	80	0.3356	0.1836	0.8210
1/29/65	8	22286	1.33	80	0.4301	0.1511	0.7389
1/29/65	8	22287	1.33	80	0.4535	0.1532	0.7108
1/29/65	8	22288	1.41	80	0.3869	0.1684	0.8057
1/29/65	8	22289	1.41	80	0.3869	0.1684	0.8057
1/29/65	8	22290	1.41	80	0.4739	0.1640	0.7048
1/29/65	8	22291	1.41	80	0.4384	0.1449	0.7630
1/29/65	8	22292	1.50	80	0.3686	0.1840	0.8495
1/29/65	8	22293	1.50	80	0.4124	0.1812	0.7951
1/29/65	8	22294	1.40	82	0.4216	0.1560	0.7718
1/29/65	8	22295	1.40	82	0.4814	0.1834	0.6765
1/29/65	8	22296	1.40	79	0.3437	0.0821	0.9149
1/29/65	8	22297	1.40	79	0.4592	0.2152	0.6743
1/29/65	8	22298	1.40	79	0.4031	0.1551	0.7933
1/29/65	8	22299	1.40	79	0.4428	0.1475	0.7524

*Data from runs 5 and 6 were not reduced by computer program. Hand calculated values are included to indicate performance trends.

Table X, Continued

Date	Run No.	Case	Inlet Mach No.	Inlet Angle (degrees)	\bar{C}_P	$\bar{\omega}$	Exit Mach No.
1/29/65	8	22300	1.21	80	0.5147	0.1364	0.6134
1/29/65	8	22301	1.20	80	0.5600	0.1534	0.5507
1/29/65	8	22302	1.00	80	0.5349	0.1049	0.5394
1/29/65	8	22303	0.90	80	0.5379	0.0974	0.4992
1/29/65	8	22304	0.80	80	0.5340	0.0837	0.4632
1/29/65	8	22305	0.70	80	0.5417	0.0779	0.4102
1/29/65	9	22307	0.69	80	0.4717	0.0808	0.4429
1/29/65	9	22308	0.69	80	0.5481	0.0830	0.3989
1/29/65	9	22309	0.69	80	0.5786	0.0949	0.3744
1/29/65	9	22310	0.80	80	0.5286	0.0889	0.4618
1/29/65	9	22311	0.89	80	0.5373	0.0989	0.4908
1/29/65	9	22312	0.89	80	0.5578	0.1020	0.4731
1/29/65	9	22313	1.01	80	0.5462	0.1157	0.5258
1/29/65	9	22314	1.01	80	0.4938	0.1070	0.5765
1/29/65	9	22315	1.13	80	0.4824	0.1047	0.6406
1/29/65	9	22316	1.13	80	0.5303	0.1108	0.5906
1/29/65	9	22317	1.13	80	0.5616	0.1263	0.5476
1/29/65	9	22318	1.20	80	0.5014	0.1271	0.6325
1/29/65	9	22319	1.20	80	0.5313	0.1466	0.5857
1/29/65	9	22320	1.40	80	0.4073	0.1885	0.7617
1/29/65	9	22321	1.40	80	0.4367	0.1947	0.7205

TABLE XI
SUBSONIC STATOR CASCADE TEST RESULTS

Date	Run No.	Case	Inlet Mach No.	Inlet Angle (degrees)	\bar{C}_P	\bar{w}	Exit Mach No.
2/2/65	10	22323*	0.49	75	0.571	0.0607	-
2/2/65	10	22324*	0.49	75	0.403	0.0984	-
2/2/65	10	22325*	0.49	75	0.605	0.0588	-
2/2/65	10	22326*	0.49	75	0.635	0.0521	-
2/2/65	10	22327	0.60	75	0.6332	0.0656	0.3118
2/2/65	10	22328	0.60	75	0.5828	0.0729	0.3345
2/2/65	10	22329	0.60	75	0.5382	0.0799	0.3535
2/2/65	10	22330	0.60	75	0.6539	0.0672	0.2998
2/2/65	10	22331	0.70	75	0.6518	0.0661	0.3471
2/2/65	10	22332	0.70	75	0.5699	0.0806	0.3897
2/2/65	10	22333	0.70	75	0.5011	0.1096	0.4147
2/2/65	10	22334	0.70	76.5	0.5901	0.0735	0.3814
2/2/65	10	22335	0.70	76.5	0.6415	0.0671	0.3529
2/2/65	10	22336	0.70	76.5	0.4989	0.1134	0.4131
2/2/65	10	22337	0.69	74.3	0.5025	0.1041	0.4149
2/2/65	10	22338	0.69	74.3	0.5902	0.0735	0.3795
2/2/65	10	22339	0.69	74.3	0.6575	0.0626	0.3437
2/2/65	10	22340	0.79	75	0.5649	0.0938	0.4298
2/2/65	10	22341	0.79	75	0.6343	0.0650	0.3985
2/2/65	10	22342	0.79	75	0.6440	0.0655	0.3908
2/2/65	10	22343	0.79	75	0.4939	0.1242	0.4582
2/2/65	10	22344	0.92	75	0.5929	0.1131	0.4492
2/2/65	10	22345	0.92	75	0.6263	0.1088	0.4246
2/2/65	10	22346*	0.90	75	0.629	0.0896	-
2/3/65	11	22347	0.50	75	0.6449	0.0753	0.2575
2/3/65	11	22348	0.50	75	0.6565	0.0715	0.2528
2/3/65	11	22349	0.50	75	0.5379	0.0834	0.2999
2/3/65	11	22350	0.50	75	0.4738	0.1037	0.3181
2/3/65	11	22351	0.60	75	0.4779	0.1213	0.3668
2/3/65	11	22352	0.60	75	0.5581	0.0943	0.3392
2/3/65	11	22353	0.60	75	0.6551	0.0716	0.2983
2/3/65	11	22354	0.70	75	0.5126	0.1190	0.4041
2/3/65	11	22355	0.70	75	0.5772	0.0971	0.3786
2/3/65	11	22356	0.70	75	0.6463	0.0741	0.3465
2/3/65	11	22357	0.70	74	0.5103	0.1162	0.4070
2/3/65	11	22358	0.70	74	0.5764	0.0987	0.3766
2/3/65	11	22359	0.70	74	0.6590	0.0696	0.3409
2/3/65	11	22360	0.70	76.5	0.5124	0.1195	0.4040

*These data points were not reduced by computer program. Hand calculated values are included to indicate performance trends.

Table XI, Continued

Date	Run No.	Case	Inlet Mach No.	Inlet Angle (degrees)	\bar{C}_P	$\bar{\omega}$	Exit Mach No.
2/3/65	11	22361	0.70	76.5	0.5800	0.0980	0.3748
2/3/65	11	22362	0.70	76.5	0.6311	0.0788	0.3537
2/3/65	11	22363	0.80	75	0.5005	0.1514	0.4439
2/3/65	11	22364	0.80	75	0.5493	0.1182	0.4305
2/3/65	11	22365	0.80	75	0.5932	0.1018	0.4095
2/3/65	11	22366	0.80	75	0.6342	0.0829	0.3918
2/3/65	11	22367	0.90	75	0.5017	0.1505	0.4910
2/3/65	11	22368	0.90	75	0.5516	0.1351	0.4616
2/3/65	11	22369	0.90	75	0.5954	0.1193	0.4370
2/3/65	11	22370	0.90	75	0.6291	0.1016	0.4218
2/3/65	11	22371	0.70	75	0.6424	0.0746	0.3503
2/3/65	12	22372	0.49	75	0.5155	0.1140	0.2918
2/3/65	12	22373	0.49	75	0.5761	0.0843	0.2791
2/3/65	12	22374	0.49	75	0.6311	0.0681	0.2620
2/3/65	12	22375	0.49	75	0.6607	0.0736	0.2460
2/3/65	12	22376	0.59	75	0.5203	0.1157	0.3459
2/3/65	12	22377	0.59	75	0.5667	0.0926	0.3329
2/3/65	12	22378	0.59	75	0.6095	0.0744	0.3194
2/3/65	12	22379	0.59	75	0.6531	0.0703	0.2977
2/3/65	12	22380	0.59	75	0.6615	0.0740	0.2909
2/3/65	12	22381	0.69	75	0.4953	0.1300	0.4050
2/3/65	12	22382	0.69	75	0.5889	0.0831	0.3745
2/3/65	12	22383	0.69	75	0.6506	0.0808	0.3370
2/3/65	12	22384	0.69	74	0.5005	0.1271	0.4034
2/3/65	12	22385	0.69	74	0.5917	0.0809	0.3740
2/3/65	12	22386	0.69	74	0.6576	0.0764	0.3347
2/3/65	12	22387	0.69	76.5	0.5038	0.1301	0.3995
2/3/65	12	22388	0.69	76.5	0.5890	0.0832	0.3740
2/3/65	12	22389	0.69	76.5	0.6377	0.0933	0.3374
2/3/65	12	22390	0.80	75	0.5096	0.1124	0.4590
2/3/65	12	22391	0.80	75	0.5723	0.0932	0.4276
2/3/65	12	22392	0.80	75	0.6312	0.0834	0.3918
2/3/65	12	22393	0.91	75	0.4960	0.1259	0.5152
2/3/65	12	22394	0.91	75	0.5464	0.1059	0.4892
2/3/65	12	22395	0.91	75	0.5953	0.0843	0.4650
2/4/65	13	22397	0.50	75	0.5271	0.1041	0.2976
2/4/65	13	22398	0.50	75	0.5650	0.0865	0.2886
2/4/65	13	22399	0.50	75	0.6124	0.0709	0.2742
2/4/65	13	22400	0.50	75	0.6124	0.0709	0.2742
2/4/65	13	22401	0.60	75	0.5057	0.0551	0.3829
2/4/65	13	22402	0.60	75	0.5569	0.1034	0.3361
2/4/65	13	22403	0.60	75	0.6044	0.0813	0.3220
2/4/65	13	22404	0.60	75	0.6388	0.0707	0.3087
2/4/65	13	22405	0.60	75	0.6592	0.0694	0.2975
2/4/65	13	22406	0.70	75	0.5286	0.1219	0.3947
2/4/65	13	22407	0.70	75	0.5637	0.1092	0.3802
2/4/65	13	22408	0.70	75	0.6270	0.0849	0.3541

Table XI, Continued

Date	Run No.	Case	Inlet Mach No.	Inlet Angle (degrees)	\bar{C}_P	$\bar{\omega}$	Exit Mach No.
2/4/65	13	22409	0.70	75	0.6517	0.0766	0.3429
2/4/65	13	22410	0.70	74	0.5412	0.1143	0.3910
2/4/65	13	22411	0.70	74	0.5788	0.0990	0.3765
2/4/65	13	22412	0.70	74	0.6262	0.0810	0.3569
2/4/65	13	22413	0.70	74	0.6480	0.0716	0.3484
2/4/65	13	22414	0.70	76.5	0.5367	0.1251	0.3880
2/4/65	13	22415	0.70	76.5	0.5840	0.1072	0.3686
2/4/65	13	22416	0.70	76.5	0.6251	0.0915	0.3513
2/4/65	13	22417	0.80	75	0.5341	0.1173	0.4413
2/4/65	13	22418	0.80	75	0.5910	0.1089	0.4060
2/4/65	13	22419	0.80	75	0.6242	0.0988	0.3881
2/4/65	13	22420	0.90	75	0.5176	0.1262	0.4936
2/4/65	13	22421	0.90	75	0.5761	0.1157	0.4545
2/4/65	13	22422	0.90	75	0.6101	0.1145	0.4273
2/4/65	14	22423	0.70	75	0.5499	0.1238	0.3776
2/4/65	14	22424	0.70	75	0.6152	0.1061	0.3459
2/4/65	14	22425	0.70	75	0.6271	0.1048	0.3387
2/4/65	14	22426	0.70	75	0.5245	0.1360	0.3857
2/4/65	14	22427	0.70	74	0.5276	0.1309	0.3866
2/4/65	14	22428	0.70	74	0.5800	0.1085	0.3669
2/4/65	14	22429	0.70	74	0.6191	0.1020	0.3455
2/4/65	14	22430	0.69	74	0.6315	0.1002	0.3379
2/4/65	14	22431	0.69	76.5	0.5536	0.1326	0.3687
2/4/65	14	22432	0.69	76.5	0.5930	0.1191	0.3516
2/4/65	14	22433	0.69	76.5	0.6047	0.1176	0.3447
2/4/65	14	22434	0.81	75	0.5036	0.1320	0.4561
2/4/65	14	22435	0.81	75	0.5812	0.1287	0.4028
2/4/65	14	22436	0.81	75	0.6038	0.1248	0.3881
2/4/65	14	22437	0.90	75	0.5343	0.1308	0.4793
2/4/65	14	22438	0.90	75	0.5938	0.1207	0.4381
2/4/65	14	22439	0.90	75	0.6039	0.1193	0.4305
2/4/65	14	22440	0.61	75	0.5443	0.1165	0.3402
2/4/65	14	22441	0.61	75	0.5920	0.1095	0.3179
2/4/65	14	22442	0.61	75	0.6311	0.1030	0.2992
2/4/65	14	22443	0.50	75	0.5247	0.1112	0.2966
2/4/65	14	22444	0.50	75	0.6180	0.1011	0.2582
2/4/65	14	22445	0.50	75	0.6332	0.0986	0.2521

TABLE XII
TANDEM CASCADE TEST RESULTS

Date	Run No.	Case	Inlet Mach No.	Inlet Angle (degrees)	\bar{C}_P	\bar{w}	Exit Mach No.
3/15/65	1	22741	0.80	80	0.5942	0.2609	0.2844
3/15/65	1	22742	1.00	80	0.5010	0.3104	0.4003
3/15/65	1	22743	1.00	80	0.6701	0.2525	0.2470
3/15/65	1	22744	1.11	80	0.5042	0.3312	0.4064
3/15/65	1	22745	1.11	80	0.5616	0.3047	0.3604
3/15/65	1	22746	1.11	80	0.6440	0.2756	0.2736
3/15/65	1	22747	1.21	80	0.5097	0.3636	0.3824
3/15/65	1	22748	1.21	80	0.6106	0.3164	0.2811
3/15/65	1	22749	1.30	80	0.5150	0.3806	0.3659
3/15/65	1	22750	1.30	80	0.5886	0.3465	0.2811
3/15/65	1	22751	1.40	80	0.4527	0.4322	0.4161
3/15/65	1	22752	1.40	80	0.5665	0.3795	0.2719
3/15/65	1	22753	1.40	80	0.5126	0.4022	0.3490
3/17/65	2	22755*	0.50	80	0.483	0.217	-
3/17/65	2	22756	0.52	80	0.5971	0.2083	0.2208
3/17/65	2	22757	0.52	80	0.6864	0.2069	0.1626
3/17/65	2	22758	0.52	80	0.4861	0.2469	0.2612
3/17/65	2	22759	0.70	80	0.5044	0.2675	0.3205
3/17/65	2	22760	0.70	80	0.6038	0.2260	0.2728
3/17/65	2	22761	0.70	80	0.6845	0.2163	0.2061
3/17/65	2	22762	0.80	80	0.5040	0.2964	0.3385
3/17/65	2	22763	0.80	80	0.5865	0.2547	0.2978
3/17/65	2	22764	0.80	80	0.6805	0.2252	0.2261
3/17/65	2	22765	1.00	80	0.4973	0.3904	0.3120
3/17/65	2	22766	1.00	80	0.6005	0.2970	0.2897
3/17/65	2	22767	1.00	80	0.6848	0.2394	0.2440
3/17/65	2	22768	1.11	80	0.4951	0.4014	0.3251
3/17/65	2	22769	1.10	80	0.6067	0.3100	0.2806
3/17/65	2	22770	1.10	80	0.6551	0.2693	0.2634
3/17/65	2	22771	1.20	80	0.5000	0.4191	0.3068
3/17/65	2	22772	1.20	80	0.5901	0.3408	0.2738
3/17/65	2	22773	1.20	80	0.6435	0.3038	0.2350
3/17/65	2	22774	1.30	80	0.5055	0.4332	0.2837
3/17/65	2	22775	1.30	80	0.6290	0.3277	0.2266
3/17/65	2	22776	1.30	80	0.5629	0.3776	0.2727
3/17/65	2	22777	1.40	80	0.4985	0.4372	0.3060
3/17/65	2	22778	1.40	80	0.4985	0.4372	0.3060
3/17/65	2	22779	1.40	82	0.4903	0.4618	0.2661

*This data point was not reduced by computer program. Hand calculated values are included to indicate performance trends.

Table XII, Continued

Date	Run No.	Case	Inlet Mach No.	Inlet Angle (degrees)	\bar{C}_P	\bar{w}	Exit Mach No.
3/17/65	2	22780	1.40	82	0.5605	0.3980	0.2394
3/17/65	2	22781	1.30	80	0.4889	0.4330	0.3220
3/19/65	3	22783	1.40	79.75	0.4353	0.4027	0.4943
3/19/65	3	22784	1.30	79.75	0.4426	0.3861	0.4806
3/19/65	3	22785	1.30	79.75	0.4426	0.3861	0.4806
3/19/65	3	22786	1.30	79.75	0.4426	0.3861	0.4806
3/19/65	3	22787	1.30	79.75	0.4268	0.1913	0.6985
3/19/65	3	22788	1.30	79.75	0.5442	0.1921	0.5604
3/19/65	3	22789	1.30	79.75	0.4635	0.1810	0.6648
3/19/65	3	22790	1.29	79.75	0.4631	0.1791	0.6660
3/19/65	3	22791	1.29	79.75	0.4619	0.1950	0.6538
3/19/65	3	22792	1.29	79.75	0.4614	0.2233	0.6291
3/19/65	3	22793	1.29	79.75	0.4611	0.2602	0.5946
3/19/65	3	22794	1.29	79.75	0.4609	0.2952	0.5591
3/19/65	3	22795	1.29	79.75	0.4661	0.1931	0.6503
3/19/65	3	22796	1.29	79.75	0.4683	0.2204	0.6234
3/19/65	3	22797	1.29	79.75	0.4681	0.2551	0.5909
3/19/65	3	22798	1.29	79.75	0.4668	0.2890	0.5579
3/19/65	3	22799	1.29	79.75	0.4667	0.2757	0.5718
3/19/65	3	22800	1.29	79.75	0.3230	0.2121	0.7970
3/19/65	3	22801	1.29	79.75	0.4969	0.1821	0.6246
3/19/65	3	22802	1.40	79.75	0.4981	0.2090	0.6309
3/19/65	3	22803	1.40	79.75	0.4488	0.2059	0.6959
3/19/65	3	22804	1.58	79.75	0.3923	0.3307	0.7014
3/19/65	3	22805	1.50	79.75	0.4359	0.2541	0.6982
3/19/65	3	22806	1.40	79.75	0.4379	0.2108	0.7057
3/19/65	3	22807	1.31	78.76	0.4457	0.2692	0.6121
3/19/65	3	22808	1.31	78.76	0.5012	0.2599	0.5497
3/19/65	3	22809	1.31	78.76	0.5343	0.2603	0.5050
3/19/65	3	22810	1.31	78.76	0.4482	0.2802	0.5953
3/19/65	3	22811	1.31	78.76	0.4484	0.3675	0.4963
3/19/65	3	22812	1.31	78.76	0.4478	0.3330	0.5386
3/19/65	3	22813	1.30	78.76	0.4496	0.3037	0.5685
3/19/65	3	22814	1.30	78.76	0.4477	0.3595	0.5068
3/19/65	3	22815	1.31	78.76	0.4461	0.3318	0.5430
3/19/65	3	22816	1.40	78.76	0.4521	0.3345	0.5568
3/19/65	3	22817	1.30	78.76	0.4396	0.3293	0.5535
3/19/65	3	22818	1.30	78.76	0.4349	0.3823	0.4969
3/19/65	3	22819	1.30	78.76	0.4337	0.3598	0.5265
3/19/65	3	22820	1.30	78.76	0.4357	0.3620	0.5209
3/19/65	3	22821	1.30	78.76	0.4346	0.4015	0.4721
3/22/65	4	22823	1.30	79.75	0.4959	0.4178	0.3365
3/22/65	4	22824	1.30	79.75	0.5473	0.3774	0.3076
3/22/65	4	22825	1.30	79.75	0.6004	0.3439	0.2592
3/22/65	4	22826	1.30	79.75	0.5014	0.3042	0.4948
3/22/65	4	22827	1.30	79.75	0.5501	0.2900	0.4416

Table XII, Continued

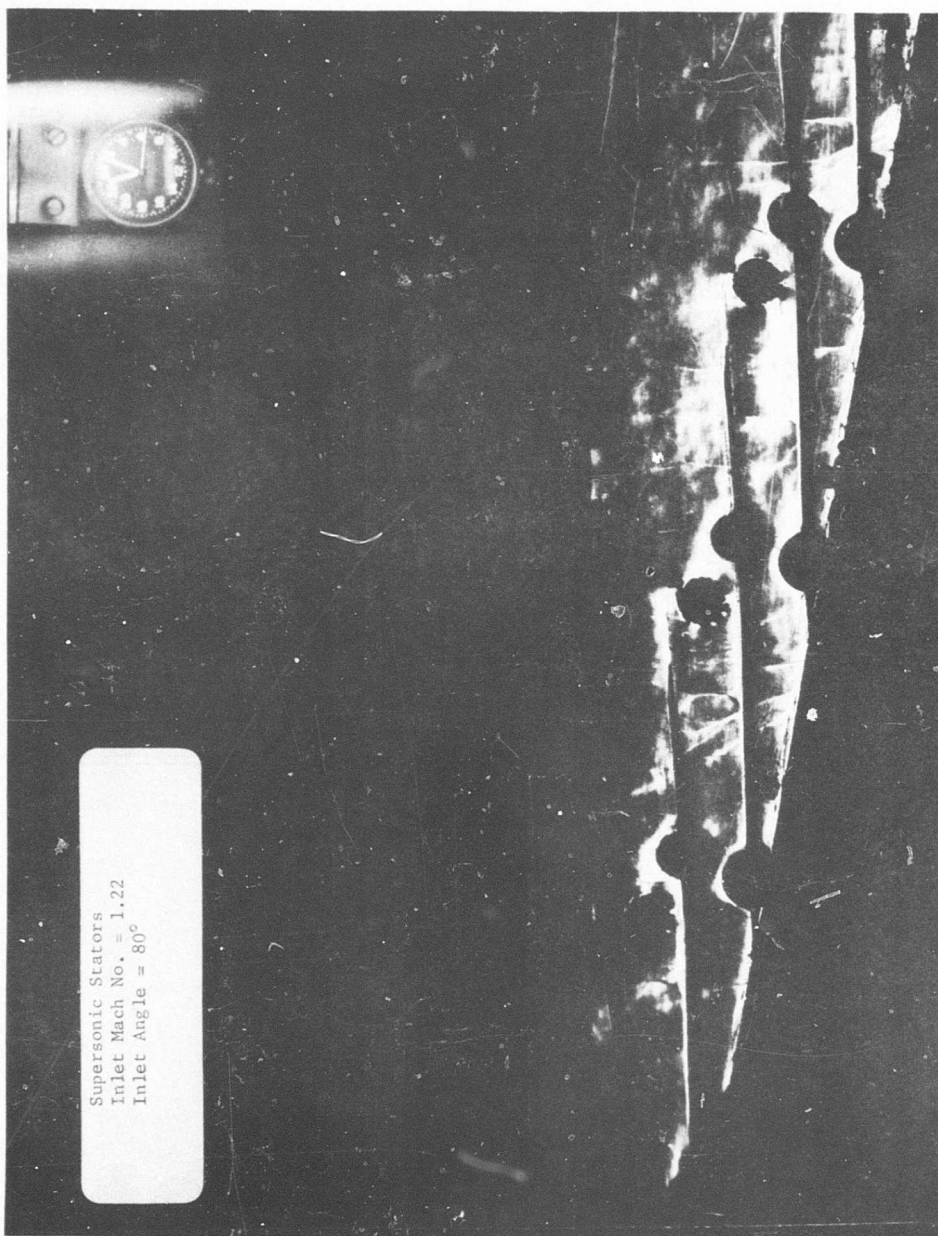
Date	Run No.	Case	Inlet Mach No.	Inlet Angle (degrees)	\bar{C}_P	\bar{w}	Exit Mach No.
3/22/65	4	22828	1.30	79.75	0.6012	0.3049	0.3343
3/22/65	4	22829	1.30	79.75	0.5653	0.2916	0.4161
3/22/65	4	22830	1.30	78	0.5739	0.2720	0.4310
3/22/65	4	22831	1.30	78	0.6219	0.2839	0.3331
3/22/65	4	22832	1.30	78	0.5478	0.2700	0.4717
3/22/65	4	22833	1.30	78	0.6125	0.2758	0.3629
3/22/65	4	22834	1.30	78	0.5002	0.2902	0.5138
3/22/65	4	22835	1.30	82	0.4918	0.3218	0.4878
3/22/65	4	22836	1.30	82	0.5484	0.3080	0.4203
3/22/65	4	22837	1.30	82	0.5930	0.3198	0.3240
3/22/65	4	22838	1.40	79.75	0.4962	0.3357	0.4882
3/22/65	4	22839	1.40	79.75	0.5503	0.3181	0.4230
3/22/65	4	22840	1.40	79.50	0.5786	0.3268	0.3561
3/22/65	4	22841	1.20	79.50	0.5540	0.2532	0.4581
3/22/65	4	22842	1.20	79.50	0.6005	0.2529	0.3948
3/22/65	4	22843	1.20	79.50	0.6358	0.2653	0.3220
3/22/65	4	22844	1.20	79.50	0.4963	0.2782	0.5042
3/22/65	4	22845	1.00	79.50	0.5042	0.2124	0.4861
3/22/65	4	22846	1.00	79.50	0.6051	0.2084	0.3868
3/22/65	4	22847	1.00	79.50	0.6600	0.2287	0.2964
3/22/65	4	22848	1.00	79.50	0.5534	0.2032	0.4458
3/22/65	4	22849	0.81	79.50	0.4915	0.1783	0.4359
3/22/65	4	22850	0.81	79.50	0.5799	0.1768	0.3698
3/22/65	4	22851	0.80	79.50	0.6606	0.2198	0.2573
3/22/65	4	22852	0.81	79.50	0.5427	0.1718	0.4024
3/22/65	4	22853	0.60	79.75	0.5380	0.1548	0.3217
3/22/65	4	22854	0.60	79.75	0.5961	0.1665	0.2816
3/22/65	4	22855	0.60	79.75	0.6642	0.2091	0.2052
3/22/65	4	22856	0.60	79.75	0.4910	0.1937	0.3278
3/23/65	5	22860	1.31	79.75	0.5012	0.3036	0.4980
3/23/65	5	22861	1.30	79.75	0.5556	0.2797	0.4486
3/23/65	5	22862	1.30	79.75	0.5556	0.2797	0.4486
3/23/65	5	22863	1.30	79.75	0.6130	0.2953	0.3300
3/24/65	6	22865	1.31	79.75	0.4898	0.3419	0.4669
3/24/65	6	22866	1.30	79.75	0.5540	0.2947	0.4309
3/24/65	6	22867	1.30	79.75	0.6008	0.2630	0.4018
3/24/65	6	22868	1.30	79.75	0.6204	0.2601	0.3740
3/24/65	6	22869	1.30	79.75	0.6512	0.2690	0.3036
3/24/65	6	22870	1.40	79.75	0.4992	0.3623	0.4444
3/24/65	6	22871	1.40	79.75	0.5549	0.3164	0.4178
3/24/65	6	22872	1.40	79.75	0.6058	0.2957	0.3587
3/24/65	6	22873	1.40	79.75	0.6074	0.3006	0.3466
3/24/65	6	22874	1.20	79.75	0.6655	0.2398	0.3119
3/24/65	6	22875	1.20	79.75	0.4953	0.3163	0.4635
3/24/65	6	22876	1.20	79.75	0.5571	0.2730	0.4305
3/24/65	6	22877	1.20	79.75	0.6062	0.2427	0.3998

Table XII, Continued

Date	Run No.	Case	Inlet Mach No.	Inlet Angle (degrees)	\bar{C}_P	\bar{w}	Exit Mach No.
3/24/65	6	22878	1.00	79.75	0.5106	0.2624	0.4370
3/24/65	6	22879	1.00	79.75	0.5351	0.2487	0.4240
3/24/65	6	22880	1.00	79.75	0.5751	0.2227	0.4057
3/24/65	6	22881	1.00	79.75	0.6891	0.2093	0.2813
3/24/65	6	22882	0.80	79.75	0.5004	0.2146	0.4051
3/24/65	6	22883	0.80	79.75	0.5481	0.1997	0.3784
3/24/65	6	22884	0.80	79.75	0.5958	0.1892	0.3469
3/24/65	6	22885	0.80	79.75	0.6902	0.1930	0.2528
3/24/65	6	22886	0.60	79.75	0.4989	0.1939	0.3229
3/24/65	6	22887	0.60	79.75	0.5438	0.1862	0.3017
3/24/65	6	22888	0.60	79.75	0.5985	0.1753	0.2746
3/24/65	6	22889	0.60	79.75	0.6912	0.1864	0.2011
3/24/65	6	22890	0.60	79.75	0.6430	0.1719	0.2481
3/25/65	7	22893	1.30	79.75	0.6128	0.2575	0.3898
3/25/65	7	22894	1.30	79.75	0.6109	0.2632	0.3848
3/25/65	7	22895	1.30	79.75	0.6404	0.2756	0.3125
3/25/65	7	22896	1.30	79.75	0.6110	0.2668	0.3796
3/25/65	7	22897	1.30	79.75	0.6495	0.2602	0.3220
3/25/65	7	22898	1.31	79.75	0.5410	0.3075	0.4339
3/25/65	7	22899	1.30	79.75	0.4941	0.3474	0.4517
3/25/65	7	22900	1.40	79.75	0.4938	0.3667	0.4476
3/25/65	7	22901	1.40	79.75	0.5429	0.3268	0.4228
3/25/65	7	22902	1.40	79.75	0.5989	0.2967	0.3701
3/25/65	7	22903	1.40	79.75	0.6039	0.2952	0.3634
3/25/65	7	22904	1.20	79.75	0.4930	0.3172	0.4656
3/25/65	7	22905	1.21	79.75	0.5613	0.2744	0.4233
3/25/65	7	22906	1.21	79.75	0.5978	0.2493	0.4034
3/25/65	7	22907	1.21	79.75	0.6689	0.2334	0.3165
3/25/65	7	22908	1.00	79.75	0.4946	0.1273	0.5586
3/25/65	7	22909	1.00	79.75	0.5535	0.1101	0.5202
3/25/65	7	22910	1.00	79.75	0.6074	0.2077	0.3853
3/25/65	7	22911	1.00	79.75	0.6910	0.2064	0.2828
3/25/65	7	22912	0.80	79.75	0.4886	0.2122	0.4157
3/25/65	7	22913	0.80	79.75	0.5453	0.1949	0.3838
3/25/65	7	22914	0.80	79.75	0.5963	0.1818	0.3520
3/25/65	7	22915	0.80	79.75	0.7014	0.1893	0.2440
3/25/65	7	22916	0.60	79.75	0.5000	0.1795	0.3289
3/25/65	7	22917	0.60	79.75	0.5436	0.1719	0.3089
3/25/65	7	22918	0.60	79.75	0.5936	0.1677	0.2820
3/25/65	7	22919	0.60	79.75	0.6978	0.1835	0.1976
3/26/65	8	22921	1.30	79.75	0.4963	0.3123	0.4932
3/26/65	8	22922	1.30	79.75	0.5445	0.2745	0.4706
3/26/65	8	22923	1.30	79.75	0.5963	0.2454	0.4322
3/26/65	8	22924	1.30	79.75	0.6418	0.2546	0.3459
3/26/65	8	22926	1.30	79.75	0.6105	0.2436	0.4130
3/26/65	8	22927	1.30	79.75	0.6104	0.2494	0.4052

Table XII. Continued

Date	Run No.	Case	Inlet Mach No.	Inlet Angle (degrees)	\bar{C}_P	$\bar{\omega}$	Exit Mach No.
3/26/65	8	22928	1.30	79.75	0.6112	0.2595	0.3895
3/26/65	8	22929	1.30	79.75	0.6110	0.2723	0.3709
3/26/65	8	22930	1.30	79.75	0.6084	0.2849	0.3555
3/26/65	8	22931	1.30	79.75	0.6094	0.2499	0.4060
3/26/65	8	22932	1.30	79.75	0.6095	0.2761	0.3673
3/26/65	8	22933	1.40	79.75	0.4952	0.3342	0.4914
3/26/65	8	22934	1.40	79.75	0.5513	0.2899	0.4623
3/26/65	8	22935	1.40	79.75	0.5984	0.2832	0.3930
3/26/65	8	22936	1.20	79.75	0.5035	0.2817	0.4917
3/26/65	8	22937	1.20	79.75	0.5516	0.2481	0.4670
3/26/65	8	22938	1.20	79.75	0.5988	0.2235	0.4332
3/26/65	8	22939	1.20	79.75	0.6655	0.2282	0.3299
3/26/65	8	22940	1.00	79.75	0.4985	0.2341	0.4747
3/26/65	8	22941	1.00	79.75	0.5519	0.1991	0.4519
3/26/65	8	22942	1.00	79.75	0.6044	0.1872	0.4089
3/26/65	8	22943	1.01	79.75	0.6866	0.2017	0.2954
3/26/65	8	22944	0.81	79.75	0.4886	0.1794	0.4394
3/26/65	8	22945	0.81	79.75	0.5455	0.1667	0.4058
3/26/65	8	22946	0.81	79.75	0.5963	0.1626	0.3689
3/26/65	8	22947	0.81	79.75	0.6961	0.1873	0.2537
3/26/65	8	22948	0.61	79.75	0.4971	0.1568	0.3462
3/26/65	8	22949	0.61	79.75	0.5438	0.1514	0.3236
3/26/65	8	22950	0.61	79.75	0.5958	0.1500	0.2944
3/26/65	8	22951	0.61	79.75	0.6939	0.1797	0.2063



Supersonic Stators
Inlet Mach No. = 1.22
Inlet Angle = 80°

Figure 136. Schlieren Photograph of Supersonic Stator Cascade Tests, Case Number 22277.

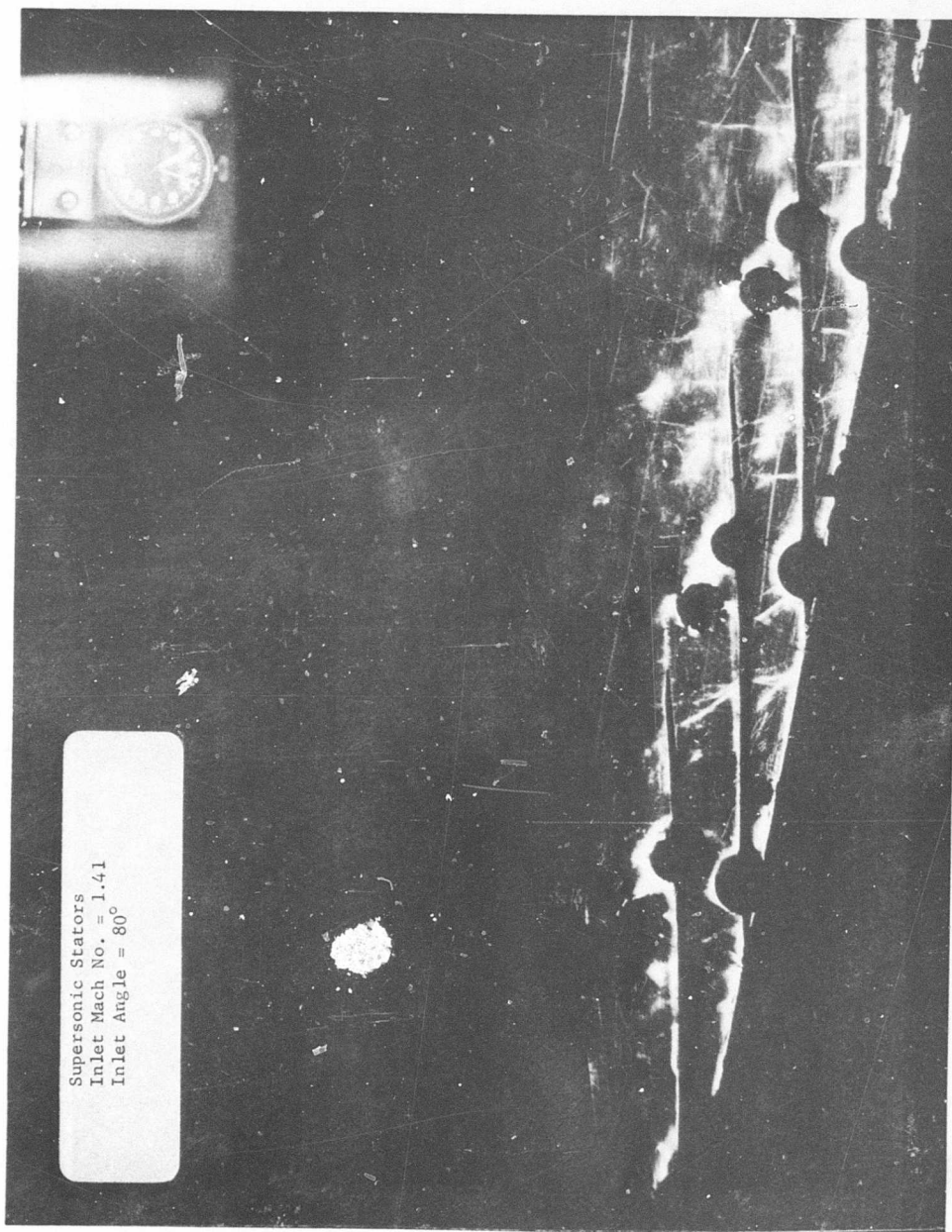


Figure 137. Schlieren Photograph of Supersonic Stator Cascade Tests, Case Number 22288.



Supersonic Stators
Inlet Mach No. = 1.41
Inlet Angle = 80°

Figure 138. Schlieren Photograph of Supersonic Stator Cascade Tests, Case Number 22291.



Figure 139. Schlieren Photograph of Supersonic Stator Cascade Tests, Case Number 22293.

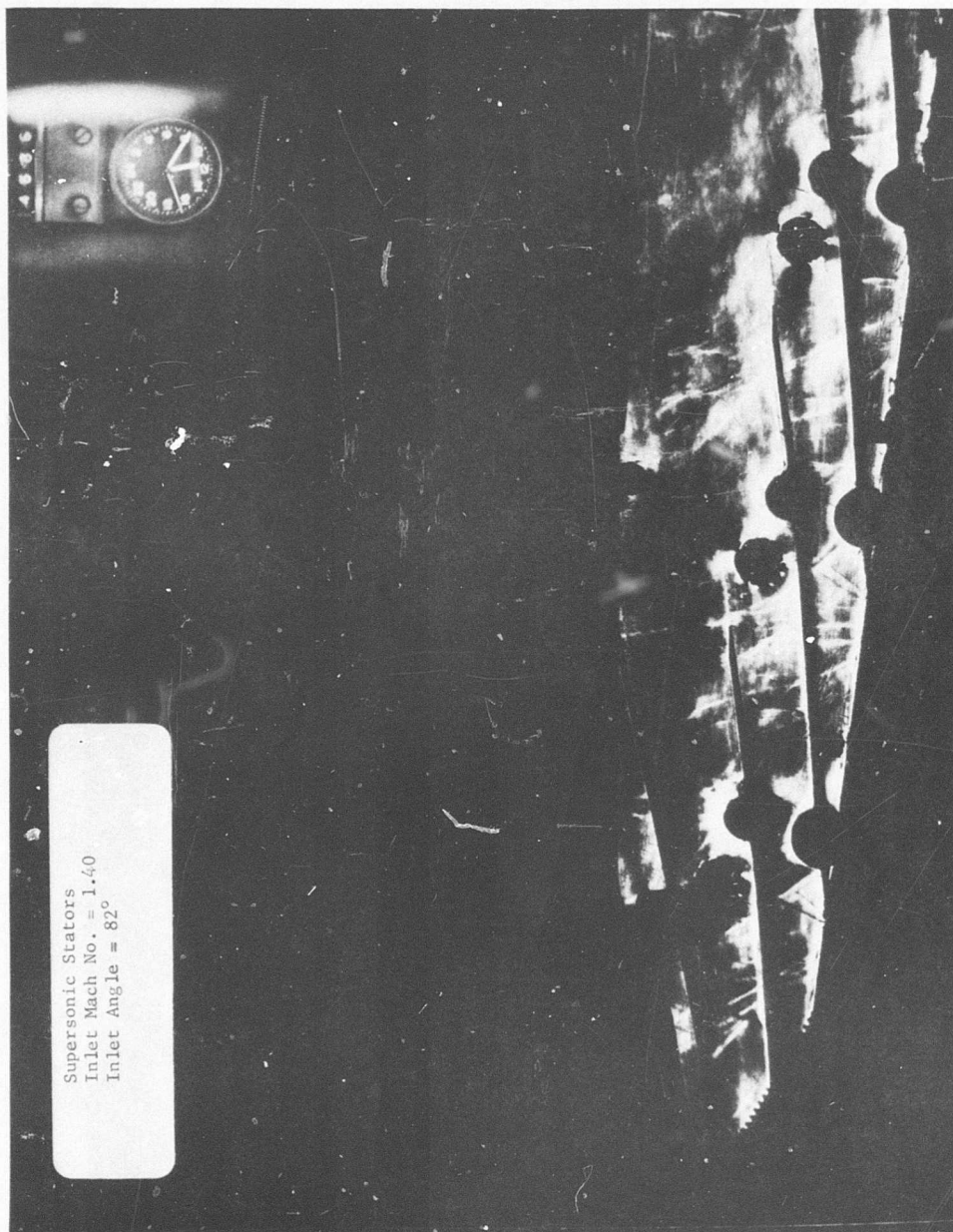


Figure 140. Schlieren Photograph of Supersonic Stator Cascade Tests, Case Number 22294.

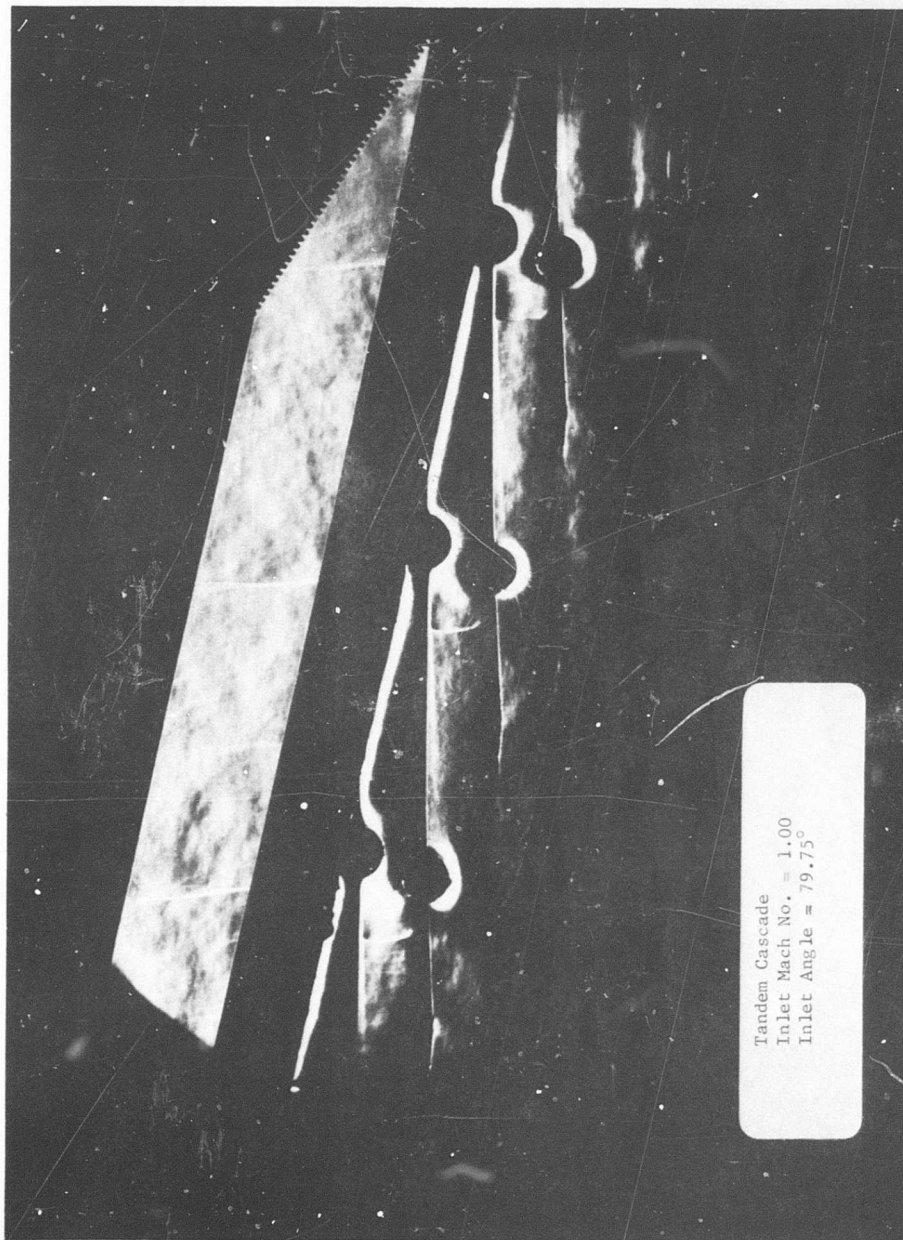


Figure 141. Schlieren Photograph of Supersonic Stator Cascade Tests, Case Number 22908.

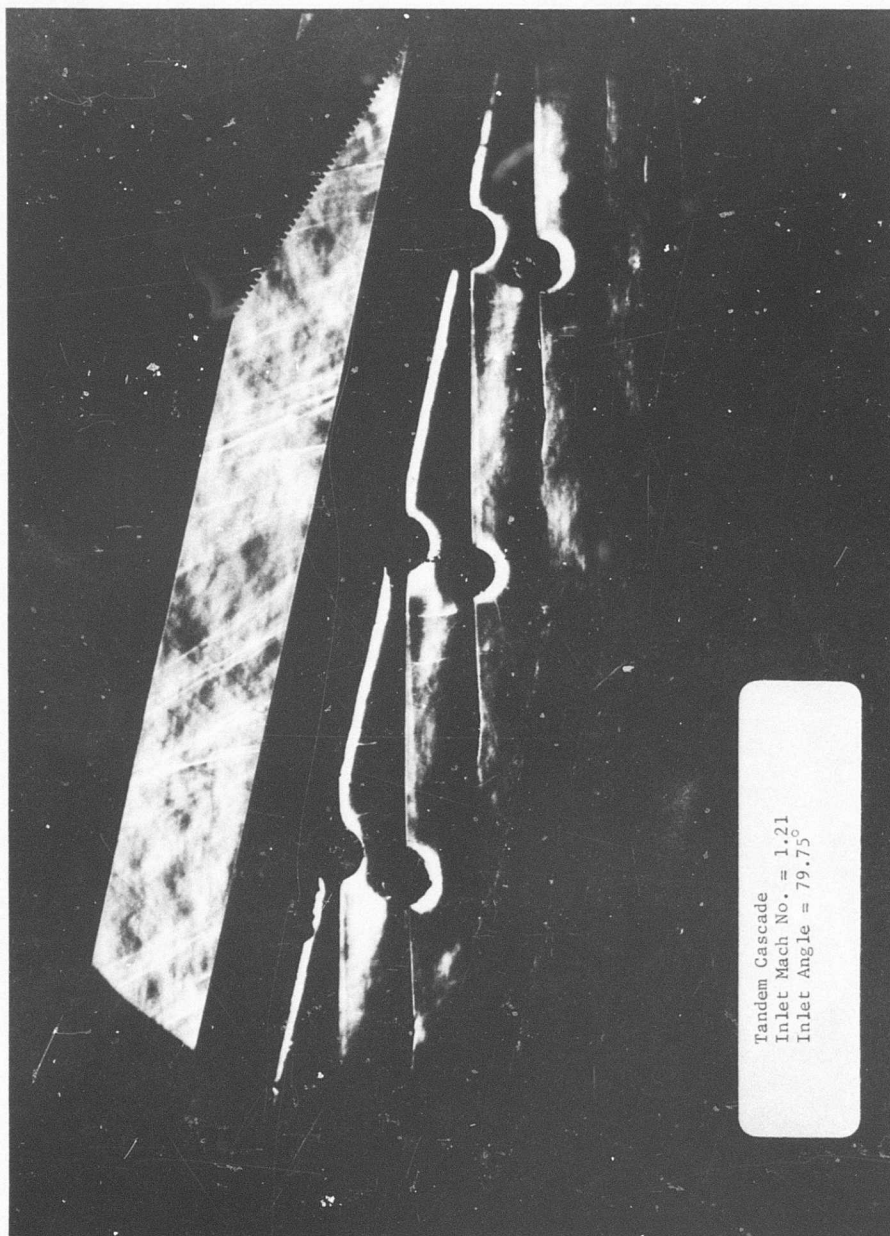


Figure 142. Schlieren Photograph of Supersonic Stator Cascade Tests, Case Number 22905.

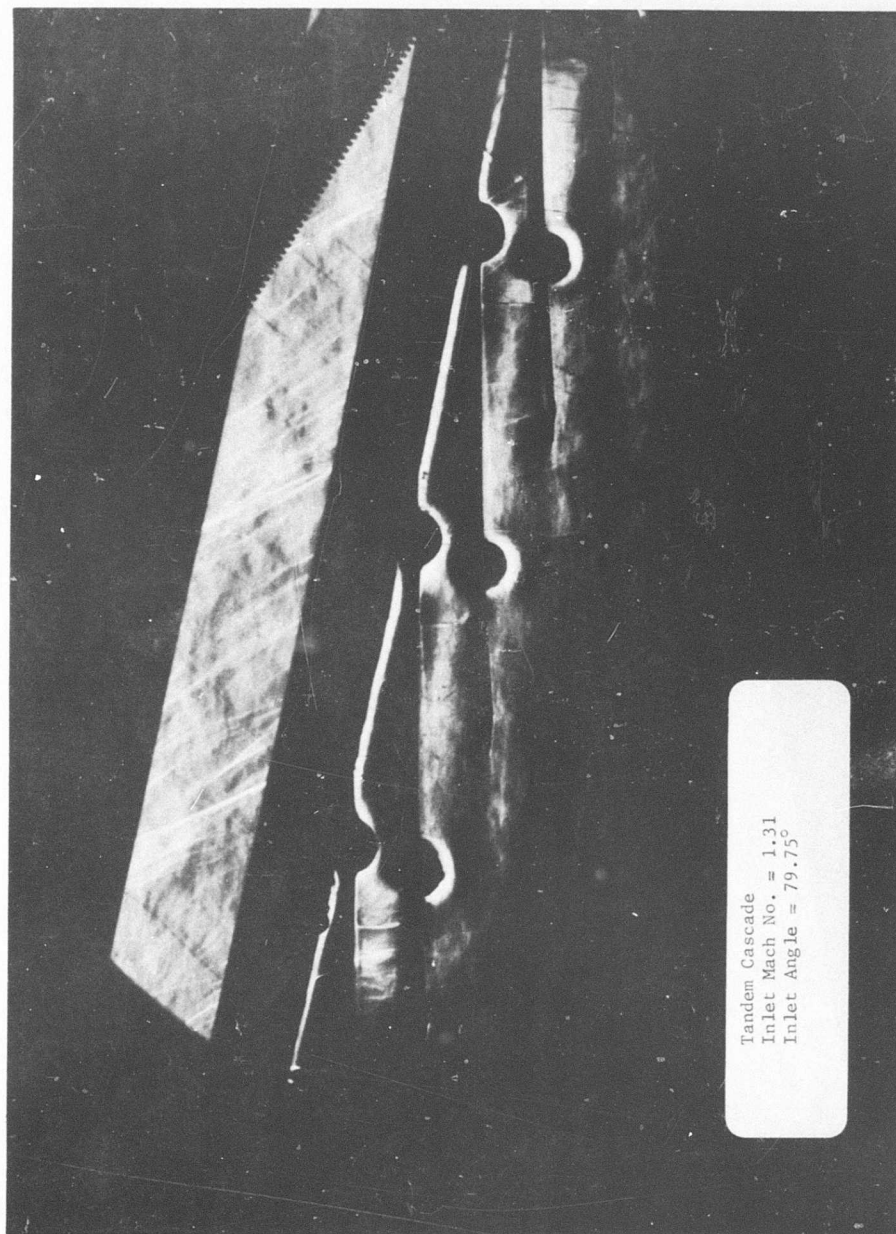
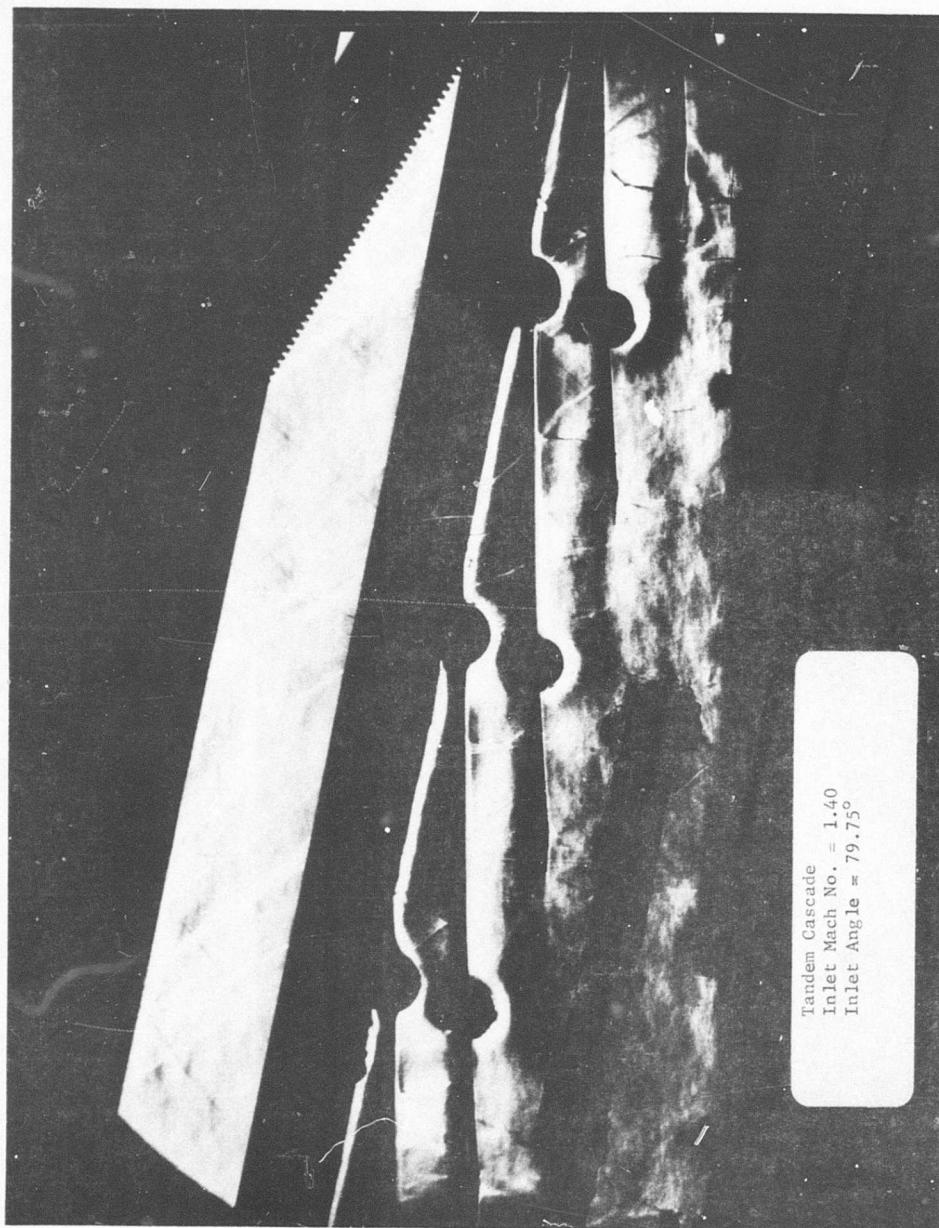


Figure 143. Schlieren Photograph of Supersonic Stator Cascade Tests, Case Number 22898.



Tandem Cascade
Inlet Mach No. = 1.40
Inlet Angle = 79.75°

Figure 144. Schlieren Photograph of Supersonic Stator Cascade Tests, Case Number 22900.

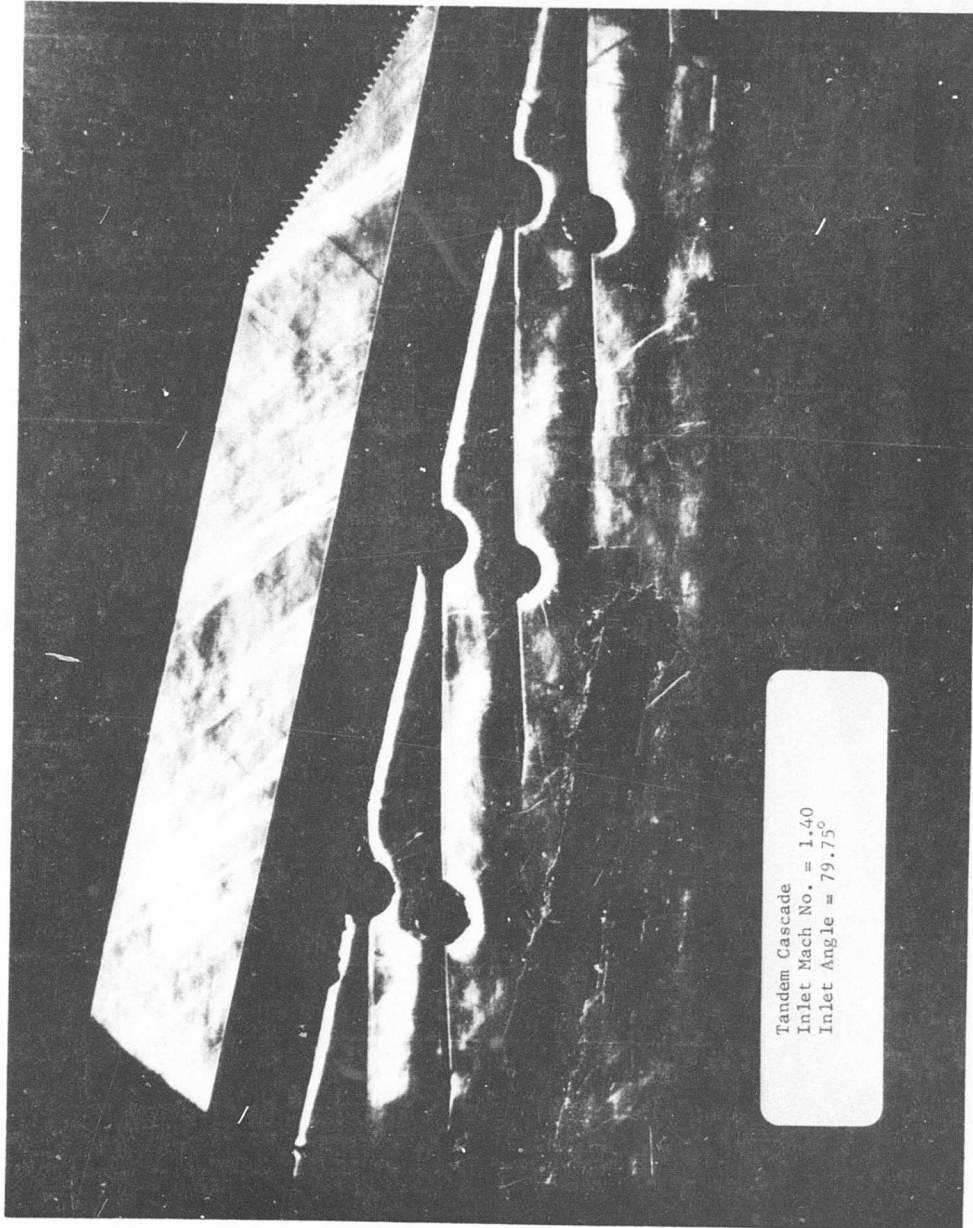


Figure 145. Schlieren Photograph of Supersonic Stator Cascade Tests, Case Number 22901.

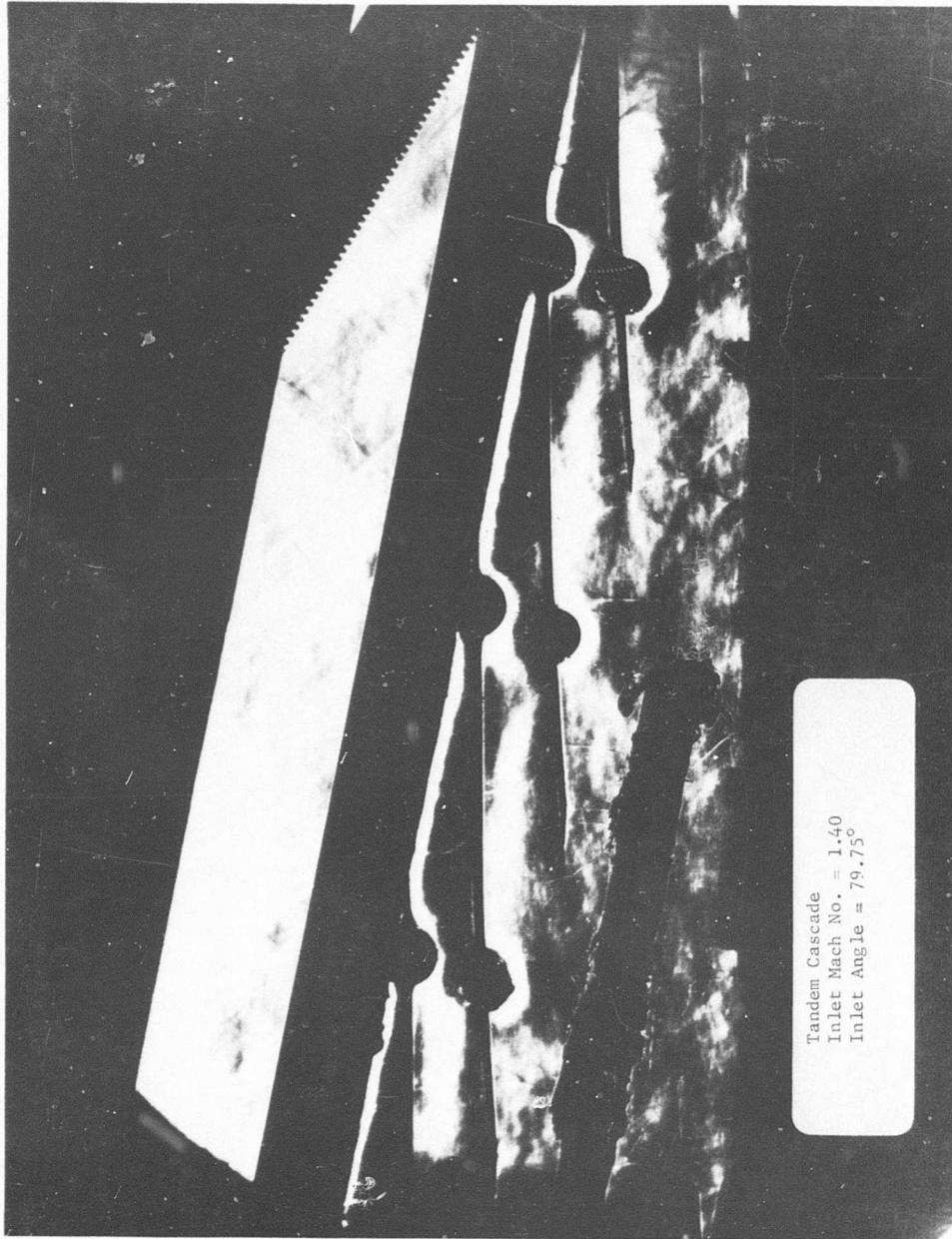


Figure 146. Schlieren Photograph of Supersonic Stator Cascade Tests, Case Number 22902.

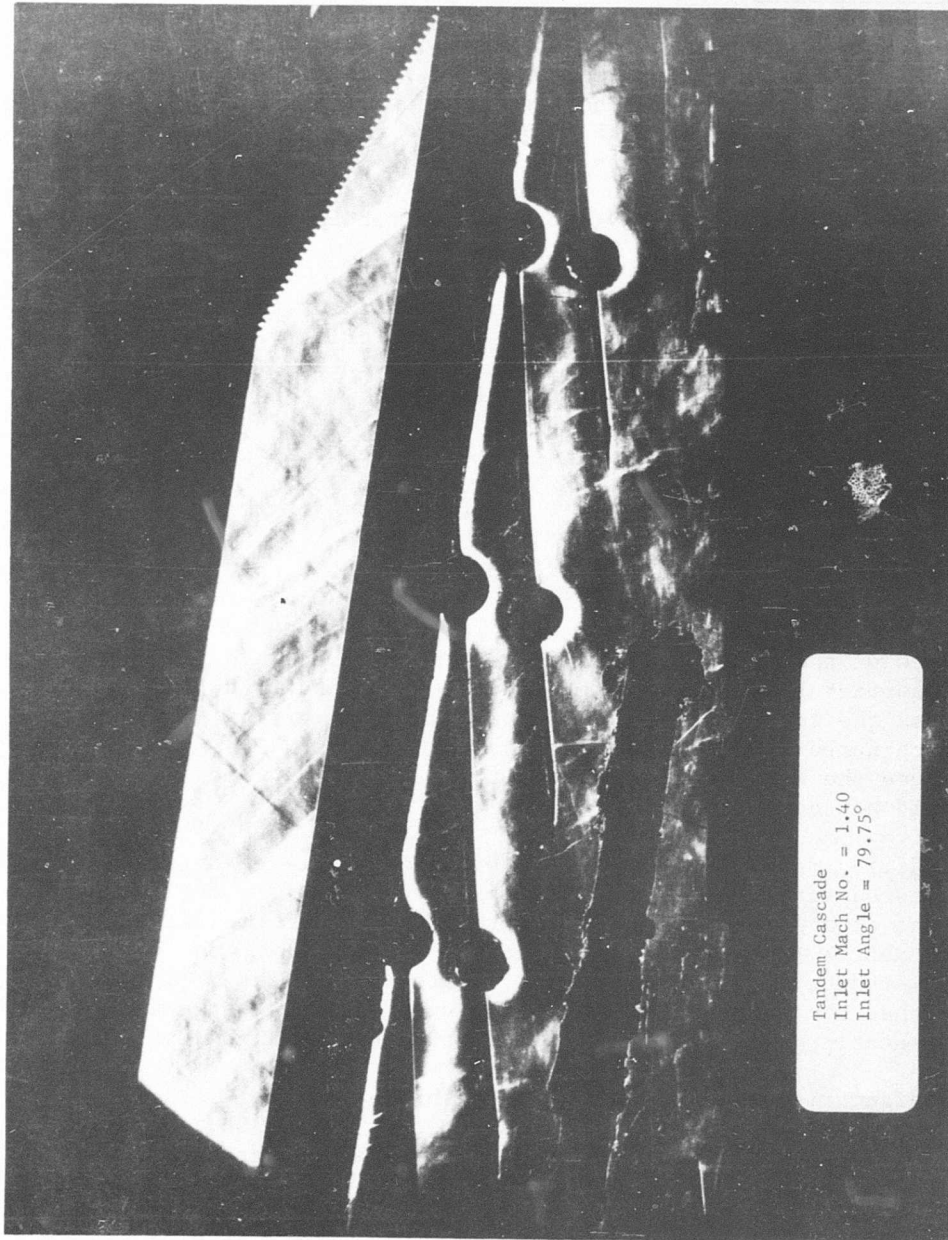


Figure 147. Schlieren Photograph of Supersonic Stator Cascade Tests, Case Number 22903.

EVALUATION

Supersonic Stators

The preliminary testing of the supersonic stator test vehicle using the original design medium length blades, with and without blade surface roughness, yielded the results shown in Figure 148. Schlieren pictures (Figures 149 through 152) of flow through the stators indicated that normal shock waves just upstream of the leading edges appear for all the Mach numbers and inlet angles tested. Failure to start supersonic flow was evident and contributed to the relatively poor performance observed.

The results of somewhat similar supersonic stator tests conducted at Evendale during 1963 were reviewed. The primary differences from the sections that gave satisfactory results in 1963 were the inlet angle (80 degrees versus 60 degrees in 1963), the section thickness and the leading edge angle (present design of 0.125 and 15 degrees, respectively). The lower aspect ratio of the present design (0.6 compared to earlier value of 0.21) was not considered a significant factor.

The supersonic stator design philosophy described earlier in this section resulted from this review. The stator blade sections were modified to reduce the leading edge wedge angle in order to weaken the strength of the initial and reflected shock waves. Additional wedges were manufactured which could be added to the modified blades to increase the contraction ratio. This was done in an attempt to reduce the Mach number at which the normal shock occurs. The objective was to reduce the Mach number of the normal shock below about 1.25 and thus to avoid boundary layer separation.

The modified design supersonic stator blades of three different lengths were tested varying inlet Mach number and inlet flow angle. In Figure 153, the data points corresponding to minimum loss coefficient at each Mach number are presented. As indicated by these data, the medium length blades produce the best supersonic stator performance. It is also noted that the configuration with the upper surface wedge added had a higher static pressure rise but at an exceedingly high loss coefficient.

The characteristics of the medium length blades were: solidity of 1.9, contraction ratio of 1.02, and area ratio of 1.15. Succeeding tests were conducted to determine the optimum value of contraction ratio and area ratio for these blades.

Increasing the contraction ratio to 1.06 was unsatisfactory because supersonic flow was seen (using the schlieren system) not to enter the passages until a Mach number of 1.49 was reached. High loss coefficients were measured as shown in Figure 154. Another configuration at a contraction ratio of 1.03 was tested. Some difficulty in starting

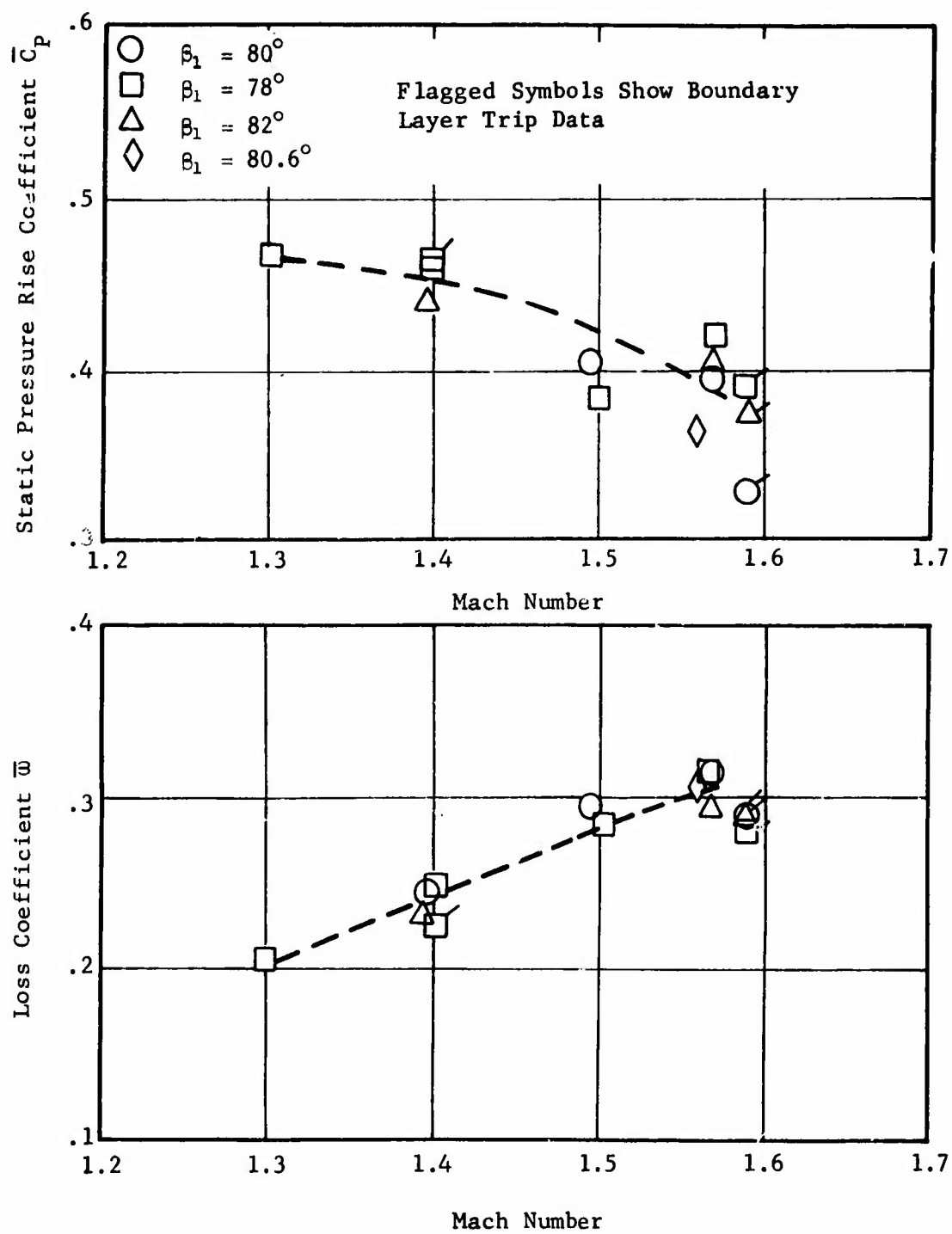


Figure 148. Results of Preliminary Testing with Original Design Medium Length Supersonic Stator Blades at Nominal Throttle Setting.

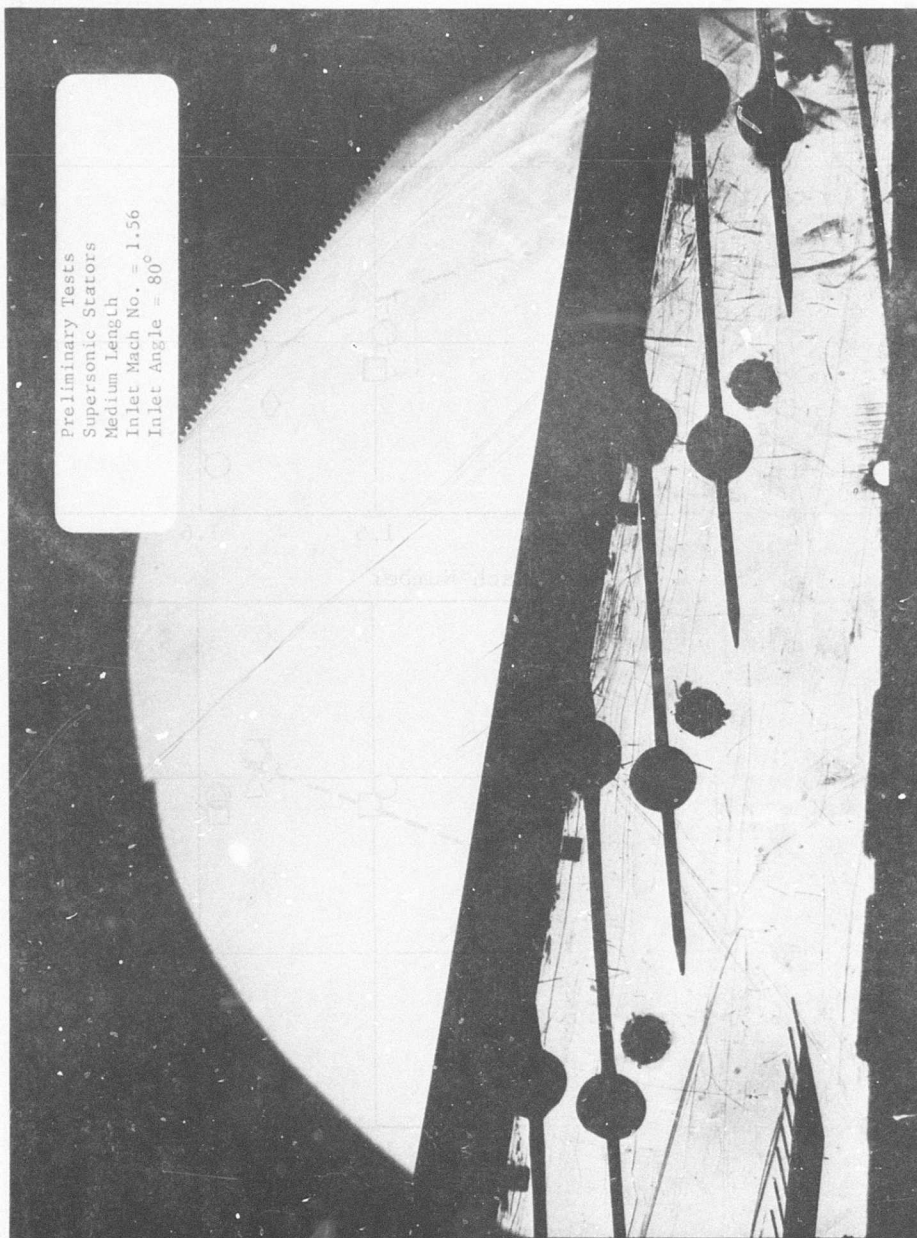
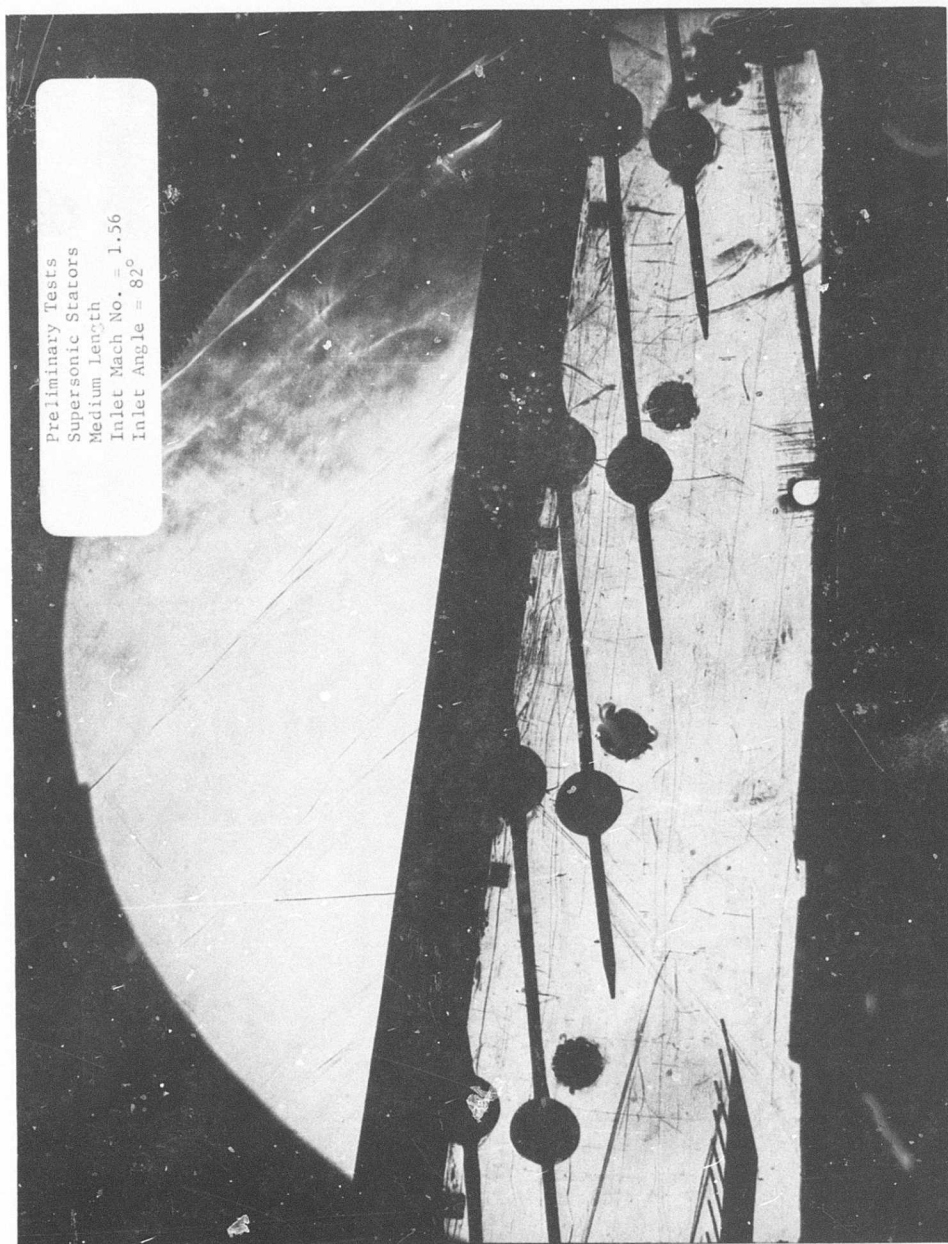


Figure 149. Schlieren Photograph of Preliminary Supersonic Stator Cascade Tests, Original Medium Length Design, Inlet Mach Number = 1.56 and Inlet Angle = 80°.



Preliminary Tests
Supersonic Stators
Medium Length
Inlet Mach No. = 1.56
Inlet Angle = 82°

Figure 150. Schlieren Photograph of Preliminary Supersonic Stator Cascade Tests, Original Medium Length Design, Inlet Mach Number = 1.56 and Inlet Angle = 82° .

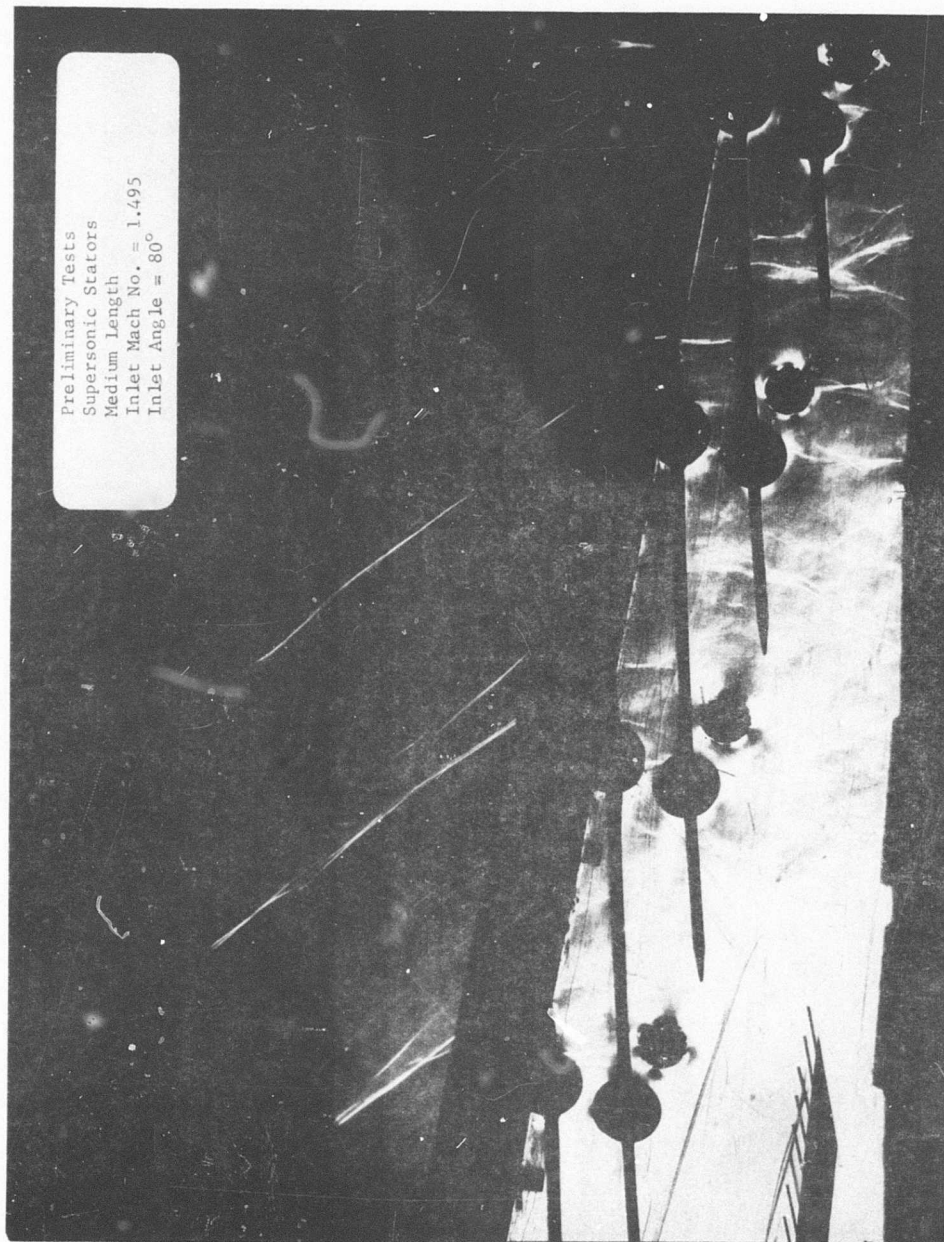


Figure 151. Schlieren Photograph of Preliminary Supersonic Stator Cascade Tests, Original Medium Length Design, Inlet Mach Number = 1.495 and Inlet Angle = 80°.

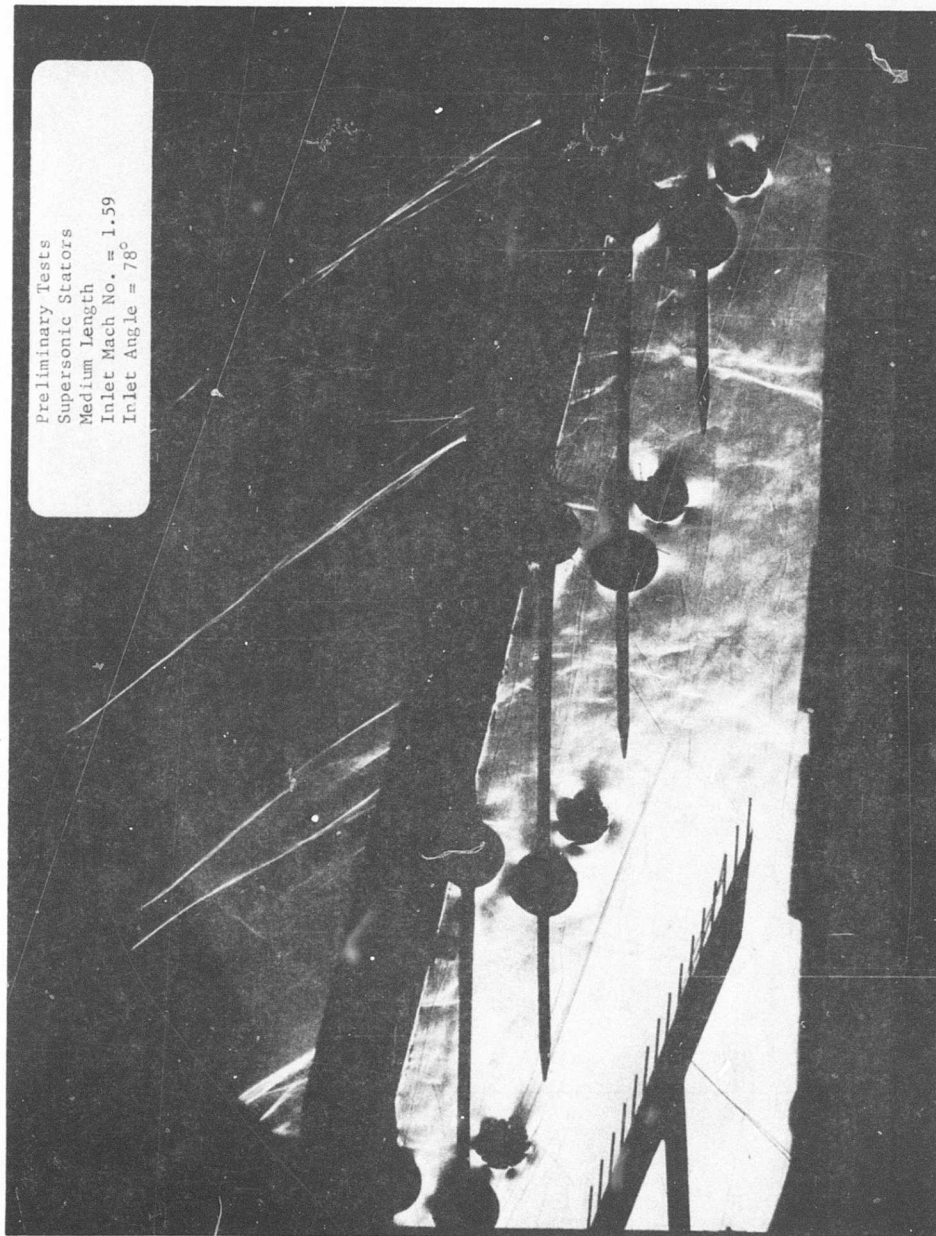


Figure 152. Schlieren Photograph of Preliminary Supersonic Stator Cascade Tests, Original Medium Length Design, Inlet Mach Number = 1.59 and Inlet Angle = 78°.

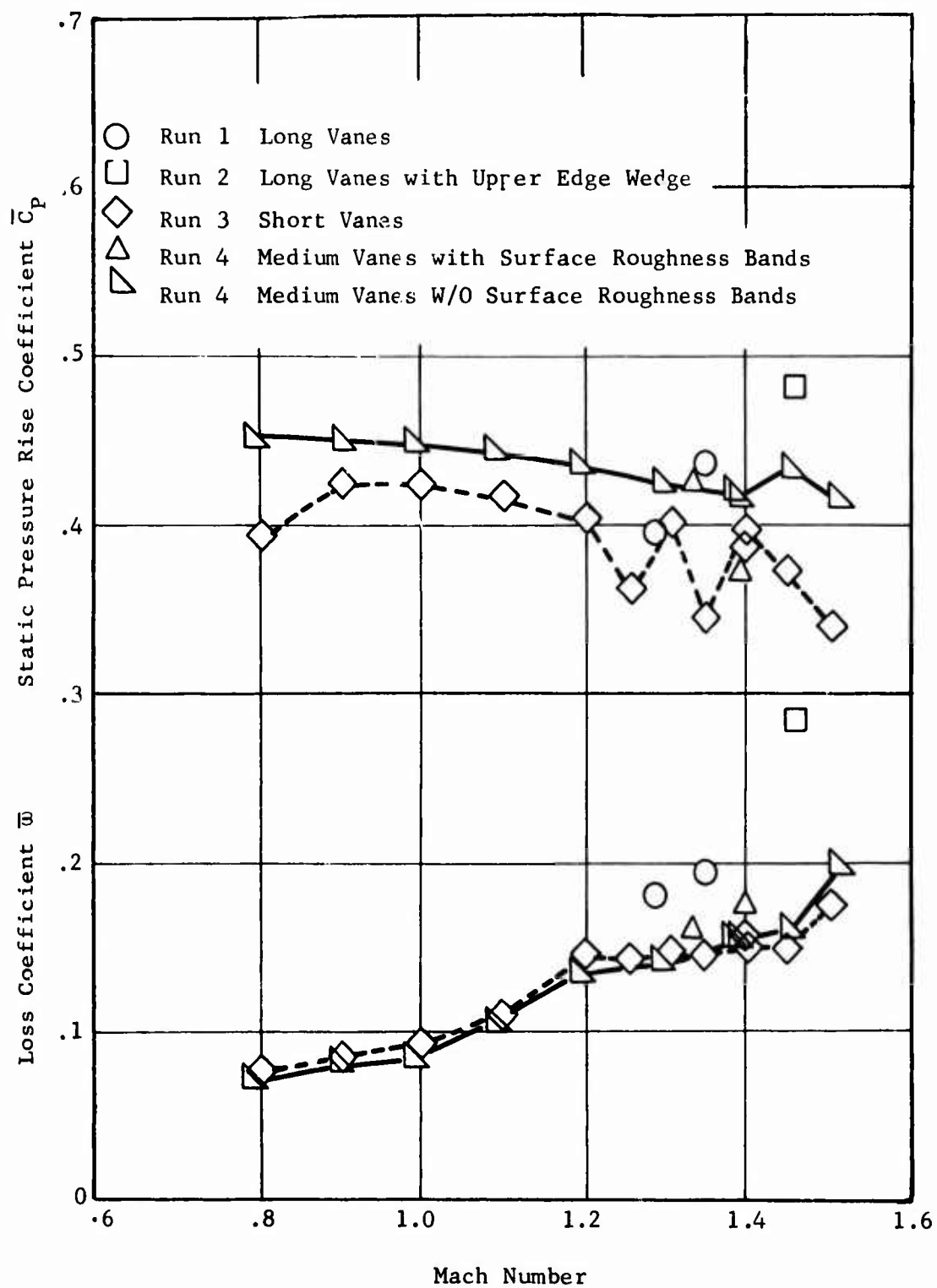


Figure 153. Performance of Modified Design Supersonic Stator Vanes of Three Different Lengths at Design Inlet Angle of 80° .

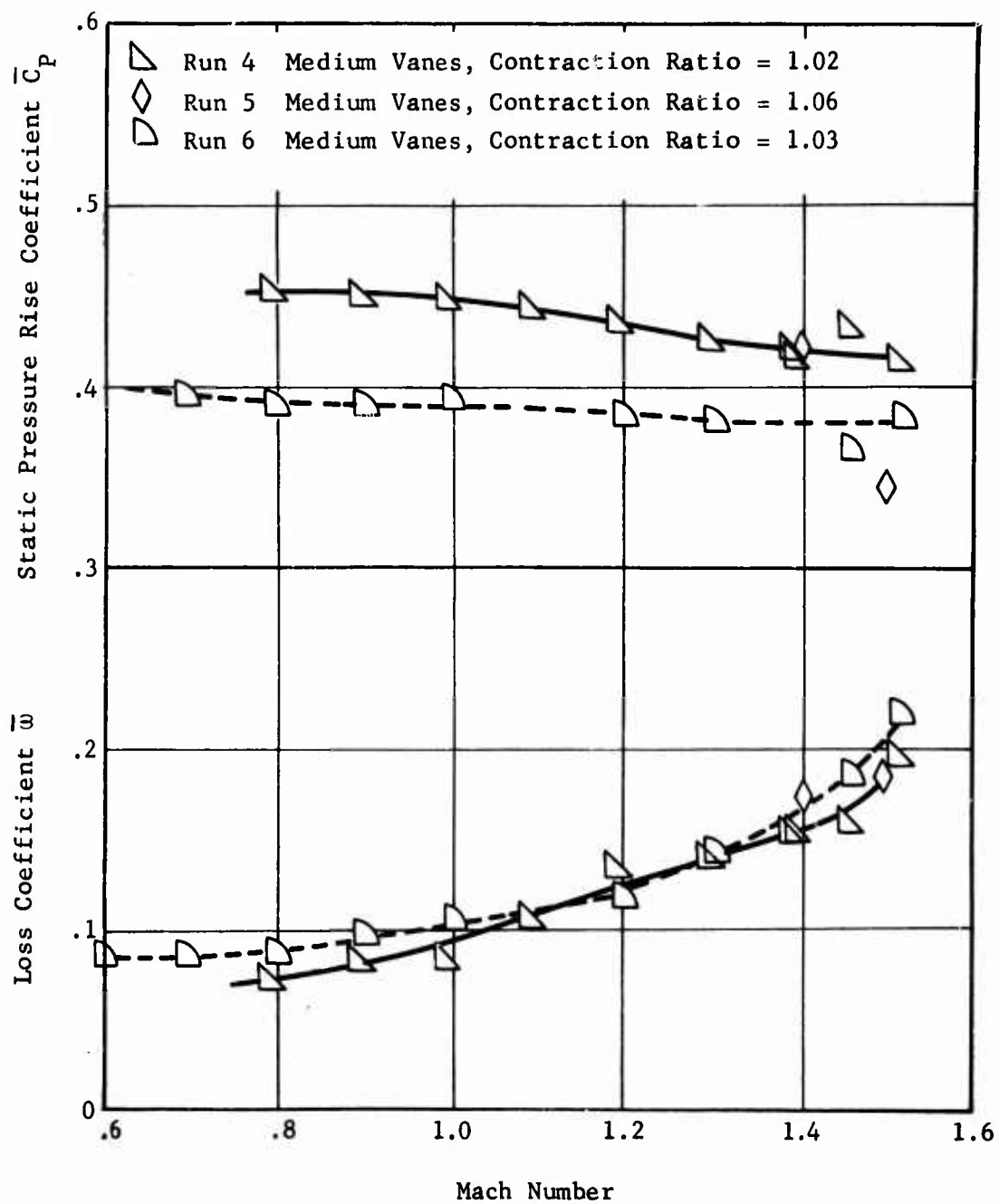


Figure 154. Effect of Contraction Ratio on Performance of Medium Length Supersonic Stators (Modified Design) at Design Inlet Angle of 80° .

supersonic flow was observed, and the loss coefficients were again higher than the original medium length configuration at a contraction ratio of 1.02.

With the contraction ratio at 1.02, the medium length supersonic stators were then tested at an area ratio of 1.23. Very satisfactory results were observed. To insure that the optimum area ratio had been obtained, the final configuration was tested with 1.02 contraction ratio and 1.28 area ratio. Reduced test data for these configurations at the contraction ratio of 1.02 are presented in Figure 155. The loss coefficients included in this figure are minimum values obtained for each test configuration at each Mach number. The static pressure rise coefficients are those which correspond to the test point for which minimum loss was obtained.

Run 4 configuration (Figure 155) is essentially the same as the original medium length supersonic stator shown as part Number 3 on Drawing 4012286-374 (see Figure 132) but with modifications as shown in Figure 156. This configuration with contraction ratio of 1.02 and area ratio of 1.15 produced low losses at Mach numbers from 0.8 to 1.2. The static pressure rise was also low over this same range of Mach numbers.

Run 8 configuration (Figure 155) is the medium length blades modified to increase the area ratio to 1.23 while maintaining the contraction ratio at a value of 1.02. This arrangement proved to have high static pressure rise coefficients and low loss coefficients over the range of Mach numbers from 0.8 to 1.2.

Run 9 configuration (Figure 155) describes the same medium length blades recambered to produce an area ratio of 1.28 while maintaining the contraction ratio at 1.02. The resulting performance showed the least losses at Mach numbers of 1.1 and 1.2 but showed appreciably higher losses at a Mach number of 1.4.

Schlieren pictures were taken of the supersonic stator configuration of test run 8. Figure 142 was taken at an inlet Mach number of 1.21 for an inlet angle of 80 degrees. The static pressure rise coefficient (\bar{C}_p) was 0.50 and the loss coefficient (\bar{w}) was 0.139 for this test condition. Figures 143 and 144 are schlieren photographs of run 8 supersonic stators at an inlet Mach number of 1.31 and an inlet angle of 80 degrees. The loss coefficient was 0.145 and the static pressure rise coefficient was 0.438 for both of these conditions. Clearly defined oblique shocks were observed within the blade passages, indicating that the flow was fully started; the flow was entirely supersonic up to the point where the normal shocks can be observed about halfway back within the confined region of the blade passage. Boundary layer growth appears to be relatively small on both the convex and the concave surfaces, with an indication that the boundary layer appears thicker on the concave (pressure) surface. These results indicate that satisfactory compressor performance should be achieved at 100 percent and slightly higher rotational

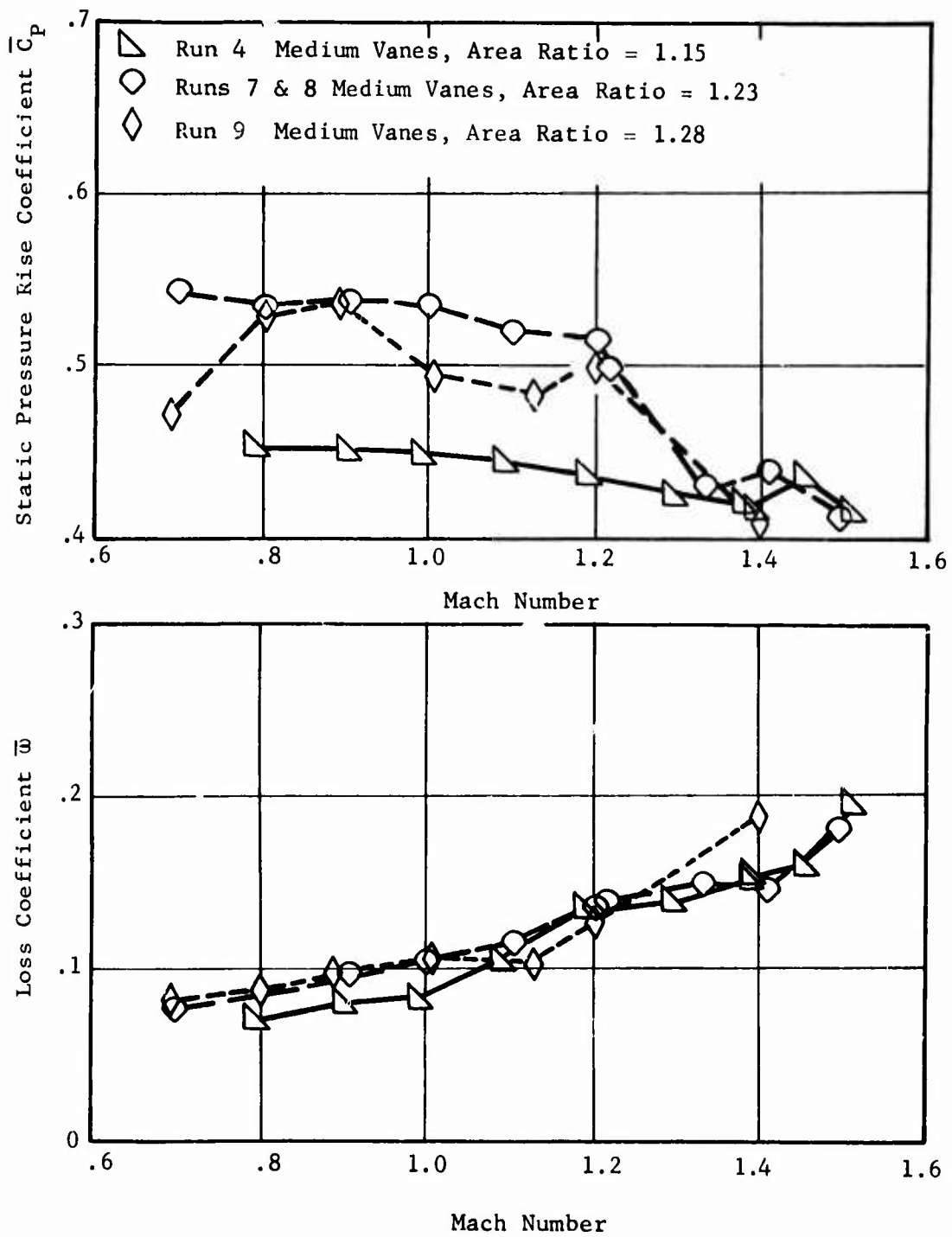


Figure 155. Effect of Area Ratio on Performance of Medium Length Supersonic Stators (Modified Design) at Design Inlet Angle of 80° .

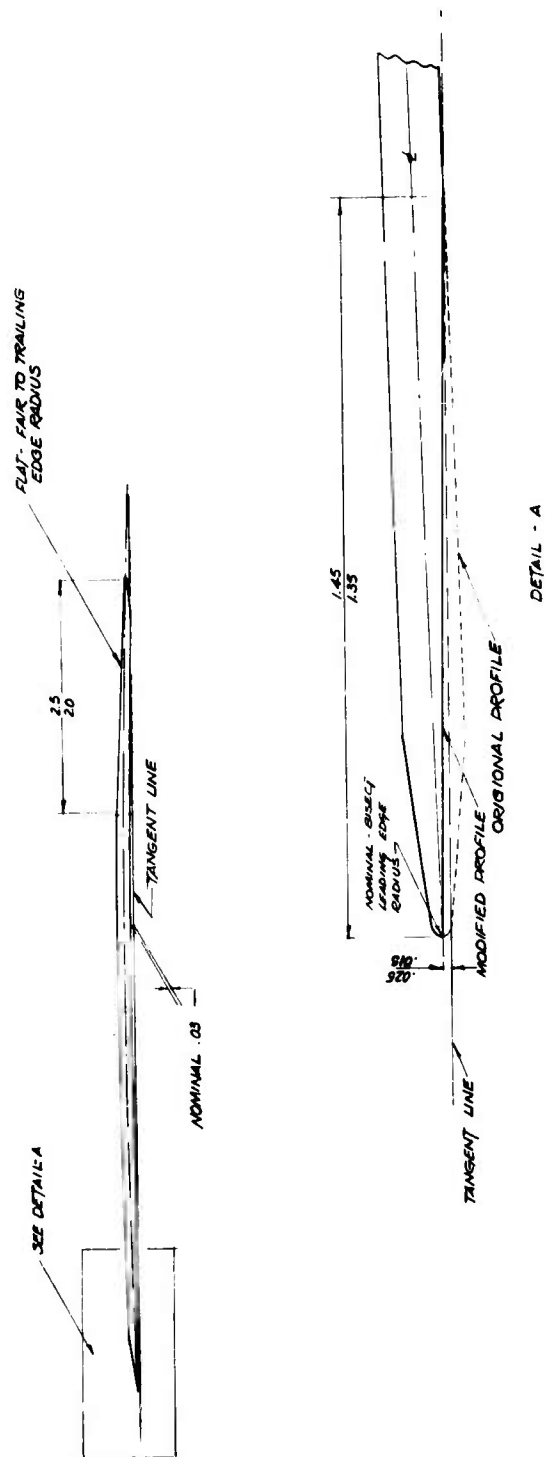


Figure 156. Modified Medium Length Supersonic Stator Vane.

speeds. The design Mach number entering the stators, with a 13.0-inch rotor diameter, is 1.28. The objective static pressure rise coefficient (\bar{C}_p) is 0.45, and the objective loss coefficient (\bar{w}) is 0.14 at the design inlet Mach number. This objective yields an exit Mach number of about 0.7, which is the design inlet Mach number for the subsonic stators.

At the supersonic stator design inlet Mach number of 1.28, the run 8 test configuration yields \bar{C}_p of 0.46 and \bar{w} of 0.144. This configuration (medium length, solidity of 1.9, contraction ratio of 1.02 and area ratio of 1.23) was selected as the best supersonic stator configuration to be used in the tandem cascade tests and as the basis for stator design in the high-speed radial outflow compressor.

Subsonic Stators

The design inlet Mach number of the subsonic stators is 0.7, and the design inlet flow angle is 75 degrees. The subsonic stators are intended to reduce the Mach number from 0.7 to 0.4. The objective pressure rise coefficient (\bar{C}_p) is 0.60, and the objective pressure loss coefficient (\bar{w}) is 0.08.

The subsonic stators of three different lengths, as shown in Figure 133, all having a nominal camber of 11 degrees and an area ratio of 1.23, were tested over the Mach number range of 0.5 to 0.90 at the design inlet angle of 75 degrees. These results are presented in Figure 157 and show that the medium length vanes had the minimum loss at Mach numbers of 0.5 to 0.8.

At the design inlet Mach number of 0.7, these same stator configurations were tested at inlet angles of 74 degrees, 75 degrees, and 76.5 degrees. These data, presented in Figure 158, show that stator performance is best at the lowest inlet angle and also that the medium length vanes are less sensitive to inlet angle change.

To establish the optimum camber or area ratio, the medium length stator blades were recambered to produce area ratios of 1.16 and 1.29 which are below and above the nominal value of 1.23. The blades were first increased in camber to produce an area ratio of 1.29, identified as run 13 in Figure 159. This setup yielded about the same performance at Mach numbers of 0.5 and 0.6 but showed increasing losses at higher Mach numbers. The camber was then decreased to produce an area ratio of 1.16. The test results are identified as run 14 and indicate that significantly higher losses were obtained with some reduction in static pressure rise coefficient.

Results of these tests indicate that the original design of the subsonic medium length stator was a very close approach to the optimum. At the design inlet Mach number of 0.7, the test results yielded values of loss coefficient and pressure rise coefficient of 0.066 and 0.652,

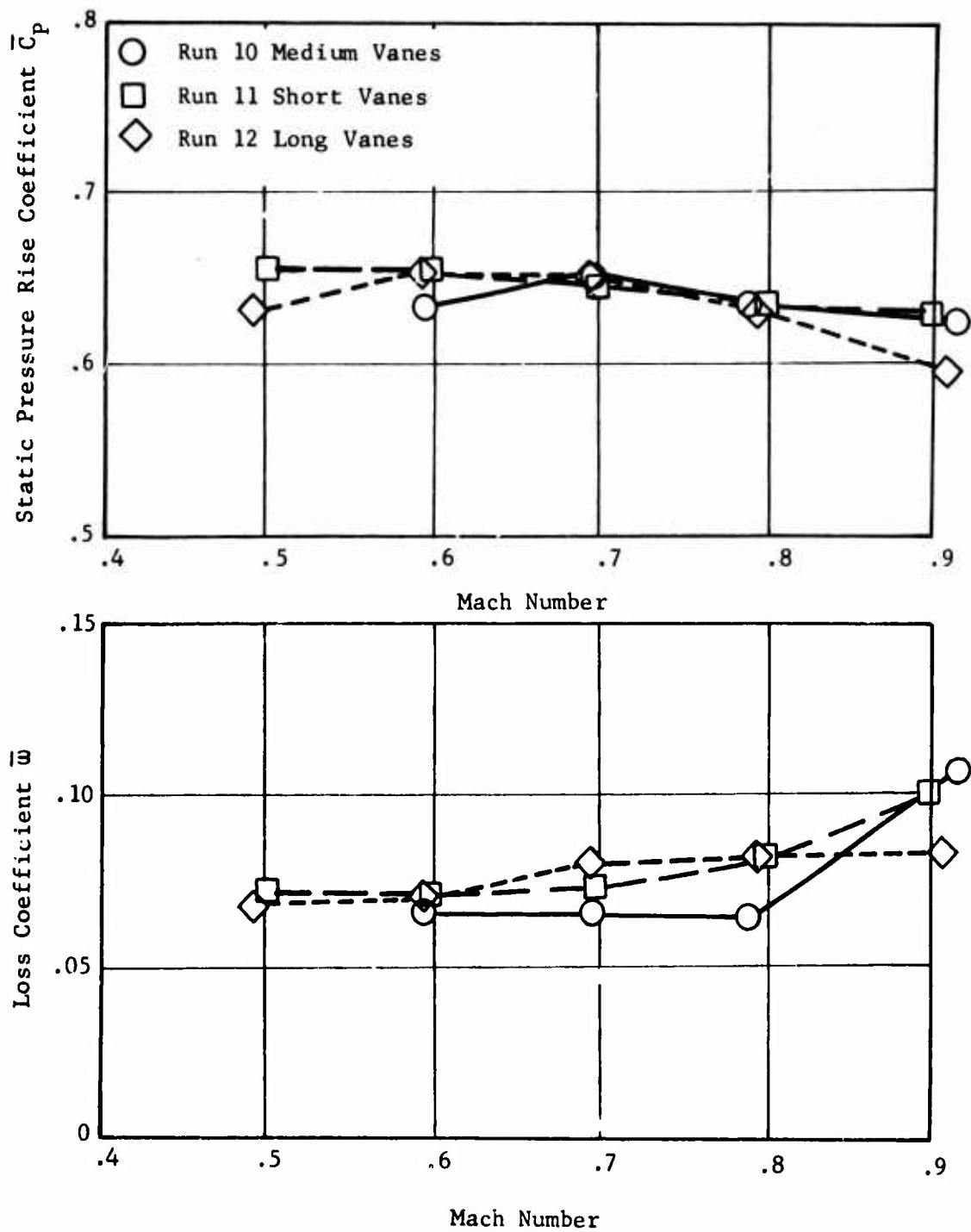


Figure 157. Performance of Subsonic Stator Vanes of Three Different Lengths at Design Inlet Angle of 75° .

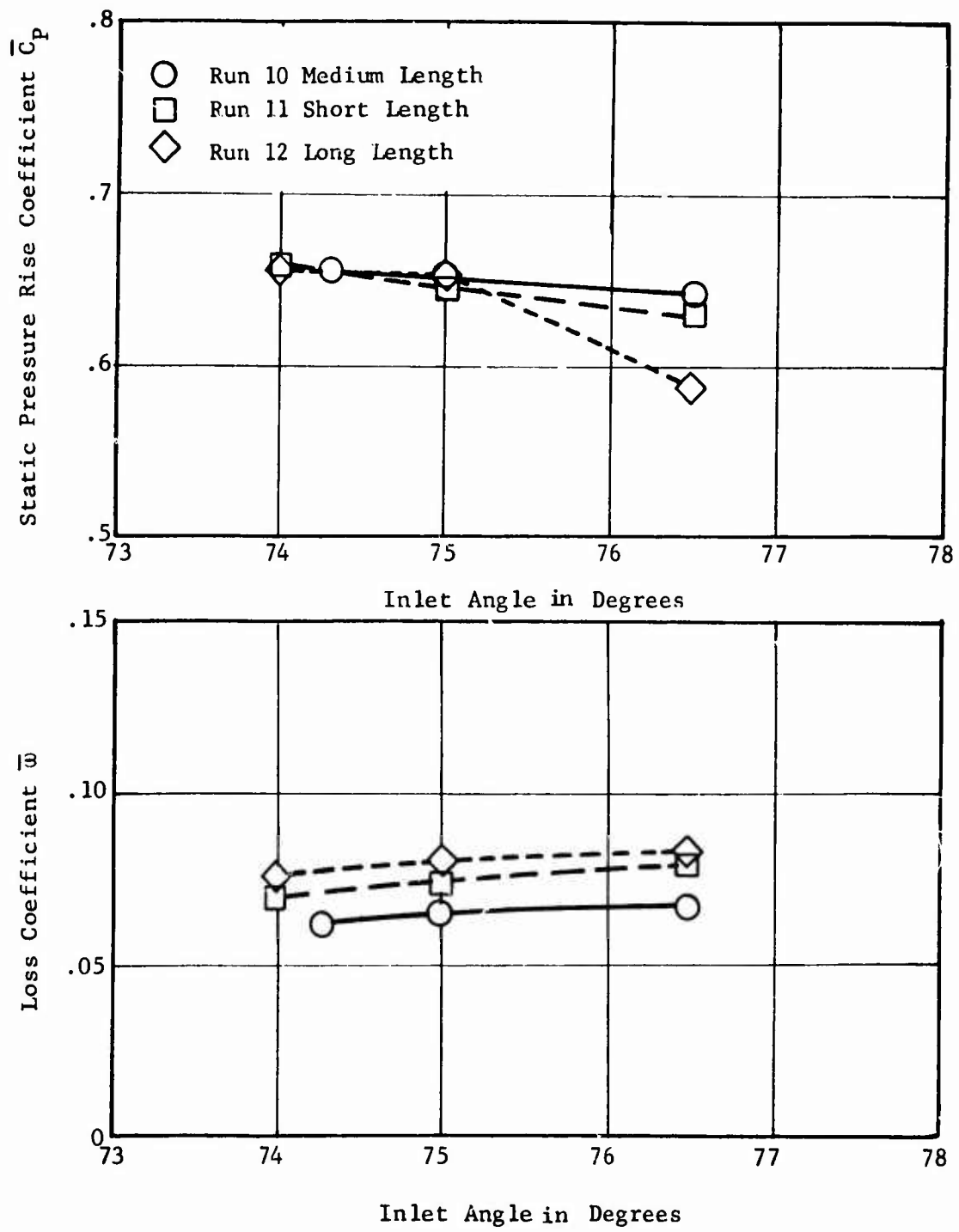


Figure 158. Effect of Inlet Angle Variation on Performance of Subsonic Stators at Design Inlet Mach Number of 0.7.

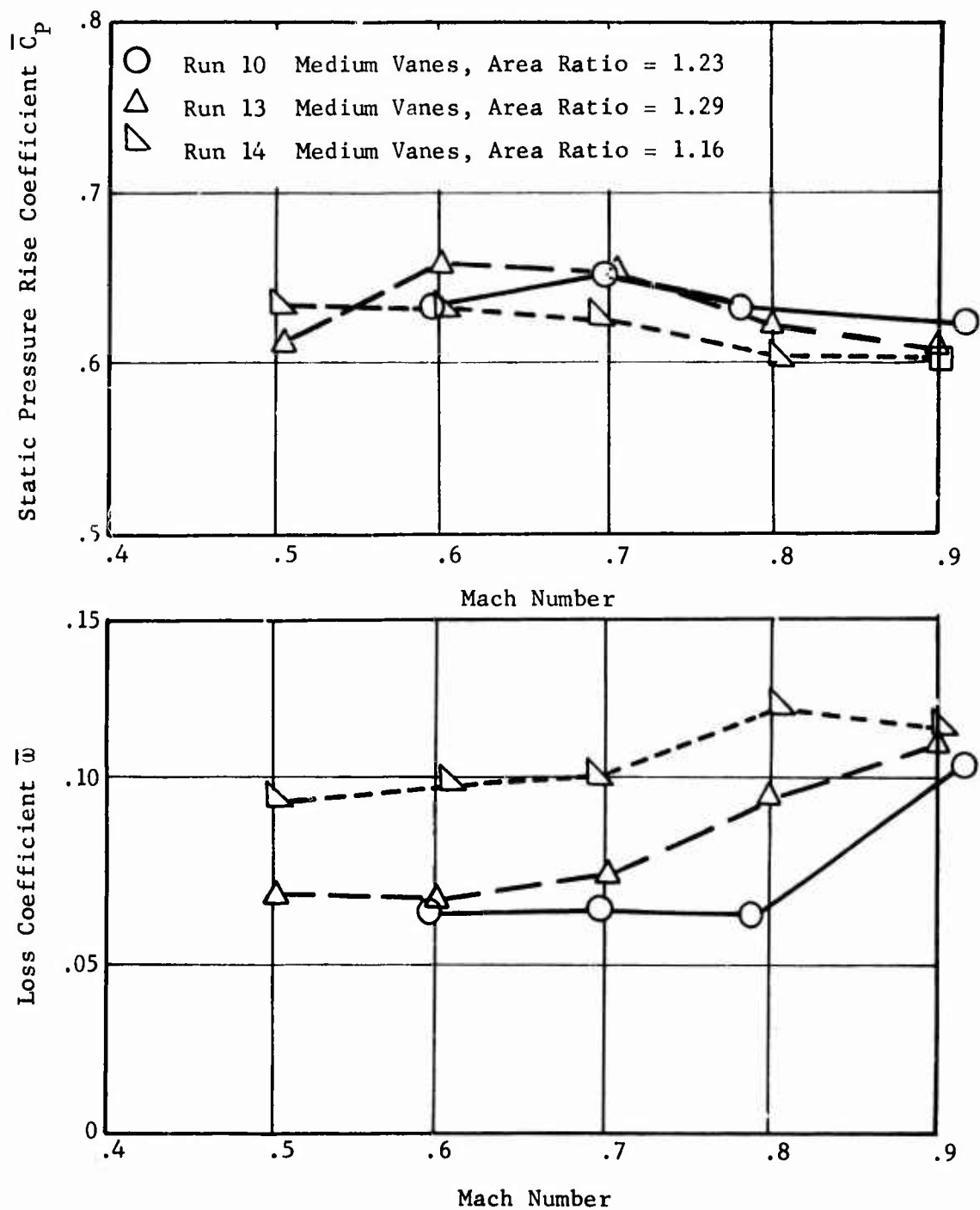


Figure 159. Effect of Area Ratio on Performance of Medium Length Subsonic Stators at Design Inlet Angle of 75° .

respectively. The objective values of 0.08 and 0.60 are exceeded. Therefore, this configuration was selected for tandem cascade testing downstream of the optimum supersonic stators previously identified and as the basis for subsonic stator design of the high-speed compressor.

Tandem Cascade

The purpose of the tandem cascade testing was to identify the best position of the subsonic stators relative to the supersonic stators. The subsonic stator blades were placed midway between the wakes of the supersonic stators to avoid regions of low energy flow. A total of four spacings between blade rows was tested. The configuration identified as nominal spacing was 2 inches in the radial direction between the trailing edge of the supersonic stators and the leading edge of the subsonic stators. Spacing in the direction of airflow was about 8 inches. All other configurations were identified relative to the nominal setting.

Three runs of tandem cascade testing were required to solve operational problems. Useful data were recorded, starting with run 4 when the subsonic stators were 1.248 inches closer to the supersonic stators in the flow direction than at the nominal setting. Data for the following test runs are presented in Figure 160.

<u>Run</u>	<u>Spacing</u>
4,5	+1.248
6	-0.624
7	0 (Nominal)
8	+0.624

Run 8 configuration has the lowest loss coefficients over the entire Mach number range, with a static pressure rise coefficient of about 0.60. The minimum loss coefficient at 1.3 Mach number observed during the test was 0.212 at a static pressure rise coefficient of 0.612. This data point, as reduced by the computer program, gave a minimum loss coefficient of 0.244 at a static pressure rise coefficient of 0.611. Upon further review, it has been determined that the values as reduced by the computer are correct, and the in-test values were only estimates used as a guide by testing personnel.

The effects of throttling the tandem cascades at constant inlet Mach number and inlet angle are shown in Figure 161. An inlet Mach number of 1.3 and an inlet angle of 80 degrees were the conditions selected for this comparison. As the cascade is throttled and static pressure rise coefficient increases, the loss coefficient decreases until a minimum value is reached. Some increase of the pressure rise coefficient occurs after the point of minimum loss coefficient is achieved. No significant changes to the upstream static pressure distributions in the cascade side

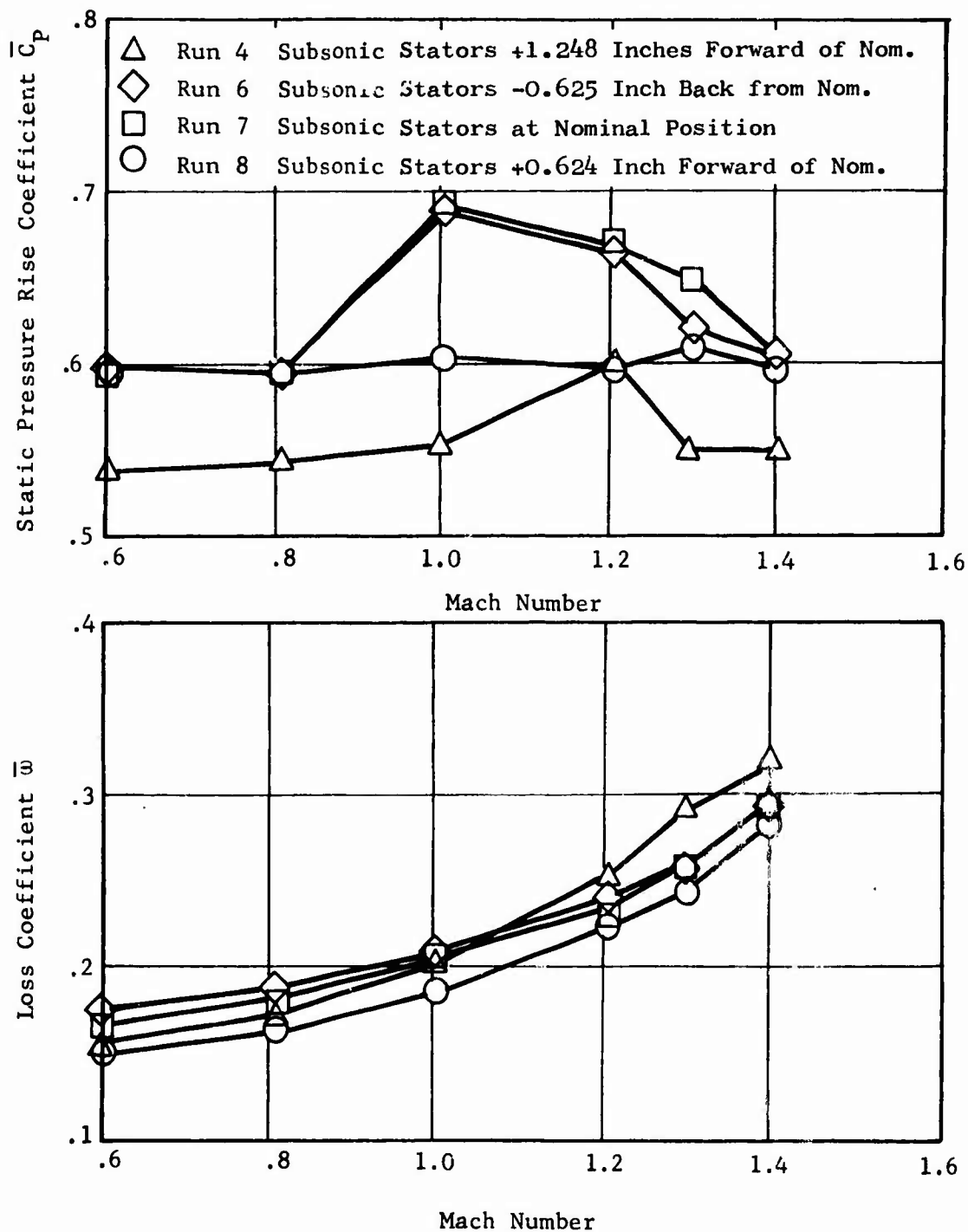


Figure 160. Effect of Spacing Between Supersonic and Subsonic Stators in Tandem Cascade Arrangement at Design Inlet Angle of 80° .

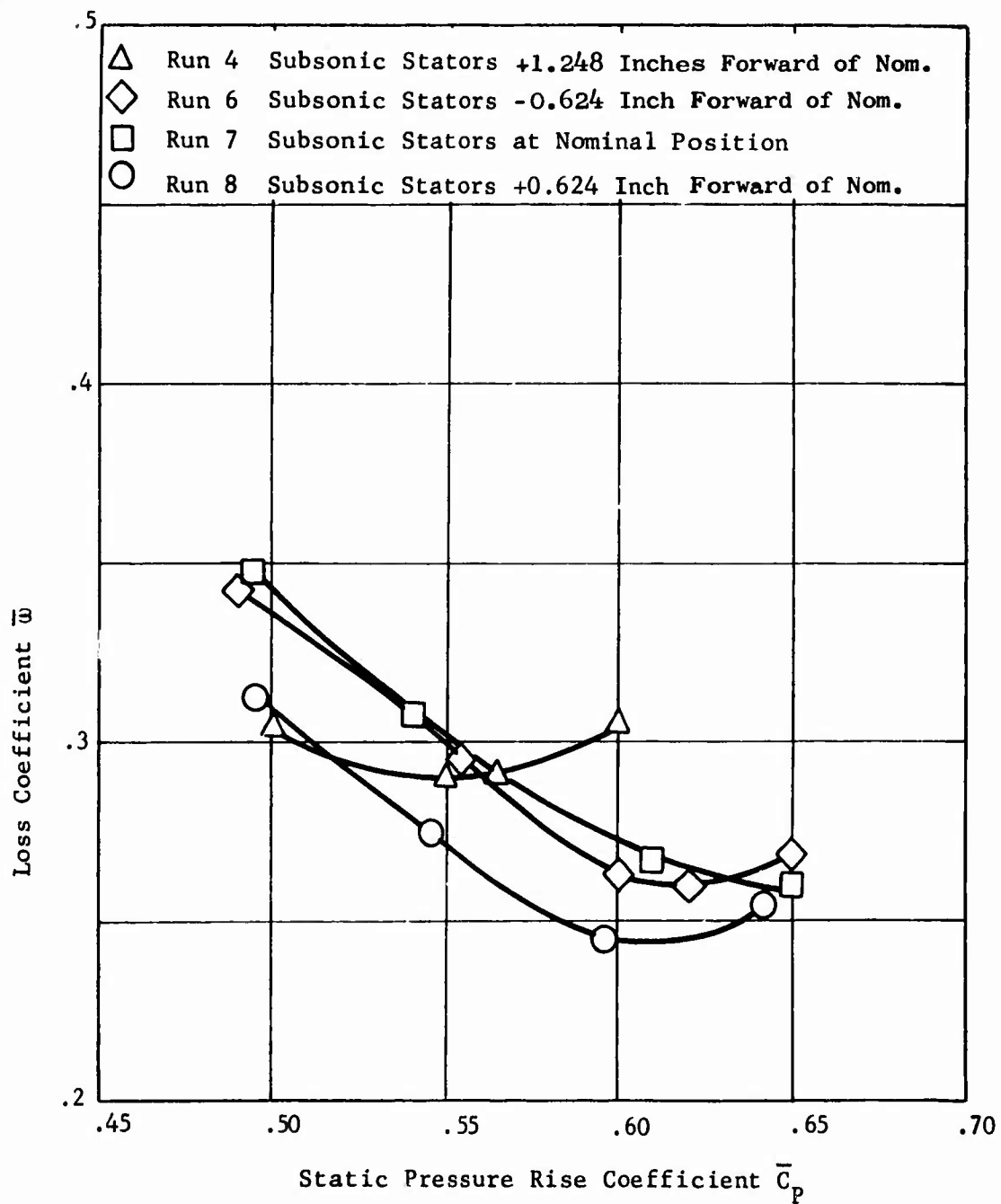


Figure 161. Effects of Throttling on Performance of Tandem Supersonic and Subsonic Stators at Inlet Mach Number of 1.3 and Inlet Angle of 80° .

walls were observed at the points tested, although the cascades were performing in a transonic manner with a normal shock upstream of the leading edges of each supersonic blade.

CONCLUSIONS

The supersonic stator performance originally anticipated was not fully achieved because of the extremely high (80 degrees) inlet flow angle and Mach number (1.4) required of the radial outflow compressor.

When the exit radius of the vaneless rotating diffuser was extended from 6.00 to 6.50 inches, the design Mach number entering the supersonic stator was reduced from 1.40 to 1.28 and the flow angle was increased from 80 to 84 degrees. Diffuser wall boundary layers will increase the radial velocity and lower the inlet angle to values near 80 degrees. Since small changes in inlet angle were found to have little effect on stator performance, this design change reduces the difficulty of achieving satisfactory supersonic stator and overall high-speed compressor performance.

Supersonic stator performance objectives were established at the design inlet Mach number of 1.28 to be a static pressure rise coefficient of 0.45 at a total pressure loss coefficient of 0.14. The optimum test configuration yielded values of 0.46 and 0.144, respectively, which is a very close approach to the objective.

Subsonic stator objectives at the design inlet Mach number of 0.7 were a static pressure rise coefficient of 0.60 at a total pressure loss coefficient of 0.08 yielding an exit Mach number of about 0.40. The optimum subsonic stator configuration produced values of 0.652 and 0.066, respectively, exceeding the objectives.

The objectives of the tandem cascade arrangement of the optimum supersonic and subsonic stators were a static pressure rise coefficient of 0.60 at a total pressure loss coefficient of 0.20. Test results at the optimum spacing between the supersonic and subsonic stators were a static pressure rise coefficient of 0.611 at a total pressure loss coefficient of 0.244. The loss coefficient objective was approached and the pressure coefficient objective exceeded.

SCROLL COLLECTOR, DIFFUSER, AND ELBOW

GENERAL

The scroll collector serves the purpose of collecting the flow coming out of the subsonic stators in the radial outflow compressor and delivering the flow to two discharge ducts. Each discharge duct contains a diffuser and a 90-degree turning elbow to conduct the flow from the scroll collector into ducts leading to the regenerator or combustor.

The Mach number of the flow leaving the stators is between 0.4 and 0.6. The tangential component of the exit velocity is much larger than the radial component. The purpose of the scroll collector is to provide a means of collecting the flow into small ducts and at the same time recovering most of the tangential velocity remaining in the airflow.

During Phase I of the radial outflow compressor program, a scroll collector, diffuser, and elbow assembly was designed, built, and tested, using the low-speed radial outflow compressor. Variations to the scroll splitter leading edge were investigated to find the best configuration for the range of flow coefficients encountered. Total and static pressure measurements were taken to provide information as to the performance characteristics of this model which will be valuable to the design of similar components for the high-speed machine.

DESCRIPTION OF TEST ITEM

The scroll collector, transition diffuser, and elbow assembly are shown mounted on the low-speed radial outflow compressor test rig in Figure 162.

The scroll collector (Figure 163) was designed with a linear increase in cross-sectional area from the splitter to the circular discharge section. The area of the scroll sections was selected so that the same tangential velocity existing at the inner diameter of the scroll would be maintained through the 180-degree arc from the splitter to the discharge. Three splitter profiles were designed and tested in order to evaluate the effects of relatively sharp and relatively blunt splitter leading edge radii on performance. Plexiglas windows were installed in the scroll exit to permit observation of tufts in the region of the splitters. The quick disconnect sections following the scroll exit permitted rapid exchange of the splitter leading edge shapes.

Following the circular discharge section on one of the scroll collector arms, an instrumentation spool piece was installed as shown in Figure 164. This piece was held with quick release clamps and could be rotated to a full circle to permit complete survey measurements of the exit duct.

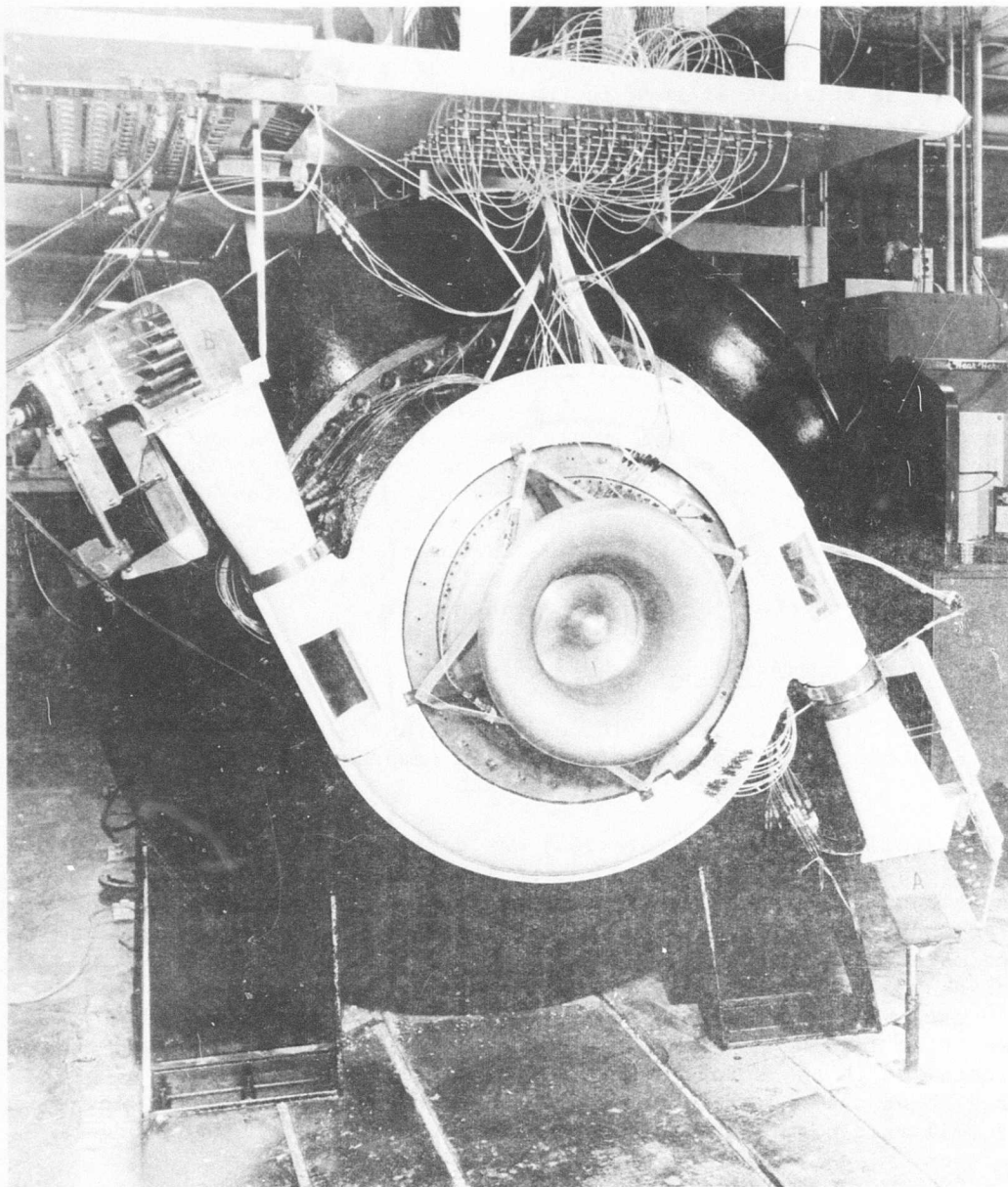


Figure 162. Installation of Scroll Collector, Transition Diffuser and Elbow on Low-Speed Radial Outflow Compressor.

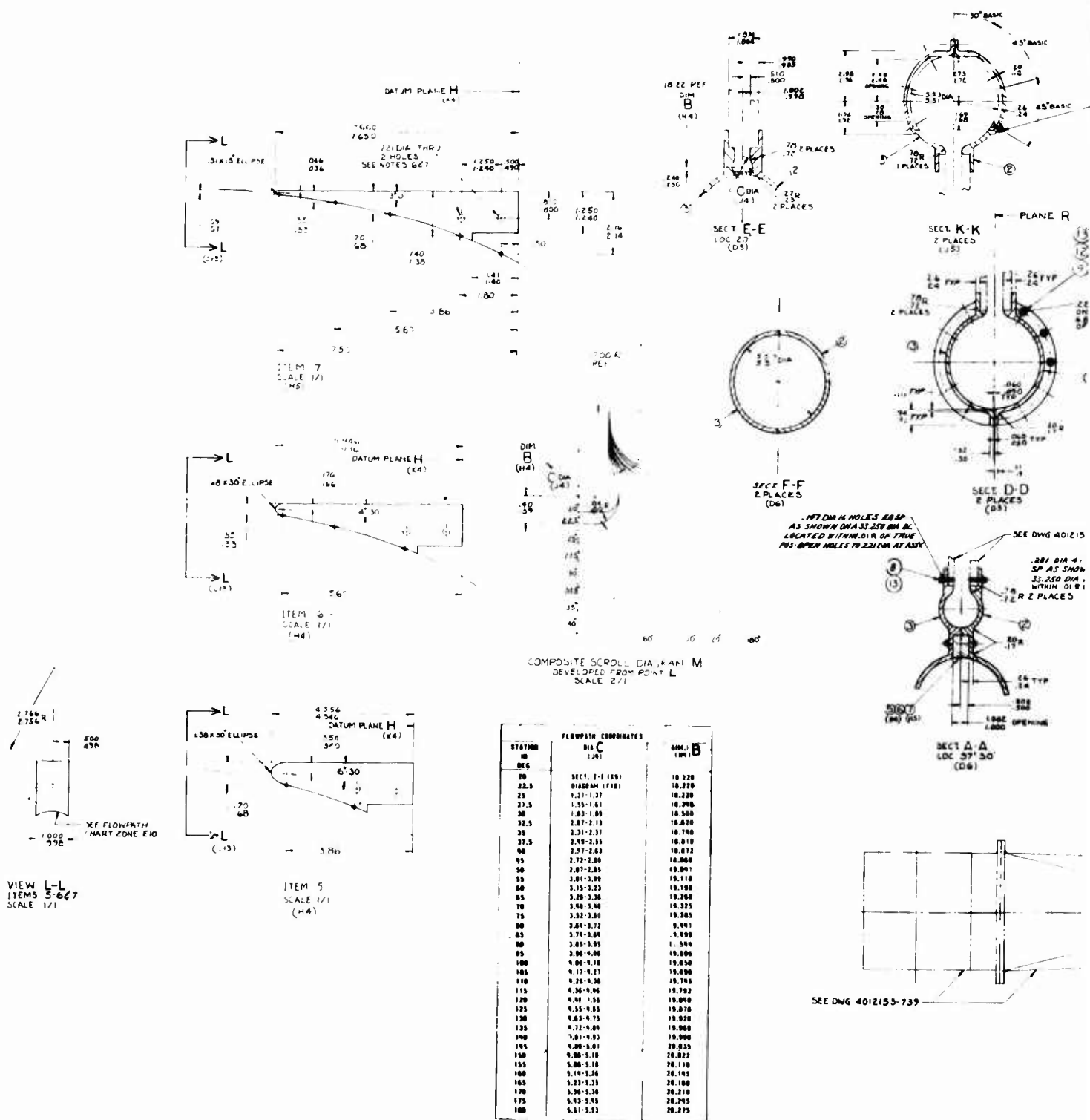
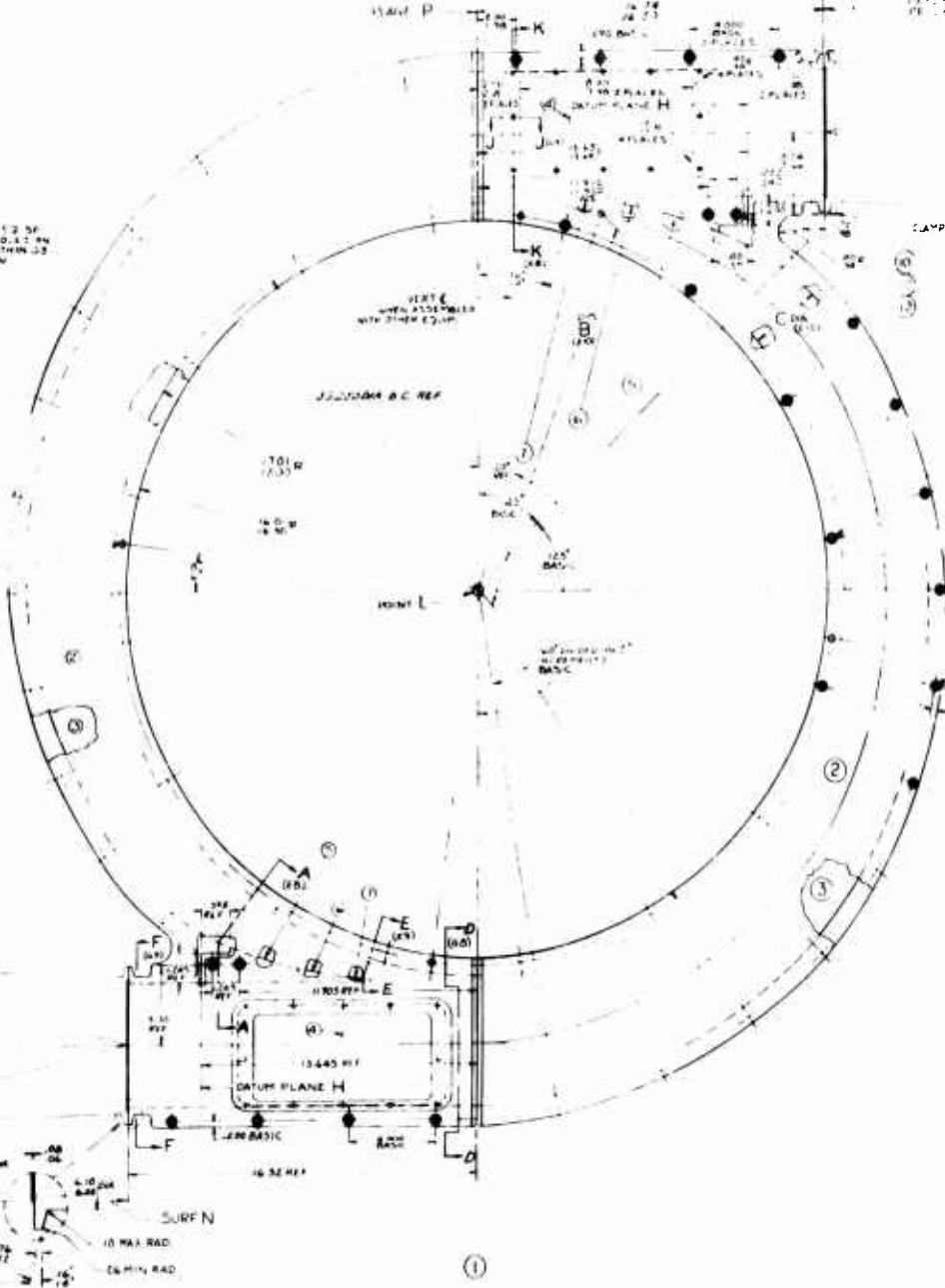
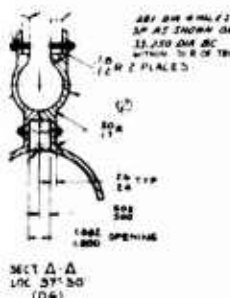
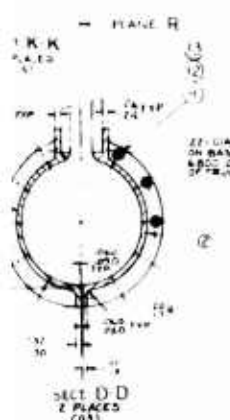


Figure 163. Scroll Collector Assembly, Low-Speed ROC.

A

PAGE		DESCRIPTION OF WORK	DATE		TIME		BY	
NO.	REV.		1	2	3	4	5	6
1		REVISIONS: 1. REVISION 1. REVISION 1.	12	1	1	1	1	1
2		2. REVISION 2. REVISION 2. REVISION 2.	12	2	1	1	1	1
3		3. REVISION 3. REVISION 3. REVISION 3.	12	3	1	1	1	1
4		4. REVISION 4. REVISION 4. REVISION 4.	12	4	1	1	1	1
5		5. REVISION 5. REVISION 5. REVISION 5.	12	5	1	1	1	1
6		6. REVISION 6. REVISION 6. REVISION 6.	12	6	1	1	1	1
7		7. REVISION 7. REVISION 7. REVISION 7.	12	7	1	1	1	1
8		8. REVISION 8. REVISION 8. REVISION 8.	12	8	1	1	1	1
9		9. REVISION 9. REVISION 9. REVISION 9.	12	9	1	1	1	1
10		10. REVISION 10. REVISION 10. REVISION 10.	12	10	1	1	1	1
11		11. REVISION 11. REVISION 11. REVISION 11.	12	11	1	1	1	1
12		12. REVISION 12. REVISION 12. REVISION 12.	12	12	1	1	1	1
13		13. REVISION 13. REVISION 13. REVISION 13.	12	13	1	1	1	1
14		14. REVISION 14. REVISION 14. REVISION 14.	12	14	1	1	1	1
15		15. REVISION 15. REVISION 15. REVISION 15.	12	15	1	1	1	1
16		16. REVISION 16. REVISION 16. REVISION 16.	12	16	1	1	1	1
17		17. REVISION 17. REVISION 17. REVISION 17.	12	17	1	1	1	1
18		18. REVISION 18. REVISION 18. REVISION 18.	12	18	1	1	1	1
19		19. REVISION 19. REVISION 19. REVISION 19.	12	19	1	1	1	1
20		20. REVISION 20. REVISION 20. REVISION 20.	12	20	1	1	1	1
21		21. REVISION 21. REVISION 21. REVISION 21.	12	21	1	1	1	1
22		22. REVISION 22. REVISION 22. REVISION 22.	12	22	1	1	1	1
23		23. REVISION 23. REVISION 23. REVISION 23.	12	23	1	1	1	1
24		24. REVISION 24. REVISION 24. REVISION 24.	12	24	1	1	1	1
25		25. REVISION 25. REVISION 25. REVISION 25.	12	25	1	1	1	1
26		26. REVISION 26. REVISION 26. REVISION 26.	12	26	1	1	1	1
27		27. REVISION 27. REVISION 27. REVISION 27.	12	27	1	1	1	1
28		28. REVISION 28. REVISION 28. REVISION 28.	12	28	1	1	1	1
29		29. REVISION 29. REVISION 29. REVISION 29.	12	29	1	1	1	1
30		30. REVISION 30. REVISION 30. REVISION 30.	12	30	1	1	1	1
31		31. REVISION 31. REVISION 31. REVISION 31.	12	31	1	1	1	1
32		32. REVISION 32. REVISION 32. REVISION 32.	12	32	1	1	1	1
33		33. REVISION 33. REVISION 33. REVISION 33.	12	33	1	1	1	1
34		34. REVISION 34. REVISION 34. REVISION 34.	12	34	1	1	1	1
35		35. REVISION 35. REVISION 35. REVISION 35.	1					

DICAL SYMBOL A
 TO FORMING SIGNA
 BLOCK
 DR 158-758



CAMP 4012153 739 TEMPS

SEE DWG 4012153

1.167 DIA 16 HOLES EQ SP
AS SHOWN IN 133.250 DIA BC
LOCATED 1.75 IN 4.0 R OF TRUE POS.
ENLARG HOLES TO 2.21 DIA AT ALL X

221 DIA 2 HOLES EQ SP
AS SHOWN LOCATED WITHIN
02 V OF TRUE POS
290 FIP 10 PLACES
BASIC

- 13 PLANE(P15) & SURF N(14) MUST BE PARALLEL
Q SQUARE WITH PLANE R (N8) WITHIN 0.1 IN/IN
- 12 MATING FLANGES ON PLANES P1 R REQUIRE
FLUSH FR ALL AROUND AT ASSY
- 11 MATCH DR ALL MATING HOLES TOGETHER
WHEN POSSIBLE
- 10 THIS ASSEMBLY TO BE FASTENED TO
PART NO 901535 1540
- 9 FASTENING DEVICES MATERIAL MUST CONFORM TO
AMS 5610 AMS 5640 3R AMS 5640
- 8 MINIMUM OF ITEMS 5 6 7 8 9 REQUIRES A SLIP FIT
ASSEMBLY DISTORTION IN ITEMS 2 3 AFTER F
- 7 ITEMS 5 6 7 8 MUST BE INTERCHANGABLE AT
EITHER OF 2 LOCATIONS WHEN ASSEMBLED
- 6 1/2 DIA HOLES IN ITEMS 5 6 7 TO BE MATCH
DR AT ASSY WITH ITEMS 2 3
- 5 PART MUST CONFORM TO MIL R 9950
TYPE I
- 4 REF ITEM 7 FOR DIMENSIONS NOT SHOWN IN ITEMS 3
- 3 ALL PARTS SHALL BE IDENTICAL
- 2 PROCEDURE FOR FIBERGLASS APPLICATION
AT EXPOSED SURFACE COT SHAEL 030
- 1 1 LAMINATE WITH FIBERGLASS CLOTH
2 LAMINATED WITH 1/8" GLASS CLOTH
3 BUILD UP WITH FIBERGLASS WITH 2000S 140 IN THK
4 FINISH WITH 1 LAMINATE 1/2 GLASS CLOTH
5 MUST CONFORM TO S1-11510 (INTERPRETATION OF DOWI
N1507942A (TORQUE)

VIEW G
SCALE 1/1

B

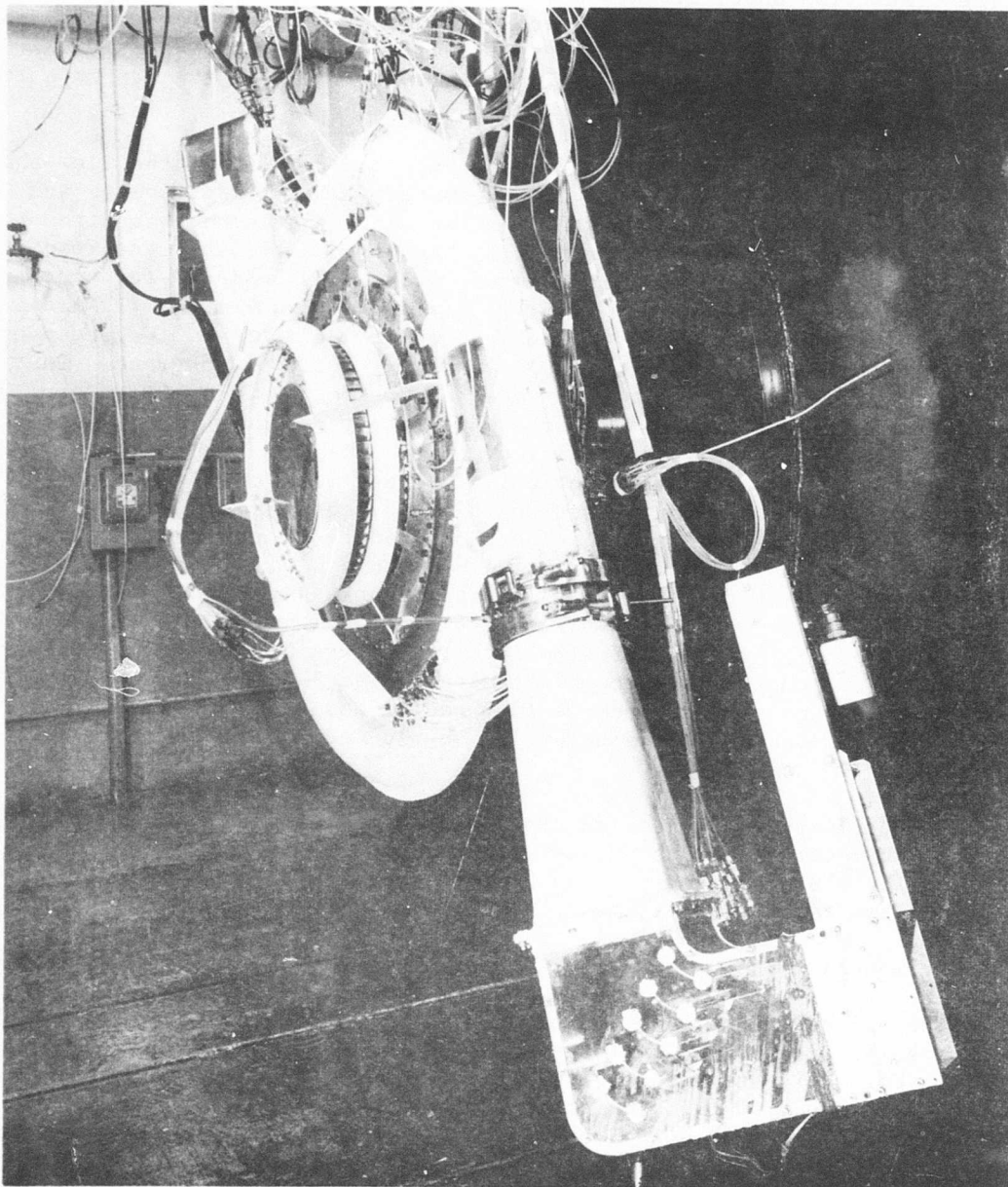


Figure 164. View of Instrumentation Spool Piece at Discharge of Scroll Exit Arm, Low-Speed Radial Outflow Compressor.

The transition duct, elbow, and throttle system are shown in Figure 165. A transition duct attaches to each circular discharge arm of the scroll collector and includes a diffuser of small area ratio. The inlet diameter of the transition section was 5.53 inches, and the square exit section was 6.3 inches on each side.

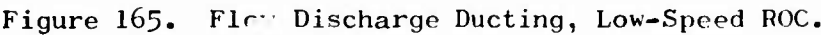
A 90-degree elbow was employed to simulate the turning of the flow that is likely to occur in an engine between the compressor discharge and the combustor. The turning vanes in the elbow section are required to turn the flow through 90 degrees with the cascade of vanes inclined at 45 degrees. An existing turning vane, previously designed for another purpose, was found to match these requirements very nearly. It had a design turning angle of 90 degrees, an inlet angle of 44.3 degrees, and an exit angle (measured from the cascade axis) of 45.7 degrees. Test results had indicated that this vane had good efficiency but under-turned the flow by about 4 degrees when set at design incidence angle. This vane, with a slightly modified camber line, was used for the turning vanes in the elbow section. The vane mean line was given 4 degrees more camber and was set to maintain the same leading edge incidence angle. The same thickness distribution was then applied to this new camber line. The solidity of this new design was also reduced from 2.26 to 2.00, but this small change should not affect the turning angle or efficiency. The resulting vane profile is shown in Figure 166. For reasons of simplicity, the turning vanes were constructed of constant section sheet metal. The leading and trailing edge wedges had a 0.015-inch maximum radius nose and the vanes incorporated 94.2 degrees of camber, which should result in 90 degrees of turning.

The throttle system consisted of a series of flat plates actuated by electric motors. The throttles were operated separately so that the same exit static pressure could be impressed on the compressor in each of the two discharge systems.

Experimental Procedure

The scroll collector, transition duct, elbow, and throttle system are shown assembled on the low-speed radial outflow compressor in Figure 162. For the test runs made for the specific purpose of investigating the performance of these components, the low-speed model incorporated the axial flow inlet guide vane system (Figure 167) and the redesigned stators in the stationary diffuser just upstream of the scroll collector. An axial flow IGV setting of zero degrees and an optimum stator angle, determined from earlier tests, of 66 degrees were used.

Three scroll splitter leading edge configurations were investigated. For each scroll splitter configuration, nine throttle valve settings, representing a range of flow coefficients from about 0.68 to 1.65, were used. At each throttle valve setting, data points were taken at rotor speed settings of 1400, 1600, and 1800 rpm. For each splitter



A

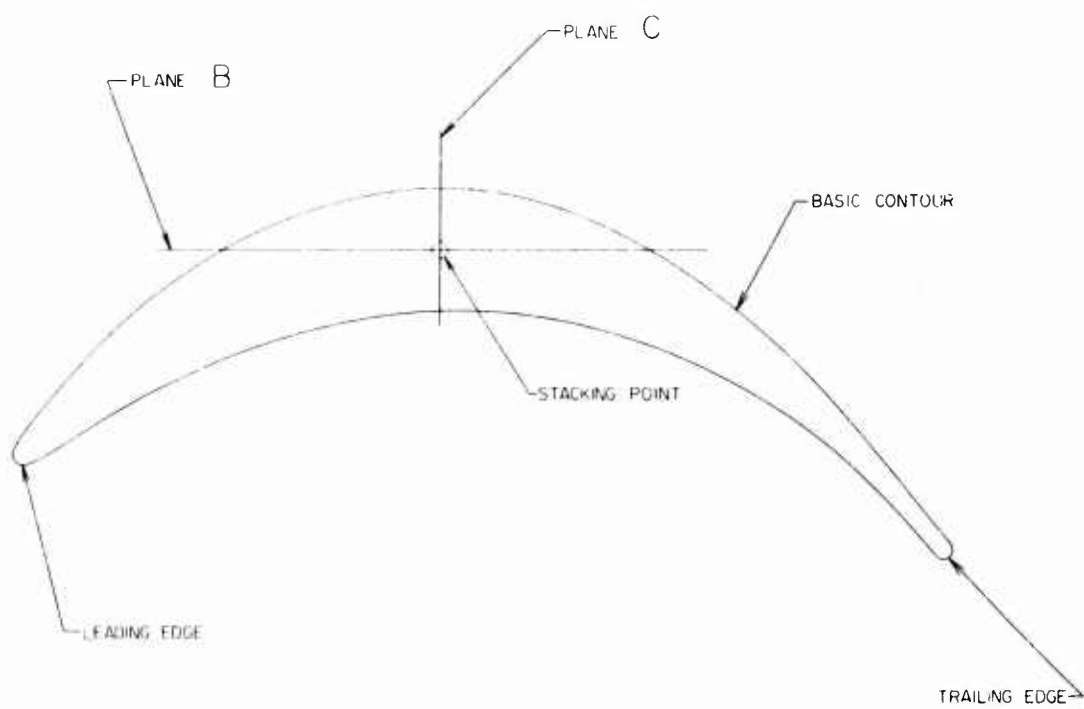


Figure 166. Elbow Turning Vane Profile.

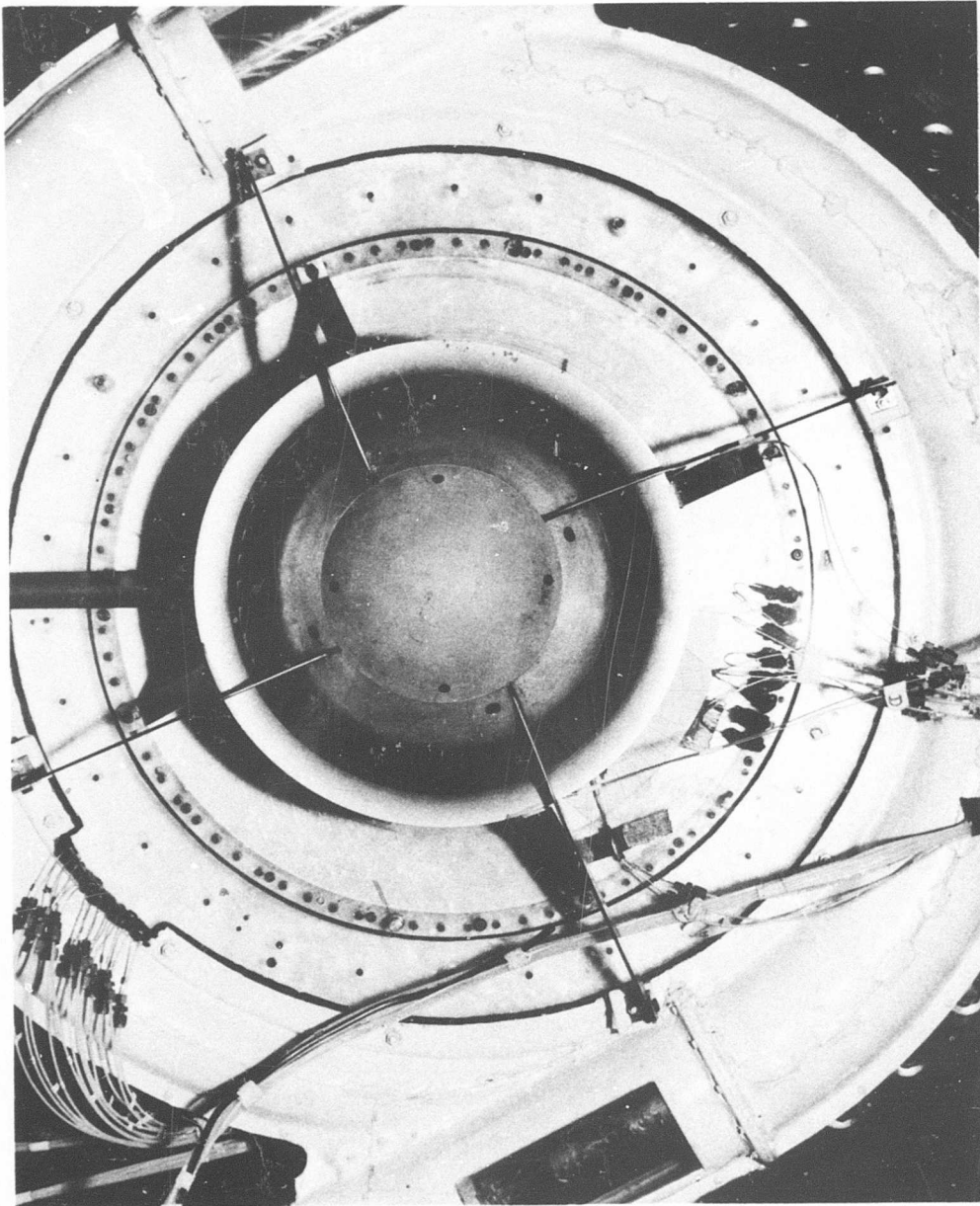


Figure 167. Low-Speed Radial Outflow Compressor with Axial Flow Inlet Installed.

configuration, total pressure surveys were taken at the discharge of one scroll exit arm and at the discharge of one elbow. This was done at all three rotor speeds at the one throttle position corresponding to design flow coefficient. A test run summary is presented in Table XIII.

The instrumentation used during this investigation is described in Table XIV. The location of the static pressure taps in the scroll collector and the transition diffuser sections A and B are shown in Figure 168. Figure 169 is a sketch of the total pressure rake which is located in the instrumentation spool at the discharge of the scroll exit arm that discharges into the transition diffuser section A. The rake was constructed so that each total pressure probe was located on the centers of equal area, permitting an area weighted average pressure to be calculated directly. An initial survey position zero is shown aligned with the centerline axis of the compressor. The compressor orientation is indicated in the lower right-hand corner of the figure. The rake (along with the spool piece to which it is attached) is rotated counterclockwise as shown by the angle θ , in increments of 30 degrees. Six rake positions are required to accomplish the complete survey.

Another total pressure survey was taken downstream of the turning vanes in one elbow section. The measuring section is square, and the rake used consisted of 10 probes equally spaced (see Figure 170). Five rake positions were used for the survey at this location.

Experimental Results

For each scroll splitter configuration, the following data are presented:

1. Pressure loss coefficient versus rake element position
2. Scroll exit arm loss coefficient map
3. Static pressure rise coefficient versus scroll collector circumferential location

The above results (Figures 171 through 179) describe the performance of the three scroll splitter configurations at the design flow coefficient and at a compressor rotor speed of 1800 rpm. Over the complete range of flow coefficient investigated for scroll splitter 1, the static pressure profile contained in 180 degrees of the scroll collector is shown in Figure 180. Figure 181 is a presentation of static pressure rise coefficient throughout the scroll collector.

Pressure loss coefficient data, based on the total pressure survey downstream of the elbow turning vanes, are presented in Figures 182 through 184.

INTERPRETATION OF TEST RESULTS

The results obtained from the scroll exit arm total pressure survey are presented as pressure loss coefficient versus rake element position in

Figures 171 through 173. For comparison purposes, the profiles obtained from all six rake positions are plotted on the same coordinate axis. The faired profile lines should intersect at the same value of pressure loss coefficient at the center of the passage. The reason that this does not happen in these data is attributed to the test procedure used to obtain these profiles. After data were obtained at each profile position, the machine had to be shut down in order to make a new setting. The inability to reset the identical flow conditions in the machine at each succeeding profile position causes the data scatter. The scatter does not seriously affect the results, especially when evaluating the relative merits of the three scroll splitter configurations. For better visualization of the losses as measured in the exit arm duct, a total pressure loss coefficient map was prepared for each splitter configuration (Figures 174 through 176). The static pressure rise coefficient as a function of circumferential position in the scroll collector (Figures 177 through 179) aids in the selection of the proper flow splitter and defines the characteristics of the scroll collector as well.

The performance of the elbow turning vanes is described in terms of loss coefficient data based on the pressure survey taken downstream of the turning vanes (Figures 182 through 184). The upstream dynamic head used in these loss coefficient calculations is based on the scroll exit arm total pressure and the transition diffuser exit static pressure (at T_3 in Figure 168).

EVALUATION

Scroll Collector and Scroll Splitter

The exit arm pressure loss coefficient map for flow splitter 1 (Figure 174) demonstrates that the minimum loss coefficient equal to 0.13 is located slightly above the flow splitter itself. Boundary layer is observed in all circumferential locations, with particularly higher losses in the first quadrant of the map. The high loss region propagates into the center of the passage. A confined lower loss region is located in the second quadrant, with uniform boundary layer against the wall. This can be attributed to the particularly better flow issuing from the front side of the nonrotating diffuser. The map is generally symmetrical about the vertical axis, with all lower loss regions in the third and fourth quadrants. The static pressure rise coefficient map (Figure 177) shows an abrupt expansion of the flow immediately downstream of the flow splitter nose. This expansion is then followed by a gradual contraction of the flow which returns the static pressure to its original reading.

For flow splitter 2, the exit arm pressure loss coefficient map (Figure 175) again indicates higher losses in the first quadrant which also propagate to the center of the passage. Lower losses are again confined to the third and fourth quadrants with the minimum loss of 0.15 indicated in the third quadrant. General uniform boundary layer

exists around the circumference and diminishes in loss value as the flow splitter region is approached. The generally symmetrical conditions about the vertical axis exist with this configuration also. Figure 178 indicates the same general static pressure distribution as was shown for flow splitter 1.

The exit arm pressure loss coefficient profiles for flow splitter 3 shown in Figure 173 indicate a very consistent set of total pressure readings. All faired lines approach a unique pressure loss coefficient reading of approximately 0.35 at the center of the passage. The exit arm loss coefficient map (Figure 176) indicates a deepening boundary layer in quadrants two and three, with the same general flow characteristics as were observed with flow splitter 1. The minimum loss coefficient is 0.16 and is again located immediately above the flow splitter with little indication of boundary layer on its upper side. A minimum pressure loss area is again observed in the second quadrant of the map. The same general static pressure distribution exists in the scroll collector except for the initial values which are somewhat lower (see Figure 179).

Figure 180 shows the scroll static pressure profile contained in 180 degrees of the scroll collector. This plot indicates that, throughout the flow coefficient range, the static pressure rise in the initial part of the duct is always returned to its initial value at or near 180 degrees of circumference. The static pressure then continues to drop slightly through the exit arm.

With the static pressure rise coefficient variation with circumferential location, shown in Figure 181 at design flow coefficient, there is an indicated rapid diffusion of the flow just downstream of the flow splitter lip, followed by a gradual increase in flow velocity through the rest of the scroll collector passage. The rapid diffusion is believed to be caused by the flow splitter lip orientation with respect to the entering flow streamlines. The lip appears to be operating at a positive angle of attack, and the inherent upwash caused by the leading edge induces additional flow in the exit arm in this region. The result is a flow-starved area just downstream of the splitter lip as indicated by the area of rapid diffusion. The area variation designed into the scroll collector passage was intended to maintain constant velocity. The influence of the flow splitter in producing the flow-starved region at the passage entrance does affect the velocity profile. The profile is indicated by the variation in the static pressure rise coefficient and is a result of the combination of area variation and the upstream influence of the flow splitter.

Of the three configurations tested, splitter 2 produces the least amount of diffusion downstream of the flow splitter lip (as indicated by the smallest change in static pressure rise coefficient). It also produces the lowest static pressure rise coefficient throughout the scroll collector. The area weighted average pressure loss coefficients

were 0.3406, 0.3075, and 0.3217 for flow splitters 1, 2, and 3 respectively. The data from this investigation show that scroll splitter 2 is the most efficient and produces the most symmetrical and consistent flow pattern in the exit arm duct.

The scroll static pressure profile can be made more uniform by improved design of the flow splitter along with maintaining the required flow area to produce constant velocity in the scroll. Based on the results of this investigation, it appears that improved performance can be realized by designing the splitter camber to match more nearly the entering flow streamlines and also by extending the splitter so that the leading edge is closer to the stationary diffuser exit. In this way, the path of the flow entering the scroll exit arms is more closely controlled, resulting in a more uniform velocity throughout the scroll collector.

Elbow Turning Vanes

Elbow turning vane loss coefficient profiles are shown in Figures 182 through 184 at design flow coefficient for all three scroll splitter configurations. These loss coefficients are based on the upstream dynamic head using the transition diffuser exit static pressure and the scroll arm exit total pressure (area averaged), assuming that the total pressure loss through the small area ratio transition diffuser is negligible.

The area averaged turning vane loss coefficients were 0.477, 0.379, and 0.387 for scroll splitters 1, 2, and 3, respectively. As indicated by Figures 174 through 176, the upstream pressure profiles are definitely not uniform and very possibly include some flow circulation in the form of secondary vortices. This kind of flow entering the turning vanes experiences high losses, and the flow downstream of the turning vanes is also nonuniform.

The nonuniform flow conditions at the scroll arm exit are influenced by the flow splitter configuration such that the lowest turning vane loss coefficient occurs when the most efficient splitter configuration is used.

From the inlet guide vane investigation on the low-speed radial outflow compressor, data were obtained which showed that the rotor exit flow conditions are strongly influenced by the rotor inlet flow conditions. Even though flow splitter configuration has some effect on flow conditions entering the elbow turning vanes, the major contribution is believed to be traceable to the inlet system.

CONCLUSIONS

Of the three scroll collector flow splitter configurations investigated, splitter 2 was identified as the most efficient at design flow coefficient. Valuable information was obtained concerning improved splitter

and scroll collector design. Static pressure measurements taken at selected circumferential locations in the scroll collector indicated that splitter design influences the downstream flow conditions. The design intent to maintain constant velocity throughout the scroll collector can be better accomplished by the use of a flow splitter cambered to match more nearly the entering flow streamlines. The splitter lip of this design should be located further upstream near the exit of the stationary diffuser to provide more control over the flow path in the scroll collector.

The performance of the elbow turning vanes was measured and was found to be a function of the entering flow conditions. The lowest total pressure loss coefficient was 0.379 at design flow coefficient with flow splitter 2 installed. With uniform upstream flow conditions, the expected loss coefficient for these turning vanes should be in the order of 0.10 to 0.12. Turning vane performance is dependent on those components of the compressor which have a strong influence on the exit flow pattern; i.e., inlet guide vanes, inlet flow path, stators, and scroll splitter design.

TABLE XIII
 SCROLL COLLECTOR, DIFFUSER AND ELBOW TEST RUN SUMMARY

Run No.	Throttle Settings	Rotor (rpm)	Scroll Splitter Configuration	Remarks
1262	47.5	1400, 1600, 1800	1 (Long)	Diffuser and turning vane rakes at zero position
	90			
	80			
	70			
	65			
	60			
	55			
	50			
	45			
1263	47.5	1400, 1600, 1800	2 (Medium)	Pressure surveys, diffuser and turning vane rakes Diffuser rake at position 5, turning vane rake at zero position
	90			
	80			
	70			
	65			
	60			
	55			
	50			
	45			
1264	47.5	1400, 1600, 1800	3 (Short)	Pressure surveys, diffuser and turning vane rakes Diffuser and turning vane rakes at zero position
	90			
	80			
	70			
	65			
	60			
	55			
	50			
	45			
	47.5			

TABLE XIV
INSTRUMENTATION SUMMARY - SCROLL COLLECTOR, DIFFUSER AND ELBOW TESTS

Item	Location	Symbol	Quantity	Description	Purpose
1	Bellmouth Inlet Static Pressures	P_{BMs}	4	Wall statics	Flow Measurement
2	Rotor Inlet Total Pressure	P_{t1}	1	Single element total with one static on each side for angular measurement	ICV Performance
3	Rotor Exit Total Pressure	P_{t3}	6	One 6 element rake	Rotor performance
4	Rotor Exit Static Pressure	P_{s3}	8	Wall statics	Rotor performance
5	Stator Exit Total Pressure	P_{t4}	12	One 6 element rake with automatic angular positioning; 6 individual elements at random angles	Compressor and static performance
6	Stator Exit Static Pressure	P_{s6}	4	Wall statics, 2 on front wall and 2 on back	Compressor and stator performance
7	Scroll Collector Static Pressure	$P_{s7.25}$	16	Wall statics - see Figure 168 for location	Scroll collector flow distribution and splitter selection
8	Scroll Exit Arm Static Pressure	$P_{s7.5}$	3	Wall statics - see Figure 168 for location	Scroll exit arm flow characteristics
9	Scroll Exit Arm Discharge Total Pressure	$P_{t7.5}$	10	One 10 element rake used in 6 angular positions for complete survey - see Figure 169	Scroll performance and splitter selection
10	Turning Vane Discharge Total Pressure	P_{t9}	10	One 10 element rake used in 5 axial location for complete survey - see Figure 170	Turning vane performance
11	Turning Vane Discharge Static Pressure	P_{t9}	8	Four wall statics at turning vane discharge of each arm	Turning vane performance

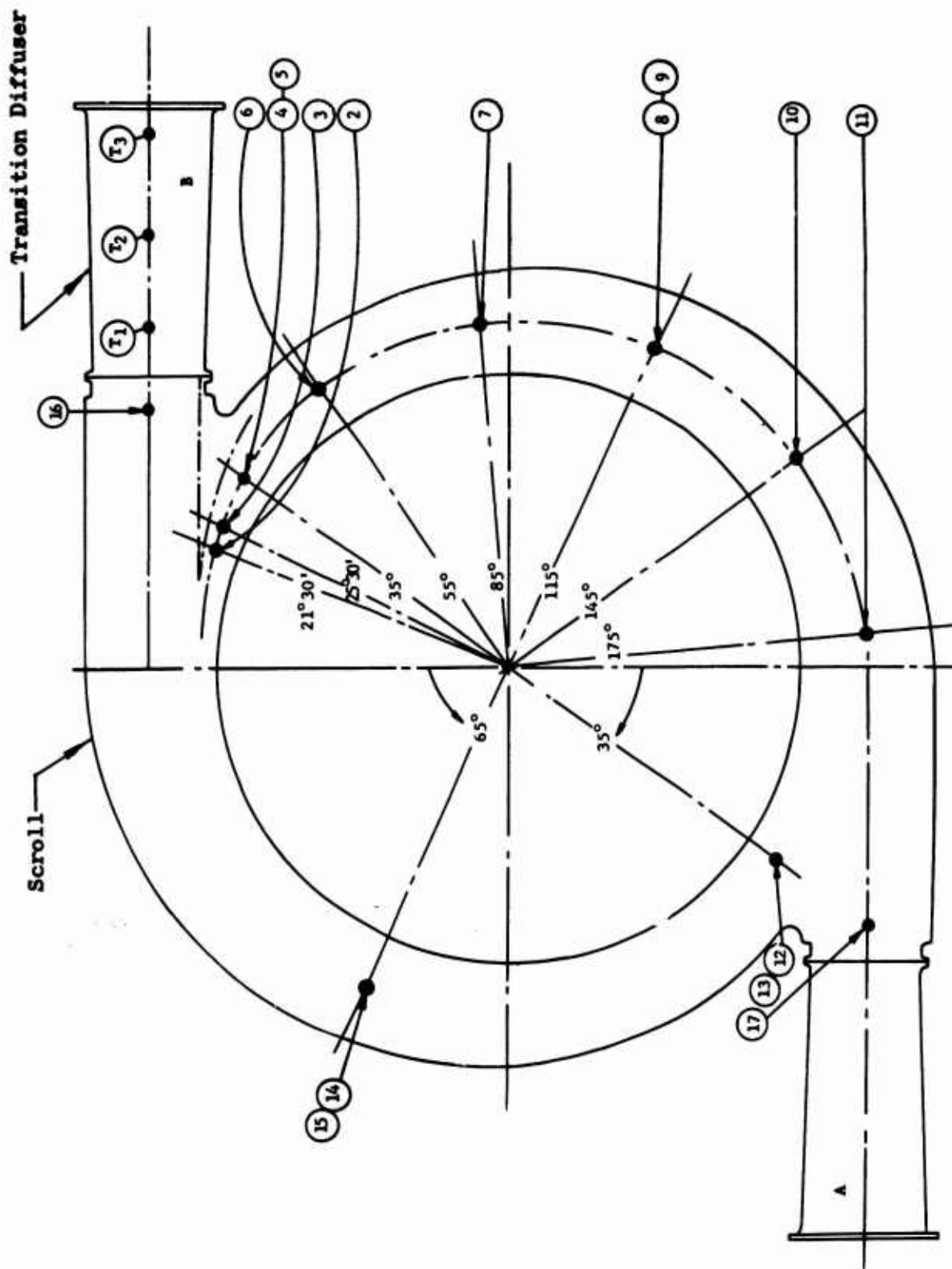


Figure 168. Scroll Collector and Transition Diffuser Static Pressure Tap Locations.

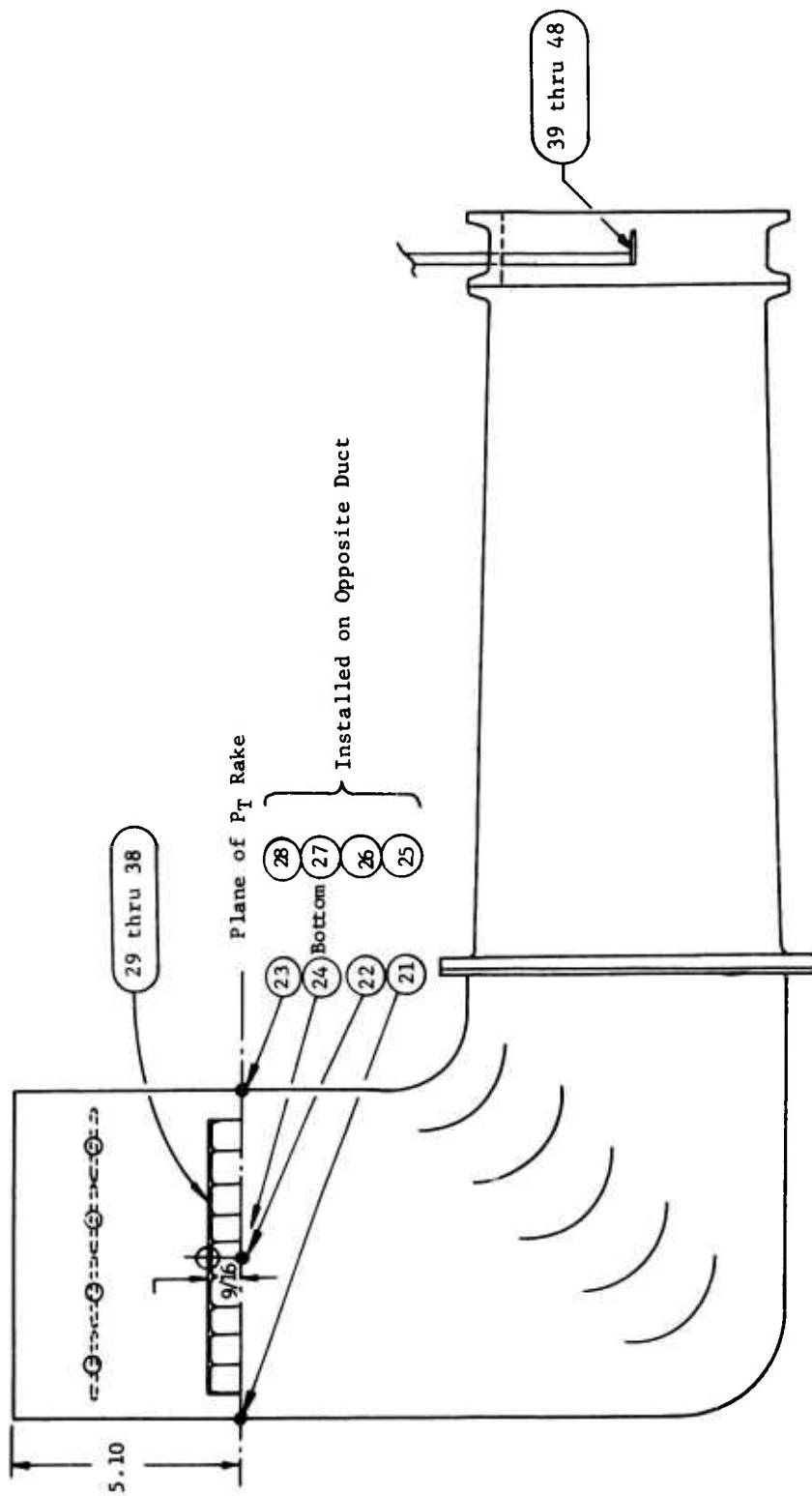


Figure 170. Total Pressure Rake, Elbow Turning Vane Discharge.

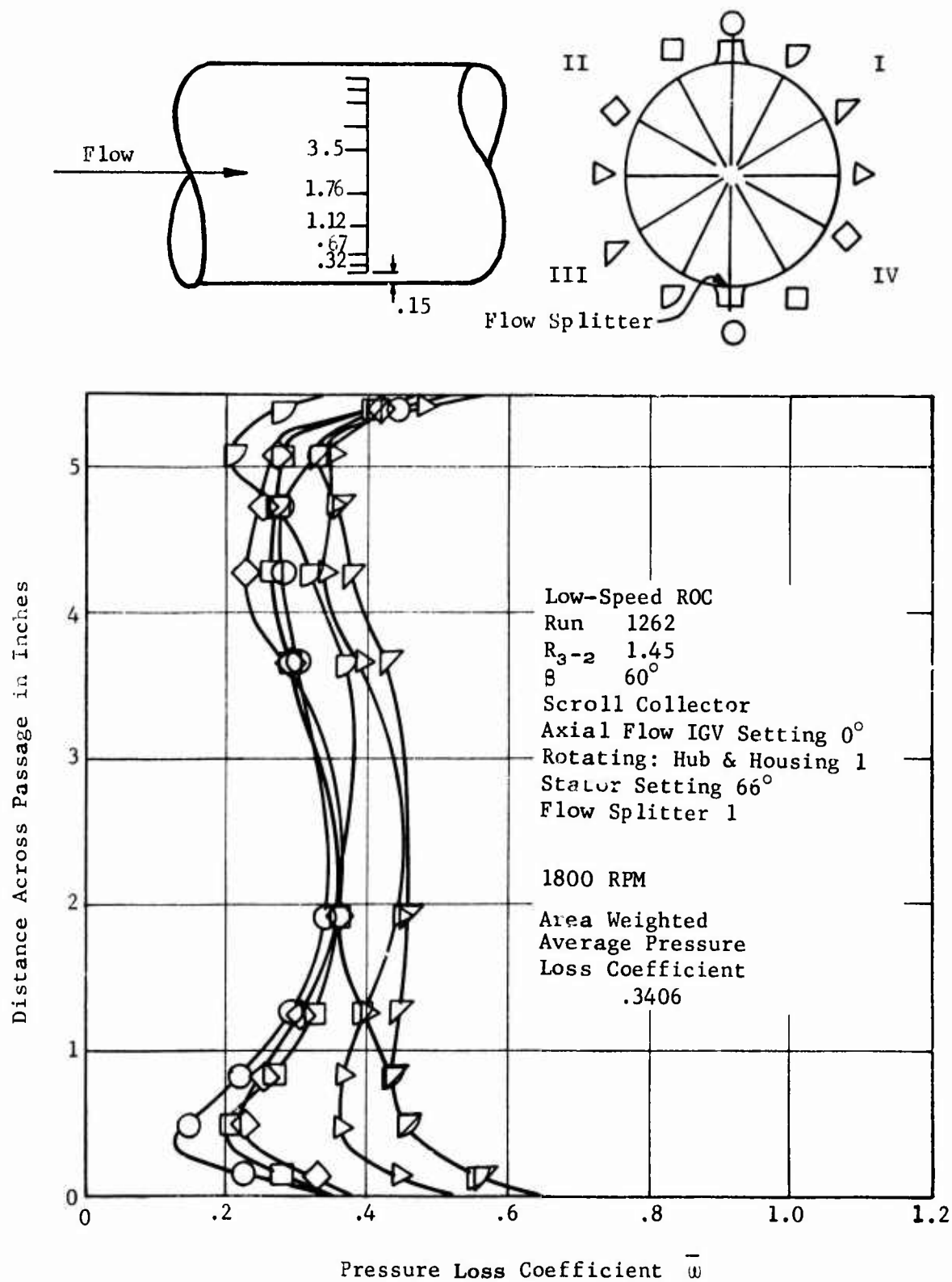


Figure 171. Scroll Collector Exit Arm Loss Coefficient Profiles, Flow Splitter 1.

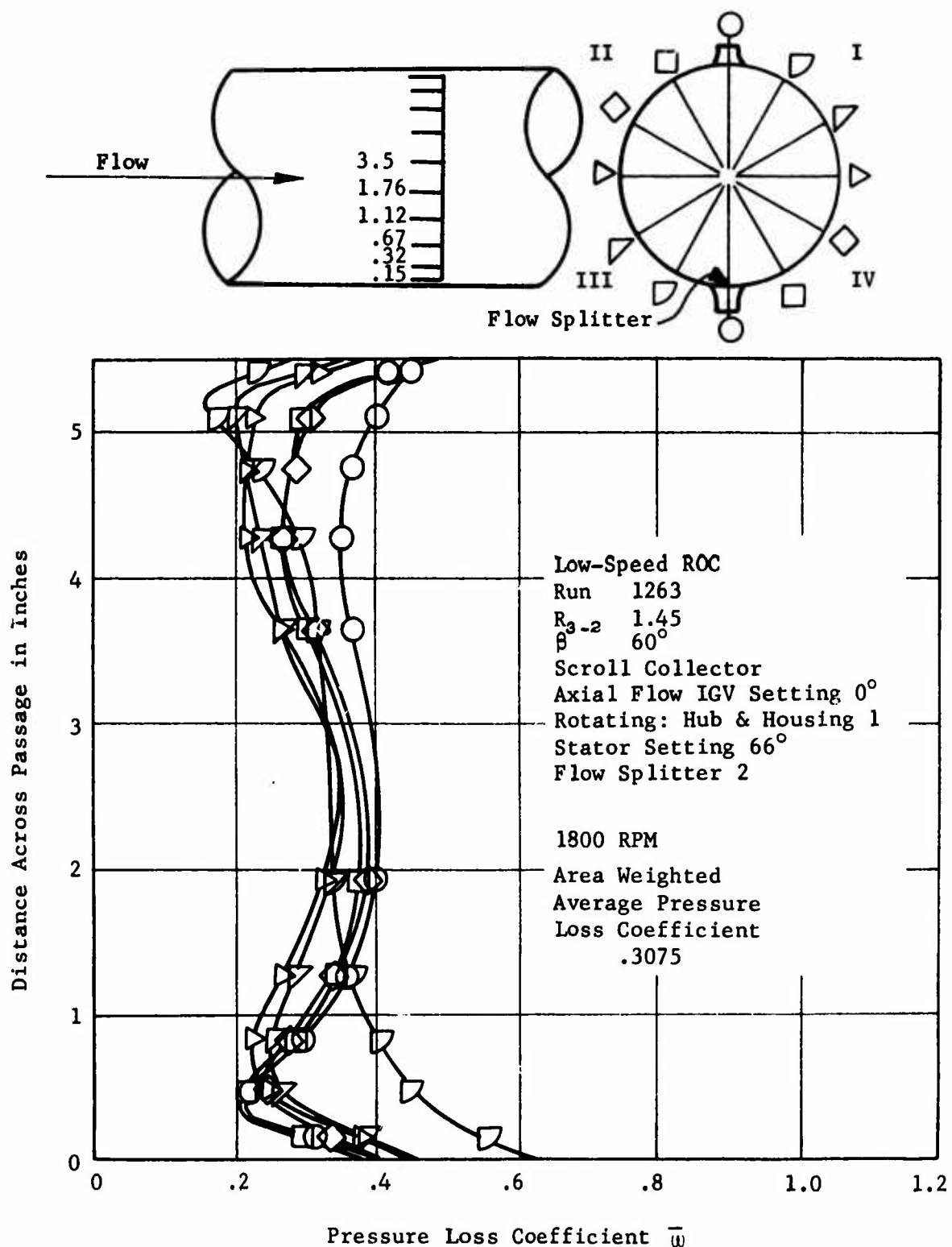


Figure 172. Scroll Collector Exit Arm Loss Coefficient Profiles, Flow Splitter 2.

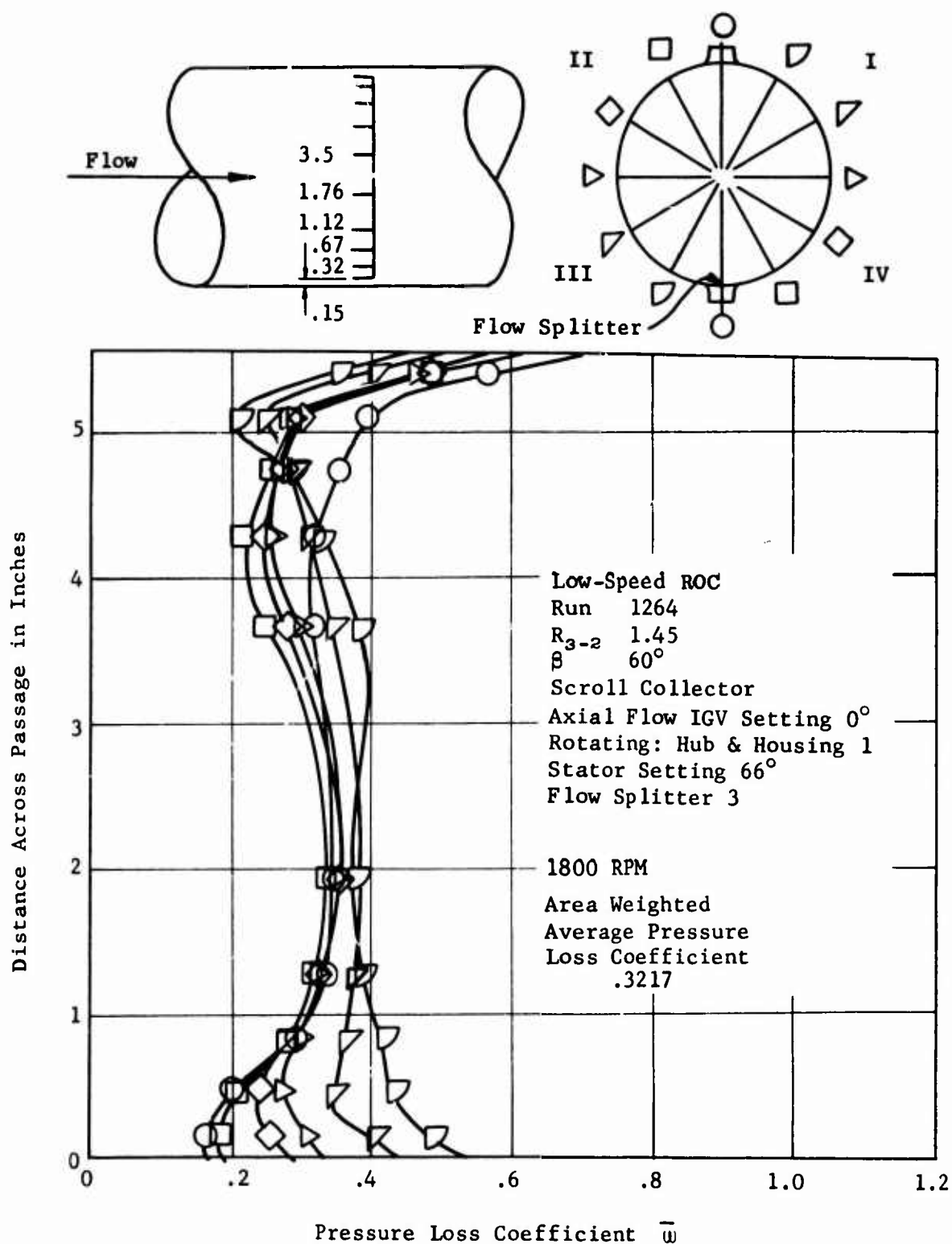


Figure 173. Scroll Collector Exit Arm Loss Coefficient Profiles, Flow Splitter 3.

Low-Speed ROC Stator Setting 66°
 Run 1262 Flow Splitter 1
 R_{3-2} 1.45 1800 RPM
 β 60°
 Scroll Collector
 Axial Flow IGV
 IGV Setting 0°
 Rotating: Hub &
 Housing 1

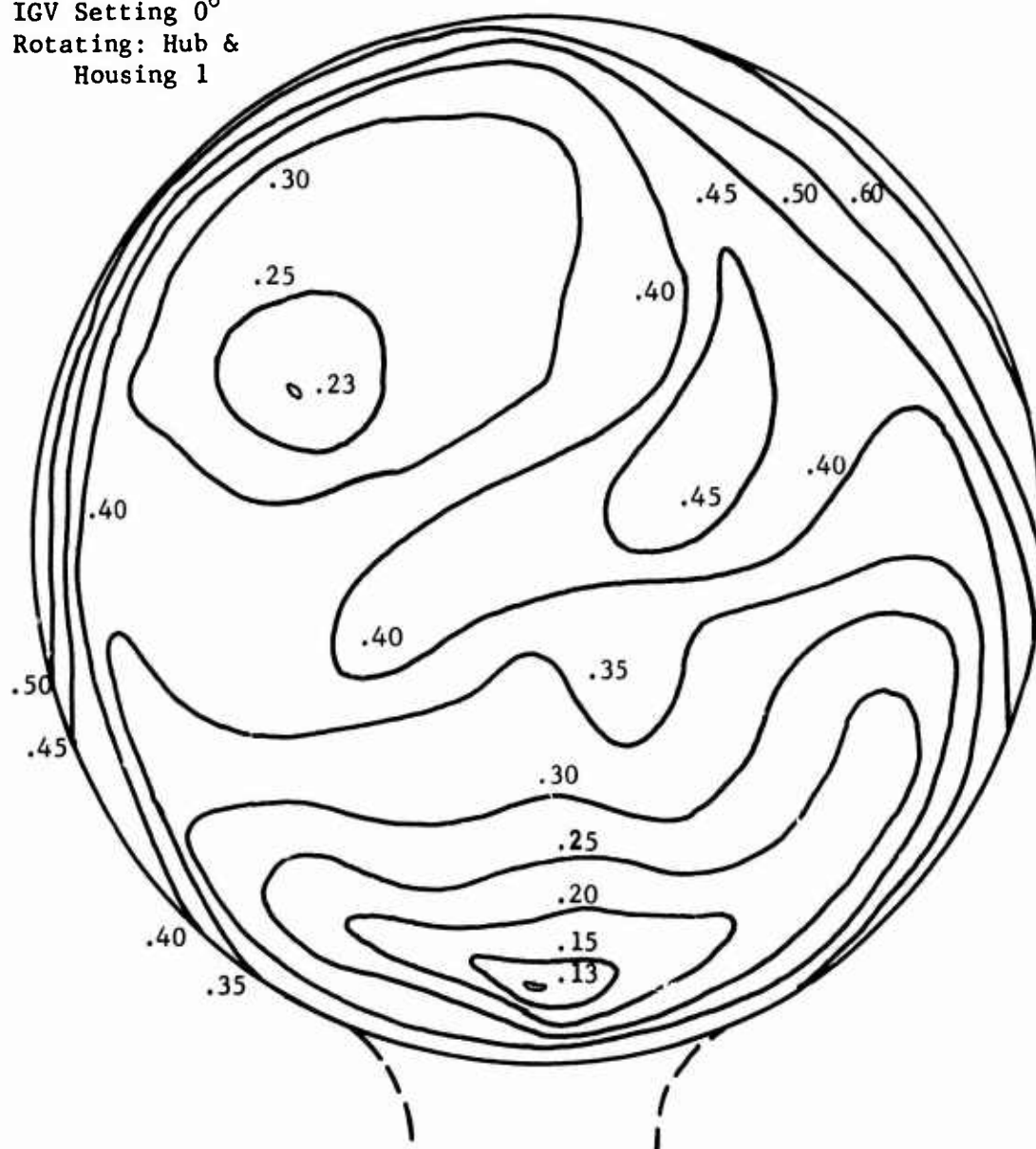
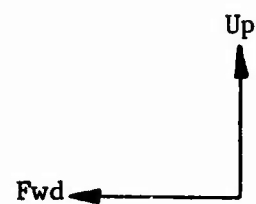


Figure 174. Scroll Collector Exit Arm Loss Coefficient Map, Flow Splitter 1.

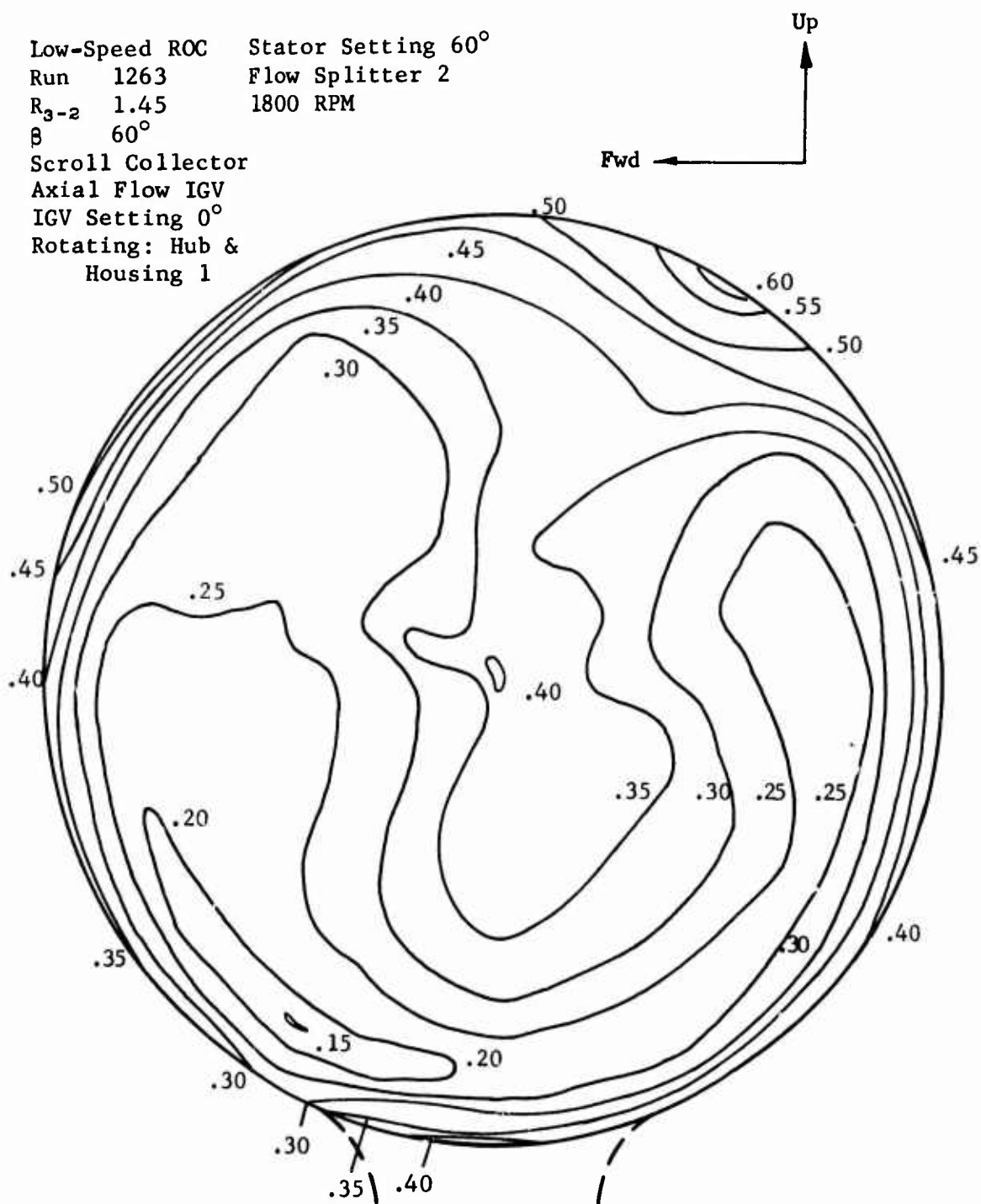


Figure 175. Scroll Collector Exit Arm Loss Coefficient Map, Flow Splitter 2.

Low-Speed ROC Stator Setting 66°
 Run 1264 Flow Splitter 3
 R_{3-2} 1.45 1800 RPM
 β 60°
 Scroll Collector
 Axial Flow IGV
 IGV Setting 0°
 Rotating: Hub &
 Housing 1

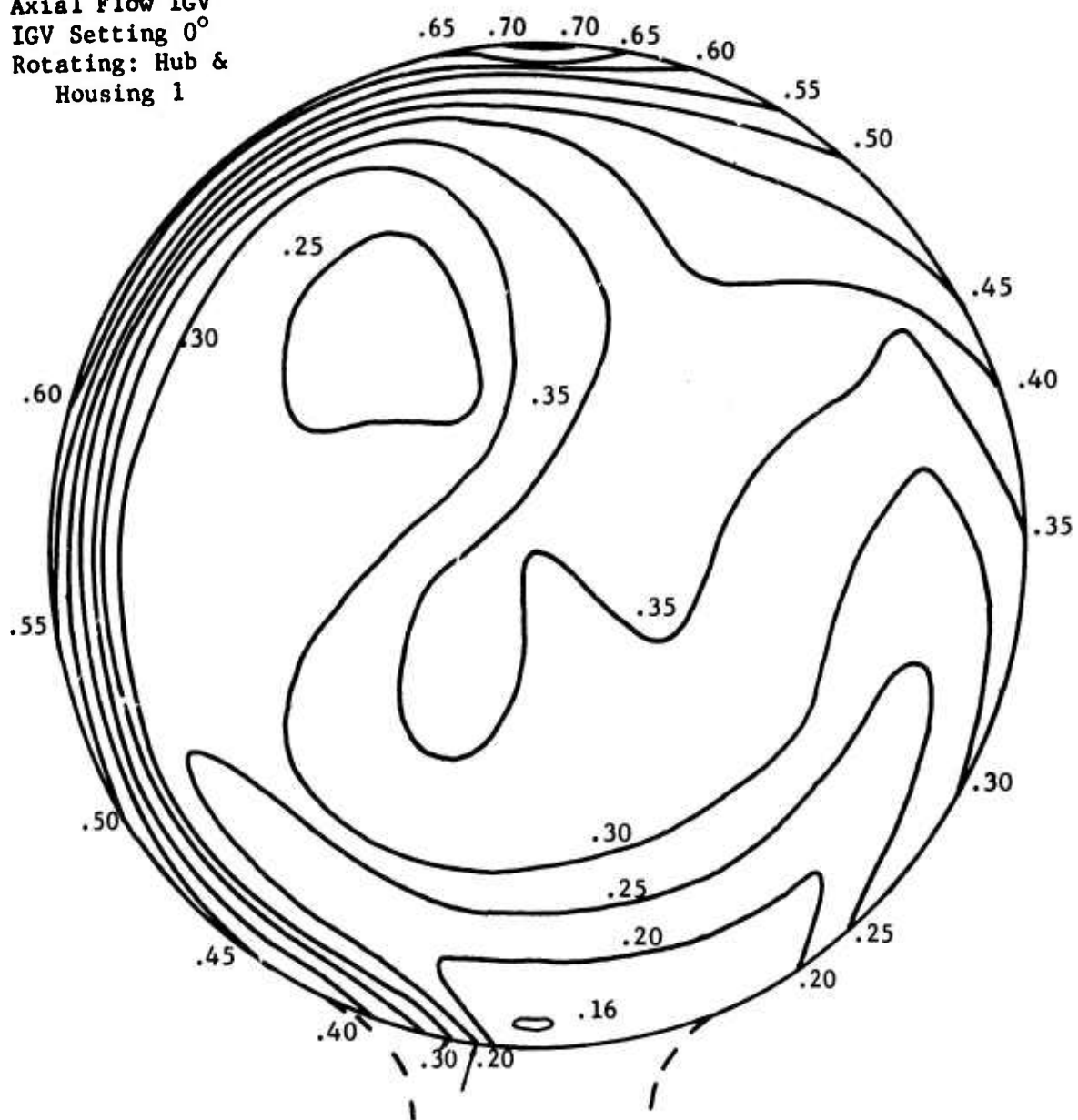
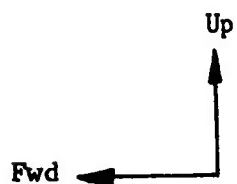


Figure 176. Scroll Collector Exit Arm Loss Coefficient Map, Flow Splitter 3.

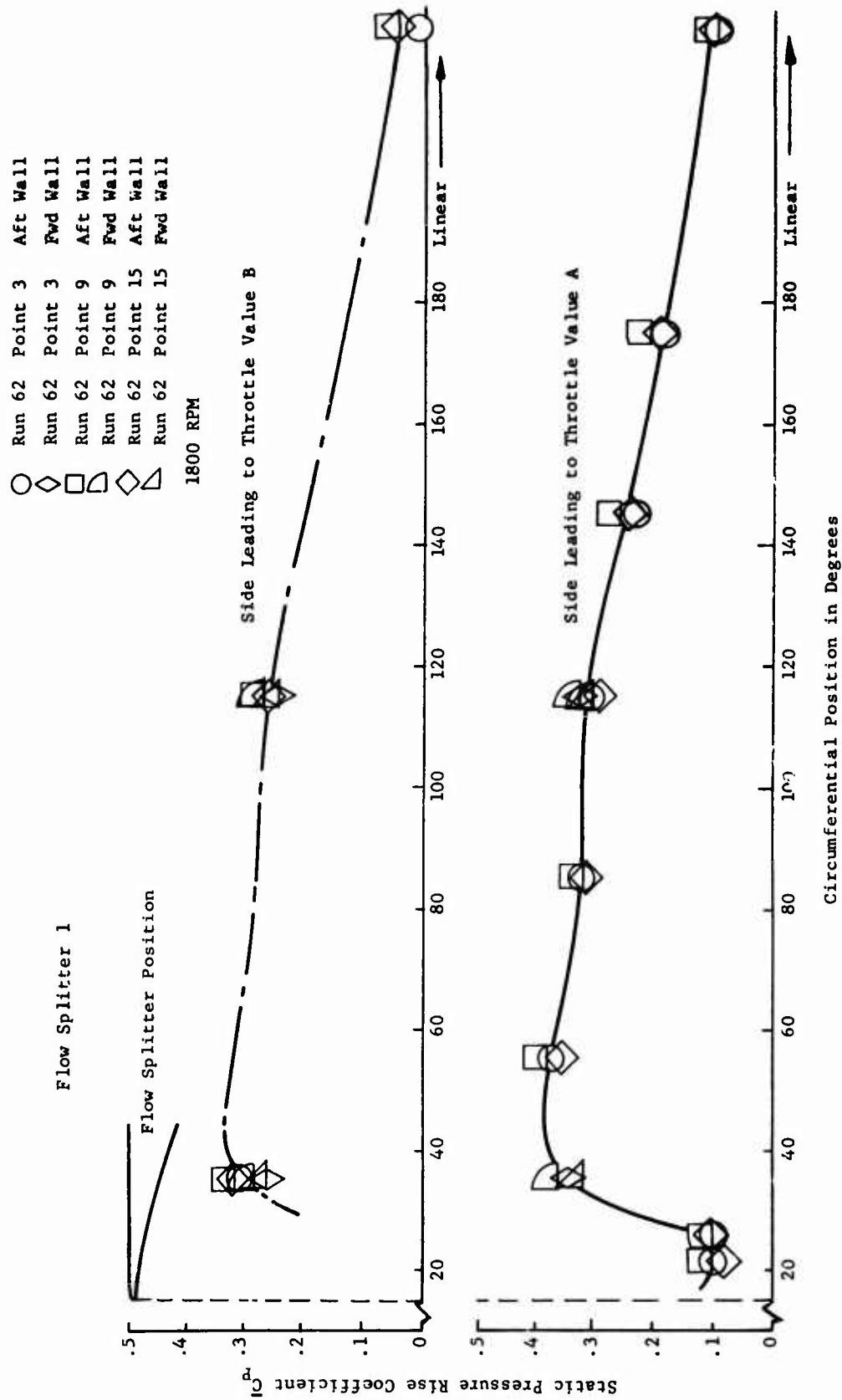


Figure 177. Scroll Collector Static Pressure Rise Coefficient, Flow Splitter 1.

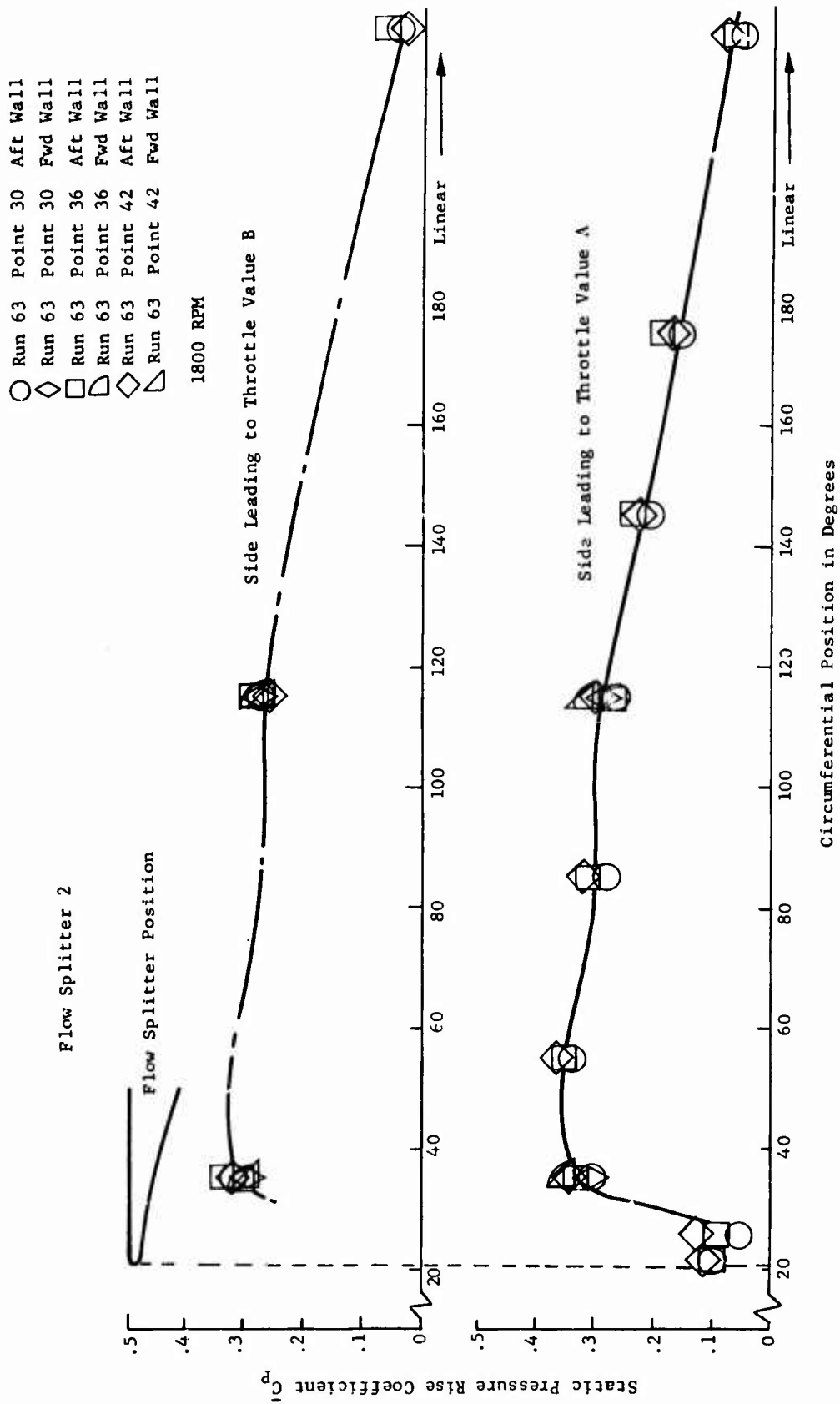


Figure 178. Scroll Collector Static Pressure Rise Coefficient, Flow Splitter 2.

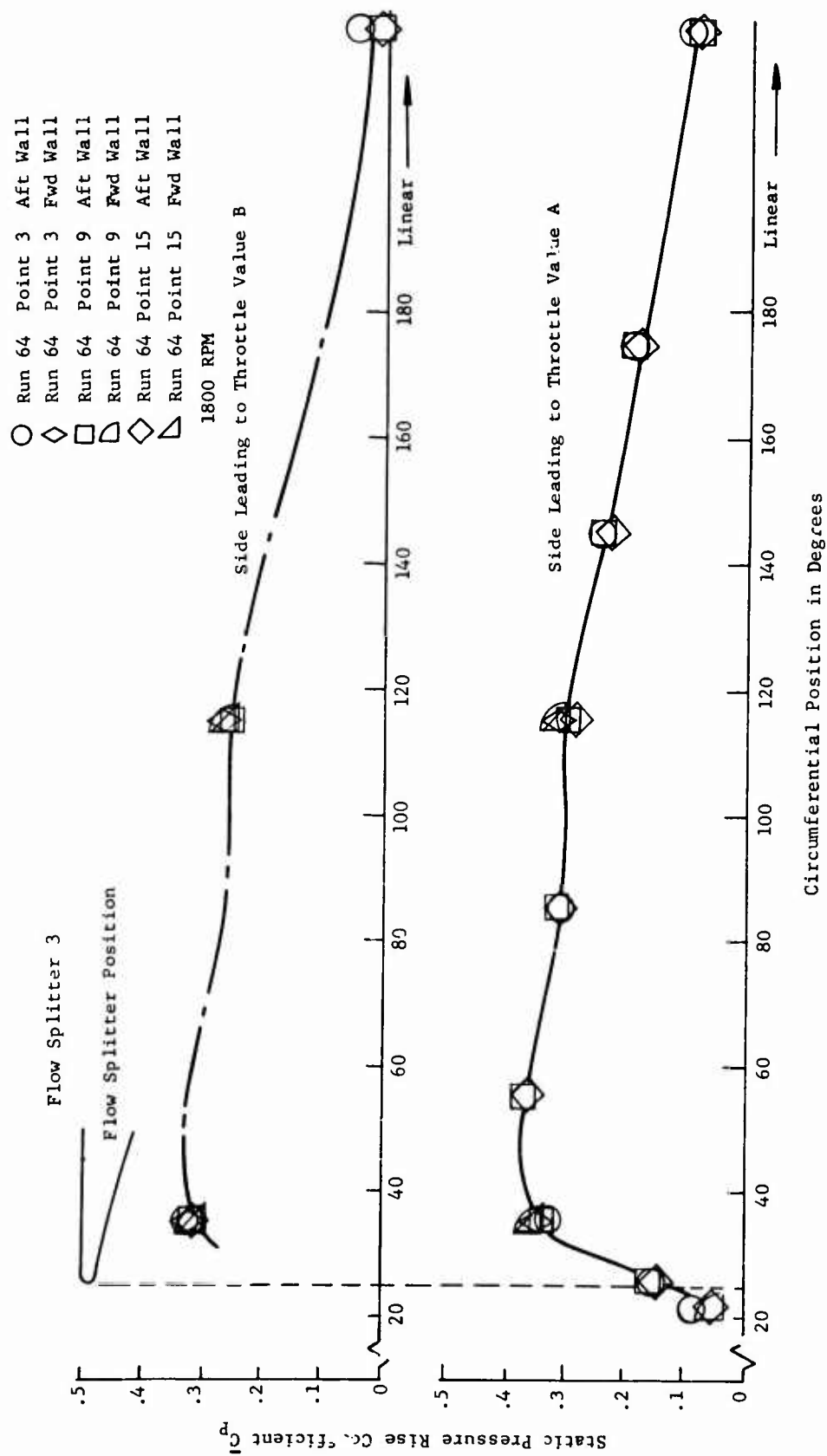


Figure 179. Scroll Collector Static Pressure Rise Coefficient, Flow Splitter 3.

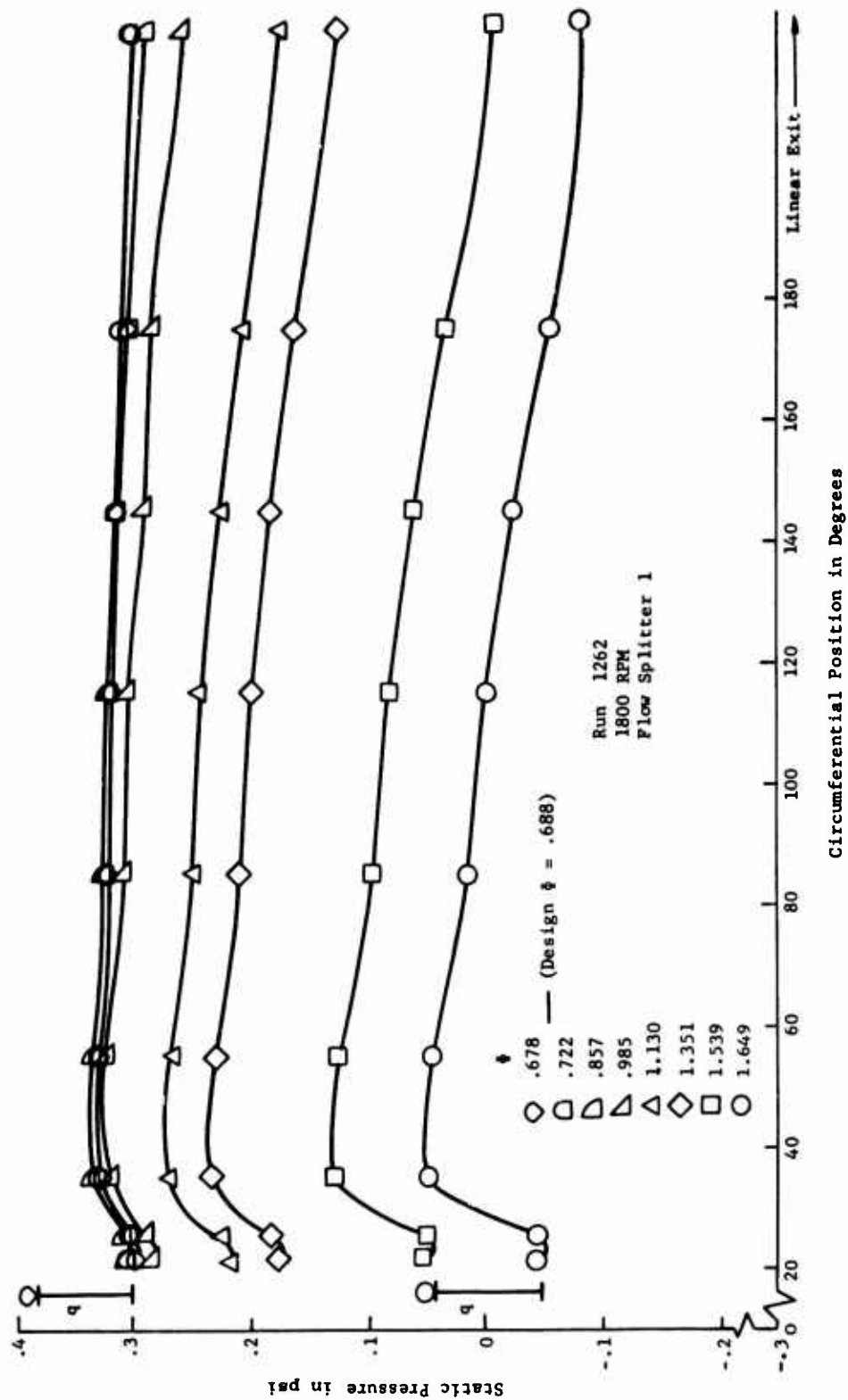


Figure 180. Scroll Collector Static Pressure Profile, Flow Splitter 1.

- Static Pressure Rise Coefficient, Splitter 1
- Static Pressure Rise Coefficient, Splitter 2
- - - - Static Pressure Rise Coefficient, Splitter 3

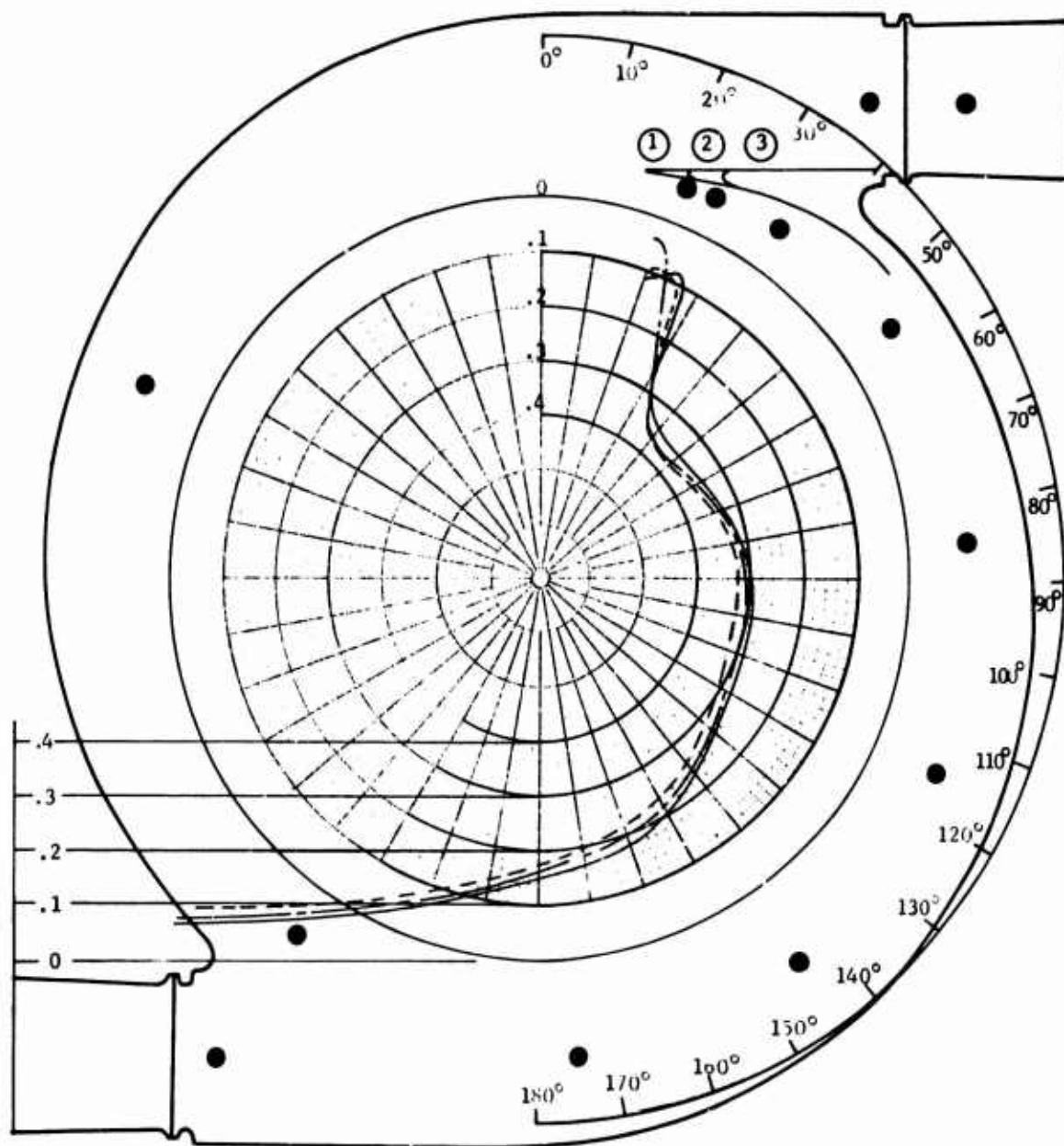


Figure 181. Scroll Collector Static Pressure Rise Coefficient Versus Circumferential Location.

Low-Speed ROC	Axial Flow IGV
Run 1262	IGV Setting 0°
R ₃₋₂ 1.45	Rotating: Hub & Housing 1
Scroll Collector	Stator Setting 66°
Flow Splitter 1	1800 RPM

Area Weighted Average Pressure Loss Coefficient 0.478

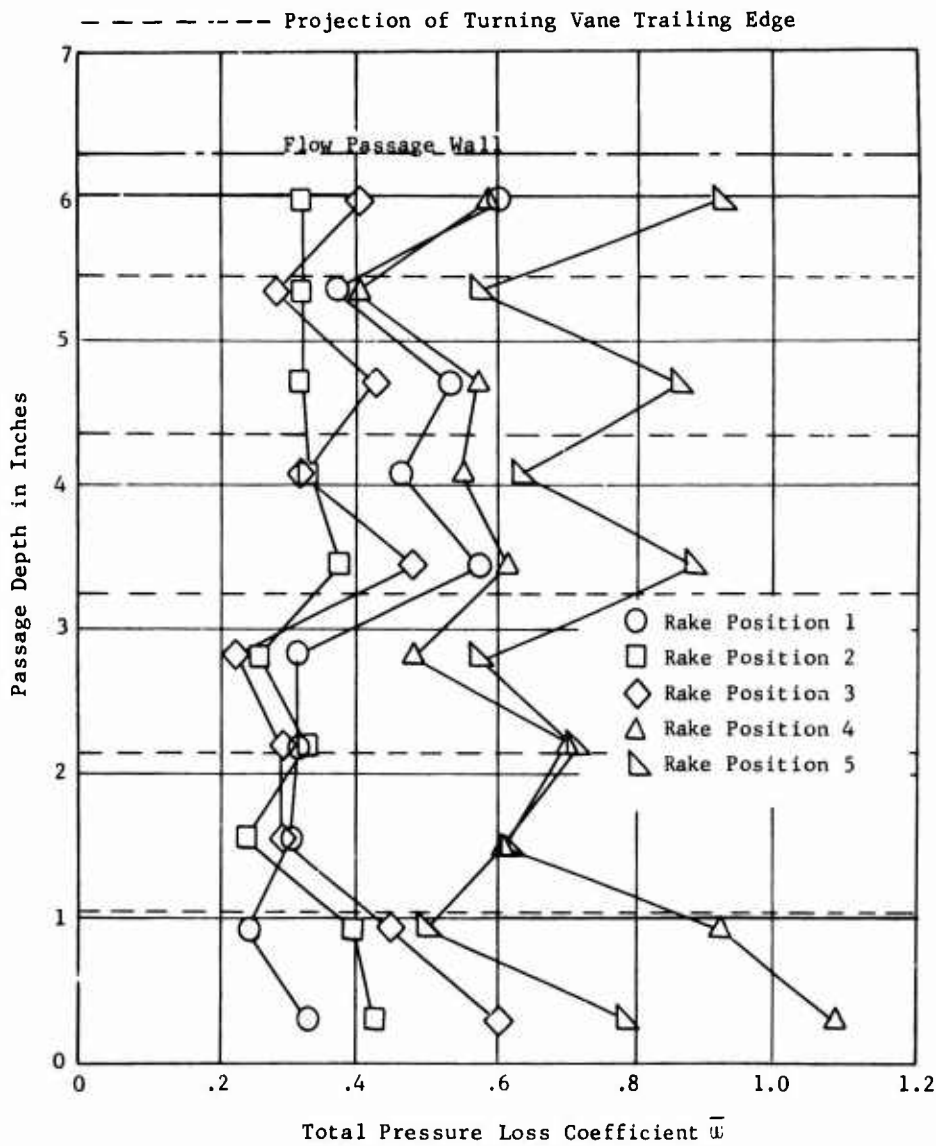


Figure 182. Elbow Turning Vane Loss Coefficient Profiles with Scroll Flow Splitter 1.

Low-Speed ROC	Axial Flow IGV
Run 1263	IGV Setting 0°
R ₃₋₂ 1.45	Rotating: Hub & Housing 1
Scroll Collector	Stator Setting 66°
Flow Splitter 2	1800 RPM

Area Weighted Average Pressure Loss Coefficient 0.379

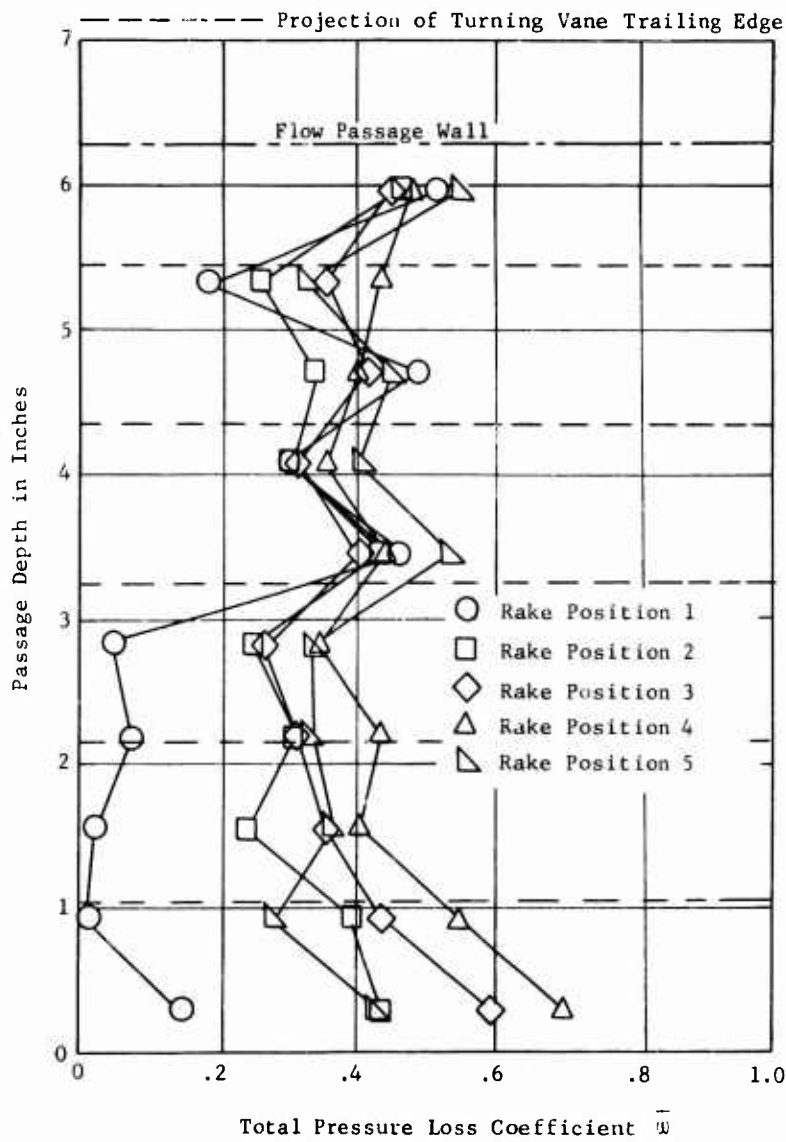


Figure 183. Elbow Turning Vane Loss Coefficient Profiles with Scroll Flow Splitter 2.

Low-Speed ROC Axial Flow IGV
 Run 1264 IGV Setting 0°
 R₃₋₂ 1.45 Rotating: Hub & Housing 1
 Scroll Collector Stator Setting 66°
 Flow Splitter 3 1800 RPM

Area Weighted Average Pressure Loss Coefficient 0.387

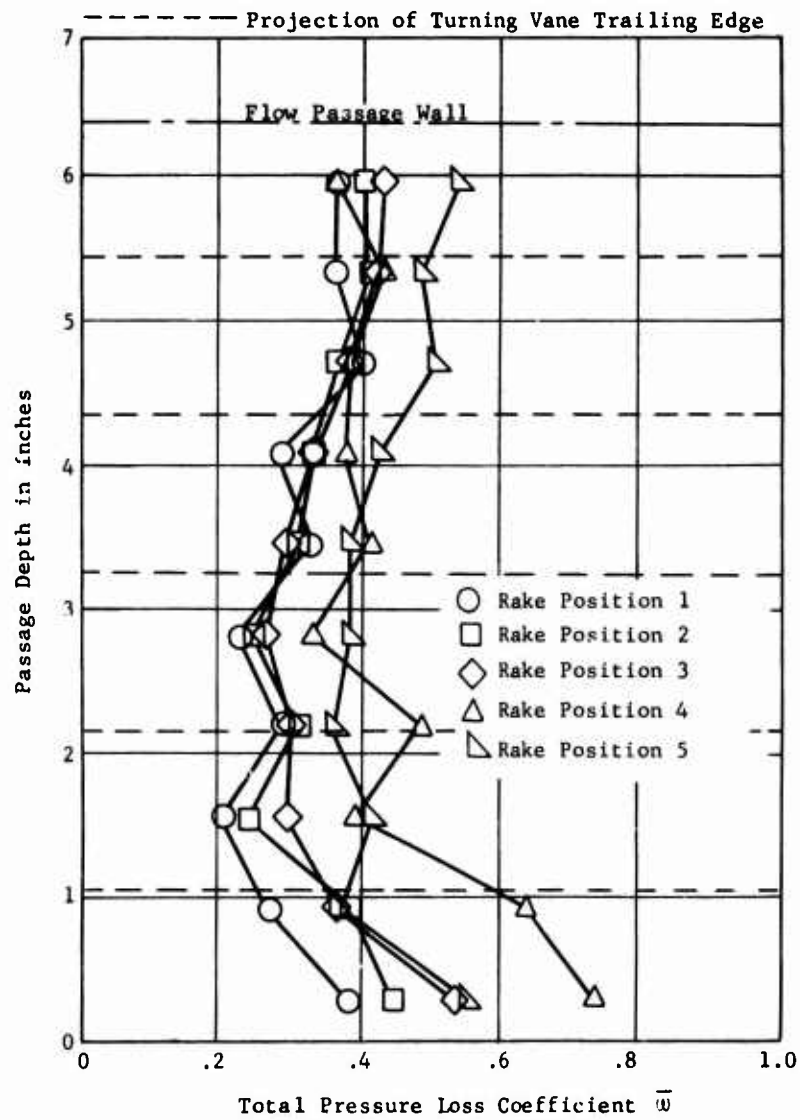


Figure 184. Elbow Turning Vane Loss Coefficient Profiles with Scroll Flow Splitter 3.

AERODYNAMIC ANALYSIS

This section of the report presents two of the major analytical studies conducted during Phase I of the small gas turbine engine compressor technology program. The compressor inlet aerodynamic analysis included calculations performed to determine flow streamlines and velocity distributions to evaluate the inlet passage contour design of the high-speed radial outflow compressor. The rotor blade aerodynamic analysis was undertaken to determine the required transformation from the two-dimensional supersonic rotor blade sections tested in the transonic cascade tunnel to the three-dimensional rotating field of the high-speed rotor. In both studies, existing computer programs were modified and adapted to accomplish the required calculations. The development of the rotor blade transformation was the more extensive and difficult task, and the detailed solution of this problem is presented.

COMPRESSOR INLET AERODYNAMIC ANALYSIS

Two computer programs were utilized to calculate the flow through the inlet section to the rotor blades. The purpose of the calculations was to evaluate the original design of the passage contours and to determine the optimum location for an axisymmetric turning vane which may be required to improve entrance flow conditions into the rotor blades.

One of the computer programs used is capable of calculating and plotting streamline contours through the inlet passage. The program is limited to incompressible flow without tangential velocity. These limitations are not significant to the intended use, since the streamline pattern served only as a guide in selecting the axisymmetric turning vane shape used as input to the second program, which calculates compressible flow. The second program also cannot accommodate tangential velocities. Inlet flow without tangential velocity is not a trivial case, however, since the initial high-speed tests will be conducted in the absence of inlet guide vanes. The design condition requires 18.4 degrees of swirl, so even then, the ratio of tangential velocity to radial velocity is relatively small. Since the pressure gradient due to tangential velocity is counter to the pressure gradient due to flow turning from axial to radial at the rotor inlet, the maximum Mach numbers calculated to exist on the surface of the shroud are higher than actual values which will occur with inlet swirl.

Preliminary calculations of a radial flow inlet were conducted before the axial flow inlet was selected and before the rotor disc shape had been selected. These calculations served to shake down the computer programs for later use and provided evidence that an inlet turning vane or splitter could be beneficial in controlling the magnitude of the maximum surface Mach number to occur on the critical surface of the shroud. These results are not presented, since they do not represent the inlet or rotor disc configuration selected.

Axial flow inlet guide vanes were selected for the high-speed radial outflow compressor because axial flow supercharging stages may be employed with this compressor and because low-speed compressor tests available at the time of selection showed more uniform conditions entering the rotor and slightly better rotor efficiency. The inlet guide vanes are placed at a mean radius with a hub-to-tip radius ratio believed to be consistent with axial flow supercharging stages. The passage area contracts in a continuous manner to accelerate the through-flow velocity uniformly from a design Mach number of 0.50 at the guide vane exit to 0.74 at the rotor blade inlet. The movable portions of the guide vanes are located in a region of the inlet passage whose inner and outer walls are sectors of spheres with a common center lying on the compressor axis of rotation. The purpose of this configuration is to maintain constant minimum clearance between the movable guide vane ends and the inner and outer walls of the passage.

The calculated streamlines of the axial inlet for incompressible flow conditions are presented in Figure 185. Since the inlet and the calculations are axisymmetric rather than two-dimensional, the streamline spacing is not directly related to velocity, as is true for the usual case of two-dimensional flow streamlines. The streamline pattern shows no irregularities, and the inlet contour appears to be quite satisfactory. When the flow through the inlet is computed using the compressible flow program with a radial Mach number of 0.50 at the rotor blade inlet, the contours of constant Mach number shown in Figure 186 are obtained. The maximum Mach number contour that is plotted is for M of 0.75. The maximum value computed in the flow was 0.81 and occurred on the shroud surface. The local static pressure rise coefficient between the minimum pressure and the rotor blade inlet, \bar{C}_p of 0.54, is not excessive and occurs over a rotating surface which should energize the boundary layer. No difficulty with flow separation or choking is anticipated for this inlet during Phase II operation, which will be limited in rotational speed and, therefore, in inlet Mach number of 0.50 presented in Figure 186.

The radial Mach number entering the rotor was increased to 0.70 and 0.75 for two additional calculations shown in Figures 187 and 188. Supersonic Mach numbers were computed for the critical region on the shroud. This calculation method, like most, is not accurate when velocities near sonic are encountered, so detailed evaluation is not warranted. Some difficulty with this inlet can be anticipated at full speed, however.

The possibility of improving the inlet flow for full speed operation by employing an axisymmetric turning vane was examined. Incompressible flow streamlines were calculated using a splitter selected to divide the inlet flow into two equal amounts. The splitter leading edge was contoured to replace the middle streamline at axial station 9.000 shown in Figure 189. The splitter trailing edge was placed on the

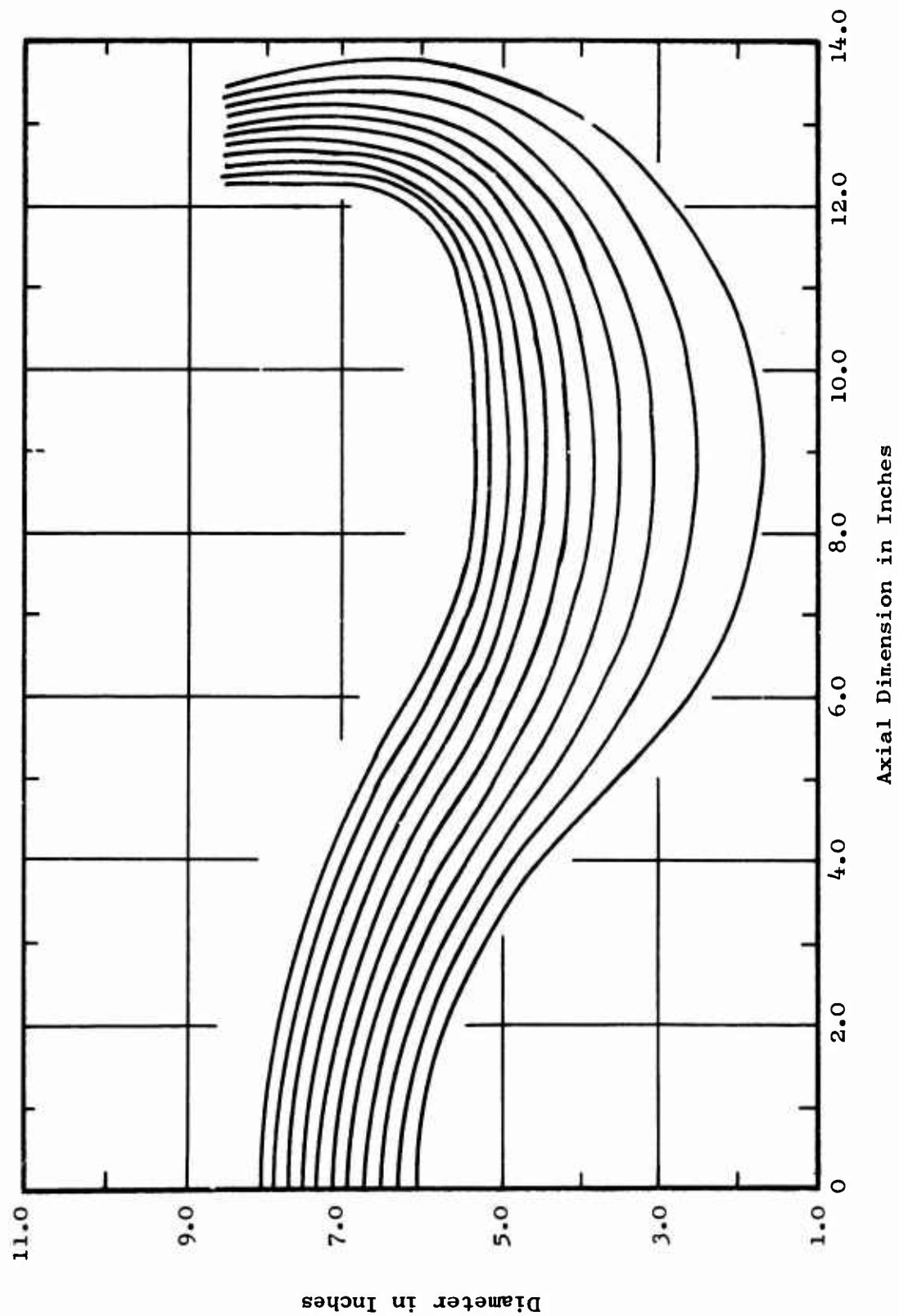
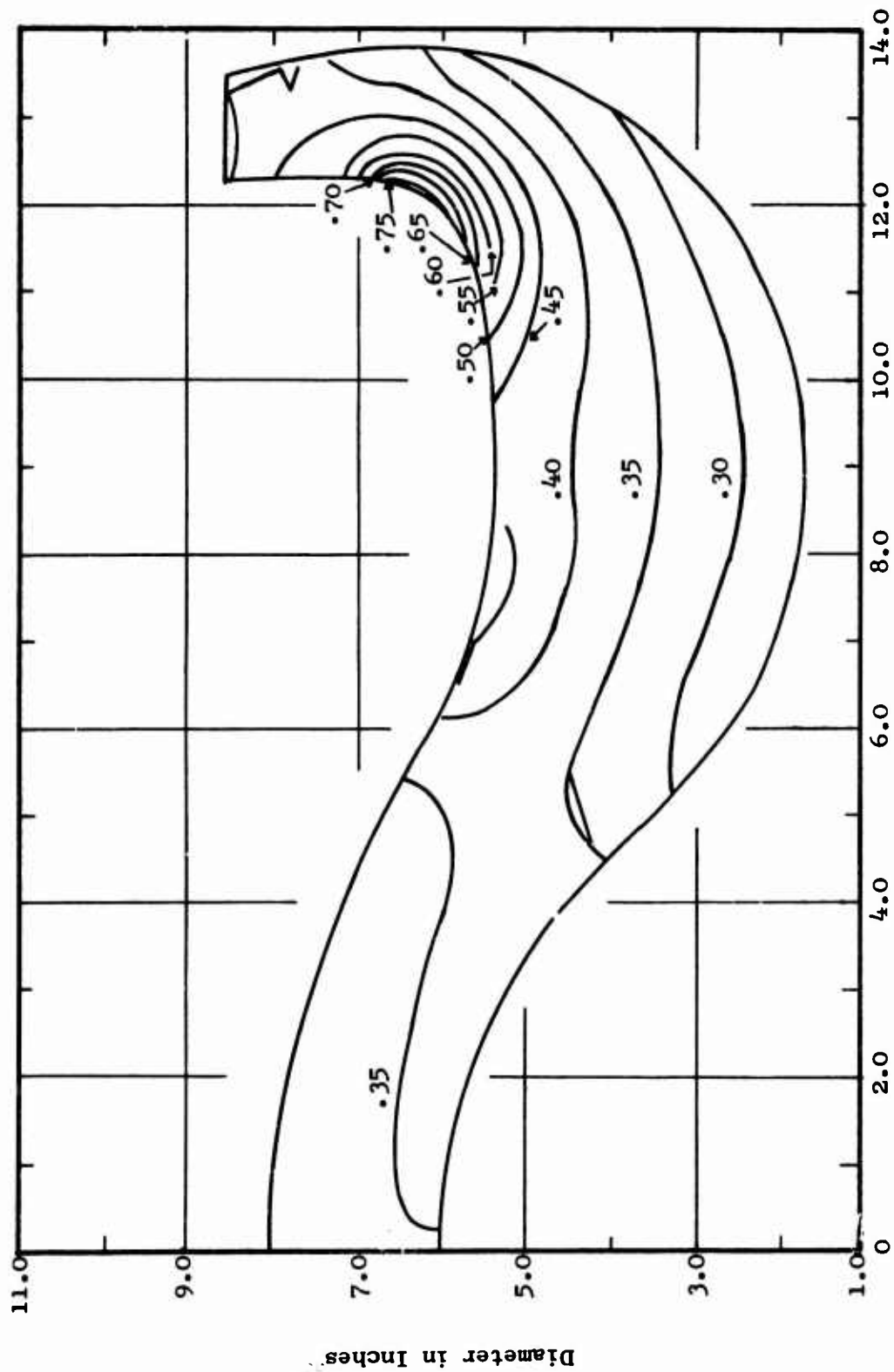


Figure 185. Axial Inlet Calculated Streamlines Based on Incompressible Flow.



Axial Dimension in Inches

Figure 186. Axial Inlet Mach Number Contours for Rotor Inlet Mach Number of 0.50

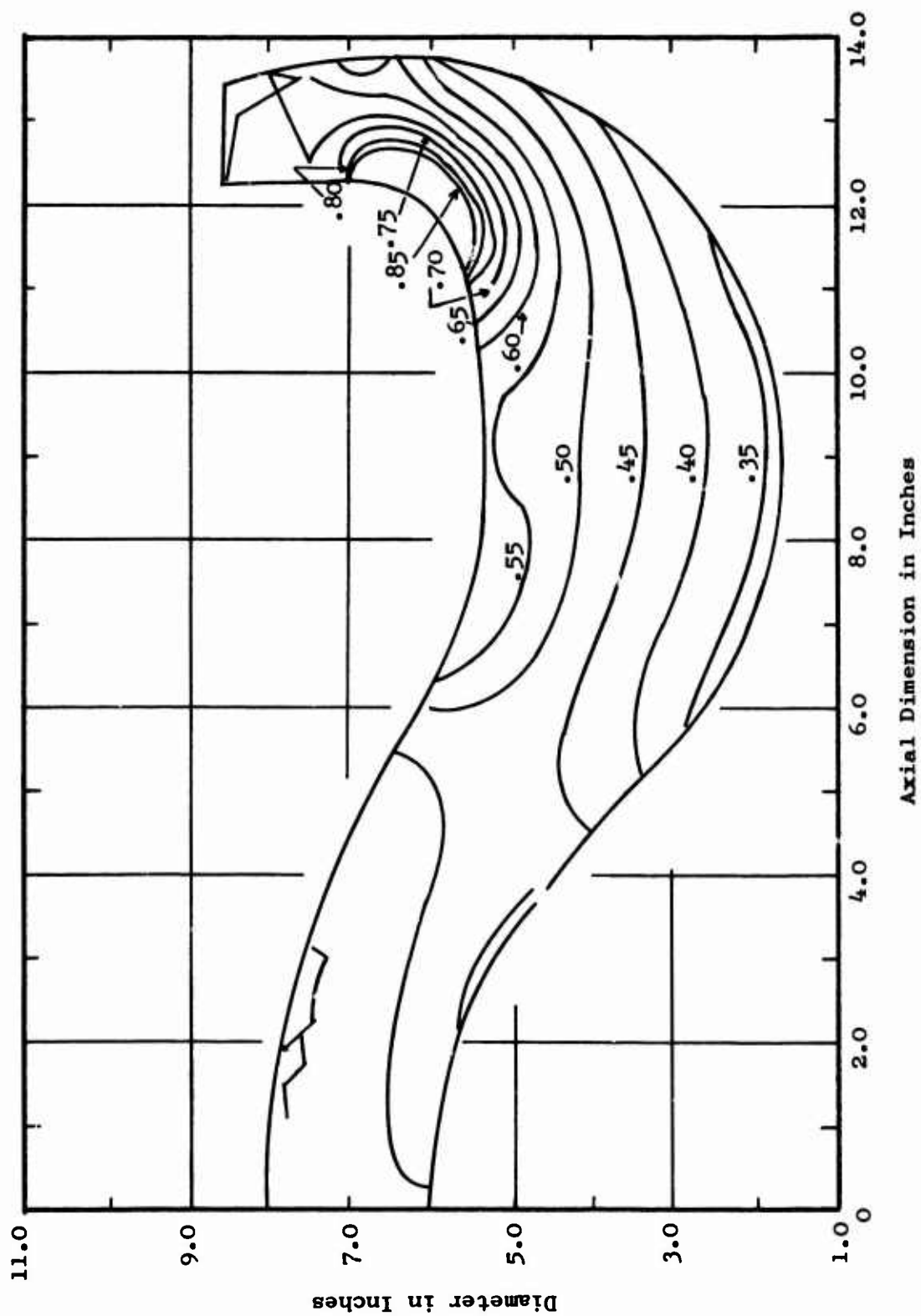


Figure 187. Axial Inlet Mach Number Contours for Rotor Inlet Mach Number of 0.70.

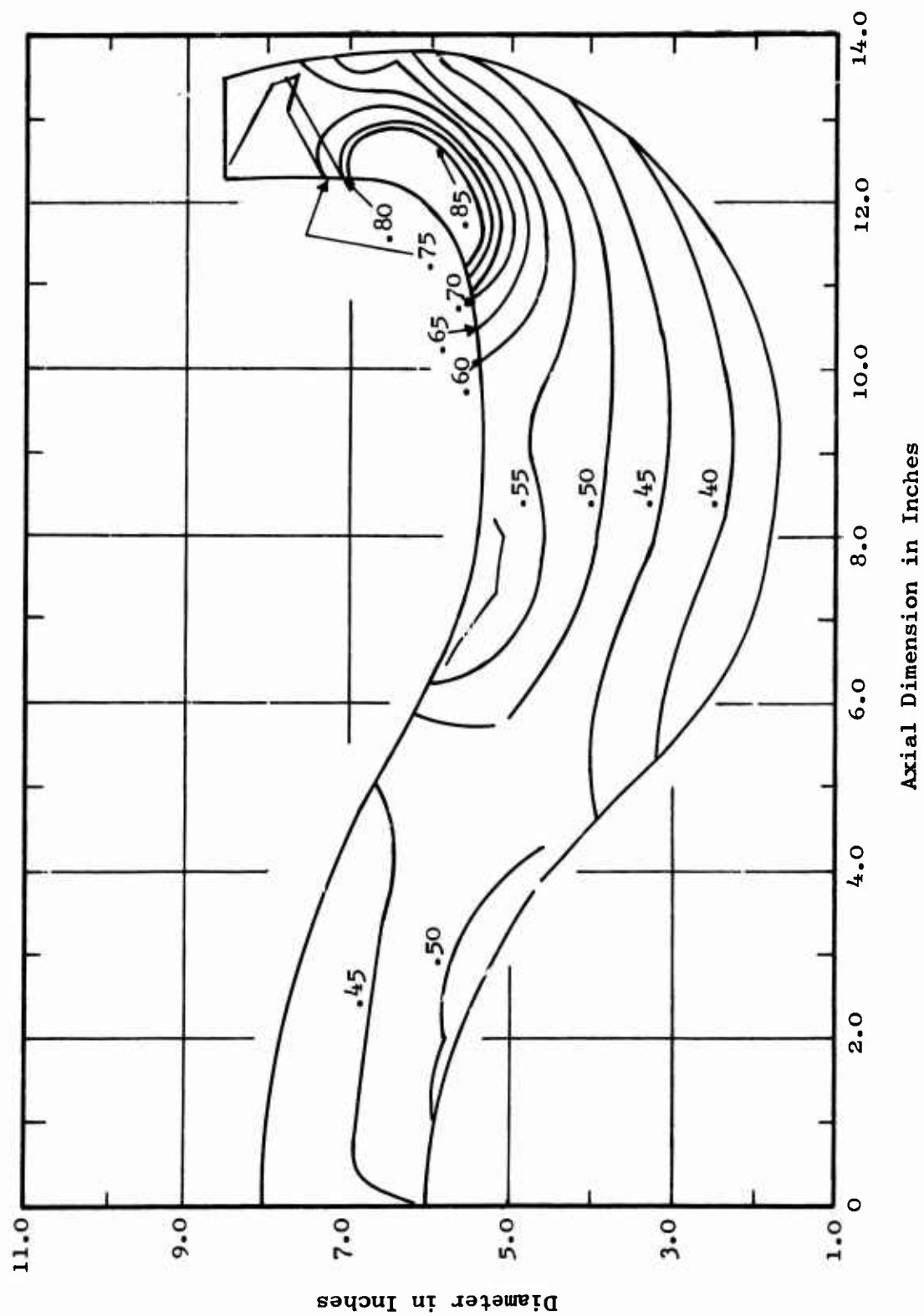


Figure 188. Axial Inlet Mach Number Contours for Rotor Inlet Mach Number of 0.75.

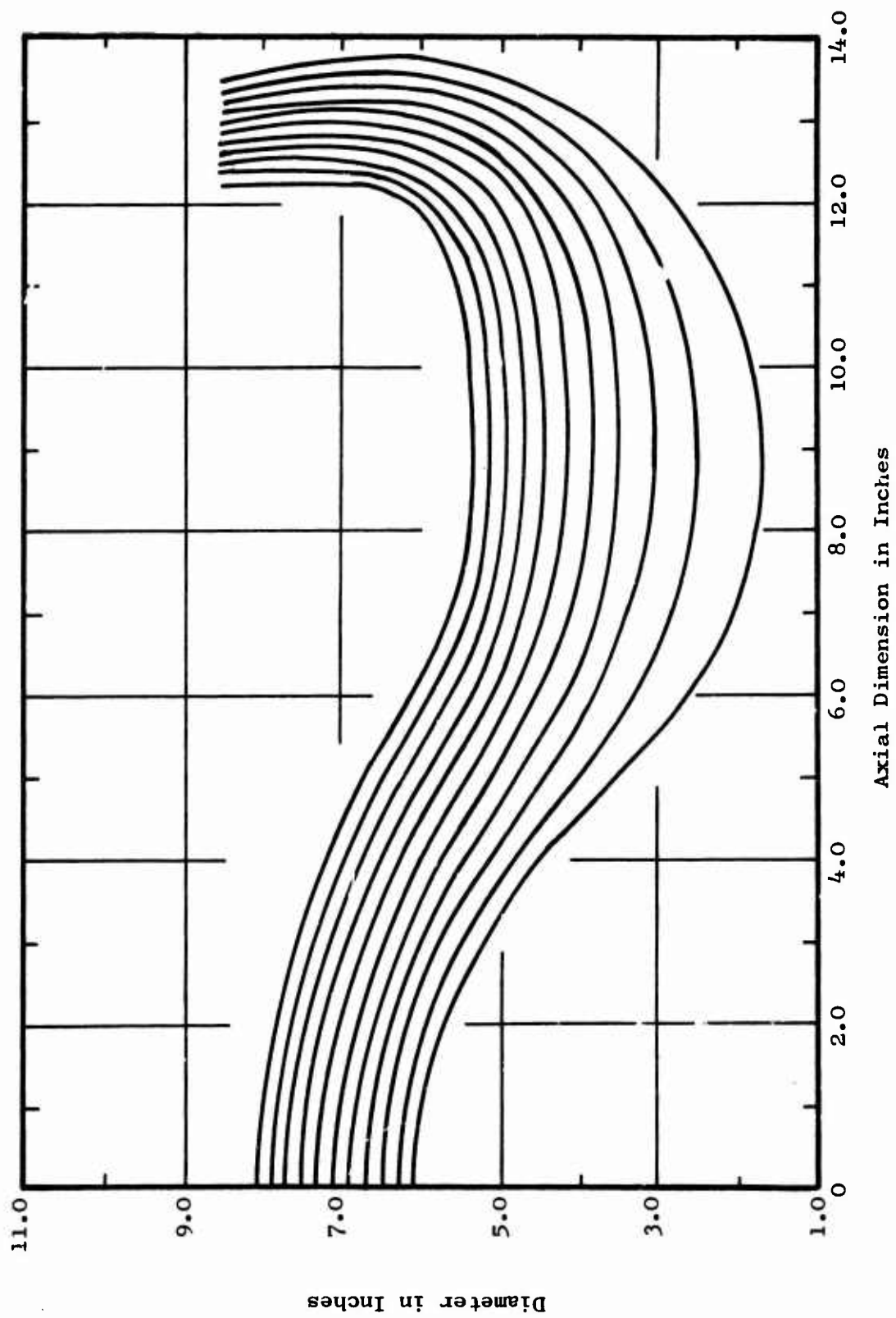


Figure 189. Axial Inlet Calculated Streamlines Based on Incompressible Flow with Splitter.

middle streamline at radial station 7,000, Figure 189. For intermediate points, the splitter was shaped to conform to a locus of passage area centers, with the areas taken normal to the undisturbed streamlines. The compressible flow plots with the splitter in place were erratic, and only the result for a rotor inlet Mach number of 0.50 can be considered presentable (Figure 190). The Mach number contour of 0.60 can be seen to occupy a smaller zone than in the plot shown in Figure 186. The maximum Mach number contour obtained with the splitter was 0.65, and the maximum local value calculated was 0.66. A reduction in the high velocities encountered in the inlet can probably be achieved by using a splitter, although it would have to be very thin in the critical region near the shroud (the calculated splitter was without thickness).

The mechanical design problems of installing a splitter having a larger diameter than the shroud opening, and of holding the splitter in place, are formidable. Preliminary studies of this problem have indicated that using a rotating splitter attached to the rotating centerbody and assembled with the rotor blades and shroud may be the best solution. It is hoped, however, that the beneficial effects of swirl will improve the inlet performance and make the use of a splitter unnecessary.

ROTOR BLADE AERODYNAMIC ANALYSIS

Introduction

The analysis of the general fluid flow problem requires a balancing of the mass, momentum, energy, and entropy conservation equations along with a number of expressions describing the behavior of the fluid properties. The general flow is impossible to solve by an available means. The analysis of a particular flow problem fortunately is not so difficult. This is true because in any given flow problem certain aspects of the flow phenomenon tend to predominate and hence govern the fluid behavior. This fact permits the division of flow problems into a number of classifications. Methods of analysis for many of the different classifications exist and yield excellent results.

The rotor blade aerodynamic analysis problem fits into the class of a steady supersonic two-dimensional isentropic adiabatic flow of an ideal gas. This class of problems can be solved by a numerical technique - the method of characteristics. The normal characteristic relationships, however, are not valid for the rotor blade passage, since this passage is defined in a coordinate system which is rotating, i.e., the rotor. Although this rotation does not affect the continuity equation, it does affect the momentum equation because the coordinate system is non-inertial. It also affects the energy equation, since the total temperature of the fluid with respect to the rotor depends on the distance from the axis of rotation. Aside from momentum and energy considerations, it may also be desired to modify the continuity equation to reflect changes in wall spacing. The applicable characteristic equations are derived in Appendix II following the method outlined in Reference 29.

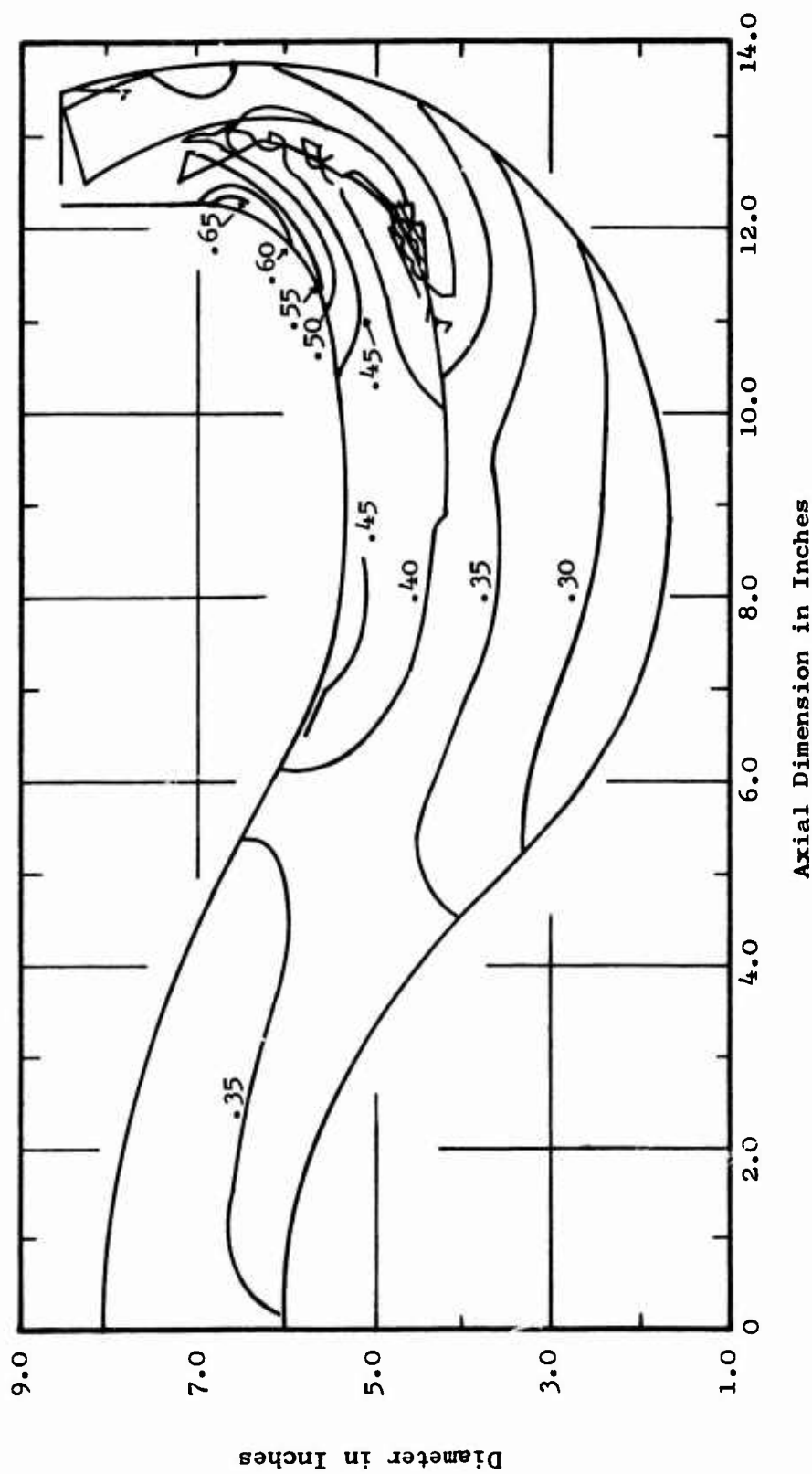


Figure 190. Axial Inlet Mach Number Contours with Flow Splitter for Rotor Inlet Mach Number of 0.50.

Verification of Derived Characteristic Equations

In order to check the derived characteristic equations, it is desirable to calculate a flow field in a rotating coordinate system by an alternate method. The calculation of the compressible free flow with a radial velocity component in a stationary coordinate system is relatively easy. This is the same flow field which exists in the rotating vaneless diffuser. If a rotating coordinate system is superimposed at the center of the free vortex field, the flow field as seen by this rotating coordinate system can be determined quite easily. A computer program was written to perform this calculation. The correlation is shown in Table XV.

Application of Method of Characteristics of Rotor Blade

An existing computer program capable of performing normal characteristic-type solutions was modified to handle the case of the rotating coordinate system. This program is capable of performing analysis-type calculations - determination of the flow field, given the blade geometry and the inlet conditions. It can also perform design type calculations - determination of rotor blade shape to obtain desired Mach number distribution on the blade surface. This dual capability was quite helpful in the rotor blade definition.

Application of Method of Characteristics Program to a Modified Two-Dimensional Blade

The first application of the computer program was made with the following objectives in mind:

1. To determine the accuracy of the method when applied to a complete blade specification.
2. To determine the magnitude and direction of the effects of radial blade orientation, coordinate rotation, and sidewall spacing on a two-dimensional blade shape (that is, a similar blade designed without consideration of these effects).
3. To determine the magnitude and direction of the changes in blade shape required to obtain an acceptable Mach number distribution in the three-dimensional (rotating) case.

In order to conform to these objectives, it was desired that the first blade shape analyzed be a slightly modified version of the rotor blade shape tested in the supersonic cascade tunnel. This modified blade has cusped leading and trailing edges and a minimum pressure surface Mach number of 1.13.

The reason for the modification in the minimum pressure surface Mach number is an inherent limitation in the method of characteristics approach. As is the case with many methods of analysis, the method of

TABLE XV
CORRELATION OF METHOD OF CHARACTERISTICS
AND TRANSFORMED FREE VORTEX FLOW SOLUTIONS

Case	Passage Contraction (percent)	Coordinate Rotation (rpm)	Radius (inches)	Characteristics		Alternate Method	
				Mach Number	Flow Angle (degrees)	Mach Number	Flow Angle (degrees)
0*	-	-	3.6000	2.0000	30.000	2.0000	30.000
1	0	0	3.6072	2.0036	28.898	2.0036	29.901
2	0	31,847	3.6072	2.0074	29.723	2.0072	29.729
2	2	31,847	3.6072	2.0047	29.748	2.0045	29.753
3	0	-31,847	3.6072	2.0037	30.025	2.0037	30.025
3	2	-31,847	3.6072	2.0010	30.048	2.0010	30.050
* Defines inlet parameters with exception of total temperature, which was 749.16 degrees Rankine.							

characteristics becomes difficult to apply or breaks down completely under certain conditions. The breakdown of the method of characteristics occurs in regions of the flow field where the Mach number approaches unity. For this reason the initial analysis was performed on a blade whose minimum Mach number is 1.13. It should be noted here that the rotor blade design criterion calls for a Mach number of unity over a considered portion of the rotor blade suction surface. It was later determined that the suction surface Mach number could be brought quite close to 1.0 (actually 1.01) without having the program encounter difficulty.

The reason for modification of the leading and trailing edge of the blade is that the finite thickness edges used in the cascade tunnel blade give rise to shock and expansion patterns which propagate upstream and modify the condition of the flow entering the blade. The detailed analysis of the resulting inlet flow pattern is not simple. It did not appear that such an analysis was necessary to achieve the previously stated initial objectives.

Method Accuracy

The ideal Mach number distribution of the modified blade is shown in Figure 191. It was natural to attempt to reproduce this distribution using the computer program in order to achieve a familiarity with the application of the program to the problem at hand, and to obtain some indication of the level of accuracy which could be expected. The results of these attempts are shown in Figure 191 as black dots. It is evident that the numerical technique employed is capable of accurately describing the Mach number distribution over the entire blade surface. No calculations were attempted on the small remaining trailing edge section of the blade.

Effects of Rotation and Wall Spacing

The generation of the input data for the case of the blade in the rotating coordinate system proceeded concurrently with the two-dimensional analysis. The specification of the inlet flow field for this case was more difficult, and hence more time consuming, than for the two-dimensional case.

The comparison of rotation and wall spacing has been made at the 25-percent chord position on the blade suction surface (point A on Figure 192).

The results at point A, corresponding to the four possible operating conditions, are:

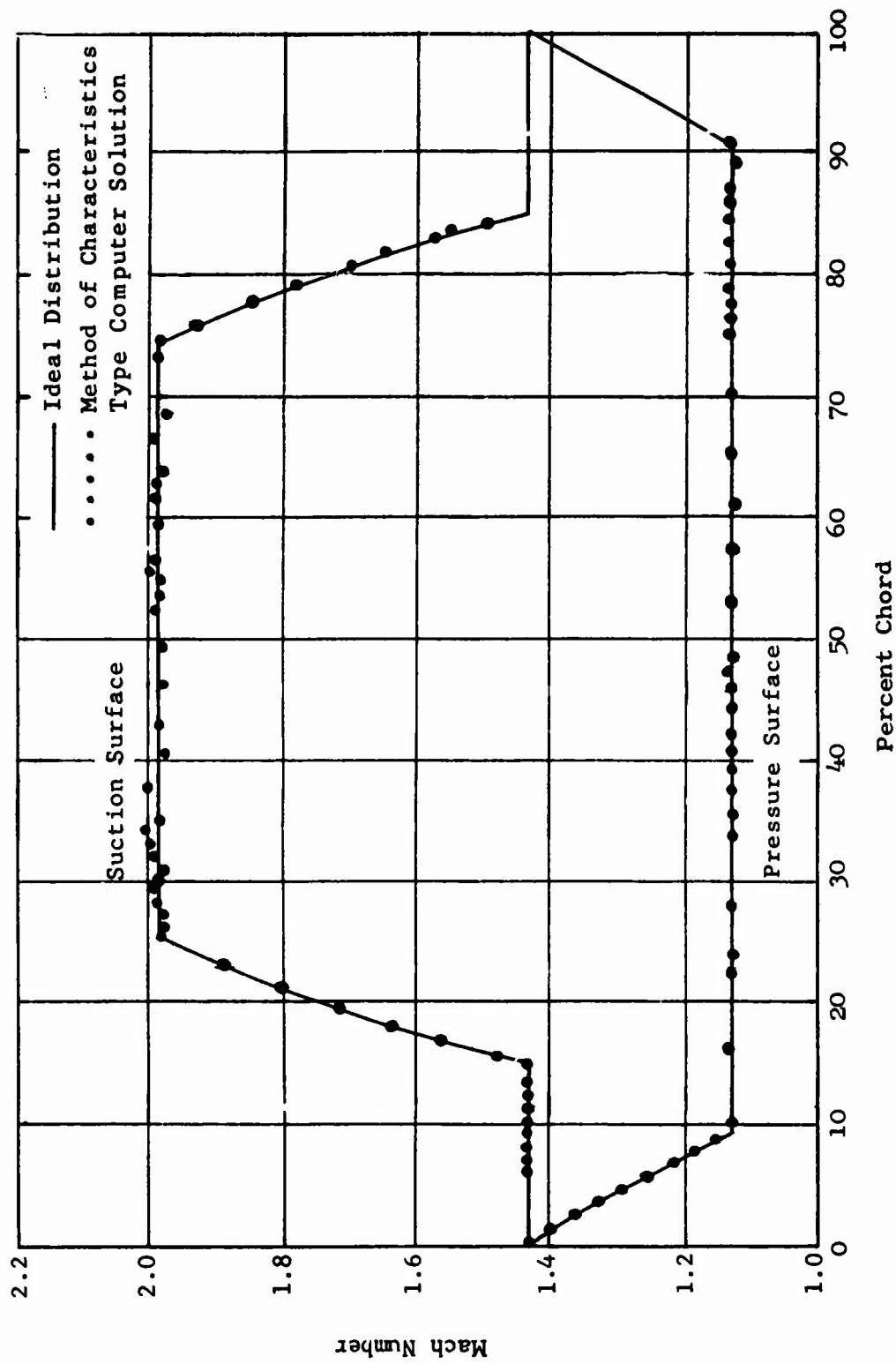


Figure 191. Two-Dimensional Rotor Blade Mach Number Distribution.

<u>Operating Conditions</u>	<u>Mach Number</u>
1. No Coordinate Rotation - Constant Wall Spacing	2.119
2. No Coordinate Rotation - Variable Wall Spacing	2.016
3. Coordinate Rotation - Constant Wall Spacing	2.246
4. Coordinate Rotation - Variable Wall Spacing	2.159

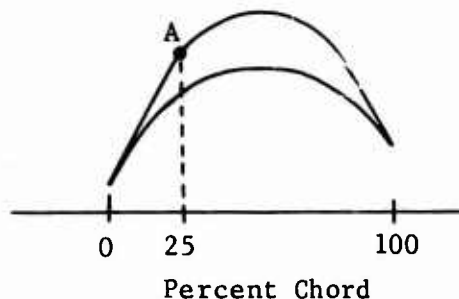


Figure 192. Rotor Blade Sketch.

The one-dimensional calculations corresponding to the above operating conditions indicate that, for the case of no coordinate rotating, the change from a constant wall spacing to a variable wall spacing should result in a decrease in Mach number of -1.9 percent. For the case with rotation, the corresponding decrease in Mach number is -1.7 percent.

The one-dimensional prediction of the effect of coordinate rotation for the case of constant wall spacing and variable wall spacing, respectively, is +1.9 percent and +2.1 percent.

The comparison of the one- and two-dimensional calculations is given below.

<u>Fixed Conditions</u>	<u>Changed Conditions</u>	<u>Two- Dimensional Prediction</u>	<u>One- Dimensional Prediction</u>
1. No Coordinate Rotation	Constant Wall Spacing to Variable Wall Spacing	-4.9%	-1.9%
2. Coordinate Rotation	Constant Wall Spacing to Variable Wall Spacing	-3.9%	-1.7%
3. Constant Wall Spacing	No Coordinate Rotation to Coordinate Rotation	6.0%	1.9%
4. Variable Wall Spacing	No Coordinate Rotation to Coordinate Rotation	7.1%	2.1%

It is evident that the one-dimensional approach is not adequate for predicting the two-dimensional effects present in the rotor.

Required Blade Shape Changes for Three-Dimensional Case

The object in applying the method of characteristics solution to a modified three-dimensional blade was to indicate what changes in rotor blade shape would be necessary to obtain an acceptable blade surface Mach number distribution. The blade shape analyzed is shown in Figure 193. The analysis was carried out to about 70-percent chord, and the results are shown in Figure 194. The passage has been divided into a number of sections in Figure 193 (i.e., Section A'CA, Section ACDB, etc.), and the corresponding surface Mach number distributions for each section have been marked on Figure 194.

The first section (Section A'CA) represents that part of the flow field which is influenced only by the lower blade. That is, the Mach number distribution in this section depends only on the blade shape from A' to C. As can be seen, the Mach number distribution from A to C is similar to the two-dimensional values shown on Figure 191, and no further modifications are necessary.

The characteristics line AC (Figure 193) indicates that changes in the blade shape at point A of the upper blade will propagate along line AC and will affect the lower blade surface flow conditions at point C. Similarly, changes made at point B will affect the lower blade at point D. The Mach number distribution along CD, therefore, is dependent on the blade shape along AB as well as the blade shape along CD.

The Mach number distribution along CD is seen, from Figure 194, first to drop slightly and then to rise rapidly to an undesirably high value. The rise in Mach number along CD can be counteracted by reducing the slope of the blade surface from A to B, as shown in Figure 193 by dashed lines.

The surface Mach number distribution also indicates a sharp drop in the suction surface Mach number at point D, owing to the oblique passage shock DE. This passage shock is generated because the inlet flow conditions and the boundary surfaces are inconsistent with an isentropic flow process through the passage. The inconsistency is due to too sharp a blade surface curvature at point B.

Because of the relatively large change in the blade surface Mach number distributions, it was decided that it would probably be more fruitful to design the three-dimensional rotor blade directly to match a desired Mach number distribution rather than to attempt to modify a two-dimensional blade design.

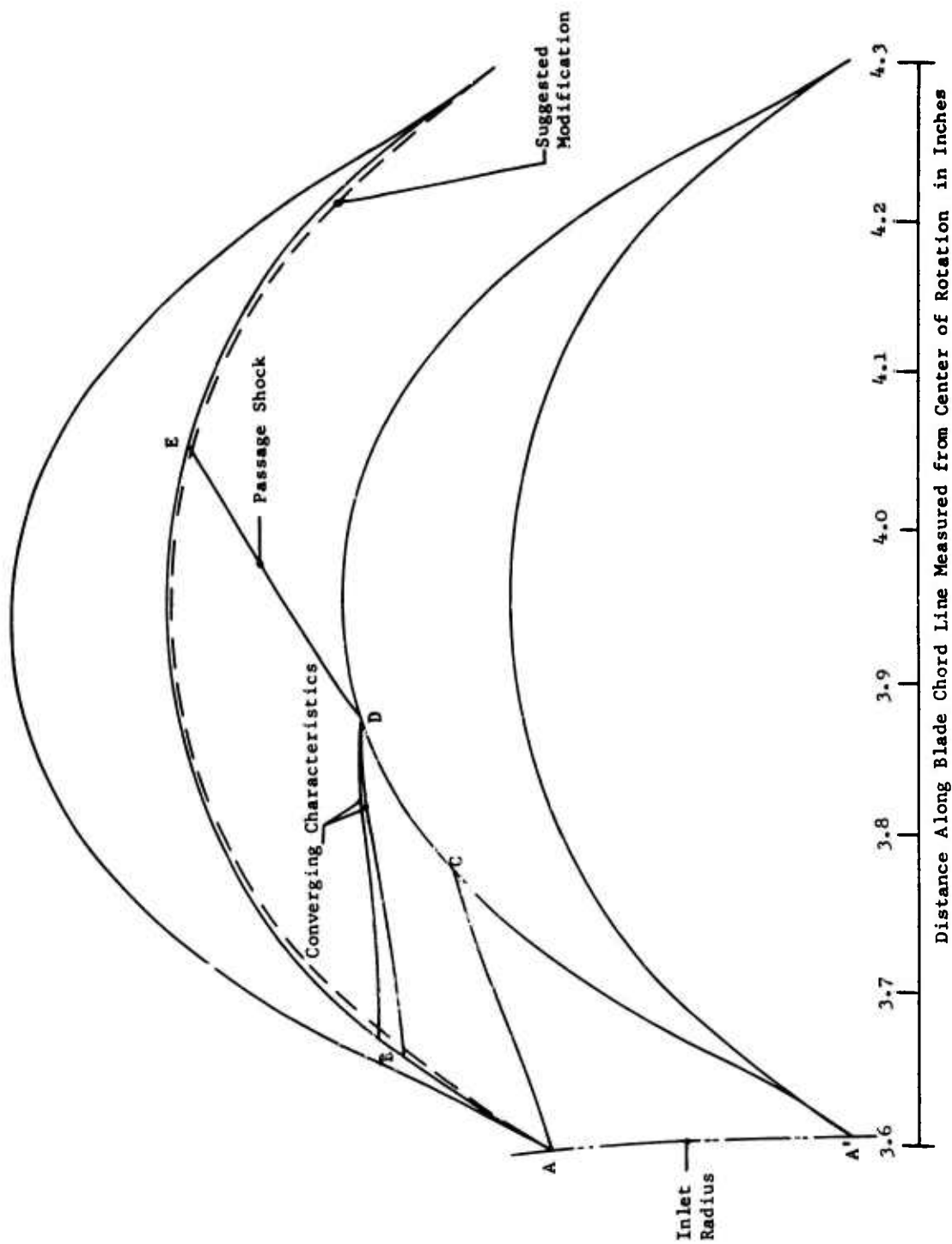
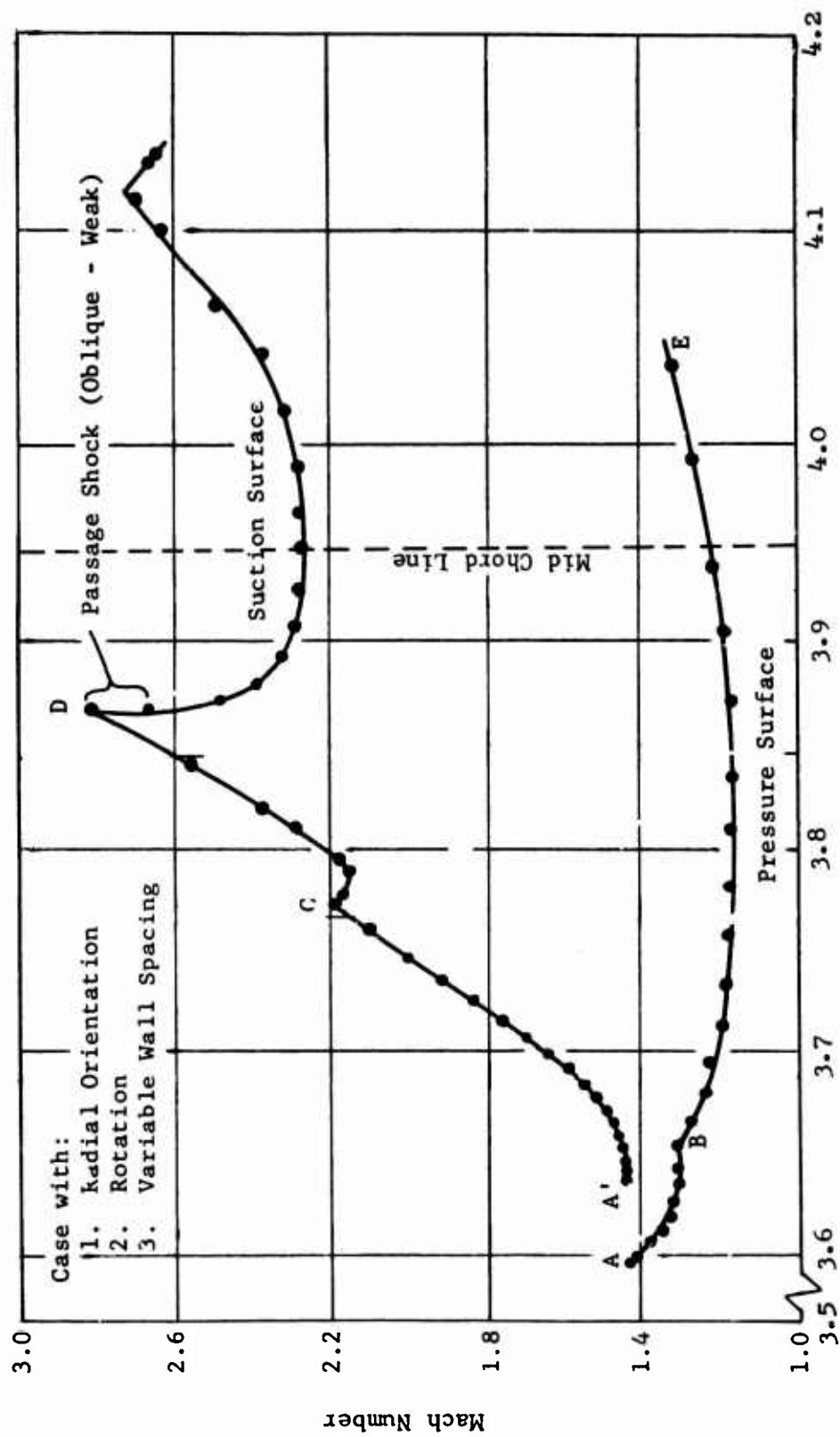


Figure 193. Three-Dimensional Rotor Blade Radial Orientation.



Distance Along Blade Chord Line Measured from Axis of Rotation in Inches

Figure 194. Three-Dimensional Rotor Blade Mach Number Distribution.

Analysis of Upstream Shock-Expansion Pattern

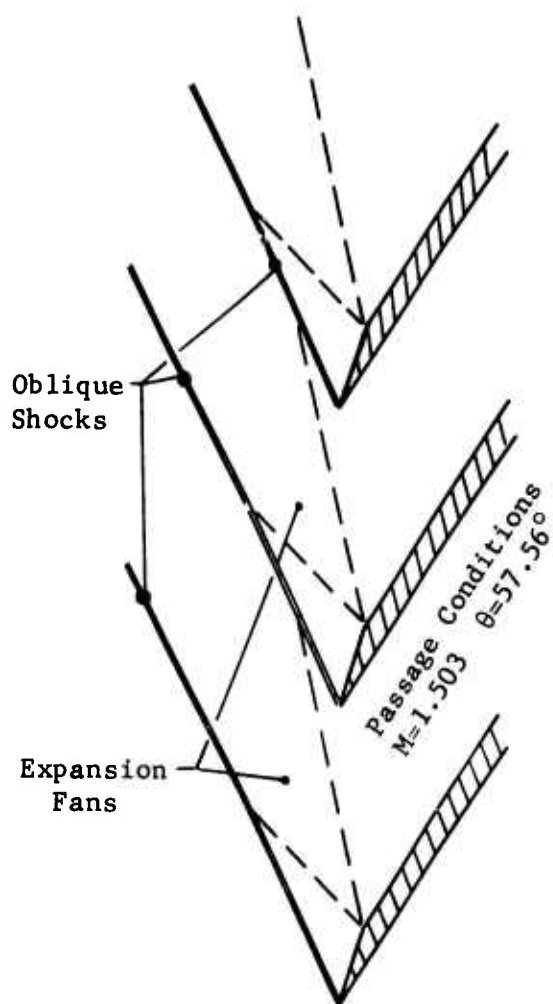
One of the major roadblocks to the successful application of the computer program to a direct three-dimensional design was the specification of the shock-expansion pattern upstream of the blade owing to the use of finite thickness leading edges. It was decided that an approximate specification of this complex flow pattern would be used in lieu of an "exact" specification. The exact specification could not be justified in the light of the additional cost in time and money and also because greater accuracy is not consistent with real dimensions that can be obtained by even the most accurate blade manufacturing methods presently available. The purpose of the approximate analysis was to describe the gross rather than the detailed effects of the finite thickness leading edges. It was based on the analysis performed on the relatively simple two-dimensional blade case. The gross effects in the two-dimensional case can be represented by considering a discontinuity to exist in the flow pattern at the blade leading edges, as shown in Figure 195.

The approximate method was applied to the three-dimensional case, and the results were used in the method of characteristics program.

Direct Design of Three-Dimensional Blade

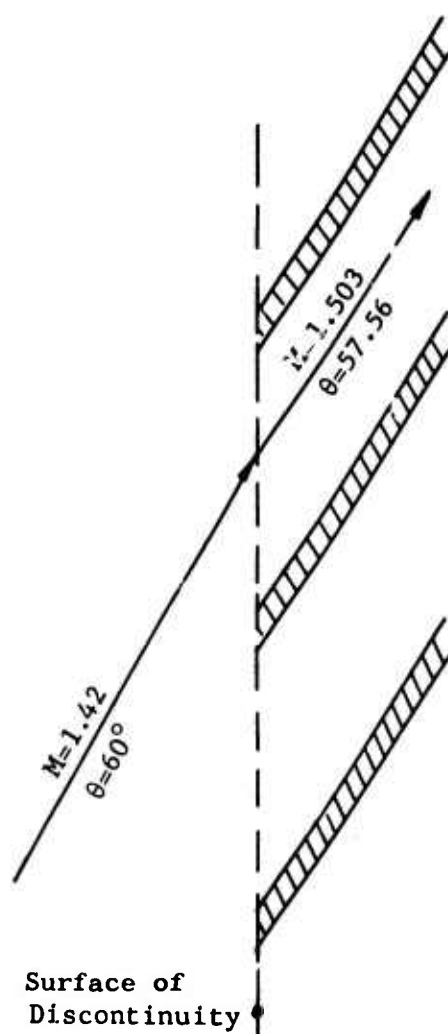
As was previously mentioned, the method of characteristics computer program employed in this analysis is capable of determining passage shape when given a surface Mach number distribution. In order that the resulting passage shape produce an acceptable blade contour, it is necessary that the Mach number distribution and resulting passage shape satisfy a number of compatibility requirements as follows:

1. The Mach number distribution must define a real blade. That is, the Mach number distribution curve defines a flow passage such that the pressure surface of this passage along with the suction surface of the adjacent passage forms the outline of a blade. A blade is considered defined if it is closed at both extremities and possesses a practical thickness in between.
2. The Mach number distribution must be capable of applying the required tangential force to the fluid. The blade tangential force is determined by integrating $P \cos \theta \, dA$ over the inner blade surface, where θ is the angle between the blade surface tangent and the local radius.
3. The minimum Mach number must be greater than 1.0 (a limitation imposed by the method of analysis).
4. The maximum Mach number should not be too large in order to reduce shear losses and to reduce the amount of diffusion necessary near the suction surface trailing edge.
5. The resulting blade shape should not have excessive wetted surface.



Upstream Conditions
 $M = 1.42$
 $\theta = 60^\circ$

Detailed Effect of Finite
 Thickness Leading Edge



Surface of
 Discontinuity

Gross Effect of Finite
 Thickness Leading Edge

Figure 195. Finite Thickness Leading Edge Effects.

6. The suction surface and pressure surface trailing edge Mach number should not be excessively different. Differences in trailing edge Mach number will result in different surface pressures just before the trailing edge. Since the fluid pressure just behind the trailing edge is assumed to be single valued, a radical flow adjustment is required if excessive pressure differences exist. This adjustment will be in the form of a trailing edge shock and expansion pattern. For blades with finite thickness trailing edges, such patterns cannot be entirely avoided, but their magnitude can be reduced by means of consistent trailing edge Mach numbers.
7. The blade passage area distribution must be such that the blade is capable of starting at the desired Mach number.

The Mach number distribution from which the final rotor blade shape was determined is shown in Figure 196. The calculated characteristics network, and the associated passage shape computed for this particular distribution, is shown in Figure 197. The blade contour was derived by rotating the upper passage surface one pitch angle counterclockwise about the rotor centerline.

In checking the preceding seven compatibility requirements, it must be borne in mind that the characteristics solution takes no account of the very significant frictional losses which occur in the actual blade. For this reason, evaluation of the Mach number distribution should be made on the basis of the one-dimensional effects calculated from the two-dimensional data obtained in the wind tunnel tests.

In order that the Mach number distribution define a real blade, it was necessary to adjust the blade shape in the trailing edge region (this adjustment is clearly seen in the rotor blade diagram, Figure 197). The magnitude of this adjustment is consistent with present knowledge of conditions at the trailing edge.

The blade surface pressure distribution, Figure 198, was used to generate the rotor blade tangential force distribution shown in Figure 199. The resultant tangential force per blade calculated from the graphical integration of the force parameter is 6.21 pounds. The required work input of the rotor blade row can be determined on the basis of the compressor efficiency and pressure ratio. For the required work input, rotor rpm, and number of blades, the individual tangential blade force can be calculated. The tangential force from this calculation is 6.24 pounds. The boundary layer would tend to decrease the work input somewhat, but it is still felt that the agreement between the two-dimensional predicted value and the one-dimensional required value is satisfactory.

The minimum Mach number of the blade is 1.0, the maximum Mach number is 2.0 (neglecting the small peak on the distribution curve, Figure 196), and the solidity is 2.5*. These values are the same values as were used in

* The solidity is indicative of the amount of wetted surface.

the design of the two-dimensional blade tested in the transonic tunnel. It is felt that these values are quite reasonable.

The blade passage starting criterion was applied and indicated that no starting problems should be expected at the design inlet Mach number of 1.42.

As can be seen in Figure 196, the trailing edge suction and pressure surface Mach numbers are significantly different from each other. This condition could not be alleviated without major blade modifications. It is believed that the frictional effects present in the actual blade will reduce this difference. In any case, it is not felt to be significant enough to warrant a redesign of the blade.

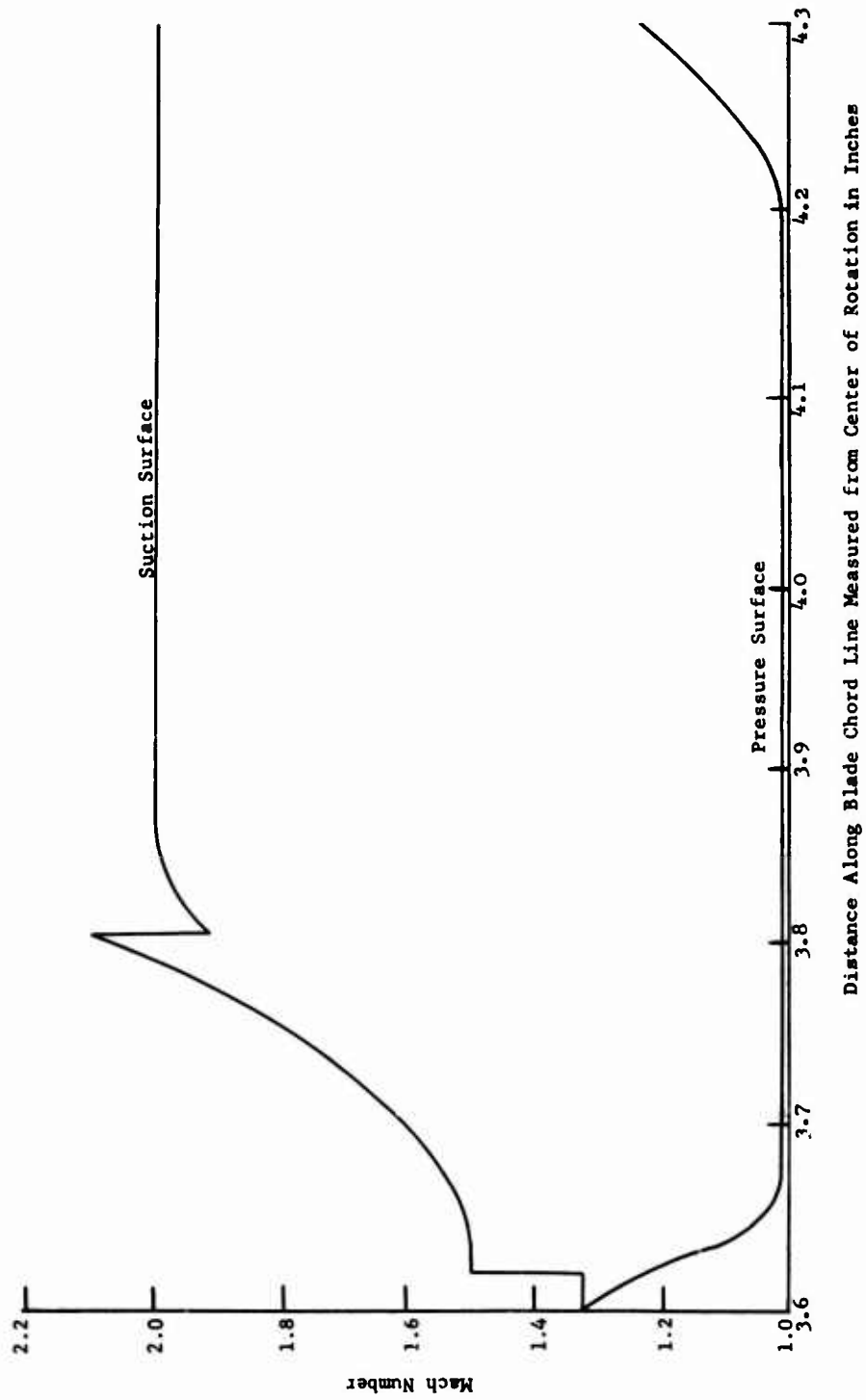


Figure 196. Mach Number Distribution for Final Rotor Blade Shape.

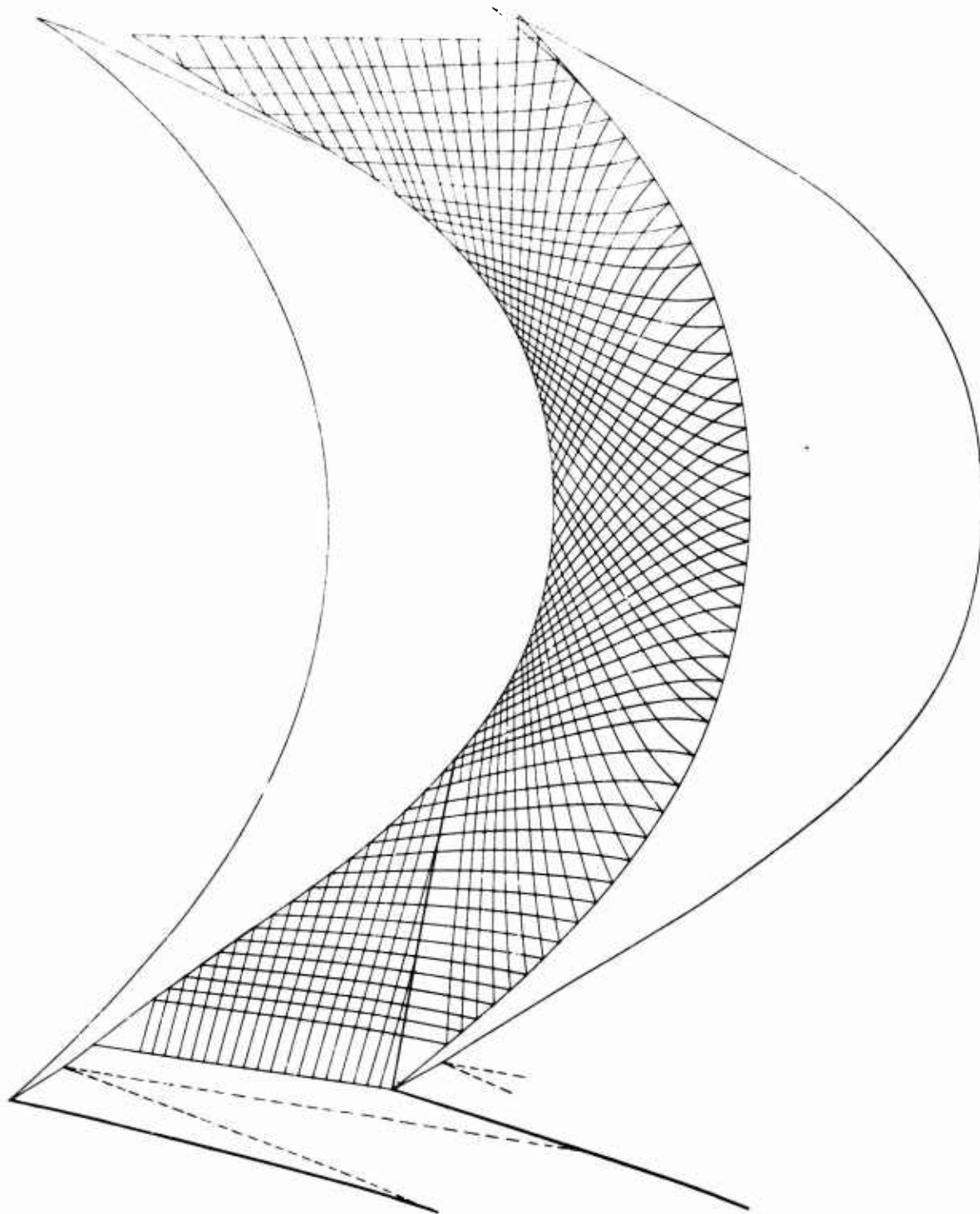


Figure 197. Characteristics Network and Passage Shape for Three-Dimensional Rotor Blade (Final Design).

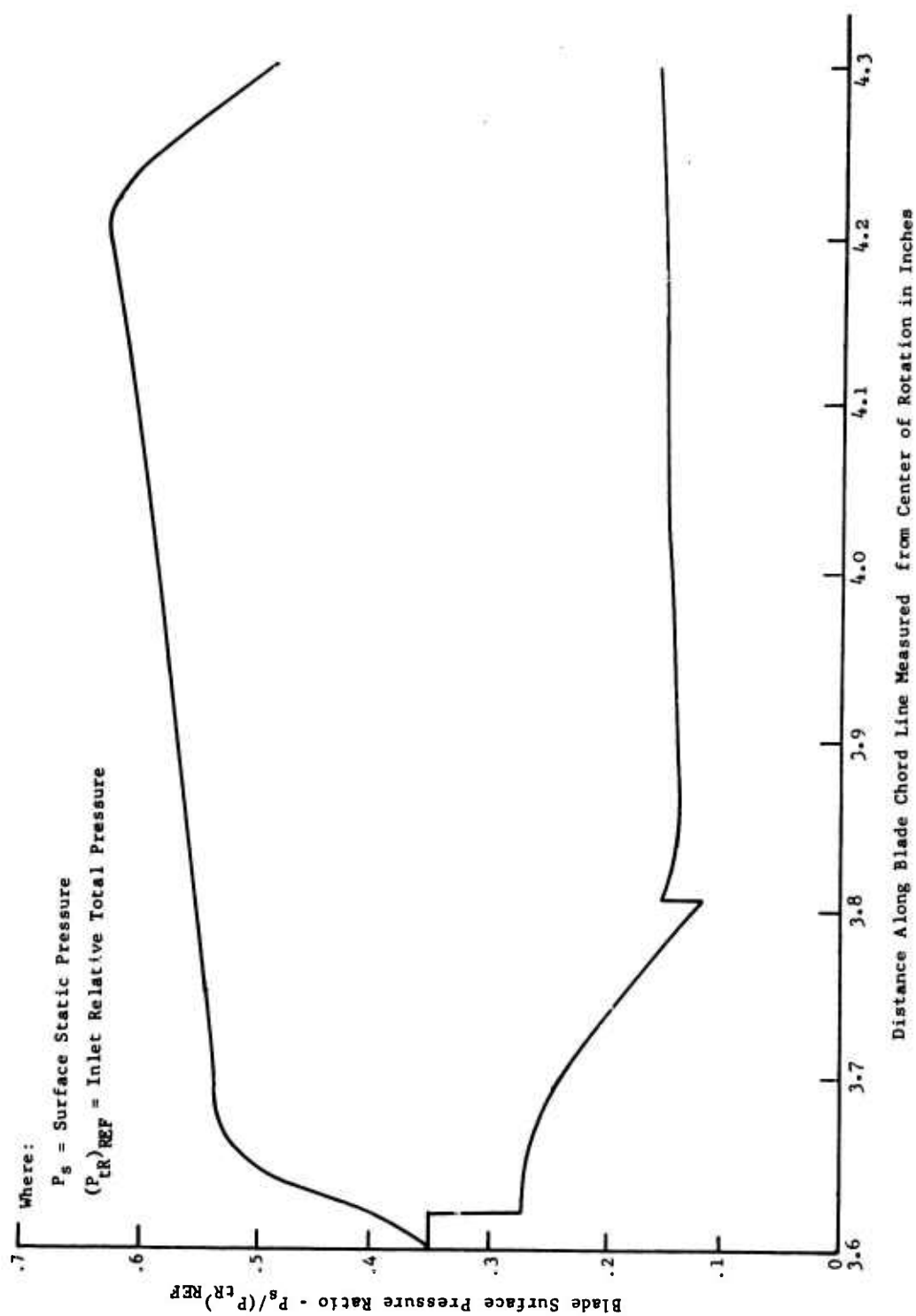


Figure 198. Rotor Blade Surface Pressure Distribution.

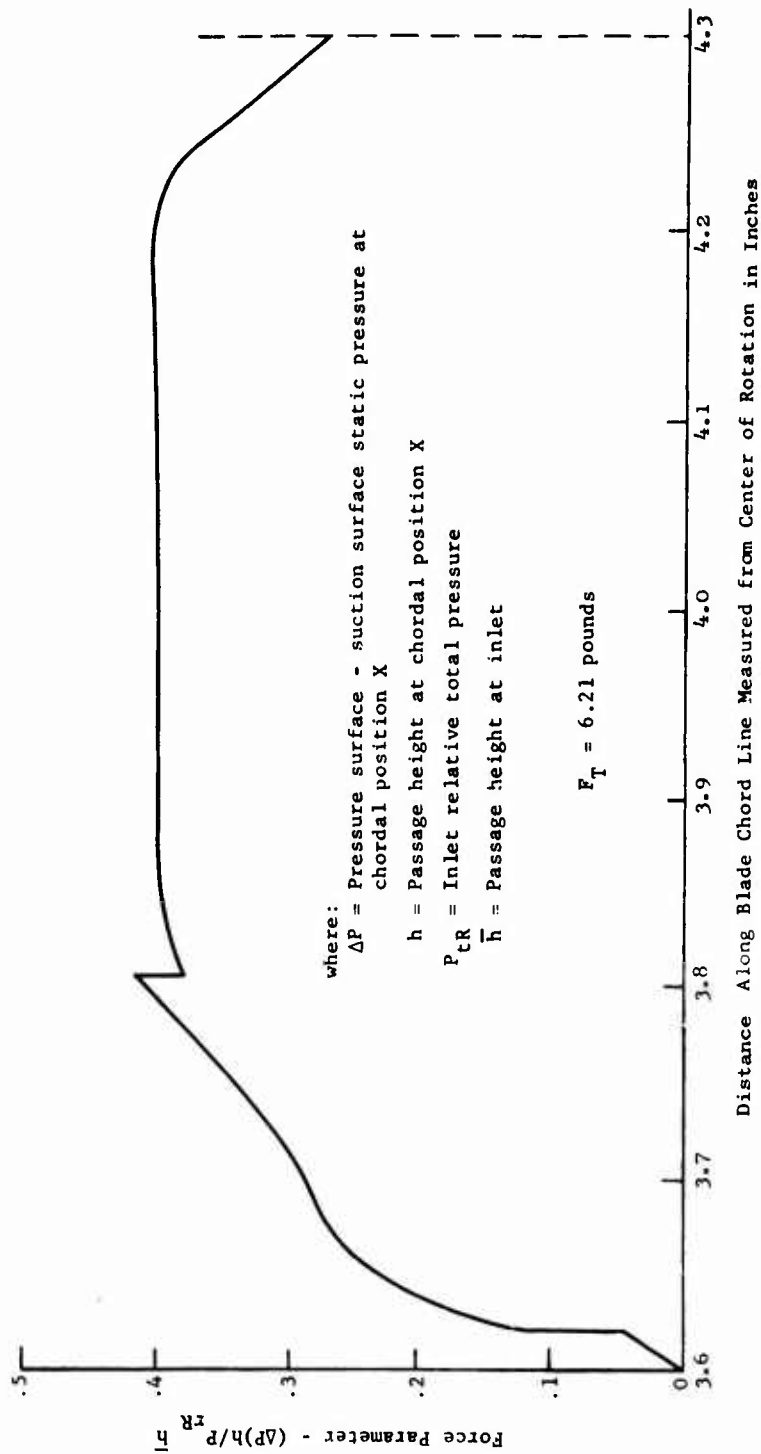


Figure 199. Rotor Blade Tangential Force Distribution.

MECHANICAL ANALYSIS

INTRODUCTION

The rotor assembly (Figure 200) is a single stage, radial flow design with blades carried axially between a disc and a rotating shroud. Disc and shroud tip diameters are 13 inches, and the blades are located on an 8-inch diameter.

The major components that make up the rotor assembly are listed below:

1. Disc
2. Blades
3. Rotating shroud
4. Centerbody
5. Shaft
6. Main bearings

The objectives of the mechanical analysis work performed during Phase I of this program were as follows:

1. To conduct an investigation of high strength aluminum, titanium, steel, and fiber glass (and possible composites of these) to determine optimum material for rotor.
2. To design a demonstrator compressor to provide maximum aerodynamic performance consistent with mechanical design requirements.

In order to meet aerodynamic performance objectives, the highest possible compressor speed is required, since efficiency of the radial outflow compressor improves significantly with rotational speed. Speed is limited, however, by allowable stresses in the rotating parts because of geometry set from aerodynamic requirements. Thus, the mechanical design envelope is set by high-speed requirements and geometry limits.

MATERIAL SELECTION

The major characteristic required in the rotor material is high strength to weight ratio, since the rotational speed is limited because of stresses in the rotor. A survey of high strength to weight ratio materials showed 6-6-2 titanium (6 percent aluminum, 6 percent vanadium, 2 percent tin, and the remainder titanium) to have definite advantages over other possible choices such as filament-wound fiber glass, X-2020 aluminum, and marage steel. Fiber glass and aluminum experience a loss in strength at the radial outflow compressor temperature levels, and marage steel has undesirable oxidation and directional properties. In addition, subsequent material property testing of 6-6-2 titanium samples (see data in report section entitled Bench Tests) showed this alloy to have excellent ductility and resistance to notch sensitivity, as well as high strength. All of these characteristics are important assets in assuring a rugged, reliable rotor.

Additional studies have been made of an improved rotor material designated 200K titanium. This alloy is a variation of the 6-6-2 titanium composition. Compared with 6-6-2 titanium, it has been found to offer the following characteristics (see reference 30):

1. 40,000 psi higher 0.2 percent yield strength
2. Less reduction in strength for thick section sizes
3. Only slightly lower ductility

Should increased radial outflow compressor performance become desirable in a growth design, 200K titanium appears to offer additional material capabilities.

MECHANICAL DESIGN FEATURES

The unique aerodynamic features of the radial outflow compressor present several difficult design requirements, among which are:

1. Flow-path walls must be formed by the rotating sides of the rotor.
2. Flow path must be a converging section.
3. Rotor blades must be supported between flow-path sides.
4. Very accurate rotor blade location contour and edge thickness are required because of small blade size and spacing.

The mechanical design features of the radial outflow compressor which meet these requirements are described here.

Disc and Shroud

Converging Flow Path

Design of a maximum speed rotor disc can be easily determined for a conventional axial flow compressor, where optimum cross sections are either the deLaval "constant stress" design for solid discs or hyperbolic sections for a disc with a bore (see Figure 201). However, a major compromise dictated by the radial outflow compressor aerodynamic requirements is that the rotating parts form the tapered sides of the flow path. Initial designs, using two rotating parts with hyperbolic cross sections which were angled to form a converging passage, were found to straighten outward at full speed, changing axial position and flow area significantly. To combat this tendency and to hold the flow-path section steady at various speeds, the centerlines of both rotating sides were selected to be radial.

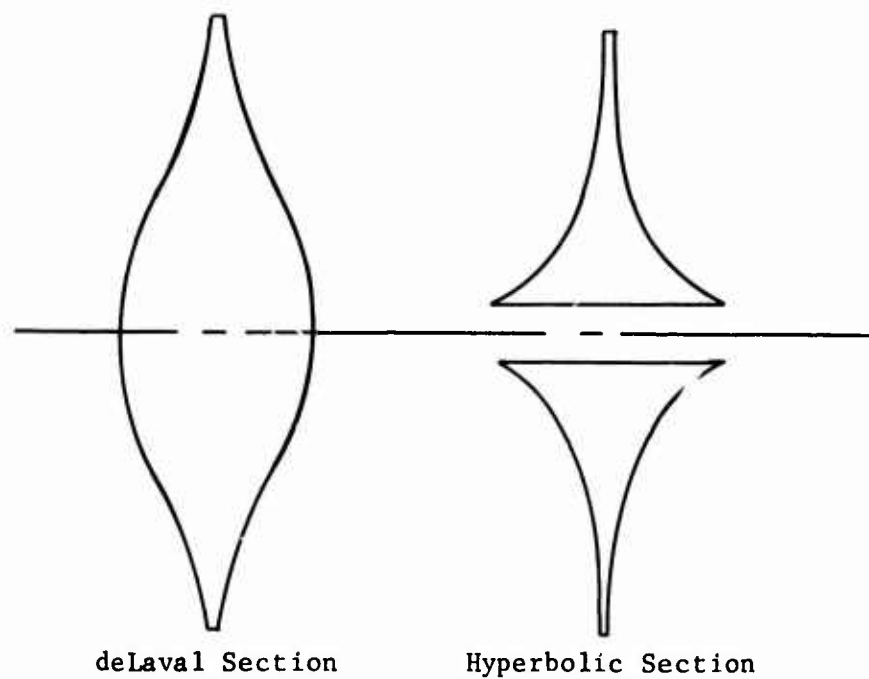


Figure 201. Disc Cross Sections for Optimum Stress Design.

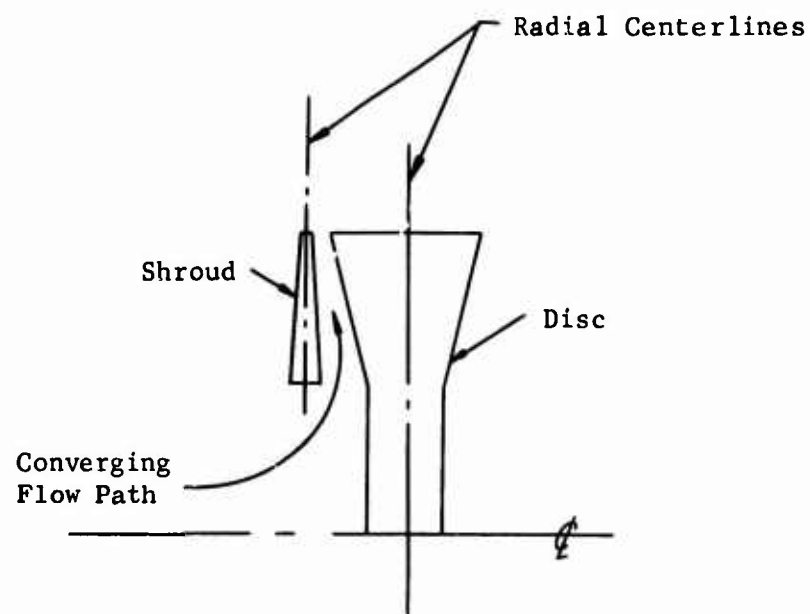


Figure 202. Stable, Converging Flow Channel Design.

Also, to design a converging passage requires the use of rotating parts with radial centerlines, where one part has positive cross section taper (decreasing thickness with increasing radius) and the other has negative taper (see Figure 202). The combination of reverse taper on adjacent rotating parts gives the desired converging flow passage while the radial centerlines give stable parts that do not shift under centrifugal load, as inclined rotating faces tend to do. Extra stability is given the shroud by providing radial centerlines in both rotating walls.

Stress Analysis

Once the concept for a stable converging flow path was set, refinement was needed to minimize stress. The most attractive possibilities were:

1. Varying rotor cross section for best stress distribution
2. Bi-material construction to use strength to density ratios to best advantage
3. Prestressing to lower the full speed rotor stress

Although tapered cross sections on both disc and shroud were found to be the key to providing a stable converging flow path, only one member could have positive taper (which decreases peak stresses). Since a central hole (which increases maximum stress) is required in the shroud to provide compressor inlet air, a trade-off was made to reduce the effect of this bore by using positive taper on the shroud. Thus, maximum stresses are permitted to be approximately the same in the shroud (having positive taper cross section and a bore) as in the disc (having reverse taper cross section and no bore).

Even though a hyperbolic tapered cross section would give slightly lower stresses in the shroud compared to a linear taper, the greater machining accuracy obtainable with linear taper (which gives a better balanced part and more accurate flow path) led to its acceptance on both the shroud and the disc. Final sizing of disc and shroud thicknesses is made by setting minimum desirable shroud tip thickness and then sizing the disc to match closely the centrifugal growth of the shroud.

Further improvement in stress distribution appeared possible with the use of a composite material rotor with prestressing (see report section entitled Bench Tests). Lower density material used in the outer rotor area would develop less centrifugal force to be carried by higher density material (having greater load capacity) in the inner rotor area. In addition, prestress applied in such a dual material rotor would further reduce the maximum stress at full compressor speed. However, complexity in attachment of the materials

to each other and questionable reliability of the prestress seemed to outweigh the advantages offered. Thus, neither of these approaches is used in the final rotor design.

Rotor Speed

Mechanical design parameters with direct influence on each other are rotor speed and rotor blade size, spacing, and location. Since compressor size and flow path had been determined in initial aerodynamic analyses, a study was made using these limits in addition to desired values of blade solidity, aspect ratio, and velocity to determine the optimum blade size, spacing, location, and rotor speed. The following mechanical design limits were found:

1. Minimum blade chord length is the limiting factor when the blades are placed at a large radius and run at reduced rpm.
2. Rotor stress is the limiting factor when large blades are placed at a small radius and run at high rpm.

The compromise design set between these two extremes has a rotor speed of 34,500 rpm with 88 blades. The blades have a 0.7-inch chord, an aspect ratio of 1, and a solidity of 2.5, and are located at a 3.95-inch radius.

Blades

The variables of blade size, spacing, and location were set in conjunction with rotor speed, and the blade contour was set by aerodynamic considerations. Blade attachment to both disc and shroud is the only major remaining blade design problem. The attachment is designed with the following requirements in mind:

1. Radial location stiffness of shroud
2. Torque transfer from disc to shroud
3. Location accuracy
4. Possible blade foreign object damage (FOD)

Listed below are what appeared to be the best attachment alternatives (see Figure 203):

1. Shear lugs - integral on each shroud and disc; fitting inside, and thus supporting, a hollow blade.
 - a. Bolts through lugs to connect shroud and disc.
 - b. Dovetail fastener - holds shear lug as alternative to using through bolts. Avoids bolt holes in shroud.

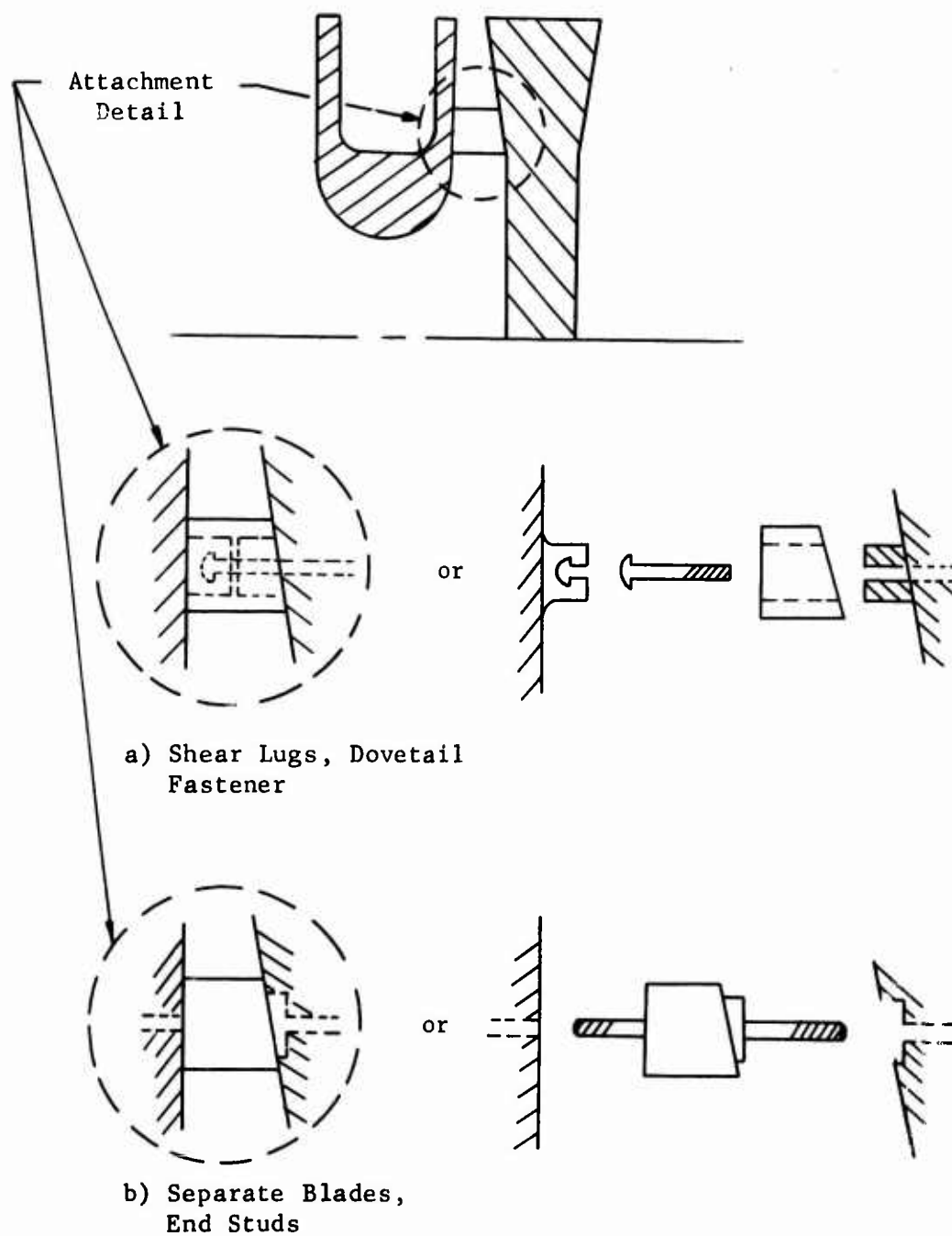


Figure 203. Blade Attachment Alternatives.

2. Integral blades - machined integral with disc, and through bolts to attach shroud.
3. Separate blades - located in recesses in disc and shroud with threaded end studs through disc and shroud.
4. Separate blades - diffusion bonded to disc and shroud.

A desirable design from a strength standpoint is the shear lug design, but manufacturing accuracy for this was an unknown. Thus, a feasibility program was initiated to produce hollow blades and a test piece with matching shear lugs to check assembly fit-up accuracy (see report section entitled Bench Tests). Also, dovetail fastener tensile specimens (compatible with the shear lugs) were ordered to evaluate their holding strength. Check-out of the shear lug test piece showed that machining accuracy and repeatability were not as good as required. Also, local shear stress was found to be excessive in the lug where effective area was reduced by the through bolt hole. Thus, an alternate design of either integral or separate blades was required. The integral design gives mechanical ruggedness and few parts to compound blade mislocation, but separate blades allow more accurate manufacture of blade contour and replaceability of blades. Since manufacturing limitations played such an important part in each design, both were presented to manufacturing firms for comments and quotes. Review of quotes showed the integral approach to be more expensive and to be manufacturable only through the use of electric discharge machining (EDM) methods. This machining process (also used in hollowing blades for the shear lug machining study) has been found to leave surfaces having poor fatigue strength properties, which cannot be tolerated in highly loaded rotating parts. In addition, further comparison of the blade attachment approaches showed the following:

- | | |
|----------------------|--|
| Integral: Advantages | 1) Few pieces |
| | 2) High shroud location stiffness |
| Disadvantages | 1) Possible scrapping of rotor due to blade manufacturing defects or FOD |
| | 2) High stress concentration at blade junction of disc |
| | 3) Manufacturability - contour and finish |
| Separate: Advantages | 1) Better blade surface contour and finish |
| | 2) Allows close fit-up of blade alignment |
| Disadvantages | 1) Bonding process involves many assembly variables |
| | 2) Number of pieces |
| | 3) Threaded titanium |

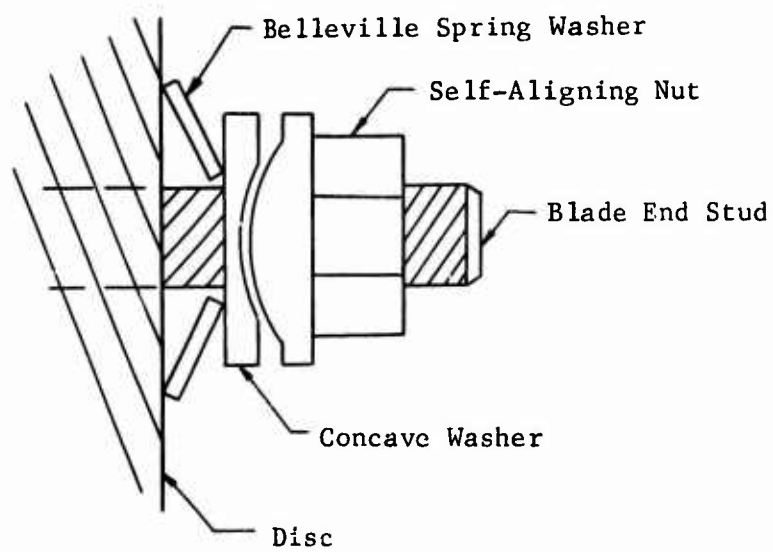
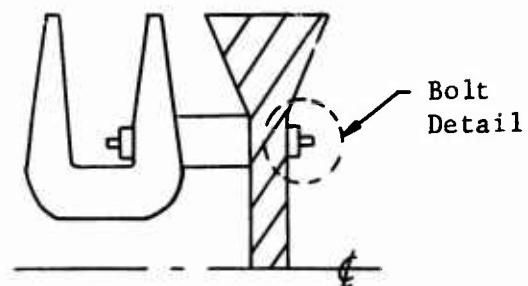


Figure 204. Preloaded Blade Attachment.

Although bonded blades are very promising (see report section entitled Bench Tests), they require much development work. Thus, separate blades with threaded studs were chosen as the best compromise design for the first rotor.

The threaded blade studs used in this separate blades design require special consideration as to nut design and preload required (see Figure 204). The nuts used are self-aligning, having a spherical base mating to a concave washer face. This feature allows full torque application to the nut on an "out of line" blade stud without the risk of bending the shank. A tension preload on the shank of 50 percent to 80 percent of yield strength is desirable to reduce possible start-stop fatigue effects. However, between start-up and 100 percent speed, both the disc and the shroud thicknesses are reduced enough by Poisson's ratio effect to cause almost 50-percent loss in shank preload. To correct this, Belleville "spring" washers are used to insure nearly constant preload during disc and shroud thickness changes.

Disc Flange

Attachment of the rotor to the driving shaft required a radially flexible coupling to allow "free" rotor stretch, yet to resist radial motion due to any unbalance in rotor or shroud. The alternative solutions considered are:

1. Curvic or radial teeth
2. Radial pins
3. Thin shear cylinder with bolted flange

Curvic or radial teeth can do the desired job but require precise, expensive grinding. Radial pins attempt the same job with less precision but inherently have undesirable clearances. A thin cylinder is an easily manufactured method of attaining the desired centering force and is radially elastic at either end. Thus, a thin shear cylinder design is used.

Centerbody

A rotating centerbody is desirable from an aerodynamic standpoint because it reduces the boundary layer growth for preswirl operation. Since it is not practical to make the centerbody integral with the disc because of the large forging that this would require, a means for centerbody attachment to the disc is required. Methods considered are:

1. Bolting through holes in the disc
2. Bolting into tapped holes partially through the disc
3. Rabbet with tie bolts

Holes through the disc near its center introduce stress concentrations in the most highly stressed region of the disc which would result in reduced test life of the disc due to low cycle fatigue cracking around

the holes. Tapped holes in the titanium disc must be made with sharp, cut threads, and they are susceptible to stripping and cracking. The rabbet provides a good locating surface for centering, while the tie bolts give a tight assembly, with the bolt holes passing through low stress material. This last method is used.

Since the centerbody is not highly stressed and sees temperatures much lower than other rotor parts, aluminum is used for the centerbody material. Use of this light material also means that centerbody unbalance is kept to a minimum.

Shaft and Main Bearings

The shaft and bearing system is a double bearing design with an overhung rotor.

Shaft

An external spline is used at the shaft-driven end with a bolted flange attachment to the rotor at the driving end. Shaft material is Nitralloy N, a well tried gear and shaft alloy that develops exceptional surface hardness when nitride case hardened. This alloy is softer than Nitralloy 135, owing to a higher nickel content, but has higher surface toughness.

Bearings

Ball bearings are used for both the forward and the rear main bearings. These are oil spray lubricated and operate at a DN value (this being a measure of surface speed where DN is the product of shaft diameter in millimeters and shaft speed in revolutions per minute) of approximately 1.6×10^6 at 100-percent speed, well below the rated DN value of approximately 2×10^6 for this type of bearing. The bearings are spring loaded in the axial direction to insure positive centering and proper load direction for both sets of angular-contact bearings.

Seals and Cooling

Seals

The two primary points for sealing against leakage are: (1) just forward of the front main bearing and (2) the forward face of the shroud. The main bearing seal is of carbon and is a double seal design using two sealing surfaces. This seal rotates with the shaft and seals against stationary surfaces. The shroud seal is a labyrinth design of aluminum attached to the housing ahead of the shroud. The seals are placed at small radii to keep surface speed of the seals at a minimum. In addition, the shroud seal is placed on a radius approximately the same as that of the blades. This

balances axial pressure on the forward and aft faces of the shroud so that no axial pressure load need be carried by the bolted blades.

A backup shroud seal designed for very low leakage has also been investigated. This seal is a hydrostatic air film design that operates with very small clearances which restrict leakage significantly compared to labyrinth seal designs. Comprehensive testing of the hydrostatic seal is indicated, however, before using this design in the compressor.

Cooling

The high surface speeds of the disc and shroud adjacent to stationary housing parts create high frictional heating in the air gap between stationary and rotating parts. To control this heating and also to regulate other thermal conditions (gradients, transients, etc.), air cooling ports are built into the compressor housing both forward and aft of the rotor. Control of leakage flow is possible by varying the pressure of the coolant air.

System Operation

Both high rotational speeds and close clearances of the radial outflow compressor demand that the vibrational characteristics be acceptable and that undesirable speed ranges be avoided. The major design areas of interest are: (1) the rotating shroud and (2) the overall rotor assembly.

Shroud

The thin outer shroud tips are dictated by steady-state stress analysis but are subject to circumferential traveling vibration waves, since the shroud is in fact a thin wheel. Any such wheel has natural nodes in the form of sine waves around its circumference which, if corresponding to the wheel rotational speed (or multiples of the speed as shown on a Campbell diagram), cause a resonance condition to exist. The shroud is designed to avoid such resonance conditions. Computer analysis was made in an idealized shroud, and the results presented in the Campbell diagram, Figure 205, show no resonance conditions occurring above the 80-percent speed range. (Note: resonance is indicated by the intersection of a node line with a speed line.) To verify this calculated data, a test piece shroud was manufactured. Bench tests showed natural frequencies (sine waves of four nodes, six nodes, etc.) to agree with the calculated values within 10 percent (note comparative data points in Table XVII). Final shroud dimensions were modified slightly, as a result of these analyses and tests, to provide an even greater margin of safety.

Rotor Assembly

Since the inlet design of the radial outflow compressor requires the use of an overhung rotor, special emphasis is placed on the design of a rotor assembly with high radial stiffness in order to avoid rotor whirl. The shaft diameter is sized as large as the bearing diameters permit within DN limits, and steel is used as the shaft material to get increased stiffness from its high elastic modulus. The shaft-to-disc cylinder coupling stiffness is maximized by giving it the largest diameter possible inside the blade circle diameter. High bolt preload is used on both blade ends to insure firm shroud to disc attachment. The centerbody is attached to the disc by preloaded tie bolts and has a small third bearing at its far end mounted to the frame through a friction damper in order to prevent large vibration deflections.

Critical speed analysis of this assembly made via computer shows a single rotor critical point occurring below 100-percent speed. The variable damping coefficient on the centerbody bearing will be set to keep this critical rpm below 70-percent speed so that the critical point can be quickly passed during spin-up to 100-percent speed.

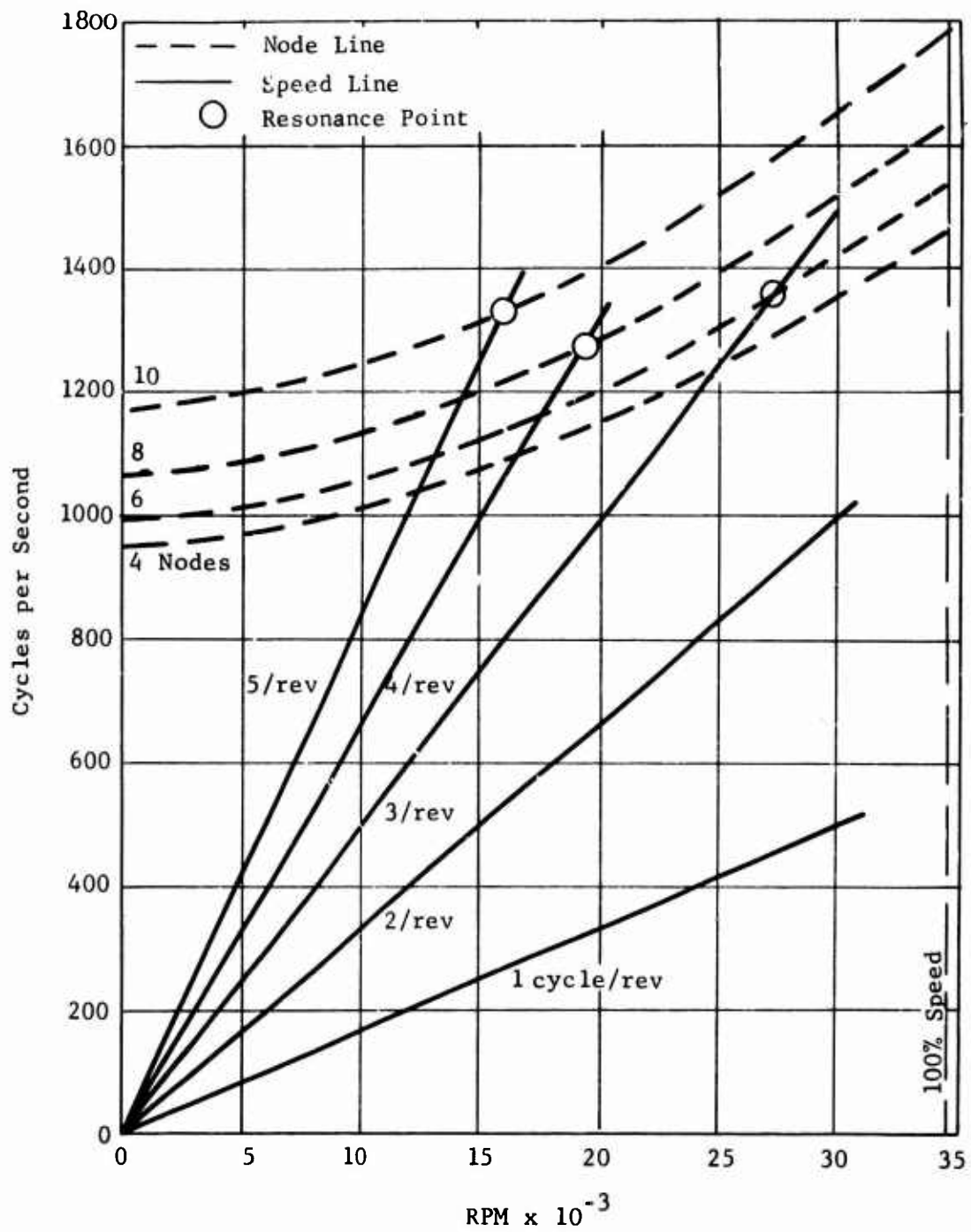


Figure 205. Campbell Diagram, Titanium Shroud.

MECHANICAL BENCH TESTS

In order to evaluate components and design ideas being considered for radial outflow compressor construction, the following work was done before finalizing the design:

1. Blade forming study
2. Blade deflection characteristics study
3. Blade attachment investigation
4. Evaluation of material properties and machinability
5. Component vibration tests
6. Rotor prestress evaluation

BLADE FORMING

Early in the preliminary design work on the radial outflow compressor, it became evident that the rotor blades would have extremely sharp edges (in the range of 0.003 inch thick). In order to evaluate whether such edges could be reasonably manufactured, several blade samples were ordered. These samples showed edges to be uniform and blade contour to be good, but final blades would need more care to get edges thinner than the samples and also to prevent edge bowing along the blade. The machining technique, however, was satisfactory and was approved for use in the manufacture of actual rotor blades.

BLADE DEFLECTION

Since these sample blades had cross sections very similar to the final blade design, they were used to check actual bending deflection values against calculated values in order to evaluate blade stress. Also, the possibility of blade edge buckling due to bending loads was examined. No edge buckling was found, however, even though applied edge compression stress approached the yield strength of the blade material.

BLADE ATTACHMENT

As noted in the Mechanical Analysis section, one of the major design problems was that of blade attachment. Several tests were made to determine the best design. Initially, the shear lug design was preferred, and two test pieces were made to evaluate the machining accuracy achievable on this design. The finished parts, shown in Figure 206, are two flat discs of 6-6-2 titanium with 12 shear lugs each. The shear lugs are grouped in sets of three and are spaced the same as a full circle of lugs. The accuracy of the lug size and location was not as good as required, primarily because the small lug spacing allowed only small milling tools to be used. These tools wear rapidly, causing variations in part dimensions.

Hollow blades were also manufactured to check fit-up with the shear lugs. These were made by taking several solid titanium blades (obtained initially for the blade forming study noted previously) and removing the center

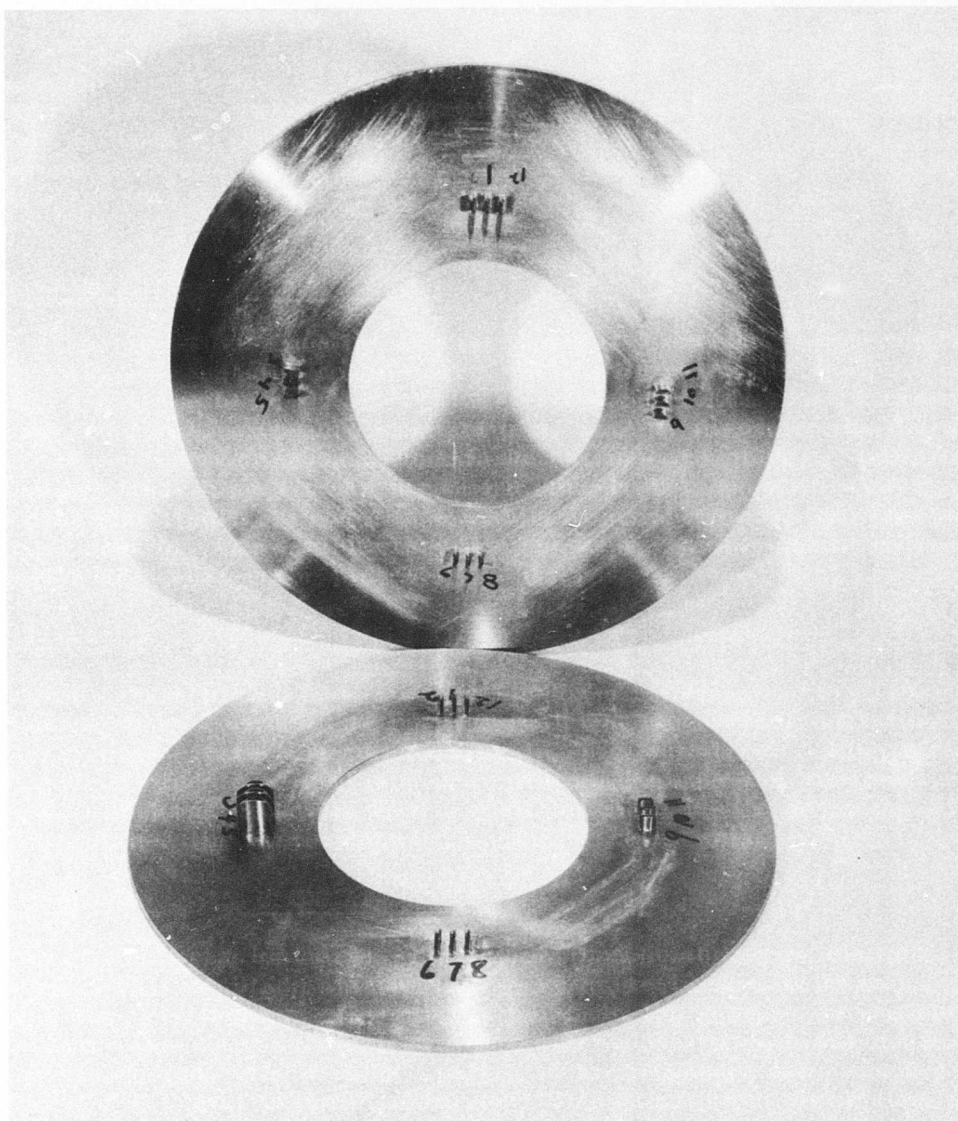


Figure 206. Blade Attachment Test Pieces of 6-6-2 Titanium With Shear Lug Design.

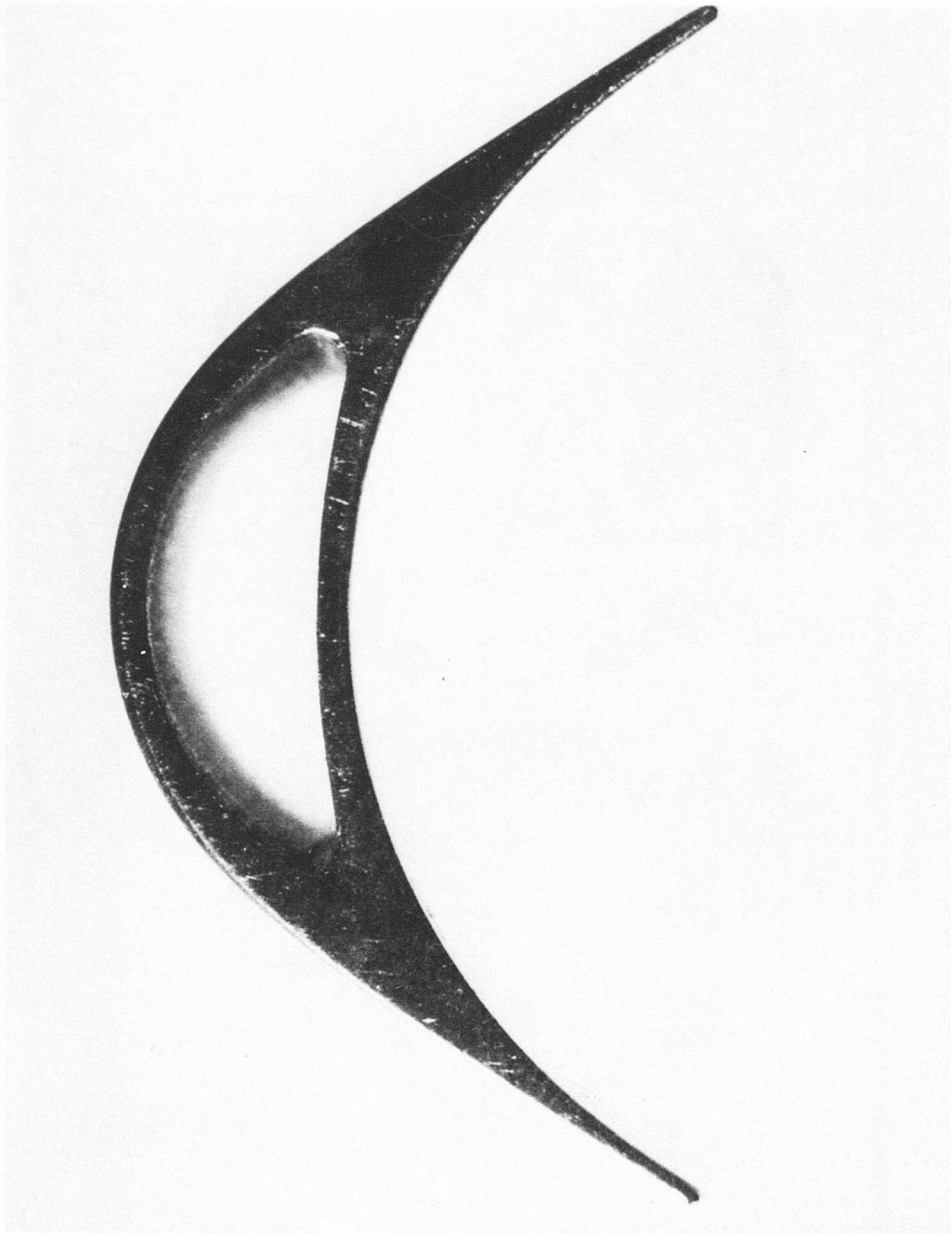


Figure 207. Hollow Titanium Blades Manufactured by Removing Center Material by Electric Discharge Machining.

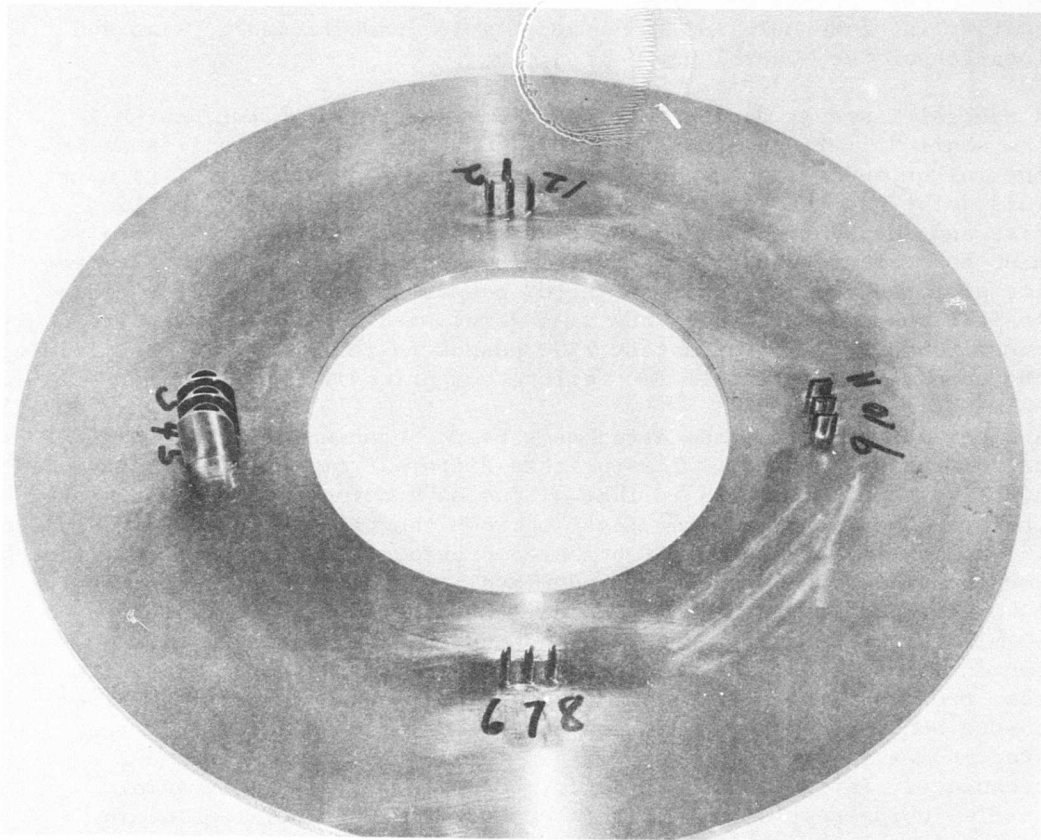


Figure 208. Assembly of Several Hollow Blades on Shear Lugs.

material by electric discharge machining, as shown in Figure 207. Assembly of several hollow blades on shear lugs is shown in Figure 208. Good dimensional accuracy was held on the blade center hole, but the electric discharge machining process left a rough hole surface with reduced strength.

Thus, the shear lug method, although offering several design advantages, is not used, partly because of the disadvantages of (1) poor surface quality in blade hole and (2) unacceptable inaccuracies in size and location of the shear lugs.

A special fastener designed to be used with the shear lug design is the small "fir-tree" stud shown in Figure 209. This stud fits a slot cut in the shear lug on the shroud. The hollow blade then fits over this joint and the stud passes through a hole in the disc, pulling disc and shroud tightly together (see Figure 210). Tensile tests were made to evaluate the fir-tree strength. Tensile loading the fir-tree in its slot required approximately 1100 pounds to spread the slot enough to fail one side. Loading the same joint with a hollow blade fit snugly over it required approximately 1700 pounds to fail the joint by yielding the shank (see Figure 211 for failure comparison).

Another approach to blade attachment is the bonding of metal to metal or "diffusion bonding". This process differs from the more widely used adhesive bonding process in that diffusion bonding requires no intermediate adhesive or bonding layer between the parts being joined. Using the hollow titanium blades fabricated previously, end plates of titanium were bonded to the blade ends under a plate pressure of approximately 1000 psi and a temperature of about 1500 degrees Fahrenheit for 30 to 60 minutes. The quality of the bond appears comparable in strength to conventional welds, yet with none of the brittleness of a heat affected zone present with welding (see Figure 212, showing a separate blade before bonding and also a bonded blade sectioned in half). Further studies are indicated, however, to determine inspection methods, repair techniques, fatigue strength, etc., before committing the radial outflow compressor design to this method. The potential gains in rotor strength and stiffness to be gained through diffusion bonding are significant.

MATERIAL EVALUATION

One of the first test programs initiated was material evaluation of 6-6-2 titanium because it showed much promise as a high strength rotor material. The results of that program, shown in Table XVI (see reference 31 for additional information), demonstrate that the material fulfilled all expectations and will be used as the radial outflow compressor disc and shroud material.

Machinability of the 6-6-2 titanium rotor material was evaluated under both high precision milling and electric discharge machining. The milling was carried out in the blade attachment program where two flat

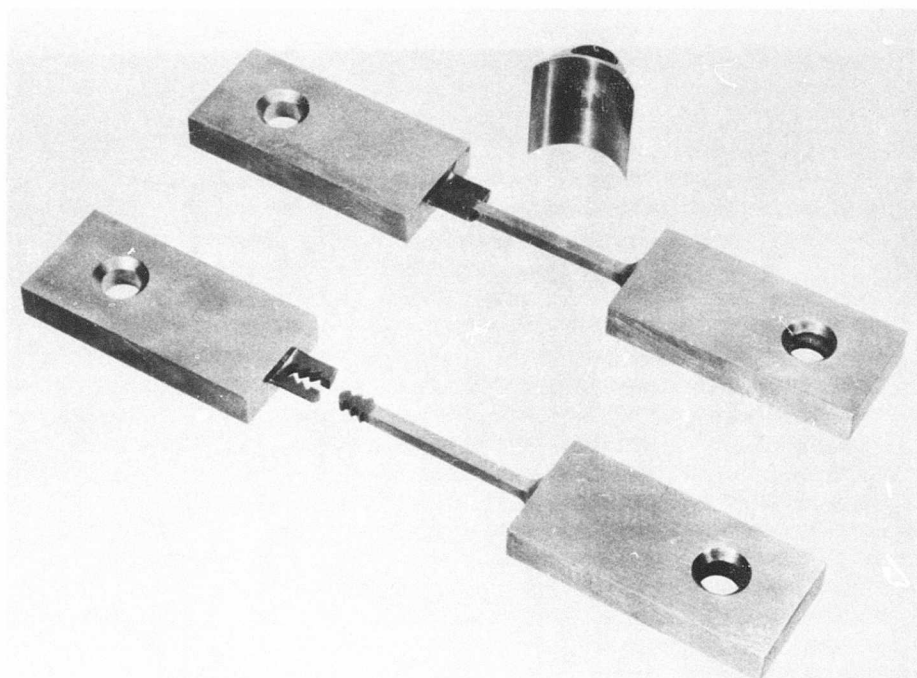


Figure 209. Fir-Tree Stud Fastener Evaluated for Use with the Shear Lug Design.

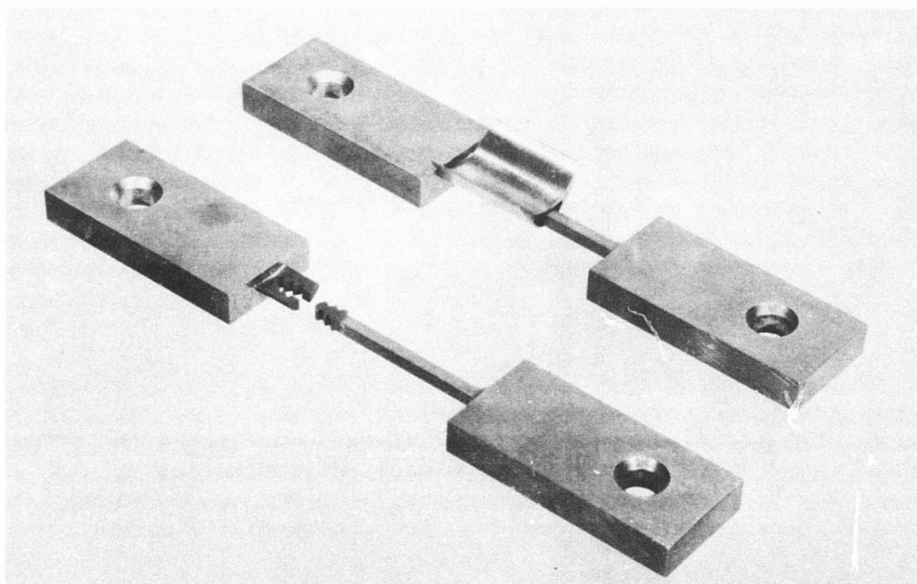


Figure 210. Illustration of Assembly of Fir-Tree Stud Fastener.

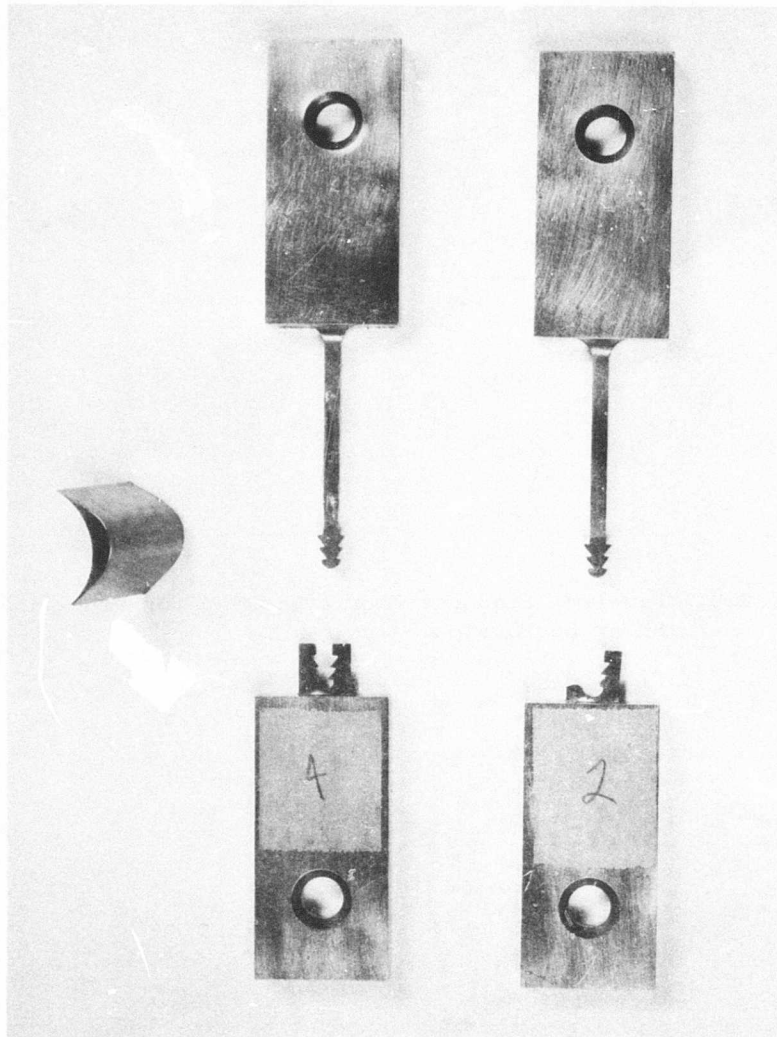


Figure 211. Tensile Test Failure Comparison with and Without Closely Fitted Hollow Blades.

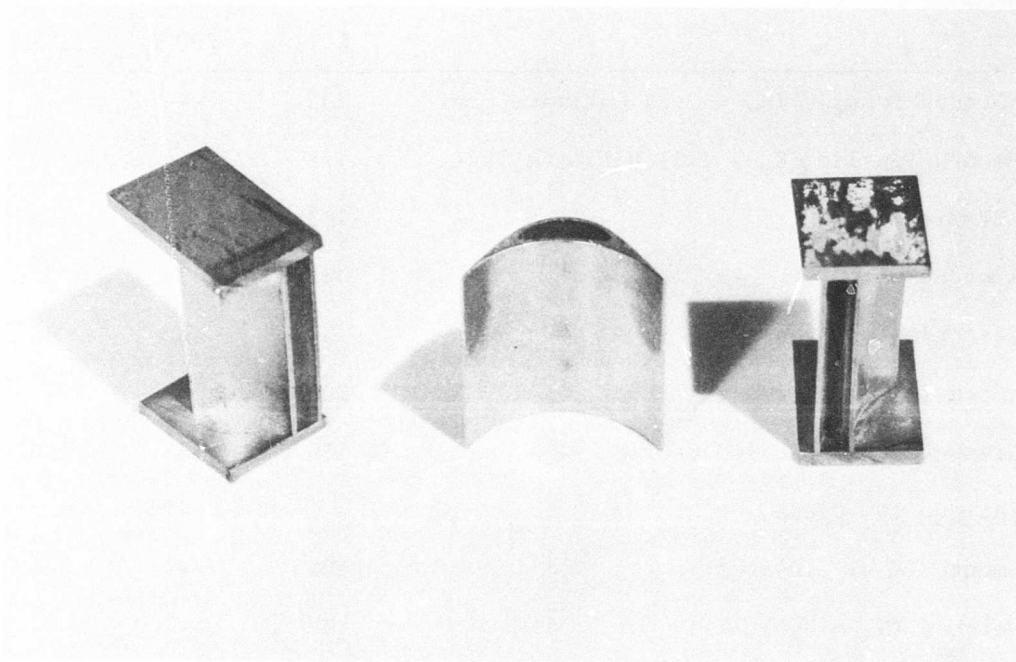


Figure 212. Half Sections of Hollow Blade with Diffusion Bonded Titanium End Plates Compared with Hollow Blade Not Bonded.

TABLE XVI
6-6-2 TITANIUM PROPERTIES

	R.T.	200°F	350°F
Notched Tensile ($K_T = 3.2$) Ultimate, ksi	235	---	---
Smooth Tensile ($K_T = 1.0$) Ultimate, ksi	173	164	150
.2% Yield, ksi	163	146	133
Elongation, %	12	12	12
Reduction of Area, %	37	43	50
Notch Time Fracture ($K_T = 3.2$), ksi	200	---	---
Creep .2% Plastic 100 Hours, ksi	150	137	120
<u>Fatigue 10^7 Cycle</u>			
Smooth ($K_T = 1.0$), ksi	102	---	---
Notched ($K_T = 3.0$), ksi	30	---	---

Where: R.T. is Room Temperature

K_T is tensile stress concentration

ksi is psi $\times 10^3$

discs with shear lugs were machined out of a 6-6-2 titanium pancake forging, using tape controlled milling equipment. The operation proceeded well except in the region of the shear lugs, where machining was slow and accuracy not as good as expected. This was due to the slightly higher surface hardness of the 6-6-2 titanium (Rockwell C hardness of 38-40) and to the small spacing between shear lugs that allowed only small milling tools, which cut slowly and wear rapidly. These problems led to the abandonment of the shear lug design and to the adoption of the separate blade design. For these separate parts, where size of milling tools is not as restricted, tungsten carbide tools will give good machining speed and accuracy in 6-6-2 titanium.

Electric discharge machining was employed to remove the centers from sample blades. Precision contoured copper electrodes were used with moderate electric power settings to maximize accuracy of the hole while keeping surface damage to the hole at a minimum. Machining time to hollow one blade was excessive (about 5 hours per 0.7-inch penetration depth), and metallographic inspection of the hole surface showed a layer of heat affected material that is susceptible to cracking and fatigue failure. So, in spite of the good contour accuracy obtained with EDM, it proved to be an unacceptable process for radial outflow compressor rotating parts because of the very long manufacturing times involved and the reduced material fatigue strength it caused.

VIBRATION AND PRESTRESS

Once the basic geometry of the compressor was set, it became evident that the thin outer edges of the shroud might be susceptible to traveling wave vibrations. Preliminary calculations of shroud natural frequency and rotor passing frequency showed a possibility of exciting a 3-cycle-per-revolution traveling wave vibration in the shroud. To evaluate the accuracy of the calculation for the unusual shroud shape, a full size aluminum shroud was built and its natural frequency checked. Results showed calculated and actual natural frequencies to be within 10 percent of each other (see Table XVII).

Preliminary rotor stress calculations included consideration of prestressed rotors and in particular aluminum or titanium parts wrapped with prestressed fiber glass around the bore.

At the same time, it was decided to evaluate methods of vibration damping and changing the shroud tip vibration frequency by laying honeycomb covered with fiber glass along the inside edges of the shroud sides (see Figure 213). The fiber glass "treated" shroud is shown in Figure 214. The natural frequencies of this modified shroud were checked and found to be 20 percent to 50 percent higher than the plain aluminum shroud (see Table XVII). No significant difference in natural frequencies was noted between the two shroud sides even though one side was a double

reinforcement of fiber glass. Of most importance, however, was the fact that vibrations excited in the modified shroud were so damped by the laminate that the vibration obtained with maximum excitation power could not be detected by touching the shroud at any point.

TABLE XVII
ALUMINUM SHROUD RESONANT FREQUENCY - CPS

Node Shape	Original Shroud Calculation	Original Shroud Tests	Tests with Fiber Glass
Four Radial Nodes	991	1028	1157
Six Radial Nodes	1034	1052	1578
Eight Radial Nodes	1108	1152	1747
Ten Radial Nodes	1220	1286	1863
Twelve Radial Nodes	1376	1464	2017

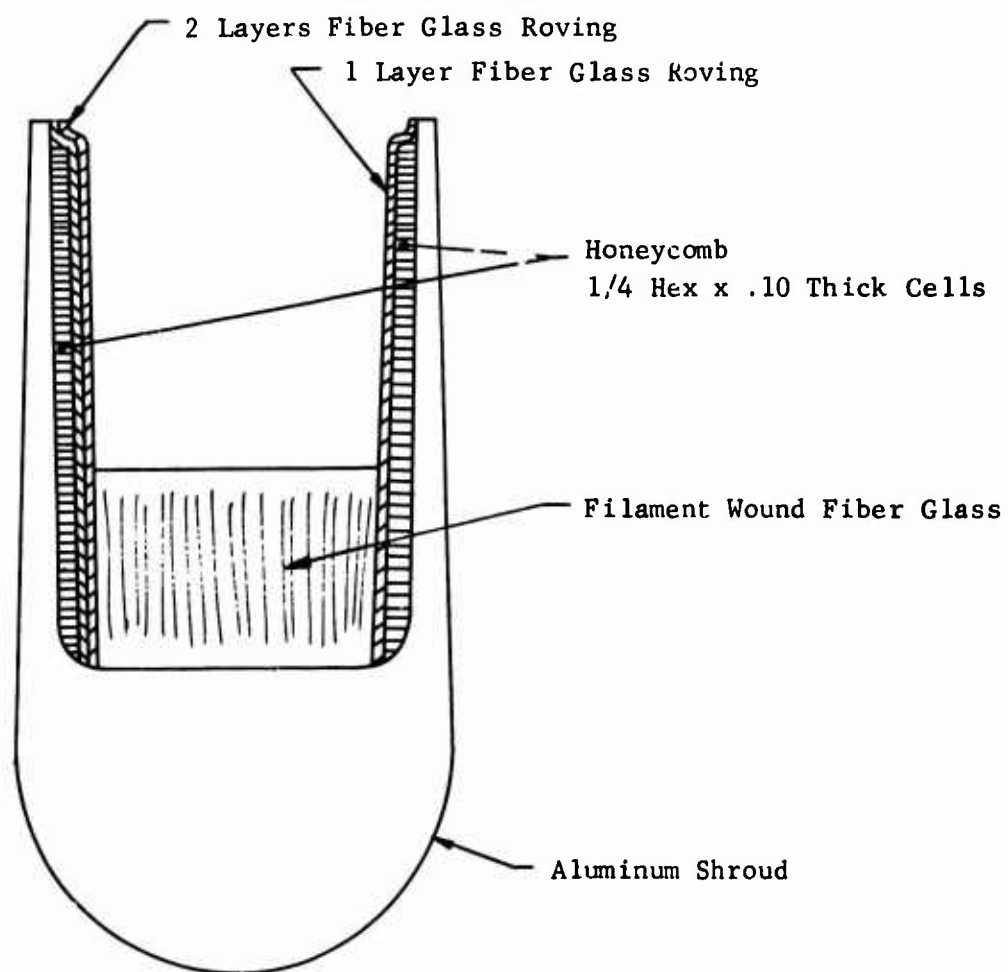


Figure 213. Fiber Glass Reinforced Shroud.

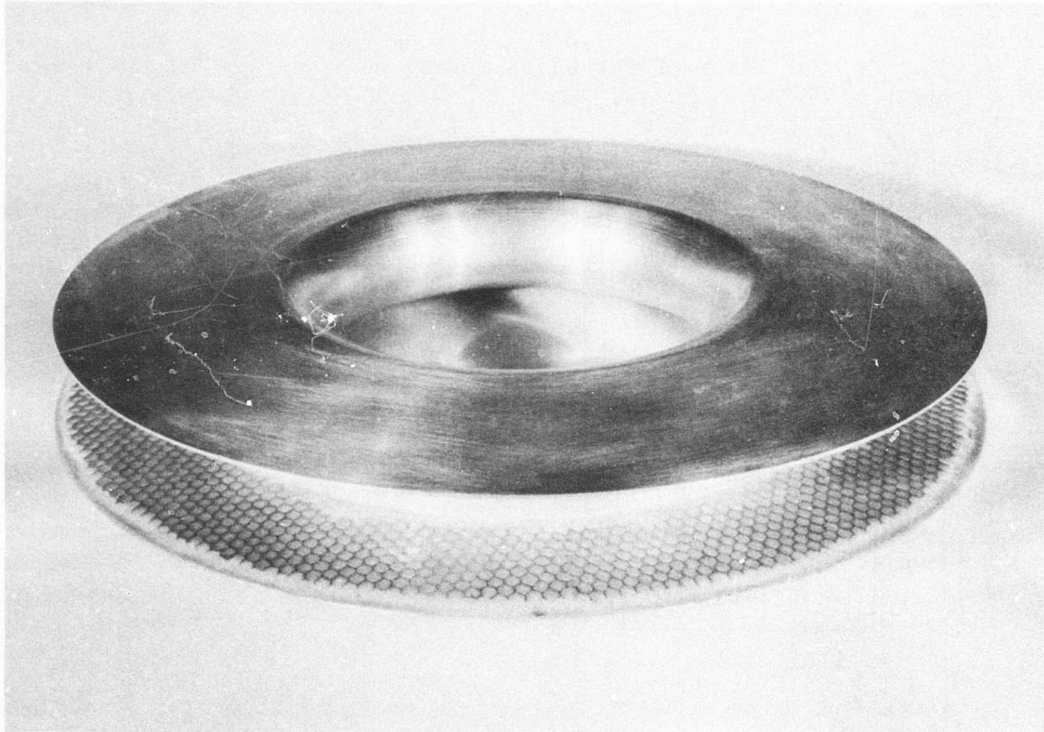


Figure 214. Shroud with Honeycomb and Fiber Glass on Inside Edges.

DESCRIPTION OF HIGH-SPEED COMPRESSOR

The radial outflow compressor design evolving from the mechanical and aerodynamic analyses performed during Phase I of the small gas turbine engine compressor technology program has the following features:

ROTOR ASSEMBLY

The rotor assembly is comprised of a shaft with two bearings supporting an overhung rotor.

Shaft Assembly

The shaft is made of Nitralloy N material with an external spline at the driven end and a bolt flange at the disc attachment end.

Both bearings are of the ball bearing type, spring loaded for a snug fit and operate at a DN value of 1.6×10^6 .

Rotor

Shroud

The shroud is to be machined from a 6-6-2 titanium pancake forging with the sides having radial centerlines to provide a stable rotating surface for the flow path. Bolt holes for the blade studs are reinforced around the edges. The bore is the inlet air passage.

Disc

The disc is to be machined from a 6-6-2 titanium pancake forging, also with radial centerline to provide a stable rotating surface for the flow path. It has reinforced bolt holes for blade studs, a cylindrical flange attachment to the shaft and a bolt flange attachment to the centerbody.

Blades

The 88 blades are to be machined from 6-6-2 titanium bar stock with end studs where half of the blades have studs extended and threaded for bolt attachment to disc and shroud.

Centerbody

The centerbody is to be machined from aluminum bar stock. One end is adapted for shrink fit onto disc attachment flange and the outer end serves as the vibration damper mount.

STATOR ASSEMBLY

Stators

The stators are to be machined from stainless steel with a double set of edge pins for support and alignment. Two stages of stators are required.

Stator Actuation

Each stage of stators are ganged together for simultaneous actuation. An eccentric cam is used for stator orientation change.

Cooling

Inlet and outlet ports for rotor cooling air are provided in the stator casing both forward and aft of the rotor.

INLET ASSEMBLY

Inlet

An axial flow design is used with bulletnose and fixed support struts.

Inlet Guide Vanes

The inlet guide vanes are to be machined from steel. Angle settings can be varied.

RADIAL OUTFLOW COMPRESSOR

The high-speed radial outflow compressor with its test cell installation is shown in Figure 215. A description of the aerodynamic instrumentation requirements for testing is presented in Appendix III.

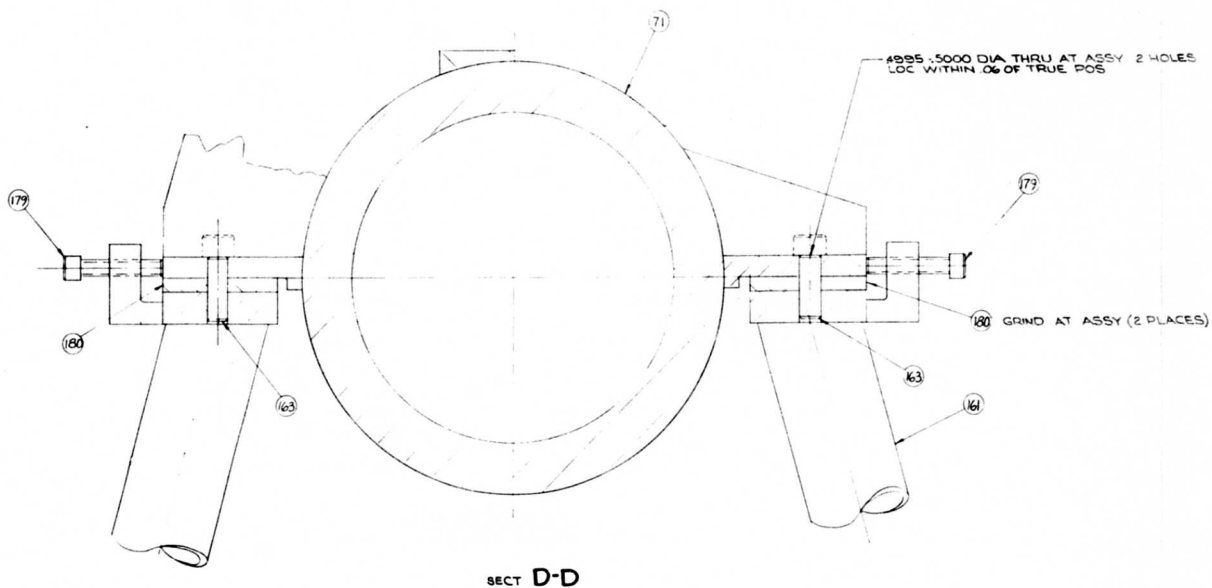
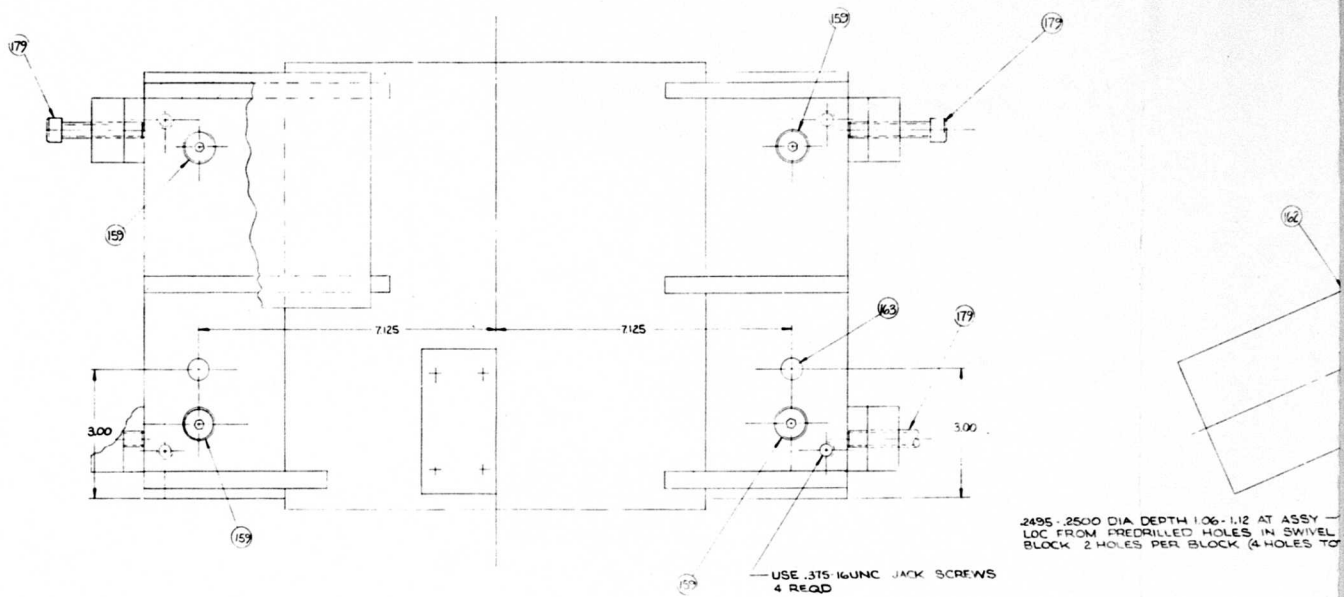
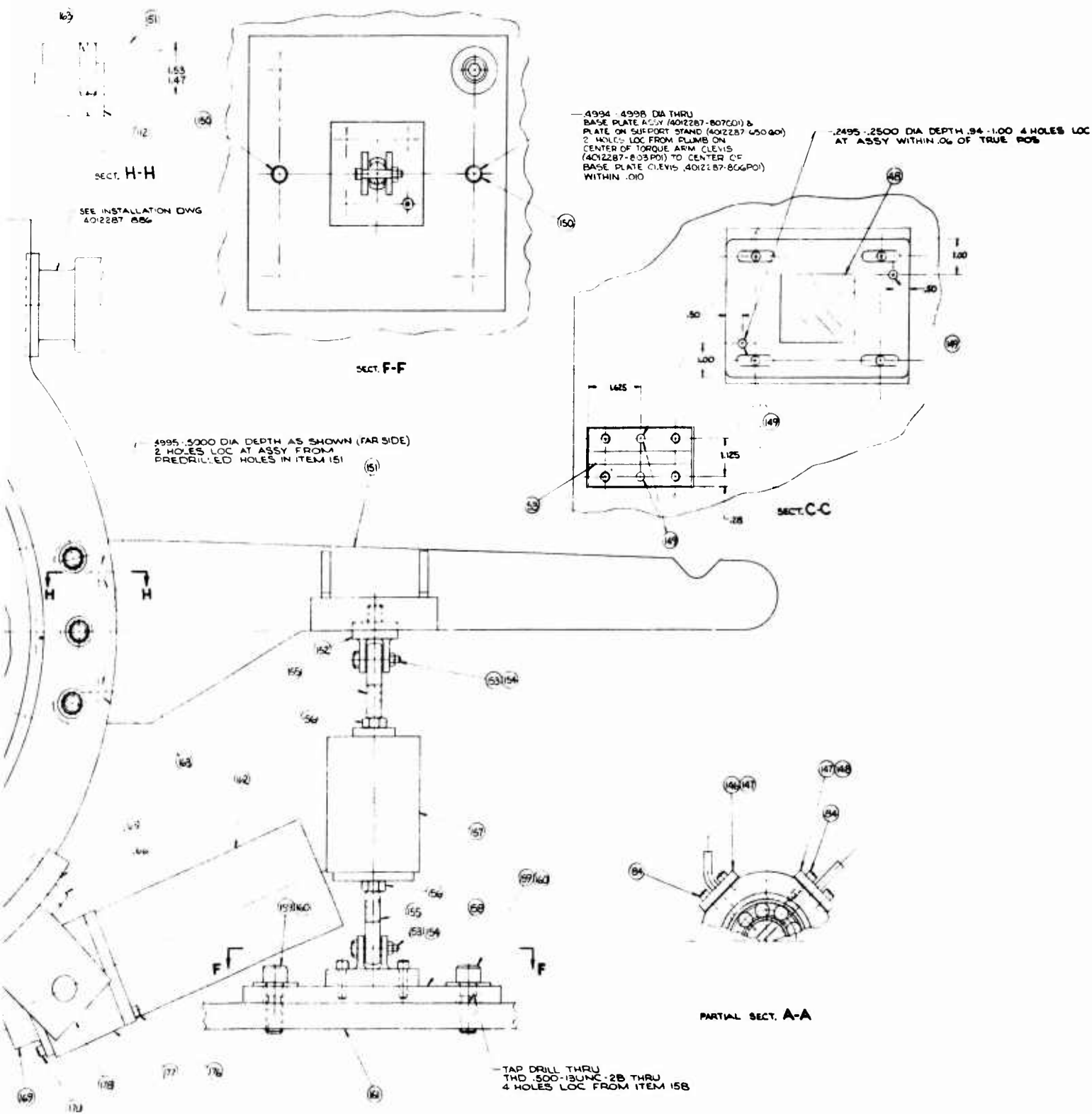


Figure 215. Radial Outflow Compressor, High Speed.

A



C

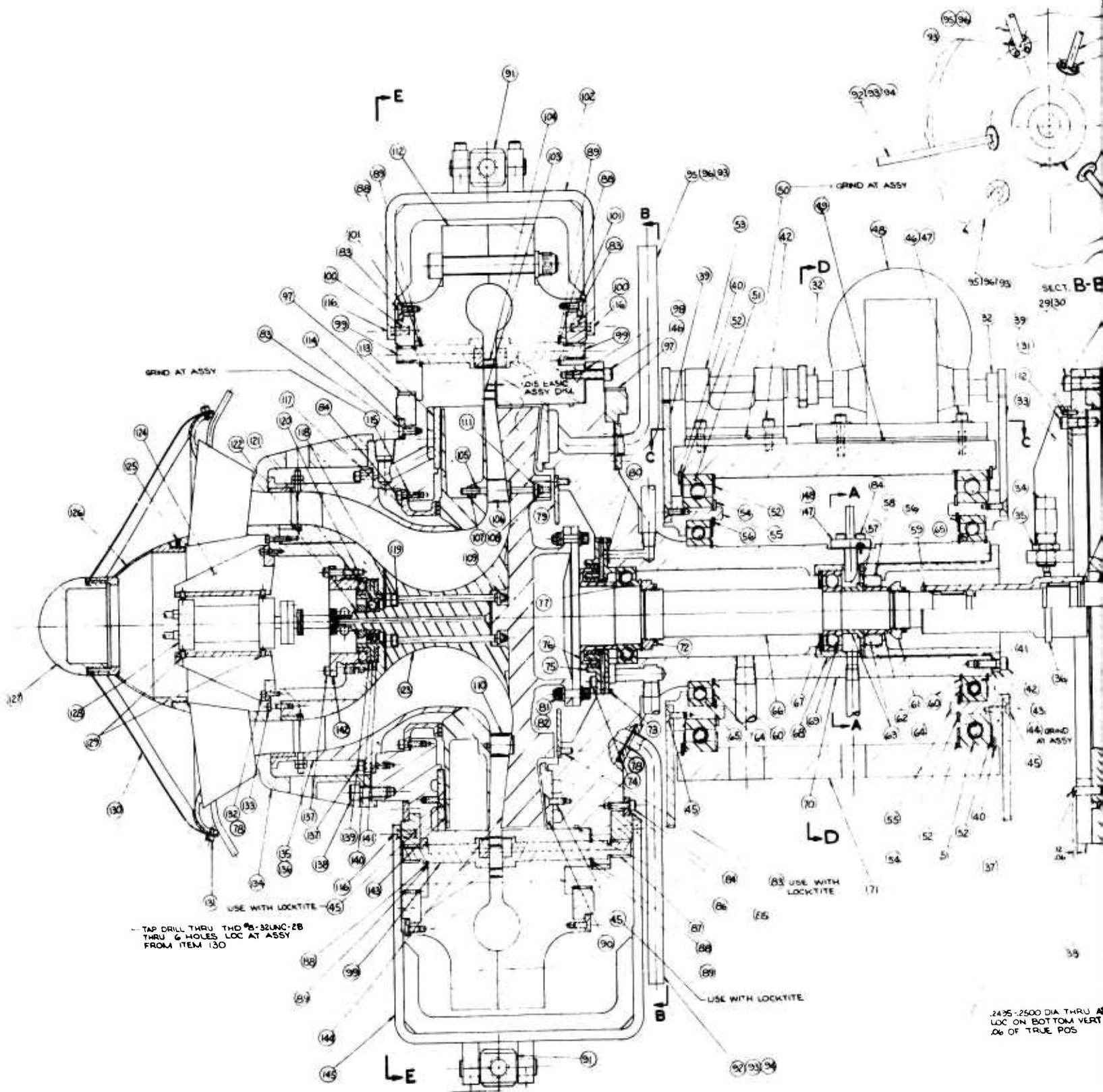
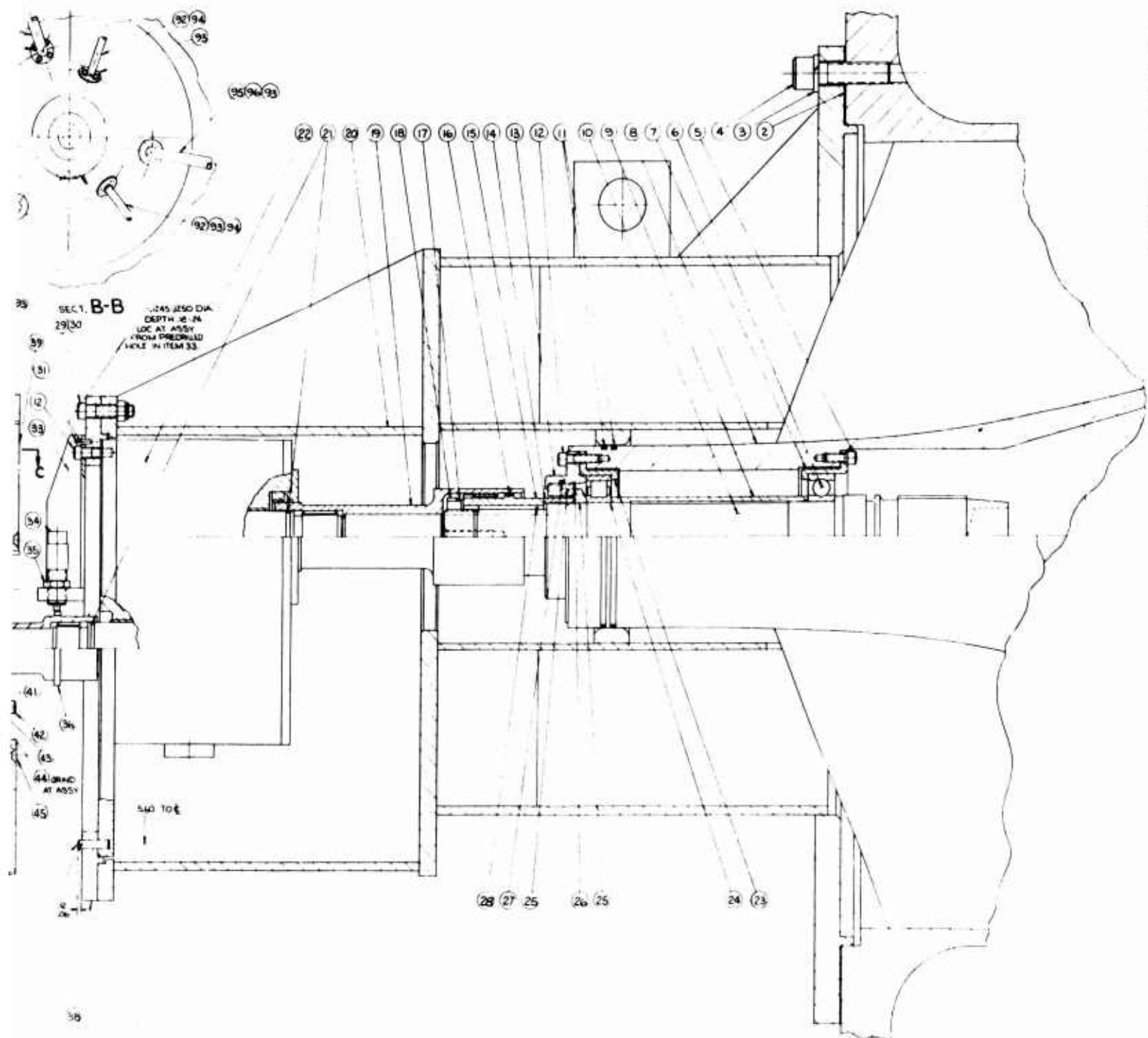


Figure 215 (Continued)

A



1	COAL
2	COAL
3	COAL
4	COAL
5	COAL
6	COAL
7	COAL
8	COAL
9	COAL
10	COAL
11	COAL
12	COAL
13	COAL
14	COAL
15	COAL
16	COAL
17	COAL
18	COAL
19	COAL
20	COAL
21	COAL
22	COAL
23	COAL
24	COAL
25	COAL
26	COAL
27	COAL
28	COAL

29	MATLIN
30	JAMES
31	DAYTON
32	DAYTON
33	DAYTON
34	DAYTON
35	DAYTON
36	DAYTON
37	DAYTON
38	DAYTON
39	DAYTON
40	DAYTON
41	DAYTON
42	DAYTON
43	DAYTON
44	DAYTON
45	DAYTON
46	DAYTON
47	DAYTON
48	DAYTON
49	DAYTON
50	DAYTON
51	DAYTON
52	DAYTON
53	DAYTON
54	DAYTON
55	DAYTON
56	DAYTON
57	DAYTON
58	DAYTON
59	DAYTON
60	DAYTON
61	DAYTON
62	DAYTON
63	DAYTON
64	DAYTON
65	DAYTON
66	DAYTON
67	DAYTON
68	DAYTON
69	DAYTON
70	DAYTON
71	DAYTON
72	DAYTON
73	DAYTON
74	DAYTON
75	DAYTON
76	DAYTON
77	DAYTON
78	DAYTON
79	DAYTON
80	DAYTON
81	DAYTON
82	DAYTON
83	DAYTON
84	DAYTON
85	DAYTON
86	DAYTON
87	DAYTON
88	DAYTON
89	DAYTON
90	DAYTON
91	DAYTON
92	DAYTON
93	DAYTON
94	DAYTON
95	DAYTON
96	DAYTON
97	DAYTON
98	DAYTON
99	DAYTON
100	DAYTON

5-2500 DIA THRU J AT ASSY
ON BOTTOM VERT & WITHIN
OF TRUE POS

B

ITEM	DESCRIPTION	REVISION	DATE	BY	APP'D
78	4012287-648P01	BAFFLE			
80	4012287-648P01	0-2 UNF x 1/2 LG			
81	EWB-0420-4-6	BOLT (H)			
82	61170-428	LOCKNUT (H)			
83	CONVL	FL HD SOC CAP SCR / NYLON			
		1/4-28 UNF x 1/2 LG			
84	CONVL	SOC HD CAP SCR / NYLON			
		1/4-32 UNF x 3/8 LG			
85	4012287-752P01	RETAINER			
86	4012287-752P01	0-2 UNF x 1/2 LG			
87	4012287-753G01	GEAR SHAFT			
88	5100-50	RETAINING RING (H)			
89	0-2 UNF x 1/2 LG	WAVE WASHER (H)			
90	4012287-651P01	LINER			
91	4012287-651P01	INLET TUBE			
92	CONVL	SOC HD CAP SCR / NYLON			
		1/4-32 UNF x 1/2 LG			
93	4012287-651P01	OUTLET TUBE			
94	4012287-651P01	GASKET			
95	4012287-651P01	RING GEAR			
96	4012287-651P01	GEAR SHAFT ASSY			
97	4012287-651P01	RING GEAR			
98	4012287-651P01	RETAINING RING			
99	4012287-651P01	STATOR VANE - SUPERSONIC			
100	4012287-651P01	STATOR VANE - SUBSONIC			
101	4012287-651P01	WASHER (H)			
102	4012287-651P01	BASE PL			
103	4012287-651P01	NUT (R)			
104	4012287-651P01	BASE PL			
105	4012287-651P01	WASHER (H)			
106	4012287-651P01	CASING ASSY			
107	4012287-651P01	LINER			
108	4012287-651P01	RETAINING RING			
109	4012287-651P01	SHAFT			
110	4012287-651P01	FL HD SOC CAP SCR / NYLON			
		1/4-20 UNC x 3/4 LG			
111	4012287-751P01	SEAL			
112	4012287-751P01	WASHER (H)			
113	4012287-751P01	WASHER (H)			
114	4012287-751P01	WASHER (H)			
115	4012287-751P01	WASHER (H)			
116	4012287-751P01	WASHER (H)			
117	4012287-751P01	WASHER (H)			
118	4012287-751P01	WASHER (H)			
119	4012287-751P01	WASHER (H)			
120	4012287-751P01	WASHER (H)			
121	4012287-751P01	WASHER (H)			
122	4012287-751P01	WASHER (H)			
123	4012287-751P01	WASHER (H)			
124	4012287-751P01	WASHER (H)			
125	4012287-751P01	WASHER (H)			
126	4012287-751P01	WASHER (H)			
127	4012287-751P01	WASHER (H)			
128	4012287-751P01	WASHER (H)			
129	4012287-751P01	WASHER (H)			
130	4012287-751P01	WASHER (H)			
131	4012287-751P01	WASHER (H)			
132	CONVL	SOC HD CAP SCR / NYLON			
		1/4-28 UNF x 1/2 LG			
133	CONVL	SOC HD CAP SCR / NYLON			
		1/4-28 UNF x 1/2 LG			
134	CONVL	SOC HD CAP SCR / NYLON			
		1/4-28 UNF x 1/2 LG			
135	4012287-753G01	GEAR SHAFT			
136	4012287-753G01	GEAR SHAFT			
137	CONVL	SOC HD CAP SCR / NYLON / ENH.			
		1/4-28 UNF x 1/2 LG			
138	CONVL	SOC HD CAP SCR / NYLON			
		1/4-28 UNF x 1/2 LG			
139	4012287-651P01	RETAINER			
140	4012287-651P01	0-2 UNF x 1/2 LG			
141	4012287-651P01	GEAR SHAFT			
142	4012287-651P01	RETAINING RING (H)			
143	4012287-651P01	WAVE WASHER (H)			
144	4012287-651P01	LINER			
145	4012287-651P01	INLET TUBE			
146	4012287-651P01	SOC HD CAP SCR / NYLON			
		1/4-32 UNF x 1/2 LG			
147	4012287-651P01	OUTLET TUBE			
148	CONVL	DOWEL PIN			
		1/4 DIA x 1 1/2 LG			
149	CONVL	DOWEL PIN			
		1/4 DIA x 1 1/2 LG			
150	4012287-651P01	GEAR SHAFT			
151	4012287-651P01	GEAR SHAFT			
152	4012287-651P01	GEAR SHAFT			
153	4012287-651P01	GEAR SHAFT			
154	4012287-651P01	GEAR SHAFT			
155	4012287-651P01	GEAR SHAFT			
156	4012287-651P01	GEAR SHAFT			
157	4012287-651P01	GEAR SHAFT			
158	4012287-651P01	GEAR SHAFT			
159	4012287-651P01	GEAR SHAFT			
160	4012287-651P01	GEAR SHAFT			
161	4012287-651P01	GEAR SHAFT			
162	4012287-651P01	GEAR SHAFT			
163	4012287-651P01	GEAR SHAFT			
164	4012287-651P01	GEAR SHAFT			
165	4012287-651P01	GEAR SHAFT			
166	4012287-651P01	GEAR SHAFT			
167	4012287-651P01	GEAR SHAFT			
168	4012287-651P01	GEAR SHAFT			
169	4012287-651P01	GEAR SHAFT			
170	4012287-651P01	GEAR SHAFT			
171	4012287-651P01	GEAR SHAFT			
172	4012287-651P01	GEAR SHAFT			
173	4012287-651P01	GEAR SHAFT			
174	4012287-651P01	GEAR SHAFT			
175	4012287-651P01	GEAR SHAFT			
176	4012287-651P01	GEAR SHAFT			
177	4012287-651P01	GEAR SHAFT			
178	4012287-651P01	GEAR SHAFT			
179	4012287-651P01	GEAR SHAFT			
180	4012287-651P01	GEAR SHAFT			
181	4012287-651P01	GEAR SHAFT			
182	4012287-651P01	GEAR SHAFT			
183	4012287-651P01	GEAR SHAFT			
184	4012287-651P01	GEAR SHAFT			
185	4012287-651P01	GEAR SHAFT			
186	4012287-651P01	GEAR SHAFT			
187	4012287-651P01	GEAR SHAFT			
188	4012287-651P01	GEAR SHAFT			
189	4012287-651P01	GEAR SHAFT			
190	4012287-651P01	GEAR SHAFT			
191	4012287-651P01	GEAR SHAFT			
192	4012287-651P01	GEAR SHAFT			
193	4012287-651P01	GEAR SHAFT			
194	4012287-651P01	GEAR SHAFT			
195	4012287-651P01	GEAR SHAFT			
196	4012287-651P01	GEAR SHAFT			
197	4012287-651P01	GEAR SHAFT			
198	4012287-651P01	GEAR SHAFT			
199	4012287-651P01	GEAR SHAFT			
200	4012287-651P01	GEAR SHAFT			

REFERENCE DRAWINGS
4012287-886 (INSTALLATION DWG)
4012287-894 (BALANCED ROTOR ASSY)

C

CONCLUSIONS

The results of the analytical and experimental investigations of both aerodynamic and mechanical design of the radial outflow compressor lead to the conclusion that this new type of compressor for small gas turbines is feasible and offers a significant advance in performance.

Either the radial inflow or the axial flow inlet guide vane system can be used satisfactorily with the ROC. The inlet contours of the axial flow inlet will be satisfactory for the conditions to be encountered in Phase II testing.

The rotor blade sections derived for and tested in cascade at supersonic speeds met the requirements very satisfactorily. The three-dimensional rotor blades transformed from the two-dimensional design, and test results should show improved performance in the high-speed compressor due to beneficial centrifugal force effects on the rotor blade and wall boundary layers.

The rotating wall vaneless diffuser performed very satisfactorily in the low-speed ROC at effective static pressure rise coefficients in the range which will exist in the high-speed compressor. Total pressure losses were found to be very low in the zone of the rotating diffuser. If this condition exists in the high-speed ROC, higher overall performance than that calculated herein may be obtained, since significant losses have been arbitrarily assigned to the rotating wall vaneless diffuser.

Supersonic stator performance measured in the transonic cascade tunnel, at Reynolds numbers less than the actual values of the high-speed ROC, was very satisfactory. The achievement of required static pressure increase at acceptable total pressure loss is particularly significant because the inlet flow angles in the required range of 80 degrees from radial represent operation at conditions much more difficult than those encountered in any previous supersonic cascade experience.

The subsonic stators performed very well as originally designed, indicating that the methods used are reliable. The combined cascade consisting of the supersonic and subsonic stators operating in tandem achieved slightly higher static pressure rise than required but at higher total pressure losses than anticipated. As a result, the rotor outside diameter was increased to obtain a lower Mach number entering the stator system.

The scroll collector, transition diffuser, and turning elbows performed satisfactorily during low-speed ROC testing, particularly at high flow coefficients.

A satisfactory mechanical design of the rotating shroud, rotor blade, disc, and attachment method was achieved. Running life at 100 percent speed is more than adequate for the Phase III program.

Vibration analyses of the rotating shroud have indicated that only higher modes of edge waves may be excited. Significant, and therefore readily detected, amplitudes will exist before dangerous stresses are developed in the thin rims.

The entire rotating system and its supports have been analyzed to determine critical rotational speeds. An outboard bearing having a variable friction damping mounting has been incorporated to permit adjustment of the lowest critical speed which will occur at less than full speed.

No barrier problem, either aerodynamic or mechanical, has been encountered during these investigations which will prevent the high performance potential of the radial outflow compressor from being demonstrated in Phases II and III of this program. On the contrary, although difficult mechanical and aerodynamic analysis, design, and development problems have been encountered, they have been solved successfully, and there is much evidence to encourage the belief that the target performance goals will be met, if not exceeded.

RECOMMENDATIONS

Further analysis of the inlet contours is recommended to decrease the maximum Mach numbers that will occur over the inner surface of the rotating shroud. An annular turning vane, or flow splitter, can accomplish this purpose, but the mechanical design problem of assembling and attaching the device is formidable. Reduced surface velocities by means of improved contours without the use of an annular turning vane are desirable.

A method of joining the rotating shroud, rotor blades, and disc into a stiff, strong assembly is desired for long running life, particularly for compressors of less airflow capacity than the present size of 4.5 pounds per second. Diffusion bonding appears to offer the capability of joining titanium alloy parts to satisfy strength requirements. The time and effort required to develop satisfactory diffusion bonding techniques for fixturing, joining, inspection, nondestructive testing, and repair are beyond the scope of this present program. It is therefore recommended that these techniques be developed under a separate program.

In general, it is recommended that Phase II be continued through the planned series of tests to determine radial outflow compressor performance up to 80 percent design speed. The planned Phase III work is then recommended. Appropriate aerodynamic and mechanical improvements will be made so that the complete performance of the ROC can be demonstrated up to 100 percent design speed.

BIBLIOGRAPHY

1. Johnston, James P., Experimental Data on Three-Dimensional Flow in a Centrifugal Compressor Diffuser, Number 27-7, Gas Turbine Laboratory MIT, Cambridge, Massachusetts, December, 1954.
2. Cardow, Ernest B., The Three-Dimensional Turbulent Boundary Layer in a Free Vortex Diffuser, Number 42, Gas Turbine Laboratory MIT, Cambridge, Massachusetts, January, 1958.
3. Jansen, Willem, Incompressible Fluid Flow in a Radial Vaneless Diffuser, Number 52, Gas Turbine Laboratory MIT, Cambridge, Massachusetts, May, 1959.
4. Jansen, Willem, Compressible Fluid Flow in a Radial Vaneless Diffuser, Number 58, Gas Turbine Laboratory MIT, Cambridge, Massachusetts, March, 1960.
5. Jansen, Willem, Quasi-Unsteady Flow in A Radial Vaneless Diffuser, Number 60, Gas Turbine Laboratory MIT, Cambridge, Massachusetts, October, 1960.
6. Michel, Donald J., Ginsburg, Ambrose, and Mizisin, John, Experimental Investigation of Flow in the Rotating Passages of a 48-Inch Impeller at Low Tip Speeds, RM E51D20, Lewis Flight Propulsion Laboratory, NACA, Cleveland, Ohio, June 26, 1951.
7. Giffin, R. G., and Erwin, J. R., Supersonic Pseudo Shock Stator Test (U), DIM 422, Applied Research Operation, General Electric Company, Evendale, Ohio, May 25, 1961. (Report Classified "Confidential")
8. Giffin, R. G., Cascade Tests of Simple and "Articulated" Variable Inlet Guide Vanes, R63FPD193, Flight Propulsion Division, General Electric Company, Evendale, Ohio, April, 1963.
9. Hawthorne, William R., Secondary Circulation in Fluid Flow, Gas Turbine Laboratory MIT, Cambridge, Massachusetts, May, 1950.
10. Hawthorne, W. R., High Speed Aerodynamics and Jet Propulsion, Volume X, Aerodynamics of Turbines and Compressors, Princeton University Press, Princeton, New Jersey, 1964, pp. 234-237.
11. Erwin, John R., and Schulze, Wallace M., Investigation of an Impulse Axial-Flow Compressor, NACA RM L9J05a, National Advisory Committee for Aeronautics, Langley, Virginia, 1950.
12. Schulze, Wallace M., Erwin, J.R., and Westphal, Willard R., Investigation of an Impulse Axial-Flow Compressor Rotor Over a Range of Blade Angles, NACA RM L50F27A, National Advisory Committee for Aeronautics, Langley, Virginia, 1950.

13. Sterrett, James R., Experimental Investigation of an Impulse-Type Compressor Rotor Having a Turning of 73° at the Mean Radius, NACA TN 4252, National Advisory Committee for Aeronautics, Langley, Virginia, 1958.
14. Goldberg, Theodore J., and Erwin, John R., Performance of an Impulse-Type Supersonic-Compressor Rotor Having a Mean Turning of 114° , NACA RM L56J01, National Advisory Committee for Aeronautics, Langley, Virginia, 1957.
15. Boxer, Emanuel, Sterrett, James R., and Wlodarski, John, Application of Vortex-Flow Theory to the Design of Supersonic Impulse Compressor or Turbine-Blade Sections, NACA RM L52B06, National Advisory Committee for Aeronautics, Langley, Virginia, April, 1952.
16. Erwin, John R., and Emery, James C., Effect of Tunnel Configuration and Testing Technique on Cascade Performance, NACA 1016, National Advisory Committee for Aeronautics, Langley, Virginia, 1951.
17. Joy Rotating Diffuser Fans, RD Series, Bulletin J-618, Joy Manufacturing Company, Henry W. Oliver Building, Pittsburgh, Pennsylvania.
18. Stewartson, K., On the Flow Between Two Rotating Coaxial Disks, Proceedings of the Cambridge Philosophical Society, Volume 49, General Electric Flight Propulsion Division Technical Information Center, Evendale, Ohio, 1953.
19. Maroit, L. A., Deak, G., and Kreith, F., Flow Phenomena of Partially Enclosed Rotating Disks, Journal of Basic Engineering, September, 1960.
20. Daily, J. W., and Nece, R. E., Chamber Dimension Effects on Induced Flow and Frictional Resistance of Enclosed Rotating Disks, Journal of Basic Engineering, March, 1960.
21. Dean, Robert C., Jr., and Senoo, Yasutoshi, Rotating Wakes in Vaneless Diffusers, Transactions of the ASME - Series D, Journal of Basic Engineering, September, 1960.
22. Moore, F. K., Three-Dimensional Boundary Advances in Applied Math, Volume IV, Academic Press, 1956, pp. 159.
23. Schulze, Wallace M., Erwin, John R., and Ashby, George C., Jr., NACA 65-Series Compressor Rotor Performance with Varying Annulus-Area Ratio, Solidity, Blade Angle, and Reynolds Number and Comparison with Cascade Results, NACA RM L52L17, National Advisory Committee for Aeronautics, Langley, Virginia, February 19, 1953.

24. Schaub, Uwe W., The Behavior of a Wake in an Adverse Pressure Gradient, Number 62, Gas Turbine Laboratory MIT, Cambridge, Massachusetts, January, 1961.
25. Hill, Philip G., Turbulent Wakes in Pressure Gradients, Number 65, Gas Turbine Laboratory MIT, Cambridge, Massachusetts, January, 1962.
26. Emmons, H. W., High Speed Aerodynamics and Jet Propulsion, Volume III, Fundamentals of Gas Dynamics, Princeton University Press, Princeton, New Jersey, 1958, pp. 110-130.
27. Kline, S. J., Abbott, D. E., and Fox, R. W., Optimum Design of Straight Walled Diffusers, Volume 81, Series D, TASME, Journal of Basic Engineering, September, 1959.
28. Donaldson, Coleman duP., and Lange, Roy H., Study of the Pressure Rise Across Shock Waves Required to Separate Laminar and Turbulent Boundary Layers, NACA TN 2770, Langley Aeronautical Laboratory, Langley, Virginia, September 1952.
29. Hayes, W. D., and Probstein, R. F., Applied Mathematics and Mechanics, Volume 5, Hypersonic Flow Theory, Academic Press, New York, New York, 1959, pp. 253-259.
30. Erdeman, V. J., Evaluation of Two High Strength Titanium Alloys as Forged Buckets - Ti-6Al-6V-2Sn and Ti-200K, DM65-278, General Electric Flight Propulsion Division, Evendale, Ohio, August 17, 1965.
31. Erdeman, V. J., Forging and Evaluation of Ti-6Al-6V-2Sn Discs, DM65-337, General Electric Flight Propulsion Division, Evendale, Ohio, August 25, 1965.

APPENDIX I, COMPRESSOR PERFORMANCE CALCULATIONS

The radial outflow compressor component aerodynamic performance goals along with performance levels demonstrated are presented in Table I, page 10. In the Summary are calculated values of overall compressor performance based on the demonstrated component performance levels. The design point conditions are illustrated here along with numerical calculations to demonstrate the methods of determining the measured component performance levels. Also, the step-by-step calculation of overall compressor performance using the demonstrated component performance levels is presented.

COMPONENT DESIGN POINT CALCULATIONS

Rotor Blade

The design inlet Mach number and inlet flow angle of the rotor blades are 1.42 and 60 degrees, respectively.

Measured performance data at the inlet and exit stations are as follows (see case 21953, Table IV):

Inlet Conditions

$P_{t1} = 108.742$ inches of fluid*
 $P_{s1} = 32.457$ inches of fluid
 $q_1 = P_{t1} - P_{s1} = 76.285$ inches of fluid
 $M_1 = 1.436$

Inlet flow angle = 60 degrees

Exit Conditions

$P_{t2} = 94.248$ inches of fluid
 $P_{s2} = 31.236$ inches of fluid

$$\bar{w} = \frac{P_{t1} - P_{t2}}{P_{t1} - P_{s1}} = \frac{108.742 - 94.248}{76.285} = 0.190$$

$$\bar{C}_p = \frac{P_{s2} - P_{s1}}{P_{t1} - P_{s1}} = \frac{31.236 - 32.457}{76.285} = -0.016$$

The performance goals for the rotor blades were $\bar{w} = 0.15$ and $\bar{C}_p = 0$.

* Manometer fluid designated "TBE" with specific gravity of 2.95.

Rotating Vaneless Diffuser

Performance of the rotating diffuser is related to the effective static pressure rise coefficient, $C_{P_{eff}}$. The design inlet flow conditions of the high-speed machine are listed below.

- | | | | |
|--------------------------------|-----------|---|----------------------|
| 1. Inlet Mach number, | M_2 | = | 2.66 |
| 2. Inlet total temperature, | T_{t2} | = | 1159 degrees Rankine |
| 3. Inlet velocity, | V_2 | = | 2856 fps |
| 4. Wheel speed, | U_2 | = | 1300 fps |
| 5. Stagnation sonic velocity, | a_{t2} | = | 1669 fps |
| 6. Inlet relative Mach number, | M_{r2} | = | 1.54 |
| 7. Inlet relative velocity, | W_2 | = | 1656 fps |
| 8. Inlet relative flow angle, | β_2 | = | 60 degrees |

The rotating vaneless diffuser geometry is:

- | | | | |
|----------------------------------|-----------|---|-------------|
| 1. Inlet diffuser passage width, | h_2 | = | 0.586 inch |
| 2. Inlet diffuser radius, | r_2 | = | 4.30 inches |
| 3. Exit diffuser passage width, | h_3 | = | 0.400 inch |
| 4. Exit diffuser radius, | r_3 | = | 6.50 inches |
| 5. Radial flow area ratio, | A_3/A_2 | = | 1.0 |
| 6. Diffuser radius ratio, | r_3/r_2 | = | 1.512 |

The effective static pressure rise coefficient is defined as

$$C_{P_{eff}} = \frac{\Delta P_{f.v.} - \Delta P_{s.b.}}{P_{t2} - P_{s2}}$$

where

$\Delta P_{f.v.}$ = free vortex pressure rise

$\Delta P_{s.b.}$ = solid body pressure rise

$P_{t2} - P_{s2}$ = absolute inlet dynamic pressure

$$C_{P_{eff}} = \frac{\left[\frac{1 - .2 \frac{V_3^2}{a_{t2}^2}}{1 - .2 \frac{V_2^2}{a_{t2}^2}} \right]^{3.5} - \left[\frac{1 + .4 \frac{U_2^2}{a_{t2}^2} \frac{R^2}{2} - 1}{1 - .2 \frac{U_2^2}{a_{t2}^2}} \right]^{3.5}}{\left(1 + .2 M_2^2 \right)^{3.5} - 1}$$

Performing the calculations:

Based on conservation of angular momentum, $V_{u3} = \left(\frac{r_2}{r_3} \right) V_{u2}$

From continuity, $\rho_2 A_2 V_{r2} = \rho_3 A_3 V_{r3}$ and $V_{r3} = \left(\frac{\rho_2}{\rho_3} \right) \left(\frac{A_2}{A_3} \right) V_{r2}$

V_3 (for free vortex flow) = 1822 fps and is defined by the calculated values of the radial and tangential components, V_{r3} and V_{u3} .

$$1 - .2 \left(\frac{V_3}{a_{t3}} \right)^2 = 1 - .2 \left(\frac{1822}{1669} \right)^2 = 0.7617$$

$$1 - .2 \left(\frac{V_2}{a_{t2}} \right)^2 = 1 - .2 \left(\frac{2856}{1669} \right)^2 = 0.4145$$

$$1 + .4 \left(\frac{U_2}{a_t} \right)^2 \left(\frac{R^2}{2} - 1 \right) = 1 + .4 \left(\frac{1300}{1669} \right)^2 \left(\frac{1.512^2}{2} - 1 \right) = 1.0347$$

$$1 - .2 \left(\frac{U_2}{a_t} \right)^2 = 1 - .2 \left(\frac{1300}{1669} \right)^2 = 0.8787$$

$$\left(1 + .2 M_2^2 \right)^{3.5} - 1 = \left[1 + .2 (2.66)^2 \right]^{3.5} - 1 = 20.9$$

$$C_{P_{eff}} = \frac{\left(\frac{0.7617}{0.4145} \right)^{3.5} - \left(\frac{1.0347}{0.8787} \right)^{3.5}}{20.9} = 0.318$$

Performance of the rotating vaneless diffuser was measured on the low-speed radial outflow compressor. The equation that follows is an equivalent definition of effective static pressure rise coefficient for the low-speed machine.

$$C_{P_{eff}} = \left(1 - \frac{1}{\sqrt{\left(1 + \phi \left(\frac{r_1}{r_2} \right)^2 \tan \beta_2 \right)^2 + \phi^2 \left(\frac{r_1}{r_2} \right)^4}} \right)^2$$

where

$$\begin{aligned} \phi & \text{ is inlet flow coefficient, } V_{r1}/U_1 &= 0.945 \\ r_1 & \text{ is radius at rotor inlet} &= 7.06 \text{ inches} \\ r_2 & \text{ is radius at rotating vaneless diffuser inlet} &= 8.27 \text{ inches} \\ \beta_2 & \text{ is angle of inlet relative velocity} &= 60 \text{ degrees} \end{aligned}$$

Flow coefficient is proportional to compressor airflow as shown by the following relationships.

$$\phi_1 = \frac{V_{r1}}{U_1}$$

Using the continuity equation, $w = \rho AV$,

$$V_{r1} = \frac{w}{\rho A_1}$$

Tangential velocity U_1 is calculated from the rotational speed of the compressor.

$$U_1 = 2\pi r_1 \frac{N}{60}$$

Then,

$$\phi_1 = \frac{w}{\rho A_1} \frac{60}{2\pi r_1 N}$$

Compressor inlet airflow is determined from the measurement of total pressure, static pressure, and total temperature in conjunction with an accurately calibrated inlet bellmouth.

The effective static pressure coefficient at the test conditions corresponding to an inlet flow coefficient of 0.945 is calculated as follows:

$$C_{P_{eff}} = \left(1 - \frac{1}{\sqrt{\left(1 + 0.945 \left(\frac{7.06}{8.27} \right)^2 \tan 60^\circ \right)^2 + (0.945)^2 \left(\frac{7.06}{8.27} \right)^4}} \right)^2 = 0.32$$

The low-speed radial outflow compressor test results indicated that maximum rotor efficiency was associated with effective static pressure rise coefficients in the range from 0.30 to 0.36.

Supersonic Stator Blades

The supersonic stators are designed for an inlet Mach number of 1.28 and an inlet flow angle of 80 degrees. Using case 22286, Table X, as typical of the test results from the transonic cascade tunnel, the following inlet and exit conditions were measured:

<u>Inlet Conditions</u>		<u>Exit Conditions</u>	
M_4	= 1.33	M_5	= 0.7389
P_{t4}	= 109.5316 inches of fluid	P_{t5}	= 98.7237 inches of fluid
P_{s4}	= 38.002 inches of fluid	P_{s5}	= 68.7667 inches of fluid
α_4	= 80 degrees	α_5	= 76.1749 degrees
T_{t4}	= 74 degrees Fahrenheit		

$$\bar{\omega} = \frac{P_{t4} - P_{t5}}{P_{t4} - P_{s4}} = \frac{109.5316 - 98.7237}{109.5316 - 38.0025} = 0.1511$$

$$\bar{C}_P = \frac{P_{s5} - P_{s4}}{P_{t4} - P_{s4}} = \frac{68.7667 - 38.0025}{109.5316 - 38.0025} = 0.4301$$

For the design inlet Mach number of 1.28 and inlet flow angle of 80 degrees, the loss coefficient is 0.144 and the static pressure rise coefficient is 0.46, as shown in Figure 155. The corresponding goals were $\bar{\omega}$ of 0.14 and \bar{C}_P of 0.45.

Subsonic Stators

The subsonic stators are designed for an inlet Mach number of 0.70 and an inlet angle of 75 degrees. Using case 22331, Table XI, the following inlet and exit conditions were measured in the transonic cascade tunnel:

<u>Inlet Conditions</u>		<u>Exit Conditions</u>	
$M_{5.25}$	= 0.6984	M_6	= 0.3471
$P_{t5.25}$	= 93.5987 inches of fluid	P_{t6}	= 91.8831 inches of fluid
$P_{s5.25}$	= 67.6444 inches of fluid	P_{s6}	= 84.5614 inches of fluid
$\alpha_{5.25}$	= 75 degrees	α_6	= 71.4732
T_{t5}	= 65 degrees Fahrenheit		

$$\bar{\omega} = \frac{P_{t5.25} - P_{t6}}{P_{t5.25} - P_{s5.25}} = \frac{93.5987 - 91.8831}{93.5987 - 67.6444} = 0.0661$$

$$\bar{C}_P = \frac{P_{s6} - P_{s5.25}}{P_{t5.25} - P_{s5.25}} = \frac{84.5614 - 67.6444}{93.5987 - 67.6444} = 0.6518$$

The goals, $\bar{\omega}$ of 0.08 and \bar{C}_P of 0.60, at the design inlet conditions were exceeded as shown by the above test case.

Tandem

The tandem arrangement of supersonic and subsonic stators has a design inlet Mach number of 1.28 and an inlet angle of 80 degrees. Case 22926, Table XII, is very close to these conditions, and the measured inlet and exit conditions are as follows:

<u>Inlet Conditions</u>		<u>Exit Conditions</u>	
M_4	= 1.3012	M_6	= 0.4130
P_{t4}	= 107.5892 inches of fluid	P_{t6}	= 90.8436 inches of fluid
P_{s4}	= 38.8470 inches of fluid	P_{s6}	= 80.8141 inches of fluid
α	= 80 degrees	α_6	= 66.8189
T_{t4}	= 75 degrees Fahrenheit		

$$\bar{\omega} = \frac{P_{t4} - P_{t6}}{P_{t4} - P_{s4}} = \frac{107.5892 - 90.8436}{107.5892 - 38.8470} = 0.2436$$

$$\bar{C}_P = \frac{P_{t4} - P_{t6}}{P_{t4} - P_{s4}} = \frac{80.8141 - 38.8470}{107.5892 - 38.8470} = 0.6105$$

These performance values are relatively close to the goals, which were $\bar{\omega}$ of 0.22 and \bar{C}_P of 0.60.

COMPRESSOR PERFORMANCE CALCULATIONS

Rotor Inlet

The design inlet conditions are:

1. Incidence angle, i = 0 degrees
2. Angle of relative velocity, β_1 = 60 degrees
3. IGV setting, α_1 = -18.4 degrees

4. Design wheel speed, $U_2 = 1300$ feet per second
5. Trailing edge radius, $r_2 = 4.30$ inches
6. Leading edge radius, $r_1 = 3.60$ inches
7. Inlet temperature, $T_{t1} = 520$ degrees Rankine
8. Inlet pressure, $P_{t1} = 1$ atmosphere

The rotor inlet velocity triangle is constructed as shown in Figure 2. The first step in solving the velocity triangle is to determine the inlet compressor tangential velocity, U_1 .

$$\frac{U_1}{U_2} = \frac{r_1}{r_2} \quad (1a)$$

$$U_1 = 1300 \left(\frac{3.60}{4.30} \right) = 1088.4 \text{ feet per second} \quad (1b)$$

From geometry, the radial velocity component, V_{r1} , can be determined.

$$\tan \beta_1 = \frac{U_1 - V_{u1}}{V_{r1}} = \frac{U_1}{V_{r1}} - \frac{V_{u1}}{V_{r1}} \quad (2a)$$

$$\tan \alpha_1 = \frac{V_{u1}}{V_{r1}} \quad (2b)$$

$$\frac{U_1}{V_{r1}} = \tan \beta_1 + \tan \alpha_1 = \tan 60^\circ + \tan (-18.4^\circ) \quad (2c)$$

$$\frac{U_1}{V_{r1}} = 1.732 - 0.333 = 1.399 \quad (2d)$$

$$V_{r1} = \frac{U_1}{(U_1/V_{r1})} = 1088.4/1.399 = 778 \text{ ft/sec} \quad (2e)$$

The remaining sides at the velocity triangle are calculated.

$$V_1 = \frac{V_{r1}}{\cos \alpha_1} = \frac{778}{\cos (-18.4^\circ)} = 819 \text{ ft/sec} \quad (3)$$

$$W_1 = \frac{V_{r1}}{\cos \beta_1} = \frac{778}{\cos 60^\circ} = 1555 \text{ ft/sec} \quad (4)$$

$$V_{u1} = V_{r1} \tan \alpha_1 = (778)(-0.333) = -259 \text{ ft/sec} \quad (5)$$

To determine the Mach number associated with the inlet velocities, inlet static temperature and sonic velocity are calculated.

$$T_{t1} - T_{s1} = \frac{V_1^2}{2gJC_p} = \frac{(819)^2}{2(32.2)(778)(.24)} = 56^\circ\text{R} \quad (6a)$$

$$T_{s1} = T_{t1} - (T_{t1} - T_{s1}) = 520 - 56 = 464^\circ\text{R} \quad (6b)$$

$$a_1 = \sqrt{\gamma g R T_{s1}} = 49.02 \sqrt{464} = 1056 \text{ ft/sec} \quad (7)$$

The significant Mach numbers are:

$$M_1 = \frac{V_1}{a_1} = \frac{819}{1056} = 0.776 \quad (8)$$

$$M_{R1} = \frac{W_1}{a_1} = \frac{1555}{1056} = 1.473 \quad (9)$$

Inlet temperature, pressure, and flow parameters are determined.

$$\frac{T_{s1}}{T_{t1R}} = 0.6975 \text{ (Isentropic Table at } M_{R1} = 1.473) \quad (10a)$$

$$T_{t1R} = \frac{T_{s1}}{(T_{s1}/T_{t1R})} = \frac{464}{0.6975} = 665^\circ\text{R} \quad (10b)$$

$$\frac{P_{s1}}{P_{t1}} = 0.671 \text{ (Isentropic Table at } M_1 = 0.776) \quad (11a)$$

$$P_{s1} = \left(\frac{P_{s1}}{P_{t1}} \right) (P_{t1}) = (0.671)(1.0) = 0.671 \text{ atmosphere} \quad (11b)$$

$$\frac{P_{s1}}{P_{t1R}} = 0.283 \text{ (Isentropic Table at } M_{R1} = 1.473) \quad (12a)$$

$$P_{t1R} = \frac{P_{s1}}{(P_{s1}/P_{t1R})} = \frac{0.671}{0.283} = 2.37 \text{ atmospheres} \quad (12b)$$

$$\text{Area} = \pi D h = \frac{\pi(7.2)(0.70)}{144} = 0.11 \text{ square foot} \quad (13)$$

$$\frac{P_{s1}}{P_{t1}} = 0.7525 \text{ (Isentropic Table at } M_1 = 0.776) \quad (14)$$

$$w_1 = \rho_{s1} A_1 V_1 = \left(\frac{\rho_{s1}}{\rho_{t1}} \right) (\rho_{t1})(0.11)(778)$$

$$w_1 = (0.7525)(0.07648)(0.11)(778) = 4.925^* \text{ lb/sec} \quad (15)$$

Rotor Blade

The rotor blade exit relative total pressure, total temperature and Mach number can now be determined. In addition to the inlet conditions, design values for the blade trailing edge tangential velocity, U_2 , of 1300 ft/sec and exit relative flow angle, β_2 , of 60 degrees are known.

$$T_{t2R} - T_{t1R} = \frac{U_2^2}{2gJC_P} - \frac{U_1^2}{2gJC_P} \quad (16)$$

$$\frac{U_2}{U_1} = \frac{r_2}{r_1} \text{ and } U_2 = U_1 \left(\frac{r_2}{r_1} \right) \quad (17)$$

$$T_{t2R} - T_{t1R} = \frac{U_1^2}{2gJC_P} \left(\frac{r_2}{r_1} \right)^2 - \frac{U_1^2}{2gJC_P}$$

$$T_{t2R} - T_{t1R} = \frac{U_1^2}{2gJC_P} \left[\left(\frac{r_2}{r_1} \right)^2 - 1 \right]$$

$$T_{t2R} - T_{t1R} = \frac{(1088)^2}{12012} \left[\left(\frac{4.3}{3.6} \right)^2 - 1 \right]$$

$$T_{t2R} - T_{t1R} = 42^\circ \text{R} \quad (18)$$

$$T_{t2R} = T_{t1R} + (T_{t2R} - T_{t1R}) = 665 + 42 = 707^\circ \text{R} \quad (19)$$

*With an assumed flow coefficient of 0.95, $w_1 = 4.68 \text{ lb/sec}$.

From rotor blade cascade tests at an inlet Mach number of 1.473, $\bar{\omega} = 0.186$. For the two-dimensional cascade tests, the loss coefficient, $\bar{\omega}$, was defined as

$$\bar{\omega} = \frac{P_{t1} - P_{t2}}{P_{t1} - P_{s1}} \quad (20a)$$

$$P_{t1} - P_{t2} = \bar{\omega} (P_{t1} - P_{s1}) \quad (20b)$$

$$\frac{P_{t2}}{P_{t1}} = 1 - \bar{\omega} \left(1 - \frac{P_{s1}}{P_{t1}}\right) \quad (20c)$$

In the three-dimensional case, the rotating cascade produces a total pressure rise from the inlet to the exit of the blade, and the following relationship is applied using the $\bar{\omega}$ value determined from the two-dimensional cascade tests.

$$\frac{P_{t2}}{P_{t1}} = \left[1 - \bar{\omega} \left(1 - \frac{P_{s1}}{P_{t1}}\right)\right] \left(\frac{P_{t2}}{P_{t1}}\right)_i \quad (21)$$

$$\frac{P_{t2R}}{P_{t1R}} = \left[1 - \bar{\omega} \left(1 - \frac{P_{s1}}{P_{t1R}}\right)\right] \left(\frac{P_{t2R}}{P_{t1R}}\right)_i \quad (22)$$

$$\left(\frac{P_{t2R}}{P_{t1R}}\right)_i = \left(\frac{T_{t2R}}{T_{t1R}}\right)^{\frac{\gamma-1}{\gamma}} = \left(\frac{707}{665}\right)^{3.5} = 1.239 \quad (23)$$

$$\frac{P_{t2R}}{P_{t1R}} = \left[1 - 0.186 (1 - 0.283)\right] 1.239 = 1.074 \quad (24)$$

$$P_{t2R} = P_{t1R} \left(\frac{P_{t2R}}{P_{t1R}}\right) = (2.37)(1.074) = 2.55 \text{ atmospheres} \quad (25)$$

$$\frac{A_2}{A_1} = \frac{r_2 h_2 \cos \beta_2}{r_1 h_1 \cos \beta_1} \quad (26a)$$

$$\beta_1 = \beta_2 = 60^\circ \quad (26b)$$

$$\frac{A_2}{A_1} = \frac{(4.3)(0.586)(0.5)}{(3.6)(0.7)(0.5)} = 1.0 \quad (26c)$$

$$\frac{A_1}{A_1^*} = 1.158 \text{ (Isentropic Table at } M_{1R} = 1.473) \quad (27)$$

$$\frac{w_1 \sqrt{T_{t1R}}}{A_1^* P_{t1R}} = \text{constant} = 0.532 \quad (28a)$$

$$\frac{w_2 \sqrt{T_{t2R}}}{A_2^* P_{t2R}} = \text{constant} = 0.532 \quad (28b)$$

$$w_1 = w_2 \quad (28c)$$

$$\frac{A_1^*}{A_2^*} = \frac{P_{t2R}}{P_{t1R}} \sqrt{\frac{T_{t1R}}{T_{t2R}}} = 1.074 \quad \frac{665}{707} = 1.0413 \quad (28d)$$

$$\frac{A_2}{A_2^*} = \left(\frac{A_2}{A_1}\right) \left(\frac{A_1}{A_1^*}\right) \left(\frac{A_1^*}{A_2^*}\right)$$

$$\frac{A_2}{A_2^*} = (1.0)(1.158)(1.0413) = 1.206 \quad (29)$$

$$M_{R2} = 1.54 \text{ (Isentropic Table at } A_2/A_2^* = 1.206) \quad (30)$$

Rotor Exit

The rotor exit velocity triangle, shown in Figure 2, is solved, and rotor discharge pressures and temperatures are determined.

$$\frac{T_{t2R}}{T_{s2}} = 1.476 \text{ (Isentropic Table at } M_{2R} = 1.54) \quad (31)$$

$$T_{s2} = \frac{T_{t2R}}{(T_{t2R}/T_{s2})} = \frac{707}{1.476} = 479^\circ\text{R} \quad (32)$$

$$a_2 = \sqrt{\gamma g R T_{s2}} = 49.02 \sqrt{479} = 1073 \text{ ft/sec} \quad (33)$$

$$W_2 = a_2 M_{R2} = (1073)(1.54) = 1656 \text{ ft/sec} \quad (34)$$

$$W_{u2} = W_2 \sin \beta_2 = 1656 \sin 60^\circ = 1434 \text{ ft/sec} \quad (35)$$

$$V_{u2} = W_{u2} + U_2 = 1434 + 1300 = 2734 \text{ ft/sec} \quad (36)$$

$$V_{r2} = W_2 \cos \beta_2 = (1656)(\cos 60^\circ) = 828 \text{ ft} \quad (37)$$

$$\alpha_2 = \arctan \frac{V_{u2}}{V_{r2}} = \arctan \frac{2734}{828} = 73.2^\circ \quad (38)$$

$$\frac{P_{s2}}{P_{t2R}} = 0.256 \text{ (Isentropic Table at } M_{R2} = 1.54) \quad (39)$$

$$P_{s2} = \left(\frac{P_{s2}}{P_{t2R}} \right) P_{t2R} = (0.256)(2.55) = 0.653 \text{ atmosphere} \quad (40)$$

$$V_2 = \sqrt{V_{r2}^2 + V_{u2}^2} = (828)^2 + (2734)^2 = 2856 \text{ ft/sec} \quad (41)$$

$$M_2 = \frac{V_2}{a_2} = \frac{2856}{1076} = 2.66 \quad (42)$$

$$\frac{T_{t2}}{T_{s2}} = 2.417 \text{ (Isentropic Table at } M_2 = 2.66) \quad (43)$$

$$\frac{P_{t2}}{P_{s2}} = 22.0 \text{ (Isentropic Table at } M_2 = 2.66) \quad (44)$$

$$T_{t2} = (T_{s2}) \left(\frac{T_{t2}}{T_{s2}} \right) = (479)(2.417) = 1159^\circ \text{R} \quad (45)$$

$$P_{t2} = (P_{s2}) \left(\frac{P_{t2}}{P_{s2}} \right) = (0.653)(22) = 14.37 \text{ atmospheres} \quad (46)$$

Rotating Vaneless Diffuser

From conservation of angular momentum,

$$V_{u3} = \left(\frac{r_2}{r_3} \right) (V_{u2}) = \frac{4.3}{6.45} (2734) = 1823 \text{ ft/sec} \quad (47)$$

$$\rho_2 = \frac{P}{RT} = \frac{(39.68)(0.653)}{479} = 0.054 \text{ lbm/ft}^3 \quad (48)$$

$$A_2 = 2\pi r h = \frac{2\pi (4.3)(0.586)}{144} = 0.11 \text{ ft}^2 \quad (49)$$

$$w = \rho_2 A_2 V_{r2} = (0.054)(0.11)(828) = 4.92 \text{ lbm/sec} \quad (50)$$

$$\frac{P_{t3}}{P_{t2}} = 0.889 \text{ (Estimated for } M_{2R} = 1.54) \quad (51)$$

$$P_{t3} = (P_{t2}) \frac{P_{t3}}{P_{t2}} = (14.30)(0.889) = 12.7 \text{ atmospheres} \quad (52)$$

$$\rho_{t3} = 39.68 \frac{P_{t3}}{T_{t3}} = \frac{39.68 (12.7)}{1159} = 0.435 \text{ lbm/ft}^3 \quad (53)$$

$$A_3 = 2\pi r_3 h_3 = \frac{2\pi (6.45)(0.4)}{144} = 0.1125 \text{ ft}^2 \quad (54)$$

To account for boundary layer growth, a blockage factor, B, of 0.63 is used.

$$A_{3F} = BA_3 = (0.63)(0.1125) = 0.071 \text{ ft}^2 \quad (55)$$

An iteration is now performed assuming values of M_3 and checking to see if the continuity relationship is satisfied. From the assumed M_3 , ρ_3 is calculated. Using the continuity equation, a value of radial velocity is calculated. Knowing V_{u3} and V_{r3} , V_3 and M_3 are calculated and compared to the assumed value. The following calculations assume an M_3 of 1.28.

$$\frac{T_{t3}}{T_{s3}} = 1.3277 \text{ (Isentropic Table at } M_3 = 1.28) \quad (56)$$

$$T_{s3} = \frac{T_{t3}}{(T_{t3}/T_{s3})} = \frac{1159}{1.3277} = 873^\circ\text{R} \quad (57)$$

$$a_3 = \sqrt{rg R T_{s3}} = 49.02 \sqrt{873} = 1448 \text{ ft/sec} \quad (58)$$

$$V_3 = a_3 M_3 = (1448)(1.28) = 1853 \text{ ft/sec} \quad (59)$$

$$\frac{\rho_{t3}}{\rho_{s3}} = 2.03 \text{ (Isentropic Table at } M_3 = 1.28) \quad (60)$$

$$\rho_{s3} = \rho_{t3} / (\rho_{t3} / \rho_{s3}) = (0.435) / (2.03) = 0.214 \text{ lbm/ft}^3 \quad (61)$$

$$V_{r3} = \frac{w}{\rho_{s3} A_{3F}} = \frac{4.92}{(0.214)(0.071)} = 324 \text{ ft/sec} \quad (62)$$

$$V_3 = \sqrt{V_{u3}^2 + V_{r3}^2} = \sqrt{(1823)^2 + (324)^2} = 1838 \text{ ft/sec} \quad (63)$$

$$M_3 = \frac{V_3}{a_3} = \frac{1838}{1448} = 1.27 \quad (64)$$

$$\alpha_3 = \arctan (V_{3u} / V_{3r}) = \arctan (1823 / 324)$$

$$\alpha_3 = \arctan 5.6265 = 79^\circ 55' \quad (65)$$

For the assumed M_3 of 1.28 and V_3 of 1853, calculated values of M_3 and V_3 were 1.27 and 1838, respectively.

Supersonic Stator

Design inlet conditions are M_4 of 1.28 and α_4 of 80 degrees. From the two-dimensional cascade test data at these conditions, the total pressure loss coefficient was 0.144 and the static pressure rise coefficient was 0.46.

$$P_{s4} / P_{t4} = 0.371 \text{ (Isentropic Table at } M_4 = 1.28) \quad (66)$$

$$P_{t4} = P_{t3} \quad \begin{array}{l} \text{Station 3 is defined as rotor exit} \\ \text{Station 4 is defined as supersonic stator inlet} \end{array} \quad (67)$$

$$P_{t4} = 12.7 \text{ atmospheres (see equation 52)} \quad (68)$$

$$P_{s4} = P_{t4} (P_{s4} / P_{t4}) = (12.7)(0.371) = 4.7 \text{ atmospheres} \quad (69)$$

$$P_{t4} - P_{s4} = 12.7 - 4.7 = 8.0 \text{ atmospheres} \quad (70)$$

$$\bar{w} = 0.144 = \frac{P_{t4} - P_{t5}}{P_{t4} - P_{s4}} \quad (71a)$$

$$P_{t4} - P_{t5} = 0.144 (8.0) = 1.15 \text{ atmospheres} \quad (71b)$$

$$P_{t5} = P_{t4} - (P_{t4} - P_{t5}) = 12.7 - 1.15 = 11.55 \text{ atmospheres} \quad (71c)$$

$$\bar{C}_P = 0.46 = \frac{P_{s5} - P_{s4}}{P_{t4} - P_{s4}} \quad (72a)$$

$$P_{s5} - P_{s4} = 0.46 (8.0) = 3.68 \text{ atmospheres} \quad (72b)$$

$$P_{s5} = (P_{s5} - P_{s4}) + P_{s4}$$

$$P_{s5} = 3.68 + 4.7 = 8.38 \text{ atmospheres} \quad (72c)$$

$$\frac{P_{s5}}{P_{t5}} = \frac{8.38}{11.55} = 0.7255 \quad (73)$$

$$M_5 = 0.693 \text{ (Isentropic Table at } P_{s5}/P_{t5} \text{ of } 0.7255) \quad (74)$$

Subsonic Stators

The station designation of the subsonic stators is 5.25 at the inlet and 6.0 at the exit. Design inlet conditions are $M_{5.25}$ of 0.71 and $\alpha_{5.25}$ of 75 degrees. From the two-dimensional cascade data at these conditions, the total pressure loss coefficient was 0.654.

$$P_{t5.25} = P_{t5} = 11.55 \text{ atmospheres} \quad (75)$$

$$P_{s5.25} = P_{s5} = 8.38 \text{ atmospheres} \quad (76)$$

The subsonic stator calculations are as follows:

$$P_{t5.25} - P_{s5.25} = 11.55 - 8.38 = 3.17 \text{ atmospheres} \quad (77)$$

$$\bar{w} = 0.066 = \frac{P_{t5.25} - P_{t6}}{P_{t5.25} - P_{s5.25}} \quad (78a)$$

$$P_{t5.25} - P_{t6} = 0.066 (3.17) = 0.21 \text{ atmosphere} \quad (78b)$$

$$P_{t6} = P_{t5.25} - (P_{t5.25} - P_{t6})$$

$$P_{t6} = 11.55 - 0.21 = 11.34 \text{ atmospheres} \quad (78c)$$

$$\bar{C}_P = 0.654 = \frac{P_{s6} - P_{s5.25}}{P_{t5.25} - P_{s5.25}} \quad (79a)$$

$$P_{s6} - P_{s5.25} = (0.654)(3.17) = 2.07 \text{ atmospheres} \quad (79b)$$

$$P_{s6} = (P_{s6} - P_{s5.25}) + P_{s5.25}$$

$$P_{s6} = 2.07 + 8.38 = 10.45 \text{ atmospheres} \quad (79c)$$

$$\frac{P_{s6}}{P_{t6}} = \frac{10.45}{11.34} = 0.921 \quad (80)$$

$$M_6 = 0.345 \text{ (Isentropic Table at } P_{s6}/P_{t6} = 0.921) \quad (81)$$

Compressor Efficiency

$$\Delta T \text{ (Isentropic)} = T_{to} \left[\left(\frac{P_{t6}}{P_{to}} \right)^{\frac{\gamma-1}{\gamma}} - 1 \right]$$

$$\Delta T \text{ (Isentropic)} = 520 \left[(11.34)^{.2857} - 1 \right]$$

$$\Delta T \text{ (Isentropic)} = 520 (2.00124 - 1)$$

$$\Delta T \text{ (Isentropic)} = 521^\circ R \quad (82)$$

$$T_{t6} = T_{t2} = 1159^\circ R \text{ (from equation 45)} \quad (83)$$

$$T_{t6} - T_{to} = 1159 - 520 = 639^\circ R \quad (84)$$

$$\eta = \frac{(T_{t6} - T_{to}) \text{ Isentropic}}{(T_{t6} - T_{to}) \text{ Actual}} = \frac{521}{639} = 0.816 \text{ or } 81.6\% \quad (85)$$

Compressor Characteristic Maps

The supersonic and subsonic compressor maps presented in Figures 216 and 217 were generated from a computer program which incorporates the above described calculation procedure along with performance characteristics determined from Phase I component tests.

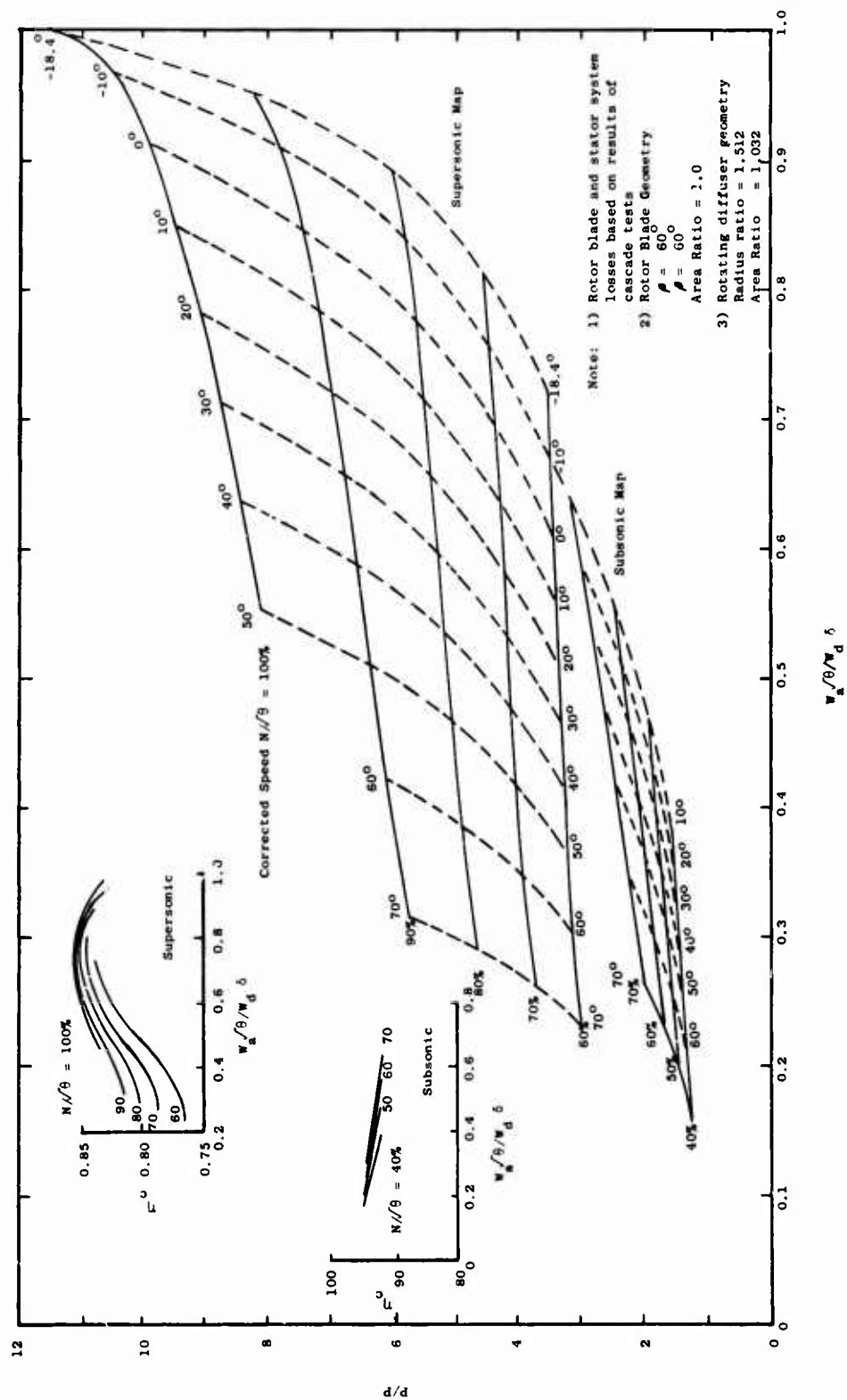


Figure 216. Radial Outflow Compressor Subsonic Map.

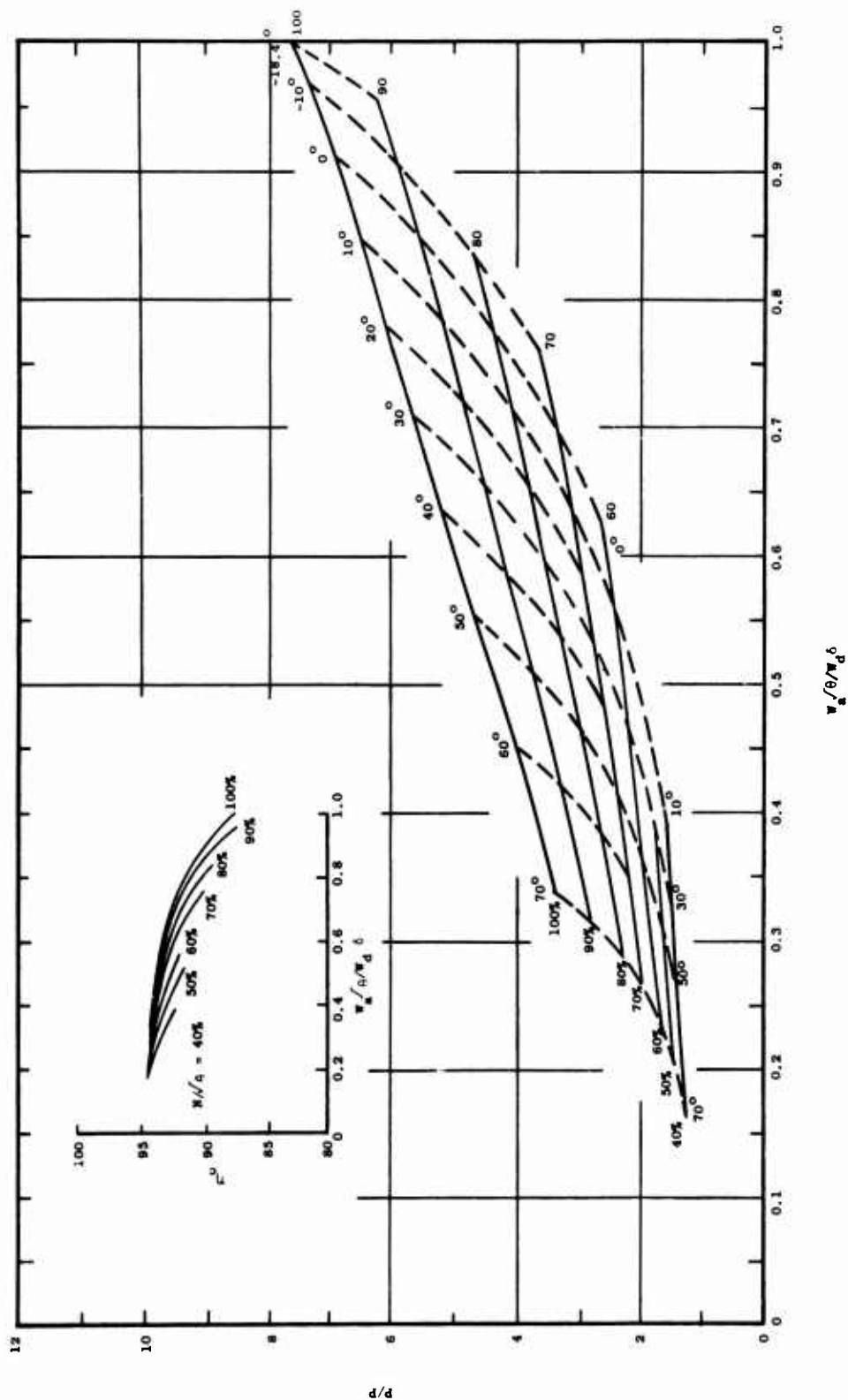


Figure 217. Radial Outflow Compressor Supersonic Map.

APPENDIX II, DERIVATION OF CHARACTERISTIC EQUATIONS

INTRODUCTION

The purpose of this analysis is to develop the equations required to perform a numerical solution of a supersonic, adiabatic, isentropic, steady, variable thickness inviscid flow of a perfect gas in a rotating reference frame. Such a solution is considered to be obtained when the significant flow field properties are known at each point in the flow field, and such properties are consistent with both the boundary conditions and the governing flow equations, within an acceptable degree of error.

Since the flow is considered isentropic, a knowledge of the flow direction and any fluid property (excluding entropy) is sufficient to specify all other significant flow properties. In the analysis to follow, it will be found convenient to specify the flow direction and the flow pressure by means of the two flow properties $\xi(+)$ and $\xi(-)$, defined as follows:

$$\xi(+) = \frac{\sqrt{M^2 - 1}}{\gamma M^2} \ln p + \theta \quad (1a)$$

$$\xi(-) = \frac{\sqrt{M^2 - 1}}{\gamma M^2} \ln p - \theta \quad (1b)$$

Basically, it is assumed that initially the values of $\xi(+)$ and $\xi(-)$ are known at every point along an input line. The analytic technique is simply concerned with the extension of the knowledge of $\xi(+)$ and $\xi(-)$ from the input line to the rest of the flow field. It is understood that, owing to the numerical nature of the method, only a finite number of points on the input line can be used; consequently, the flow field can be determined only at a finite number of field points. These field points constitute what may be called a solution mesh. If it is desired to know the flow conditions at an off-mesh point, one may either use interpolation between on-mesh points or redefine the initial input points so as to produce a mesh containing the desired point. If it is deemed that a solution mesh is not accurate enough, an increase in the number of input points will increase the mesh fineness and the solution accuracy. Incidentally, one method for estimating the accuracy of a solution mesh is simply to compare it to a finer solution mesh. A brief discussion of the process of constructing a solution mesh from the corresponding input points is given below.

Unlike many numerical techniques, the method of characteristics does not require the solution for all the mesh points simultaneously. Rather, the mesh points are determined in a consecutive manner with the conditions

at each new mesh point generally calculated from the knowledge of conditions at two previously calculated upstream mesh points. This procedure is possible because of the nature of supersonic flow. In the special case of a mesh point at a solid boundary, or a free surface, only one previously calculated mesh point is required.

To specify an unknown mesh point completely, it is necessary to determine its location and its $\xi(+)$ and $\xi(-)$ values. Consider two mesh points whose location and associated flow properties are known. It is desired to find the next consecutive mesh point. Theoretically, through each mesh point two curves called physical characteristics may be drawn. To distinguish the two curves, one is called the positive (+) characteristic and the other the negative (-) characteristic. The location of the next consecutive mesh point corresponding to the two given mesh points is defined by the intersection of a positive and a negative characteristic from each mesh point as shown in Figure 218.

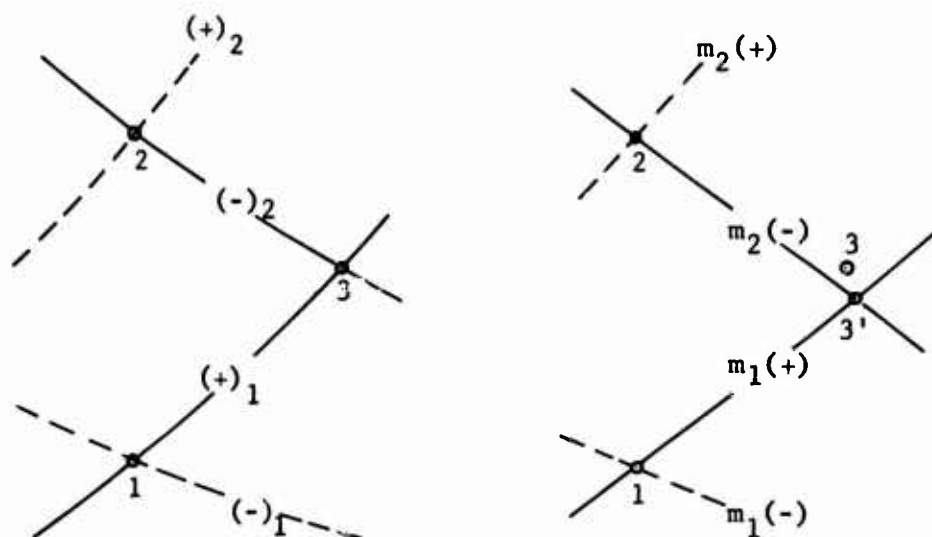


Figure 218. Mesh Point Location by Characteristic Curves and by Characteristic Slopes.

In practice, only the slopes of the characteristic curves are generally known at each mesh; and in lieu of an exact specification of the mesh point location, an approximate location, based on the intersection of two straight lines, must be accepted. The slopes of the characteristic curves at any mesh point are, in general, a function only of the flow properties at the mesh point. It will be shown later that for the particular problem under study, the positive and negative characteristic slopes are, respectively,

$$m_1(+) = \tan(\theta_1 + \mu_1) \quad (2a)$$

$$m_2(-) = \tan (\theta_2 - \mu_2) \quad (2b)$$

where

$$\tan \mu = \frac{1}{\sqrt{M^2 - 1}}$$

With the location of the mesh point determined, an initial approximation of the flow properties at the point can be made. As will be shown later, $\xi_3(+)$ may be determined using an equation of the form

$$\xi_3(+) = \xi_1(+) + \epsilon_1(+) \cdot \Delta_{1-3}^1 \quad (3)$$

where

$\xi_3(+)$ is the value of $\xi(+)$ at mesh point 3

$\xi_1(+)$ is the value of $\xi(+)$ at mesh point 1

$\epsilon_1(+)$ is a function which depends on the flow properties at mesh point 1

Δ_{1-3}^1 is the distance from mesh point 1 to mesh point 3

Similarly, the value of $\xi_3(-)$ can be determined from:

$$\xi_3(-) = \xi_2(-) + \epsilon_2(-) \cdot \Delta_{2-3}^1 \quad (4)$$

where

$\xi_3(-)$ is the value of $\xi(-)$ at mesh point 3

$\xi_2(-)$ is the value of $\xi(-)$ at 2

$\epsilon_2(-)$ is a function which depends on the properties at mesh point 2

Δ_{2-3}^1 is the distance from mesh point 2 to mesh point 3

With $\xi_3(+)$ and $\xi_3(-)$ known, the rest of the flow properties at point 3 may be determined. In addition, the positive and negative characteristic slopes may be calculated at point 3. It is apparent that a better approximation of the position of point 3 can be obtained if the straight lines drawn through mesh points 1 and 2 are drawn with appropriate average slopes as shown in Figure 219. The subscript "1-3" indicates an average of $m_1(+)$ and $m_3(+)$.

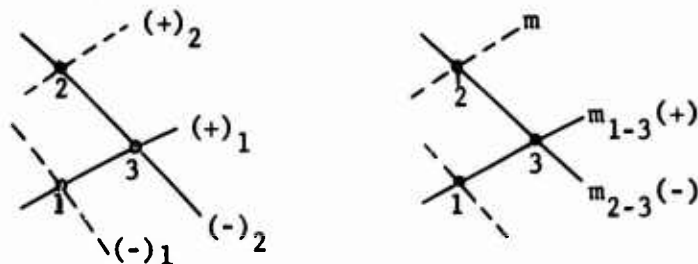


Figure 219. Mesh Point Location by Characteristic Curves and by Characteristic Average Slopes.

It can be seen that the new mesh point will be very close to its exact location if the mesh is reasonably fine with respect to the curvature of the characteristics.

With a new position for mesh point 3, a new determination of $\xi_3(+)$ and $\xi_3(-)$ should be made. In the new determination, the average of the $\epsilon_1(+)$ and $\epsilon_3(+)$ values should be used in place of $\epsilon_1(+)$ in equation 3; and the average of $\epsilon_2(-)$ and $\epsilon_3(-)$ used in place of $\epsilon_2(-)$ in equation 4. That is,

$$\xi_3(+) = \xi_1(+) + \epsilon_{1-3}(+) \Delta l_{1-3} \quad (5a)$$

$$\xi_3(-) = \xi_1(-) + \epsilon_{2-3}(-) \Delta l_{2-3} \quad (5b)$$

The iterative correction of location and properties is continued until adequate conversion is obtained. It may be noted here that although the above iteration can be made as close as desired, an absolute error in location and value will always exist which can only be reduced by going to a smaller mesh size. Fortunately, this error is very small for reasonably fine meshes.

The remainder of this analysis will be devoted to a derivation of the characteristic functions $m(+)$, $m(-)$, $\epsilon(+)$, and $\epsilon(-)$.

ANALYSIS

Reference Frame

The reference frame used for the development of the characteristic relationships is a Cartesian coordinate system whose origin is fixed in space, but which possesses an angular velocity ω about its z axis. A region surrounding the point A in the flow field is to be investigated. The point A and the associated nomenclature are shown in the rotating coordinate system in Figure 220.

The unit vectors \bar{i} and \bar{j} are the intrinsic unit vector at the point A. The vector \bar{i} is parallel to the relative velocity vector at A, and the vector \bar{j} is normal to \bar{i} as shown. Since the vectors \bar{i} and \bar{j} are fixed with respect to the reference Cartesian system, they possess both a translation and a rotation with respect to fixed space. The conservation equations will be developed at the point A with respect to the directions of \bar{i} and \bar{j} .

Steady-State Conservation of Mass

Consider the stream element bounded by streamline (1), streamline (2), the upper and lower flow passage walls, and stream filament faces A and B, as shown in Figure 221. There is no flow of mass across the passage

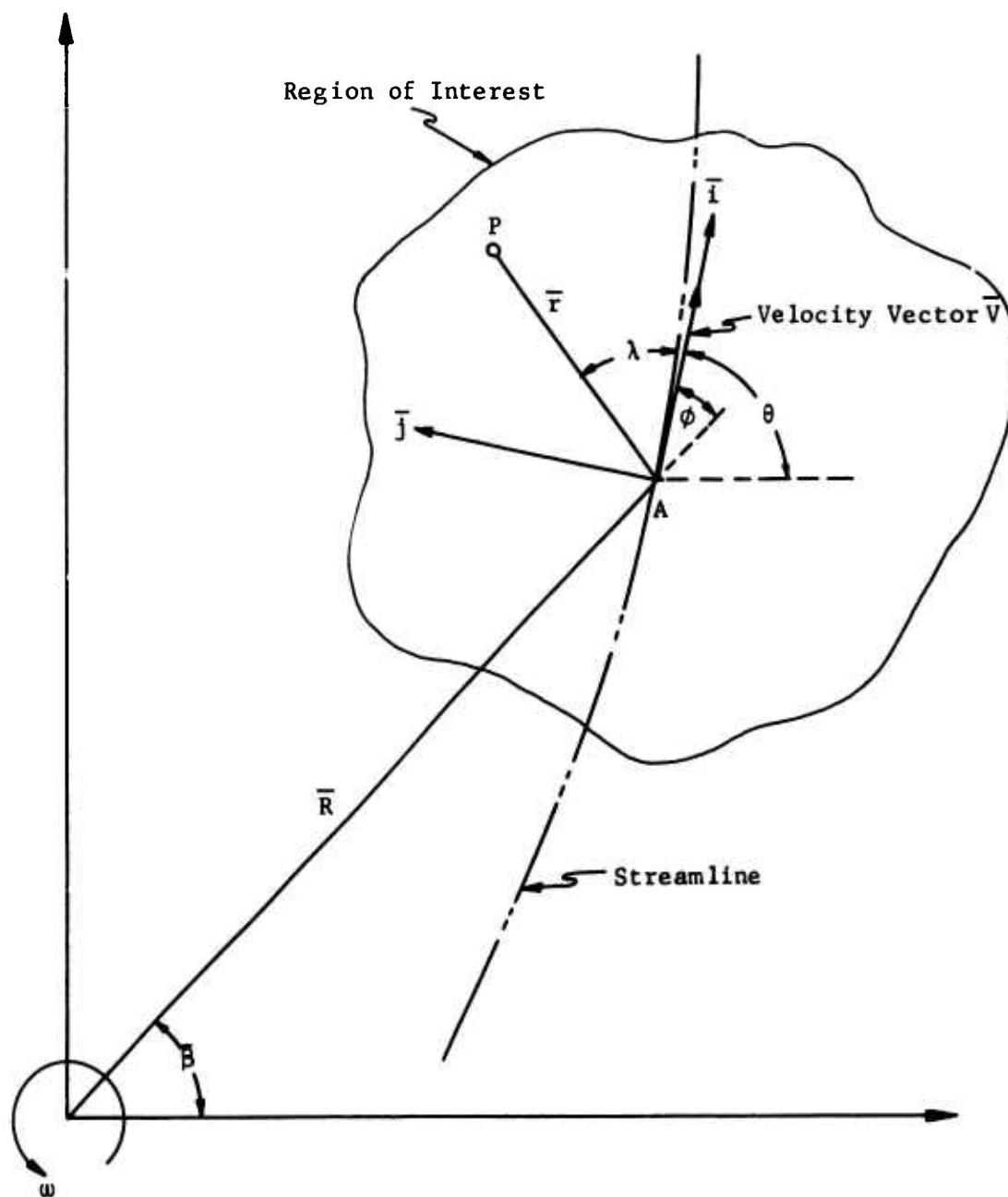


Figure 220. Rotating Reference Frame.

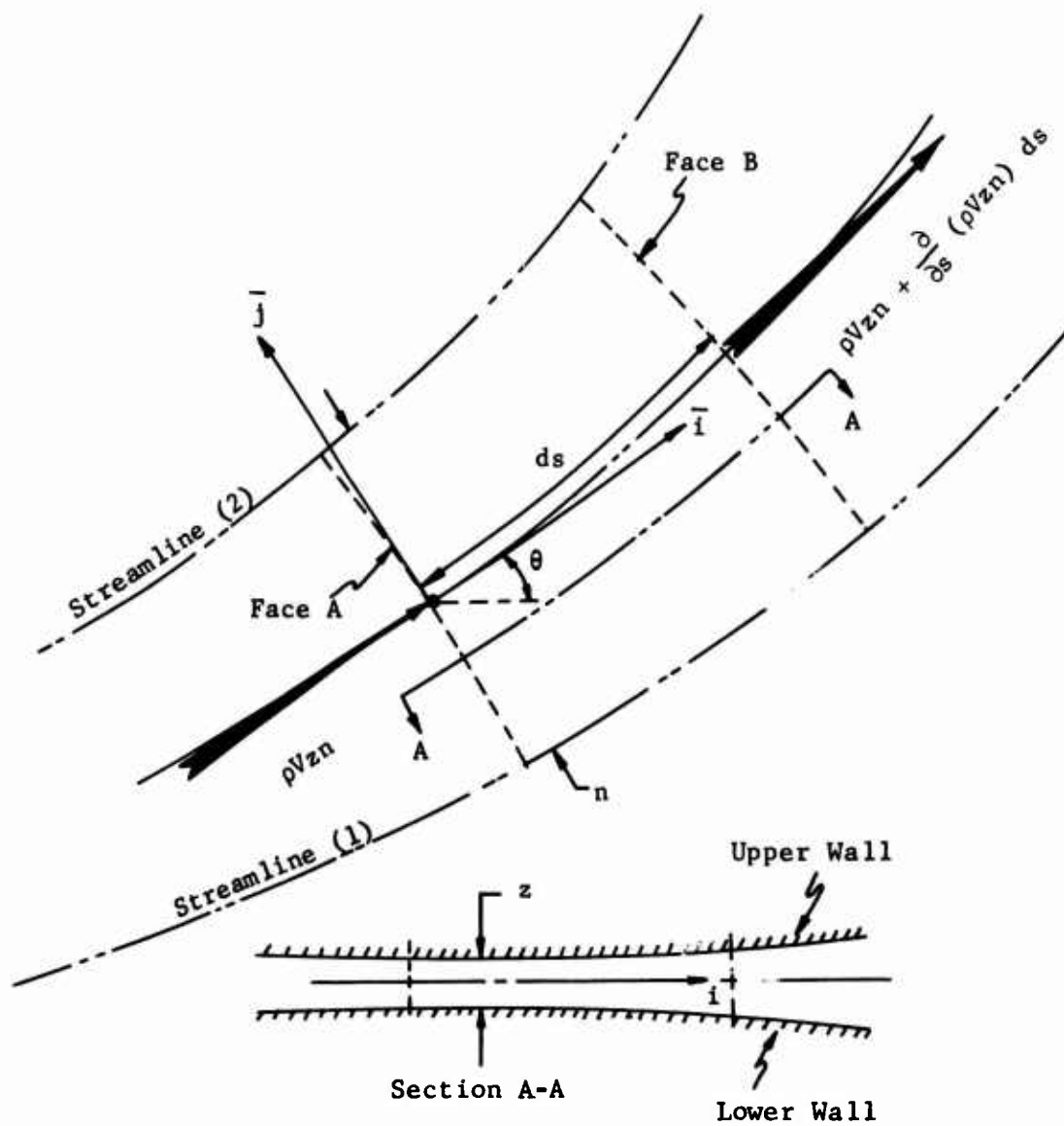


Figure 221. Stream Element.

walls or across the bounding streamlines. The mass flow out of the element through face A and face B respectively is given by:

$$\dot{M}_A = -(\rho V z n)_A \quad (6a)$$

$$\dot{M}_B = (\rho V z n)_A + \frac{\partial(\rho V z n)}{\partial s} ds \quad (6b)$$

Since the flow field is steady,

$$\dot{M}_A + \dot{M}_B = 0 \quad (7)$$

$$\frac{\partial}{\partial s} (\rho V z n) = 0 \quad (8)$$

In expanded form, equation 8 becomes

$$\rho \frac{\partial V}{\partial s} + V \frac{\partial \rho}{\partial s} + \rho V \frac{\partial}{\partial s} \ln(z) + \rho \frac{V}{n} \frac{\partial n}{\partial s} = 0 \quad (9)$$

The last term in equation 9 represents the effect of streamline divergence. It is possible to describe streamline divergence in an alternate and more desirable manner, i.e., in terms of the rate and change of streamline angle with respect to the normal direction \bar{j} .

$$\frac{1}{n} \frac{\partial n}{\partial s} = \frac{\partial \theta}{\partial n} \quad (10)$$

If z is assumed to be a function of R only (as in a rotor with an axisymmetric passage width distribution), then the term $\frac{\partial}{\partial s} \ln(z)$ may be rewritten as

$$\frac{\partial}{\partial s} \ln(z) = \frac{d \ln(z)}{dR} \cos(\theta - \bar{\beta}) \quad (11)$$

Substituting equation 10 and equation 11 into equation 9 and rearranging terms imparts the following form to the continuity equation at point A.

$$-\frac{1}{V} \frac{\partial V}{\partial s} = + \frac{1}{\rho} \frac{\partial \rho}{\partial s} + \frac{\partial \theta}{\partial n} + \frac{d \ln(z)}{dR} \cos(\theta - \bar{\beta}) \quad (12)$$

Steady-State Conservation of Momentum

Consider a particle P a distance r from point A, and at an angle λ with \bar{i} as shown in Figure 220. The acceleration of this point in an inertial reference frame is

$$\bar{A} = \ddot{\bar{R}} + \bar{r}'' + 2\bar{\omega} \times \bar{r}' + \dot{\bar{\omega}} \times \bar{r} + \bar{\omega} \times \bar{\omega} \times \bar{r} \quad (13)$$

In equation 13 the dots represent differentiation with respect to time in the inertial frame and the primes represent differentiation with respect to time in the non-inertial ($\bar{i} - \bar{j}$) frame.

The terms of equation 13, expanded in terms of the \bar{i} and \bar{j} directions, are:

$$\ddot{\bar{R}} = -\omega^2 R \cos(\theta - \beta) \bar{i} + \omega^2 R \sin(\theta - \beta) \bar{j} \quad (14a)$$

$$\bar{r}'' = u' \bar{i} + v' \bar{j} \quad (14b)$$

$$2\bar{\omega} \times \bar{r}' = -2\omega v \bar{i} + 2\omega u \bar{j} \quad (14c)$$

$$\dot{\bar{\omega}} \times \bar{r}_1 = 0 \quad (14d)$$

$$\bar{\omega} \times \bar{\omega} \times \bar{r} = -\omega^2 r \cos \lambda \bar{i} - \omega^2 r \sin \lambda \bar{j} \quad (14e)$$

where

u = particle velocity in the \bar{i} direction

v = particle velocity in the \bar{j} direction

The components of 14b may be rewritten as

$$u' = u \frac{\partial u}{\partial s} + v \frac{\partial u}{\partial n} \quad (15a)$$

$$v' = u \frac{\partial v}{\partial s} + v \frac{\partial v}{\partial n} \quad (15b)$$

Combining equations 13 and 14a to equations 14e, 15a, and 15b yields

$$\begin{aligned} \bar{A} = & [-\omega^2 r \cos(\theta - \beta) + u \frac{\partial u}{\partial s} + v \frac{\partial u}{\partial n} - 2\omega v - \omega^2 r \cos \lambda] \bar{i} \\ & + [\omega^2 r \sin(\theta - \beta) + u \frac{\partial v}{\partial s} + v \frac{\partial v}{\partial n} + 2\omega u - \omega^2 r \sin \lambda] \bar{j} \end{aligned} \quad (16)$$

To determine the acceleration of a particle at A, the radius r is allowed to approach zero.

$$\lim_{r \rightarrow 0} u = V \quad (17a)$$

$$\lim_{r \rightarrow 0} v = 0 \quad (17b)$$

$$\lim_{r \rightarrow 0} u \frac{\partial v}{\partial s} = V^2 \frac{\partial \theta}{\partial s} \quad (17c)$$

Hence, the acceleration at the point A is

$$\bar{A} = [-\omega^2 R \cos(\theta - \bar{\beta}) + V \frac{\partial V}{\partial s}] \bar{i} + [\omega^2 R \sin(\theta - \bar{\beta}) + V^2 \frac{\partial \theta}{\partial s} + 2\omega V] \bar{j} \quad (18)$$

The force per unit mass of fluid due to the flow field pressure gradients is

$$\frac{dF}{dM} = \frac{-\nabla P}{\rho} \quad (19)$$

Expanding the terms of the \bar{i} and \bar{j} directions yields

$$-\frac{\nabla P}{\rho} = \frac{1}{\rho} \frac{\partial P}{\partial s} \bar{i} + \frac{1}{\rho} \frac{\partial P}{\partial n} \bar{j} \quad (20)$$

Equating 20 (the force per unit mass) to 18 (the acceleration) and separating i and j components yields the two momentum equations:

$$\frac{1}{\rho} \frac{\partial P}{\partial s} + V \frac{\partial V}{\partial s} - \omega^2 R \cos(\theta - \bar{\beta}) = 0 \quad (21a)$$

$$\frac{1}{\rho} \frac{\partial P}{\partial n} + V^2 \frac{\partial \theta}{\partial n} + 2\omega V + \omega^2 R \sin(\theta - \bar{\beta}) = 0 \quad (21b)$$

Characteristic Equations

It is desired at this point to have equations 21a and 21b contain only the partials of the pressure P and flow angle θ . The continuity equation (equation 12) can be used to eliminate the partial of V at the expense of introducing the partial of ρ (introduction of the partial of z is of no consequence since it is assumed that the behavior of z is known). However, since the flow is assumed to be isentropic, the partial of ρ can be related to the partial of P by

$$\frac{\partial \rho}{\partial s} = \frac{1}{a^2} \frac{\partial P}{\partial s} \quad (22)$$

Combining 21a and 21b with 22 and noting that $M^2 = V^2/a^2$ and that $\rho V^2 = \gamma P M^2$ yields

$$\frac{\Theta}{P} \frac{\partial P}{\partial s} + \frac{\partial \Theta}{\partial n} = -K \quad (23a)$$

$$\frac{1}{\rho V^2} \frac{\partial P}{\partial n} + \frac{\partial \Theta}{\partial s} = -\sigma \quad (23b)$$

where $\Theta = \frac{M^2 - 1}{\gamma M^2}$

$$K = \frac{\omega^2 R}{V^2} + \frac{d}{dR} \ln(z) \cos(\theta - \bar{\theta})$$

$$\sigma = \frac{2\omega}{V} + \frac{\omega^2 R}{V^2} \sin(\theta - \bar{\theta})$$

In addition to equations 18a and 18b, two more equations for the partials of P and θ can be written, as follows:

$$\frac{\partial P}{\partial s} ds + \frac{\partial P}{\partial n} dn = dP \quad (24a)$$

$$\frac{\partial \theta}{\partial s} ds + \frac{\partial \theta}{\partial n} dn = d\theta \quad (24b)$$

Equations 23a, 23b, 24a and 24b are four equations in the four partials of P and θ with respect to s and n, and can be represented in matrix form by

$$NX = C \quad (25)$$

where

$$N = \begin{bmatrix} ds & dn & 0 & 0 \\ 0 & 0 & ds & dn \\ \frac{\Theta}{P} & 0 & 0 & 1 \\ 0 & \frac{1}{\rho V^2} & 1 & 0 \end{bmatrix}$$

$$X = \begin{bmatrix} \frac{\partial P}{\partial s} \\ \frac{\partial P}{\partial n} \\ \frac{\partial \theta}{\partial s} \\ \frac{\partial \theta}{\partial n} \end{bmatrix} \quad (26)$$

$$C = \begin{bmatrix} dP \\ d\theta \\ -K \\ -\sigma \end{bmatrix}$$

Forming the determinant of N yields

$$\text{DET}(N) = ds^2 - (M^2 - 1) dn^2 \quad (27)$$

and hence the determinant of N is zero in the direction

$$\frac{dn}{ds} = \pm \frac{1}{\sqrt{M^2 - 1}} \quad (28)$$

Note: $M > 1$

The directions in which the determinant of N is zero are called characteristic directions, and curves along which the determinant of N is zero are called characteristic curves, or simply characteristics.

From the definition of the Mach angle, the following relationships are valid if $M > 1$:

$$\sin \mu = 1/M \quad (29a)$$

$$\cos \mu = \sqrt{M^2 - 1} / M \quad (29b)$$

$$\tan \mu = 1/\sqrt{M^2 - 1} \quad (29c)$$

It is seen that the directions defined by equation 28 are coincident with the directions of the Mach lines passing through the point A.

The assumption that the first derivatives of the dependent variables have finite values requires that the four numerator determinants in Cramer's Rule also be zero in the direction of the Mach lines through

point A. In each of the four Cramer's Rule determinants, this requirement reduces to:

$$\Gamma \frac{dP}{P} \pm d\theta \pm \sigma ds + K \tan\mu ds = 0 \quad (30)$$

where

$$\Gamma = \frac{\sqrt{M^2 - 1}}{\gamma M^2}$$

The distance ds in the \bar{i} direction can be related to the distance dl in a characteristic direction by

$$ds = dl \cos\mu \quad (31)$$

A positive dl corresponds to a movement in the upstream direction, while a negative dl corresponds to a movement in the downstream direction. Besides changing ds to dl , a further modification of equation 30 can be made by defining two new fluid properties, $\xi(+)$ and $\xi(-)$, such that

$$d\xi(+) = \Gamma \frac{dp}{p} + d\theta \quad (32a)$$

$$d\xi(-) = \Gamma \frac{dp}{p} - d\theta \quad (32b)$$

Substituting 31, 32a and 32b into 30 yields

$$d\xi(\pm) + (\pm \sigma \cos\mu + K \sin\mu) dl = 0 \quad (33)$$

Equation 33 may be put in finite difference form by noting that

$$d\xi(+) \approx \xi(+) - \xi_0(+) \quad (34a)$$

$$d\xi(-) \approx \xi(-) - \xi_0(-) \quad (34b)$$

$$dl \approx \Delta l \quad (34c)$$

where

$$\xi(+) = \Gamma \ln \left(\frac{P}{\bar{P}_t} \right) + \theta \quad (35a)$$

$$\xi(-) = \Gamma \ln \left(\frac{P}{\bar{P}_t} \right) - \theta \quad (35b)$$

and \bar{P}_t is an arbitrary constant

Substituting 34a to 34c into 33 yields

$$\xi(\pm) = \xi_0(\pm) - (\pm \sigma \cos\mu + K \sin\mu) \Delta l \quad (36)$$

If the definitions

$$\epsilon(+) = -\sigma \cos\mu - K \sin\mu \quad (37a)$$

$$\epsilon(-) = a \cos\mu - K \sin\mu \quad (37b)$$

are made, then equation 36 becomes

$$\xi(\pm) = \xi_0(\pm) + \epsilon(\pm) \quad \Delta 1 \quad (38)$$

Characteristic Functions

To summarize the analysis, it has been shown that the functions $m(+)$, $m(-)$, $\epsilon(+)$, and $\epsilon(-)$ described in the introduction are:

$$m(+) = \tan(\theta + \mu) \quad (39a)$$

$$m(-) = \tan(\theta - \mu) \quad (39b)$$

where

$$\mu = \arctan \frac{1}{\sqrt{M^2 - 1}}$$

and

$$\epsilon(+) = -\sigma \cos\mu - K \sin\mu \quad (39c)$$

$$\epsilon(-) = \sigma \cos\mu - K \sin\mu \quad (39d)$$

$$\text{where } K = \left(\frac{\omega_R^2}{v^2} + \frac{d}{dR} \ln(z) \right) \cos(\theta - \tilde{\beta})$$

$$\sigma = \left(\frac{2\omega}{v} + \frac{\omega_R^2}{v^2} \right) \sin(\theta - \tilde{\beta})$$

Evaluation of Field Properties from $\xi(+)$ and $\xi(-)$

With $\xi(+)$ and $\xi(-)$ known at a point A, the nondimensionalized pressure at A may be obtained by addition of equations 35a and 35b, i.e.,

$$\frac{P}{P_t} = \exp \frac{\xi(+) + \xi(-)}{2\Gamma} \quad (40)$$

In equation 40, \bar{P}_t is an arbitrary reference pressure which will, for convenience, be chosen as the actual total pressure (relative to the rotating reference frame) at some reference radius R^* . If the total temperature at R^* (relative to the rotating reference frame) is \bar{T}_t , then since the flow is isentropic, the temperature and pressure at any other radius are related as follows:

$$\frac{T}{\bar{T}_t} = \left(\frac{P}{\bar{P}_t} \right)^{\frac{\gamma-1}{\gamma}} \quad (41)$$

Hence, substituting 41 into 40,

$$\frac{T}{\bar{T}_t} = \exp \frac{\xi(+) + \xi(-)}{\frac{2\gamma\Gamma}{\gamma-1}} \quad (42)$$

But since the flow is adiabatic, the increase in total temperature with radius due to reference frame rotation is

$$\frac{T_t}{\bar{T}_t} = \frac{\omega^2}{2 C_p \bar{T}_t} (R^2 - R^{2*}) \quad (43)$$

Also noting that

$$\frac{T_t}{T} = 1 + \frac{\gamma-1}{2} M^2 \quad (44)$$

$$\Gamma = \frac{\sqrt{M^2-1}}{\gamma M^2} \quad (45)$$

and multiplying 42 by 44 and equating to 43 yield

$$\left(1 + \frac{\gamma-1}{2} M^2 \right) \exp \frac{\xi(+) + \xi(-)}{\frac{2}{M^2} \frac{\sqrt{M^2-1}}{\gamma-1}} = 1 + \frac{\omega^2}{2 C_p \bar{T}_t} (R^2 - R^{2*}) \quad (46)$$

The equation may be solved for the Mach number M . Once M is known, the other fluid properties can be easily evaluated by the usual methods. The flow angle may be obtained from equations 35a and 35b by simple subtraction.

$$\theta = \frac{\xi(+) - \xi(-)}{2} \quad (47)$$

APPENDIX III, ROC INSTRUMENTATION

INTRODUCTION

The purpose of the ROC instrumentation is to provide sufficient information to:

1. Evaluate the compressor performance.
2. Aid in locating and diagnosing mechanical and aerodynamic deficiencies.
3. Insure that the compressor is operated within prescribed safe limits.

The fulfillment of the instrumentation function in general entails both a data collection operation and a data reduction operation. The data collection operation ordinarily consists of five steps, as follows:

1. Definition of parameter to be monitored, and the region of interest.
2. Definition of a suitable "signature" which may be monitored if it is not possible to monitor the parameter directly, either because of its nature or because of its location.
3. Measurement of the signature (or the parameter directly) in terms of a transmittable signal.
4. Transmission of the signal to the display station.
5. Display of the signal by means of a suitable read-out device.

The data reduction operation entails:

1. Compensating for bias introduced by the transmission system or the display system (relating value on read-out device to transducer signal).
2. Relating the transducer signal to the value indicated (requires transducer characteristic curves).
3. Relating the value of the signature to the value of the parameter in the region of interest (in most cases, an attempt is made to determine the value that the parameter would have had if the instrumentation were not in place).
4. Combining the value of the parameter measured with other parameters to evaluate the significant system variables (efficiency, thermal distribution, stress levels, etc.).

STATION AND INSTRUMENTATION DEFINITIONS

The regions in the compressor at which aerodynamic measurements will be made are listed in Table XVIII and are shown diagrammatically in Figure 222. A listing of the quantities to be measured at the above stations is given in Table XIX. The first column of Table XIX indicates the symbol which shall be used to designate the quantity. The second column indicates the number of probes or measurement heads which will be used to collect the data. The set of four columns which follows indicates the particular buildup during which each specific measurement will be required, and the last column briefly describes the quantity to be measured.

The configurations corresponding to the buildup numbers referred to in the table are as follows:

<u>Buildup Number</u>	<u>Configuration</u>
1	Rotor only
2	Rotor and supersonic stator
3	Rotor and supersonic stator
4	Rotor, supersonic and subsonic stators
5	Rotor, supersonic and subsonic stators
6	Rotor, supersonic, subsonic stators, and IGV.

Required instrumentation is indicated by an X in the appropriate buildup number column. An asterisk by the instrument identification indicates traversable instrumentation.

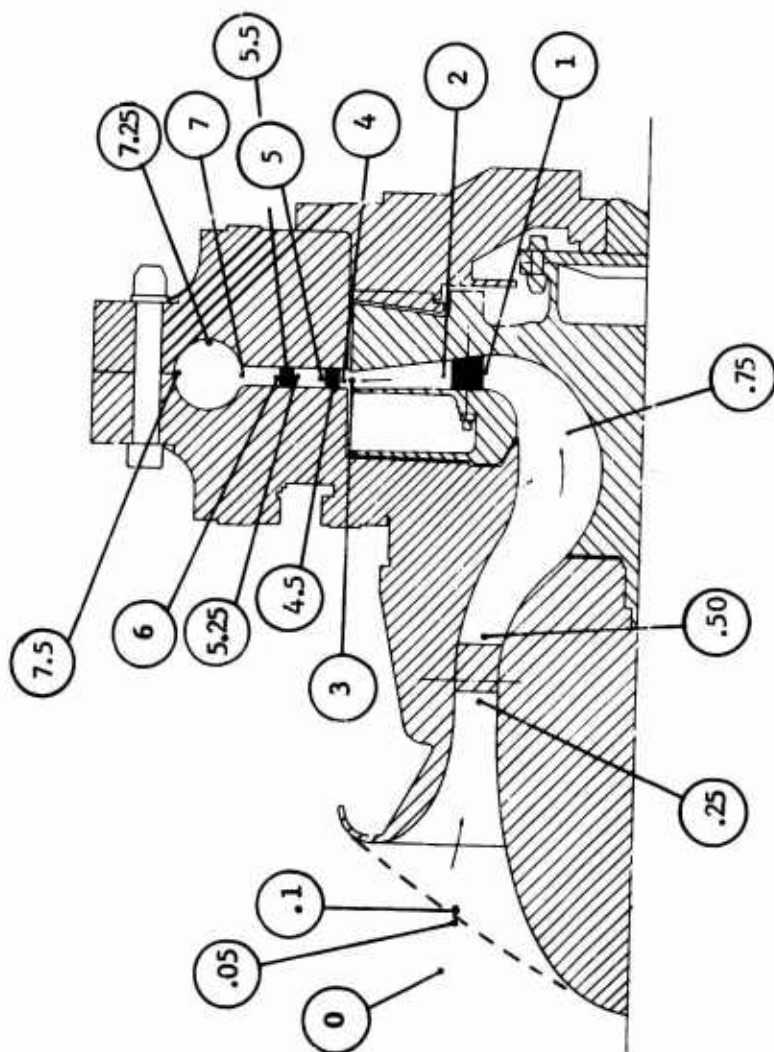
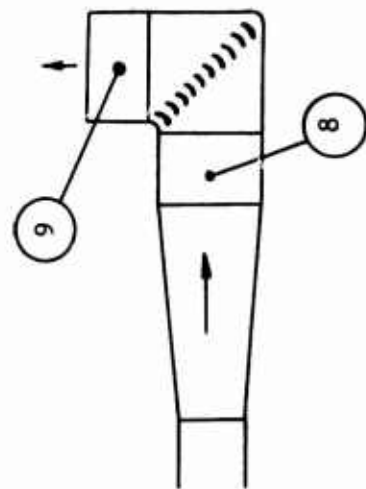


Figure 222. Radial Outflow Compressor Instrumentation Station Numbers
(See Table XVIII).

TABLE XVIII
ROC STATION DEFINITION

Station	Description
0	Tank Condition or Compressor Inlet
0.05	Inlet Screen Inlet
0.1	Inlet Screen Exit
0.25	IGV Inlet
0.50	IGV Exit
0.75	Inlet Duct
1.0	Rotor Blade Inlet
2.0	Rotor Blade Exit
3.0	Rotor Exit
4.0	Supersonic Stator Inlet
4.5	Supersonic Stator Passage
5.0	Supersonic Stator Exit
5.25	Subsonic Stator Inlet
5.50	Subsonic Stator Passage
6.0	Subsonic Stator Exit
7.0	Scroll Inlet
7.25	Scroll Centerline
7.50	Scroll Outside Diameter
7.75	Splitter Lip
8.0	Diffuser
9.0	Elbow

TABLE XIX
RADIAL OUTFLOW COMPRESSOR RESEARCH INSTRUMENTATION (PHASE II)

Identification	Number	Buildup Number				Description
		1	2-3	4-5	6	
<u>Pressures</u>						
ΔP_V-1	2	X	X	X	X	Venturi ΔP
$UP_t V-1$	2	X	X	X	X	Venturi upstream total
OP_2-1	6	X	X	X	X	Tank static pressure
$0.25 P_t$	4	X	X	X	X	IGV inlet totals
$0.25 P_s$	8	X	X	X	X	IGV inlet statics
$*0.50 P_t$	1				X	IGV exit total pressure and angle
$0.50 P_s$	8				X	IGV exit statics
$0.75 P_s$	2	X	X	X	X	Inlet duct static pressure
$3.0 P_s$	18	X	X	X	X	Rotor exit static pressure
$*3.0 P_t$	1	X				Rotor exit total pressure and yaw
$4.0 P_s$	6		X			Supersonic stator inlet
$4.5 P_s$	2	X	X	X	X	Supersonic stator passage statics
$*5.0 P_t$	1	X	X			Supersonic stator exit total and yaw
$*5.0 P_{tR}$	1		X			Supersonic stator exit total rake
$5.0 P_s$	8	X	X	X	X	Supersonic stator exit statics
$5.5 P_s$	3		X	X	X	Subsonic stator passage statics
$*5.5 P_t$	1	X	X			Subsonic stator spindle cobra probe
$*6.0 P_t$	1			X	X	Subsonic stator exit total rake
$7.0 P_s$	6	X	X	X	X	Scroll inlet statics
$7.25 P_s$	8			X	X	Scroll centerline statics

TABLE XIX, Continued

Identification Number	Buildup Number				Description	
	1	2-3	4-5	6		
<u>Pressures</u> (Continued)						
*7.25 P _t	1		X		Scroll centerline total and yaw traverse	
7.5 P _s	2		X		Scroll outside diameter statics	
7.75 P _s	7		X		Splitter lip statics	
8.0 P _s	16		X	X	Diffuser wall statics	
*8.0 P _t	15		X		Diffuser totals	
9.0 P _s	8		X	X	Elbow statics	
*9.0 P _t	15			X	Elbow exit totals	
Additional Pressure Instrumentation						
UCV-ΔP	2	X	X	X	X	Upstream coolant flow orifice ΔP
UCV-P _t	1	X	X	X	X	Upstream coolant flow orifice total
DCV-ΔP	2	X	X	X	X	Downstream coolant flow orifice ΔP
DCV-P _t	1	X	X	X	X	Downstream coolant flow orifice total
DRP _s -1	4	X	X	X	X	Disc rear static pressure (radius - 4.25)
DRP _s -2	4	X	X	X	X	Disc rear static pressure (radius - 5.733)
<u>Temperatures</u>						
UTV-T _t	3	X	X	X	X	Venturi upstream total
OT _t	2	X	X	X	X	Tank air temperature
0.05 T _t	4	X	X	X	X	Screen inlet total
3.0 T _t	1	X				Rotor discharge total rake
5.0 T _t	1		X			Supersonic stator exit rake

TABLE XIX, Continued

Identification Number	Buildup Number				Description	
	1	2-3	4-5	6		
<u>Temperatures</u> (Continued)						
*8.0 T _t	1	X	X	X	Diffuser exit total rake	
*9.0 T _t	1			X	X	Elbow exit total rake
Additional Temperature Instrumentation						
UCV-T _t	2	X	X	X	X	Upstream coolant orifice total
DCV-T _t	2	X	X	X	X	Downstream coolant orifice total
DTT-1	2	X	X	X	X	Disc tip thermocouple
DRT-1	2	X	X	X	X	Disc rear thermocouple
RTE-1	2	X				Rotor trailing edge thermocouple

Unclassified

Security Classification

DOCUMENT CONTROL DATA - R & D		
(Security classification of title, body of abstract and indexing annotation must be entered when the overall report is classified)		
1. ORIGINATING ACTIVITY (Corporate author) General Electric Company Cincinnati, Ohio		2a. REPORT SECURITY CLASSIFICATION Unclassified
		2b. GROUP
3. REPORT TITLE RADIAL OUTFLOW COMPRESSOR COMPONENT DEVELOPMENT - VOLUME I - PHASE I - AERODYNAMIC AND MECHANICAL DESIGN ANALYSIS AND DIFFUSER TESTS		
4. DESCRIPTIVE NOTES (Type of report and inclusive dates)		
5. AUTHOR(S) (First name, middle initial, last name) John R. Erwin Nickolas G. Vitale		
6. REPORT DATE May 1969	7a. TOTAL NO. OF PAGES 403	7b. NO. OF REFS 31
8a. CONTRACT OR GRANT NO. DA 44-177-AMC-180(T)	8b. ORIGINATOR'S REPORT NUMBER(S) USAAVLABS Technical Report 68-38A	
8c. PROJECT NO. Task 1M121401D14413	8d. OTHER REPORT NO(S) (Any other numbers that may be assigned this report)	
10. DISTRIBUTION STATEMENT This document is subject to special export controls and each transmittal to foreign governments or foreign nationals may be made only with prior approval of US Army Aviation Materiel Laboratories, Fort Eustis, Virginia 23604.		
11. SUPPLEMENTARY NOTES Volume 1 of a 3-volume report	12. SPONSORING MILITARY ACTIVITY US Army Aviation Materiel Laboratories Fort Eustis, Virginia	
13. ABSTRACT This report covers investigations conducted during Phase I of the Radial Outflow Compressor Component Development Program. This phase consisted of compressor component analyses and investigations conducted using an existing low-speed compressor model and a transonic cascade tunnel. Aerodynamic information for the design of the high-speed radial outflow supersonic compressor to be investigated in Phase II was obtained. A stress analysis and bench tests of several possible rotor designs were conducted as well as an investigation of methods of fabricating and joining blades, rotating shroud, and discs. Target performance values are 11:1 pressure ratio with 81% adiabatic efficiency at 4.5 lb/sec airflow. No problem areas were discovered that would prevent the achievement of the design performance levels to be tested in Phase II of the program.		

DD FORM 1473

REPLACES DD FORM 1473, 1 JAN 64, WHICH IS
OBSOLETE FOR ARMY USE.

Unclassified

Security Classification

Unclassified

Security Classification

14.	KEY WORDS	LINK A		LINK B		LINK C	
		ROLE	WT	ROLE	WT	ROLE	WT
	Compressor						
	High-Pressure-Ratio Compressor						
	Radial Outflow Compressor						
	Variable Geometry Diffuser						
	Rotating Diffuser						

Unclassified

Security Classification

4312-69